Schriftenreihe Lasertechnik

Prof. Dr.-Ing. C. Emmelmann (Hrsg.)

Band 4

INSTITUTE OF LASER AND SYSTEM TECHNOLOGIES
HAMBURG UNIVERSITY OF TECHNOLOGY

Olaf Rehme

Cellular Design for Laser Freeform Fabrication

Technische Universität Hamburg-Harburg • Institut für Laser- und Anlagensystemtechnik

Cellular Design for Laser Freeform Fabrication

Vom Promotionsausschuss der
Technischen Universität Hamburg-Harburg
zur Erlangung des akademischen Grades
Doktor-Ingenieur
genehmigte Dissertation

von

Dipl.-Ing. Olaf Rehme

aus Hamburg

2009

Bibliografische Information der Deutschen Nationalbibliothek
Die Deutsche Nationalbibliothek verzeichnet diese Publikation in der Deutschen Nationalbibliografie; detaillierte bibliografische Daten sind im Internet über http://dnb.d-nb.de abrufbar.
1. Aufl. - Göttingen : Cuvillier, 2010
Zugl.: (TU) Hamburg-Harburg, Univ., Diss., 2009

978-3-86955-273-6

1. Gutachter: Prof. Dr.-Ing. Claus Emmelmann

2. Gutachter: Prof. Dr. habil. Ph.D. Michael Morlock

Tag der mündlichen Prüfung: 27.08.2009

© CUVILLIER VERLAG, Göttingen 2010
Nonnenstieg 8, 37075 Göttingen
Telefon: 0551-54724-0
Telefax: 0551-54724-21
www.cuvillier.de

Alle Rechte vorbehalten. Ohne ausdrückliche Genehmigung des Verlages ist es nicht gestattet, das Buch oder Teile daraus auf fotomechanischem Weg (Fotokopie, Mikrokopie) zu vervielfältigen.
1. Auflage, 2010
Gedruckt auf säurefreiem Papier

978-3-86955-273-6

Acknowledgements

I wrote this present thesis in my function as a research assistant at the Institute of Laser and System Technologies (iLAS) at Hamburg University of Technology (TUHH), Germany. I would sincerely like to thank the primary supervisor of my thesis Prof. Dr.-Ing. Claus Emmelmann for his continuous support and confidence in my work on a topic where starting from scratch was required and the road sometimes seemed to never end. Secondly, I would also like to thank the secondary supervisor Prof. Dr. habil. Ph.D. Michael Morlock for never stopping to ask questions as to what the key benefits are and what feasible applications can be derived from the considered technology and the developments made in this thesis.

Throughout my time working at the institute I was pleased with a harmonic atmosphere which helped keeping a positive mindset. I would like to thank all my former colleagues with whom I had the opportunity to work with for their support and ideas. Additionally, I would especially like to thank the ‘additive manufacturing crew’ who I worked with for several years, i.e. Dr.-Ing. Maren Petersen, Dr.-Ing. Andreas Lorenz, Dipl.-Ing. Hendrik Vogel and M.Sc. Maximilian Munsch as well as Dr. rer.nat. Jan Stupl as a ‘non-additive manufacturing crew-member’. I found our exchange of ideas always very fruitful.

I would also like to mention the effort of numerous students who worked on the topic of this thesis or related topics during their specialized labs or while accomplishing their project, bachelor and master theses. Without their contributions the results in this thesis would not have been possible.

Finally, I must admit that the foundation to all my achievements was layed much earlier, therefore, I would sincerely like to thank my family for providing the opportunities that I had and for their continuous love and support. Thanks to all of you for bearing with me and my priorities.

I Abstract .... **v**

II Zusammenfassung .... **vii**

III Abbreviations .... **ix**

IV List of symbols .... **xi**

V List of figures .... **xvii**

VI List of tables .... **xxi**

1 Introduction **1**

2 Cellular design and manufacturing processes **3**

2.1 Cellular materials 3
  2.1.1 Classification 3
  2.1.2 Product quality objectives 5
  2.1.3 Occurrence and applications 6
  2.1.4 Mechanical properties 11
2.2 Conventional fabrication processes for cellular materials 39
  2.2.1 Overview 39
  2.2.2 Periodic cellular materials: lattice and truss structures 42
  2.2.3 Constraints of existing fabrication processes for cellular materials 45
2.3 Summary 46

3 Laser Freeform Fabrication **47**

3.1 Motivation for cellular design with Laser Freeform Fabrication 47
3.2 Development of Laser Freeform Fabrication 49
  3.2.1 Technological evolution 49
  3.2.2 State-of-the-art of industrial processes 50
3.3 Selective Laser Melting 51
  3.3.1 SLM principle and process characteristics 51
  3.3.2 Influence parameters on SLM 52
3.4 Analysis and advances of SLM influence parameters 54
  3.4.1 Part geometry and CAD data 54
  3.4.2 Material 54
  3.4.3 Process 60
  3.4.4 Post-processing 72
3.5 Product quality and manufacturing cost and time in applications of SLM solids 73
  3.5.1 Dominating influence parameters in SLM processes 73
  3.5.2 Quality properties of solid SLM parts 75
  3.5.3 Applications 82
  3.5.4 Considerations of manufacturing cost and time 85
3.6 Summary 86

4 Fundamental analysis of cellular part design for SLM 87
4.1 Process development and precursor experiments 87
4.2 Analysis and assessment of process conditions 89
4.2.1 General influence parameters 89
4.2.2 Material 90
4.2.3 SLM system 92
4.3 Approach to assessment of mechanical properties 97
4.4 Summary 98
5 Theoretical analysis of SLM cellulars 99
5.1 Structural hypotheses for isotropic cellular materials 99
5.1.1 Strength and elastic properties of low density cellular materials 99
5.1.2 Bending- and stretch-dominated behaviour 104
5.1.3 Strength and elastic properties of high density cellular materials 105
5.2 Structural hypotheses for anisotropic SLM lattice structures 106
5.2.1 Approach to a generalized SLM lattice structure theory 106
5.2.2 Anisotropy of SLM solids 108
5.2.3 Characterization of elastic deformation for SLM lattice structures 109
5.2.4 Characterization of plastic deformation for SLM lattice structures 113
5.2.5 Matrix structural analysis for low density SLM lattice structures 117
5.2.6 Effective material properties for high density SLM lattice structures 124
5.2.7 Determination of relative density for SLM lattice structures 125
5.2.8 General model for SLM lattice structures of low and high relative density 127
5.3 Development of SLM lattice structure designs 128
5.3.1 General producibility 128
5.3.2 Tesselation of 3D space 131
5.3.3 Selected SLM lattice structures 133
5.4 Theoretical analysis of preselected SLM lattice structures 136
5.4.1 Evaluation of expected critical relative densities 136
5.4.2 Matrix structural analysis of preselected SLM lattice structures 139
5.5 Summary 142
6 Experimental analysis of SLM solids and cellulars 143
6.1 Mechanical properties of SLM solids 143
6.2 Producibility of SLM lattice structures 148
6.2.1 Minimum positive feature size 148
6.2.2 Stability of SLM lattice structures 152
6.3 Development of test procedures 157
6.3.1 Test utilities, test conditions and sample sizes 157
6.3.2 Compression strength tests 159

6.3.3 Tensile strength tests 160
6.3.4 Shear tests 161
6.4 Test of specific strength in dependence of cell type 162
6.5 Selection of cell types for tests in dependence of cell size 169
6.6 Test of elasticity in dependence of cell size 171
6.6.1 Elastic compression tests 171
6.6.2 Elastic shear tests 173
6.7 Test of strength in dependence of cell size 174
6.7.1 Compression strength tests 174
6.7.2 Tensile strength tests 177
6.7.3 Shear tests 179
6.8 Results discussion 179
6.8.1 Comparison to literature results 179
6.8.2 Comparison to theory 181
6.8.3 Conclusion 181
6.9 Summary 182
7 Development of cellular design for SLM parts 183
7.1 Development of scaling laws for engineering design 183
7.1.1 Conversion of relative density into the main design parameters 183
7.1.2 Scaling laws in dependency of aspect ratio in the low relative density regime 184
7.1.3 Scaling laws in dependency of aspect ratio for the full range of relative densities 185
7.2 General design rules for SLM lattice structures and for hybrid parts 187
7.2.1 Design rules for stand-alone SLM lattice structures 187
7.2.2 Design rules for hybrid parts 188
7.3 Cellular Design for SLM lattice structures in medical implants 190
7.3.1 Advantages of SLM lattice structures in implant applications 190
7.3.2 Example 1: Optimization of bending stiffness of a hip endoprosthesis stem 190
7.3.3 Example 2: Optimization of bending stiffness of a tibial base plate 191
7.3.4 Example 3: Optimization of extensional stiffness of a tibial base plate 192
7.3.5 Example 4: Verification of compressive yield strength of a tibial base plate 192
7.3.6 Example 5: Optimization of manufacturing time and cost of a tibial base plate ... 193
7.4 Summary 193
8 Conclusion 195
9 Bibliography 197
10 Appendices 227
10.1 Cellular material properties 227
10.1.1 Acoustical properties 227
10.1.2 Mechanical damping properties 230

- 10.1.3 Permeability 231
- 10.1.4 Thermal properties 233
- 10.1.5 Electrical properties 236
- 10.1.6 Specific surface area........ 238
- 10.1.7 Buoyancy........ 239

10.2 Fabrication of stochastic cellular materials: foams and sponges........ 241

- 10.2.1 Pressing from solid phase........ 241
- 10.2.2 Foaming from solid phase........ 243
- 10.2.3 Foaming from liquid phase 244
- 10.2.4 Casting from liquid phase 247
- 10.2.5 Deposition techniques from vapor or ionic phase........ 248

10.3 Simulation results: relative densities and compressive yield strengths........ 250

10.4 Average strut diameter in dependence of melt energy 252

10.5 Results for stability of SLM lattice structures 255

10.6 Results of elasticity in dependence of cell size........ 261

10.7 Results of compressive strength in dependence of cell size 264

10.8 Results of tensile strength in dependence of cell size........ 267

I Abstract

Cellular materials are spread all across the world. They can be found in nature, e.g. in bone and wood, as well as in engineering applications such as honeycomb sheets and aluminum foams to name but a few. Cellular materials have some unique properties which allow new and innovative applications beyond the scope of solid engineering materials. Especially their low density and therefore their outstanding stiffness-to-weight-ratio is of greatest importance in most applications. Functions of cellular materials could be lightweight structures of high stiffness, damping and absorption of mechanical energy, vibration control, acoustic absorption, heat exchange, filtering and numerous other tasks. Generally, a combination of these tasks in one part exhibits an optimized and therefore innovative overall performance.

One recent development in production technologies is the field of Laser Freeform Fabrication (LFF) processes where parts are manufactured by application of thin layers of powder or sometimes liquid material. A laser beam melts and solidifies the material along contour lines and hatch areas according to slices of a corresponding 3D-CAD model. Among these processes the Selective Laser Melting (SLM) technology was advanced based upon the work in this thesis to allow the manufacture of periodic, open-cell lattice structures from engineering materials such as stainless steel, titanium, etc. In contrast to other cellular materials these lattice structures can be of well-defined, nearly arbitrary shape. Due to the layerwise fabrication the SLM process is also capable of creating lattice cores surrounded by solid shells allowing new degrees of geometric freedom in engineering design that was never experienced before in conventional machining. This allows the development of interesting new applications such as medical implants where the main issues are the improvement of osseointegration and realization of physioelastic material properties for an optimized bond between the implant and surrounding tissue. Lattice structures obtained from the SLM process can meet these requirements.

This thesis contributes to the understanding of the mechanical properties of the new material class of SLM lattice structures. Their future incorporation in engineering designs requires a profound knowledge of failure mechanisms and operational limits. Therefore, a comprehensive summary is given on the state-of-the-art of cellular materials followed by a dedicated analysis on Laser Freeform Fabrication and an in-depth validation of the Selective Laser Melting capabilities. Readers with advanced knowledge on cellular materials or Laser Freeform Fabrication may skip ***sections 2*** or ***3***, respectively. Next, all process constraints and boundary conditions for the manufacture of SLM lattice structures are elaborated. Then a bilateral approach was chosen to derive scaling laws and optimize the SLM lattice structures for given tasks. Firstly, a theoretical analysis comprises the examination of structural hypotheses for isotropic cellular materials before a generalized theory is developed for anisotropic SLM lattice structures. Different cubic, polyhedral and rhombic cell types are evaluated towards their producibility. Some of these cell types are preselected and are subject to numerical analysis where their mechanical properties are derived on the basis of the space framework theory. Secondly, an extensive experimental evaluation of test specimens is given. This includes examinations of the properties of SLM solids, the producibility of SLM lattice structures in terms of dimensions and testing of their mechanical properties such as strength and elasticity in compression, tension and shear load. The test procedures are divided in three stages. The first stage comprises the examination of the specific strength in dependence of the cell type to narrow down few optimum cell types for different applications. In the second and third stage these cell types are investigated towards their elasticity and strength in dependence of the cell size. Finally, this thesis concludes with scaling laws provided in accordance with the theoretical and experimental results. Opposed to simple power laws used for cellular materials these newly developed scaling laws consider leaps in properties at higher, so-called critical relative densities which can be obtained from SLM due to its high degree of design freedom. At the critical relative density SLM lattice structures cease being frameworks and become rather solids with pores.

For future applications these scaling laws can be applied by design engineers to match particular requirements that can only be fulfilled by Laser Freeform Fabrication and its degrees of freedom in design. For the sake of completeness some sample applications in the field of medical implants are given in this thesis, which involve these scaling laws.

II Zusammenfassung

Zelluläre Werkstoffe existieren in der gesamten bekannten Welt. Es lassen sich sowohl in der Natur als auch in der Technik verschiedenste zelluläre Werkstoffe finden, wie z.B. Knochen und Holz oder Wabenkernstrukturen und Aluminiumschäume, um nur einige zu nennen. Zelluläre Werkstoffe weisen einige einzigartige Eigenschaften auf, die neue und innovative Anwendungen jenseits der Möglichkeiten massiver technischer Werkstoffe gestatten. Insbesondere ihre geringe Dichte und ihr damit im Zusammenhang stehendes hervorragendes Verhältnis von Festigkeit zu Gewicht ist von größter Bedeutung in den meisten Anwendungen. Die Funktionen von zellulären Werkstoffen können beispielsweise Leichtbaustrukturen hoher Festigkeit sein oder Dämpfung und Absorption mechanischer Energie, Schwingungsdämpfung, Schallabsorption, Wärmeaustausch oder Filterung neben vielen anderen Aufgaben. Allgemein bietet die kombinierte Anwendung derartiger Aufgaben in einem Bauteil eine optimierte und damit innovative Gesamtleistung.

Eine noch junge Entwicklung auf dem Gebiet der Fertigungstechnik ist die Lasergeneriertechnologie, mittels derer Bauteile durch das Auftragen dünner Schichten eines Pulvers oder seltener einer Flüssigkeit hergestellt werden. Durch einen Laserstrahl wird Werkstoff entlang von Konturlinien und Schraffurflächen aufgeschmolzen und verfestigt sich entsprechend von Schichtflächen eines zugehörigen 3D-CAD Modells. Als ein solches Verfahren wurde die Selective Laser Melting (SLM) Technologie im Rahmen dieser Arbeit weiter entwickelt, um die Herstellung von periodischen, offen-zellulären Gitterstrukturen aus technischen Werkstoffen, wie z.B. Edelstahl, Titan, etc. zu ermöglichen. Im Gegensatz zu anderen zellulären Werkstoffen können diese Gitterstrukturen genau definierte und dabei nahezu beliebige Formen annehmen. Aufgrund der schichtweisen Fertigung ist der SLM Prozess auch in der Lage, innere Gitterstrukturen mit massiver Umhüllung herzustellen, wodurch neue geometrische Freiheitsgrade in der Konstruktion ermöglicht werden, die zuvor mit konventioneller Bearbeitung undenkbar waren. Auf diese Weise können interessante neue Anwendungen erschlossen werden, wie z.B. medizinische Implantate, die die Verbesserung der Osseointegration und die Umsetzung physioelastischer Eigenschaften für eine optimierte Verbindung zwischen Implantat und umgebenden Gewebe zum Ziel hat. Die mit dem SLM Prozess herstellbaren Gitterstrukturen können diese Anforderungen erfüllen.

Diese Arbeit leistet einen Beitrag zum Verständnis der mechanischen Eigenschaften der neuen Werkstoffklasse der SLM Gitterstrukturen. Ihre zukünftige Verwendung durch Konstrukteure erfordert eine grundlegende Kenntnis ihrer Versagensmechanismen und Betriebsgrenzen. Daher wird zunächst der Stand der Technik von zellulären Werkstoffen umfassend analysiert, gefolgt von einer dedizierten Analyse der Lasergeneriertechnologie mit einer eingehenden Validierung der Möglichkeiten des Selective Laser Melting. Leser mit vertieften Kenntnissen über zelluläre Werkstoffe oder der Lasergeneriertechnologie können ***Kapitel 2*** bzw. ***3*** überspringen. Danach erfolgt die Darstellung aller prozessseitigen Randbedingungen zur Herstellung von SLM Gitterstrukturen. Für die Ableitung von Skalierungsgesetzen und zur Optimierung von SLM Gitterstrukturen für gegebene Einsatzzwecke wird daraufhin ein zweigleisiger Ansatz verfolgt. Erst werden durch eine theoretische Analyse Festigkeitshypothesen für zelluläre Werkstoffe untersucht, bevor eine verallgemeinerte Theorie für anisotrope SLM Gitterstrukturen entwickelt wird. Verschiedene kubische, polyedrische und rhombische Zelltypen werden hinsichtlich ihrer Herstellbarkeit bewertet. Einige dieser Zelltypen werden ausgewählt und darauf einer numerischen Analyse unterzogen, in der ihre mechanischen Eigenschaften auf der Basis der dreidimensionalen Tragwerktheorie erforscht werden. Danach folgt die Darstellung einer ausgedehnten experimentellen Untersuchung von Probekörpern. Diese beinhaltet sowohl die Untersuchung der Eigenschaften von SLM Festkörpern, die Herstellbarkeit von SLM Gitterstrukturen im Hinblick auf Größenverhältnisse als auch ihre mechanische Prüfung hinsichtlich Festigkeit und elastischer Eigenschaften unter Druck-, Zug- und Scherbelastung. Die mechanische Prüfung ist in drei Stufen aufgeteilt. Die erste Stufe umfasst die Untersuchung der spezifischen Festigkeit in Abhängigkeit des Zelltyps mit dem Ziel, wenige optimale Zelltypen für verschiedene Anwendungen zu finden. In der zweiten und dritten Stufe werden diese Zelltypen hinsichtlich ihrer Elastizität und Festigkeit in Abhängigkeit von der Zellgröße untersucht. Letztlich schließt die vorliegende Arbeit mit Skalierungsgesetzen, die im Einklang mit den gefundenen theoretischen und experimentellen Ergebnissen aufgestellt werden. Im Gegensatz zu einfachen Potenzgesetzen, wie sie für zelluläre Werkstoffe verwendet werden, ziehen diese neu entwickelten Skalierungsgesetze Unstetigkeiten von Eigenschaften in Betracht, welche bei höheren, sog. kritischen relativen Dichten auftreten können, die durch die großen Gestaltungsfreiheitsgrade von SLM möglich sind. Bei der kritischen relativen Dichte gehen SLM Gitterstrukturen von einer Tragwerkstruktur über zu einem Festkörper mit Poren.

Für zukünftige Anwendungen können diese Skalierungsgesetze von Konstrukteuren herangezogen werden, um spezielle Anforderungen erfüllen zu können, die sich nur durch die gestalterischen Freiheitsgrade der Lasergeneriertechnologie ermöglichen lassen. Der Vollständigkeit halber sind abschließend in dieser Arbeit einige Beispiele aus dem Gebiet der medizinischen Implantologie gegeben, in denen diese Skalierungsgesetze zur Anwendung gelangen.

III Abbreviations

1D	one-dimensional
2D	two-dimensional
3D	three-dimensional
Al	Aluminum
ASTM	American Society for Testing and Materials
B	Boron
Ba	Barium
bcc	Body-centered cubic or body diagonals
bcc_z	Body-centered cubic, body diagonals with vertical struts in z-direction
Be	Beryllium
BET	Brunauer, Emmet and Teller: volumetric-static multi point method
C	Carbon
CAD	Computer Aided Design
CAM	Computer Aided Manufacturing
Ca	Calcium
CMMC	Ceramic metal matrix composites
Co	Cobalt
c.p.	commercially pure
Cr	Chromium
CT	Computer Tomography
Cu	Copper
CVD	Chemical Vapor Deposition
CVI	Chemical Vapor Infiltration
DIN	Deutsches Institut für Normung e.V.
DLF	Direct Laser Forming
DMLS	Direct Metal Laser Sintering
EDXRF	Energy Dispersive X-Ray Fluorescence
EDM	Electric Discharge Machining
EN	European Norm
ERG	Energy Research and Generation, Inc., Materials and Aerospace Corporation
fcc	Face-centered cubic or single face diagonals
fcc_z	Face-centered cubic single face diagonals with vertical struts in z-direction
f_2cc	Face-centered cubic, double face diagonals
f_2cc_z	Face-centered cubic, double face diagonals with vertical struts in z-direction
f_2bcc	Face-centered cubic, double face diagonals and body diagonals
f_2bcc_z	Face-centered cubic, double face diagonals and body diagonals with z-struts
FE	Finite Element
Fe	Iron
FEM	Finite Element Method
H	Hydrogen
hcp	hexagonal closest packing

HIC	Head Injury Criterion
HIP	Hot Isostatic Pressing
hp	Hexagonal packing
HRC	Rockwell hardness
ICP-OES	Inductively coupled plasma optical emission spectrometry
iLAS	Institute of Laser and System Technologies
ISO	International Organization for Standardization
LDC	Low Density Core
LENS	Laser Engineered Net Shaping
LFF	Laser Freeform Fabrication
LOM	Laminated Object Manufacturing
Mg	Magnesium
Mn	Manganese
Mo	Molybdenum
N	Nitrogen
N/A	Not applicable
Nb	Niobium
Nd	Neodymium
Ni	Nickel
O	Oxygen
P	Phosphorus
PEEK	Polyetheretherketone
PVD	Physical Vapor Deposition
RD	Rhombic dodecahedron
sc	simple cubic packing
SFF	Solid Freeform Fabrication
Si	Silicon
SLA	Stereolithography Apparatus
SLM	Selective Laser Melting
SLS	Selective Laser Sintering
Sn	Tin
Sr	Strontium
STL	Standard Triangulation Language
TCO	Total cost of ownership
Ti	Titanium
TRD	Trapezo-rhombic dodecahedron
TUHH	Hamburg University of Technology
V	Vanadium
Y	Yttrium
Yb	Ytterbium
YAG	Yttrium Aluminum Garnet
Zr	Zirconium

IV List of symbols

All symbols used in this thesis comply with the associated international standards, if available, as follows:

- DIN 1304-1, 1994, [81]
- DIN 32532, 2006, [83] (draft)
- DIN 50100, 1978, [84]
- DIN EN ISO 10534-1, 2001, [92]
- DIN EN ISO 10534-2, 2001, [93]
- DIN EN ISO 11145-1, 2002, [94]
- DIN EN ISO 11146-1, 2005, [95]
- DIN EN ISO 12737, 2005, [96]
- DIN ISO 4022, 1990, [97]
- DIN ISO 9277, 2003, [98]
- DIN ISO 80000-8, 2006, [99]

Variable sub- and superscripts

$(\cdot)^*$	Property of a cellular material
$(\cdot)'$	Local coordinate system
$(\cdot)_0$	Initial value of a property
$(\cdot)_{86.5}$	Property of a laser beam which includes 86.5 % of the total beam energy
$(\cdot)_{at}$	Value of a property at ambient conditions / standard atmosphere
$(\cdot)_{cell}$	Property of one unit cell
$(\cdot)_{eff}$	Effective value of a property
$(\cdot)_{fluid}$	Property of an arbitrary fluid
$(\cdot)_{gas}$	Property of a gas (or generally of a fluid) trapped inside closed-cell porosities
$(\cdot)_h$	Property at h^{th} level of structural hierarchy
$(\cdot)_i$	Index (e.g. of a vector) or sequential numbering, also $(\cdot)_j$, $(\cdot)_k$, $(\cdot)_l$, $(\cdot)_\alpha$, $(\cdot)_\beta$, $(\cdot)_\gamma$
$(\cdot)_{ij}$	Index of a matrix
$(\cdot)_{max}, (\cdot)_m$	Maximum value of a property
$(\cdot)_{p0.2}$	Property at yield point, i.e. 0.2 % plastic strain, also $(\cdot)_{p1}$, i.e. 1 % plastic strain
$(\cdot)_{solid}$	Property of bulk material (non-cellular)
$(\cdot)_t$	Tangent function of a non-linear property
$(\cdot)_x$	Property in x-direction
$(\cdot)_y$	Property in y-direction
$(\cdot)_{yield}$	Occurrence of yield in a property due to plastic failure
$(\cdot)_z$	Property in z-direction

Symbols

Throughout this thesis some symbols may represent vectors or matrices as well as scalars. Vectors and matrices are always denoted in bold print while scalars are denoted in italics. The following table of symbols employs the scalar notation where both types apply and the vector/matrix notation where scalars are not applicable.

A	[m²]	Area
A	[m/m]	Break strain
a	[m]	Cell size in x-direction
a	[m^2/s]	Thermal diffusivity
a	[m]	Crack length
a	[m/s^2]	Acceleration / deceleration
a_m	[nm^2]	Average surface area covered by one adsorbate molecule
a_s	[m^2/g]	Specific surface area
b	[m]	Cell size in y-direction
b	[m]	Neck radius between adjacent particles
b	[1]	Number of bars in a framework
C	[1]	Proportionality constant or coefficient
$\mathbf{C}$		Elasticity tensor
COD	[m]	Crack opening displacement
$CTOD$	[m]	Crack-tip opening displacement
Cw	[m]	Warping coefficient
c	[m]	Cell size in z-direction
c	depends	Proportionality constant or coefficient
c_p	[J/kgK]	Specific heat
D	[m]	Melt pool depth
D	[N/m]	Spring constant
d	[m]	Diameter (e.g. micro strut, powder particle or tensile specimen)
$d_{0,86.5}$	[m]	Laser beam focus diameter
E	[MPa]	Young’s modulus
E	[J/mm^2]	Energy density, i.e. energy per unit area [J/mm^2], per unit length [J/mm] or per unit volume [J/ mm^3]
E_{melt}	[J]	Melt energy
e	[1]	Euler’s constant ($e = 2.71828\ldots$)
$\mathbf{e}$	[1]	Unit vector
F	[N]	Force
f	[1]	Geometric constant
f	[m]	Focal length
f	[1]	Fraction of volume
G	[MPa]	Shear modulus
g	[m/s^2]	Standard gravity ($g = 9.80665$ m/s^2)
g	[W/m^3]	Heat source function

HB	[1]	Brinell hardness
HV	[1]	Vickers hardness
h	[1]	Order of hierarchy
h	[W/m^{2}K]	Radiation transfer coefficient
h	[W/m^{2}K]	Convection coefficient
h_s	[m]	Hatch distance
I	[W/m^2]	Laser beam intensity
I	[m^4]	Area moment of inertia
I	[MPa]	Invariant of a stress tensor’s characteristic polynomial
$\mathbf{I}$	[1]	Identity matrix
J	[1]	Janssen factor
J	[MPa]	Invariant of a deviatoric tensor’s characteristic polynomial
J	[MPa]	Polar area moment of inertia (or torsion constant)
J	[1]	Colburn factor
J_{Ic}	[N/m]	Initiation toughness
j	[1]	Number of frictionless joints in a framework
K	[1]	Arbitrary property in generalized percolation theory
K	[MPa]	Bulk modulus
K_s	[MPa]	Shear correction coefficient
$K_{Ic\text{-}IIIc}$	[Nm$^{-3/2}$]	Fracture toughness, modes I, II and III
K	[]	Ludwik-Hollomon correlation material constant
$\mathbf{K}$		Global stiffness matrix
k	[1]	Number of constraints of a framework
k	[1]	Structural factor
$\mathbf{k}$		Element stiffness matrix
$\bar{k}_0$	[m^{-1}]	Propagation constant of a sound absorber
k_B	[J/K]	Boltzmann constant ($k_B = 1.380650 \cdot 10^{-23}$ J/K)
L	[J/kg]	Latent heat
L	[mol^{-1}]	Avogadro constant ($L = 6.0221415 \cdot 10^{23}$ mol^{-1})
L	[m]	Length (e.g. scan vector, bending beam or tensile specimen)
L_P	[dB]	Sound power level
L_p	[dB]	Sound pressure level
l	[m]	Layer dimensions (e.g. l_z is the layer thickness)
l	[m]	Length
M	[1]	Laser beam quality factor
M	[Nm]	Moment, couple
M	[1]	Number of degrees of freedom of a framework
Ms	[°C]	Martensitic transformation temperature
m	[kg]	Mass
m	[1]	Integer number to count items
m	[1]	Power law exponent
Nu	[1]	Nusselt number

n	[1]	Integer number to count items or dimensions
n	[1]	Power law exponent (e.g. for effective material property)
n_a	[mol/g]	Amount of adsorbate molecules per monomolecular layer
n_m	[mol/g]	Specific amount of adsorbate molecules per monomolecular layer
P	[W]	Power (e.g. of a laser beam or a sound wave)
p	[Pa]	Pressure (also partial or differential) of gas, vapor or sound wave
p	[1]	Probability
p	[1]	Correction term
p_c	[1]	Probability at percolation threshold
Q	[J/mol]	Activation energy
Q	[m^3/s]	Volume stream velocity
q	[1]	Number of mechanisms of a framework
q_3	[µm^{-1}]	Volumetric density distribution
R	[J/molK]	Gas constant (R = 8.314472 J/molK)
R	[Ω]	Electrical resistance
R	[1]	Reflectivity
R	[µm]	Surface roughness (R_z - ten point, R_T - total roughness)
R	[MPa]	Strength
R^2	[1]	Coefficient of determination
Re	[1]	Reynolds number
R	[MPa]	Strength
$RMSE$	[1]	Root mean square error
R_{th}	[K/W]	Thermal resistance
r	[m]	Radius or length of radius vector
r	[1]	Amplitude ratio of reflected and incident sound wave ($r \leq 1$)
$\mathbf{S}$		Compliance tensor
S/N	[1]	Signal-to-noise-ratio
s	[1]	Load ratio in fatigue tests
s	[1]	Number of self-stress states of a framework
s	[MPa]	Deviatoric stress
s^2	depends	Statistical variance
T	[K]	Temperature
t	[s]	Time
t	[m]	Thickness
t	[MPa]	Traction, i.e. stress or force
u	[m]	Displacement in x-direction
V	[m^3]	Volume
V_a	[mm^3/g]	Specific adsorbed volume per monomolecular layer
v	[m/s]	Speed
v	[m]	Displacement in y-direction
W	[J]	Work and energy, respectively
W	[m]	Melt pool width
w	[m]	Laser beam waist radius

w	[m]	Displacement in z-direction
x	[m]	x-coordinate
x	[m]	Overlap length at critical strut angle
y	[m]	y-coordinate
$\bar{y}$	depends	Mean value of desired part quality parameter
Z	[m^4]	Plastic section modulus
$\bar{Z}$	[kg/m^{4}s]	Characteristic impedance of a sound absorber
z	[m]	z-coordinate
z_R	[m]	Rayleigh length
α	[1]	Sound absorption coefficient
α	[W/m^{2}K]	Heat transfer coefficient
α	[rad]	Surface angle vs. x-y-plane or rotation angle
α	[rad]	Rotation angle about x-axis
β	[1/m]	Effective absorption coefficient
β	[1]	Distance between particles in relation to the mean particle size
β	[rad]	Rotation angle about y-axis
γ	[1]	Length of heat conduction in solid divided by mean particle size
γ	[rad]	Angular strain due to shear forces
γ	[rad]	Rotation angle about z-axis
Δ	[1]	Substitute for lengthy expressions
$\boldsymbol{\Delta}$		Displacement vector
δ	[1]	Ratio of solid conduction area to total area of a cross section plane
δ	[m]	Shrinkage
δ	[m]	Deformation
ε	[m/m]	Strain
$\dot{\varepsilon}$	[s^{-1}]	Strain rate
ε_r	[1]	Electrical permittivity
ε	[1]	Emissivity
η	[1]	Efficiency
η	[Ns/m^2]	Dynamic viscosity
Θ	[rad]	Angle of divergence of a laser beam
θ	[°]	Leverage angle against the x-y-plane
θ	[rad]	Rotational displacement
ϑ	[1]	Loss factor in damping processes
Λ	[m/m]	Normalized contact conductivity
λ	[W/mK]	Thermal conductivity
λ	[m]	Wave length
μ	[1]	Load ratio in incremental calculation of the tangent stiffness
ν	[1]	Poisson's ratio
π	[1]	Pi constant ($\pi = 3.1415926$)

ρ	[kg/m^3]	Density
ρ	[Ωm]	Electrical resistivity
σ	[MPa]	Mechanical stress
σ	[S/m]	Electrical conductivity
σ	[Wm^{-2}K^{-4}]	Stefan-Boltzmann constant ($\sigma = 5.670400 \cdot 10^{-8}$ Wm^{-2}K^{-4})
σ_0	[MPa]	Material-dependent constant in creep equation
τ	[MPa]	Shear stress
$\mathbf{\Phi}$		Rotation matrix
ϕ	[1]	Fraction of mass concentrated in the cell struts or edges opposed to the cell walls
ϕ	[1]	Length of heat conduction in gas related to the mean particle size
φ	[rad]	Angle of layer warpage
φ	[°]	Azimuth angle in the x-y-plane
$\mathrm{\varphi}$		Rotation matrix
Ψ_i	[m]	Inertia permeability coefficient
Ψ_v	[m^2]	Laminar permeability coefficient
Ω	[1]	Atomic volume

V List of figures

Figure 1.1: Impact of cellular design combined with Laser Freeform Fabrication on product innovations ... 2
Figure 2.1: Classification of cellular structures ... 3
Figure 2.2: Examples for open- (left) and closed-cell porosity (right) [316] ... 4
Figure 2.3: Classification and industrial relevance of cellular materials [256] ... 5
Figure 2.4: Influences on the quality of cellular material products ... 6
Figure 2.5: Natural sandwich cores: human skull (left) and a bird's wing (right) [122] ... 7
Figure 2.6: Skeleton of the deep-sea sponge Euplectella sp. [116] ... 7
Figure 2.7: Application groups of cellular materials ... 8
Figure 2.8: Ishikawa diagram of cellular material properties ... 10
Figure 2.9: Small clusters (left) and one percolating cluster (right) [278] ... 11
Figure 2.10: General compressive behaviour of cellular solids ... 13
Figure 2.11: Formation of plastic hinges in cell corners [270] ... 14
Figure 2.12: General tensile behaviour of cellular solids ... 18
Figure 2.13: Wöhler-curve (stress-life curve) ... 31
Figure 2.14: Strain-life curve ... 32
Figure 2.15: House of Quality for Cellular Material Products ... 39
Figure 2.16: Fabrication processes for cellular metals ... 40
Figure 2.17: Capability range of cellular metal making processes ... 41
Figure 2.18: Periodic cellular materials made by compaction from solid phase [9] ... 42
Figure 2.19: Periodic cellular materials made by forming from solid phase [304] ... 43
Figure 2.20: Periodic cellular materials made by joining from solid phase [304], [232], [280] ... 44
Figure 2.21: Periodic cellular materials made by casting from liquid phase [303], [166] ... 44
Figure 3.1: Cross section through SLM process chamber and operating principle ... 51
Figure 3.2: Ishikawa diagram of SLM influence parameters ... 53
Figure 3.3: Propagation of an ideal Gaussian beam and a real laser beam ... 60
Figure 3.4: Simple process map for Laser Freeform Fabrication processes [139] ... 64
Figure 3.5: Balling effect model based on multi-layer powder bed model ... 68
Figure 3.6: Examples for curl development in SLM parts (Rehme, 2007) ... 70
Figure 3.7: Dominant control parameters in SLM processes ... 74
Figure 3.8: Critical quality properties for SLM parts ... 76
Figure 3.9: Positive and negative minimum feature size [250] ... 80
Figure 3.10: Process chain for a customized acetabulum endoprosthesis [254] ... 84
Figure 4.1: First SLM lattice structure precursor experiment ... 87
Figure 4.2: Point-like exposure strategy vs. hatch scan strategy ... 88
Figure 4.3: Improved SLM lattice structure from point-like exposure strategy ... 89
Figure 4.4: SLM machine subsystems ... 92
Figure 4.5: SLM machine housing, CAD model and sketch of process chamber [198], [105] ... 93

Figure 4.6: Beam quality factor, focus diameter and Rayleigh length vs. laser beam power ... 95
Figure 5.1: 2D example of a frame which has one mechanism and one corresponding state of self-stress [50] ... 104
Figure 5.2: Ishikawa diagram of a generalized theory for SLM lattice structures ... 107
Figure 5.3: Hill vs. v. Mises yield surfaces for SLM solids ... 108
Figure 5.4: Theoretical trend of yield strength in dependence of leverage angle between force and x-y-plane ... 109
Figure 5.5: 3D stress state of a volume element dV ... 110
Figure 5.6: Von Mises and Tresca yield surfaces for isotropic materials [318] ... 114
Figure 5.7: Yield surface for SLM lattice structure ... 117
Figure 5.8: Nodal forces and moments acting on a framework member in local coordinates ... 118
Figure 5.9: Coordinate transformation from local to global coordinates by means of 3 consecutive rotations ... 120
Figure 5.10: Intersection of two struts of radius r_1 and r_2 ... 125
Figure 5.11: Suitable functions which can describe a property over the full range of relative densities ... 127
Figure 5.12: FEM calculation of melt front propagation in unconsolidated powder ... 129
Figure 5.13: Space-filling polyhedra (1st and 2nd row: [317], 3rd row: [151]) ... 132
Figure 5.14: Octet truss framework [263] ... 133
Figure 5.15: Selected cubic unit cell types ... 134
Figure 5.16: Selected polyhedral unit cell types ... 135
Figure 5.17: Tetrahedral unit cell types ... 136
Figure 5.18: Determination of overlap length between two adjacent struts ... 137
Figure 6.1: SLM tensile specimens orientated in directions normal to the surface of a hemisphere ... 143
Figure 6.2: Directional dependence of tensile yield strength $R_{p0.2}$ for SLM solids ... 144
Figure 6.3: Directional dependence of ultimate strength R_m for SLM solids ... 145
Figure 6.4: Directional dependence of break strain for SLM solids ... 145
Figure 6.5: Directional dependence of Young's modulus for SLM solids ... 147
Figure 6.6: Lattice strut diameter vs. melt energy ... 150
Figure 6.7: Normalized strut diameter in dependency of laser beam power ... 151
Figure 6.8: Build errors in SLM lattice structures ... 153
Figure 6.9: Obtainable aspect ratio experiment for cell type *bcc* ... 154
Figure 6.10: Results for obtainable stability of cell type *bcc* ... 155
Figure 6.11: Best fit evaluation of obtainable aspect ratios for all cell types ... 156
Figure 6.12: Bracket for retaining one flange of a tensile specimen ... 160
Figure 6.13: Test specimens for specific strength tests on all cell types ... 163
Figure 6.14: Results of compression tests at constant cell size in x-direction ... 166
Figure 6.15: Results of compression tests at constant cell size in y-direction ... 166
Figure 6.16: Results of compression tests at constant cell size in z-direction ... 167
Figure 6.17: Typical failure modes for SLM lattice structures (type I, II and III) ... 168

Figure 6.18: Compressive test specimens of cell types *fcc* and f_2bcc_z for effective elasticity at variable cell sizes 171
Figure 6.19: Results for effective Young's modulus of cell type f_2bcc_z 172
Figure 6.20: Shear specimens of cell type *fcc* 174
Figure 6.21: Results for effective compressive yield strength of cell type f_2bcc_z 175
Figure 6.22: Crushed compressive specimens (cell types *fcc* top left, f_2bcc_z top right, f_2cc_z bottom) 176
Figure 6.23: Results for effective tensile yield strength of cell type f_2bcc_z 177
Figure 6.24: Crushed tensile specimens of cell types *fcc*, f_2cc_z and f_2bcc_z (from left to right) 178
Figure 7.1: Relative density in dependency of aspect ratio 184
Figure 7.2: Compressive yield strengths in y-direction of different cell types vs. aspect ratio 186
Figure 7.3: Bonding of SLM lattice structures with solid walls in hybrid parts 189
Figure 7.4: Redesigned tibial base plate as an example of a hybrid part with SLM lattice structure 191
Figure 10.1: Adsorption isotherm (left) and BET diagram (right) [98] 239
Figure 10.2: Stochastic cellular materials made by pressing from solid phase [28], [303], [271], [106], [67] 241
Figure 10.3: Stochastic cellular materials made by foaming from solid phase [61], [15] .. 243
Figure 10.4: Stochastic cellular materials made by foaming from liquid phase [76], [316], [244], [158], [28] 244
Figure 10.5: Stochastic cellular materials made by casting from liquid phase [316], [60]. 247
Figure 10.6: Stochastic cellular materials made by deposition techniques [28] 248
Figure 10.7: Test specimens for examination of obtainable aspect ratio 255
Figure 10.7 (continued) 256
Figure 10.7 (continued) 257
Figure 10.7 (continued) 258
Figure 10.8: Results for obtainable stability of SLM lattice structures 258
Figure 10.8 (continued) 259
Figure 10.8 (continued) 260
Figure 10.9: Results for effective Young's modulus of cell type *fcc* 261
Figure 10.10: Results for effective Young's modulus of cell type f_2cc_z 262
Figure 10.11: Results for effective compressive yield strength of cell type *fcc* 264
Figure 10.12: Results for effective compressive yield strength of cell type f_2cc_z 265
Figure 10.13: Results for effective tensile ultimate strength of cell type *fcc* 267
Figure 10.14: Results for effective tensile yield strength of cell type *fcc* 268
Figure 10.15: Results for effective tensile ultimate strength of cell type f_2cc_z 269
Figure 10.16: Results for effective tensile yield strength of cell type f_2cc_z 270
Figure 10.17: Results for effective tensile ultimate strength of cell type f_2bcc_z 271

VI List of tables

Table 2.1: Applications based on metallic cellular materials ... 9
Table 2.2: Influence of various cross section profiles on parameter C_1 ... 23
Table 2.3: Influence of various cross section profiles on parameter C_2 ... 26
Table 2.4: Extremal Poisson's ratios and their engineering consequences ... 27
Table 2.5: Evaluation matrix of current fabrication processes for periodic cellular metals ... 46
Table 4.1: Chemical analysis of stainless steel powder ... 91
Table 4.2: Chemical analysis of SLM parts ... 91
Table 4.3: Approach to assessment of mechanical properties of SLM lattice structures ... 97
Table 5.1: Estimation of critical relative densities ... 138
Table 5.2: Resulting theoretical power laws for preselected cell types ... 141
Table 6.1: Best fit coefficients for average strut diameter ... 150
Table 6.2: Best fit coefficients for SLM lattice structure stability criterion in *eq. (6.9)* . 155
Table 6.3: Results for average relative density, strengths, specific strengths and energy absorption ... 164
Table 6.4: Failure modes of various SLM lattice structure cell types ... 168
Table 6.5: Evaluation matrix of all cell types ... 170
Table 6.6: Results for elastic shear tests ... 174
Table 6.7: Results for shear strength testing ... 179
Table 6.8: Ratios of tensile and compressive yield strengths of SLM lattice structures . 180
Table 6.9: Comparison of power laws for the low relative density regime ... 180
Table 7.1: Relative density in dependency of aspect ratio ... 183
Table 7.2: Compressive yield strength in dependency of aspect ratio in the low relative density regime ... 185
Table 7.3: Best fits for compressive yield strength over full range of relative density ... 185
Table 10.1: Calculated relative density for all cell types and cell sizes ... 250
Table 10.2: Calculated yield strengths [MPa] in x-, y- and z-direction for all cell types and cell sizes ... 251
Table 10.3: Results for average strut diameters for variable melt energies ... 252
Table 10.3 (continued) ... 253
Table 10.3 (continued) ... 254
Table 10.4: Elasticity in dependence of cell size for cell type *fcc* ... 261
Table 10.5: Elasticity in dependence of cell size for cell type f_2cc_z ... 262
Table 10.6: Elasticity in dependence of cell size for cell type f_2bcc_z ... 263
Table 10.7: Compressive yield strength in dependence of cell size for cell type *fcc* ... 264
Table 10.8: Compressive yield strength in dependence of cell size for cell type f_2cc_z ... 265
Table 10.9: Compressive yield strength in dependence of cell size for cell type f_2bcc_z ... 266
Table 10.10: Tensile ultimate strength in dependence of cell size for cell type *fcc* ... 267
Table 10.11: Tensile yield strength in dependence of cell size for cell type *fcc* ... 268
Table 10.12: Tensile ultimate strength in dependence of cell size for cell type f_2cc_z ... 269

Table 10.13: Tensile yield strength in dependence of cell size for cell type f_2cc_z 270
Table 10.14: Tensile ultimate strength in dependence of cell size for cell type f_2bcc_z 271
Table 10.15: Tensile yield strength in dependence of cell size for cell type f_2bcc_z 272

1 Introduction

Industrial production technologies are strongly committed to optimizing the major market goals of product quality as well as manufacturing cost and time in order to strive for better competitiveness. Simultaneous optimization of two or even all three of these factors is often conflicting and in most cases merely resolved by innovative technologies. Therefore, innovations are the driving force for the improvement of product quality and the reduction of manufacturing cost and time.

This typically involves innovations in product design which are often derived from new developments in production technologies. These can help meet the above mentioned market goals. One such technology, which emerged recently, is the field of Laser Freeform Fabrication (LFF) meaning laser-based additive solid freeform fabrication processes. These processes typically consist of layered application of liquid or powder material on a building platform. Solidification of targeted geometries in each layer derived from a sliced 3D-CAD model is being achieved with heat induced by partial absorption of laser beam energy. For rapid production of functional or non-functional plastic parts (e.g. prototypes) this technology has been successfully used over the past 20 years. However, the demand for functional parts made from engineering materials rather than plastics has propelled the technology towards the latest developments such as so-called Selective Laser Sintering and Selective Laser Melting (SLM). Both processes, introduced in the late 1990's, allow fast freeform fabrication of functional parts from different metallic alloys that yield required quality properties. The greatest advantages of these manufacturing technologies are a fundamental CAD-CAM-integration, potential for fabrication of virtually randomly complex geometries and the capability of delivering individual part geometries with quick time-to-market response.

Until a few years ago typical applications for LFF processes were only deployed in the field of Rapid Prototyping and Rapid Tooling. Now, over the recent years, applications are shifting towards Rapid Manufacturing which focus engineering materials. Thus industries from medical technologies or tool and mould makers became aware of the potential of making product innovations available which are inherent in this production method. However, the powder materials used are typically very costly compared to solid engineering materials and today, the machine operation cost is still expensive, too. Therefore, the production cost for LFF parts can be considerably high.

Apparently, if cellular design is employed with LFF processes the manufacturing cost and time can be reduced while the product quality can be enhanced. This requires innovative part designs which incoroporate cellular approaches to make use of the geometric degrees of freedom available with LFF processes. ***Fig. 1.1*** shows the impact this innovative combination of methodology (cellular design) and technology (LFF) has on product quality as well as manufacturing cost and time due to the numerous advantages listed under the bullets. An example for a realization of this combination could be a tailored part design where internal solid volume is substituted with a lattice structure in order to obtain stiff but lightweight parts designed specifically for given load situations.

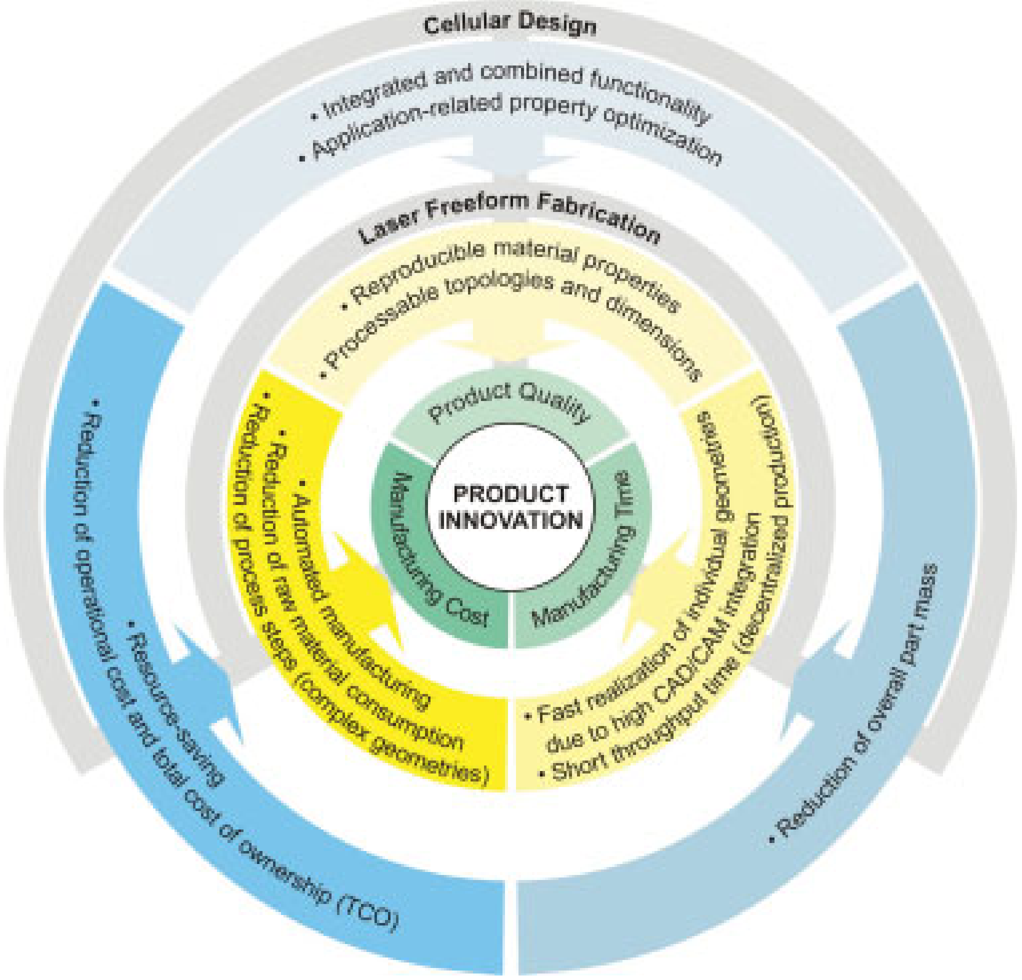
Cellular Design
• Integrated and combined functionality
• Application-related property optimization
Laser Freeform Fabrication
• Reproducible material properties
• Processable topologies and dimensions
Product Quality
PRODUCT INNOVATION
Manufacturing Cost
Manufacturing Time
• Automated manufacturing
• Reduction of raw material consumption
• Reduction of process steps (complex geometries)
• Fast realization of individual geometries due to high CAD/CAM integration
• Short throughput time (decentralized production)
• Reduction of operational cost and total cost of ownership (TCO)
• Resource-saving
• Reduction of overall part mass

Figure 1.1: Impact of cellular design combined with Laser Freeform Fabrication on product innovations

Any optimization effort for LFF processes has to take into account that the quality properties for laser fabricated parts demanded by the customer must be achieved. This leads to the need of developing an engineering process for designing and manufacturing laser fabricated lattice structures at reproducible industrial quality standards. Therefore, the scope of the work presented in this thesis is to develop and analyze the design and the manufacturing of lattice structures made from Selective Laser Melting and to characterize their mechanical behaviour in regard of resulting product quality versus manufacturing cost and time. After a close scrutiny of the current state of technology in cellular material engineering and LFF processes, theoretical approaches to model SLM fabricated solids as well as failure mechanisms for SLM lattice structures are developed in order to design products with appropriate periodic, cellular structures. Subsequently, a comprehensive experimental analysis of SLM solids and lattice structures is carried out. Results of test specimens fabricated on a SLM machine developed by the company Realizer GmbH are evaluated in regard of their producibility and their material properties such as strength in compression, tension and shear load. According scaling laws are derived for the most promising cell types to answer the question of what part design should be aspired to if design engineers wish to incorporate SLM lattice structures into new applications. Finally, these laws are applied to suggested applications in medical implant design where cellular materials can be useful to improve ingrowth of bone tissue and to adjust the effective stiffness of implants to the surrounding tissue.

2 Cellular design and manufacturing processes

2.1 Cellular materials

2.1.1 Classification

Cellular materials can be found in nature as well as numerous engineering applications. They have a number of unique properties which allow new and innovative applications beyond the scope of solid engineering materials. They exhibit low density and therefore low mass along with high strength, high stiffness, high thermal conductivity (or in contrast high thermal insulation), high acoustic absorption as well as high gas permeability. Thus they make excellent lightweight structures with high stiffness-to-weight-ratios e.g. for sandwich cores loaded in bending. Their superior specific strength allows outstanding kinetic energy absorption characteristics while their high surface-to-mass ratio permits exceptional heat transfer capabilities. According to their properties introduced in ***section 2.1.4*** they are also well usable for acoustic absorption, for damping and absorption of mechanical energy, for vibration control, for filters, for thermal insulation, for heat exchange, for electric insulation and conduction, respectively and for catalyst usage among many other possible applications. Suitable design and configuration in terms of optimizing the cellular structure allows even the simultaneous fulfillment of multiple part functions. Often cellular materials do not necessarily excel over conventional materials in single properties and most often their costs are higher. Glass wool for instance can achieve much better sound absorption than any cellular material, however, it cannot be used for any kind of structural load. Therefore, using cellular materials in combined applications like e.g. lightweight, load-bearing heat exchangers is most promising.

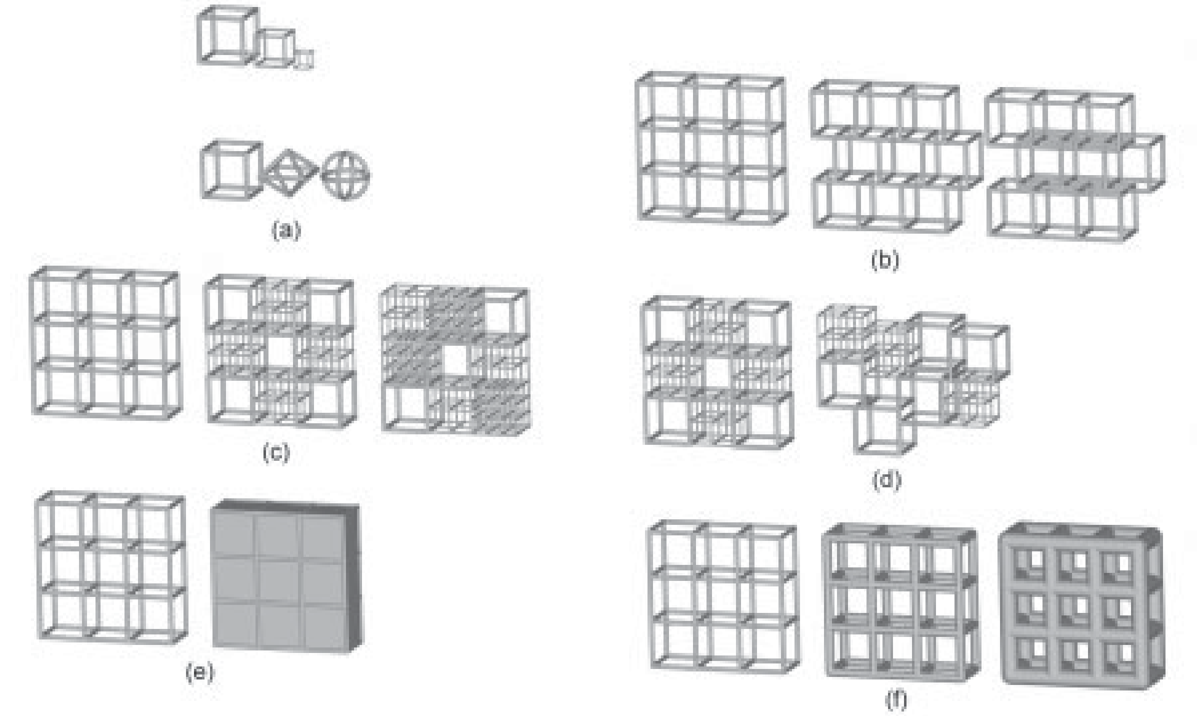

Figure 2.1: Classification of cellular structures

Cellular structures as illustrated in ***fig. 2.1*** can be classified by what shall be called the design parameters such as

- material,
- cell size and shape (a),
- topology (b),
- cell size variability (c),
- 2D- or 3D-periodic or stochastic appearance (d),
- type of porosity (open- or closed-cell structure) (e),
- relative density (f) and
- hierarchical structure.

Cell dimensions can typically range from several tens of microns to centimeters. They may also vary within periodic cellular materials featuring repetitive patterns that can either be the result of a characteristic, inherent in the manufacturing process, or the result of constructed design. If the repetitive pattern is translated in two dimensions, a prismatic material also known as honeycomb results. Three dimensional periodicity, however, yields a lattice structure (sometimes also named truss structure). Materials that cannot be described with a single unit cell and a repetitive pattern are named stochastic materials and they often show a distinct statistical variation of cell size and shape depending on manufacturing process parameters. Generally, better mechanical properties can be expected from regularly arranged cell structures than from randomly distributed formations which show low connectivity of the joints due to a small number of cell walls or struts linked in edges or vertices, respectively (Scheffler, 2005, p. 5, [270]).

The porosity of a cellular material can be described by either an open-cell or a closed-cell structure as depicted in ***fig. 2.2***. Open-cell porosity in a periodic cellular material occurs in lattice and honeycomb structures. Honeycomb, however, can be pseudo closed-cell if applied in its preferential environment in sandwich cores where both faces are typically bonded to sheet material. Open-cell stochastic cellular materials are refered to as sponges, whereas their closed-cell counterparts represent the wide spread group of foams. Only structures composed from hollow spheres can be periodic or, if post-processed e.g. by Hot Isostatic Pressing (aka HIPing), the cell size and shape of hollow spheres will become stochastic. Hollow spheres can

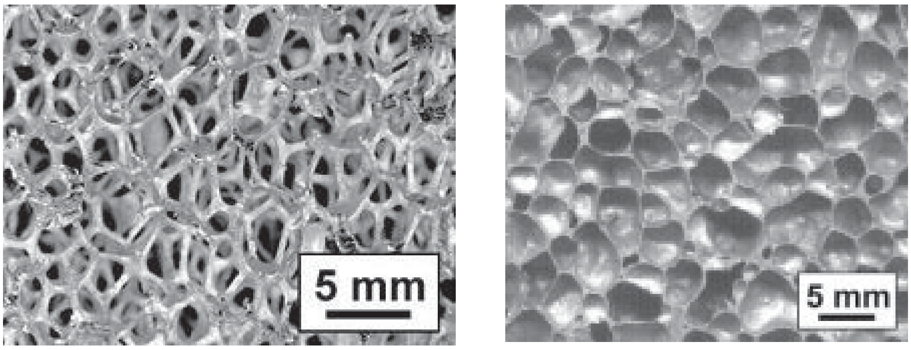

Figure 2.2: Examples for open- (left) and closed-cell porosity (right) [316]

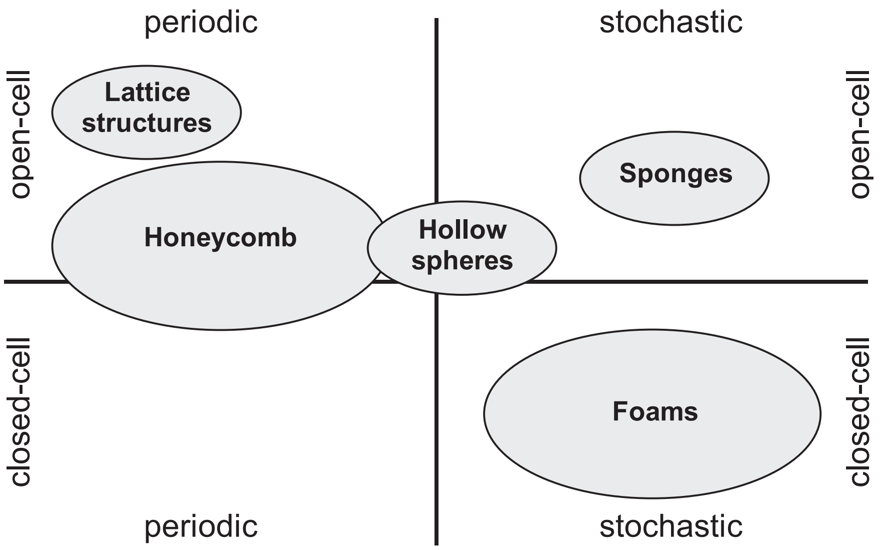

Figure 2.3: Classification and industrial relevance of cellular materials [256]

also show complex internal porosity, therefore, they should partially be added to the group of closed-cell materials. ***Fig. 2.3*** summarizes these categories for different metallic cellular materials and qualitatively specifies their current industrial relevance by giving a binary state of size for each category in which the bigger sized ellipse reflects a higher relevance.

The relative density of a cellular material is strongly influenced by the previously mentioned parameters of cell size, cell shape, cell size variability, type of porosity and thickness of cell walls and struts. Beyond these it can be influenced further by structural hierarchy, i.e. if structural features occur on different size scales. A typical example are e.g. cell walls and struts that comprise internal truss structures or voids. Structural hierarchy can contribute to improved strength properties compared to the same material without structural hierarchy that has the same relative density (Lakes, 1993, p. 511, [174]).

2.1.2 Product quality objectives

Quality is typically defined as the capability of the entirety of inherent properties of a product, a system or a process to fulfill the customer's demands (DIN EN ISO 9000, 2005, p. 18, [91]). For products which incorporate cellular materials quality is mainly influenced by the cellular material properties and the functionality the cellular material provides. Both are subject to the design parameters as ***fig. 2.4*** illustrates. The most important design parameters and resulting cellular material properties required for comparing different cellular materials are

- obtainable dimensions such as cell size,
- relative density,
- obtainable degree of periodicity,
- flawlessness,
- resulting strength of a cellular structure (e.g. in mechanical applications) and
- its potential to be tailored for topology optimization (e.g. in mechanical or thermal applications).

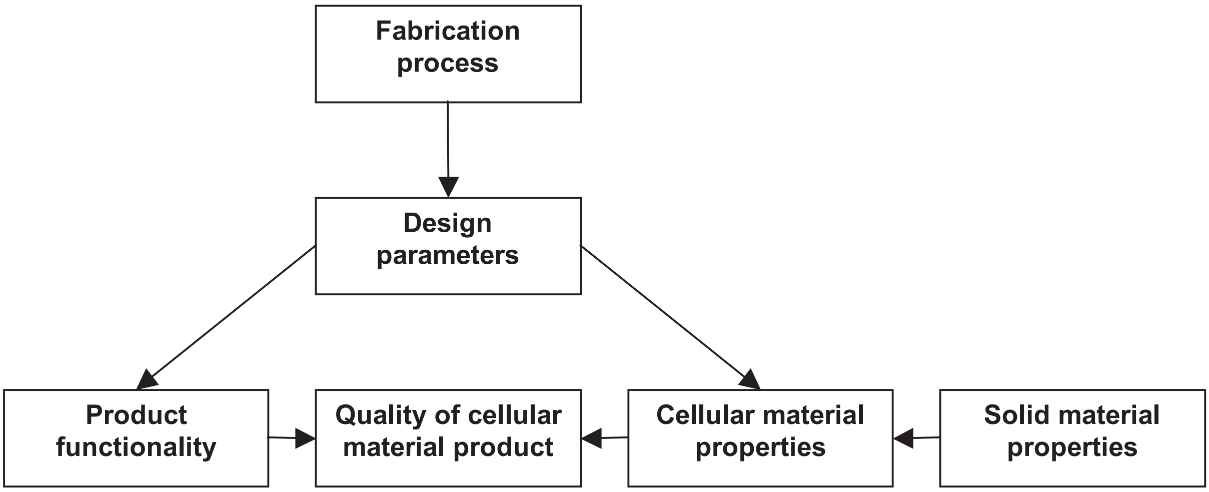
Fabrication process
Design parameters
Product functionality
Quality of cellular material product
Cellular material properties
Solid material properties

Figure 2.4: Influences on the quality of cellular material products

For most available cellular materials the design parameters are governed and hence limited by constraints of their fabrication processes as also shown in ***fig. 2.4***. Therefore, exploiting the possibilities for new product functionality implies that the according fabrication processes and the engineering design methods have to be mastered in order to obtain the desired product quality.

This thesis focuses solely on metallic materials though cellular structures made from plastics or ceramics should not be considered of lesser industrial relevance due to many investigations conducted with polymer foams and rapidly growing interest in ceramic foams although the latter are the least well characterized materials (Scheffler, 2005, p. 3, [270]). However, metallic, cellular materials are expected to allow the highest degree of freedom in the design parameters. Thus achievement of the product quality objectives like e.g. high strength at low weight or high heat transfer capability with structural integrity can be fulfilled. This chapter presents the occurrence of metallic, cellular materials, their typical fields of application, their properties in regard of achievable product quality and the various manufacturing processes available today. In ***section 2.2.3*** all these manufacturing processes are evaluated in respect to the design parameters.

2.1.3 Occurrence and applications

In nature one can find cellular materials nearly everywhere related to living tissue of plants, animals and humans. Such materials are e.g. wood, cancellous bone and sponge. Gibson (2005, p. 393, [122]) gives some typical examples how nature involves these materials in ‘sandwich core type’ items such as the human skull in ***fig. 2.5 (left)*** where overall robustness at minimum weight is important to protect the brain and a bird’s wing in ***fig. 2.5 (right)*** where high bending stiffness at low weight is required. Furthermore, of high interest is the glassy skeleton structure of the deep-sea sponge Euplectella sp. in ***fig. 2.6*** that was recently described by Aizenberg (2005, pp. 275-278, [6]). It overcomes the brittleness of its constituent solid, glass, due to seven hierarchical levels of structure at different length scales.

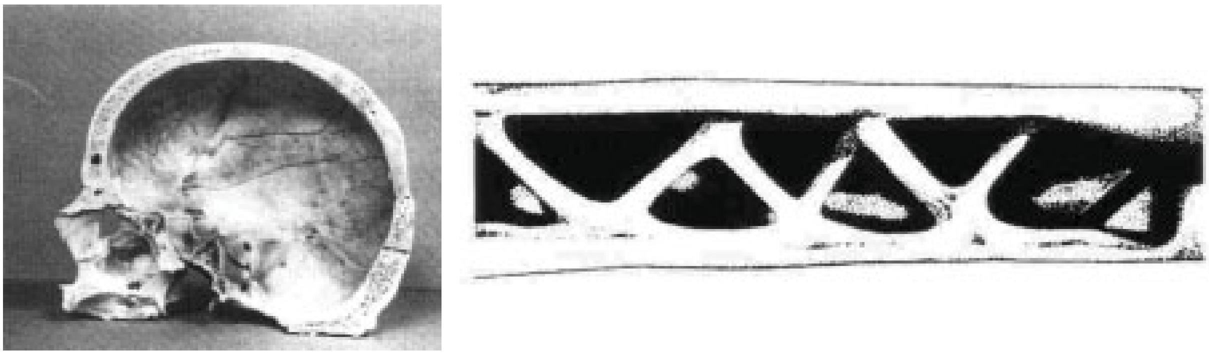

Figure 2.5: Natural sandwich cores: human skull (left) and a bird's wing (right) [122]

Three of these levels are situated on microscopic dimensions beyond the interest of this thesis. However, the four levels that can be found on a macroscopic scale deal with the formation of a very specific grid into a cylinder and build-up of helical surface ridges altogether making the sponge stiff against random load types and protecting it from ovalization which would weaken its strength against bending caused by underwater currents.

The properties of metallic cellular materials listed in ***section 2.1.4*** result in a variety of possible engineering applications. However, not all materials fulfill a designated purpose as well as others. Therefore, possible application groups are shown in ***fig. 2.7***. In a matrix that distinguishes open- and closed-cell as well as periodic and stochastic cellular materials, these groups are placed in the most probable position (Rehme, 2006). Apparently, the positioning of each group is not a definitive must, however, in those applications shown in the upper half of the figure where media such as gas, fluid or solid pass the cellular material or where tissue grows into it, only open-cell structures can serve the purpose. On the other hand only closed-cell materials allow suitable design for buoyancy devices and thermal insulation. However, in structural applications closed-cell materials should be used since they offer at least hypothetically better performing strength properties than open-cell materials as explained in detail in ***section 2.1.4.15***. Additionally, the greatest benefit for structural applications such as energy absorbers or implants of high stiffness can be found in periodic structures due to the same reason. Other applications such as filters and heat exchangers should as well be made from periodic materials as less pressure drop per unit length can be expected. Those application groups shown on the right hand side of ***fig. 2.7*** are typically made from stochastic materials as the use of periodic materials has no evident advantage. In contrast the

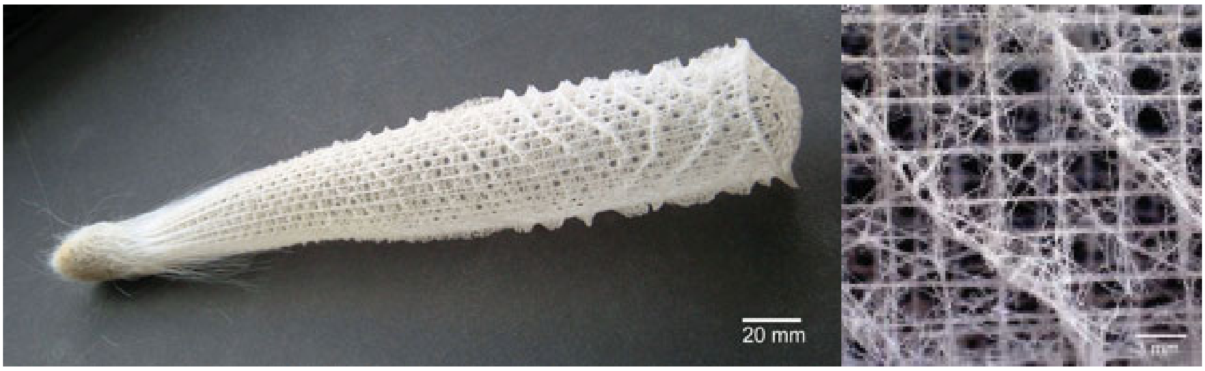

Figure 2.6: Skeleton of the deep-sea sponge Euplectella sp. [116]

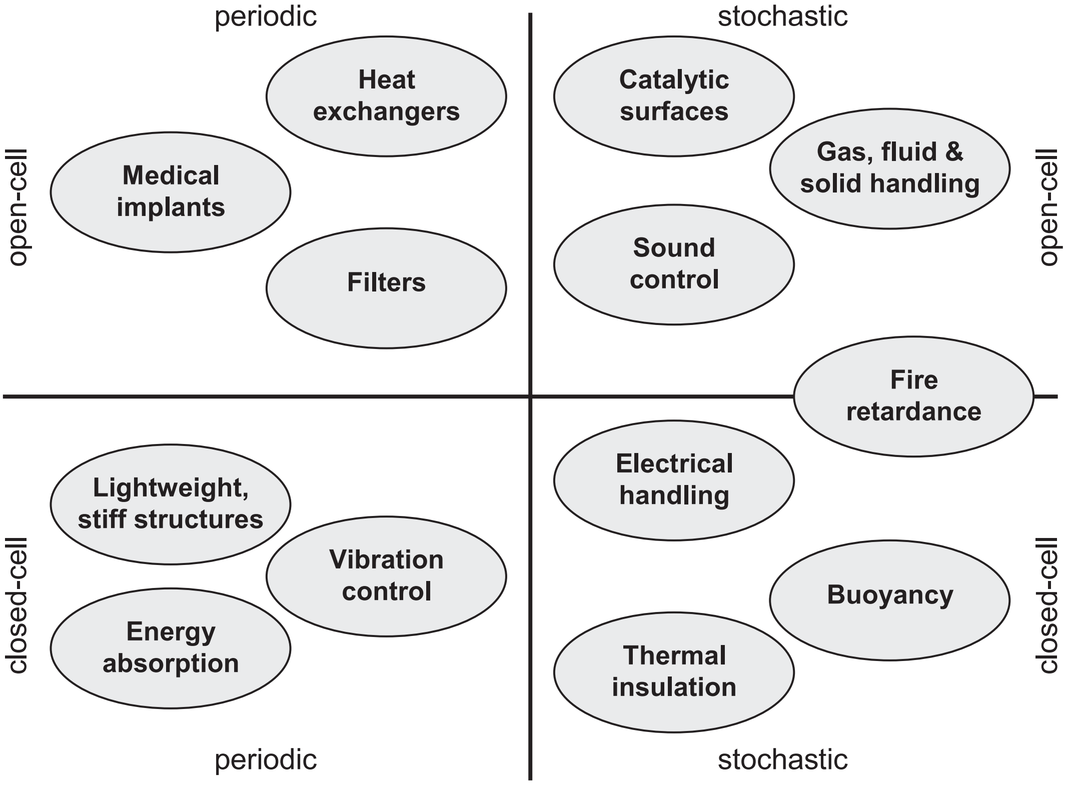
periodic
stochastic
open-cell
open-cell
Heat exchangers
Medical implants
Filters
Catalytic surfaces
Gas, fluid & solid handling
Sound control
Fire retardance
Electrical handling
Lightweight, stiff structures
Vibration control
Energy absorption
Buoyancy
Thermal insulation
closed-cell
closed-cell
periodic
stochastic

Figure 2.7: Application groups of cellular materials

manufacture of periodic cellular materials is often more costly per volume unit. It is therefore the task of the design engineer to make the best compromise between the options from ***fig. 2.7*** and the choice of materials, cell sizes, cell shapes, cell topologies, cell size distributions and relative densities for a given engineering application.

All these different application groups have resulted in numerous existing applications and in a number of currently developed implementations which were given by Ashby (2000, pp. 3-5, [17]), Banhart (2000, pp. 503-504, [26]), (2001, p. 609-621, [28]), ERG (2006, p. 4, [107]), Gibson (2005, pp. 391-395, [122]), Nieh (2000, p. 105, [217]), Stöbener (2003, p. 285, [281]), Wang (2005, pp. 21-23, [307]), Wicklein (2003, pp. 369-374, [315]) and various other authors. The span of industries making use of cellular materials has become quite wide. A summary of all these applications can be found in ***table 2.1*** sorted by their current importance in engineering design. This list may be comprehensive, however, not complete as new applications keep constantly emerging.

Table 2.1: Applications based on metallic cellular materials

Application group	Applications
Lightweight structures	High strength core structures for aircraft wing panels; stiff and lightweight structural panels in aerospace fuselage applications; stiff and low inertia robotic arms; lightweight and stiff cores for automobile hoods, trunk lids, sliding roofs, bulkheads and passenger compartment walls; structural lightweight bulkheads in shipbuilding; lightweight and stiff cores for mirrors in space applications
Energy absorption	Automobile bumpers; blast shock wave protection; space debris protection for satellites, crash energy absorber for suburban railcars; reinforcements of car's A- and B-pillars; space vehicle landing pads
Gas, fluid & solid handling	Pressure reducers; fluid pulse dampers; vacuum chucks; fuel tank baffles; porous rollers for regulated application of fluids; hover cushions; gas spargers for fluids; flow restrictors for fluids; storage devices for fluids; gas diffusers for semiconductor etch and deposition equipment; flow straightener in wind tunnels; containment and burn rate enhancers for solid propellants
Heat exchangers	Heat sinks for electronic components; gas and liquid heat exchanger with little pressure drop; regenerator for thermal engines; transpiration coolers
Thermal insulation	Heat resistant and self-supporting sound insulation in car chassis; heat shielding for aircraft exhaust; thermal shock resistant materials
Sound control	Sound dampers; silencers for jet engine intakes; pneumatic tool mufflers; sound absorbers along motorways and in railroad tunnels; impedance adaptors for ultrasound sources
Filters	Precipitation of solid or liquid particles from gasses; precipitation of solid particles or fibers from fluids; mist elimination of water and oils; sea water rejecters for ship ventilation
Fire retardance	Flame arresters; lightweight firedoors; fire resistant panels underneath house facades
Vibration control	Vibration reducers; gas-tight seals between engine stages in turbines; machine housings
Catalytic surfaces	Automobile catalytic converters; matrix for chemical beds and scrubbers; water purification (redox reaction of ions contained in the water)
Electrical handling	Electromagnetic pulse attenuation; porous electrodes in fuel cells and electrolytic processes; battery plates; electromagnetic shielding in machine housings
Medical implants	Scaffolds in tissue engineering; bone implants
Buoyancy	Floater for measuring fill levels in hot or corrosive media
Others	Preforms for metal-ceramic composites; artificial wood

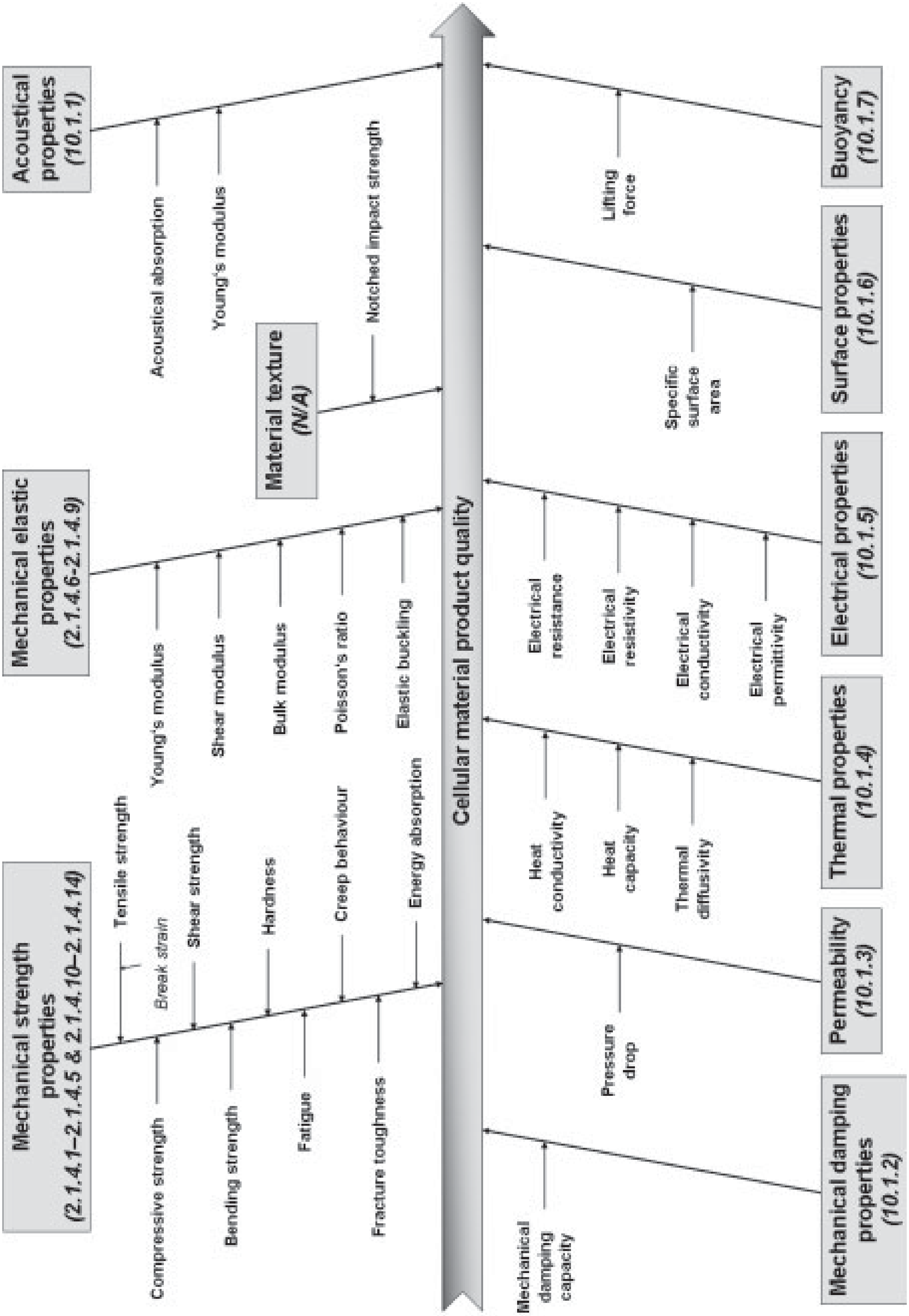
Acoustical properties (10.1.1)
Acoustical absorption
Young's modulus
Material texture (N/A)
Notched impact strength
Mechanical elastic properties (2.1.4.6-2.1.4.9)
Young's modulus
Shear modulus
Bulk modulus
Poisson's ratio
Elastic buckling
Mechanical strength properties (2.1.4.1–2.1.4.5 & 2.1.4.10–2.1.4.14)
Tensile strength
Break strain
Shear strength
Hardness
Creep behaviour
Energy absorption
Compressive strength
Bending strength
Fatigue
Fracture toughness
Cellular material product quality
Buoyancy (10.1.7)
Lifting force
Surface properties (10.1.6)
Specific surface area
Electrical properties (10.1.5)
Electrical resistance
Electrical resistivity
Electrical conductivity
Electrical permittivity
Thermal properties (10.1.4)
Heat conductivity
Heat capacity
Thermal diffusivity
Permeability (10.1.3)
Pressure drop
Mechanical damping properties (10.1.2)
Mechanical damping capacity

Figure 2.8: Ishikawa diagram of cellular material properties

2.1.4 Mechanical properties

The quality of a product made from a cellular material can in part be derived from the properties the cellular material has, as shown in ***fig. 2.4***. The most relevant property groups and their subordinated properties which typically define this quality are shown in ***fig. 2.8***. These properties depend mainly on the solid material the cellular material was made from (Ashby, 2000, p. 40, [17]). Secondly, they depend on the design parameters such as cell size, cell shape, periodicity (and the resulting connectivity between cell walls or struts), porosity type and relative density the cellular material possesses. However, not all cellular material fabrication processes necessarily allow taking direct influence on these design parameters.

In the literature quite a few sources describe the properties of cellular materials made from metal very detailed. However, since the publishing of the definitive book by Gibson (1997, pp. 52-343, [123]) none of the sources from the past 10 years gave a complete overview on the up-to-date insights on all important properties simultaneously. In order to precisely describe the impact that the properties in ***fig. 2.8*** have on the resulting product quality, this section contains a comprehensive summary of all mechanical properties. Other properties are given in ***appendix 10.1*** according to the section numbers in the figure. Certain details on how to measure the properties are mentioned as well.

Before explaining these properties one approach commonly used by many researchers has to be mentioned. This approach is the percolation theory which according to the definition of Stauffer (1994, p. 4, [278]) deals with clusters formed of nearest neighbours in a number of sites where each site is randomly occupied with probability p completely independent of all other sites. All sites together, regardless of their being occupied or unoccupied, are conjunct in a finite shape such as a rectangular grid comprising one cell for each site serving here as a simple two-dimensional example shown in ***fig. 2.9 (left)***. If the probability p reaches a certain critical value p_c, i.e. the so-called percolation threshold, then at least one cluster extends from all faces or borders of that shape as seen in ***fig. 2.9 (right)***. The cluster now 'percolates' through the system. The calculation of percolation thresholds for various grid types, dimensions, definition of nearest neighbours and site or bond percolation can be found in the

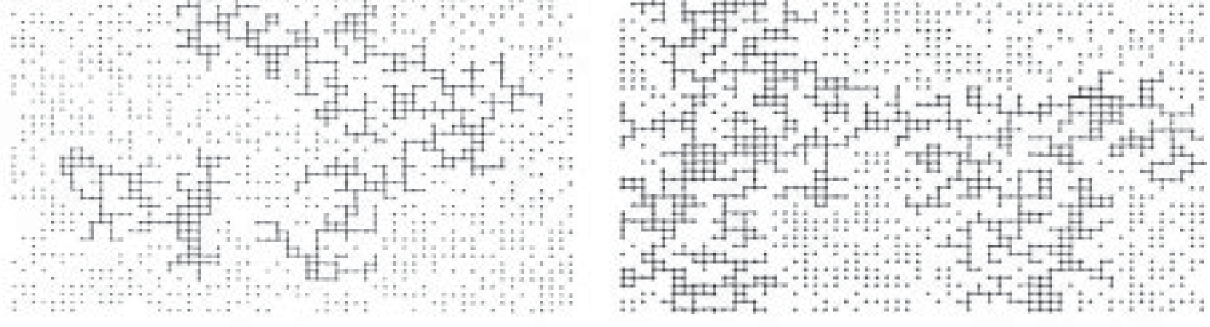

Figure 2.9: Small clusters (left) and one percolating cluster (right) [278]

literature. Those researchers who have considered percolation theory in context with cellular materials simplified the resulting correlations by assuming that only those cellular materials are of interest that do not disintegrate and provide certain mechanical stability. Thus they always form a percolating cluster and only the range above the percolation threshold is of interest. Since quite low relative densities can be obtained for cellular materials, Kováčik (1998, p. 239, [165]) assumed that the percolation threshold can be fixed at zero density which is generally followed by all other authors. It is widely perceived that the probability p can be equated with the distribution of mass in a cellular material and therefore with its relative density. When Last (1971, pp. 1719-1721, [178]) performed first experiments on the electrical conductivity of graphite paper with randomly punched holes in it, it became evident that the examined property and the relative density are not linearly proportional above the percolation threshold. Stauffer (1994, p. 91, [278]) gives a reasonable explanation for this behaviour by stating that clusters growing beyond the percolation threshold develop branches representing so-called ‘dead ends’. These do not contribute to a property K^* unlike the so-called ‘backbone’. Thus Last (1971, pp. 1719-1721, [178]) obtained a non-linear dependency of the conductivity from relative density which can be best fitted with a power function of the generalized form in ***eq. (2.1)***. If the percolation threshold p_c is set to zero, if the probability p becomes the density ρ and if the effective property is expressed in dependency of the relative density, then ***eq. (2.2)*** results. The proportionality factor C must always be unity since a fully dense specimen must exhibit the same property as the solid material (Kováčik, 1998, p. 240, [165]). The percolation theory appears to be applicable especially for the mechanical, thermal and electrical properties of cellular materials presented below.

$$K^* \propto (p - p_c)^n \tag{2.1}$$

$$\frac{K^*}{K_{solid}} = C \cdot \left(\frac{\rho^*}{\rho_{solid}} \right)^n \tag{2.2}$$

Depending on the cell parameters depicted in ***fig. 2.1*** and on the material they were made from, cellular solids can generally exhibit failure by elastic buckling, plastic deformation and brittle fracture of cell walls or struts (Scheffler, 2005, pp. 7-8, [270]). Elastic buckling is preferably applicable on elastomeric foams and brittle fracture on ceramics. However, these failure modes will be included in the considerations made here despite of the ductility of most metals. Alltogether strength, elasticity and stiffness of cellular structures also strongly depend on whether they show bending-dominated or stretch-dominated behaviour. Both these terms will be explained in detail in ***section 5.1.2***.

2.1.4.1 Compressive strength

Typically, two different compressive stress-strain curves can be observed when testing ductile cellular materials uniaxially (Rehme, 2006, pp. 0K10-0K11, [251]). These depend on whether bending-dominated or stretch-dominated behaviour prevails. In ***fig. 2.10*** the solid line shows the initial settling that often occurs due to broken cell edges received from post-processing of a cellular material such as cutting, etc. Next, the solid line displays the reversible linear-elastic deformation applicable for both curves. The curve along the dotted line represents bending-dominated structures and shows a peak stress after failure initiation before a nearly constant plateau stress is obtained well below the peak stress. In some cases the peak strength can be less distinct or even unexistent in contrast to the diagram shown. When the increasing compaction causes densification of the part at relative densities near unity, the stress bursts to infinity. The second curve along the dashed line exhibits a stretch-dominated behaviour where after failure initiation the stress grows again linearly, however, the slope is much lower compared to the elastic regime and the deformation is irreversible. Eventually, the identical densification process takes place and the stress increases rapidly.

To a priori avoid confusion with the theory and various findings on compressive strength properties presented below, bending-dominance should in most cases be associated with open-cell or with stochastic materials while stretch-dominance can often be correlated with their closed-cell or sometimes open-cell periodic counterparts. Ideal bending-dominated structures are typically dominated by a non-linear rise of relative yield strength over relative density with exponents around 1.5, whereas ideal stretch-dominated structures nearly approximate a linear rise (Scheffler, 2005, p. 16, [270]). Since the relative yield strength in both curves should approach unity for nearly dense materials it follows that at given relative density a stretch-dominated cellular material always shows higher relative strength.

Gibson (1997, pp. 203-208, [123]) developed the most acknowledged model for the strength of open-cell and closed-cell metallic materials derived from assumptions of cell strut and cell

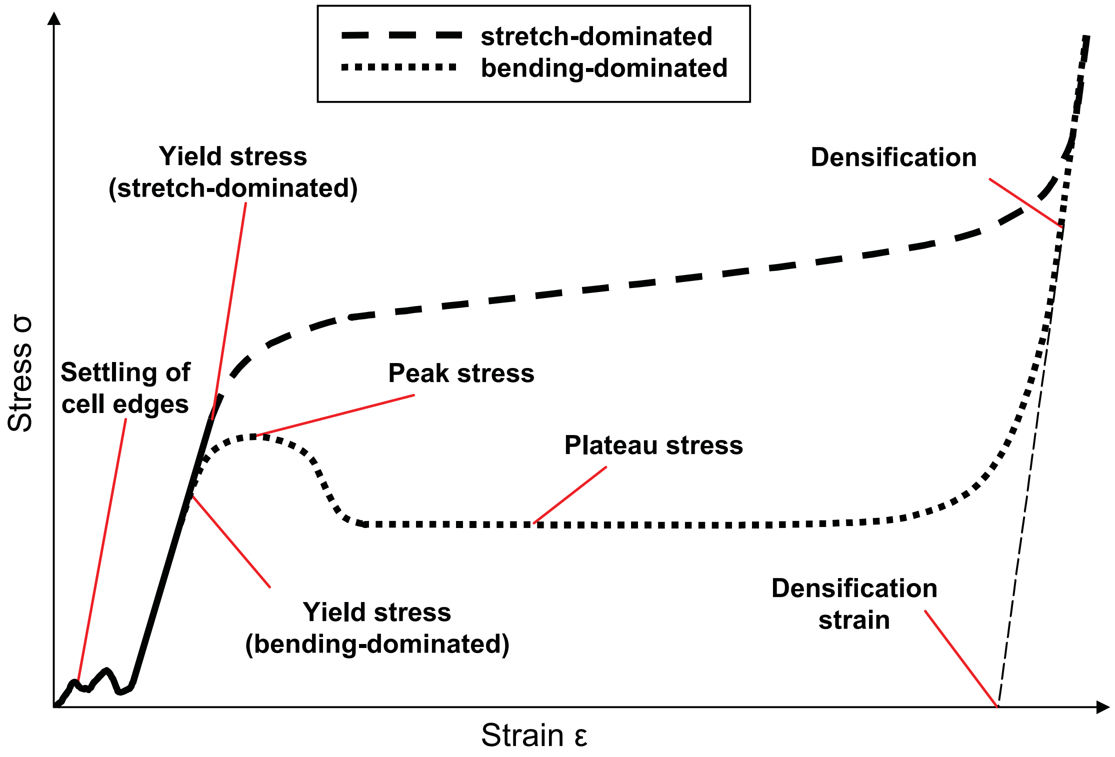

Figure 2.10: General compressive behaviour of cellular solids

wall deformation and failure. In the open-cell model cubic unit cells comprising struts of square cross section and equal length in all three directions of space serve this purpose. In further considerations additional connective struts are attached perpendicularly at the center of the struts of the unit cell (***fig. 2.11***). Thus a force exerted on the unit cell will cause a bending moment in those struts that are orientated perpendicularly to the direction of the force. Due to the centered attachment of the connective struts a worst case consideration of the bending moment takes place regardless of how the real material comprising numerous unit cells is structured. The corners of the unit cell are regarded as fixed hinges. After deformation of the struts when the bending force on the surface of an exposed strut exceeds the strength of the solid material, the corners become plastic hinges.

The use of the bending moment in this model as well as the geometrical dimensions of cell strut length and cross section, which correlate well with the relative density, leads to ***eq. (2.3)*** where n_5 was derived to 1.5. C_5 was determined to 0.3 by experimental effort. Thus the relative yield strength, i.e. the cellular's strength divided by the strength of the solid, apparently depends mainly on the relative density of the cellular material and its solid properties. This matches conclusions drawn by Deshpande (2001, pp. 6275-6276, [78]), Scheffler (2005, pp. 7-8, [270]) and other researchers. However, some constraints apply to this model. Gibson (1997, p. 205, [123]) gave a density correction to ***eq. (2.3)*** which, however, is almost insignificant. Furthermore, this model fails at relative densities greater than 0.3 (Gibson, 1997, p. 205, [123]) since the beam-bending concept does not hold under this condition. The closed-cell equivalent of the model comprises the same network of cell struts which become cell edges supplemented with cell faces of a different thickness. Due to the nature of most foaming processes these cell walls typically contain a small amount of the solid and are therefore less thick. If again the unit cell is exposed to an external force, then stretching of the cell walls occurs. Therefore, ***eq. (2.4)*** accounts for the additional membrane stress derived from the plastic work performed through bending of the cell edges and stretching of the cell walls in regard to the fraction of solid mass ϕ contained in each one of

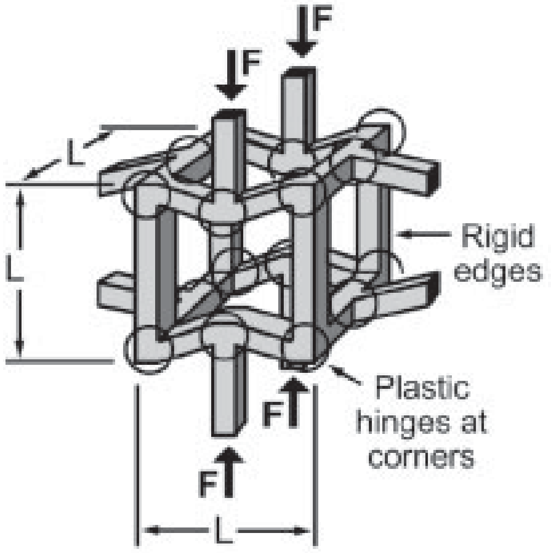

Figure 2.11: Formation of plastic hinges in cell corners [270]

them. In the case of $\phi = 1$ (open-cell) all mass is concentrated in the cell edges and the formula becomes ***eq. (2.3)*** with $C_5' = C_5$. A value of 0.44 is suggested for C_5'' for relative densities below 0.2 while in the case of $\phi = 0$ (closed-cell) it should rather be approximately unity as the relative yield strength must become unity when the density of the bulk material is reached.

$$\frac{\sigma^*_{yield}}{\sigma_{yield,solid}} = C_5 \cdot \left(\frac{\rho^*}{\rho_{solid}} \right)^{n_5} \tag{2.3}$$

$$\frac{\sigma^*_{yield}}{\sigma_{yield,solid}} = C_5' \cdot \left(\phi \cdot \frac{\rho^*}{\rho_{solid}} \right)^{n_5'} + C_5'' \cdot (1-\phi) \cdot \left(\frac{\rho^*}{\rho_{solid}} \right) \tag{2.4}$$

Experimental analysis of open- and closed-cell materials made from different solids was conducted by a number of researchers. Ashby (2000, p. 53, [17]) performed extensive tests on polymeric foams and gives a range of 0.1 to 1 for C_5, 1.5 for n_5, a range of 0.05 to 0.5 for C_5', an unusual value of 2/3 for n_5' and a range of 0.03 to 0.3 for C_5'' where $\phi = 1$ in the left term of ***eq. (2.4)*** while $\phi = 0$ in the right term. Andrews (1999, pp. 116-122, [10]) tested a number of commercially available open-cell and closed-cell aluminum foams and sponges with relative densities between 0.08 and 0.20. The results confirmed ***eq. (2.3)*** for open-cell materials, however, the closed-cell foams stayed far behind the expectations from ***eq. (2.4)*** and the above mentioned values given by Gibson (1997, p. 208, [123]). Nieh (2000, p. 108, [217]) found that the deviation between the hypothetic and the obtainable yield strength can generally be one order of magnitude. This result was determined from testing open-cell ERG (Energy and Research Group, Inc.) Duocel sponges with relative densities between 0.05 and 0.1. When McCullough (1999, p. 2326, [196]) examined the closed-cell aluminum foam Alulight with densities between 0.15 and 0.35, they exhibited yield strengths more in the expected range of open-cell materials with a best fit of values for C_5 between 0.28 and 0.376 and $n_5' = 1.5$ for ***eq. (2.3)***. This is yet further evidence that closed-cell aluminum foams perform worse than expected. According to McCullough (1999, p. 2326, [196]) the main reasons leading to premature plastic failure in stochastic foams and sponges can be found in

- cell edge curvature,
- concentration of material at cell edges rather than in the cell walls and
- non-uniform density of the cellular material.

Additionally, Nieh (2000, p. 105, [217]) confirmed that the cell shape effects the strength only slightly, whereas a variation of the cell size at fixed density is negligible.

Ni-Al and Ni-Cr-Al superalloy open-cell sponges with relative densities between 0.026 and 0.035 manufactured from a 2.2 % dense pure Ni sponge by aluminization and chromation were investigated by Choe (2004, p. 1291, [56]). The compressive yield strengths obtained were in rough agreement with ***eq. (2.3)*** and the values given by Gibson (1997, p. 206, [123]). The maximum deviation for relative densities between 0.03 and 0.4 was determined to a factor of 2. Another open-cell sponge made from Zr-based amorphous metal alloy Vit106 with relative densities ranging from 0.14 to 0.28 and with pore sizes between 150 to 355 µm was examined by Brothers (2005, pp. 4433-4435, [46]). Remarkable about this cellular material was the significantly increased compressive ductility compared to the bulk material. Opposed to only 2 % strain that bulk Vit106 metal alloy allows, strain rates of up to 80 % were obtained. Here ***eq. (2.3)*** could be applied where $C_5 = 0.25$ and $n_5 = 1.9$. A Finite Element Method (FEM) analysis of hollow-sphere foams including simple, body-centered and face-centered cubic configurations under consideration of the neck geometry of the bond between spheres was conducted by Sanders (2003, pp. 150-161, [264]). The variety of resulting structures could be well described using ***eq. (2.3)*** where C_5 ranges from 0.65 to 1 and n_5 from 1.3 to 1.36. Apparently, here the face-centered cubic (*fcc*) configuration has superior properties over simple cubic (*sc*) or body-centered cubic (*bcc*) packing since it yields the smallest exponent n_5. For tetrahedral lattice truss sandwich structures made from perforated and folded aluminum sheets, Kooistra (2004, pp. 4229-4237, [164]) established hypothetical and experimental results on their compressive behaviour at relative densities between 0.02 and 0.08. It was found that the tetrahedral lattice trusses are superior to open-cell foams and comparable to the hypothetically high strength of closed-cell foams. At low relative densities, however, they definitely outperform closed-cell, stochastic materials. Typical yield strength values for cellular materials made from aluminum range between 1.39 and 12.7 MPa at relative densities between 0.079 and 0.25. Their specific yield strengths result in a bandwidth from 17.59 to 50.58 MPa/kg.

High strain rate experiments with cellular materials were conducted by only few researchers. Mukai (1999, pp. 365-371, [212]) tested the sensitivity to strain rate of the plateau stress of an open-cell AZ91 magnesium alloy sponge with a relative density of 0.03 as well as the bulk material. Over 6 orders of magnitude in the range of $1\cdot10^{-3}$ s^{-1} to $1.8\cdot10^{3}$ s^{-1} the bulk material showed only 10 % increase in plateau stress, whereas for the sponge material the plateau stress was approximately doubled for strain rates between $1\cdot10^{-3}$ s^{-1} and $1.4\cdot10^{3}$ s^{-1}. Very similar results were obtained by Kanahashi (2000, pp. 349-353, [155]) who analyzed an open-cell SG91A aluminum sponge with relative densities ranging from 0.03 to 0.06. The bulk material showed only 10 % increase in stress during plastic deformation for strain rates from $1\cdot10^{-3}$ s^{-1} to $1.5\cdot10^{3}$ s^{-1}, whereas the cellular material showed approximately 60 % increase in plateau stress for strain rates from $1\cdot10^{-3}$ s^{-1} to $1.4\cdot10^{3}$ s^{-1}. Further observations were that for the open-cell material the yield strength did not change at dynamic strain rates compared to quasi-static strain rates and that the higher the strain rate was the more distinct the peak stress appeared to be. For open-cell sponges with very low density (below 0.1) Lankford Jr. (1998, p. 104, [175]) investigated the air flow through the tortuous structure, compared the results to high strain rate experiments conducted under a partial vacuum and found that the strain rate takes no influence on strength values. Such open-cell behaviour can be confirmed with data acquired by Dannemann (2000, pp. 157-164, [72]) who examined open-cell as well as closed-cell aluminum foams at strain rates from $1\cdot10^{-3}$ s^{-1} to $2.5\cdot10^{3}$ s^{-1} with relative densities ranging from 0.074 to 0.15. For closed-cell foams it was found that their yield strength exhibits a significant dependency on the strain rate. The inertia of gas movement through the cells as they rupture was identified to be the main reason for this phenomenon. Therefore, over a raise of 6 orders of magnitude in strain rate an increase of 60 to 120 % in yield strength was determined.

Some results on multiaxial compressive loads can be found (Gioux, 2000, pp. 1097-1117, [124]) that were obtained for an open-cell ERG Duocel sponge (relative density 0.07) and for a closed-cell Alporas foam (relative density 0.08). Though both materials were stochastic, these specimens failed under biaxial compressive load rather by stretching of cell walls and struts in contrast to uniaxial load which noticably raised the yield strength. However, in triaxial (i.e. hydrostatic) loading, failure was bending-dominated again and yield strengths were near the values of uniaxial loading. Typical yield surfaces for failure mechanisms such as elastic buckling, plastic yielding and brittle fracture of cellular materials under multiaxial compressive and tensile loads were developed theoretically and verified experimentally by Triantafillou (1991, pp. 9-14, [298]).

$$\frac{\sigma^*_{yield,h}}{\rho^*_h} = \frac{E_{solid}}{\rho_{solid}} \cdot ck^h \cdot \left(\frac{\rho^*_h}{\rho_{solid}} \right)^{n_1 - 1 + \frac{n_2 - n_1}{h}} \tag{2.5}$$

Lakes (1993, pp. 513-514, [174]) introduced the concept of hierarchical structure where cellular materials themselves are made from structural elements like e.g. porous struts. This concept gives rise to much lighter weight at a given strength. This was shown for open-cell lattice, honeycomb and tubular geometries where each level of hierarchy represents a different size scale. Vice versa at a given weight the hierarchical structure enhances strength. The reason for the improved strength is the suppression of buckling which occurs in solid slender parts (like e.g. struts) without hierarchical structure significantly before the onset of yield. The higher the level of hierarchy h the greater the buckling strength becomes. Typically beyond the hierarchical order of 3 the buckling strength exceeds the yield strength, therefore no further gain can be anticipated. The strength-to-density ratio of a structure of hierarchical order h can be described by ***eq. (2.5)*** where the multiplier c and the exponents n_1 and n_2 are parameters which depend on the failure mode of the material's cell walls and struts and k is a structural factor which deviates from unity only for frameworks. ρ_h is the density that the material still posseses at h^{th} order of hierarchy. Experiments showed that a second order hierachical honeycomb yields an increase in compressive strength by a factor of up to 3.8, whereas the theory even predicts an improvement by a factor of 4.6.

2.1.4.2 Tensile strength

The tensile stress-strain curve of cellular materials deviates substantially from the compressive curve. First an initial settling and a linear-elastic regime can be observed with increasing strain of a specimen under tension. According to Gibson (1997, pp. 217-218, [123]) the same mechanism of bending of cell edges or struts is responsible for the onset of plastic yield. However, no plateau stress can be observed since rotation of cell edges or struts ceases as soon as they are aligned with the tensile axis. Therefore, the stress rises much faster with increasing strain when the second mechanism of plastic extension of cell edges or struts prevails.

Fig. 2.12 documents how the growth of first cracks can slightly relax tension during this phase before the ultimate tensile strength is reached and the propagation of at least one major crack triggers fracture and thus complete failure of the part (Rehme, 2006). As the strain further increases, two different response curves should be distinguished for cellular materials. Some of them, which behave ductile under compressive forces, exhibit brittle failure under tension (McCullough, 1999, p. 2329, [196]) while others are ductile under tension as well. Therefore, bending- and stretch-dominance can be established again. The dotted line represents a ductile behaviour under tension where the force decreases exponentially with strain such that typically long elongations can be obtained before rupture of the part happens. This case of bending-dominance where the bending of cell edges or struts can take place over a wide elongation length should be accounted for open-cell materials or closed-cell materials of low edge connectivity. Along the dashed line the force decreases slower at an approximately linear rate until sudden rupture occurs. This case shows the rather brittle, stretch-dominated behaviour where cell walls or struts are stretched and hence fail at lower strains compared to the previous case. Either curve shows typical strain hardening response, a mechanism well known from solid metals on the level of grain boundaries. In cellular materials this effect has an apparent macroscopic impact whenever the transition from rotation to stretching of cell walls or struts takes place in one layer of cells.

Gibson (1997, p. 217, [123]) stated that due to the similarity of failure mechanisms under compression and tension ***eq. (2.3)*** and ***eq. (2.4)*** hold as well for the estimation of tensile yield strength. Experimental and calculative results from other researchers support this assumption

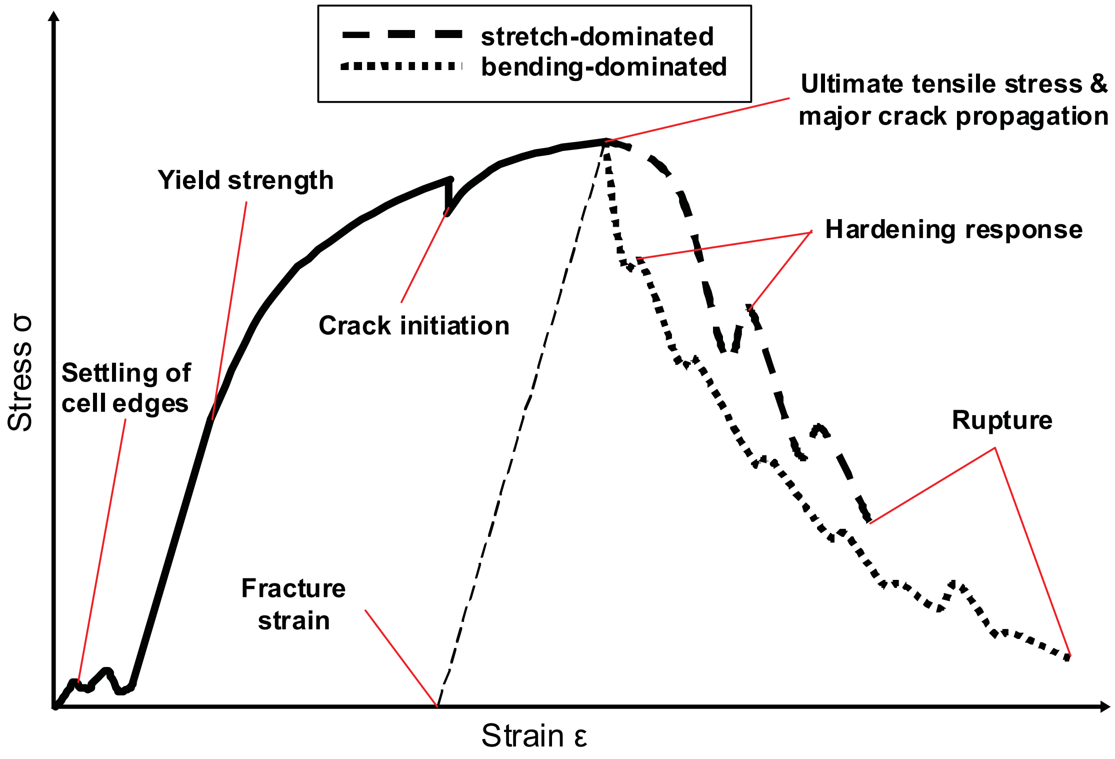

Figure 2.12: General tensile behaviour of cellular solids

for a variety of open-cell and closed-cell materials such as ERG Duocel, Alporas, Alulight und hollow spheres (Harte, 1999, p. 2513, [135]), (McCullough, 1999, p. 2325, [196]) and (Sanders, 2003, p. 160, [264]). In this specific context Brothers (2005, p. 4435, [46]) suggested that for open-cell materials C_5 in ***eq. (2.3)*** can be fitted best if the geometric mean of the compressive and the tensile yield strength of the according bulk material is used. However, other findings like those obtained by Ashby (2000, p. 53, [17]) document that tensile strength is for both open-cell and closed-cell materials greater by a factor between 1.1 and 1.4. Nonetheless, this result remains unclear since no comment was made on the choice of materials and other boundary conditions. In contrast, Andrews (1999, p. 121, [10]) found for the above mentioned aluminum foams and sponges tensile yield strength values of only 0.40 to 0.89 times the compressive yield strength.

Apart from these slightly confusing correlations Motz (2001, p. 2467, [210]) obtained representative results on tensile strength properties of closed-cell aluminum foams by examination of Alporas foams. Relative densities were 0.093 and 0.148 at an average cell size of 3.5 mm. Measured characteristic values included the yield strength with average values of 0.71 MPa for the lower and 1.79 MPa for the higher relative density, the ultimate tensile strength (1.70 MPa and 3.95 MPa), the unloading Young’s modulus (1630 MPa and 3680 MPa), the fracture strain (2.3 % and 3.1 %), the work-hardening exponent (0.34 and 0.30) and the plastic Poisson’s ratio (0.332 and 0.420). The work-hardening exponent was deduced from the slope of the plastic regime of the tensile stress-strain curve in a double logarithmic plot, whereas the plastic Poisson’s ratio resulted from the slope of the curve of the transverse versus the longitudinal strain. Values for specific yield strength were presented by Jancek (2003, pp. 132-134, [154]) who analyzed foams made from compacted AlSi10 powder regarding their behaviour under tensile load. After manufacturing the foam had a relative density of around 0.15 and a skin of metal, oxide and compressed pores. In the foam core gradually distributed cell sizes were found with the largest cells in the center. The yield strength of dog-bone shaped specimens was in the range of 1 to 1.5 MPa and the specific yield strength between 24.92 and 37.38 MPa/kg.

2.1.4.3 Shear strength

Little is known from the literature on the shear strength of cellular materials. According to Andrews (2001, pp. 703-707, [12]) a characteristic stress-strain diagram of a specimen in shear load matches roughly the diagram for tensile load displayed in ***fig. 2.12***. In this context a closed-cell Alporas aluminum foam with relative densities in the range of approx. 0.067 to 0.079 was investigated. The dimensions of the specimens were selected from 5 different thicknesses from 6 to 30 mm, a width of 55 mm and a constant length to thickness ratio of 12. In the according shear tests ultimate shear strengths between 1.11 and 1.64 MPa were obtained where on average the strength rose with the specimen’s relative density. Similar results were received in a study conducted by Saenz (1998, p. 88, [262]) who tested a different closed-cell aluminum foam with relative densities between 0.35 and 0.38. The average shear strength was around 1.03 MPa and the average specific shear strength was 0.0029 MPa/kg·m^3, respectively. However, this second foam turned out to show extremely brittle behaviour such that the point of rupture directly followed the yield point unlike the scenario in ***fig. 2.12***. Both analyses did not give a correlation of shear strength and relative density of the material used.

Other experimental results can be found (von Hagen, 1998, pp. 63-64, [133]) where two commercially available closed-cell aluminum foams were tested and the ultimate shear strength was measured. Here, the results suggest that the relative shear strength can be described by a simple power law as presented in ***eq. (2.3)***. In the case of the rather ductile foam (Alporas) an exponent n_5 of 1.40 was obtained while the other more brittle foam (Alcan) showed an almost linear dependency of relative shear strength on relative density with an exponent n_5 of 0.99.

Rising shear strength with increasing relative density was also found by Sanders (2003, p. 159, [264]) who developed formulae for the relative yield shear stress of open- and closed-cell materials. Here, the relativity was implemented not in regard to the yield strength in shear of the according bulk material but to the yield strength in compression using the yield criterion derived by Deshpande (2000, pp. 1280-1281, [79]). The resulting ***eq. (2.6)*** represents the open-cell case while ***eq. (2.7)*** is the equivalent for closed-cell materials.

$$\frac{\tau^*_{yield}}{\sigma_{yield,solid}} = 0.21 \cdot \left(\frac{\rho^*}{\rho_{solid}} \right)^{1.5} \tag{2.6}$$

$$\frac{\tau^*_{yield}}{\sigma_{yield,solid}} = 0.23 \cdot \left(\frac{\rho^*}{\rho_{solid}} \right)^{2} + 0.30 \cdot \left(\frac{\rho^*}{\rho_{solid}} \right) \tag{2.7}$$

2.1.4.4 Bending strength

Cellular materials are attractive core materials for sandwich structures. Their low relative density allows the manufacture of sandwich panels with cores of nearly arbitrary thickness and with solid face sheets attached to them. These panels offer high bending stiffness around axes parallel to the face sheets which contribute most to the area moment of inertia. The theory of the strength of sandwich structures and their optimum design for stiffness under three-point bending load was discussed by Gibson (1997, pp. 348-370, [123]). It explains four different modes that are mainly responsible for the failure of sandwich panels:

- face sheet yield (the side that is exposed to tensile forces)
- face sheet wrinkle (the side that is exposed to compressive forces)
- core shear
- decohesion of the interfacial bond between core and face sheet

Other failure modes such as indentation of the face sheets can usually be avoided by properly distributing the load over a greater contact area or length. For optimum design one can create a so-called failure mode map where the load equations for the first three failure modes are equated. The solutions are constraints for the design parameters which, if displayed in the diagram, divide this into fields showing the dominating failure mode in dependency of the geometric variables of sandwich panel design.

Although sufficient theoretical background exists, not much experimental data is available on the bending behaviour of sandwich panels containing cellular materials in their cores. Deshpande (2001, pp. 6275-6276, [78]) conducted tests on sandwich beams manufactured from investment cast tetrahedral truss cores. The materials used were an Al-Si alloy as well as a silicon brass alloy. All specimens were between 110 and 190 mm long and 65 to 130 mm wide. They were equipped with either solid face sheets or with connective struts between unit cell vertices in the planes where otherwise the face sheets would have been placed. The latter were the so-called triangulated face sheets. In the case of solid face sheets the specimens of both materials failed by core shear which, however, occurred only in the center region of the specimens instead of across their full length. The Al-Si alloy showed yield strengths of roughly 2000 N while the silicon brass alloy sustained roughly 2500 to 3000 N. As often observed in tensile tests, a similar crack propagation and strain-hardening response occurred before the ultimate strength was reached at values typically two or three times higher than the yield strength. The sandwich beams with triangulated face sheets made from the Al-Si alloy failed from face yielding, whereas those made from the silicon brass alloy suffered from face wrinkling. Here, the yield strengths ranged roughly between 1000 and 2000 N for the former alloy and between 1500 and 3000 N for the latter.

2.1.4.5 Elastic buckling

When metal foams and sponges collapse they typically show plastic deformation. However, in the case of very low relative densities it is possible for elastic failure to precede plastic collapse. This occurs by elastic buckling of cell walls or struts which exhibit a greater extension the smaller the relative density is. Gibson (1997, pp. 198-199, [123]) derived ***eq. (2.8)*** from the Euler formula for elastic buckling of slender columns with a factor C_4 of 0.05. This correlation is valid for the failure strength σ^*_{buckle} of open-cell sponges with a relative density below 0.3. If the relative density resides above this value, then elastic buckling is less likely to occur, therefore ***eq. (2.9)*** gives a density correction where the factor C_4' is 0.03. In the case of closed-cell sponges ***eqs. (2.8)*** and ***(2.9)*** apply as well, however, an additional term $(p_{cell} - p_{at})$ is added to σ^*_{buckle} where p_{cell} is the pressure of the gas or fluid inside the cells and p_{at} is the environmental pressure. Inner excess pressure accounts for tension on the cell walls which needs to be overcome for buckling to occur.

$$\sigma^*_{buckle} = C_4 \cdot E_{solid} \cdot \left(\frac{\rho^*}{\rho_{solid}} \right)^2 \tag{2.8}$$

$$\sigma^*_{buckle} = C_4^{'} \cdot E_{solid} \cdot \left(\frac{\rho^*}{\rho_{solid}} \right)^2 \left(1 + \sqrt{\frac{\rho^*}{\rho_{solid}}} \right)^2 \tag{2.9}$$

To correctly predict the failure strength in compressive load situations it is required to estimate which one is lower: the elastic buckling strength or the yield strength according to ***eqs. (2.8)*** and ***(2.3)***. Solved for the relative density one obtains the stability criterion in ***eq. (2.10)*** which gives the minimum relative density at which failure by elastic buckling can still occur. An important consideration in this context is the applicable exponent n_5 from

eq. (2.3) as it can cause a significant transition of the threshold. Typical values for the quotient of yield strength and elastic modulus can attain values between 0.00238 and 0.00666 for the metallic materials considered in this thesis. Therefore, for values of n_5 near 2 elastic buckling might never occur since the fabrication of relative densities below 0.05 is hardly feasible due to stability reasons.

$$\frac{\rho^*}{\rho_{solid}} > \left(\frac{C_5}{C_4} \cdot \frac{\sigma_{yield,solid}}{E_{solid}} \right)^{\frac{1}{2-n_5}} \tag{2.10}$$

2.1.4.6 Young's modulus

The stress-strain curves in ***fig. 2.10*** and ***2.12*** both show the linear-elastic regime of compressive and tensile loads where deformation is reversible and linearly proportional to the applied stress. The Young's modulus E is a measure of the stiffness which for small strains ranging in this linear-elastic regime is defined as the slope of the curve $\Delta\sigma/\Delta\varepsilon$ also known as Hooke's law. In cellular materials the reduced density results in decreased stiffness. Thus the relative effective modulus of elasticity is obtained from the reduced stiffness divided by the Young's modulus of the bulk material.

Ko (1965, pp. 49-50, [163]) considered hexagonal closest (*hcp*) and face centered cubic (*fcc*) packing of identical spheres. These two ways of packing yield the highest known density of 0.74 or, if the spheres are taken as voids, the highest known porosity and thus a minimum density of 0.26. If the spheres were expanded such that their surfaces become flat wherever a neighbour sphere is contacted, then the *hcp* composition would become a space-filling array of trapezo-rhombic dodecahedrons, whereas the *fcc* packing would show a space-filling array of rhombic dodecahedrons. All dodecahedrons were then reduced to their cell edges by removing the cell walls. The dependency of Young's modulus on the relative density of the resulting lattice structure was calculated. In the case of *hcp* a linear proportionality was found suggesting that the overall elasticity is dominated by stretching of struts. For the *fcc* packing a quadratic dependency was calculated, implying that bending appears to be the dominant mechanism of elasticity.

The same model for the strength of cellular solids established in ***eqs. (2.3)*** and ***(2.4)*** is used (Gibson, 1997, pp. 184-197, [123]) to explain Young's modulus of open-cell and closed-cell materials. Derived from this concept the stiffness of open-cell structures depends on beam bending of the struts and leads to ***eq. (2.11)*** where the constants were analytically determined to $C_1 = 1$ and $n_1 = 2$. In contrast, closed-cell structures show a distribution of their solid mass where a fraction ϕ resides in the cell edges while another fraction $(1-\phi)$ is found in the cell walls. All explanations from ***eq. (2.4)*** on the mechanisms of cell-edge bending (giving a quadratic term) and cell wall stretching (resulting in a linear term) hold here as well and give rise to ***eq. (2.12)***. In this formula the same values for constants C_1 and n_1 were suggested as in ***eq. (2.11)*** and C_1' is expected to be equal to C_1. However, two mechanisms are missing in ***eq. (2.12)*** because their influence is often ignored, i.e. cell wall bending which would give another cubic term and the compression of fluid contained inside the cells which depends on the inverse of unity minus the material's relative density. Both mechanisms result in very small numbers compared to the rest of ***eq. (2.12)*** and are thus often ignored.

$$\frac{E^*}{E_{solid}} = C_1 \cdot \left(\frac{\rho^*}{\rho_{solid}} \right)^{n_1} \tag{2.11}$$

$$\frac{E^*}{E_{solid}} = C_1 \phi^2 \cdot \left(\frac{\rho^*}{\rho_{solid}} \right)^{n_1} + C_1^{'} (1 - \phi) \frac{\rho^*}{\rho_{solid}} \tag{2.12}$$

In their micromechanical analysis of open-cell and closed-cell materials with tetrakaidecahedral unit cells Warren (1997, pp. 791-793, [311]) suggested that, besides bending of cell edges and stretching of cell walls, homogenous deformation is also accompanied by torsion of the struts or cell edges, respectively, which was declared an important strut-level deformation mechanism. ***Eq. (2.11)*** was used to derive models for different strut or cell edge geometries. The variations of parameter C_1 depending on the according cross section profile is given in ***table 2.2*** while the exponent n_1 maintained a value of 2. The hypercycloidial profile is also known as the so-called Plateau border shape and is explained best with a triangular profile obtained from three touching circular arcs.

The general affinity to the tetrakaidecahedral unit cell model stems from its realistic cell wall arrangement compared to actual metallic foams as it represents a state of minimum surface energy for closed-cell foams (Thomson, 1887, p. 507, [292]). One unit cell consists of six square and eight hexagonal faces and is obtained by truncating the corners of a cube such that the faces from all truncated corners are in contact with each other. The advantage of this model is its low anisotropy since e.g. its elastic modulus varies within less than 10 % with direction of loading (Roberts, 2001, p. 190, [259]). Therefore, like many others, Zhu (1997, pp. 336-337, [333]) employed this model in an analysis for open-cell foams based on beam theory. For different cross sections ***eq. (2.13)*** was obtained where equilateral triangular cross sections of cell struts resulted in values of 0.726 and 1.09 for factor C_a and factor C_b, respectively. In contrast, the hypercyloidial shape leads to the values 1.009 and 1.514.

$$\frac{E^*}{E_{solid}} = \frac{C_a \cdot \left(\frac{\rho^*}{\rho_{solid}} \right)^2}{1 + C_b \cdot \frac{\rho^*}{\rho_{solid}}} \tag{2.13}$$

Table 2.2: Influence of various cross section profiles on parameter C_1

Shape of cross section profile of a strut		C_1
Circular	○	0.593
Square	□	0.619
Equilateral triangle	△	0.710
Hypercycloidial		0.979

Yet a different approach was used by Roberts (2001, pp. 192-193, [259]) who applied a Voronoi tesselation model. In this model spheres grow with uniform velocity from seed points that were randomly distributed in space. Wherever two spheres make contact, growth is stopped while elsewhere growth is continued. This results in a typical distribution of cells and cell sizes similar to actual metallic foams. Besides, a *bcc* distribution of seed points would lead to the above mentioned tetrakaidecahedral unit cell structure. In their study the result of a random Voronoi tesselation was evaluated with FEM calculations in which the relative density was changed by varying the thickness of the cell faces. For small relative densities between 0.1 and 0.3 of closed-cell foams a simple power law like ***eq. (2.11)*** was found to describe the dependence of the relative effective stiffness where C_1 and n_1 were determined as 0.563 and 1.19. Calculcations for open-cell sponges were derived from Voronoi tesselations where the cell faces were removed by defining only the cell edges as solid. The obtained relative densities between 0.04 and 0.5 resulted in values of $C_1 = 0.930$ and $n_1 = 2.04$, respectively (Roberts, 2002, p. 42, [260]). However, as relative density approaches unity this simple power law cannot hold if C_1 is not equal to 1. Therefore, ***eq. (2.14)*** was suggested, i.e. for relative densities between 0.15 and 1 with values of $p = -0.140$ and $n = 2.09$ for the closed-cell case or in the open-cell case for relative densities between 0.04 and 1 with values of $p = -0.0056$ and $n = 2.12$, respectively.

$$\frac{E^*}{E_{solid}} = \left(\frac{\frac{\rho^*}{\rho_{solid}} - p}{1 - p} \right)^n \qquad \textbf{\textit{(2.14)}}$$

Most other investigations typically delivered a simple power law similar to ***eq. (2.11)*** as well. An aluminum foam with relative densities between 0.15 and 0.3 and cell sizes between 0.45 to 1.35 mm was examined by Kováčik (1998, p. 245, [165]). Elasticity was obtained from the resonant frequencies of free vibrations of the samples. Here, an exponent n_1 with a value of 1.65 was found, whereas the proportionality factor C_1 showed almost no deviation from unity. Ströhla (2000, p. 445, [282]) applied a beam-bending model on 5 x 5 x 5 cell blocks of tetrakaidecahedral and rhombic dodecahedral unit cells in order to calculate the elastic properties of cellular materials. These calculations resulted in values for the exponent n_1 and factor C_1 of 2.12 and 1.35 for the tetrakaidecahedral unit cell while the rhombic dodecahedral structure delivered values of 2.47 and 1.32. All values are derived from according diagrams.

Often metallic cellular materials turn out to be less strong in experiments than predicted by the according theory (McCullough, 1999, p. 2326, [196]) as explained above. Grenestedt (1998, pp. 7-12, [131]) made an analytical evaluation of the influence of imperfections inside closed-cell materials on their stiffness. Among different possible mechanisms like waviness or thickness variations of cell walls and shape variations of cells, stiffness was found to be especially sensitive to waviness of cell walls but insensitive to thickness variations of cell walls and shape variations of cells. Sanders (1998, p. 53, [265]) assessed own FEM calculations and rather held the cell wall curvature and cell wall corrugations responsible for a reduction of up to 70 % in strength and elasticity modulus.

As previously explained for ***eq. (2.5)*** Lakes (1993, p. 513, [174]) developed a concept of modeling the behaviour of hierarchical structures where the material in cellular solids exhibits small size scale structures leading to less weight. Thus the resulting stiffness is decreased and for material with h orders of hierarchy ***eq. (2.15)*** was suggested. The exponent n_1 should attain a value of 2 in the case of open-cell foams where bending of struts dominates while it should be 1 if axial loading of struts dominates (e.g. expected in honeycombs loaded out of plane or in frameworks). This basically complies with the considerations made for ***eq. (2.11)*** and ***eq. (2.12)***. Except for 3D-frameworks where the structural factor k is less than unity, k is exactly 1 in all other instances. Therefore, hierarchical structure has practically no influence on Young's modulus unless 3D-frameworks are applied.

$$\frac{E_h^*}{E_{solid}} = k^h \cdot \left(\frac{\rho^*}{\rho_{solid}} \right)^{n_1} \tag{2.15}$$

2.1.4.7 Shear modulus

Similar to Young's modulus the shear modulus G describes a material's reversible linear-elastic deformation under shear load. The shear modulus (or modulus of rigidity) and Young's modulus are related to each other by ***eq. (2.16)*** which incorporates the Poisson's ratio ν (see ***section 2.1.4.9***).

$$G = \frac{E}{2 \cdot (1+\nu)} \tag{2.16}$$

Analogous to both assumptions of beam bending of struts or cell edges and of cell wall or cell edge stretching, established for the effective Young's modulus of open- and closed-cell materials, Gibson (1997, pp. 186-197, [123]) derived formulae for the according effective shear moduli given in ***eqs. (2.17)*** and ***(2.18)*** where the values of parameters C_2 and C_2' were suggested as 3/8 and n_2 as 2. Here, the effective shear modulus G^* was correlated with the elasticity modulus of the bulk material rather than its shear modulus due to the fact that shear strain is proportional to this material constant. If, however, the real relative shear modulus was needed, it could be easily calculated by substitution of E_{solid} with the help of ***eq. (2.16)***.

$$\frac{G^*}{E_{solid}} = C_2 \cdot \left(\frac{\rho^*}{\rho_{solid}} \right)^{n_2} \tag{2.17}$$

$$\frac{G^*}{E_{solid}} = C_2 \phi^2 \cdot \left(\frac{\rho^*}{\rho_{solid}} \right)^{n_2} + C_2^{'} (1-\phi) \frac{\rho^*}{\rho_{solid}} \tag{2.18}$$

Warren (1997, p 791, [311]) presumed that the shear modulus of cellular solids is sensitive to its topology and to the cross section shape of its struts or cell edges. ***Eq. (2.17)*** was also employed in the according tetrakaidecahedral unit cell model where exponent n_2 was fixed at a value of 2 as well. However, C_2 resulted in values given in ***table 2.3*** depending on the cross section profile.

Table 2.3: Influence of various cross section profiles on parameter C_2

Shape of cross section profile of a strut		C_2
Circular	○	0.20008
Square	□	0.20950
Equilateral triangle	△	0.24194
Hypercycloidial		0.33639

Other investigations with analytical approach (Ströhla, 2000, p. 446, [282]) delivered values $C_2 = 0.50$ and $n_2 = 2.39$ for tetrakaidecahedral unit cells while the rhombic dodecahedral structure showed values of $C_2 = 0.41$ and $n_2 = 2.28$. Alternatively, ***eq. (2.19)*** was suggested also based on a tetrakaidecahedral unit cell model (Zhu, 1997, p. 337, [333]).

$$\frac{G^*}{E_{solid}} = \frac{0.2333 \cdot \left(\frac{\rho^*}{\rho_{solid}}\right)^2}{1 + 0.700 \cdot \frac{\rho^*}{\rho_{solid}}} \tag{2.19}$$

2.1.4.8 Bulk modulus

The bulk modulus K is the incompressibility of a material, i.e. its resistance against uniform or hydrostatic pressure in the regime of reversible linear-elastic deformation. The bulk modulus is as well related to Young's modulus by the expression in ***eq. (2.20)***.

$$K = \frac{E}{3 \cdot (1 - 2\nu)} \tag{2.20}$$

In their analytical investigation Warren (1997, p. 791, [311]) found that in contrast to the shear modulus the relative bulk modulus does not appear to depend on specific geometry of a foam or sponge. Instead it exhibits a linear correlation to the material's relative density according to ***eq. (2.21)*** which was also confirmed by Zhu (1997, p. 337, [333]).

$$\frac{K^*}{E_{solid}} = \frac{1}{9} \cdot \frac{\rho^*}{\rho_{solid}} \tag{2.21}$$

2.1.4.9 Poisson's ratio

The Poisson's ratio ν gives a relation of the negative transverse strain to the longitudinal strain of a material exposed to uniaxial tension or compression. The longitudinal strain occurs in the load direction, whereas the transverse strain is found normal to this axis. The Poisson's ratio links the elastic moduli and can be found from the formulae in ***eqs. (2.16)***, ***(2.20)*** and ***(2.22)*** where E is Young's modulus, G is the shear modulus and K is the bulk modulus.

$$\nu = \frac{3K - 2G}{6K + 2G} \tag{2.22}$$

In tension a material's volume can increase or remain constant while the behaviour in compression is vice versa. If quadratic strain terms are disregarded for small strains, then the relative volume change of the material is proportional to longitudinal strain by a factor of (1–2ν) due to thermodynamic considerations of strain energy (Lakes, 1987, p. 1038, [173]). Therefore, the Poisson's ratio of a material cannot exceed 0.5, typical values range between 0 and 0.5 where 0.5 is an incompressible material. The main materials considered in this thesis such as stainless steel, aluminum and titanium show values of 0.3, 0.33 and 0.34, respectively. However, some materials can exhibit negative values between –1 and 0 which can e.g. happen in the case of foam, sponge and specially designed materials. These are also referred to as auxetic materials. ***Table 2.4*** summarizes typical materials which represent special cases of Poisson's ratio (Lakes, 1993, p. 696, [172]). Values greater than 0.5 can occur if cells are elongated such that the cellular structure shows significant anisotropic mechanical properties as it can be the case in undeformed hexagonal honeycombs or strongly deformed foams (Wang, 2001, p. 380, [309]). Materials with a negative Poisson's ratio are envisaged in applications for artificial intervertebral discs or for the damping of vibrations and sound as well as impact energy (Martz, 1996, p. 230, [193]).

A negative Poisson's ratio in isotropic materials can be obtained in the following ways (Lakes, 1991, pp. 2288-2290, [171]), (Choi, 1992, p. 5373, [59]), (Chen, 1991, p. 5400, [54]), (Prall, 1997, p. 305, [231]):

- non-affine deformation kinematics (i.e. unfolding of unit cells in foams and sponges),
- rotational degrees of freedom in lattice nodes connected by some ligaments of negative

Table 2.4: Extremal Poisson's ratios and their engineering consequences

Material	***v***	**Characteristics**	**Engineering consequences**
Rubber	0.5	$\lim\limits_{\nu\to 0.5}\left(K = \frac{2G(1+\nu)}{3(1-2\nu)}\right) = \infty$ $\lim\limits_{\nu\to 0.5}\left(G = \frac{3K(1-2\nu)}{2(1+\nu)}\right) = 0$	• incompressible • minimum shear strength
Cork	0	$\lim\limits_{\nu\to 0}\left(K = \frac{2G(1+\nu)}{3(1-2\nu)}\right) = \frac{2}{3}G$ $\lim\limits_{\nu\to 0}\left(G = \frac{3K(1-2\nu)}{2(1+\nu)}\right) = \frac{3}{2}K$ $\lim\limits_{\nu\to 0}\left(E = 2G(1+\nu)\right) = 2G$	• shear strength exceeds compressibility • stiffness exceeds shear strength • transverse strain equals zero in tension and compression
Ideal re-entrant cellular material	-1.0	$\lim\limits_{\nu\to -1}\left(K = \frac{2G(1+\nu)}{3(1-2\nu)}\right) = 0$ $\lim\limits_{\nu\to -1}\left(G = \frac{3K(1-2\nu)}{2(1+\nu)}\right) = \infty$ $\lim\limits_{\nu\to -1}\left(E = 2G(1+\nu)\right) = 0$	• easy to compress • maximum shear strength • minimum stiffness

stiffness (due to prestrain) or
- noncentrosymmetry (chirality) where a structure differs from its mirror image and has therefore no center of symmetry.

If negative Poisson's ratio materials are not obtained from specifically designed materials they can also be manufactured from conventional metallic foams and sponges. The most investigated material is the so-called re-entrant structure where the cell walls or struts protrude rather inward than outward giving rise to a concave shaped unit cell. Since the theory of elasticity has no length scale a coarse cellular structure should not be required which allows to expect that even the transformation of microstructures smaller than 1 μm into re-entrant structures is possible. Their manufacture from conventional low-density foams and sponges made from random metallic materials incorporates permanent compression in three orthogonal directions. Some materials can be transformed by simple application of triaxial hydrostatic pressure, however, for ductile metal foams and sponges a subsequent uniaxial compression at room temperature is necessary until yield occurs. The major modifications induced are the formation of plastic hinges and the plastic buckling of cell walls or struts. The strain applied in each direction determines the alterations of the structure and thus the total volumetric compression ratio (Friis, 1988, p. 4407, [117]). Another method was suggested by Martz (1996, p. 234, [193]) for closed-cell foams where the foam is exposed to a vacuum such that the cell walls stretch as the gas entrapped in the cells expands. The reintroduction of atmospheric or higher pressure causes the cell walls to buckle plastically, creating a re-entrant structure. It was observed that this method results in a negative Poisson's ratio along only one of three orthogonal axes. The most important parameters in transforming a foam or sponge into a re-entrant structure are temperature, time and volumetric compression ratio (Wang, 2001, p. 374, [309]). Typically, in testing of re-entrant materials the volumetric compression ratio is considered preferentially. Choi (1995, pp. 117-127, [58]) derived a model for the theoretical Poisson's ratio at small linear elastic strains according to ***eq. (2.23)*** where φ is the angle of a specific cell strut pointing inwards into the unit cell at ranges of $0.25\pi < \varphi < 0.5\pi$ (45 to 90°). In this model theoretical volumetric compression ratios between 1.4 and 4.8 are required for the creation of re-entrant foams and sponges. According to the theory the lowest Poisson's ratio can be obtained at the highest volumetric compression ratio of 4.8 which is expected to be valid for elasto-plastic as well as brittle materials.

$$\nu = -\frac{\sin(\varphi - 0.25\pi)}{\cos(\varphi - 0.25\pi)} \tag{2.23}$$

Gibson (1997, p. 193, [123]) observed large scatter and no trend for the dependency of Poisson's ratio on relative density in the compression of conventional foams and sponges. However, Ströhla (2000, p. 445, [282]) and Warren (1997, p. 793, [311]) noticed that Poisson's ratio reaches 0.5 for relative densities approaching zero and found that it decreases exponentially to the value of the bulk material towards relative densities near unity.

Compressive tests were conducted by Friis (1988, pp. 4408-4410, [117]) on a conventional open-cell copper sponge with initial relative density of 0.053 transformed into a re-entrant structure by triple uniaxial compression with a total volumetric compression factor of 1.7. Infered from the author's diagrams the conventional sponge showed yield strengths of roughly 0.25 MPa at 3.5 % elastic strain while the re-entrant structure failed only at 1 MPa stress and 15 % elastic strain with significantly reduced Young's modulus. The Poisson's ratio of the conventional copper sponge exhibited values of around 0.42, whereas the re-entrant sponge showed a value of –0.39 in the initial stages of compression with progressively increasing values as the magnitude of axial strain increased. More detailed results were obtained by Choi (1992, pp. 5374-5375, [59]) who also determined that strain-hardening does not occur with re-entrant foams and sponges in both tension and compression. Copper sponges with initial relative densities of 0.04, 0.08, 0.09 and 0.1 were transformed into re-entrant structures by sequential deformation in three orthogonal directions. The smallest Poisson's ratio obtained from these specimens was –0.8 at zero strain for the sponge with an initial relative density 0.1 and a volumetric compression ratio of 2.13. In the correlation of Poisson's ratio versus compression ratio at different relative densities the Poisson's ratio attains a minimum value at a specific volumetric compression ratio for each relative density. This specific compression ratio is the smaller the higher the initial relative density was. Young's modulus is influenced by the volumetric compression ratio such that compressive stiffness increases with volumetric compression while tensile stiffness behaves vice versa. The influence of volumetric compression ratio on yield strength was found to be similar. In conventional foams and sponges the yield strength in tension and in compression was mostly observed to be similar (see above). In re-entrant foams and sponges, however, the yield strength decreased under tensile load with the compression ratio and increased in compressive load. Explanations of the strength's decrease in tension rely on the weakness of the plastic hinges formed in the cell walls or struts while in compression the contact of cell walls or struts accounts best for the increase in strength.

At zero strain the Poisson's ratio of conventional foams and sponges will generally show a significant non-linear dependency on the amount and direction of strain. The Poisson's ratio drops in compression, however, remains greater than zero. In tension it will rise to a maximum close to 0.5 before it slightly decreases at continued strain. If the cell size is increased, the maximum Poisson's ratio should be obtained at smaller tensile strains. However, re-entrant structures on the other hand show their minimum Poisson's ratio at zero strain. Both compressive and tensile strain increase the Poisson's ratio which although remains below zero. If in the case of a re-entrant structure the cell size is increased, then the minimum Poisson's ratio decreases since the bending of cell walls or struts can occur more easily allowing e.g. concave cell struts to bulge out (Wang, 2001, p. 380, [309]).

Table 2.4 as well as some material testing results give insight into the advantages of negative Poisson's ratio materials which can mainly be found in high shear strength and high resilience. Besides these properties the resistance against indentation can also be maximized by applying materials with negative Poisson's ratio since indentation is proportional to the impinging pressure by the factor $(1-\nu^2)/E$ which equals zero in the case of $\nu = -1$ (Lakes, 1987, p. 1040, [173]). Likewise, the fracture toughness (further explained below in

section 2.1.4.13) of negative Poisson's materials can be increased. Choi (1996, p. 79, [57]) investigated an open-cell copper sponge and found K_{Ic}-values of 120 kPa·m$^{0.5}$ for the conventional sponge with initial relative density of 0.08 and 180 kPa·m$^{0.5}$ for the re-entrant sponge obtained after a volumetric compression by the factor of 2.0. At volumetric compression ratios of 2.0, 2.5 and 3.0 the same re-entrant sponge delivered J_{Ic}-values of 1.4, 1.8 and 2.1 kPa·m while the conventional structure showed only 0.8 kPa·m. These experimental results document a clear rise of fracture toughness for re-entrant materials obtained from subsequent volumetric compression in three orthogonal directions with fracture toughness enhancements of up to 162.5 %.

2.1.4.10 Hardness

In engineering and material sciences hardness is typically referred to as indentation hardness. It characterizes the resistance of a material's surface against plastic deformation caused by an indenter of well defined geometry which varies depending on the test principle used. Most common hardness tests are the Brinell, the Rockwell and the Vickers test. The only literature reference on the hardness of cellular materials is the data available from Tabata (1990, pp. 95-98, [290]) and Lee (1998, pp. 34-35, [179]). The former authors conducted Brinell and Vickers tests on porous sintered copper, aluminum and iron specimens to determine the correlation between hardness and yield strength of the specimens in dependence of the relative density. The latter used these findings to compare them with FEM calculations for porous copper specimens of identical dimensions. Both approaches are in good agreement and show a linear increase of Brinell hardness with increasing relative density according to ***eq. (2.24)*** which was derived from the figures in (Lee, 1998, p. 35, [179]). This formula assumes a value of 45 HB for bulk copper in accordance with literature values between 40 to 50 HB. However, ***eq. (2.24)*** is not valid below the measured relative densities of 0.7 and higher. Below a relative density of 0.52 it would even yield negative hardness values.

$$\frac{HB^*}{HB_{solid}} = 93 \cdot \left(\frac{\rho^*}{\rho_{solid}} \right) - 48 \qquad \textbf{\textit{(2.24)}}$$

2.1.4.11 Fatigue

Fatigue life is defined as the number of cycles a part can sustain when loaded with alternating stress. It should allow giving estimates on the dynamic failure behaviour of a part. Typically, the upper and lower limit of the stress applied are both either in compression or in tension. The load ratio s is thus derived from the lower stress limit divided by the upper stress limit. However, tension-compression or shear fatigue tests can be performed as well. According to DIN 50100 (1978, pp. 3-4, [84]) fatigue strength is defined as the maximum oscillating load at which a part can bear an indefinite number of load cycles without showing fracture or inadmissible strain. If several identical test specimens are either loaded at a constant mean stress σ_m or a constant lower stress limit σ_l, while the stress amplitude σ_a or the upper stress limit σ_u, respectively, is varied, one obtains the so-called Wöhler-curve in a plot of the given varied stress levels versus a logarithmic grading of the number of cycles to failure (stress-life curve). This curve features a nearly asymptotic progression towards high cycle numbers as displayed in ***fig. 2.13***. In the case of steel that is $10 \cdot 10^6$ cycles and for light metals $100 \cdot 10^6$ cycles. Hence, the endurance limit can be defined as the maximum upper stress divided by the yield strength of monotonic, quasi-static loading. This factor yields the fraction of stress that can be applied on a part in a dynamic load situation when fatigue strength is expected.

Banhart (1999, p. 617-619, [27]) examined closed-cell foams under cyclic compressive load which were made from powder with relative densities between 0.203 and 0.348. The upper stress limit was chosen between 50 and 80 % of the compressive yield strength while the load ratio applied was 0.1 and the testing frequency varied between 3 and 10 Hz. The tests revealed an endurance limit of approximately 0.5 at which the parts failed after 10^4 to 10^5 cycles. It was observed that before failure the deformation of the test specimens increased only slightly at constant linear pace (q.v. sample diagram in ***fig. 2.14***). Then at the moment of failure the foam yielded strongly within a few hundred cycles and the strain grew at a much higher rate. Finally, after this phase the strain rate decreased again to a moderate linear value.

Similar results were found by Harte (1999, p. 2511-2515, [135]) who investigated the open-cell ERG Duocel sponge with a relative density of 0.07 and the closed-cell Alporas foam with a relative density of 0.11. Compression-compression tests were conducted at a frequency of 20 Hz with load ratios of 0.1 and 0.5 where a comparable strain-life behaviour was found like mentioned above. The sudden rise and fall of the strain rate occurred at strains of about 2 % and is assumed to be caused by the sequential formation of crush bands. In tension-tension tests at the same frequency with a load ratio of 0.1 both materials tested failed at axial strains of 1 to 2 % after 10^4 to 10^5 cycles due to macroscopic crack initiation and propagation. Since

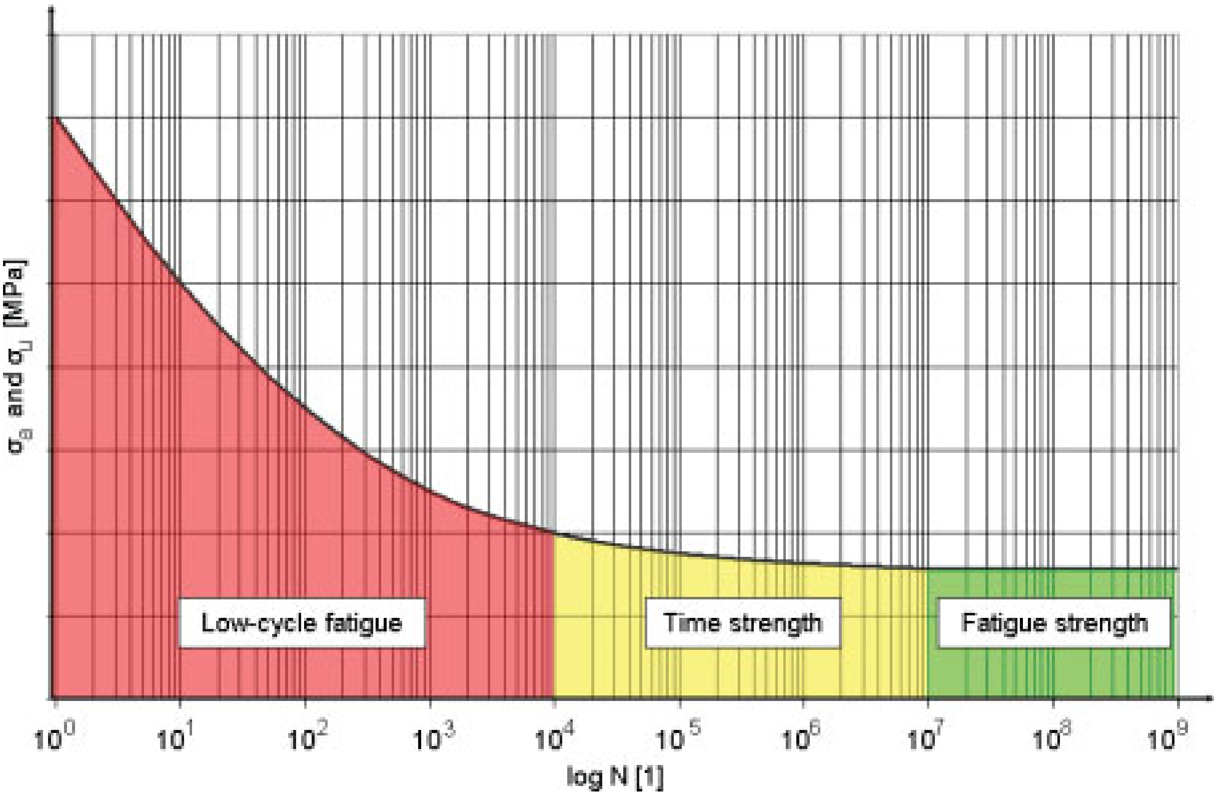

Figure 2.13: Wöhler-curve (stress-life curve)

there is no densification possible in pure tensile testing the strain-life curve is in fact similar to the pure compression curve in ***fig. 2.14*** but after fracture it lacks the decreased linear strain rate. It was found that for an endurance limit of 0.6 fatigue strength is achieved as test specimens survived more than 10^7 cycles. Furthermore, according to Ashby (2000, p. 34, [17]) the strain-life curve in shear fatigue testing is similar to the curve in tension-tension testing.

An alternative method for the determination of the lifetime of foamed aluminum samples was suggested by Zettl (1998, p. 100, [329]). A reduction of the specimens resonance frequency while their weight and volume remained constant indicated a change of stiffness. As soon as a reduction of 50 Hz was observed a specimen was considered to have reached its lifetime since crack initiation was often found at this point.

Further analysis includes the development of formulae for the number of cycles to failure in dependence of the material's relative density and for the growth rate of macrocracks under fatigue loading (Huang, 1998, pp. 29-31, [147]). It also involves an investigation on how Young's moduli of specimens change as strain is increased either caused by monotonic, quasi-static loading or caused by fatigue loading (Harte, 1999, pp. 2521-2522, [135]). It was found that cyclic loading shows only a slightly greater loss of stiffness with growing strain.

2.1.4.12 Creep

Creep typically occurs in metallic materials at loads significantly below yield strength and at temperatures above 30 % of the absolute melting temperature (i.e. measured on the Kelvin

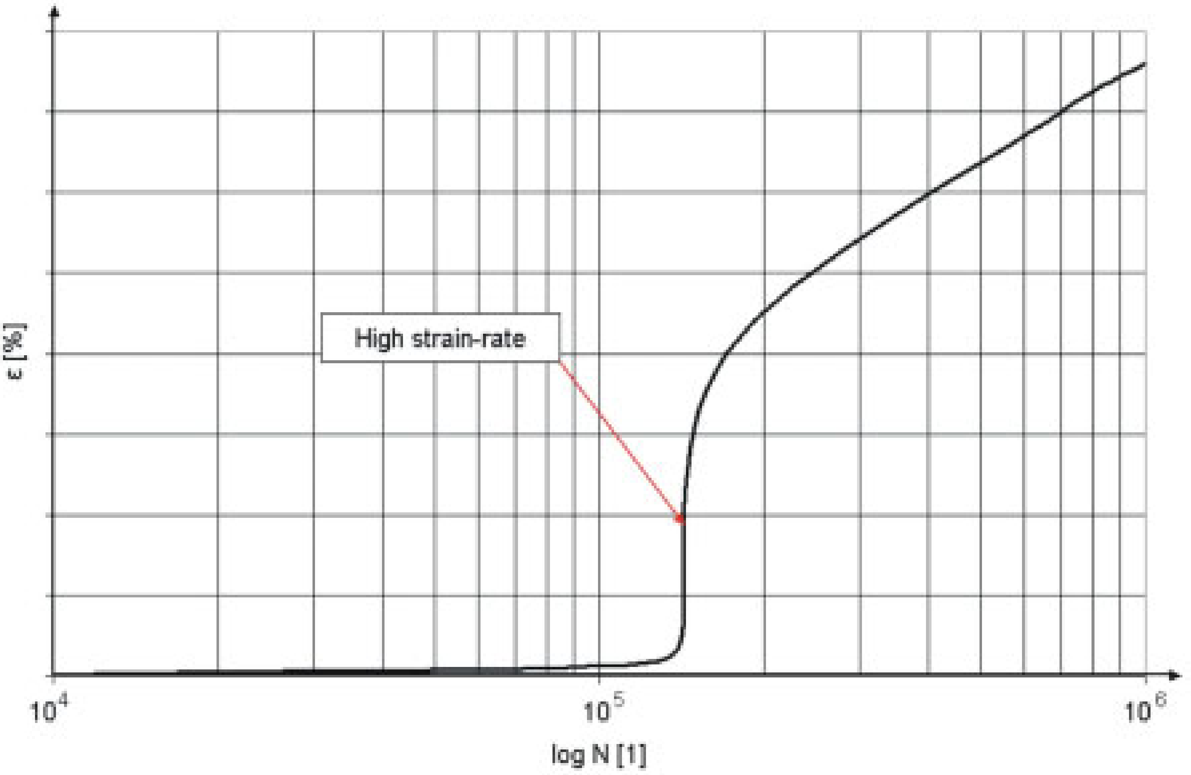

Figure 2.14: Strain-life curve

scale). When a material bears according load and temperature over an extended amount of time it exhibits time-dependent strain. The strain rate increases after exposing the material for a specific amount of time, similar to fatigue failure as explained above. Generally, the creep of solids is being described by the power law in ***eq. (2.25)*** where $\dot{\varepsilon}_{solid}$ is the strain rate, σ is the uniaxial stress responsible for the occurrence of creep, σ_0, n and C are material constants, e is Euler's constant, Q is the activation energy, R is the gas constant and T is the absolute temperature.

$$\dot{\varepsilon}_{solid} = \dot{\varepsilon}_{0,solid} \cdot \left(\frac{\sigma}{\sigma_0} \right)^n \qquad \text{where: } \dot{\varepsilon}_{0,solid} = Ce^{-\frac{Q}{RT}} \tag{2.25}$$

$$\dot{\varepsilon}^* = \dot{\varepsilon}_{0,solid} \cdot \frac{0.6}{n+2} \cdot \left(\frac{1.7(2n+1)}{n} \frac{\sigma}{\sigma_0} \right)^n \cdot \left(\frac{\rho_{solid}}{\rho^*} \right)^{\frac{(3n+1)}{2}} \tag{2.26}$$

Andrews (1999, pp. 2853-2863, [13]) derived from the rate of curvature change of cell walls dependent on strain rate that theoretically for open-cell materials the parameters n and Q remain constant while the creep rate $\dot{\varepsilon}^*$ is proportional to the inverse of relative density to the power of $(3n+1)/2$ according to ***eq. (2.26)***. An experimental assessment of this model was conducted using the open-cell ERG Duocel sponge where at constant temperature T the slope of log $\dot{\varepsilon}^*$ versus log σ yielded parameter n while $-Q/R$ was determined from the slope of log $\dot{\varepsilon}^*$ versus the inverse of temperature. The examinations revealed that the compressive and tensile data are very similar. For a relative density of 0.09 and a temperature of 275°C the power law creep exponent n was 4.2 (compression) and 5.0 (tension) where the solid showed a value of 4.0. The values for the activation energy Q were 203 kJ/mol (compression), 226 kJ/mol (tension) and 173 kJ/mol (solid). Both types of load deliver typical time-dependent strain curves. Under compression a similar curve like in ***fig. 2.14*** is obtained where the regime of secondary creep shows the maximum strain rate and failure of the material due to collapse of one layer of cells. Under compressive load the relative density was varied from 0.06 to 0.14 resulting in a slightly decreasing value of n with increasing relative density, whereas Q remained approximately constant. An important observation was that despite significant differences in the failure mechanisms of compressive and tensile creep the lifetime expectancy under creep is proportional to the reciprocal of the creep strain rate.

Similar examinations were conducted for the closed-cell foam Alporas with a relative density of 0.087 (Andrews, 1999, pp. 2927-2935, [11]). Again the resulting parameters n and Q in both compression and tension were close to the values of the solid. However, at higher stresses the power law exponent n increased to values of 15.0 in compression and 14.4 in tension while at higher temperatures the activation energy Q increased to values of 555.4 kJ/mol in compression and 404 kJ/mol in tension where the model from ***eq. (2.27)*** suggested 71 kJ/mol. The best explanation found was that due to inhomogeneities in the microstructure of some cell walls local stress peaks develop causing these cell walls to enter a power law breakdown regime. The consequence from this is that the according cell walls behave as if they were missing which leads to rapid creep rates.

$$\dot{\varepsilon}^* = \dot{\varepsilon}_{0,solid} \cdot \left(\frac{3}{2} \frac{\sigma}{\sigma_0} \frac{\rho_{solid}}{\rho^*} \right)^n \tag{2.27}$$

The creep of open-cell NiAl sponges with relative densities of 0.05 and 0.066 was examined by Hodge (2003, pp. 2354-2360, [143]) at temperatures between 800°C and 1100°C and compressive stresses between 0.1 and 1.5 MPa. At stresses below 0.5 MPa the secondary creep behaviour of both relative densities followed the power law behaviour of bulk NiAl material with best fits of 3.4 for the creep exponent n and an activation energy Q of 206 kJ/mol suggested by the model based on ***eq. (2.28)*** where the assumption was made that approximately one third of all struts contribute to creep compression while the assumption of creep bending from ***eq. (2.25)*** was neglected. At higher stresses the same phenomenon of increasing values for n could be observed resulting in a power law breakdown for the foam of least relative density.

$$\dot{\varepsilon}^* = \dot{\varepsilon}_{0,solid} \cdot \left(3 \frac{\sigma}{\sigma_0} \frac{\rho_{solid}}{\rho^*} \right)^n \tag{2.28}$$

Typically, creep is dominated by bending and stretching of cell walls or struts. However, according to Cocks (2000, p. 3399, [63]) they can buckle elastically under creep conditions, i.e. elevated temperatures or increased stress far below the yield threshold and well below the cellular material's elastic buckling stress.

2.1.4.13 Fracture toughness

Fracture toughness describes the ability of a material to sustain fracture despite the existence of cracks, at a given state of stress and crack length. The intensity factor of stress around the tip of one crack under tensile load (opening mode, perpendicular to the direction of crack propagation) is given by ***eq. (2.29)*** (DIN EN ISO 12737, 2005, p. 4, [96]) where σ is the stress, a is the crack length and f is a factor depending on the geometry of the part and the crack. If the load is in shear in direction of crack propagation (sliding mode) or in shear perpendicular to the direction of propagation (tearing mode), the stress intensity factor is denoted K_{IIc} and K_{IIIc}, respectively. The critical value of K_{Ic} is a material property that indicates the condition under which a crack will propagate. The solid materials considered in this thesis are typically ductile and exhibit values of fracture toughness around 50 $\text{MPa}\cdot\text{m}^{0.5}$ for steel alloys, around 36 $\text{MPa}\cdot\text{m}^{0.5}$ for aluminum alloys and roughly between 44 and 66 $\text{MPa}\cdot\text{m}^{0.5}$ for titanium alloys. In ductile materials the propagation of cracks is often ceased by yield and dislocation of material. Typical materials showing brittle fracture exhibit stress intensity factor values of at least one order of magnitude less (e.g. about 3 to 5 $\text{MPa}\cdot\text{m}^{0.5}$ for aluminum oxide ceramics).

$$K_{Ic} = \sigma \sqrt{\pi a} \cdot f \tag{2.29}$$

Generally, the K-values are suitable to describe brittle material behaviour by linear-elastic fracture mechanics. For ductile materials the theory of yield fracture mechanics is more appropriate. It comprises the concept of the *J*-integral J_{Ic} (aka initiation toughness) that describes the potential energy due to crack growth Δa and the concept of COD (crack opening displacement) or CTOD (crack-tip opening displacement) measurements, where the displacement in direction of tension is measured either at a fixed position on the notch flank (e.g. 5 mm behind the initial crack-tip, i.e. COD_5) or at a position behind the current crack-tip (e.g. 5 mm distance, i.e. $CTOD_5$), respectively.

$$K_{Ic} = 0.65 \cdot \sigma_{solid} \sqrt{\pi a} \cdot \left(\frac{\rho^*}{\rho_{solid}} \right)^{1.5} \tag{2.30}$$

To describe the dependency of K_{Ic} for open-cell materials on their relative density Gibson (1997, pp. 219-220, [123]) inferred ***eq. (2.30)*** on the basis of ***eq. (2.29)***. Experimental investigations of the closed-cell Alporas foam that was made from a very ductile aluminum alloy and of the also closed-cell Alulight foam (made from a more brittle aluminum alloy) revealed that no reasonable K_{Ic}-values can be acquired for the cellular material containing the ductile alloy due to a rather longish non-linear stress-strain curve during rupture of the specimens (Motz, 2002, pp. 2016-2033, [211]). However, due to too small specimen sizes, where the total displacement in the stress-strain curve during rupture is too short, the foam made from the brittle alloy did not deliver valid K_{Ic}-values, either. Apparently, valid fracture toughness values were obtained from the *J*-integral tests with J_{Ic}-values ranging from 39 to 410 N/m for relative densities between 0.093 and 0.148. It was found that the COD_5-values showed even less scatter and the results were independent of the size of the specimens. The obtained values ranged between 0.22 and 1.03 mm. The validity of the *J*-integral tests was confirmed by McCullough (1999, pp. 2334-2338, [195]) who also examined closed-cell Alulight foams of relative densities between 0.13 and 0.32. Both fracture and initiation toughness were found to increase with relative density according to ***eqs. (2.31)*** and ***(2.32)*** where the K_{Ic}-value is given in $\mathrm{MPa \cdot m^{0.5}}$ and the J_{Ic}-value in kN/m.

$$K_{Ic} = 41 \cdot \left(\frac{\rho^*}{\rho_{solid}} \right)^{1.65} \tag{2.31}$$

$$J_{Ic} = 37 \cdot \left(\frac{\rho^*}{\rho_{solid}} \right)^{1.52} \tag{2.32}$$

2.1.4.14 Energy absorption

Cellular materials are well capable of absorbing impact energy preferably under compressive deformation. Ideal absorbers dissipate energy at constant deceleration and make use of the maximum strain before the onset of significant densification and exposure of the impinging object to unacceptable forces. In a stress-strain diagram this correlates with an initially very steep incline of the curve and a sharp transition to constant stress at the appropriate stress level. The above described elastic and plateau behaviour of cellular materials under compression satisfies this requirement. The capacity W of an energy absorber is defined as the amount of absorbed energy which equals the integral of the stress σ along the strain ε due to its deformation according to ***eq. (2.33)***. It allows to compare different absorbers in absolute quantities, however, the efficiency η can yield better estimations by giving relative figures. Several definitions exist for the latter, one being the capacity divided by the maximum energy that is hypothetically possible, denoted in ***eq. (2.34)*** (Rausch, 2002, p. 10, [243]).

$$W(\varepsilon) = \int_0^{\varepsilon} \sigma(\varepsilon) d\varepsilon \tag{2.33}$$

$$\eta(\varepsilon) = \frac{W(\varepsilon)}{\sigma_{max}(\varepsilon) \cdot \varepsilon} \tag{2.34}$$

Another method of obtaining the efficiency of an energy absorber is the Janssen factor J which relates the real deceleration of an object to the ideal deceleration. The J factor is then displayed versus the dissipated energy per unit volume, i.e. the relative capacity (Gibson, 1997, pp. 316-317, [123]). The real deceleration a_{real} is derived from the plateau stress σ_{pl}, the cross section area A of the absorber and the mass m of the object impinging it according to ***eq. (2.35)***. The object receives ideal deceleration of its mass m containing the kinetic energy W_{kin} if significant densification of the absorber is neglected and its full thickness t is used to dissipate the energy as given in ***eq. (2.36)***. The Janssen factor J then results from these two equations according to ***eq. (2.37)*** where the volume V of the energy absorber is deduced from its cross section A and its thickness t.

$$a_{real} = \frac{\sigma_{pl} \cdot A}{m} \tag{2.35}$$

$$a_{ideal} = \frac{W_{kin}}{m \cdot t} \tag{2.36}$$

$$J = \frac{a_{real}}{a_{ideal}} = \frac{\sigma_{pl} \cdot V}{W_{kin}} \tag{2.37}$$

Miyoshi (1999, pp. 1056, 1059, [207]) examined the closed-cell aluminum foam Alporas with a relative density of around 0.106 and cell sizes of 4.5 and 3 mm. At quasi-static strain rates of 10^{-3} s^{-1} and a strain of 0.5 average relative capacities of 0.94 MJ/m^3 were obtained for the cell size 4.5 mm and 1.32 MJ/m^3 for 3 mm, respectively. These results showed that at constant relative density the microstructure of a cellular material can take great influence on the capacity and the efficiency of an energy absorber.

Often the annihilation of energy takes place at dynamic conditions. Therefore, Mukai (1999, pp. 925-926, [213]) conducted tests with high strain rates of approx. $2.5 \cdot 10^3$ s^{-1} as well as quasi-static strain rates of 10^{-3} s^{-1} for specimens of the same material. These comprised relative densities between 0.093 and 0.102 and showed an average cell size of 2.6 mm. Like mentioned above in ***section 2.1.4.1*** over six orders of magnitude increase in strain rate a rise of 50 % in yield and plateau strength was found here, too. On average at a strain of 0.55 a relative capacity of 1.00 MJ/m^3 resulted from the quasi-static tests while the dynamic loading yielded 1.51 MJ/m^3.

For many applications it is of utmost importance to increase the capacity as much as possible. This is mainly achieved by increasing or extending the plateau strength. In addition to the cell size and the strain rate, the relative density takes great influence on it. If the relative density is increased the plateau strength increases, too. However, the plateau typically extends with decreasing relative density. Flaws inside the material can also extend and simultaneously reduce the plateau strength (Pawlicki, 2003, p. 235, [226]). Therefore, each application requires an individual optimum of the relative density as Kretz (2002, p. 783, [167]) discovered while investigating the Head Injury Criterion (HIC) of aluminum foams when used as deformation elements in car pillars. Gradinger (1999, pp. 145-148, [130]) reported that local fluctuations of the relative density in an absorber have a weakening effect. Experiments and simulations showed that the yield and the plateau strength and thus the capacity are reduced if inhomogeneities exist. This fact was substantiated by Wöß (2004, pp. 135, 138, [323]) who analyzed periodic lattice structures similar to those in this thesis. It was found that the yield strength and the capacity can be varied by a factor of three by changing the unit cell structure and by translating it. The highest yield strength and capacity was obtained for a translated simple cubic structure (like the one in ***fig. 2.1 (b), middle***), followed by a reinforced *bcc* structure.

2.1.4.15 Scaling laws for properties of cellular materials

Not only is it convenient for design engineers to have scaling laws available that allow the customization of cellular material properties for a given task. In fact, the complex geometries typically found in cellular solids do not admit easy handling of calculations without the use of e.g. FEM software. Therefore, establishing simple scaling laws should be considered a must. In this regard the percolation theory as explained at the beginning of ***section 2.1.4*** is useful in finding power laws to describe the properties of cellular materials explained in the previous sections and in the appendix such as: strength, elasticity, creep behaviour, fracture toughness, energy absorption, damping capability, thermal conductivity, thermal diffusivity, electrical resistance, electrical conductivity, electrical permitivity and permeability. Especially the property of mechanical stiffness is a paramount example for the diversity of the percolation theorem. As shown in ***section 2.1.4*** different mechanisms can dominate the resulting scaling laws. For each mechanism a certain power law exponent can be derived analytically from e.g. beam theory that is in good agreement with experimental results. The stretch-dominated behaviour e.g. implies axial strain of struts which is correlated linearly to the responsible stress while bending-dominated behaviour causes struts to sag perpendicularly to their length which follows a quadratic dependency on the applied stress. The mechanism of cell wall bending gives rise to even cubic terms. Since real cellular materials often exhibit all these mechanisms to a greater or lesser extent the best fitted power law exponent is often a non-integer value in the range between 1 and 3. Generally, a material property is more attractive if it yields a small exponent close to unity because the loss of the property progresses slower with decreasing relative density.

General observations in comparing the mechanical properties of open- and closed-cell materials as well as stochastic and periodic materials according to ***fig. 2.3*** were made and can be summarized as follows. Closed-cell materials should generally show greater strength than open-cell materials due to a higher number of mechanisms resisting the material's deformation. However, especially closed-cell, stochastic materials stay behind the expectations (McCullough, 1999, p. 2326, [196]) and they do not outperform open-cell materials which often operate near their predicted limits. The main reason for this is the occurrence of flaws in the walls of closed-cell materials (Grenestedt, 1998, pp. 7-12, [131]). Additionally, periodic materials have superior strength, stiffness and energy absorption capability compared to stochastic materials (Sypeck, 2002, p. 760, [288]). This was confirmed by a number of other researchers (Scheffler, 2005, pp. 15-16, [270]) who showed that the power law exponents of periodic materials have the potential of approaching unity. Hohe (2005, pp. 931-932, [144]) also calculated that microstructural disorder of a foam or sponge leads to a general weakening of the strength properties of up to 30 % and causes an increasing scatter of experimental results thus making forecasts obtained from scaling laws more inaccurate. According to Bram (2000, p. 500, [44]) this scatter can also be more distinct the greater the pores of a stochastic material are due to their contribution to inhomogeneous failure.

A comprehensive collection of scaling laws can be found elsewhere (Ashby, 2000, pp. 53-54, [17]), however, the literature rarely gives information on the valid range of relative density for all scaling laws. This is indeed a major problem which most theories have that were derived for cellular materials as they can only be applied in a narrow band of relative densities typically below a value of 0.3. As shown in ***fig. 2.4*** the design parameters cannot be chosen freely for most cellular materials since they typically depend on the fabrication process. Therefore, the existing theories are sufficient for cellular materials such as metal foams. However, for future developments it is desirable to have scaling laws available which on one hand directly incorporate the design parameters rather than employing pseudo design parameters dictated by constraints of the fabrication process. On the other hand they should account for a broader range of design parameter values, e.g. relative densities up to unity, if possible. Apparently, this will require a new class of cellular material and a new fabrication process which allows the degree of freedom of varying the design parameters more than previously possible. In order to help envision a new link chain of influences on the quality of a cellular material product the so-called 'House of Quality for Cellular Material Products' is defined. Derived from ***fig. 2.4*** it consists of

- a basement and a ground floor which contain all predetermined or fixed conditions,
- several floors of product functionalities and cellular material properties as well as
- a roof which contains the quality objectives of the cellular material product.

Like in a real environment the visibility of characteristic features of this house from a remote point of view, i.e. the customer's point of view, increases from bottom to top as shown in ***fig. 2.15***. The left part of it contains the rather methodical approaches while its right part comprises all technical issues. Realizing the goals of a House of Quality for Cellular Material Products will enable design engineers to use design parameters of their choice in order to optimize the product functionality provided that the design parameters are covered by accepted scaling laws.

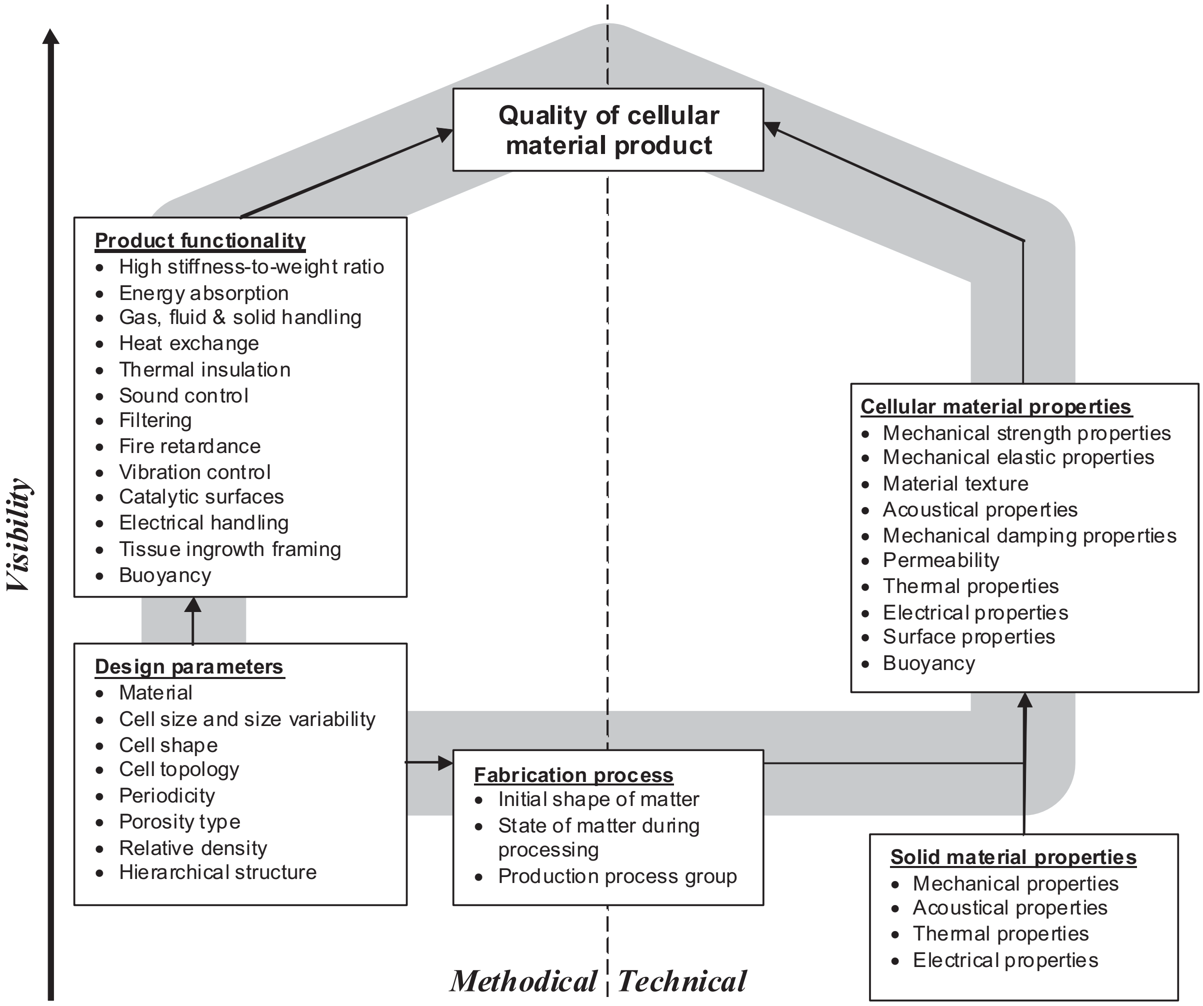
Quality of cellular material product
Product functionality
High stiffness-to-weight ratio
Energy absorption
Gas, fluid & solid handling
Heat exchange
Thermal insulation
Sound control
Filtering
Fire retardance
Vibration control
Catalytic surfaces
Electrical handling
Tissue ingrowth framing
Buoyancy
Design parameters
Material
Cell size and size variability
Cell shape
Cell topology
Periodicity
Porosity type
Relative density
Hierarchical structure
Fabrication process
Initial shape of matter
State of matter during processing
Production process group
Cellular material properties
Mechanical strength properties
Mechanical elastic properties
Material texture
Acoustical properties
Mechanical damping properties
Permeability
Thermal properties
Electrical properties
Surface properties
Buoyancy
Solid material properties
Mechanical properties
Acoustical properties
Thermal properties
Electrical properties
Visibility
Methodical
Technical

Figure 2.15: House of Quality for Cellular Material Products

2.2 Conventional fabrication processes for cellular materials

2.2.1 Overview

Many different fabrication processes and a variety of base materials are available for cellular materials although here the focus remains solely on metallic materials. Most existing manufacturing technologies for cellular materials employ the processing of a powder or a melt and yield structures of stochastic composition. Thus they have limited degrees of design freedom preventing the creation of an ideal, periodic microstructure. However, few methods are available that allow the manufacture of such designed structures. The overview on current fabrication methods for metallic cellular materials in ***fig. 2.16*** (Emmelmann, 2007, p. 530, [111]) was adopted and advanced with information given in various sources from Ashby (2000, pp. 8-21, [17]), Banhart (2001, pp. 563-598, [28]), Wadley (2002, p. 728, [303]) and Degischer (2003, p. 46, [76]). It comprises all different states (solid, liquid, vapor and ionic) of various raw materials (powder, melt, spheres, sheet metal, trusses, gas and metal salt). For better recognition powder metallurgical processes can be followed along blue lines, melt processes along red lines and fabrication from hollow spheres can be found along green lines.

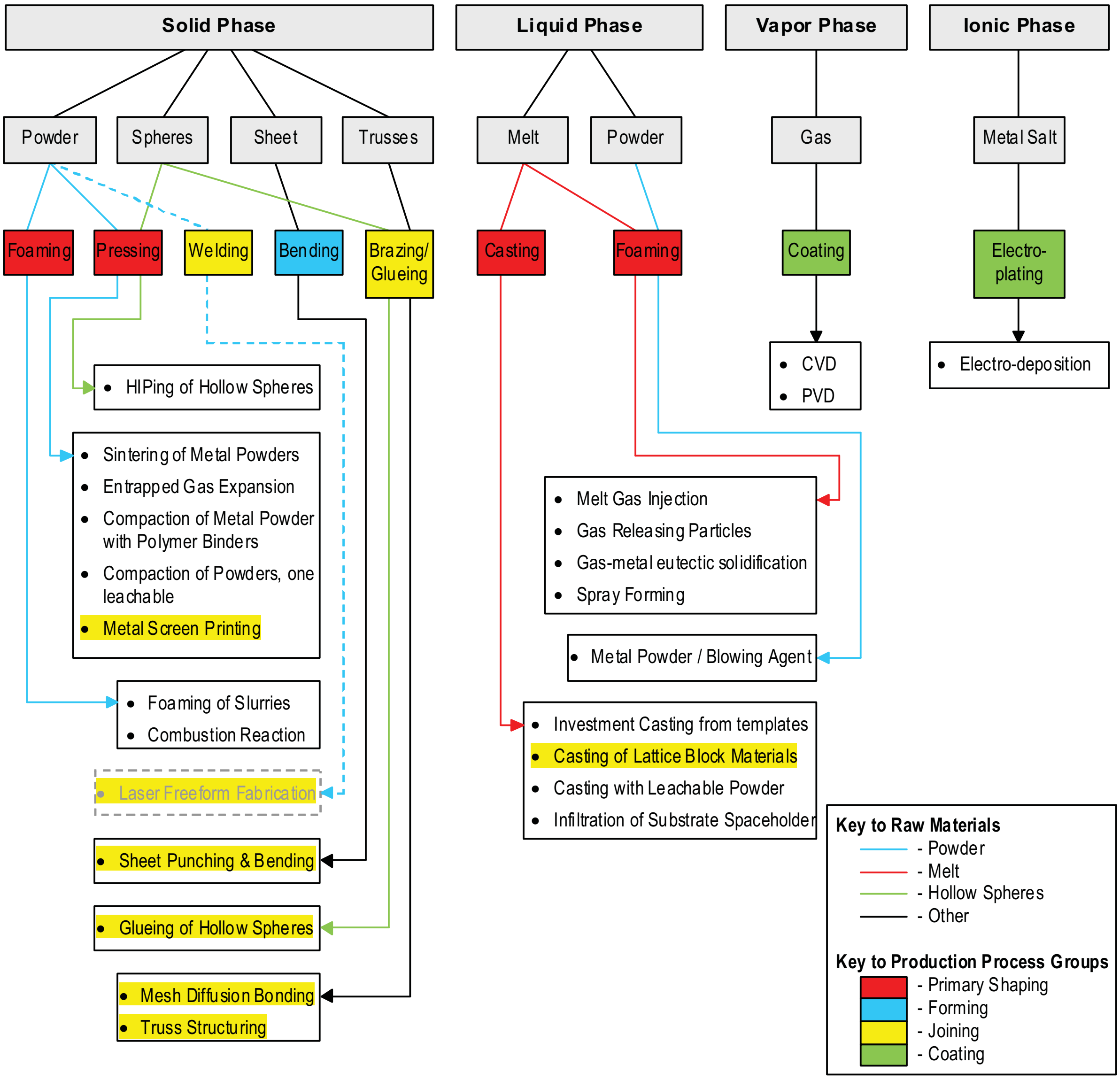
Solid Phase
Liquid Phase
Vapor Phase
Ionic Phase
Powder
Spheres
Sheet
Trusses
Melt
Powder
Gas
Metal Salt
Foaming
Pressing
Welding
Bending
Brazing/ Glueing
Casting
Foaming
Coating
Electro-plating
CVD
PVD
Electro-deposition
HIPing of Hollow Spheres
Sintering of Metal Powders
Entrapped Gas Expansion
Compaction of Metal Powder with Polymer Binders
Compaction of Powders, one leachable
Metal Screen Printing
Foaming of Slurries
Combustion Reaction
Laser Freeform Fabrication
Sheet Punching & Bending
Glueing of Hollow Spheres
Mesh Diffusion Bonding
Truss Structuring
Melt Gas Injection
Gas Releasing Particles
Gas-metal eutectic solidification
Spray Forming
Metal Powder / Blowing Agent
Investment Casting from templates
Casting of Lattice Block Materials
Casting with Leachable Powder
Infiltration of Substrate Spaceholder
Key to Raw Materials
- Powder
- Melt
- Hollow Spheres
- Other
Key to Production Process Groups
- Primary Shaping
- Forming
- Joining
- Coating

Figure 2.16: Fabrication processes for cellular metals

Below the raw materials each route can branch to one or several fabrication methods each of which belongs to one of the main production process groups described in DIN 8580 (2003, p. 7, [82]). This norm contains a systematic summary of all production process groups and their subordinated manufacturing processes. In ***fig. 2.16*** the relevant process groups from this norm are distinguished by coloured boxes:

• primary shaping (red):	1.1.1: casting, 1.1.6: foaming, 1.4.1: pressing
• forming (blue):	2.4.1: bending (by straight tool movement)
• joining (yellow):	4.6.2: welding, 4.7.x: brazing, 4.8.x: glueing
• coating (green):	5.8.1: vapor deposition, 5.9.1: electro-plating

Further below each fabrication method finally leads to a set of processes and technologies that are available today either commercially or in laboratory environment. Some of these processes are highlighted in yellow. Only these allow the manufacture of periodic microstructures from metallic materials. The scope of the work presented in this thesis is to extend the current state-of-the-art by the powder welding process using Laser Freeform Fabrication which, in the above figure, has dotted lines and pale font. All other fabrication processes for periodic cellular materials are briefly explained in ***section 2.2.2*** and for stochastic cellular materials in ***appendix 10.2***. Additional information and schematic illustrations of these processes can be found in the corresponding chapters from Ashby (2000, pp. 6-21, [17]) and Banhart (2001, p. 563-598, [28]). However, for completeness of this overview another diagram is given in ***fig. 2.17*** (Emmelmann, 2007, p. 531, [111]) where all processes are grouped according to their achievable cell size and relative density to present the capability range of metallic cellular materials at a glance. Precursors for this diagram were suggested by Ashby (2000, p. 7, [17]) and Wadley (2002, p. 727, [303]). Additional information is given through colours that represent the according type of porosity each process typically delivers. Those which yield periodic, open cells are shown in light green, whereas those with periodic, closed cells are dark green. Processes giving open-cell, stochastic materials are orange while those with closed-cell, stochastic cells are dark red. Thus light colours generally stand for open-cell and dark colours for closed-cell porosities while greenish colours show periodic and reddish colours a stochastic structure. In some cases text boxes have more than one colour where the dominating colour shows the cell type of prevailing occurence.

Beyond these methods some fabrication processes can be combined with the use of moulds and profiles to directly manufacture functional parts (Stöbener, 2003, pp. 282-283, [281]). These are preferably foaming processes applied inside empty shells or profiles where the void is filled with an internal foam or sponge structure. Thus parts can be produced which are solid on the outside while showing low weight and high strength.

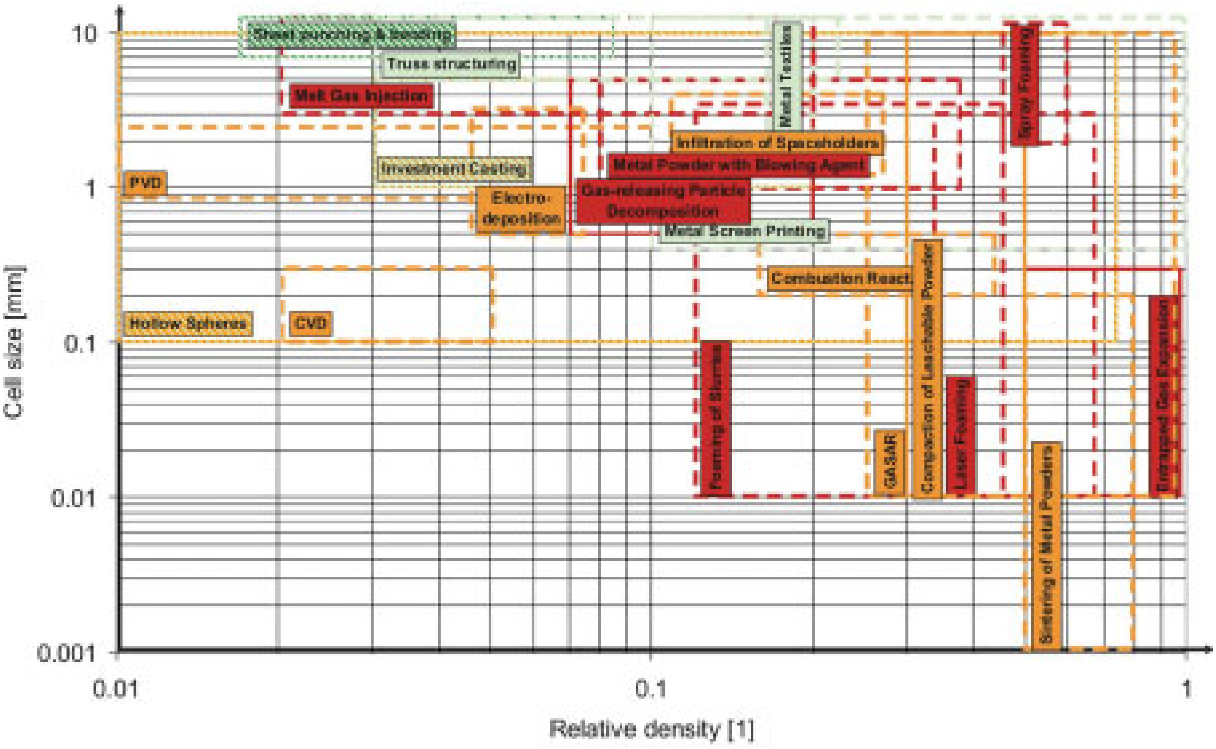

Figure 2.17: Capability range of cellular metal making processes

2.2.2 Periodic cellular materials: lattice and truss structures

Opposed to the manifold processes for the manufacture of stochastic cellular materials presented in ***appendix 10.2*** it is evident that the total number of processes which result in periodic cellular materials is much smaller. Quite a few of these processes typically require more production time per volume unit due to structuring procedures.

2.2.2.1 Compaction from solid phase

Metal screen printing

A new technology entitled ‘direct typing’ and its application on stainless steel powder was presented by Andersen (2004, p. 2, [9]). In a screen printing process step a blend of metal powder and organic binder is printed onto a substrate and hardened before the next layer is printed (Fackler, 2005, p. 11, [113]). Finally, a debindering and sintering step is performed to remove the binder from the green and to obtain a diffusive metallic bond. This way metallic 3D structures (see sample in ***fig. 2.18***) can be obtained with minimum wall thickness of 160 μm and void width of 250 μm to several millimeters. A process which has a lot in common with this procedure though it requires additional infiltration with bronze was described by Dormal (2004, p. P4011.1- P4011.2, [100]). In this so-called Prometal process a full powder layer is applied and an organic binder is printed on top of the layer and dried thermally. After infiltration a part can consist of up to 40 % bronze and of only 60 % steel.

2.2.2.2 Forming from solid phase

Constructed truss structures by deformation shaping

A simple way of obtaining periodic open-cell structures can be found in joining single trusses or struts. One method suggested by Sypeck (2002, p. 761, [288]) uses perforated stainless steel sheets with equilateral hexagonal holes and a deformation process that bends the sheets along aligned nodes of adjacent hexagons, i.e. perpendendicular to some of their edges, giving the structure in ***fig. 2.19 a)***. During the deformation annealing treatment is required to soften the strain-hardened struts. Kooistra (2004, pp. 4231-4233, [164]) used aluminum sheets with elongated hexagonal holes that were bent along aligned nodes perpendicular to the long edge

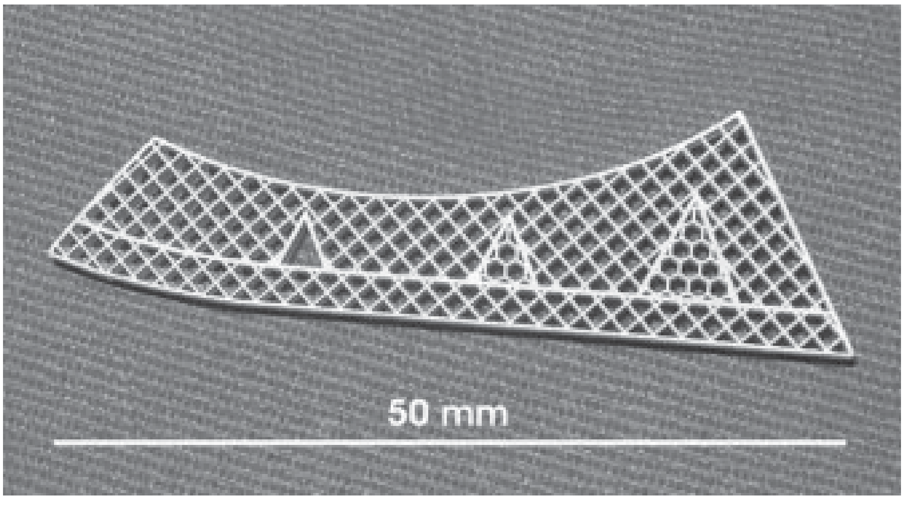

Figure 2.18: Periodic cellular materials made by compaction from solid phase [9]

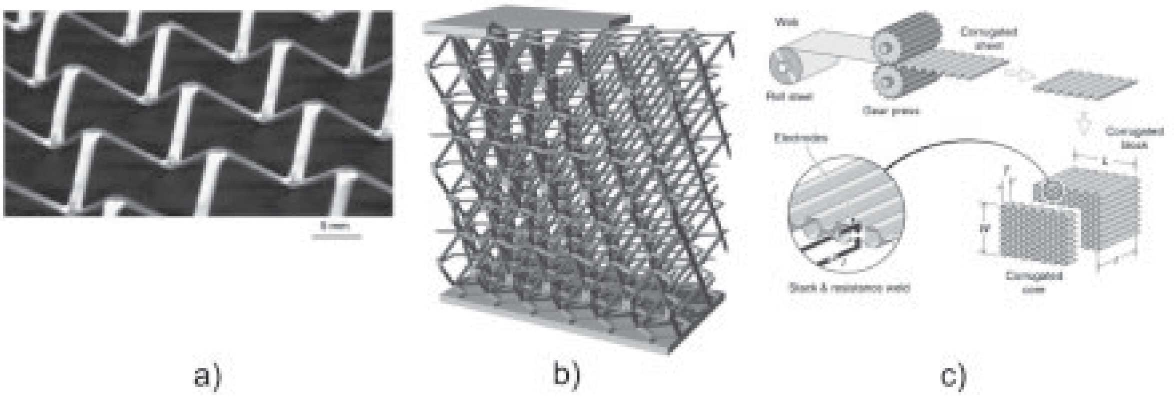

Figure 2.19: Periodic cellular materials made by forming from solid phase [304]

of the hexagons. This way single layers of a tetrahedral truss structure result. Relative densities between 0.017 and 0.083 were achieved by variation of the sheet thickness while cell sizes remained more or less constant at approx. 10 mm. For the use as cores in sandwich panels the layers were attached to face sheets by brazing or transient liquid phase bonding as suggested in ***fig. 2.19 b)***. An even simpler approach (Wadley, 2003, pp. 2331-2332, [304]) consists merely of deformation shaping of solid sheets to e.g. egg-box topology or corrugated shapes that can be stacked and bonded by resistance welding as shown in ***fig. 2.19 c)***.

2.2.2.3 Joining from solid phase

Constructed truss structures by structuring and bonding

A different approach is the assembly and joining of metal wires and tubes. Wadley (2003, pp. 2332-2335, [304]) stated that all metal alloys that can be drawn into wire are usable for weaving, braiding and sewing processes which result in the open-cell woven structures illustrated in ***fig. 2.20 a)***. These are also called metal textiles and the perfectness of their periodicity depends on dispersion of their cell sizes which are typically in the range of few millimeters. 3D cellular structures can be obtained by stacking and joining the nodes of single layers using transient liquid phase bonding. If single layers of what was initially a square wire orientation are bent along aligned nodes 45° to the direction of the wires, then pyramidal layers can be obtained comparable to those produced from bending of perforated sheet metal. A typical value for their relative density is around 0.18.

A similar but non-woven method was introduced by Queheillalt (2005, pp. 305-308, [232]) who fabricated similar structures by layering stainless steel wires and tubes in a tool where they were joined together by brazing. This method yields open-cell truss structures of either square or diamond orientation with relative densities between 0.03 and 0.23 at a cell size of 5 mm. In a similar tool Queheillalt (2005, pp. 132-133, [236]) arranged hollow stainless steel tubes and created single layers of tubes overlaying at 60°. This diamond pattern was vacuum brazed at the nodes and then bent to receive a pyramidal structure. Here, the relative density was 0.028 at a cell size of approx. 10 mm. Examples for both, solid and hollow as well as square and diamond patterns are given in ***fig. 2.20 b)***.

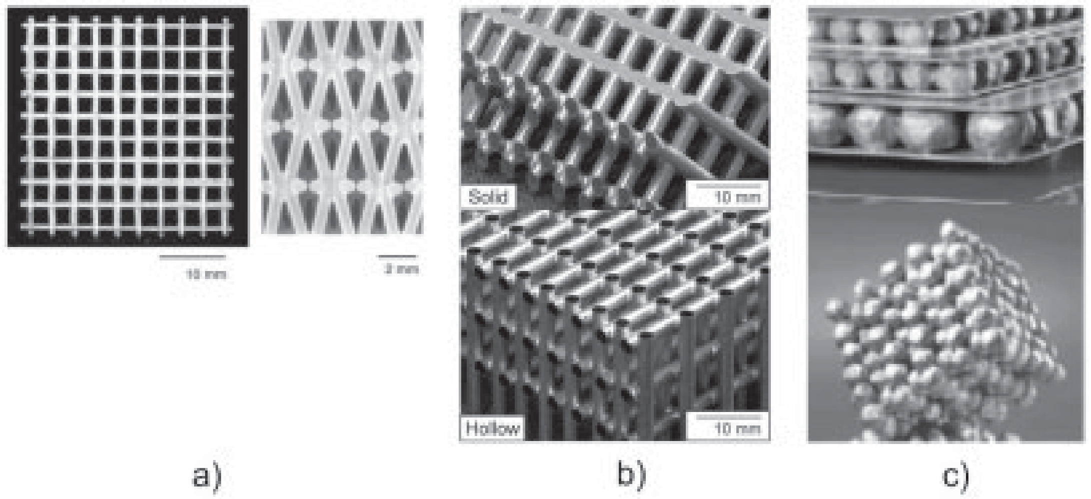

Figure 2.20: Periodic cellular materials made by joining from solid phase [304], [232], [280]

Joining of hollow spheres

Production processes which include the powder metallurgical method with use of a blowing agent as explained in ***appendix 10.2.3*** can be used to manufacture spheres that are solid outside but possess internal porosity. The process of glueing, brazing or sintering such spheres to structured elements of desired shape was suggested by Stöbener (2005, pp. 13-15, [280]) and is documentend in ***fig. 2.20 c)***. However, before the final step of joining the spheres an ordered alignment of the spheres e.g. in *hcp* configuration has to be ensured in order to obtain a periodic structure. This product is commercially available under the brand name Advanced Pore Morphology technology.

2.2.2.4 Casting from liquid phase

Lattice Block Materials

Using the above mentioned investment casting process for the manufacture of periodic cellular structures like the one shown in ***fig. 2.21 a)*** was reported by Wadley (2002, pp. 730-731, [303]). According to Ott (2003, pp. 8-14, [222]), who investment casted lattice blocks as seen in ***fig. 2.21 b)*** from the nickel-based IN718 superalloy, the main concerns for the casting

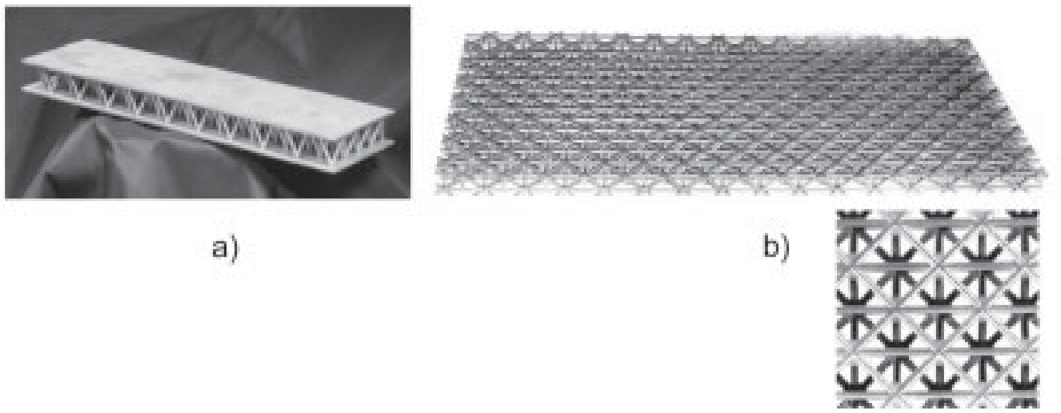

Figure 2.21: Periodic cellular materials made by casting from liquid phase [303], [166]

of periodic materials are the feature producibility (e.g. no missing ligament sections) and the size constraints. Compared to lattice block materials like the above mentioned constructed truss structures, cast cellulars are better suitable if complex geometries and a near-net-shape are required, castable alloys are used and the likelihood of ligament defects is acceptable. The superalloy lattice block produced from this method showed a relative density of 0.15 (Hebsur, 2002, p. 20, [140]) at a cell size of obviously greater than 10 mm.

2.2.3 Constraints of existing fabrication processes for cellular materials

Basically, all fabrication processes that yield stochastic foams and sponges (see ***appendix 10.2***) lack sufficient control on pore size or pore size distribution and on pore positioning. As mentioned before, periodic cellular materials exhibit higher strength and stiffness due to their structure, therefore, their associated processes should be preferred. However, specific constraints in each fabrication method might exempt it from particular applications. In the case of metal screen printing apparently only prismatic, open-cell structures with vertical walls can be manufactured. All processes where the struts of cellular materials are shaped by bending and structuring with or without bonding, typically a lower limit for cell size and strut diameter exists that lies in the range of 5 to 10 mm. This includes the casting process for lattice block materials where sometimes whole sections of struts can be missing after casting if the feature size becomes too small. Therefore, no parts with micro structure can be obtained from these methods.

It should be noted that none of the approaches for periodic cellular materials delivers closed-cell porosities which in theory should by far be superior to open-cell structures if no flaws occur. Only one exception exists, i.e. if corrugated sheets are bonded such that closed-cells result. However, such a material has apparently not been investigated yet as emphasized in ***fig. 2.3***. The existing processes for the structuring of periodic materials still incorporate certain limitations. Therefore, ***table 2.5*** gives the achievable cell size and relative density for the different manufacturing methods for periodic materials introduced above. It evaluates

- how well periodicity can be achieved,
- the likelihood of the occurrence of flaws in the structure after manufacturing,
- the typical mechanical strength compared to a genuine engineering material
- and the potential for topology optimization of the structure to a given load situation.

In the evaluation matrix good fulfillment of a property is represented by a '+', a mediocre fulfillment by a '○' and a poor fulfillment by a '–'. It reveals that no process exists that can achieve the fabrication of small scale structures with possible cell sizes significantly lower than 5 mm, relative densities below 0.2 and a sufficient performance in the mentioned categories. Moreover, none of the processes delivers a good fulfillment of all criteria simultaneously and those that show triple '+' all lie in the range of large cell sizes. Furthermore, a true topology optimization which can incorporate the enhancement or removal of certain struts or where struts receive a freeform positioning and orientation is hardly feasible with these fabrication processes if not at all for cell sizes below 10 mm. Therefore, a new fabrication process is required that overcomes this restriction.

Table 2.5: Evaluation matrix of current fabrication processes for periodic cellular metals

Process	Cell size [mm]	Relative density [kg/kg]	Periodic	Flaws	Strength	Topology optimization
Metal screen Printing	0.4 – 10	0.1 – 1	+	+	○	–
Deformation shaping	≥ 7	0.017 – 0.083	+	+	+	○
Metal textiles	≥ 2	0.15 – 0.2	○	+	+	○
Truss structuring	≥ 5	0.03 – 0.23	+	+	+	○
Joining of hollow spheres	0.5 – 10	0.01 – 0.73	○	○	+	○
Investment casting	≥ 10	0.1 – 0.2	+	○	+	+

2.3 Summary

This chapter reports on the state-of-the-art of metallic, cellular materials and gives information how to classify them. An important aspect that is followed throughout this chapter is the quality of products that involve cellular materials. Typically, the product quality depends directly on the properties of the cellular material and on the product functionality, which both depend on the design parameters that are also defined in this chapter. However, for commercially available cellular materials, the design parameters are subject to constraints of the according fabrication process. Hence, they cannot be chosen freely and the resulting product quality is limited.

After giving examples of typical applications for cellular materials and analyzing their properties the first section of this chapter suggests a ‘House of Quality for Cellular Material Products’ where the product quality is mainly driven by the design parameters instead of constraints of the fabrication process. It is found that this can only be achieved by introducing suitable fabrication processes.

Then, the second section of this chapter analyzes conventional fabrication processes for metallic, cellular materials. Since generally higher mechanical strength can be expected from periodic cellular materials their according fabrication processes are evaluated in regard of some fundamental design parameters introduced earlier. The main finding is that of the existing fabrication processes none is capable of producing cellular materials of cell sizes down to 1 mm or even in the submillimeter range while simultaneously fulfilling the goals of high periodicity, flawlessness, high strength and potential for topology optimization.

3 Laser Freeform Fabrication

3.1 Motivation for cellular design with Laser Freeform Fabrication

All manufacturing methods for metallic cellular materials presented in ***section 2.2*** suffer from the limitations mentioned in ***section 2.2.3***, which are

- insufficient degrees of freedom for the design parameters, i.e. the range of cell sizes and relative densities,
- insufficient periodicity,
- flaws in the resulting cellular framework,
- low strength and
- lack of potential for topology optimization.

The use of additive fabrication processeses appears obvious to promote the forthcoming of truly periodic, cellular structures in the shape of regular lattices which show superior mechanical properties on one hand and which satisfy the design engineer's need for defining almost arbitrary structures on the other hand including the possibility for topology optimization. In contrast to the well-known subtractive manufacturing processes like e.g. turning or milling, additive fabrication is typically based on a layerwise buildup of parts from liquid or powder materials. Due to the formation of parts from single material layers this type of production is also called generative manufacturing. Its advantage is the ability of producing nearly any arbitrary geometry from initially shapeless materials allowing for undercuts or internal freeforms in hollow parts that cannot be manufactured with subtractive machining. Until today numerous additive fabrication methods have been developed which can process plastic, ceramic and metallic materials (Wohlers, 2003, pp. 13-17, [324]). They do not merely distinguish by the type of material they process, but also by the type of material feed and the way energy is deployed to achieve solidification of material particles at the required location. Material feed concepts can incorporate powder or liquid beds, powder injection, inkjets and other methods. The energy delivery can take place locally for a small amount of material at a time by means of e.g. a laser or electron beam which melts or sinters the material or it can take place for a complete layer by thermal treatment. Most of these processes are summarized by the generic term 'Rapid Prototyping', however, a more exact and therefore better term is 'Solid Freeform Fabrication' (SFF).

SFF gives new degrees of freedom in design due to the layered build-up of parts. Therefore, Stampfl (2003, pp. 660-661, [277]), Wöß (2004, p. 135, [323]), Naing (2005, p. 257, [214]) and Almeida (2006, pp. 1-3, [8]) recently suggested to manufacture scaffolds and lattice structures for medical purposes from thermoplastic processable materials such as Polyamide or PEEK. This was already close to the idea of manufacturing metallic lattice structures which Williams (2005, p. 219, [319]) then suggested to achieve by additive manufacturing processes that use metal powder. The most prominent of these processes involve a laser as their source of energy, therefore, the subgroup of 'Laser Freeform Fabrication' (LFF) and among this the Selective Laser Melting (SLM) process will be scrutinized further in this section.

Most LFF processes exhibit small process speeds. Typical for processing stainless steel with e.g. SLM is a generated part volume of 0.9504 cm³/h to 9.36 cm³/h when varying the dominant process parameters such as layer thickness from 30 to 100 µm, scan speed from 80 to 200 mm/s and hatch distance from 110 to 130 µm at a laser beam power of 100 W. Apparently, these figures are not competitive compared to conventional machining. Thus there is the need to find a way of simultaneously using the advantages that LFF processes offer and increasing the process speed. This becomes especially important under the aspect of expensive cost of machine operation that is still common since this technology was only developed over the recent years. One obvious solution to this problem would be avoiding solid parts of full density which require high exposure time and thus a high consumption of process time and powder material hence increasing the cost. Therefore, one major goal of the work presented in this thesis is the development of fundamental design rules for alternative product designs which help finding an acceptable compromise between e.g. process speed on one hand and part strength on the other hand. This idea is realized by substitution of solid material with lattice structures of particular design. In addition this approach leads to a whole new class of materials since the SLM process which will be introduced below is capable of creating very fine lattice structures comprising thin micro struts. The design of cell types, cell size and micro strut diameter allows customization of these lattice structures to desired material properties for many applications beyond simple reduction of density of a formerly solid part. The focus in this thesis is placed on the analysis of mechanical properties and the development of scaling laws which allow deriving design rules for the modification of existing product design. Thus new applications can be created based on lattice structures manufactured with SLM. This innovative approach of combining cellular design with LFF can overcome the constraints of limited degrees of design freedom which were mentioned in ***section 2.2.3***. Thus the goals of improving product quality while reducing manufacturing cost and time set out in ***fig. 1.1*** can be achieved.

This will give engineers innovative design possibilities in various applications where e.g.
- lightweight design is required,
- different functionalities have to be combined in one part (such as structural strength, heat exchange, energy or sound absorption, filtering, etc.) or where
- internal solid mass should be partially or completely substituted by a SLM lattice that is meant to bear a given load.

In order to support this intention, typical loads such as compression, tension and shear as well as the elastic behaviour of SLM lattice structures will be analyzed in this thesis. The special motivation for the analyses conducted is the desire to optimize the strength-to-density-ratio, meaning what design and what process parameters can be used to obtain optimum part properties like e.g. minimum weight at given strength. The methods used here incorporate theoretical analyses presented in ***section 5*** as well as destructive material testing presented in ***section 6***. Eventually, the results presented help optimizing all three factors of product quality and manufacturing cost and time by cellular design of SLM parts. To conclude the work of this thesis examples of SLM lattice structure applications are given in ***section 7***.

3.2 Development of Laser Freeform Fabrication

3.2.1 Technological evolution

For several thousand years the fabrication of freeform parts like e.g. gold jewelry was performed using the lost wax process where the necessary molds were made with tremendous manual effort. Then, with industrialization the machining of parts developed which allowed for increased manufacturing speed and part quality. With the advent of computer technology the automation of manufacturing processes in CAD/CAM process chains became feasible. At the same time, over the past three decades laser beam sources for material processing were developed. Due to the good focusability of laser beams paired with high beam intensity, i.e. power per surface area unit, lasers proved to be suitable for production processes with even higher manufacturing speeds and further improved product quality.

Early Solid Freeform Fabrication research already involved laser beam sources such as the exposure of a photosensitive polymer by two intersecting laser beams (Swainson, 1977, [287]). Further examples are the concept of fusible particles of a suitable plastic or plastic-coated sand which are employed to form layers where a laser beam selectively fuses an area in each layer which defines a portion of the part (Housholder, 1981, [146]) and many other contributions. However, none of these concepts were commercialized. The first patent on the field of LFF as it is known today was granted to Hull (1986, [148]) for an invention called Stereolithography Apparatus (SLA). This system was then licensed to 3D-Systems and it is capable of directly proceeding from a 3D-CAD model to a physical object by polymerizing the according slice geometries in layers of a light-sensitive liquid polymer with an ultraviolet laser (Jacobs, 2002, p. 2, [152]). Subsequent layers in this process are manufactured by lowering all previous layers into the polymer reservoir such that the object in progress is covered on top by one layer of liquid polymer. This repetitive process of laser beam exposure and lowering of the part is then repeated until all individual layers are attached to their adjacent layers.

Almost simultaneously a related process was developed by Deckard (1988, pp. 10-12, [75]) where thin layers (125 µm) of heat fusible plastic powder particles are deposited consecutively onto a substrate and exposed to laser light. Thus, 3D objects are built layerwise from CAD data with the use of a 100 W Nd:YAG laser. Micrographs of laser sintered plastic parts give the association of sinter metal textures due to neck formation between adjacent powder particles which are fused together. This is a main characteristic of this process and, therefore, it was named Selective Laser Sintering (SLS) despite the lack of pressure during the process. Later it was commercialized by DTM Corp. and extended to the manufacture of metal parts by using plastic coated metal powder particles. Limitations in laser beam intensities as well as limitations in the absorption of laser beam energy due to improper wavelengths required that only the melted plastic provides inter-particle adhesion (Jacobs, 2002, p. 6, [153]). In this process the plastic binder is burned out and the metal (e.g. steel) sintered during one furnace run. In a second furnace run the residual porosity is infiltrated with a metal of lower melting point (e.g. 90 % copper and 10 % bronze) than the powder material (Stucker, 2000, p. 133, [284]). This method was therefore named Indirect Laser

Sintering and it yields nearly fully dense metal parts. In contrast, Stereolithography can only yield metal parts through subsequent investment casting.

In the 1990's the metal powder processing LFF systems matured. Wohlers (2003, pp. 13-17, [324]) gives a summary of the different systems that appeared on the market during this and the following decade. Quite a few companies went into business then, however, some of them only to disappear soon after. The most important LFF process developments from this time are listed as follows. In 1991 Laminated Object Manufacturing (LOM) was introduced to the market where sheet material (paper, ceramic, plastic or aluminum foil) is cut by a laser to the proper contour geometry and bonded onto previous layers. In 1994 the Direct Metal Laser Sintering (DMLS) process was established by EOS which is based on SLS. It allows a direct one-step manufacturing by using two-phase powder in a liquid-phase sintering process. Thus nearly fully dense parts were obtained without subsequent furnace runs. Another method by the name of Laser Engineered Net Shaping (LENS), also known as laser cladding, was presented in 1998 where a laser melts metal powder supplied coaxially to the laser beam through a deposition nozzle. The object is formed in layers on a x-y-table moved in raster fashion underneath the combined laser beam and powder stream, respectively. Since two-phase powder materials still did not match the properties of engineering materials, Fockele & Schwarze (today Realizer GmbH) introduced the concept of Selective Laser Melting (SLM) in 1999 where single-phase metal powder is fully remelted giving properties similar to those of cast parts. In 2001 Concept Laser established a system based on the principle of SLM which also incorporates laser marking and laser ablation in the same machine under the name of Laser Cusing. Another machine system derived from the SLM principle was brought onto the market in 2003 by Trumpf under the name of Direct Laser Forming (DLF). This technology provided a heating system beyond the temperature capabilities of other systems to reduce temperature gradients and thus thermally induced stresses in parts.

3.2.2 State-of-the-art of industrial processes

Due to the advantages in material properties achieved with SLM processes only few LFF systems remained in the market of which some are powder bed-based and some are laser cladding processes. Among the powder bed-based processes only the systems sold by EOS (Direct Metal Laser Sintering), Concept Laser (Laser Cusing), MCP-HEK (Selective Laser Melting) and Phenix (Selective Laser Melting) are currently available on the market. This is due to the fact that these are one-step processes which deliver better part properties e.g. in terms of part accuracy than indirect processes with follow-up procedures such as furnace runs. Recently, these systems were subject to miscellaneous benchmarks e.g. conducted by Levy (2003, pp. 593-601, [181]), Dalgarno (2004, pp. 261-264, [70]), Castillo (2005, pp. 4-30, [53]) and Abdel Ghany (2006, pp. 87-94, [1]) where they were compared with each other and other Solid Freeform Fabrication processes. Other LFF systems disappeared due to lack of commercial success or were taken from the market as it was the case in 2004 when EOS acquired all patent rights from DTM and 3D Systems (Santos, 2006, p. 1460, [267]).

All currently available processes have similar advantages and disadvantages. Their preferred field of application is the one-step manufacture of complex geometries in low production numbers, ideally with lot sizes of 1 where conventional machining would require a much longer overall production time due to a high number of processing steps. Today, LFF methods still exhibit some deficiencies such as limited resolution, limited material selection, poor surface finish which may require extensive post-processing, in some cases poor material properties and sometimes further post-processing in terms of support removal for overhanging part structures. The manufacture of periodic, cellular micro structures, however, necessitates processes that allow fabrication of cell sizes smaller than 2 mm with wall thicknesses smaller than 500 µm from engineering materials such as steel, titanium, etc. where a density of close to 100 % is achieved (Williams, 2005, pp. 219-220, [319]). Regarding these and other related issues such as accuracy, part strength, etc. leads to the selection of Selective Laser Melting (SLM) as the process of choice for the realization of LFF open-cell lattice structures as disclosed in the following sections of this thesis.

3.3 Selective Laser Melting

3.3.1 SLM principle and process characteristics

The LFF process used for the manufacture of specimens in this thesis is Selective Laser Melting (SLM). Like most other LFF processes involving powder material, the SLM process

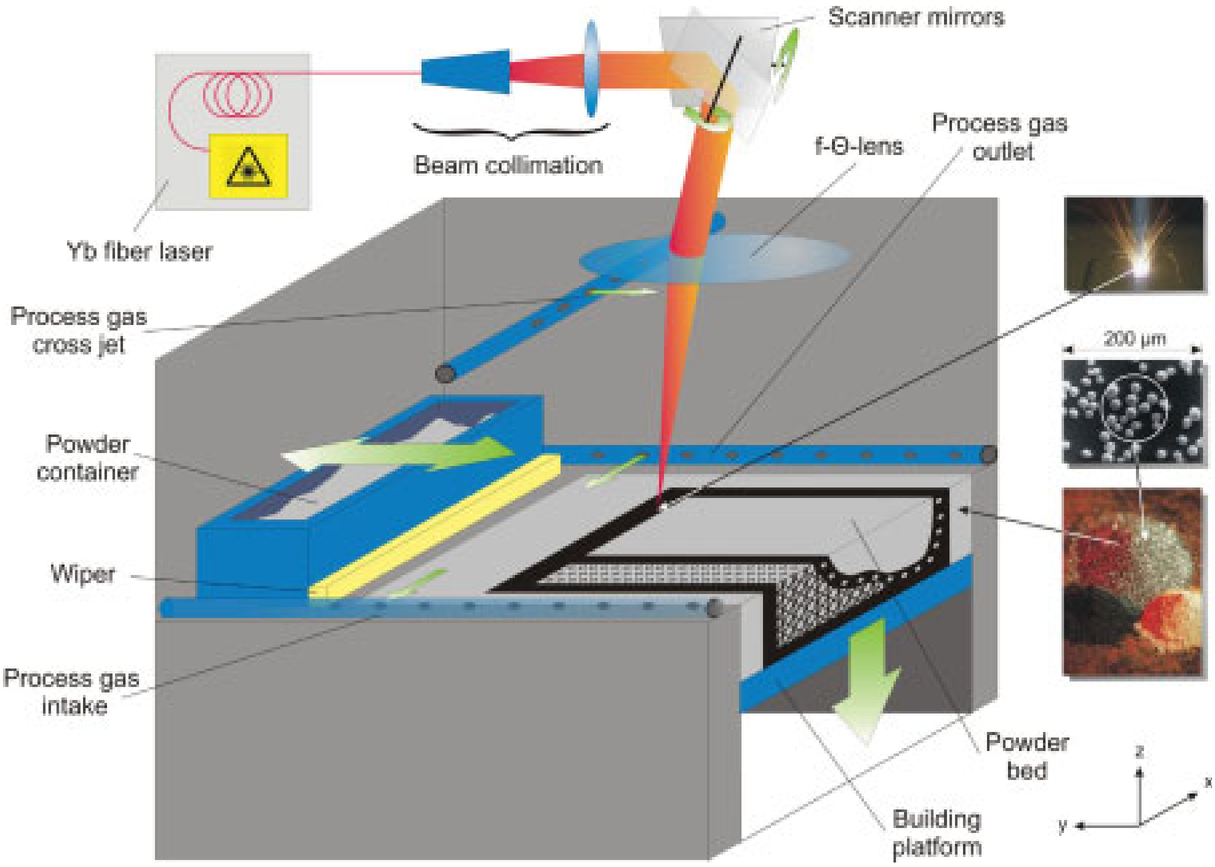
Scanner mirrors
Yb fiber laser
Beam collimation
f-Θ-lens
Process gas outlet
Process gas cross jet
Powder container
Wiper
Process gas intake
200 µm
Powder bed
Building platform
z
x
y

Figure 3.1: Cross section through SLM process chamber and operating principle

is based on a principle in such manner that the powder is applied in very thin layers on a building platform and melted due to the thermal energy induced by a laser beam. The powder particles have a statistical distribution of size from 5 µm to between 20 and 60 µm. Therefore, the thickness of each layer is at least 20 to 100 µm (Emmelmann, 2007, p. 250, [110]). In each layer the laser beam exposes a cross-section area of the part that is built by melting and resolidification of the powder particles, before the building platform is lowered and coated with a new layer of powder. In order to achieve this, a coating device with a silicon wiper applies the new layer of powder onto the previous layer as seen in ***fig. 3.1***. The laser beam is being redirected across the surface of the powder bed (identified as the x-y-plane) by scanner optics (pivoted mirrors) in such a way that the powder particles can be selectively melted where desired. The surface tension of each powder particle changes due to melting which allows neck formation between adjacent particles, resulting in coalescence of the powder particles and creation of a solid layer attached to the previous one underneath.

3.3.2 Influence parameters on SLM

Recently, more than 130 different influence parameters which take effect on the SLM process were identified (Rehme, 2005, p. 228, [250]) where some preliminary work by Wagner (2003, pp. 30-41, [305]) and Führer (2002, pp. 66-75, 79-84, 93-99, [114]) was included. However, meanwhile 157 different influence parameters were distinguished (Rehme, 2007). These are presented in ***fig. 3.2*** where above and below the main arrow a chronological order of process steps and process constraints can be found from left to right and top to bottom according to the sequence of actions and conditions concerned with SLM. Therefore, the resulting Ishikawa diagram contains the influences of

- the user,
- process preparation,
- the part geometry,
- the geometry's data representation,
- the base material properties,
- the LFF system (which is a SLM machine in this Ishikawa diagram),
- the process itself which is governed by the process parameters and
- post-processing.

Alltogether these parameters take influence on the quality of solid SLM parts as well as their manufacturing cost and time. The part quality depends on all influence groups named under the bullets, however, the manufacturing time and hence the manufacturing cost is merely influenced by the two last bullets, i.e. the user's choice of process parameters as well as the number of post-processing steps and their duration. If neglecting the only marginally represented influences on manufacturing cost and time the Ishikawa diagram from ***fig. 3.2*** is related to the box 'solid material properties' in the basement of the 'House of Quality for Cellular Material Products' introduced in ***fig. 2.15*** which gives ***fig. 3.2*** a very fundamental meaning for all following considerations of this thesis.

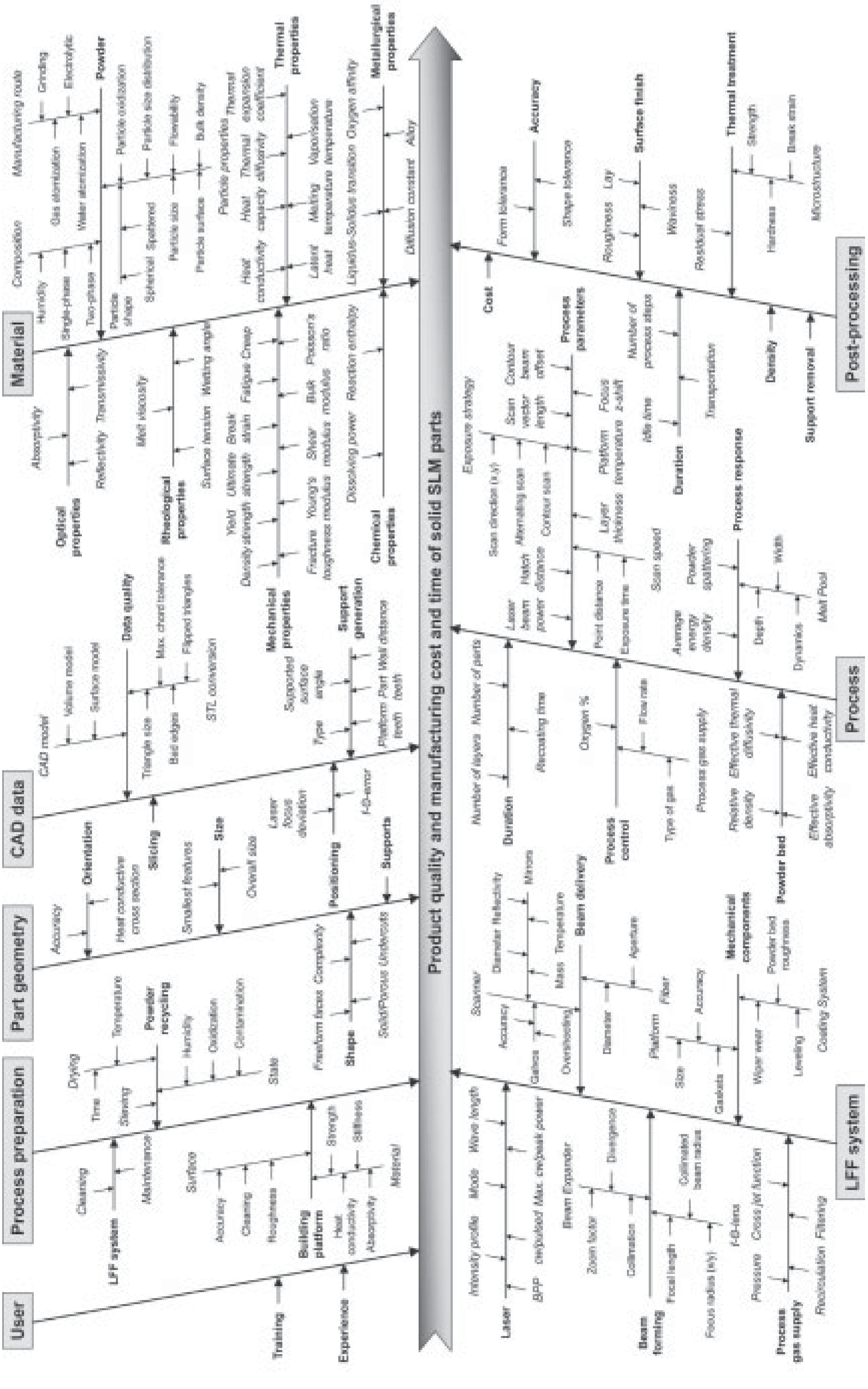
Product quality and manufacturing cost and time of solid SLM parts
User
Training
Experience
Process preparation
LFF system
Cleaning
Maintenance
Building platform
Surface
Accuracy
Cleaning
Roughness
Heat conductivity
Absorptivity
Material
Strength
Stiffness
Powder recycling
Time
Sieving
Drying
Temperature
Humidity
Oxidation
Contamination
State
Part geometry
Accuracy
Orientation
Heat conductive cross section
Smallest features
Size
Overall size
Freeform faces
Complexity
Shape
Solid/Porous
Undercuts
CAD data
CAD model
Volume model
Surface model
Data quality
Triangle size
Max. chord tolerance
Bad edges
Flipped triangles
STL conversion
Slicing
Laser focus deviation
Positioning
f-θ-error
Supports
Support generation
Type
Supported surface angle
Platform teeth
Part teeth
Wall distance
Material
Absorptivity
Optical properties
Reflectivity
Transmissivity
Melt viscosity
Rheological properties
Surface tension
Wetting angle
Mechanical properties
Yield strength
Ultimate strength
Break strain
Fatigue
Creep
Density
Fracture toughness
Young's modulus
Shear modulus
Bulk modulus
Poisson's ratio
Chemical properties
Dissolving power
Reaction enthalpy
Composition
Humidity
Single-phase
Two-phase
Manufacturing route
Gas atomization
Water atomization
Grinding
Electrolytic
Powder
Particle shape
Spherical
Spattered
Particle size
Particle surface
Particle oxidation
Particle size distribution
Flowability
Bulk density
Particle properties
Thermal properties
Heat conductivity
Heat capacity
Thermal diffusivity
Thermal expansion coefficient
Latent heat
Melting temperature
Vaporisation temperature
Liquidus-Solidus transition
Oxygen affinity
Metallurgical properties
Diffusion constant
Alloy
LFF system
Laser
Intensity profile
Mode
Wave length
BPP
cw/pulsed
Max. cw/peak power
Beam forming
Beam Expander
Zoom factor
Divergence
Collimation
Collimated beam radius
Focal length
Focus radius (x/y)
f-θ-lens
Process gas supply
Pressure
Cross jet function
Recirculation
Filtering
Scanner
Accuracy
Galvos
Overshooting
Diameter
Reflectivity
Mirrors
Mass
Temperature
Beam delivery
Diameter
Aperture
Fiber
Platform
Size
Gaskets
Accuracy
Mechanical components
Wiper wear
Leveling
Coating System
Powder bed roughness
Process
Duration
Number of layers
Number of parts
Recoating time
Process control
Oxygen %
Flow rate
Type of gas
Process gas supply
Powder bed
Relative density
Effective thermal diffusivity
Effective absorptivity
Effective heat conductivity
Laser beam power
Hatch distance
Scan direction (x,y)
Alternating scan
Contour scan
Exposure strategy
Scan vector length
Contour beam offset
Process parameters
Layer thickness
Platform temperature
Focus z-shift
Point distance
Exposure time
Scan speed
Average energy density
Powder splashing
Process response
Depth
Width
Dynamics
Melt Pool
Post-processing
Cost
Form tolerance
Accuracy
Shape tolerance
Number of process steps
Idle time
Duration
Transportation
Roughness
Lay
Surface finish
Waviness
Residual stress
Thermal treatment
Strength
Hardness
Break strain
Microstructure
Density
Support removal

Figure 3.2: Ishikawa diagram of SLM influence parameters

3.4 Analysis and advances of SLM influence parameters

The Ishikawa diagram in ***fig. 3.2*** is the guideline for this following section. Its most important influence groups, i.e. part geometry, CAD data, material, process and post-processing are analyzed and recent advances presented. The influence groups of user and process preparation are not covered here due to lack of recent progress in these fields. An analysis of an LFF system is postponed to ***section 4.2.3*** where the SLM machine used for the experimental stage of this thesis is presented in the context of the assessment of process conditions. Besides that the LFF system analysis is not required at this point for an understanding of the influence parameters on the quality of SLM solids.

3.4.1 Part geometry and CAD data

3.4.1.1 Part orientation

The orientation of parts on the building platform can vastly influence the process duration as secondary process steps such as the application of new powder layers are very time consuming. Part orientation, however, also comprises the issue of accuracy since the staircase effect due to finite layer thickness limits accuracy (Rehme, 2005, p. 229, [250]). Rattanawong (2004, pp. P4050.1-P4050.5, [242]) suggested an algorithm to optimize build directions by minimizing the volumetric build error caused by the staircase effect. However, for metal processing LFF methods it is unlikely to allow arbitrary build directions since heat conduction issues of the emerging part and the powder bed limit the degrees of freedom. The same constraints apply for the considerations of Xu (1999, pp. 56-57, [326]) who suggested to optimize the part orientation depending on

- material cost,
- manufacturing time,
- build error and
- surface finish

in that order. This is generally a comprehensive choice of parameters between which a reasonable compromise has to be made. In this recommendation the material is influenced by the amount of necessary support structures that result from the build direction. Some further comments on part orientation (Lin, 2001, pp. 74-78, [183]) advised that build errors can also be caused by the shape of part boundaries in as-processed layers depending on the type of Solid Freeform Fabrication process (e.g. concave or convex layer boundary) and by deviations from the desired part geometry due to resolution errors in the part’s Standard Triangulation Language (STL) surface model. An algorithm was presented to account for these errors, helping to e.g. improve the issues of build error and surface finish.

3.4.2 Material

3.4.2.1 General properties and processability of materials

Metals and metallic alloys represent the largest group of materials currently developed for the SLM process. Generally, the viscosity of metals is several orders of magnitude greater than that of polymers even near the melting point. Therefore, solid state binding mechanisms are not feasible for metallic materials (Bourell, 1992, p. 371, [43]), however, some alloys can be processed with moderate effort such as stainless steel while others cannot be handled easily. The reason for such different behaviour can be found in the material properties such as melting point, thermal elongation, heat conductivity, viscosity of the melt and particle wettability. Today most SLM machines are equipped with solid state lasers that offer wavelengths between 1064 and 1090 nm which allow better beam absorption for melting metals than the CO_2 wavelength of 10600 nm.

The choice of single-phase metallic materials for LFF is limited because the properties of the solid are of great importance. Van der Schueren (1995, p. 26, [300]) emphasized that the wetting characteristics of the liquid over the solid particles are very critical. This affects the wetting angle which should be as small as possible to achieve low surface tension forces of the melt. Particle wetting is also difficult when oxide layers exist on the powder particles, therefore, their surface condition is of considerable importance as well. Generally, the wetting issue can be improved with chemical additives like flux media such as phosphorus which is found in some powder materials commercialized by EOS (Agarwala, 1995, p. 30, [4]), such as Cu_3P (Zhu, 2005, p. 80, [332]) or zinc chloride (Manriquez-Frayre, 1990, p. 105, [191]). All these issues led to the concurrent development of two-phase materials which allow liquid-phase sintering that is an easier to control binding mechanism than full melting because balling is avoided due to adjusted interparticle wetting. Two-phase materials can be arranged either as a mixture of two powders or one phase of powder can exhibit a coating made from the second phase. Tolochko (2003, pp. 72-77, [295]) tested both possibilities with Fe-Cu and Ni-alloy-Cu mixtures as well as Cu-coated Fe-powder and Cu-coated Ni-alloy powder. The findings revealed that either the low melting point component, i.e. copper in the Fe-Cu mixture, or the powder of higher absorptance, i.e. the nickel-alloy in the Ni-alloy-Cu mixture melts first and acts as a binder material. In coated powders, however, only the coating material can bind the particles, therefore, it must exhibit the lower melting point. Two-phase materials do not offer the same properties as engineering materials do in functional, engineering applications. Therefore, this thesis focusses only single-phase materials.

These can be grouped into four different material groups which are elements, alloys, superalloys and intermetallics each of which show characteristic challenges of their own in the laser melting of their powders. Pure elements such as gold or silver show very high reflectivity thus reducing the absorptivity of their powders and increasing the risk of process instabilities due to so-called back reflections. These elements as well as copper also exhibit very little absorptivity in the above mentioned wavelength ranges of solid-state lasers. Their absorptivity increases remarkably towards the wavelengths of visible light. Despite these problems Pogson (2003, pp. 335-343, [229]) and Ramos (2004, p. 212, [241]) tried to process copper powder with Nd:YAG and Yb:YAG lasers, respectively. They used steel and copper substrates, however, all experiments yielded widely scattered part densities where on average the test specimens were incomplete or not fully dense with densities between 60 and 96 % of the value given in the literature. Much more promising results with elemental powder were achieved by Emmelmann et al. (2006, p. 30, [108]) who processed c.p. grade 1 titanium and obtained average densities around 98 %.

Alloys are the most SLM-tested group of materials. Early developments by Meiners (1999, pp. 76-99, [201]) yielded first successful processing of single-phase materials such as stainless steel 1.4404 (316L) and 1.4332 (309L) and achieved densities above 99 % of the values given in the literature. These materials show quite docile behaviour while other alloys are less easy to handle. The reason can be found in the nature of the SLM process due to its rapid cooling of the material. Stainless steel alloys e.g. show martensitic hardening when cooled down quickly enough from the melting point to ambient temperature because carbon is forced to dissolve while their lattice structures change from *fcc* to *bcc*. In titanium alloys, however, the martensitic transformation is accompanied with a transition from *bcc* to *hcp* without dissolving elements. Therefore, the change of volume is even greater for titanium alloys and they suffer residual stresses leading to undesired consequences for the process which are explained in detail in ***section 3.5.2***. Due to this other steel alloys were the first to be adapted for the SLM process. Initially, tool steels 1.3343 (M2) and 1.3344 (M3/2) were examined by Niu (1998, pp. 67-72, [218] and 1999, pp. 25-31, [219]). These alloys, however, delivered a rather insufficient density around 70 % as found by Akhtar (2003, p. 666, [7]) and Hauser (2003, pp. 645-647, [138]) who both confirmed that the alloy composition has a significant influence on the resulting density since identical powder fractions of the tool steel alloy 1.2343 (H13) allowed obtainable densities of up to 90 % of the literature value. Regardless of the above mentioned residual stress problems associated with titanium alloys Over (2003, pp. 22-76, [223]) managed to develop SLM for TiAl6V4 and obtained densities of up to 99.5 % by using sufficient preheating of the building platform. Experimental analysis of the commercial SLM machine from MCP-HEK at Hamburg University of Technology (TUHH) has involved the successful processing of some the above mentioned as well as many new different engineering materials such as stainless steel 1.4404 and 1.4410 (Eisen, 2004, pp. 29-59, [104]), tool steels 1.2344 and 1.3342 and Cu90Sn10 (Lemke, 2005, pp. 105-109, [180]) as well as the titanium alloy TiAl6Nb7 (Berggreen, 2005, pp. 38-74, [37]). Other researchers contributed results with nearly full part density for the aluminum alloys AlSi25, AlSi10Mg and AlMg3 (Zhang, 2004, pp. 51-82, [330]) and CoCr (Uckelmann, 2007, pp. 22-30, [299]).

Super alloys are materials of complex composition based on nickel, cobalt or nickel-iron. Typically, they exhibit high mechanical strength and creep resistance at high temperature since they are often used in processes with directional solidification where single crystal parts with no grain boundaries are obtained. This effect avoids creep at high temperatures. The SLM process does not allow directional solidification of the processed material, nevertheless, especially some nickel-based superalloys were subject to scrutiny such as 2.4668 (Inconel 718) by Klocke (2002, p. 196, [160]), Mar-M247 by Ramos (2002, pp. 213-215, [240]) and 2.4851 (Inconel 601) as well as 2.4856 (Inconel 625) by Lemke (2005, pp. 92-100, [180]). All researchers obtained high densities with little pores slightly varying among the different materials. Klocke reported that strength and hardness of the SLM processed Inconel 718 material stayed far behind those values of the conventionally processed material, however, Lemke found both to be equal for Inconel 625.

The fourth group of single-phase materials are intermetallics which are typically characterized by lattice structures that deviate remarkably from those of their constituent metals. They show strong internal order and metallic with covalent or ionic bonding. Thus these materials offer a compromise between metallic and ceramic materials in terms of hardness and resistance to high temperatures. Only few such materials were tested so far, one of which was the intermetallic $Fe50Cu15Ni20Fe_3P15$ which allowed to obtain a dense structure with few pores (Kruth, 2003, pp. 139-142, [168]). The well-known shape memory alloy TiNi was processed by Kyogoku (2003, pp. 674-675, [170]) but the shape memory effect was not observed in the produced parts unless they were made from a two-phase powder with identical amounts of elemental titanium and nickel.

Using powder mixtures of more than one material to achieve in-process alloying of a material similar to likewise procedures performed in conventional sintering processes was indicated by Kruth (2004, pp. 55-58, [169]) and suggested by Rehme (2005, p. 229, [250]). The manufacture of parts from graded materials by implementing a special deposition technique where alternate layers of different materials are applied could also be available in the near future. Beal (2004, pp. 189-195, [35]) obtained some preliminary results with different grades of tool steel 1.2344 and copper. More future perspectives were presented by Petersen (2007, pp. 139-147, [227]) who developed the laser sintering process for metal-ceramic composites such as materials called Fe-s-MAC, i.e. $Fe60Al7Al_2O_333$, and CMMC, i.e. [ZrO_2, TiC, SiC](1-10)-[Fe-Ni](90-99). These materials showed promising results for functional surfaces, e.g. in applications where high resistance to wear is required.

3.4.2.2 Special properties and processability of powder materials

Practical experience with the SLM process reveals that the process capability of the powder material used is most crucial. Despite that the solid material properties promise sufficient processability, it might still occur that a particular material is not available as a suitable type of powder. The desired goals are homogeneous layerwise application of the powder, high relative powder density and thin layer thickness in respect to the quality properties mentioned in ***section 3.5.2***. In order to achieve this, several requirements must be met. Of utmost importance is the the ability of a powder to flow freely otherwise no homogeneous powder layers can be deposited. This property can be tested by measuring the time it takes the powder to pass through a funnel with an orifice of given diameter according to the norm ASTM B 213 (2003, pp. 2-3, [18]). This method gives an indication whether an arbitrary powder is suitable for the SLM process at all. Derived from these constraints five important requirements were found (Rehme, 2006) which are presented as follows.

Bulk density

A general rule is that higher density of the base material results in better flow characteristics of its powder. Practical experience with the SLM process has therefore shown that for stainless steel powders (1.4404) with a bulk density of approx. 7.85 g/cm³ the flowability is sufficient, whereas for titanium alloy powder such as TiAl6Nb7 which shows a bulk density of approx. 4.51 g/cm³, other factors such as particle size distribution, etc. need to be optimized to ensure sufficient flowability. For aluminum powder like e.g. AlSi10 (bulk density approx. 2.7 g/cm³) the flow characteristics deteriorate such that hardly any useful powder layers can be obtained using the standard SLM process which provides a silicon wiper to spread the powder (Rehme, 2005). Similar results for different materials were found by Zhang (2004, pp. 44-45, [330]) who used a prototype SLM machine with different powder spread facilities and therefore managed to obtain nearly acceptable powder layers for aluminum.

A second issue in terms of density is the relative density of the powder bed. The goal of obtaining fully dense parts from the process requires a high relative density of the powder bed. Powder beds of e.g. stainless steel 1.4404 powder with nearly spherical particles are slightly compressed by the silicone wiper in the SLM machine and can achieve relative densities of around 0.618. Compared to the theoretical maximum density of 0.74 for spherical particles in *hcp* configuration this value is significantly lower. Karapatis (1999, p. 259, [157]) annotated that the relative density of very thin layers of powders on solid material from previous layers underneath is even much lower due to so-called wall effects. These are caused by powder particles of sizes in the order of the layer thickness which allow less volume to be filled with smaller particles directly between them and the adjacent solid material. Apparently, practical observations in the SLM process showed that the influence of the powder bed density is only of minor significance to the density of the resulting part. It generally occurs that each consecutively deposited powder layer is thicker than the selected layer thickness due to the shrinkage of the previous powder layer upon melting and solidification. This way the shrinkage which helps to obtain full part density is counterbalanced well. Thus, if each deposited layer of powder is thicker than the selected layer thickness, the above mentioned observations made by Karapatis will be of minor importance only.

Particle size

Best process results will only be obtained if the particle size of the powder material is restricted to a certain range. The upper limit controls the minimum layer thickness which is responsible for the quality property of surface roughness due to the staircase effect. The maximum particle size should be chosen at least 10 % less than the layer thickness to avoid the above mentioned wall effect. Secondly, the upper limit must be chosen such that a physical bond between consecutive layers is guaranteed in respect to the consumed amount of energy per volume unit in the powder bed. The bottom limit has major influence on the flow characteristics of any powder. If chosen too small, the flowability will be severly constricted due to small particles exhibiting strong inter-particle forces. According to Zhang (2004, p. 36, [330]) restricting the bottom limit also increases the process stability since small particles vaporize more easily and enhance powder spattering. Therefore, the SLM process can be handled best if for layers of 75 µm thickness as used in the test parts presented in this thesis the particle size ranges between 10 and 65 µm.

Particle size distribution

Furthermore, the distribution of different particle sizes should follow a specific pattern to receive a high relative density of the powder bed. According to German (1989, pp. 136-137,

[120]) a relative density of 95 % is achieved for a so-called trimodal distribution with relative particle diameters of 49 to 7 to 1. Considering the particle size range of 10 to 65 µm given above it is comprehensible that this requirement cannot be fulfilled. Hence, Karapatis (1999, p. 261, [157]) suggested using approx. 30 weight-% fine powder and 70 weight-% coarse powder with a size ratio of 1:10 which could be realized if the size ratio or the smallest acceptable particle size is slightly reduced. SLM parts fabricated by Wolfangel (2006, pp. 47-79, [325]) with a variety of different customized particle size distributions revealed that part density can be increased if bimodal particle size distributions are applied.

Typically, commercially available powders offer a continuous particle size distribution rather than discrete particle sizes. It is therefore a realistic compromise to aim at exponentially declining distributions with a relative high number of small particles, a medium number of mid-sized particles and a small number of large particles literally leading to a multimodal distribution. This should approximately match a relation of 4 to 1 regarding the amount of smallest particles compared to the amount of largest particles. For the SLM process this particle distribution can be stated as

$$n(d) = n_0 \cdot e^{cd} \tag{3.1}$$

where n is the number of particles and d is the particle diameter (Rehme, 2005). For a particle size range of 10 to 65 µm as mentioned above the constants in this formula result to $n_0 = 1.287$ and $c = -0.02521$ provided that d is given in µm and e is Euler's constant.

Particle shape

If possible, all powder particles should be rather spherical than spattered since this helps improving the powder's flow characteristics. This is important for mainly two reasons. Firstly, the maximum relative density of a multimodal powder particle distribution is only obtained if particles of different diameters are spread homogeneously within the powder bed which is a rather theoretical assumption. However, spherical particles allow better ordering (Van der Schueren, 1995, pp. 27-28, [300]) and can fill residual gaps in the powder bed more easily because of reduced friction. Secondly, due to this effect spherical particles will increase the ability of a powder to flow freely and ensure a homogeneous application of powder across a layer. The only advantage for spattered powder particle appears to be their greater surface-to-mass-ratio which can improve the process kinetics of fusing particles together by increased laser beam absorption (Niu, 1999, p. 1233, [220]). However, this advantage is only marginal since powder beds generally show very high absorption as explained in ***section 3.4.3.1.***

Humidity and oxidization

Moisture contents in the powder is definitely undesired as it will increase inter-particle forces leading to a possible loss of the powder's ability to flow freely. However, exposing a powder to ambient atmosphere e.g. during recycling or sieving can increase its humidity. Thus, the process chain has to provide drying if necessary. Some powder materials can show sensitive reactions to ambient gases such as oxygene. Oxidization might lead to a deterioration of the powder's wetting characteristics which is explained above in ***section 3.4.2.1***.

3.4.3 Process

3.4.3.1 Laser beam and material interaction

Sun (1991, p. 21, [285]) established a model for the understanding of the process of solidifying metallic materials in a powder bed. This is divided into the optical submodel accounting for the interaction between the laser beam and the powder material, the thermal submodel describing the heat transfer and melt front propagation in the powder bed as well as the solidified material and the sintering submodel. Generally, the term 'sintering submodel' should be replaced by 'coalescence and solidification submodel' as a variety of binding mechanisms can be held responsible for powder bed consolidation. The overall process model was extended by Klocke (2003, pp. 387-392, [162]) who added a chemical submodel to account for chemical reactions such as oxidization. These need to be controlled to enhance the wetting of powder particles in the melt pool.

Initially, the laser beam source is responsible for the amount of energy applied onto the powder bed. Typically, the laser beam focus which exhibits a specific waist diameter $d_{0,86.5}$ is positioned exactly on the powder bed surface or slightly above or below it. Due to losses in the optical system of a SLM machine the beam power P_L is reduced while the beam parameter product is increased, which results from multiplication of the laser beam's waist radius $w_{0,86.5}$ and half of its divergence angle $\Theta_{86.5}$. Compared to an ideal Gaussian beam a real laser beam exhibits both waist diameter $d_{0,86.5}$ and divergence angle $\Theta_{86.5}$ increased by factor M as shown in ***fig. 3.3*** according to ***eq. (3.2)*** and ***eq. (3.3)*** (Eichler, 2003, p. 228, [102]). The figure was derived from a drawing given by Eichler (2004, p. 64, [103]), however, here the true beam waist diameters are given. This increase of focus diameter broadens the intensity distribution of the laser beam perpendicular to the direction of propagation according to ***eq. (3.5)***.

$$d_{86.5,real}(z) = M \cdot d_{86.5,ideal}(z) \tag{3.2}$$

$$\Theta_{86.5,real} = M \cdot \Theta_{86.5,ideal} \tag{3.3}$$

Sun's optical submodel (1991, pp. 22-26, [285]) assumed that the incident laser beam energy on the powder bed is partially absorbed and mainly conducted into the powder bed. A small fraction of it is lost at the surface through radiation and convection. Transmission of laser

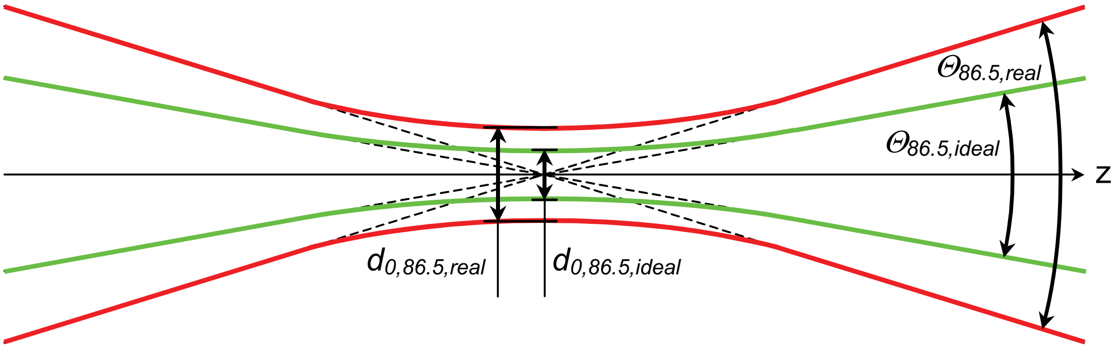

Figure 3.3: Propagation of an ideal Gaussian beam and a real laser beam

light through the powder bed can be neglected since typical penetration depths are rather small. Therefore, the absorptance of laser beam energy, which is the reflectivity *R* deducted from unity, is a major factor in the following considerations. The full laser beam intensity I_0 decreases with penetration depth *z* according to ***eq. (3.4)*** where β is the effective absorption coefficient and *e* is Euler's constant. The effective absorption coefficient is approximately the inverse of the particle size *d* because laser light is easily attenuated by metallic powders due to a complex sequence of reflections and scattering on powder particle surfaces.

$$I(z) = (1 - R) \cdot I_0 e^{-\beta z} \quad \text{where: } \beta = \frac{1}{2d} \tag{3.4}$$

Tolochko (2000, p. 157, [294]) found that a powder material generally shows higher absorptance than the according bulk material. In metallic materials this property is mainly dominated by electrons located in states close to the Fermi level. 50 to 120 % higher absorptance of metallic powder materials was confirmed by Laoui (2000, p. 455, [176]) who verified the complex reflection situation in a powder bed using ray-tracing simulations as well as experiments by means of Nd:YAG laser beam radiation.

Substitution of I_0 with the intensity distribution of a real laser beam source, e.g. a Gauss mode laser beam, which depends on the radial distance *r* from the center of the beam, yields ***eq. (3.5)*** and ***eq. (3.6)*** in cartesian coordinates where *w* is the beam radius and *x* and *y* are the powder bed coordinates. A moving laser beam can be modeled if the time *t* is introduced and the scan speed v_x in x- and v_y in y-direction is considered, thus giving ***eq. (3.7)***. ***Eq. (3.4)*** combined with ***eq. (3.7)*** results in ***eq. (3.8)*** which gives the local intensity distribution of laser beam light inside the powder bed at a given point of time.

$$I(r) = (1 - R) \cdot I_0 \cdot e^{-\frac{2r^2}{w^2}} \tag{3.5}$$

$$I(x, y) = (1 - R) \cdot I_0 \cdot e^{-\frac{2x^2 + 2y^2}{w^2}} \tag{3.6}$$

$$I(x, y, t) = (1 - R) \cdot I_0 \cdot e^{-\frac{2(x - v_x t)^2 + 2(y - v_y t)^2}{w^2}} \tag{3.7}$$

$$I(x, y, z, t) = (1 - R) \cdot I_0 \cdot e^{-\frac{2(x - v_x t)^2 + 2(y - v_y t)^2}{w^2} - \beta z} \tag{3.8}$$

If the intensity distribution *I(x,y,z,t)* is partially differentiated with respect to *z*, then the amount of energy *g(x,y,z,t)* is derived which is absorbed per volume and time unit at a given set of coordinates of the powder bed. This yields the so-called heat source function specified in ***eq. (3.9)*** which is required for heat transfer calculations as shown in ***section 3.4.3.2***.

$$g(x, y, z, t) = -\frac{\partial I}{\partial z} = (1 - R) \cdot I_0 \cdot \beta \cdot e^{-\frac{2(x - v_x t)^2 + 2(y - v_y t)^2}{w^2} - \beta z} \tag{3.9}$$

3.4.3.2 Heat and mass transfer

The calculation of heat transfer in the powder bed was also detailed by Sun (1991, pp. 32-39, [285]) who suggested the Fourier differential equation of effective heat conduction in ***eq. (3.10)*** to describe the propagation of heat (where T is the temperature) in a powder bed which exhibits a stochastic distribution of randomly sized powder particles by effective parameters. Since powder beds consist of powder particles with gas-filled voids they show a relative density ρ_{eff} and thus a specific heat $c_{p,eff}$ proportional to ρ_{eff} as shown in ***eq. (3.11)***. Numerous approaches were made to establish appropriate approximations for the effective thermal conductivity λ_{eff} of a powder bed to allow treating it like a solid. Different considerations of the three mechanisms of heat conduction between powder particles, convection in the gas-filled voids and radiation across the voids leads to various results. The most simple approach was given by Williams (1998, p. 93, [321]) who only related λ_{eff} in ***eq. (3.12)*** to the solid fraction of the powder bed thus neglecting convection and radiation. Tolochko (2003, pp. 320-323, [296]), however, assumed a vacuum between the powder particles and subsequently declared thermal radiation between particles and heat conduction through particle necks the dominant influences on λ_{eff}. Hence, the left term in ***eq. (3.13)*** is the derived radiation where d is the particle size and σ is the Stefan-Boltzmann constant. The right term accounts for the conduction where Λ is the normalized contact conductivity which depends on the structure of the powder bed packing and b is the neck radius. All three mechanisms of heat transfer were considered by Yagi (1957, pp. 373-381, [327]) in ***eq. (3.14)*** where the left term stands for heat conductivity, the middle term for convection and the right term for radiation. Here, δ is the relation of solid conduction area to the total area of a cross section plane, β is the distance between particles in relation to the mean particle size, γ is the length of conduction in solid divided by the mean particle size, ϕ is the length of conduction in gas related to the mean particle size, h_{rs} is the solid to solid radiation transfer coefficient and h_{rv} is the void to void radiation transfer coefficient. Bugeda (1999, pp. 21-26, [49]) tried to simplify this correlation and developed ***eq. (3.15)*** where ϕ was merely found empirically.

$$\rho_{eff} c_{p,eff} \frac{\partial T}{\partial t} = \frac{\partial}{\partial x}\left(\lambda_{eff} \frac{\partial T}{\partial x}\right) + \frac{\partial}{\partial y}\left(\lambda_{eff} \frac{\partial T}{\partial y}\right) + \frac{\partial}{\partial z}\left(\lambda_{eff} \frac{\partial T}{\partial z}\right) + g(x,y,z,t) \tag{3.10}$$

$$c_{p,eff} = c_{p,solid} \cdot \rho_{eff} \tag{3.11}$$

$$\lambda_{eff}(T) = \lambda_{solid}(T) \cdot \rho_{eff} \tag{3.12}$$

$$\lambda_{eff}(T) = \frac{16}{3} d\sigma \cdot T^3 + \Lambda \lambda_{solid}(T) \cdot \frac{2b}{d} \tag{3.13}$$

$$\lambda_{eff}(T) = \delta \lambda_{solid}(T) + \frac{\left(\frac{\rho_{eff}}{\rho_{solid}} - \delta\right) \cdot \beta}{\frac{\gamma}{\lambda_{solid}(T)} + \frac{1}{(\lambda_{gas}(T)/\phi) + dh_{rs}}} + \left(1 - \frac{\rho_{eff}}{\rho_{solid}}\right) \beta d h_{rv} \tag{3.14}$$

$$\lambda_{eff}(T) = \frac{\rho_{eff} / \rho_{solid} \cdot \lambda_{solid}(T)}{1 + \phi \cdot \lambda_{solid}(T) / \lambda_{gas}(T)} \tag{3.15}$$

These formulae only yield the properties of static powder beds. In LFF processes, however, mass transfer takes place due to melting and solidfication of powder. In sintering as well as in melting of powder particles, shrinkage of the powder bed material occurs because its porosity is reduced. The mass transfer at the powder bed surface is nearly neglectable as the initial powder bed roughness is not exceeded considerably (Tolochko, 2003, p. 321, [296]). Remelted or sintered regions in the powder bed will approach the heat conductivity λ_{solid} of the solid material.

A dynamic consideration of the in-process heat conductivity, especially around the melt pool area, is more complicated. Sih (1994, p. 322, [275]) proposed to include heat transfer through

- conduction and radiation of adjacent powder particles where incomplete solid contact prevails,
- conduction and radiation of melt in powder particle interstices where incomplete solid contact prevails,
- conduction and radiation of melt in the melt pool and
- conduction where complete solid contact prevails.

These mechanisms are listed in the order of their occurrence in one specific spot on the powder bed surface where the laser beam moves across. From this a rather lengthy thermal transport formula was suggested which is not repeated here. It completely neglects convection mechanisms which is supported by Tolochko's confirmation (2003, p. 323, [296]) that conductivity and radiation are of the same order of magnitude and that process dynamics are strongly influenced by radiative heat transfer as it determines the melt front propagation through the powder bed.

After all parameters from ***eq. (3.10)*** are estimated, it can be solved provided that the following boundary conditions are assumed. ***Eq. (3.16)*** accounts for the loss of heat at the surface of the powder bed to the surrounding atmosphere through convection where h is the convection coefficient. It also accounts for the loss of heat through radiation at the interface between the powder bed and its surrounding chamber where ε is the powder bed's surface emissivity and σ is the Stefan-Boltzmann constant. Since the bottom of the powder bed container is considered adiabatic such that no heat is lost there, the boundary condition in ***eq. (3.17)*** can be derived where Sun (1991, p. 33, [285]) suggested that this condition can even prevail at a finite value of z equal to the depth of the powder bed. In fact typical LFF machines possess a heated building platform which keeps the temperature at the bottom of the powder bed at a constant level. The third important boundary condition is ***eq. (3.18)*** which assumes the initial condition of a homogenous temperature distribution before the process starts.

$$-\lambda_{eff}(T)\left.\frac{\partial T}{\partial z}\right|_{z=0} = h\left(T_{environment} - T_{z=0}\right) + \varepsilon\sigma\left(T^4_{chamber\ surface} - T^4_{z=0}\right) \qquad \textbf{(3.16)}$$

$$-\lambda_{eff}(T)\left.\frac{\partial T}{\partial z}\right|_{z=-\infty} = 0 \qquad \textbf{(3.17)}$$

$$T(x,y,z,t=0) = T_0 \qquad \textbf{(3.18)}$$

3.4.3.3 Numerical process models

Full factorial experimental analysis of LFF processes to obtain a process map as given in ***fig. 3.4*** requires much effort. Therefore, it is helpful to use numerical models to narrow down the manifold influences of all dominant process parameters. The effective heat conductivities as introduced in ***section 3.4.3.2*** are indeed suitable for calculations of powder bed temperatures, however, interparticle temperatures, the transition from powder to liquid material at the melt pool border as well as melt pool dynamics are not covered in such considerations. Thus, it is useful to employ FEM models based on ***eqs. (3.9)*** to ***(3.10)*** and ***(3.16)*** through ***(3.18)*** which allow a realistic modelling of the process around the melt pool, the solidified portion of the part and the powder bed. Typically, homogenous powder particle distributions are assumed to limit the complexity of calculations. The most important models are presented below.

Meiners (1999, pp. 25-41, [201]) developed a 2D model to calculate the temperature distribution in single powder particles derived from the incident laser beam light and the absorption characteristics of the powder particles which allows an estimation of possible scan speeds. After incorporating a 2D-model of the scanning of layers, the melt pool geometry in scaning direction and along the z-axis could be determined such that reasonable values for the layer thickness and refined values for the scan speed were derived.

In a much simpler 1D FEM model Das (2001, pp. 358-360, [74]) considered the heat transfer through a powder bed with effective heat transfer properties as suggested in ***section 3.4.3.2***. However, in this model the melt front propagation in z-direction was more sophisticated due to incorporating the Stefan condition from ***eq. (3.19)*** which gives a boundary condition for the heat flux balance at the melt interface where the transition from solid to liquid takes place.

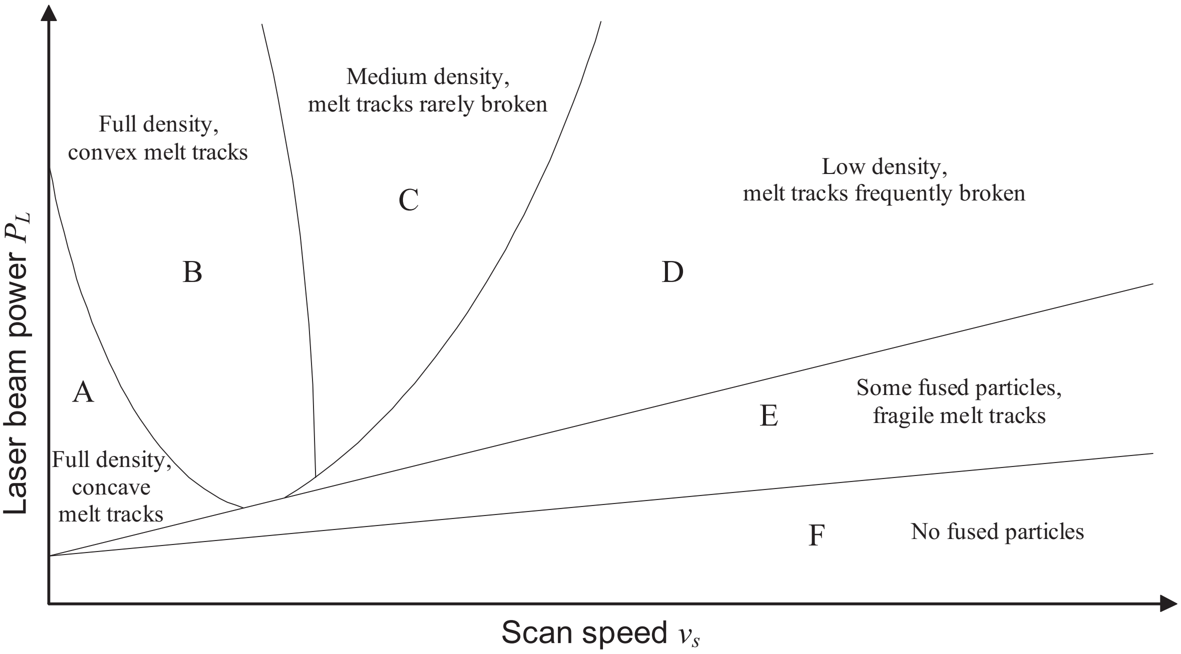
Full density,
convex melt tracks
Medium density,
melt tracks rarely broken
Low density,
melt tracks frequently broken
A
B
C
D
E
F
Full density,
concave
melt tracks
Some fused particles,
fragile melt tracks
No fused particles
Laser beam power P_L
Scan speed v_s

Figure 3.4: Simple process map for Laser Freeform Fabrication processes [139]

Here, the speed of the melt front propagation is the z-coordinate differentiated with respect to time *t*. *L* is the latent heat required for the phase change and both temperature gradients are considered in their respective solid or liquid environments towards the border at $z = z_{melt\ front}$. Later this model was slightly refined by Chung (2002, pp. 322-330, [62]).

$$\frac{dz}{dt}\rho_{solid}L = \lambda_{solid}\frac{\partial T_{solid}}{\partial z} - \lambda_{liquid}\frac{\partial T_{liquid}}{\partial z} \qquad \textbf{\textit{(3.19)}}$$

A true 3D FEM process model was presented by Over (2003, pp. 36-50, [223]) who focussed on the temperature dependent development of thermal stresses and strains in application of single scan tracks and adjacent scan tracks for complete layers. A comprehensive summary on the thermodynamics behind single scan tracks on powder beds, single scan tracks on previous layers and adjacent scan tracks for complete layers on previous layers can be found in Chen's work (2005, pp. 358-366, [55]).

A similar model was developed by Wagner (2003, pp. 90-96, [305]) who conducted 3D FEM calculations for the temperature distribution in single powder particles exposed to laser beam light, for point-like exposure of powder bed surfaces and for line scan exposure of powder bed surfaces. This was as well based on the assumptions for laser beam and material interaction and for heat and mass transfer introduced in the above sections. However, chemical and metallurgical processes (Wagner, 2003, pp. 67-81, [305]) were supplemented to round off this approach. Petersen (2007, pp. 175-183, [227]) supplied methods to obtain numerical solutions for the same type of problems where individual strategies, e.g. multiple exposure for adapted temperature control, need to be applied.

3.4.3.4 Process stability

Successful coupling of the laser beam energy into the powder bed and achieving a suitable heat and mass transfer around the melt pool is not necessarily sufficient to obtain a stable LFF process. The stability of the solidified material depends significantly on the dominating process parameters which are summarized in ***section 3.5.1***. Typical process maps as suggested by Hauser (2004, pp. 452-456, [139]) and Klocke (2003, p. 180, [161]) exhibit regions of different material consolidation in diagrams of laser beam power versus scan speed. Hauser's finite element process modelling showed a distribution of different levels of powder material consolidation upon solidification according to ***fig. 3.4*** which is in good agreement with experimental findings. In this diagram A and B are regions of full part density with scan tracks of concave cross sectional shape in region A. In region B the scan track cross sections show a rather convex shape due to insufficient powder particle wetting of the melt. This raises the issue of undesired process instabilities due to melt beads that rise higher than the level of the powder bed surface plus one layer thickness and, therefore, obstruct the coating mechanism from depositing the next powder layer (Rehme, 2005). In regions C and D the shape of the scan track cross sections remain convex, however, the density of the solidified material decreases and scan tracks are occasionally broken in region C and more frequently in region D. In region E the powder material is only partially melted and the scan tracks are extremely fragile. Finally, region F comprises no fused particles at all. ***Fig. 3.4*** summarizes these regions qualitatively in a diagram of laser beam power vs. scan speed without giving explicit values because the scaling depends substantially on the powder material and the LFF system.

3.4.3.5 General process handling

Generally, the handling of single-phase metallic materials is more complicated than two-phase materials. Therefore, it took roughly a decade before materials like e.g. stainless steel were successfully processed with LFF systems. Nevertheless, typical issues arise with most single-phase metallic materials that are discussed as follows.

Hauser (1999, pp. 266-270, [136]) started early development of process maps for powder material from stainless steel 314S where laser beam power vs. scan speed were considered. The corresponding diagrams showed areas where melting and bonding occurs with low surface tension phenomena in dependency of average particle sizes. It was found that with the elimination of oxygen in the process chamber the surface tension forces of the melt became less dominant. Thus, liquid metal can flow more easily and wet other solid powder particles to create an improved bond of high strength and density. For the elimination of oxygen, flooding of the process chamber with argon process gas was recommended.

High thermal gradients are the main contributor to surface tension forces which increase the so-called balling effect and lead to high residual stresses (both explained in ***sections 3.4.3.6*** and ***3.4.3.7***). Morgan (2001, p. 160, [209]) suggested to preheat the metallic powder bed in order to reduce these problems as previously applied on polymer powder beds (Sauer, 2005, p. 40, [268]). However, polymer powder beds are maintained just below the glass transition temperature which cannot be associated with the metallic materials considered here since their melting point is far beyond the temperature which the optics, sensors and mechanics inside the process chamber can withstand. Nevertheless, most commercially available LFF systems were subsequently equipped with building platform heaters to achieve powder bed temperatures between 150 and 300°C. Only the no longer available DLF system introduced by Trumpf could achieve preheating of up to 500°C. Observations made at the Institute of Laser and System Technologies (iLAS) at Hamburg University of Technology (TUHH) showed that with the use of preheated powder beds less laser beam power is required to obtain fully dense parts (Rehme, 2005).

3.4.3.6 Material consolidation

Process stability as introduced in ***section 3.4.3.4*** depends vastly on the dominant process parameters. Especially high energy densities and low thermal conductivity of the powder bed can lead to a serious process instability, the so-called balling effect. The areas of high laser beam power P_L in Regions C and D of ***fig. 3.4*** are typical regimes where balling is likely to occur. This effect is enhanced, if the laser beam exposure takes place over unconsolidated powder with no solid part or the building platform directly underneath.

The balling effect was characterized by Tolochko (2003, p. 325, [296]) who described the formation of large spherical droplets which degrade the structure of the powder due to surface tension forces. This happens when rapid heating conditions due to high laser beam intensities and too little effective heat conduction into the powder bed promote the formation of droplets of the size of or greater than the laser beam focus diameter. In this case the period of solid-state sintering before melt formation is too short and the strength of necks between solid particles is insufficient to resist the surface tension of the melt. This tension is an effect where a liquid surface contracts to minimize its surface energy. This was further explained by Niu (1999, pp. 1229-1234, [220]) who observed that for solid-state and liquid-phase sintering no balling effect occurs. However, when full melting of the material is conducted, the melt pool exhibits a steep temperature gradient and surface tension is a function of temperature. Due to this the melt pool shows high surface tension at the edge and low surface tension near its center, respectively. This causes Marangoni forces which produce a flow of material from a region of low to a region of high surface tension and thus initiates the balling effect. Oxygen content in the powder even increases the surface tension temperature coefficient and promotes the balling effect. A method to counteract the balling effect was suggested by Morgan (2001, p. 166, [209]) who showed that using a q-switched Nd:YAG laser can modify the melt pool shape and thus overcome the surface tension. Other methods can be found in suitable process handling. In an experimental analysis Tolochko (2004, pp. 79-84, [297]) observed the formation of a flat lens-shaped scan track cross section. With increasing duration of laser beam exposure this shape deformed such that the edges bent upwards until they met and formed a sphere. This was explained with a simple geometrical model where the powder bed consists of layers of spherical particles. Its topmost layer receives the highest amount of heat energy compared to the sublayers underneath since more heat is lost sideways into the powder bed the deeper the according sublayer is located. Therefore, the horizontal and vertical shrinkage of each sublayer decreases with increasing depth and the probability of bending of the melt pool track edges increases. This model revealed mainly increasing powder bed length, or more specific increasing melt pool width, as an important influence on the balling effect.

More influence factors can be derived from the following multi-layer model (Rehme, 2006) where the intensity of the balling effect is described by the angle φ in ***fig. 3.5*** which should be kept as low as possible. The initial state before laser beam exposure is given in the left part of ***fig. 3.5*** where W_0 is the melt pool width, D_0 is the melt pool depth and d is the powder particle diameter. The number of particles n in one layer gives the following correlation.

$$W_0 = n \cdot d \tag{3.20}$$

For small angles φ the condition in ***eq. (3.21)*** can be established where the index i denotes the number of the layer.

$$\varphi = \min! \qquad \text{and } \varphi = \frac{W_i}{r_i} \tag{3.21}$$

This gives the consequences that the melt pool width W_i be minimized and radius r_i be maximized.

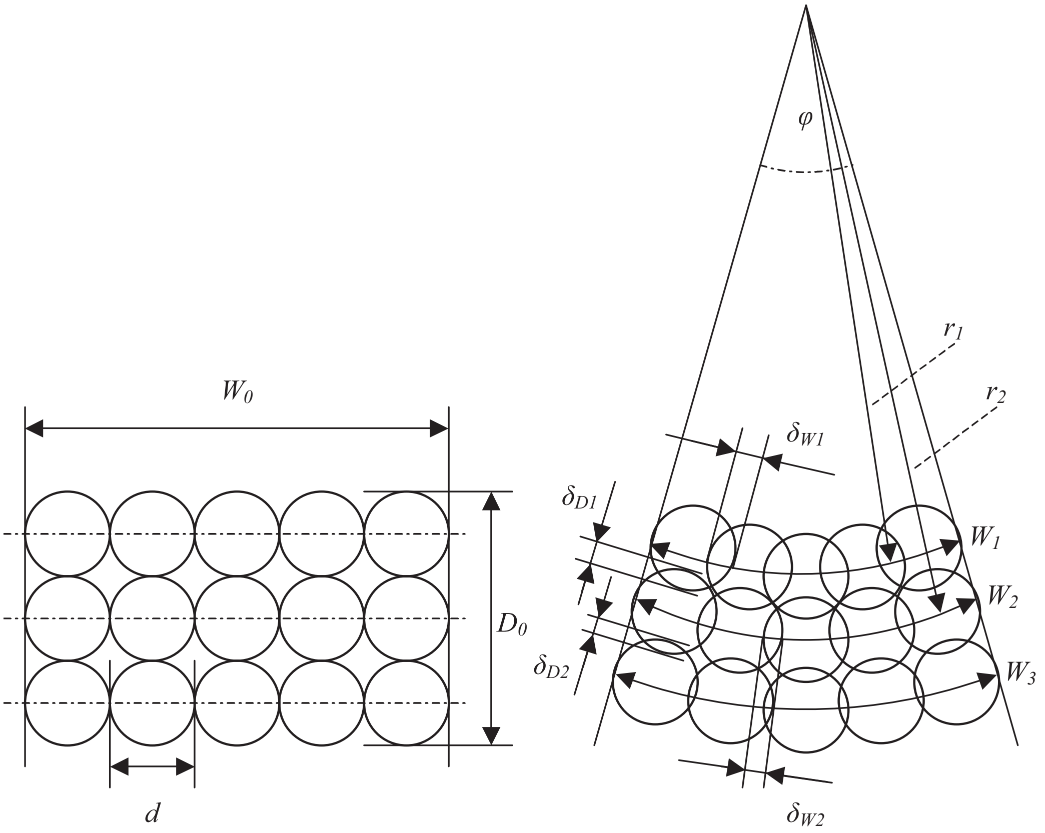

Figure 3.5: Balling effect model based on multi-layer powder bed model

$$W_i = \min! \qquad \text{and } r_i = \max! \tag{3.22}$$

The number of particles *n* in one layer does not change during shrinkage thus the consolidated width of each layer W_i can be expressed by subtracting the horizontal shrinkage between all adjacent particles in one layer δ_{W_i} from the initial melt pool width W_0.

$$W_i = W_0 - (n-1) \cdot \delta_{W_i} \tag{3.23}$$

The radius of each layer r_i can be obtained by simple adding of the topmost layer's radius and and the according number of particle diameters reduced by each previous layer's vertical shrinkage $\delta_{D_{i-1}}$.

$$r_i = (r_1 - d) + \sum_i \left(d - \delta_{D_{i-1}}\right) \qquad \text{for } i \geq 2 \tag{3.24}$$

It is assumed that each powder particle has a nearly uniform temperature distribution. Therefore, the vertical and the horizontal shrinkage of one layer is expected to be approximately identical.

$$\delta_{D_i} \approx \delta_{W_i} \tag{3.25}$$

Derived from ***eq. (3.24)*** this gives the following correlation.

$$r_i = (r_1 - d) + \sum_i \left(d - \frac{W_0 - W_{i-1}}{n-1} \right) \qquad \text{for } i \geq 2 \qquad (3.26)$$

From ***eqs. (3.23)*** and ***(3.26)*** it becomes apparent that W_i is minimized when W_0 is minimized and r_i is maximized when d is maximized and W_0 is minimized as well.

Thus the main conditions for the occurrence of balling is a large melt pool width which is increased by high laser beam power, low scan speed, large laser beam focus diameter and low effective heat conductivity of the powder. Further factors are small powder particle diameters and oxygene content in the powder. These conditions were developed for single-phase materials. Agarwala (1995, pp. 28, [4]) and Chen (2005, pp. 357, [55]) commented on two-phase materials that using two materials with substantially different melting points are also suitable to prevent the balling effect since the high melting point powder remains solid during laser beam exposure hence reducing the overall shrinkage.

3.4.3.7 Part warping

The layerwise manufacturing in LFF processes leads to thermal gradients between layers. The most recently manufactured layer shrinks as it cools down but the layers underneath obstruct it from complete shrinkage. Therefore, these layers exert a tensile force on the top layer while in return this one causes compressive forces on the layers underneath. This effect is stronger for greater thermal expansion coefficients of the material used. As the number of layers increases during build-time the result is either a part that has no internal stress but shows curl (in the state of equilibrium), i.e. the ends of a planar part bend in positive z-direction, or the result is a part with internal stress but without curl if it has a support structure securing it firmly to the building platform. In the second case cutting the part from the building platform will relieve the internal stress and still cause the part to warp.

This issue can be overcome by suitable post-processing methods or by proper process handling. In an attempt to understand this warpage phenomenon Dalgarno (1996, p. 559, [68]) discovered that two different curl radii can develop. If a part has one preferred direction of longitudinal elongation, then a small radius develops at both ends and a bigger radius develops between its middle and the ends. This can be seen quite well on samples prepared at iLAS (Rehme, 2007) in ***fig. 3.6 (right)*** where 25 layers of 75 µm thickness were built from stainless steel powder. The maximum deflection of this sheet metal-like part was 11 mm whereas the part consisting of 10 layers on the left showed only 1.5 mm deflection. The part on the right shows varying radii along the curved side as predicted by Dalgarno.

Important influence factors on residual stress and the curl effect, respectively, were determined by Pohl (2001, pp. 368-371, [230]). According to his research the level of residual stress becomes greater for decreasing hatch distance, increasing number of layers and increasing laser beam energy per unit area. Niebling (2005, pp. 79-80, [216]) found that especially the process speed takes major influence on residual stresses. E.g. increasing laser beam power and scan speed can still yield the same energy density and a nearly identical microstructure of the material but the cooling rate is changed such that higher internal stress

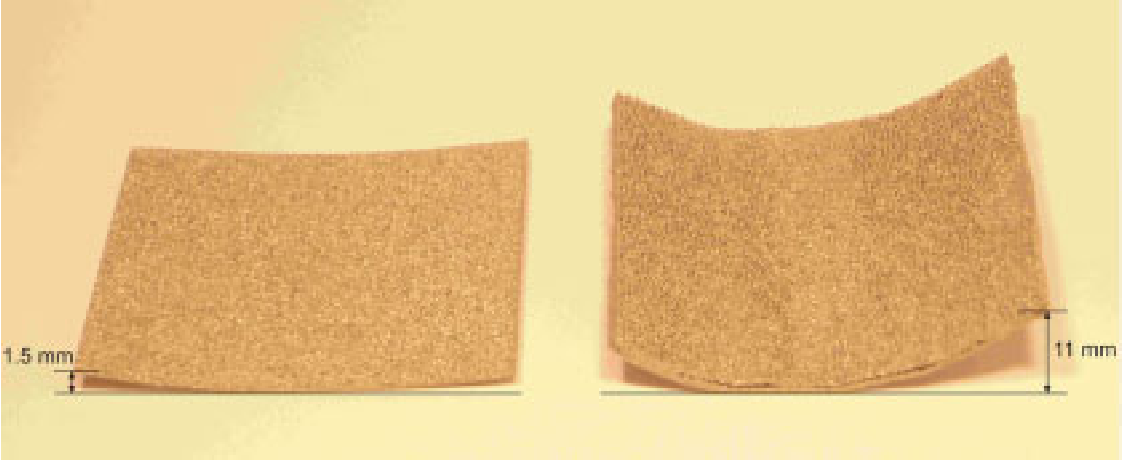

Figure 3.6: Examples for curl development in SLM parts (Rehme, 2007)

levels develop which might even lead to delamination of layers. The exposure strategy influences warping as well in such a way that short scan vectors perpendicular to the part's elongation yield the lowest internal stresses. This is realized best with a square exposure pattern where all squares are filled perpendicularly to the elongation. In contrast, spiral exposure patterns yield the greatest stress levels. The overall stress level of a part typically increases with the number of layers and with increasing yield strength of a material (Mercelis, 2005, p. 116, [203]). The preheating of powder beds as mentioned above generally helps to reduce thermal gradients and thus warping of parts. In fact if no preheating is used for single-phase metal powders, then typical scan vector lengths should remain below an order of magnitude of 15 mm (Hauser, 1999, p. 276, [137]).

An analytical description of part curl developing from residual stress was suggested by Uckelmann (2007, pp. 64-66, [299]) who described the curl of SLM parts through means of an elastic curve which is given as a second-order polynomial according to ***eqs. (3.27)*** where v is the deflection of a beam-shaped part in global z-direction, depending on the global x- and y-coordinates according to ***fig. 3.1***. The proportionality constants c_i and thus the overall deflection depend on the geometry of the part, the process parameters and the material.

$$v(x) = c_1 x^2 + c_2 x \text{ and } v(y) = c_3 y^2 + c_4 y \tag{3.27}$$

3.4.3.8 Process parameter optimization

As shown in ***section 3.3.2*** a tremendous amount of influence parameters act on LFF processes. Only a limited number of these parameters can be controlled by the user and even less parameters yield dominant influence. However, typically the number of free process parameters is still too large to conduct full factorial experiments if one intends to find optimum process parameters. Different methods were suggested by various authors to handle the complex interaction of these process parameters. Ghanekar (2003, pp. 353-355, [121]) proposed to use the D-optimality technique which involves the concept of least squares and gives accurate parameter estimates with least computing time.

For many production processes it is sufficient to obtain a robust process independent of all disturbance variables rather than finding the optimum of all involved process parameters. The inherent variance of the disturbance variables is typically responsible for the tolerance of process results around the desired mean value which is mainly influenced by the control parameters. The smaller the accepted tolerance is, the higher the process capability becomes resulting in process robustness. Finding of the dominant disturbance variables and the appropriate control parameter values on which the disturbance variables take least influence can be achieved for LFF processes using the Taguchi method (Lorenz & Rehme, 2005, pp. 92-95, [185]). In this method each factor level combination of control parameters is tested against all factor levels of disturbance variables. The variance becomes minimal when the so-called signal-to-noise-ratio (*S* to *N*) in ***eq. (3.28)*** becomes maximum which depends on the mean value of the desired part quality parameter $\bar{y}$ and the statistical variance s^2.

$$\frac{S}{N} = 10 \cdot \log\left(\frac{\bar{y}^2}{s^2}\right) \qquad \textbf{\textit{(3.28)}}$$

A more general approach based on the system theory of statistical test methodologies and the derived modelling was presented for LFF systems by Fährer (2002, pp. 35-54, [114]). Van Elsen (2007, pp. 65-95, [301]) suggested to transform process parameters into dimensionless values to achieve better comparability on one hand. On the other hand this method supposedly leads to results of higher validity but the number of independent process parameters cannot be reduced. Yet another although completely different approach to optimize process parameters of LFF processes was chosen by Steinberger (2001, pp. 115-126, [279]) who used FE simulations to obtain some optimum process parameters. However, it should be noted that this method yields not necessarily the optimum for all the dominant process parameters.

3.4.3.9 Process duration

As mentioned in ***section 3.4.1.1*** the part orientation can influence the process duration to a great extent. One of the approaches in this thesis is to reduce manufacturing time by filling solids with internal lattice structures. This can show impressive results with savings of up to 90 % of the layer scan time depending on the mechanical requirements of the parts (Rehme, 2006, p. 15, [252]).

Apparently, the major process parameters such as scan speed, hatch distance and layer thickness can also take serious influence on process duration. However, this possibility cannot be exploited arbitrarily. In ***section 3.5.2*** it will be shown that important LFF part quality properties will suffer severe losses if the process parameters are chosen unappropriately. This becomes obvious especially from ***eq. (3.29)***.

Other, though less efficient, ideas to reduce the process duration of solid LFF parts involve e.g. adapted exposure patterns. Rajan (2001, pp. 231-240, [239]) suggested an algorithm which identifies the optimum angle in the x-y-plane for the scan line direction of each layer such that each layer is fabricated with a minimum number of scan lines. This helps reduce so-called sky-writing where the scanner path is continued beyond the layer due to the scanner mirrors' inertia. A similar approach was found by Yang (2002, pp. 35-37, [328]) who calculated equidistant (similar to spiral) exposure patterns to reduce scan time. This method can lead to a significant reduction of scan time since sky-writing is avoided as much as possible. However, experiments at the iLAS at TUHH showed that spiral exposure patterns increase residual stresses in SLM parts made from TiAl6Nb7 (Rehme, 2005). Therefore, this procedure is not recommendable.

Another attempt to reduce the layer scan time of supposedly up to 20 % was achieved by Miramahdi (2006, pp. P6006.2- P6006.4, [205]) who improved the jump path plan of the laser beam in LFF processes according to the Ant Colony System method applied to the Traveling Salesman Problem.

3.4.4 Post-processing

The necessity of post-processing of LFF parts depends strongly on the required quality properties, on the desired functionality in terms of prototype or functional parts and on the type of material used. Generally, prototype parts do not necessarily require the same strict demands as functional parts and less post-processing might be sufficient. In the case of functional parts, however, typical quality properties might be specified to targeted values.

If a material is applied that only allows to achieve relative bulk densities below 0.95 (like e.g. two-phase powder), then subsequent HIPing processes are useful to improve the density. Agarwala (1995, p. 40, [5]) reported increases in relative bulk density from initial values of 0.72 to final values of as much as 0.98 within one to three hours. Two- or multi-phase materials are also typical candidates for subsequent liquid-phase sintering between solidus and liquidus temperature of one of the components. This process can be employed to also increase a part's density and thus its strength and hardness. In liquid-phase sintering temperature and time are important non-monotonic, non-linear key factors (Agarwala, 1995, p. 39, [5]).

The nature of LFF processes is characterized by notably rapid cooling and solidification of material once the melt-pool has moved on. For some materials such as steel this yields martensitic micro structures of high strength and hardness with well acceptable levels of break strain (Brettschneider, 2006, pp. 48-51, [45]). However, some materials such as titanium alloys embrittle due to prevailing high temporal cooling gradients and, therefore, rather low break strain values are obtained. A change of the material's micro structure can be achieved by subsequent annealing processes which help increase strength, ductility and hardness due to removal of crystal defects and the internal stresses they cause and due to nucleation of new grains in the recrystallization phase. Annealing also relieves residual thermal stresses which result from the layerwise manufacturing in LFF as explained in ***section 3.4.3.7***. Examples of successful application of annealing as a post-process were given by Emmelmann (2007, p. 54, [109]) where the break strain of TiAl6Nb7 parts was slightly improved from 0.5 % to 2.2 % and by Wirtz (2005, pp. 106-114, [322]) where the break strain of TiAl6V4 specimens was increased from 5.2 % to 11.5 %. Karapatis (1998, pp. 82-85,

[156]) showed how proper control of temperature and time has to be conducted to obtain minimum geometrical distortions and desired porosity and hardness values after thermal treatment.

Still a great issue for LFF parts is the surface quality. If surface roughnesses R_z equal or below 20 µm are needed, then, depending on the part geometry, processes such as sand blasting, grinding (e.g. vibratory grinding), shot peening or polishing (e.g. electrolytic polishing) are required which can deliver satisfying results. Of these methods shot peening is also capable of increasing the near-surface density. In certain applications, however, these processes may damage a part due to unwanted changes of shape. A typical example is the rounding off of edges from sand blasting which makes it unsuitable for LFF injection mould tools.

These parts are also critical in terms of accuracy. Some injection tool moulds require tolerances of 5 µm or better. Commercial LFF processes for metallic materials can deliver roughly ±0.1 mm tolerance. If functional surfaces are needed, oversized measures have to be provided in according part regions where only subsequent milling and turning processes can yield the desired part accuracy.

3.5 Product quality and manufacturing cost and time in applications of SLM solids

3.5.1 Dominating influence parameters in SLM processes

Of all influence parameters mentioned in ***fig. 3.2*** only approximately 13 are crucial to the resulting quality properties of the manufactured parts. The influence parameters can be divided into control parameters and disturbance variables. Control parameters are beam power P_L, the speed v_s of the laser beam focus $d_{0,86.5}$ as it moves across the powder surface, the hatch distance h_s (i.e. the distance between adjacent scan tracks in the scanned area), layer thickness l_z and exposure sequence strategy of which the scan vector length L is an important factor. All these parameters are displayed in ***fig. 3.7*** among some other process parameters. For each specific material used only a small range of values for each process control parameter, i.e. the so-called process window, will result in acceptable part quality properties as introduced below in ***section 3.5.2***. The inherent variance of disturbance parameters on the other hand is responsible for the tolerance of process results (Rehme, 2005, p. 229, [250]). The smaller the accepted tolerance is, the higer becomes the achievable process quality.

Despite the large number of process parameters the above mentioned, dominant control parameters in LFF processes became quite obvious during the early process developments made by Deckard (see ***section 3.2.1***). The fundamental work for SLM of single-phase, metallic materials conducted by Meiners (1999, pp. 52-65, [201]) was aimed at obtaining parts of high density by application of high energy densities. The energy density is significantly influenced by the laser beam power divided by the product of scan speed, hatch distance and layer thickness (see ***eq. (3.29)***). Therefore, the optimization path was to find a

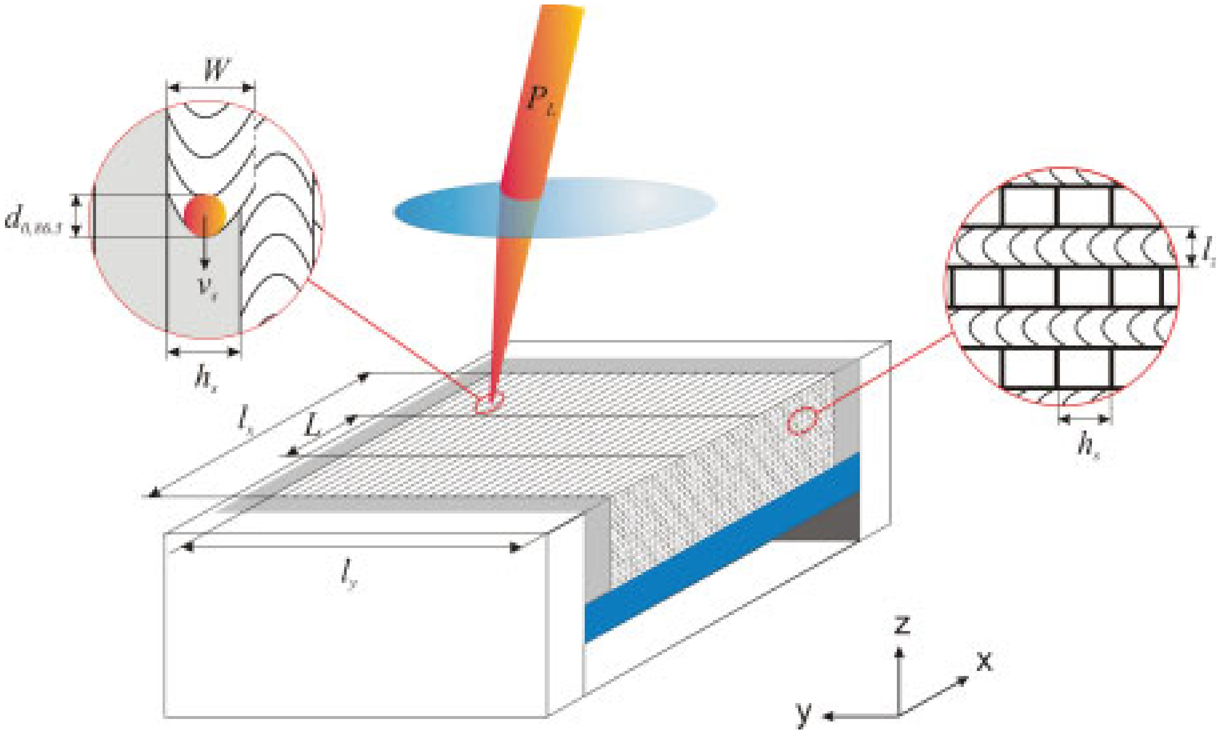

Figure 3.7: Dominant control parameters in SLM processes

suitable process window for laser beam power versus scan speed first, where part densities of close to 100 % are realized, if possible. Then, secondly, the ranges of layer thickness and hatch distance, which still allow high part densities, were evaluated. Laser beam power and scan speed both strongly interact with these two parameters as they influence the depth D and width W of the melt pool and therefore the connectivity of adjacent layers and scan tracks.

In order to find an optimum process window for the use of arbitrary SLM systems with any kind of material it is necessary to know the dominant process parameters on one hand and to balance their conflicting influences on part quality and on productivity on the other hand.

Laser beam power

It is required to apply high laser beam power to obtain high part density. However, maximum power is limited by material evaporation which leads to spattering powder particles, reduced density and increased surface roughness due to powder particles adhering to part surfaces. Increasing the laser beam power is also at the cost of part accuracy since the laser beam focus diameter typically increases with rising power which yields a wider melt pool. On one hand this constricts the smallest possible size of features that can be fabricated. On the other hand neglection of the changed melt pool size will result in inaccurate part dimensions.

Scan speed

For high process productivity the scan speed should be increased, but this is exactly counterproductive to the demand for high part density as explained above. The upper limit of scan speed can also be estimated from two factors. The first factor is the minimum coalescence time required for powder particles to fuse together. Klocke (2003, p. 178, [161]) examined the fundamental binding mechanisms of single-phase powders in two-grain experiments. Depending on the laser beam power, on the absorption and on the material’s heat conductivity coalescence times between 5 and 35 ms were measured for fusing two particles. This sets the absolute upper limit for scan speed by dividing the melt pool length (in scan direction) by the coalescence time. However, it must be considered that additional powder particles may reside between the surface powder particles and the previously solidified layer. In order to obtain proper attachment of all powder particles to the previous layer the scan speed must therefore be decreased further. The second factor is a limitation of the maximum scan speed due to melt pool instabilities which can arise if the scan speed exceeds the speed of heat transportation through the powder bed which posseses reduced effective thermal conductivity. Such melt pool instabilities also lead to increased development of spattering.

Hatch distance
If the hatch distance is chosen too large, then the productivity is increased but the part density is significantly reduced, powder particles might remain unexposed and residual stresses, which are not reduced by the increased hatch distance, can exceed the material’s yield strength (Niebling, 2005, p. 98, [216]). If the hatch distance is chosen too small, too much powder is drawn into the melt pool from the still unmelted adjacent scan track leaving behind too little powder for this adjacent scan track which in turn will also reduce the part density.

Layer thickness
Increasing the layer thickness will increase the productivity of the process, however, the vertical resolution is reduced and thus the surface roughness of a part increased. The layer thickness must be smaller than the melt pool depth otherwise the currently fabricated layer will not be properly attached to the previous layer and suffer from delamination.

Exposure Strategy
The exposure strategy can be a very dominant influence parameter with effects on the density, surface quality and residual stress of a part. It has little interaction with other process parameters and should be chosen very carefully in terms of proper scan vector length, number of contour scans and sequence of hatch and contour scan.

The investigations conducted by various researchers in order to find the dominant process parameters were usually performed on a strictly empirical basis. Generally, the dominant process parameters can also be obtained systematically by employing established methods for design of experiments. A suitable method is e.g. the Shainin method which reveals the few dominant process parameters from a group of parameters (Lorenz, 2005, pp. 92-95, [185]).

3.5.2 Quality properties of solid SLM parts

SLM parts can be characterized by a few critical quality properties. According to ***fig. 3.8*** these are surface finish (surface roughness), strength (ultimate strength, yield strength, Young’s modulus, break strain), accuracy to shape and to size, hardness as a value for resistance to wear, density in terms of pore-free microstructure and residual stress behaviour (leading to warping or cracking of parts during the process or after).

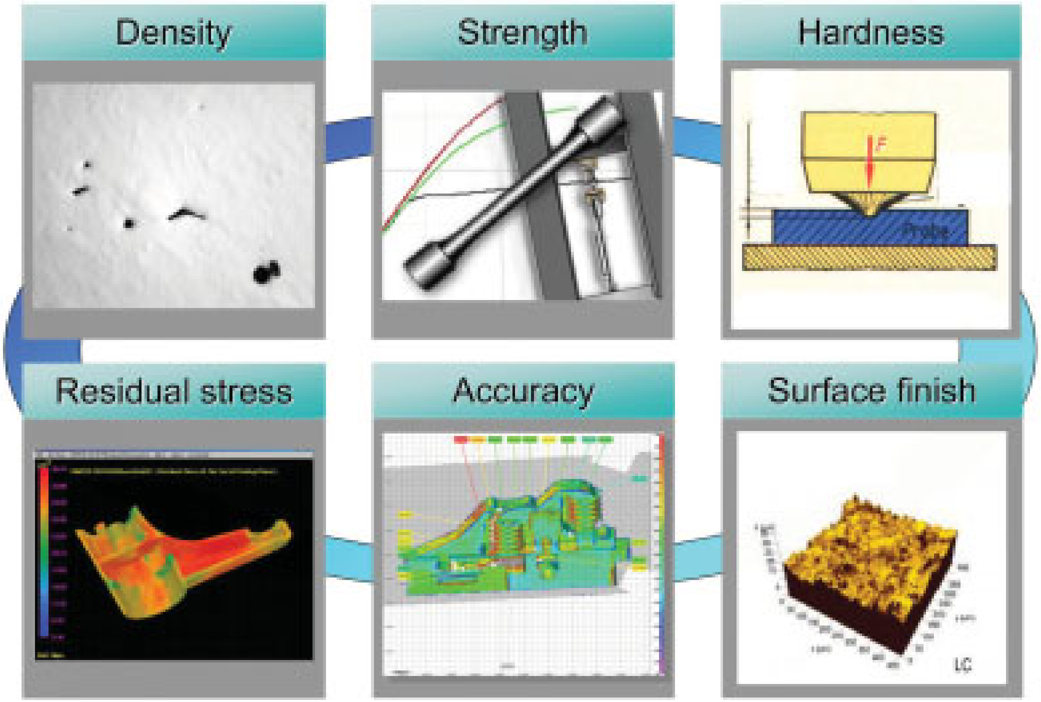

Figure 3.8: Critical quality properties for SLM parts

The achievement of a high reproducibility of quality in SLM parts according to the quality properties given here, mainly depends on how small the process tolerances can be maintained. Nevertheless, the need for small process tolerances also depends on the required part tolerances. Irrelevance of one or more quality properties can greatly simplify the task of maintaining small process tolerances. Additionally, much effort is also required in the design of SLM parts because it can show severe influence on the process tolerances. A simple example is the choice of bad geometry leading to poor heat conductivity from the currently processed layer through the part into the building platform which might result in insufficient powder particle coalescence and e.g. reduced strength properties.

Density

The bulk density of solid LFF parts should be the most relevant issue of all initial examinations for new materials since other part quality properties such as high strength and high hardness require little porosity. Ideally, the density should always be near the theoretical maximum, i.e. it should be above 99 % of the value obtained for rolled material which is not flawless either. Many sources have reported similar results on the dependency of the density of metallic LFF parts on the dominant process parameters as explained in ***section 3.5.1***. Agarwala (1995, p. 33, [4]), Williams (1998, p. 95, [321]) and Meiners (1999, pp. 52-53, [201]) postulated a linear proportionality between a part’s bulk density ρ and the energy density E of the laser beam per unit length as given in ***eq. (3.29)***.

$$\rho \propto E \text{ where } E = \frac{P_L}{v_s} \text{ or } E = \frac{P_L}{v_s \cdot h_s} \text{ or } E = \frac{P_L}{v_s \cdot h_s \cdot l_z} \qquad \textbf{\textit{(3.29)}}$$

Lemke (2005, p. 75, [180]) confirmed this correlation for the energy density per unit area which includes considerations of the hatch distance h_s while Uckelmann (2007, pp. 26-27, [299]) did the same for the energy density per unit volume which incorporates the layer thickness l_z. Since some of the energy delivered to the powder bed is lost due to heat conduction and radiation between two consecutive layers it is, however, highly recommended to use the energy density per unit area (Rehme, 2005, p. 230, [250]). Other results stating that the bulk density also depends on the scan speed for constant energy density (Zhang, 2004, p. 57, [330]) are of minor relevance.

Strength

Due to the characteristics of the SLM process where extremely short times of melting and solidification of material prevail (a typical temperature gradient is several 10^2 K/s) higher tensile strengths than for rolled material can be achieved. This can be derived from the effect that the crystal lattice of e.g. a metallic alloy develops small grain sizes, hence increasing the strength when cooled down quickly enough. However, in this case special attention has to be given to the break strain which might result in values below expected standards due to embrittlement of the material.

Williams (1996, p. 551, [320]) proposed the model given in ***eq. (3.30)*** to estimate the yield strength σ of LFF parts made from polymer powders under flexural load where c_1 and c_2 are empirical constants. This model holds as well for metallic materials (Rehme, 2007) at least for a limited bandwidth of energy densities since the strength depends directly on the bulk density represented by the first term in the formula. The second term accounts for reduction of strength due to increased scan rate, i.e. the area of laser beam exposure per time unit. This occurs because higher scan rates increase the temporal cooling gradients which induce residual stresses in metallic materials. Generally, this raises the risk of delamination of layers of consolidated material. Like the yield or ultimate stress the flow curve of the stress σ in dependency of the strain ε depends just as well on the porosity of a bulk material. The flow stress can be described by constitutive formulae such as the Ludwik-Hollomon correlation given in ***eq. (3.31)*** where K is a material constant and n is the work-hardening exponent. This equation was advanced by Miani (2001, pp. 385-388, [204]) for LFF processed materials with a bulk density ρ of less than the theoretical, pore-free material's density ρ_{solid} which would tolerate a strain ε_{solid} leading to ***eq. (3.32)***.

$$\sigma_{yield} = c_1 \cdot \frac{P_L}{v_s \cdot h_s} - c_2 \cdot v_s \cdot h_s \tag{3.30}$$

$$\sigma(\varepsilon) = K\varepsilon^n \tag{3.31}$$

$$\sigma(\varepsilon) = K \cdot \left(1 - \frac{3}{4}\left(1 - \frac{\rho}{\rho_{solid}}\right) + \frac{1 - \frac{\rho}{\rho_{solid}}}{\varepsilon_{solid}} \varepsilon \right) \varepsilon^n \tag{3.32}$$

The anisotropic strength behaviour of metallic LFF parts was first noticed by Meiners (1999, pp. 96-99, [201]) who found characteristic variations of these properties for tensile test specimens built from stainless steel in the x-y-plane and in z-direction. The yield strength $R_{p0,2}$ as well as the ultimate tensile strength R_m were approx. 50 MPa lower in z-direction at average values of 460 and 510 MPa, respectively, than in directions of the x-y-plane. The break strain A showed no dependency on spatial direction. However, the anisotropy of LFF parts is more complex and some refined results for SLM solids are presented in ***section 6.1***. Other correlations found by Uckelmann (2007, pp. 40-45, [299]) were that for constant laser beam energy density and part densities greater than 0.995 all three strength properties mentioned here decrease with increasing scan speed and increasing layer thickness. Additionally, the break strain is proportional to the average grain diameter of the part's microstructure which in turn is directly proportional to the laser beam energy density (Uckelmann, 2007, pp. 52-53, [299]).

Hardness

High hardness of a material depends much on low porosity because it is defined as the resistance against indentation (see ***section 2.1.4.10***) which is in fact another strength property. Hardness is also often found to follow similar behaviour as strength properties. Typically, hardness values above those of rolled materials are obtained due to the extremely short solidification times of local material areas in LFF processes.

Santos (2002, p. 182, [266]) measured the Vickers hardness of SLM titanium specimens fabricated at different laser beam power settings and scan speeds. As expected the hardness increases with rising energy density of the laser beam according to ***eq. (3.33)***.

$$HV \propto E \tag{3.33}$$

Residual stress

Since the SLM process involves laser light which is partially absorbed and converted to thermal energy the parts built can suffer from warping or cracking due to residual stresses. This strongly depends on the used material and on the process parameters as explained above in ***section 3.4.3.7***. Residual stresses in SLM parts develop from mainly two reasons. One reason is the volume change due to changes in an alloy's crystal lattice as the material cools down from the melting point to ambient temperature. The resulting stress level can occur in all three spatial dimensions of the part and it might lead to microscopic and macroscopic cracks as well as other effects such as deviations of the part from the desired geometry (Over, 2003, pp. 35-36, [223]). The second reason for residual stresses in SLM parts is the influence of shrinkage in the currently produced layer against the solid layers underneath. This leads to two-dimensional residual stresses perpendicular to the build direction which can result in curl development as mentioned above. Niebling (2005, pp. 72-75, [216]) determined the occurring stresses and found that the current layer shows merely tensile stresses in scan direction whereas the contact zone to the previous layers also suffers from in-plane tensile stresses perpendicular to the scan direction. The layers underneath accordingly suffer from compressive stresses along and perpendicular to the scan direction. Stresses in scan direction are higher than those perpendicular to it. Altogether the resulting multi-axial stresses should be considered by calculating equivalent stress levels (e.g. von Mises stress).

The level of internal stress in SLM parts is an important property and must be kept as low as possible to avoid part quality deficiencies. The counter measures against part curl described in ***section 3.4.3.7*** all help to reduce the stress level significantly. However, it should be noted here that the material used takes major influence and that certain popular engineering materials such as tool steel 1.2344 and the titanium alloy TiAl6V4 develop rather high residual stress levels. More research is necessary in the development of suitable alloys.

Accuracy

The quality property of shape and size accuracy has only limited correlation to quantitative values such as the process parameters since it depends much more on the abilities of the LFF system. It strongly correlates with factors of process control concerned with the melt pool width which mainly depends on the effective heat conductivity of the powder bed, the laser beam power, its focus diameter and the scan speed. The resulting melt pool width takes effect on size accuracy depending on the quality of the corrective beam offset at contour scan lines of each exposed layer. Other factors for shape accuracy are position tolerances from the scanning system or warping due to residual stress.

Nelson (1995, p. 161, [215]) showed that the beam delivery and the thermal process control take major influence on the part accuracy. Factors like the positional accuracy of the scanner system, its repeatability, its dynamic errors caused by acceleration and deceleration of the mirrors or by coordination of the laser “on”/”off”-signal to manage sky-writing and the f-theta-lens-correction (Rehme, 2005, p. 230, [250]) are responsible for deviations of the desired beam delivery to the powder bed surface. Inaccuracies due to the melt pool width in the powder bed surface are typically regarded and corrected by the LFF system, provided that all influence factors are considered. The melt pool width W, which is equal to the scan track width, is a function of laser beam power P_L focus diameter $d_{0,86.5}$, scan speed v_s and effective heat conduction $\lambda_{eff}(T)$ of the powder bed according to ***eq. (3.34)*** (Rehme, 2005, p. 231, [250]).

$$W = f\left(P_L, d_{0,86.5}, v_s, \lambda_{eff}(T)\right) \tag{3.34}$$

However, in the context of scan track width, another important influence factor on part accuracy is the achievable minimum feature size (Rehme, 2005, p. 231, [250]). The minimum feature size (resolution) is of high importance in design of functional parts e.g. for thin walls, for small apertures or in context of this thesis for small micro struts in SLM lattice structures. Thin walls are an example for so-called positive minimum feature size (smallest solid part possible) while small apertures are an example for negative minimum feature size (smallest gap size possible). As apparent from ***fig. 3.9*** the minimum positive feature size in z-direction has to be distinguished between layers that are built on previously melted powder which is now solid and layers that are built on the powder bed without support structures. Besides that both positive and negative minimum feature size in z-direction mostly depend on the layer

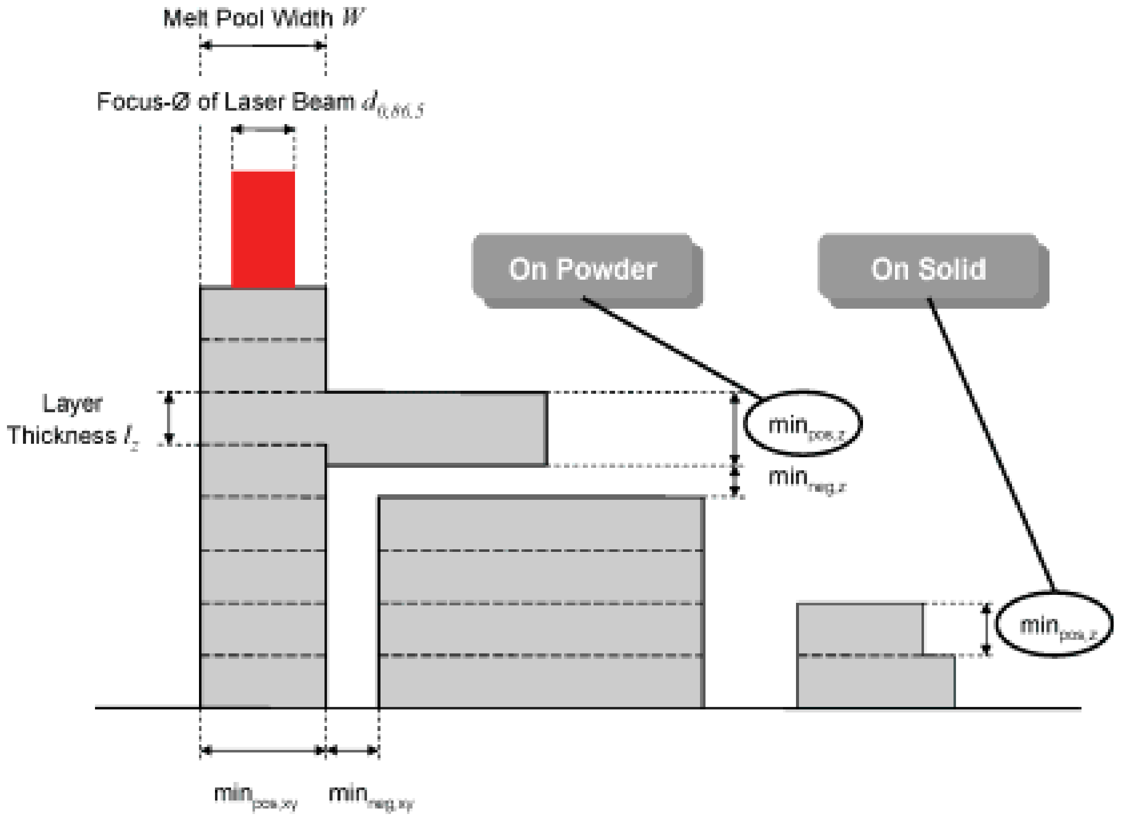

Figure 3.9: Positive and negative minimum feature size [250]

thickness l_z whereas the positive and negative minimum feature size in the x-y-plane depend mainly on the melt pool width W. Therefore, the layer thickness is the only process parameter taking influence on part accuracy due to the staircase effect aside from the less significant part orientation which can help minimize resolution errors. Experimental analysis conducted at iLAS by Tangwiriyasakul (2004, p. 74, [291]) showed that inaccuracy in z-direction can occur due to the fact that the thickness of the first few layers, i.e. between 10 and 15 layers at a a layer thickness of e.g. 75 µm, is often larger than desired. It is thus recommended to build parts on a sufficient number of layers of support material which is cut off after the process.

A third and not less important reason for part inaccuracies are thermal effects. Part warping as introduced in ***section 3.4.3.7*** can evidently cause severe inaccuracies due to layerwise shrinkage either during the process or after the process when the occurring thermal stresses are relieved. If heat transfer through the finished layers is not uniform at build-time e.g. due to the part geometry, this might also lead to deviations from the desired geometry or even to the development of melt beads which may disturb the process stability and change the part dimensions.

If all three major issues for part accuracy are controlled appropriately, then typical part tolerances in the magnitude of ±0.1 mm or 0.1 to 0.2 % for larger parts were achieved by Pintat (1995, p. 74, [228]). One decade later accuracy was improved only slightly as obtainable tolerances decreased to values between ±25 and ±100 µm (Rehme, 2005, p. 228, [250]).

Surface quality

The roughness of LFF part surfaces has been an issue since LFF processes were established and only little improvements were made since. Owing to both facts that powder materials of finite size are processed and that only a finite layer thickness can be applied, it is difficult to achieve surface qualities as found in machined parts. Therefore, certain applications require post-processing as described in ***section 3.4.4*** unless applications are found that are independent of surface quality or that even need high surface roughness.

The lowest achievable surface roughness even on surfaces in the x-y-, y-z- and x-z-planes, where no staircase effect occurs, is currently around $R_z = 30$ µm due to partially melted powder particles that adhere to the surface and their particle size distribution, respectively (Rehme, 2005, p. 228, [250]). The influence of the powder particle size distribution on surface roughness was elaborated at iLAS by Wolfangel (2006, pp. 65-66, [325]) who developed a bimodal powder particle size distribution from stainless steel powder with two peaks in the volumetric density distribution where peak values q_3 of 2.656 μm^{-1} at a particle diameter d of 11.8 µm and 4.878 μm^{-1} at 47.9 µm, respectively, were realized. This powder particle size distribution is most balanced in terms of good powder flowability, high part density and small surface roughness as it fulfills the demand for suitable size and weight ratio between small and large particles from ***section 3.4.2.2*** more than any other powder composition. The surface roughness on faces of test specimens in the x-y-plane made from this powder yields values for R_z around 53.3 µm.

A second option are high contour scan speeds which allow better surface quality due to less adherent powder particles. This, however, might lead to decreased near surface density and hence decreased hardness.

In addition to the roughness from adherent powder particles, the roughness of surfaces that are not parallel to the x-y-, y-z- or x-z-plane depends vastly on the staircase effect which inevitably develops due to the finite layer thickness. Therefore, the roughness increases by an amount which depends on the angle α between the x-y-plane and the part surface. Simple geometrical considerations (Rehme, 2005, p. 228, [250]) yield the correlations

$$\begin{aligned} R_T &\approx R_{adherent\ powder\ particles} + R_{staircase\ effect} \\ R_T &\approx R_{adherent\ powder\ particles} + \sqrt{\cos\alpha \cdot \sin\alpha \cdot mh_s \cdot nl_z} \end{aligned} \qquad \textbf{(3.35)}$$

which take into account the width and height of each step which must be multiples m of the hatch distance h_s and multiples n of the layer thickness l_z. Here, the contribution of the staircase effect to overall roughness is set equal to the maximum distance between the surface envelope and the corner of a step, in a direction perpendicular to the surface envelope. This simple model, however, neglects the effect that small melt beads due to contour scans can have on surface roughness. These melt beads can exceed the predetermined height of a layer due to the surplus of energy that is transmitted into the material during contour scanning. Therefore, the distance between the surface envelope and the corner of a step could be increased as shown by Rehme (2005, p. 228, [250]). Depending on the surface angle, the number of contour scans, the laser beam power and the exposure sequence (hatch first, then contour scan or vice versa) these melt beads can show arbitrarily complex geometries. Further research should be carried out to investigate optimum scan strategies combined with adaptive laser beam power to obtain better qualities on freeform surfaces.

3.5.3 Applications

One major strength of LFF is the rapid production of a small number of parts with complex geometry. Nevertheless, until today only a small number of typical applications have evolved for metallic LFF parts in the markets of Rapid Prototyping, Rapid Tooling and Rapid Manufacturing. Rapid Prototyping is understood as quick manufacturing of samples for demonstration purposes, assembly and installation simulation in one process step, if possible. Rapid Tooling, however, means direct manufacturing of dies, moulds and other tools of high precision and durability to use as means of manufacture for other products. In contrast, Rapid Manufacturing means direct manufacturing of near-net-shape, functional parts from engineering materials comprising reproducible properties in one process step, if possible. Among the above named markets, applications in Rapid Manufacturing offer the largest industrial potential as they open the possibility to allow new product designs and reduce the production cost and time while maintaining high quality standards.

Early developments of applications for LFF parts from metallic materials were mainly focussed on Rapid Prototyping. Soon after, Rapid Tooling applications started to grow as well as the demand for parts with high quality properties. The early polymer coated laser sintered materials were used by Badrinarayan (1992, p. 141, [24]) to produce copper electrodes for Electric Discharge Machining (EDM). However, these electrodes suffered from a too high rate of erosion compared to the investment cost due to their high porosity of approx. 52 %. Next, Stucker (1995, pp. 280-281, [283]) managed to turn the lack of density into an asset by laser sintering EDM electrodes from polymer coated zirconium diboride particles and infiltrating the voids with copper such that the electrical and thermal conductivities of the ZrB_2/Cu material were the same as those of pure copper while expecting these electrodes to last 16 times longer. Lower initial porosities of 23.3 % were obtained by E-Eleser (2000, pp. 31-32, [101]) who infiltrated laser sintered bronze-nickel and steel-copper electrodes with tin and silver solder. The results after spark erosion of C45 and X210Cr12 steel materials appeared to be promising, especially for the steel-copper electrodes. The lowest wear was observed for electrodes infiltrated with silver solder. Some newer examinations (Martínez-García, 2004, pp. P4079.2-P4079.3, [192]) report the use of other two-phase materials with indirect and direct laser sintering, however, no further improvements were achieved and the ratio of metal removal to tool wear was still found to be worse than that of conventional copper or graphite electrodes (Meena, 2006, pp. 227, [200]). Future use of laser melting of single-phase materials could be a new incentive for this type of application.

An important application in the field of Rapid Tooling is the manufacture of tools for injection moulding of plastic materials. Dalgarno (2001, pp. 176-178, [69]) was the first to suggest this application and make use of conformal cooling channels inside the mould tools for cooling but also for heating. The benefit from optimized heat flux inside the tool is optimum temperature of the injected polymer which allows to reduce cycle times and improve process control. In complex shaped injection moulding parts LFF is the only method that can produce such channels that are located near the surface of the tool independent from its shape. Recently, however, more benefits arose from Rapid Tooling applications. The conventional process chain in the production of mould tools typically consists of many different process steps such as milling, turning, drilling, grinding, ageing, EDM and polishing to name but a few. This results in rather longish lead times. A representative example is the production of mould tools for mobile phone housings which takes 10 weeks using the conventional process chain. This could be reduced to 5 weeks using LFF processes due to massive reduction of the required process steps (Rehme, 2004, pp. 20-29, [248]). Glaßer (2004, p. P4015.3, [125]) confirmed the usability of plastic parts from LFF injection moulds since they show properties like identical series products from conventional mould tools. However, it has to be noted that this is only valid for prototype mould tools which have a durability of up to one million injection moulded plastic parts. Future development of LFF mould tools from single-phase tool steel materials will extend this application to series mould tools with much higher output quantities (Emmelmann, 2007). Regenfuß (2004, p. 716, [245]) managed to apply Laser Micro Sintering for the production of mould tools for very small plastic parts with features in the submillimeter range.

With the ability of meeting higher demands towards product properties due to the possibility of using single-phase, metallic materials the era of Rapid Manufacturing finally began to supersede many prototyping applications with the production of functional, near-net-shape parts. These could involve tools, sliders or inserts for die casting tools and other functional parts (Meiners, 1999, pp. 659-660, [202]) or tools for the handling of fibers, aspiration boxes for fiber holders, tweezers for mechanical fiber fixation and grip bits for optical lenses (Regenfuß, 2004, p. 421, [246]) or micro coils (Regenfuß, 2007, p. 28-29, [247]) all made from materials such as stainless steel (e.g. 1.4404), tool steel (e.g. 1.2343), titanium alloys (e.g TiAl6V4), aluminum alloys (e.g. AlSi30), tungsten and molybdenum. Other functional parts manufactured with LFF processes such as metallic dental camera housings that are customized to the anatomy of the dentist's hand or helicopter turbine parts where the time and cost of manufacture were reduced by 50 % compared to conventional production processes were reported by Glaßer (2006, p. P6032.5, [126]). It was also shown that even for small series of up to 900 identical metal parts LFF processes can be economically more efficient than conventional processes (Shellabear, 2004, p. 440, [273]).

An apparently strong growing market for LFF products is the field of medical applications. Early ideas involved making the high porosity of laser sintered parts an asset and thus porous matrices made from LFF were suggested for use as drug delivery devices which allow controlled release of medication in the human body over a prolonged period of time without the hazard of under- or overdosage (Low, 2001, p. 263, [186]). However, the possibility to manufacture individual single piece products for each customer makes LFF a perfect solution for many other health related items. Therefore, applications were developed where individual geometries are scanned directly from a patient's body parts e.g. via computer tomography (CT) or fringe projection and subsequently processed in a CAD-CAM chain. This applies well to medical devices and instruments (Dalgarno, 2006, pp. 2-4, [71]) such as patient individual drill guides for spinal surgery where single vertebrae are isolated from load or displacement by frame support. After a CT scan the drill guide is designed around the desired vertebrae and the required screw position is inserted. Then the product is manufactured in the LFF process with a material that only needs to be approved for temporary use inside the body. Similar drill guides were also suggested for complicated bores in the jaw bone and the mastoid. Other instruments suggested are customized orthoses which are externally applied devices used to modify the structural or functional characteristics of the neuromuscoskeletal system. These are used as in-shoe inserts for patients with deformed feet and the customized design is derived from motion capture data and the 3D foot geometry. However, the use of a CAD-CAM chain also applies well to parts for permanent use inside the human body which are implants. Laoui (2004, pp. 479-480, [177]) proposed to use state-of-the-art dentistry equipment to scan patient's teeth and reproduce them from titanium by means of SLM. Meanwhile the production of dental crowns and bridges was industrialized (Uckelmann, 2007, p. 15, [299]) at approximately half the cost of casting and milling technologies. The manufacture of customized endoprostheses by SLM from commercially pure (c.p.) titanium and from TiAl6Nb7 for various parts of the human body was suggested by Rehme in different sources (2005, pp. 8-14, [249]), (2006, p. P6001.5, [253]), (2007, p. 8, [255]) which is useful for trauma or tumour patients who often cannot receive standard implants. As also reported by Emmelmann (2007, p. 250, [110]) in 2006 the first patient received an artificial acetabulum endoprosthesis manufactured from SLM exactly to the specific needs of the patient according to the process chain depicted in ***fig. 3.10*** where a CT scan was taken and converted into CAD data. The following CAD design delivered an implant with customized fixtures which was

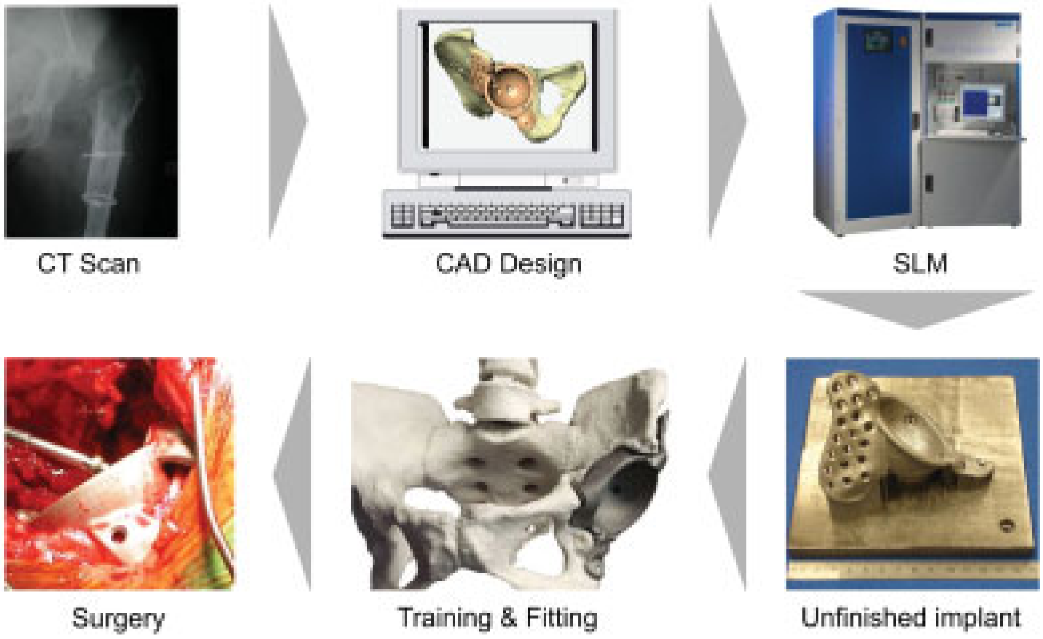

Figure 3.10: Process chain for a customized acetabulum endoprosthesis [254]

directly converted into STL data processed by the SLM machine. After the implant was fabricated, the support structures were removed and the surface finished accordingly. Before the ready-to-use endoprosthesis was implanted the surgeon practiced the surgery on a plastic Rapid Prototyping model of the pelvis which was derived from the same CT scan as well. One benefit of this process chain was a much reduced manufacturing time of 24 hours compared to 2 weeks usually required for individual implants fabricated from CT scans. Other benefits were the reduction of surgery duration from 3 to 2 hours which involved less loss of blood for the patient and better fit of the implant.

Many more applications than the above mentioned are currently subject to thorough examination by various companies in different industries. However, in order to not lose competitiveness most companies decide not to publish their ideas or their results, respectively.

3.5.4 Considerations of manufacturing cost and time

The use of LFF systems in industrial applications depends strongly on fulfillment of the criteria of product quality as well as manufacturing cost and time obtained for a specific part. Mere substitution of an existing manufacturing process with e.g. SLM without taking advantage in at least one of the above mentioned criteria and without impairing the remaining criteria is unthinkable from an economic point of view in industrial environments. If e.g. the SLM process allows the fabrication of new designs that conventional processes cannot deliver, then the product's quality is improved provided that the quality demands according to ***fig. 3.8*** are satisfied. In terms of cost an example was given in ***section 3.5.3*** where the capability of SLM was shown to produce small sized, patient-individual dental products at half the cost of milled or cast parts. In other industries time is a critical factor where SLM systems can contribute. A study conducted by Rehme (2004, pp. 20-29, [248]) revealed that the fabrication of tools for polymer injection moulding with SLM can speed up the process chain immensely if the manufactured cavities possess complex geometries and need to be produced in single quantity. In this industry an increase in cost is sometimes even acceptable if it is counterbalanced by the benefits of time reduction.

An economical evaluation of LFF processes for a given application must consider quality, cost and time by making suitable compromises between these three interconnected factors. Typical SLM systems are sold at prices around 0.5 million Euros. Calculating the investment cost, depreciations, interest on the investment cost, staff, space, maintenance and cost of operation leads to typical rates of approximately 100 Euros per hour of machine operation. The process duration is determined mainly by the part volume, the part orientation (see ***section 3.4.3.9***) and the process parameters. However, the process parameters may not be chosen arbitrarily due to the quality demands towards the part. Thus, the process parameters restrict the lower limit of process duration and hence the cost.

Therefore, a sufficient command of the major process parameters is required for an ability of estimating the minimum duration of SLM processes. Maximum scan speed is limited by the amount of time required for single powder particles to fuse together. Wagner (2003, pp. 98-103, [305]) found that the time required for the fusing of two powder particles depends on laser beam power and on the flowability and surface tension of the material. In the case of stainless steel 1.4404 the range was between 3 and 35 ms for the highest and the lowest laser beam power, respectively. For an assumed laser beam focus diameter of 110 µm at a laser beam power of 100 W (see ***section 4.2.3***) this would yield a scan speed of 36.67 mm/s, however practical experience with the same material at iLAS showed that much faster scan speeds still lead to parts with nearly full density (Eisen, 2004, p. 59, [104]). Another important influence on process duration is the maximum layer thickness that can be derived from the temperature development in a currently processed layer. According to calculations contributed by Zhang (2004, p. 35, [330]) a combination of large laser beam power and high scan speed would yield high temperatures in the upper powder particles of the currently processed layer while the lower powder particles above the previous layer achieve only low temperatures. In extreme cases this could mean evaporation of the upper powder particles while the lower powder particles do not even melt which would lead to delamination. Also relevant for an economical evaluation due to its influence on process duration is the hatch distance. If chosen too large to increase the build volume per time unit, unmelted powder remains between adjacent scan tracks as explained in ***section 3.5.1***.

3.6 Summary

This chapter shows how insufficient quality for metallic, cellular material products obtained from conventional manufacturing processes due to unabilities of influencing the process can be overcome by using Laser Freeform Fabrication (LFF) which gives completely new degrees of freedom for cellular design. It explains how the development of LFF came about and what industrial processes currently are state-of-the-art.

Next, the Selective Laser Melting (SLM) process is presented and an in-depth analysis for the fabrication of solid parts is conducted. This analysis reveals the influence parameters and summarizes advances achieved by the author and other researchers in order to better understand how the influence parameters affect product quality as well as manufacturing cost and time. From the variety of influence parameters the most dominating are derived and their effects on the main quality properties of SLM solids are discussed. After giving examples for typical industrial applications of SLM solids the influences on manufacturing cost and time are discussed as well.

4 Fundamental analysis of cellular part design for SLM

4.1 Process development and precursor experiments

As shown in ***section 3.5.3*** LFF has found numerous applications in different industries for solid parts with high quality demands made from a variety of materials. Many such applications involve geometries beyond the possibilities of conventional machining processes, however, the approach to manufacturing cellular materials with SLM is even more complex. First precursor experiments showed that cellular specimens obtained from 3D-CAD design cannot fulfill the demand for optimum SLM lattice structures in terms of micro-sized dimensions and error-free fabrication. ***Fig. 4.1*** shows a sample manufactured with state-of-the-art SLM technology where the smallest possible strut diameter is 1.2 mm and the cell size is 6 mm. The solid circle points out a horizontal strut with a fabrication error due to poor heat conduction into the powder bed. It should be noted that horizontal struts of this diameter dimension can be manufactured with clear coherence and stability although they exhibit typical deviations from the desired circular cross section shape again due to the heat conduction issue as seen inside the dashed circle. Such shape deviations increase the notch effect on single struts which decreases their mechanical strength due to inhomogeneous stress concentration. Furthermore, the strut diameters in this present example do not allow small cell sizes since minimum cell size must always be greater than the strut diameter. This implies that the struts also require a certain minimum length. Therefore, if the design is derived from 3D-CAD, the strut dimensions are such that warpage due to thermal stresses develops in horizontal struts which results in deformed vertical struts like the one shown inside the dotted circle.

One explanation for this misachievement using 3D-CAD geometries to obtain SLM lattice structures can be found in the state-of-the art exposure strategies that SLM processes employ. Each exposure strategy provides specific movement patterns of the laser beam across the powder bed, also called the scan path. These paths consist of scan vectors in either x- , y-, or x- and y-direction in all layers or they consist of layerwise alternating x- and y-scan vectors.

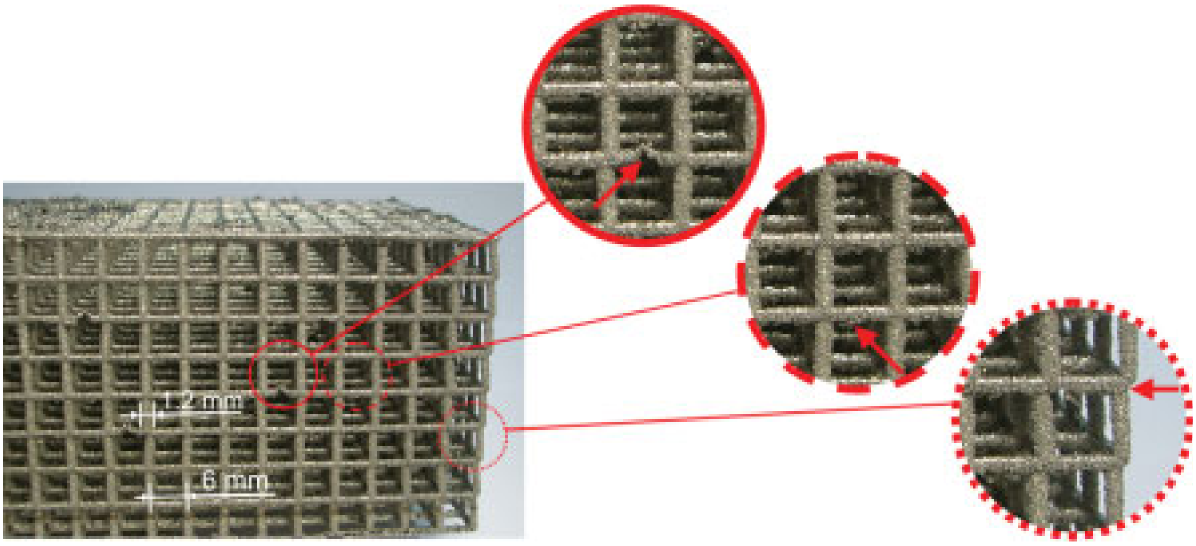

Figure 4.1: First SLM lattice structure precursor experiment

Placement of multiple scan vectors parallel to each other in such distance that allows for overlapping the melt pool of adjacent scan tracks ensures a dense and pore-free slice of the part to be built firmly connected to the previous slice. Scanning in both x- and y-direction on each layer appears uneconomical due to increased process time. X-only or y-only scan vectors appear unsuitable to obtain parts with orthotropic strength properties. Thus for solid parts the alternating x-y-scan strategy is most favourable. Depending on the powder material properties (e.g. due to the phase changes of its crystal lattice structure as it cools down) it might also be desirable to limit the scan vector length to reduce resulting residual stresses in the part as previously explained in ***section 3.5.2***. These strategies for solid SLM parts are well suitable for typical dimensions of 3D-CAD geometries. When attempting to realize micro-sized structures, however, they show a major disadvantage due to the splitting of the exposure into a sequence of adjacent scan tracks for the so-called hatch and the contour scan which is conducted to achieve a smoother part surface rather than a wavy surface at the ends of all neighbouring scan tracks. This severely limits the minimum feature size that can be obtained because hatch and contour scan together require a certain minimum of area on the powder bed. The second important explanation for the above misachievement is the fact that the desired finest structures are a problem when using standard 3D-CAD software because typically resolution errors occur during the required conversion into the STL surface model representation (Sutcliffe, 2005, p. 1083, [286]).

The above presented precursor experiment and constraints in terms of exposure strategies for solid parts suggest that a different approach is required to manufacture SLM lattice structures with finest struts which allow for parts with e.g. least density or a high strength-to-weight ratio. This raises the question of what the realms of these struts' producibility are. For finest structures minimum exposure time and exposure of minimum area of the powder bed to laser beam radiation is necessary. In this case time is an important factor since increased exposure duration enlargens the size of the melt pool such that finest structures seem out of reach.

Therefore, a special approach is used here that employs merely a point-like exposure style rather than using elongated scan vectors for hatch and contour scan as shown in ***fig. 4.2*** where the right hand side of the powder bed receives a 40 mm^2 area of point-like exposure while on the left hand side another same-sized area is fully exposed with a conventional hatch scan method. The time required to expose one layer in each area is 4.5 s for the point-like exposure

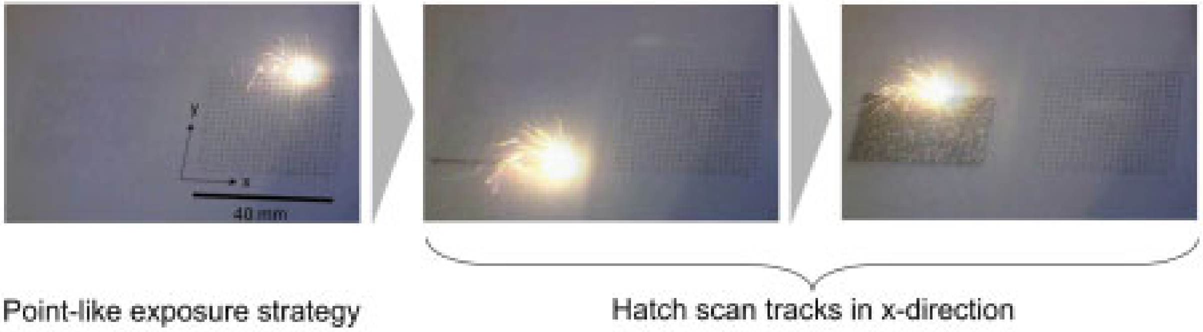
y
x
40 mm
Point-like exposure strategy
Hatch scan tracks in x-direction

Figure 4.2: Point-like exposure strategy vs. hatch scan strategy

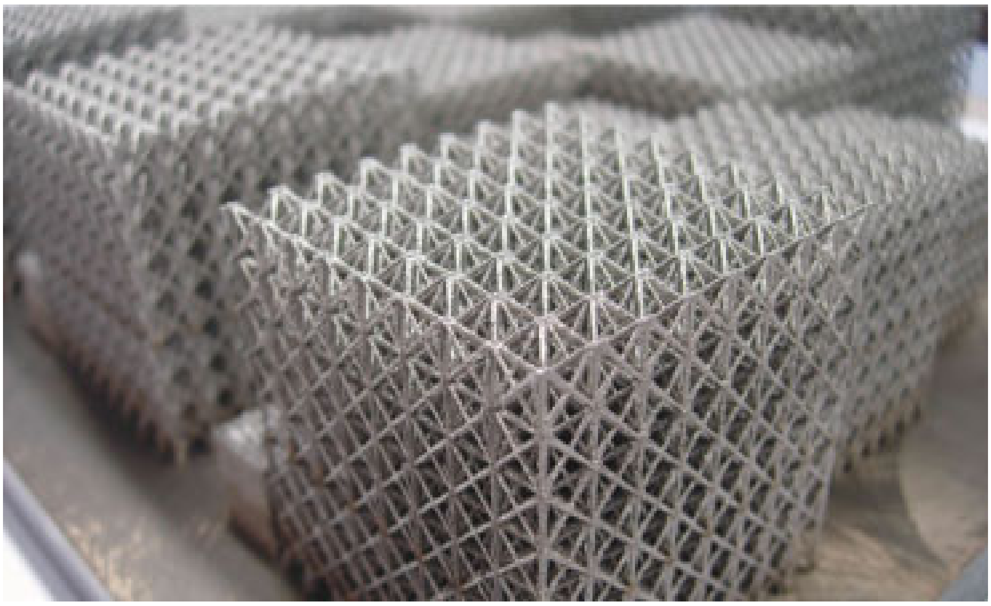

Figure 4.3: Improved SLM lattice structure from point-like exposure strategy

and 58 s for the hatch scan method where the newly realized exposure style yields a lattice structure like the one in ***fig. 4.3*** while the conventional method results in a solid block of material.

In order to achieve the point-like exposure a special C++ computer program was developed within the framework of this thesis that creates an arbitrary lattice structure as a set of vectors with finite length from given parameters. From these vectors it directly calculates the necessary scanner positions in each layer according to the intersection of each vector with the considered layer and creates a so-called slice file in the proprietary code of the SLM machine used. This results in lattice structures that possess struts with virtually no thickness since no diameter is defined. Instead, in the process their diameter is a result of the amount of beam energy coupled into the material as shown below in ***section 6.2.1***.

4.2 Analysis and assessment of process conditions

4.2.1 General influence parameters

By application of the point-like exposure strategy the precursor experiments were successfully concluded with fabrication of SLM lattice structures which offer cell sizes in the range of few millimeters and strut diameters in the submillimeter range. Before conduction of an extensive experimental investigation (presented in ***section 6***) an assessment of the process conditions is necessary to ensure reliable and reproducible results on one hand and to assure the quality of all test specimens according to ***fig. 3.8*** on the other hand. Therefore, the Ishikawa diagram from ***fig. 3.2***, which names all SLM influence parameters that have impact on product quality as well as manufacturing cost and time of a part, is employed to derive a suitable structure for this task. These influence parameters are divided in eight different categories which determine

- user capabilities,
- process preparation qualities,
- part geometry,
- qualities of the 3D-CAD data representation of the part geometry,
- material properties,
- capabilities of the SLM system,
- process constraints and
- post-processing qualities.

Most of these categories can be specified with little effort, however, some must be scrutinized carefully. The experimental stage of this thesis was conducted by the author with help from students who were all well trained in fabrication of solid SLM parts and in the newly developed approach to produce SLM lattice structures (user capabilities). Before each process run a thorough cleaning of the used SLM system was conducted and the powder material was sieved using a 75 µm mesh. Only small quantities in the range of approx. 2 % of unused powder were added to the recycled powder since ageing and deterioration of the material properties due to repeated use of the powder material were not discovered. The steel building platforms were milled, ground and sandblasted to obtain a levelled surface of high absorptance for laser beam energy with the required powder application properties (process preparation qualities). For SLM lattice structures the test specimen geometries and their according slice file data representation (rather than conventional 3D-CAD data) were prepared as mentioned in ***section 4.1***. Solid test specimens (mainly tensile specimens) were designed in the 3D-CAD software SolidWorks (part geometry). Among the process constraints the exact process parameters were subject to experimental investigation and were hence not predetermined. Other aspects such as process control and powder bed conditions were considered at an earlier stage where no distinction between solid SLM parts and SLM lattice structures is necessary. Both types of parts require identical processing which includes conformal preheating of the powder bed as explained in ***section 4.2.2***, the use of a minimum of 3 l/min of argon gas to achieve a protective atmosphere with residual oxygen contents of less than 0.5 % and a powder bed prepared from stainless steel powder which was measured to a packed density of 4.883 g/cm^3 or 61.54 %, respectively (Crames, 2005, p. 81, [66]). The post-processing involved wire EDM to separate all specimens from the building platform. SLM lattice structures were not treated further but solid parts such as tensile specimens were turned to conform to standard diameters and to avoid the notch effect due to poor surface quality. The issue of material properties and the capabilities of the SLM system deserve closer consideration. Therefore, their assessment is presented seperately in the following two sections.

4.2.2 Material

All test specimens examined in this thesis were manufactured from commercially available powder material from one single supplier. The commercial powder name is Stellite JET KOTE alloy 7330 which according to Deloro Stellite (2006, p. 1, [77]) possessed a particle size distribution from 0 to 70 µm where 97.4 % of the powder mass ranged between 20 and

53 µm. A chemical analysis (EDXRF and ICP-OES) confirmed the composition of this powder sold as stainless steel 1.4404 (also known as 316L) given in ***table 4.1***. The literature (Wegst, 2004, p. 335, [314]) gives an approximate density value of 8 g/cm^3 for 1.4404. From the composition of the powder and its element's densities at ambient temperature a theoretical density of 7.897 g/cm^3 was calculated.

Table 4.1: Chemical analysis of stainless steel powder

Element	Fe	C	Cr	Ni	Si	Mn	Mo
Mass [%]	66.477	0.023	16.6	12.2	0.6	1.6	2.5

The SLM process does apparently take effect on the composition of the material. Parts manufactured from the above mentioned powder material have a slightly different composition than the constituent powder as chemical analysis revealed (Brettschneider, 2006, p. 66, [45]). It is quite obvious that a small portion from all elements given in ***table 4.2*** except for iron vanishes during the process. The reason for this behaviour was not further investigated but could possibly be found in evaporation of the other elements. A combustion analysis of the soot that develops on the inside of the process chamber showed that it contains 0.92 % carbon which is noticeably higher than the initial 0.023 % of the powder but yet negligibly small. Thus the soot must consist of the other elements as well. The changed composition of the material in the SLM parts is still very close to the initial 1.4404, however, it is 1.1 % short on chromium. According to Wegst (2004, pp. 300-304, [314]) it is even closer to 1.4910 and 1.4919 where only 0.6 % chromium and 0.7 % nickel would be missing. Disregarding the fact that the chemical analysis could not measure carbon the calculated density of this new compositions yields 7.898 g/cm^3. However, virtually pore-free, solid SLM samples delivered an average density of 7.934 g/cm^3. Throughout the following sections of this work this reference value will henceforth be used for solid material obtained from the SLM process. More mechanical properties of solid SLM parts are presented in ***section 6.1***.

Table 4.2: Chemical analysis of SLM parts

Element	Fe	C	Cr	Ni	Si	Mn	Mo
Mass [%]	69.41	N/A	15.4	11.3	0.5	1.19	2.2

An important issue in terms of process control is the powder bed preheating which should be selected appropriately to reduce residual stresses in SLM parts on one hand. On the other hand, to meet the product quality demands introduced in ***section 3.5.2***, it is also important to obtain a uniform microstructure throughout any part. This must not be taken for granted due to repeated reheating of parts during each layer's laser beam exposure. Therefore, Costa (2004, p. 647, [64]) suggested to pre-heat the substrate of a LENS process (explained in ***section 3.2.1***) near the martensitic transformation temperature Ms of the processed material. This temperature can be estimated in centigrades for steels using Andrews' empirical formula (1965, pp. 721-727, [14]) in ***eq. (4.1)*** where the temperature is calculated from the percentage of carbon ($\%C$) and of chromium ($\%Cr$) contained in the according alloy. The composition of the stainless steel used in this thesis yields a lower temperature estimation of 252.6°C according to ***table 4.1*** and an upper estimation of 281°C according to ***table 4.2*** where the Cr contents is lower and the C contents is set to zero due to lack of information. Since preheating of the powder bed only near these temperatures is required, a heating of the building platform to a temperature of 200°C is considered sufficient.

$$Ms = 512 - 453 \cdot (\%C) - 15 \cdot (\%Cr) \qquad \textbf{\textit{(4.1)}}$$

In this context a potential embrittlement of the powder material may develop from preheating which can cause precipitation of carbon and nitrogen on the grain boundaries and thus ageing of steel. Nevertheless, this is considered of lesser importance since the material used here is alloyed with silicon and remelting of the material should reverse the precipitation process.

4.2.3 SLM system

The test specimens examined in this thesis were all built on a 2004 SLM machine named MCP Realizer manufactured by Realizer GmbH, Paderborn, Germany which was made available to the Institute of Laser and System Technologies (iLAS) at Hamburg University of Technology (TUHH) by MCP-HEK GmbH, Lübeck, Germany. Prior to fabrication of the test specimens, the machine properties were thoroughly tested in order to derive the specific factors limiting the accuracy and reproducibility of further results.

Any laser processing system can be divided into different subsystems which may consist of

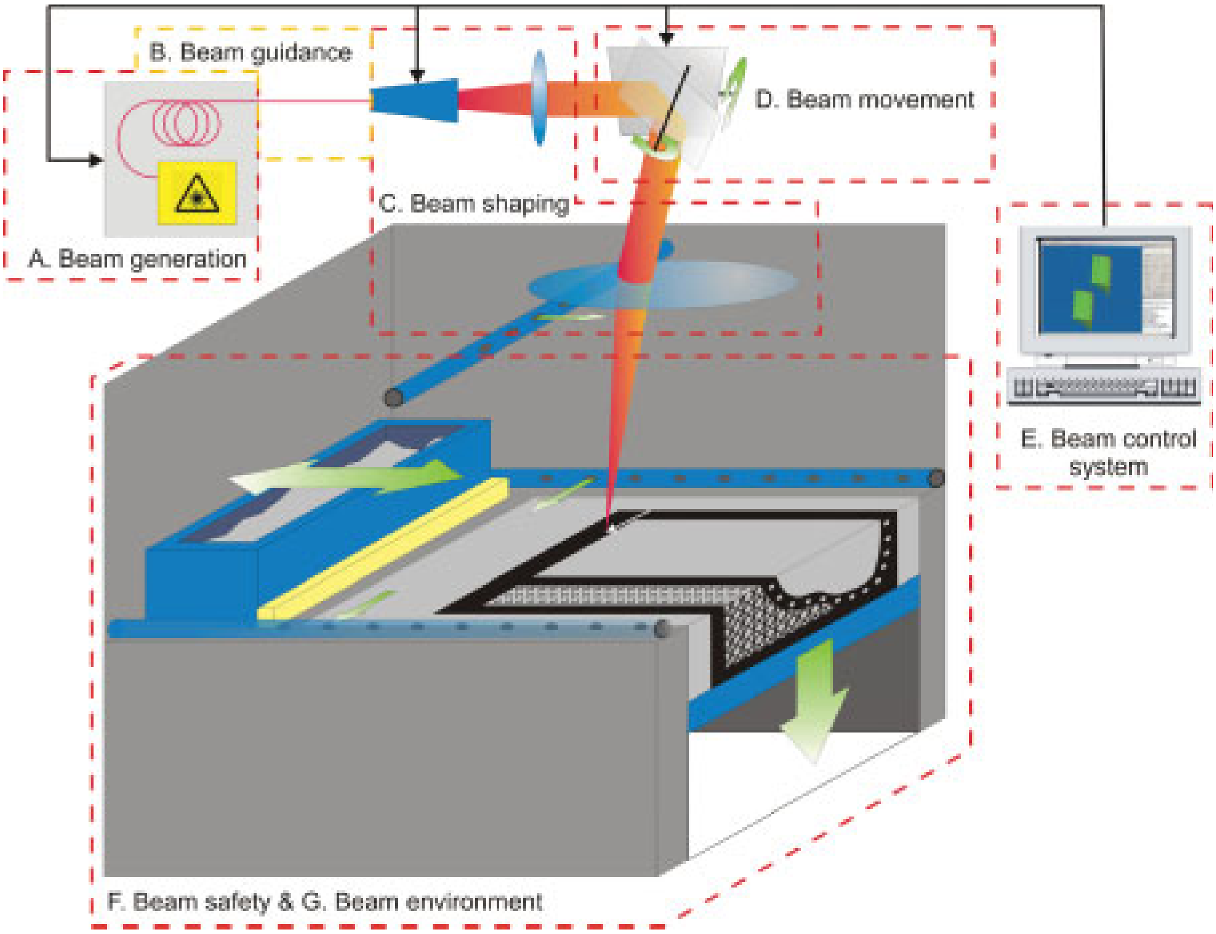

Figure 4.4: SLM machine subsystems

various components that are selected according to the required characteristic machine capabilities. Typical subsystems according to Emmelmann (2007, pp. 5-7, [112]) as shown in ***fig. 4.4*** are:

- A. Beam generation
- B. Beam guidance
- C. Beam shaping
- D. Beam movement
- E. Beam control system
- F. Beam safety
- G. Beam environment

The subsystems B, C and D together yield the beam delivery.

The SLM machine used for the fabrication of test specimens in this thesis is shown in ***fig. 4.5*** where ***a)*** is the complete machine housing, ***b)*** is a CAD model of the process chamber and ***c)*** is the beam delivery into the process chamber. This system is characterized by the following components from each of the above listed subsystems according to the specified capital letters A. to G.:

- A.: - 100 W Ytterbium fiber laser (IPG YLR-100), wavelength 1077.1 nm,
- B.: - step-index glas fiber, 60 µm diameter
- C.: - fiber end collimator (aperture 5 mm)
  - collimator (Sill optics beam expander, fixed zoom factor 8, variable divergence angle),
  - f-theta-lens (300 mm focal length)
- D.: - scanner system (Cambridge Technology Model 6650)
- E.: - one user workstation
  - one process computer
  - various interface cards for motors, valves, pumps, laser and sensors
- F.: - process chamber
  - process gas circulation

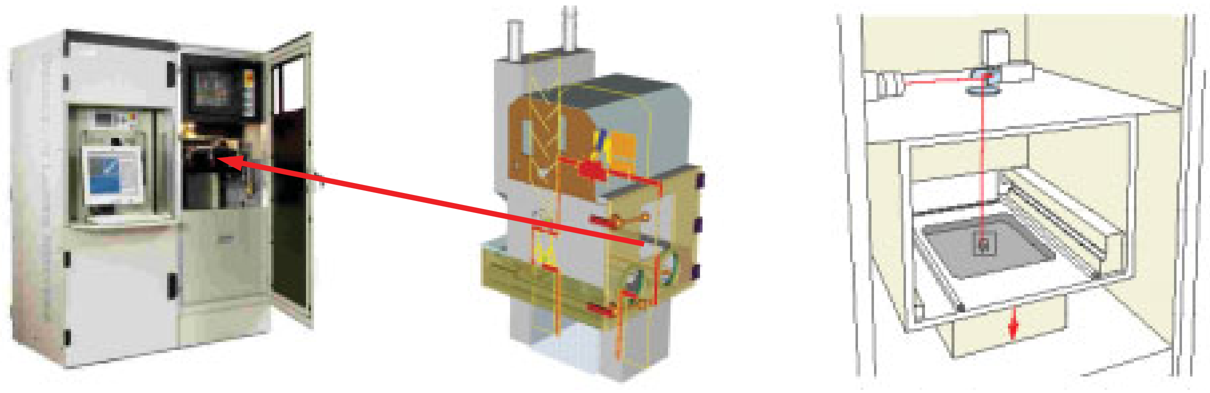

a) **b)** **c)**

Figure 4.5: SLM machine housing, CAD model and sketch of process chamber [198], [105]

- G.: - coating system
  - powder tank
  - heated platform system

In order to let the design parameters govern the product quality rather than the fabrication process as introduced in the 'House of Quality for Cellular Material Products' in ***fig. 2.15*** it is mandatory to allow as few constraints as possible from the fabrication process. This implies as few constraints as possible from the according LFF system. Therefore, those subsystems and components of the SLM machine used in this thesis are of special importance which take direct influence on the dominant process parameters according to ***section 3.5.1*** and hence on the product quality as well as the manufacturing cost and time in respect to ***sections 3.5.2*** and ***3.5.4***. Hence, a brief interpretation of the most important subsystem properties acquired for this particular machine is presented in the following paragraphs.

A. Beam generation

For the fabrication of fine lattice structures it is mandatory to have best resolution capabilities and thus the smallest focus diameter possible. ***Eq. (4.2)*** gives the theoretical focus diameter $d_{0,86.5,ideal}$ of an unperturbed laser beam according to geometrical constraints such as the collimation of the optical fiber $d_{86.5,input}$, the wave length λ and the focal length f of the f-theta lens. For the present system a theoretical focus diameter of 20.6 µm results from measured or given values for beam collimation of 5 mm, wave length of 1077.1 nm and focal length of 300 mm. However, as shown in ***fig. 3.3*** the cauterization of a real beam deviates significantly from the theoretical beam propagation. This is described by the beam quality factor M^2 which is the ratio of the beam parameter product of a real laser beam to that of an ideal Gaussian beam leading to an increased focus diameter $d_{0,86.5,real}$ as given in ***eq. (4.3)***.

$$d_{0,86.5,ideal} = \frac{f \cdot \lambda}{d_{86.5,input} \cdot \pi} \tag{4.2}$$

$$d_{0,86.5,real} = \frac{f \cdot \lambda}{d_{86.5,input} \cdot \pi} \cdot M^2 \tag{4.3}$$

The factor M^2 that is obtainable on the powder bed is therefore relevant for the smallest feature size that the SLM process can deliver according to ***eq. (3.34)***. The beam quality factor M^2 of the laser beam source was determined to equal or less than 1.05 directly after the fiber end collimator of the laser unit. This still allows a slightly increased theoretical focus diameter of 21.6 µm.

A Primes FocusMonitor was used according to the rotating aperture methodology proposed in DIN EN ISO 11146-1 (2005, p. 4, pp. 11-17, [95]) to acquire the actual in-process constraints of the laser beam source (Crames, 2005, pp. 20-30, [66]). This was conducted such that all laser beam properties were measured directly on the powder bed level. The laser beam power was tested in the range between 12.2 and 100.7 W output power setting. Due to losses in components such as collimator, scanner mirrors and f-theta-lens the resulting laser beam power was measured to slightly decreased values between 12.1 to 94 W with a nearly linear

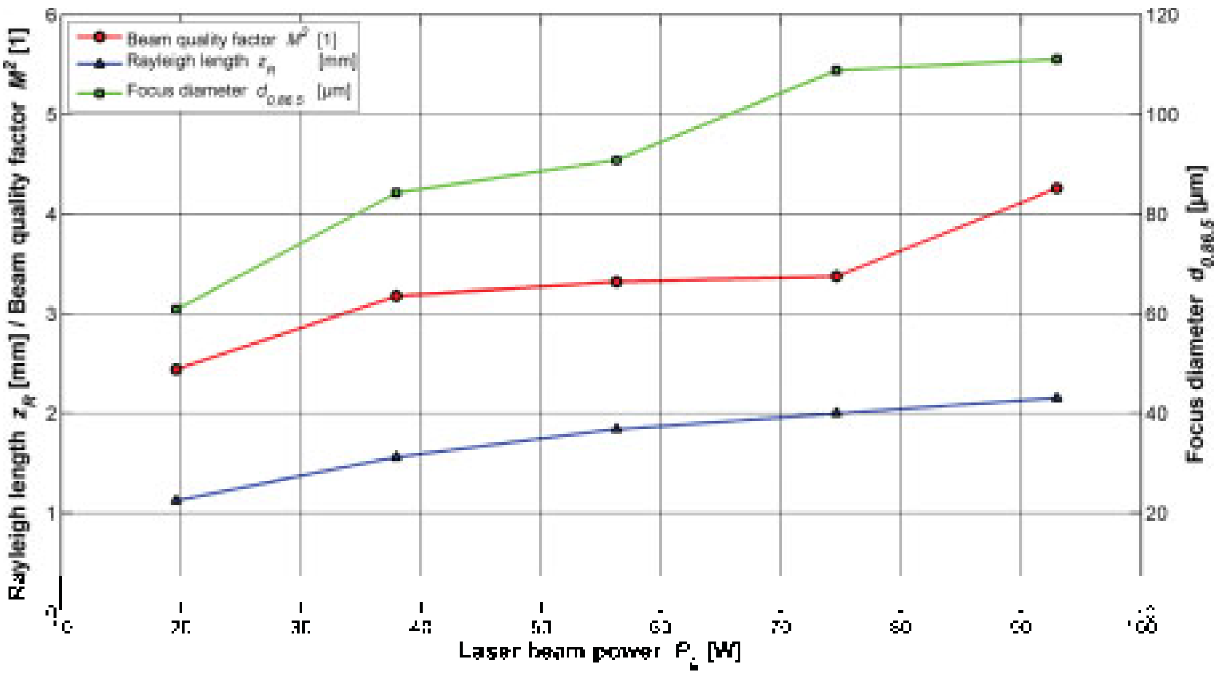

Figure 4.6: Beam quality factor, focus diameter and Rayleigh length vs. laser beam power

correlation between selected and obtained power as approximated in ***eq. (4.4)***. This is important for future considerations of energy density transferred into the powder bed as well as for the parameters of beam quality factor M^2, focus diameter $d_{0,86.5}$ and Rayleigh length z_R which were measured at given laser beam power settings $P_{L,selected}$ of 20, 40, 60, 80 and 100 W. ***Fig. 4.6*** shows the obtained average values for beam quality factor in red circles, focus diameter in green rectangles and Rayleigh length in blue triangles versus the true laser beam power at the powder bed surface according to ***eq. (4.4)***.

$$P_L = 0.9171 \cdot P_{L,selected} + 1.2496\ \mathrm{W} \tag{4.4}$$

The measured values for the beam quality factor M^2 ranged between 2.11 and 4.52 at the lowest and highest laser beam power, respectively. This confirms a massive deterioration of laser beam quality additionally to the loss of some laser beam power. As a result the theoretical focus diameter can by far not be met. The measurement yielded values between 60.9 and 111 µm at the lowest and highest laser beam power, respectively. This is roughly five times the theoretical value calculated above which is in good agreement with the measured values of M^2. Focus diameter of this order of magnitude still appear suitable to produce micro-sized features with expected smallest positive feature sizes within few hundreds of microns. The measured Rayleigh lengths ranged from 1.125 to 2.155 mm, again from the lowest to the highest laser beam power. This information is important since further measurements performed on the effects of the beam expander unit gave a minimum of 16.35 mm focus shift along the z-axis over the full range of beam collimation. Thus the focus shift is one order of magnitude larger than the Rayleigh length of the focussed beam which can lead to reduced laser beam intensity on the powder bed and process failure.

C. & D. Beam delivery

The scanner system was tested in terms of dynamics and resulting accuracy with regard to the new scan strategy introduced in ***section 4.1*** which features mostly short sky-writing paths in the millimeter length range between two consecutive exposure points. In order to reduce auxiliary process time between two points these paths must be travelled at highest possible speed to ensure the competitiveness over hatch scan methods. Measurements suggest that in this distance range the scanner can accelerate to speeds of above 1 m/s (Crames, 2005, pp. 50-53, [66]) which is considered sufficient for the new scan strategy. According to the manufacturer the so-called small angle step response time is 3.5 ms (Cambridge Technologies, 2007, [52]) which in manufacturing of SLM lattice structures might not be adequately small enough and might influence the minimum allowed exposure time of single exposure points.

The quality property of accuracy to shape and size as defined for solid SLM parts in ***section 3.5.2*** depends strongly on the repeatability of the scanner positioning. Additionally, the size accuracy also depends on the so-called f-theta-lens correction. Both influence factors are as well important for the fabrication of micro-sized lattice struts. However, for SLM lattice structures the repeatability of the scanner positioning mainly influences the shape of the struts whereas the f-theta-lens correction mainly influences the position of the struts.

The repeatibility of the scanner positioning accuracy controls the cross section profile of each strut. If the repeatibility is low then struts are composed of subsequent weld spots that are located at positions deviating from the center line of each strut. This position variance must be kept as small as possible and should be considered critical since it can increase the notch effect on loaded struts. Measurements of obtained exposure positions showed that the standard deviation depends on the length of the path travelled to each position because the scanner mirrors can accelerate more the longer the path is. The longer the acceleration period is the higher the tendency becomes for the mirrors to overshoot. On average the relative standard deviation, i.e. the standard deviation divided by the average path length, yielded an overshoot value of 0.314 %. If calculated for the triple standard deviation, this value suggests that 3 out of 1000 exposure points show a dislocation of more than 0.942 % of the travelled path length. If the largest expected unit cells are e.g. equilateral with a side length of 10 mm, then the longest expected sky-writing path will be 14.14 mm diagonally. Even at this path length 99.7 % of all exposure points will fall within a range of ±133 µm of the nominal position. Examinations of the melt pool width indicated that at a size of approximately 200 µm it is significantly greater than the focus diameter due to the heat affected zone as denoted in ***eq. (3.34)***. This gives rise to the assumption that at full laser beam power and a resulting focus diameter of 111 µm an acceptable minimal value of 99.7 % of all exposure points will overlap with the exposure points from the previous layer such that a firm connection between powder material exposed in consecutive layers is obtained.

In order to assess the f-theta-lens correction error for an estimation of strut position accuracy various geometries were exposed onto photographic paper and measured. Linear, size-dependent errors were found where geometries along the x-direction were on average 4.05 %

too large while in the y-direction they showed an average oversize of 2.9 %. This systematic error occurred due to simple misadjustment of the f-theta-lens correction and is not critical for the experimental work on SLM lattice structures as long as all obtained dimensions rather than the defined dimensions are used in subsequent calculations of stresses. Nevertheless, to achieve the highest degree of periodicity in SLM lattice structures the f-theta-lens correction should be adjusted corrrectly.

G. Beam environment

The positioning accuracy of other mechanical machine components is also an important issue. However, in this context mainly the movement of the building platform in z-direction should be considered. Measurements showed that even after 227 steps at 75 µm layer thickness, the total deviation along the z-axis is never more than 30 µm which would result in 0.176 % inaccuracy in part height which is one order of magnitude less than the inaccuracies in x- and y-direction.

4.3 Approach to assessment of mechanical properties

Further assessment of the mechanical properties of SLM lattice structures is performed throughout the two following sections of this thesis by means of theoretical and experimental

Table 4.3: Approach to assessment of mechanical properties of SLM lattice structures

Theoretical modelling	Experimental investigation
Anisotropy of SLM solids	Anisotropy of SLM solids
-	Producibility of SLM lattice structures
-	Experimental determination of suitability of various cell types for specific applications Decision for three most suitable cell types for further in-depth investigation
External failure model (continuum mechanics, yield surface) Internal failure model for low relative densities (matrix structural analysis) Internal failure model for high relative densities (solid with pores approach)	Experimental determination of tensile, compressive and shear strength and elasticity for SLM lattice structures of low and high relative densities
Mathematical functions to unify both models for low and high relative density which consider a given critical relative density	Fitting of experimental data to unified model, conversion of results into main design parameter *a*/*d* (aspect ratio)
Producibility of SLM lattice structures	-
Simulation of strength and elasticity of various cell types and cell sizes in the low relative density regime	Comparison of experimental results in the low relative density regime with simulation

methods. All involved steps are pointed out in ***table 4.3*** in order to clarify the general approach. Additionally, steps in the theoretical as well as the experimental assessment, which aim at similar objectives, are compared in this table by placing them in identical lines. Among these objectives all steps are processed in parallel except for the investigation of producibility of SLM lattice structures which in theoretical modelling is foreseen to be examined only before a decision for specific cell types is required in the simulation whereas in the experimental investigation it is required before any of the desired test specimens are examined.

4.4 Summary

This chapter shows how first attempts failed to fabricate open-cell lattice structures with SLM based on 3D-CAD data. Only the development of a new point-like exposure strategy allows the manufacture of SLM lattice structures with micro-sized struts in the submillimeter range and cell sizes in the range of few millimeters down to the submillimeter range.

The important aspects of product quality as well as manufacturing cost and time considered for solid SLM materials in ***section 3.5*** count as well for the fabrication of SLM lattice structures. Therefore, this chapter determines the general influence parameters that take effect on the fabrication of SLM lattice structures. In preparation of the experimental analysis in ***section 6*** the process conditions are analyzed and assessed. These are mainly the constraints from the material and the SLM system. The material composition is examined by chemical analysis and its process suitability is considered. The SLM system is divided into different subsystems of which the most important ones are analyzed by theoretical considerations compared with measurements conducted on the machine used for fabrication of specimens in this thesis.

Finally, the approach of the theoretical and experimental investigations of the mechanical properties of SLM lattice structures given throughout the two following sections is pointed out as a guideline for further reading.

5 Theoretical analysis of SLM cellulars

5.1 Structural hypotheses for isotropic cellular materials

5.1.1 Strength and elastic properties of low density cellular materials

Before fabrication and examination of numerous test specimens in order to assess the mechanical properties of SLM lattice structures it is compulsory to reduce the potential amount of specimens. Therefore, it is required to derive e.g. suitable cell types, cell sizes, strut diameters, etc. by utilizing appropriate theoretical considerations. Furthermore, theories developed on the mechanical properties of the test specimens and derived scaling laws should be in good agreement with future experimental results. Here, the focus is the deduction of the expected elastic and failure behaviour of SLM lattice structures under uniaxial compressive and tensile loads as well as shear loads.

In ***section 2.1.4*** a number of scaling laws were given which all are similar to ***eq. (2.2)***. According to the percolation theory introduced in ***section 2.1.4*** these scaling laws are based on power laws as a function of the cellular material's relative density. This implies that any cellular material is considered a continuum consisting of the bulk material but of lesser density. This approach appears quite suitable for stochastic cellular materials such as foams and sponges with expected isotropic mechanical properties where the stochastic structure does not allow a straightforward analytical approach. The precursor experiments mentioned in ***section 4.1*** indicate that describing the mechanical properties of SLM lattice structures can be conducted likewise, i.e. power laws based on relative density, as presented by Rehme (2006, p. P6001.4, [253]). However, this procedure is detrimental since it neglects the fact that SLM lattice structures have a highly ordered framework structure which substantially influences the mechanical properties due to its prevailing failure modes. Thus it would allow the consequence of predicting identical mechanical properties for two different cell types which comprise identical relative densities. This is evidently inadmissable, therefore, a more suitable approach based on beam theory for 3D frameworks is required.

In fact, even though stochastic cellular materials like foams and sponges can be considered a continuum, results for these materials were also derived analytically based on elastic beam bending theory in which simple unit cells such as cubic frames (see ***fig. 2.11***, Gibson, 1997, pp. 203-208, [123]) or tetrakaidecahedral polyhedrons (Grenestedt, 1999, pp. 1474-1475, [132] and Zhu, 1997, pp. 323-331, [333]) were assumed. These approaches allow to obtain an estimation of the effective strength and effective Young's modulus of bending- and stretch-dominated cellular materials as shown in ***eqs. (5.1)*** through ***(5.21)***, provided that certain simplifications are admitted. One simplification is the assumption of equal cell size in all three dimensions, meaning that all unit cells are cubic and of the same size, and the second one is that only small relative densities are considered because of repeated inclusion of mass concentrated in cell corners where two or more struts intersect. In this context effective strength or modulus means the proportion of the obtained value compared to the bulk material's value. The following introductive derivations only include considerations of open-cell materials since closed-cell materials are irrelevant for SLM lattice structures and are hence not needed for the subsequent development of scaling laws. Some similar derivations can be found in the literature, however, no source is available which gives a complete overview and a clear distinction between bending-dominated and stretch-dominated behaviour as follows.

Relative yield strength

The yield strength σ^*_{yield} of a bending-dominated cellular material is proportional to the force F^*_{yield} applied onto its cross section area A^* which will cause plastic deformation. Assuming that this macroscopic consideration can as well be referred to a single unit cell and simplyfing the geometry of this unit cell such that is has cubic shape and that the length of all unit cell edges become identical ($a = b = c$), the cross section area can be rewritten as $A = a^2$ and the new result is proportional to σ^*_{yield}. Deriving the plastic force from the plastic bending moment $M_{yield,solid}$ in a cell strut of length a gives

$$\sigma^*_{yield} = \frac{F^*_{yield}}{A^*} \propto \frac{\frac{M_{yield,solid}}{a}}{a^2}. \tag{5.1}$$

According to beam bending theory (Timoshenko, 1961, p. 164, [293]) the maximum internal stress in a beam under bending deformation occurs in its remotest fiber from the neutral axis and is defined as

$$\sigma_{yield,solid} = \frac{M_{yield,solid}}{I} \cdot \frac{d}{2} \tag{5.2}$$

where I is the area moment of inertia, which is

$$I = \frac{\pi d^4}{4} \tag{5.3}$$

for struts of circular cross section with strut diameter d. ***Eq. (5.2)*** assumes the neutral axis in the exact middle of the strut, thus the factor 2 is explained. Solving ***eq. (5.2)*** for the moment $M_{yield,solid}$ and and substituting the area moment of inertia I according to ***eq. (5.3)*** the cellular material's yield strength becomes

$$\sigma^*_{yield} \propto \sigma_{yield,solid} \cdot \frac{d^3}{a^3}. \tag{5.4}$$

Since the volume of one unit cell is constant whether made from cellular or from bulk material

$$V = \frac{m}{\rho} = const = \frac{m_{solid}}{\rho_{solid}} = \frac{m^*}{\rho^*} \tag{5.5}$$

it follows that relative density of a cellular material is

$$\frac{\rho^*}{\rho_{solid}} = \frac{m^*}{m_{solid}}. \tag{5.6}$$

Furthermore, for a cellular material comprising unit cells made of circular struts the mass of a unit cell is always proportional to the square of the strut diameter divided by the square of the cell size as ***eq. (5.7)*** shows.

$$\frac{\rho^*}{\rho_{solid}} \propto \frac{\rho_{solid} \cdot a\pi \frac{d^2}{4}}{\rho_{solid} \cdot a^3} \propto \frac{d^2}{a^2} \tag{5.7}$$

Equating this with ***eq. (5.4)*** gives the relative yield strength for a bending-dominated cellular material in dependence of its relative density

$$\frac{\sigma^*_{yield}}{\sigma_{yield,solid}} \propto \left(\frac{\rho^*}{\rho_{solid}}\right)^{1.5}. \tag{5.8}$$

In contrast, for stretch-dominated cellular materials no bending occurs and the force F^*_{yield} from ***eq. (5.1)*** acting on the material's full cross section area becomes the much smaller value $F_{yield,solid}$ causing plastic strain in one cell strut. Therefore, the yield strength of one strut due to longitudinal strain is given by

$$\sigma_{yield,solid} = \frac{F_{yield,solid}}{d^2} \cdot \frac{4}{\pi}. \tag{5.9}$$

Assuming that the force $F_{yield,solid}$ in one strut is proportional to the overall force F^*_{yield} and equating ***eqs. (5.9)*** and ***(5.1)*** gives

$$\sigma^*_{yield} \propto \frac{F_{yield,solid}}{a^2} = \sigma_{yield,solid} \cdot \frac{d^2}{a^2} \cdot \frac{\pi}{4}. \tag{5.10}$$

Rewriting this correlation with ***eq. (5.7)*** shows a linear dependency of the relative yield strength on the relative density of a stretch-dominated cellular material.

$$\frac{\sigma^*_{yield}}{\sigma_{yield,solid}} \propto \frac{\rho^*}{\rho_{solid}} \tag{5.11}$$

This result must be considered rather critically. It would be convenient to obtain a cellular material whose strength diminishes only linearly with reduction of its relative density. However, in stretch-dominated frameworks not all struts can be subject to elongation, some are always exposed to compression. This allows the occurrence of failure due to buckling. Buckling-dominated behaviour can be expressed, if ***eq. (5.1)*** is altered such that the consideration of macroscopic stress is related to a consideration of stress on one unit cell strut caused by a critical force $F_{critical}$ equal to the Euler load.

$$\sigma^*_{yield} = \frac{F^*_{yield}}{A^*} \propto \frac{F_{critical}}{a^2} \propto \frac{\frac{E_{solid} I}{a^2}}{a^2} . \qquad \textbf{\textit{(5.12)}}$$

Using ***eqs. (5.3)***, ***(5.7)*** and ***(5.12)*** gives a quadratic dependence of a cellular material's yield strength in relation to its Young's modulus depending on its relative density as shown in ***eq. (5.13)***. This formula allows to derive a critical density below which buckling-dominated strength is smaller than stretch-dominated strength. The relation of Young's modulus E_{solid} and yield strength σ_{yield} at 0.2 % plastic strain of bulk stainless steel as used in the experimental section of this thesis gives an approximate factor of 400.

$$\frac{\sigma^*_{yield}}{E_{solid}} \propto \left(\frac{\rho^*}{\rho_{solid}} \right)^2 \qquad \textbf{\textit{(5.13)}}$$

This allows to evaluate ***eq. (5.13)*** and obtain a relative density of 0.05 above which, for stainless steel, the absolute values of buckling-dominated yield strength are indeed greater than those of stretch-dominated behaviour. This is valid for most cellular materials since relative densities below 0.05 are difficult or for some processes even impossible to obtain.

Eqs. (5.8), ***(5.11)*** and ***(5.13)*** may as well be applied on the shear strength of bending- and stretch-dominated cellular materials by replacing σ^*_{yield} with the macroscopic shear strength τ^*_{yield} which can be easily shown by using the same approaches.

Relative Young's modulus

The definition of the Young's modulus of a material is the proportionality factor between applied stress σ and resulting strain ε. This is also true for the macroscopic consideration of a cellular material's effective Young's modulus, i.e. its stiffness E^*. ***Eq. (5.14)*** breaks this correlation down to the fundamental variables of a force F^* applied onto its cross section area A^* which causes a deformation δ^* along its length l in the direction of the force.

$$E^* = \frac{\sigma^*}{\varepsilon^*} = \frac{\frac{F^*}{A^*}}{\frac{\delta^*}{l}} \qquad \textbf{\textit{(5.14)}}$$

Assuming a simplyfied unit cell geometry like above, this correlation can be equated with the dimensions of one unit cell on which the force F acts causing the deformation δ. Rewriting with $A^* = a^2$ and $l = a$ gives

$$E^* = \frac{F}{a \cdot \delta} . \qquad \textbf{\textit{(5.15)}}$$

For a bending-dominated structure the force F exerted onto a single strut inside the unit cell at a given location, i.e. a in this case, divided by the bending stiffness EI of the strut is, according to beam bending theory (Timoshenko, 1961, p. 6, [293]), proportional to the deformation δ of the strut:

$$\delta \propto \frac{Fa^3}{E_{solid} I} \tag{5.16}$$

Substituting the area moment of inertia for struts with circular cross section area according to ***eq. (5.3)*** and equating ***eqs. (5.15)*** and ***(5.16)*** gives

$$\frac{E^*}{E_{solid}} \propto \frac{d^4}{a^4}\,. \tag{5.17}$$

Hence with the aid of ***eq. (5.7)*** the quadratic dependence of the relative Young's modulus on the relative density of a bending-dominated cellular material is obtained:

$$\frac{E^*}{E_{solid}} \propto \left(\frac{\rho^*}{\rho_{solid}}\right)^2 \tag{5.18}$$

For a stretch-dominated structure, however, a significant deviation exists for the relative Young's modulus. The force F applied onto a single strut in direction of its axis multiplied with the undeformed cell size and divided by the compressive stiffness $E_{solid} \cdot A$ of the strut equals the deformation δ of the strut:

$$\delta = \frac{Fa}{E_{solid} A} \tag{5.19}$$

Under consideration of the cross section area for circular struts

$$A = \frac{\pi d^2}{4} \tag{5.20}$$

and substituting ***eq. (5.19)*** into ***eq. (5.15)*** a linear correlation between the relative Young's modulus and the relative density of a stretch-dominated cellular material is obtained:

$$\frac{E^*}{E_{solid}} \propto \frac{d^2}{a^2} \propto \frac{\rho^*}{\rho_{solid}} \tag{5.21}$$

The shear moduli of bending- and stretch-dominated cellular materials can be obtained from likewise approaches where the effective Young's modulus E^* in ***eqs. (5.18)*** and ***(5.21)*** is replaced with the effective shear modulus G^*.

As shown in ***section 2.1.4*** the idealized scaling laws from ***eqs. (5.8)***, ***(5.11)***, ***(5.18)*** and ***(5.21)*** can hardly be reproduced in practical experiments due to e.g. flaws or low strut connectivity within the cellular structure of a material. The response in scaling laws is typically an increased exponent compared to the ideal value. The higher the exponent is the worse the performance of the cellular material becomes since the same relative density will yield e.g. a lower strength value. Therefore, it is of high interest to obtain small exponents near the theoretical value.

5.1.2 Bending- and stretch-dominated behaviour

As seen above, the knowledge whether a unit cell shows bending- or stretch-dominated behaviour is significant to develop characteristic scaling laws. A simple criterion on the stability of frameworks was found by Maxwell (1864, pp. 294-299, [194]) from the equilibrium conditions in a network of pin-jointed straight bars connected by frictionless joints in which a stiff framework is defined as one in which the distance between any two joints cannot be altered without altering the length of one or more of the framework's bars. Maxwell's rule implies that a 3D-framework having j frictionless joints requires $b = 3j\text{-}6$ bars to be just stiff. If, however, more bars exist than degrees of freedom of the joints less the number of constraints, i.e. $b > 3j\text{-}6$, then states of self-stress are possible which make the framework even stiffer. In contrast, if fewer bars exist than degrees of freedom of the joints less the number of constraints, i.e. $b < 3j\text{-}6$, then the framework becomes a mechanism which can fold up or out when loaded externally. As Maxwell supposed, frameworks which are exceptions to his rule are possible. These lack stiffness because of the existence of an infinitesimal mechanism although, nominally, they show no degrees of freedom due to a corresponding state of self-stress. Calladine (1978, pp. 164-167, [50]) gave an according example for 2D space where Maxwell's rule $b = 2j\text{-}3$ is satisfied while one mechanism and one state of self-stress coexist. ***Fig. 5.1*** shows such an example constructed from 9 bars and 6 joints in which the left part of the frame has one too many bars to be just stiff and, therefore, has one state of self-stress, while the right part has one too few bars and thus has an infinitesimal mechanism. Hence, Calladine accounted for the possible states of self-stress s and the number of mechanisms q by extending Maxwell's rule to ***eq. (5.22)***.

$$M = b - nj + k = s - q \tag{5.22}$$

In this formula n is the number of dimensions and k the number of constraints while the absolute value of M stands for the number of degrees of freedom a bending-dominated

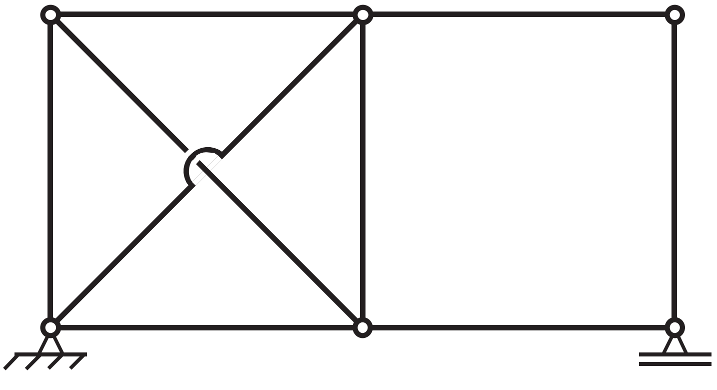

Figure 5.1: 2D example of a frame which has one mechanism and one corresponding state of self-stress [50]

framework has (if $M < 0$) or for the number of additional constraints a stretch-dominated framework has (if $M > 0$). It is often used to predict the rigidity of cellular materials. In ***eq. (5.22)*** s is obtained from determining the rank of the $(nj)\times(k+6)$ equilibrium matrix in a relation where the sum of all forces is zero and q is derived from determining the rank of the $(k+6)\times(nj)$ compatibility matrix in a kinematic relation which equates all bar extensions with all nodal displacements.

For SLM lattice structures made from only one type of unit cell that is periodically repeated the counting of self-stress states and mechanisms can be neglected. However, if a unit cell yields $M \geq 0$ then stretch-dominated behaviour should be assumed while bending-dominated behaviour should be anticipated in the case $M < 0$. However, all considerations presented in this section were developed for isotropic materials. Therefore, it is expected that for SLM lattice structures each individual cell type can simultaneously show bending- and stretch-dominated behaviour in different directions of load. Therefore, it must be hypothesized that the explanation of the inner behaviour of SLM lattice structures cannot be derived by means of simple models as represented by ***eq. (5.22)***.

5.1.3 Strength and elastic properties of high density cellular materials

In contrast to materials of low relative density, the structure inherent in porous solids cannot be approximated by frameworks or network structures but rather by approaches of two-phase materials in which the second phase consists of geometrically defined inclusions. If these inclusions are vacuum or gas phase, i.e. they represent pores, the general formula in ***eq. (5.23)*** can be employed for calculations of the material's relative Young's modulus where ν is the Poisson's ratio of the solid material. For high relative densities near unity it exhibits nearly linear behaviour.

$$\frac{E^*}{E_{solid}} = \frac{2 \cdot \frac{\rho^*}{\rho_{solid}}}{2 + \big(3(1-\nu)+1\big)\cdot\left(1 - \frac{\rho^*}{\rho_{solid}}\right)} \tag{5.23}$$

$$\frac{\sigma^*_{yield}}{\sigma_{yield,solid}} = \frac{\rho^*}{\rho_{solid}} \tag{5.24}$$

The yield strength of porous solids is governed by mainly two effects (Rice, 1993, p. 2188, [258]). These are on one hand the reduced cross section area, leading to a linear decrease of yield strength, and on the other hand the occurrence of stress concentrations, i.e. notch stresses, around the pores. However, Rice stated that such stress concentrations are merely significant if the yield strength is proportional to the material's Young's modulus and the fracture energy. This is true for brittle materials where failure due to fracture prevails. For ductile metallic materials this influence can be neglected, therefore, the yield strength scales linearly with relative density for relative densities near unity (Boccaccini, 1994, pp. 15-16, [40]) according to ***eq. (5.24)***.

5.2 Structural hypotheses for anisotropic SLM lattice structures

5.2.1 Approach to a generalized SLM lattice structure theory

The scaling laws and methods to derive the mechanical properties and failure behaviour introduced in the previous section work sufficiently well for isotropic materials such as metallic foams. However, for SLM lattice structures these approaches fail completely since it is obvious that the unit cell design can dictate deviating properties in different directions of space. Therefore, a different method needs to be implemented for an ability to specifiy scaling laws by means of continuum mechanics. A suitable tool for this approach is the tensorial representation of effective Young's moduli and effective strengths. Various authors (Bažant, 1991, p. 748, [34]) agree that analytical solutions become ineffective or impossible for three dimensional, anisotropic structure analysis. Therefore, it appears mandatory to incorporate all valid analytical methods available for single bars and trusses into the greater context of a numerical approach for frameworks which contain a high number of interacting correlations. Thus standard procedures for structural engineering such as the displacement method can be used to evaluate different unit cell configurations in terms of elastic and plastic behaviour.

Beyond a critical point of high relative density the framework model will fail because the lattice structure becomes a solid with pores as already introduced in ***section 5.1.3***. This leads to a different theory for the effective material properties of high density SLM lattice structures.

This ***section 5.2*** will guide through all the theoretical background required for an understanding of the development of a generalized theory for SLM lattice structures as shown in the Ishikawa diagram in ***fig 5.2***. Therefore, some light is shed on the anisotropy of SLM solids due to the layerwise processing of material as introduced in ***section 3.5.2***. Next, the anisotropy of SLM lattice structures is investigated to answer the questions how does it affect the mechanical properties and how can these properties be sufficiently represented. Thus the tensor representation of mechanical elasticity and strength properties is introduced. To assess the according effective properties of low relative density SLM lattice structures, matrix structural analysis is presented next. This is followed by the calculation of effective material properties in the high relative density regime. Then, the general relative density of SLM lattice structures is derived and the basis is laid for determination of the critical relative density above which framework models break down. Next, both approaches for low and high relative densities are combined to form a generalized theory for SLM lattice structures.

In order to not complicate the generalized theory the main design parameters considered are the unit cell size a and the micro strut diameter d and the derived aspect ratio a/d, respectively. This implies that all unit cell dimensions are set equal, i.e. $a = b = c$, if applicable like in e.g. in the case of orthorhombic unit cells. This is also quite reasonable in terms of optimization of the mechanical properties of SLM lattice structures since unbalanced unit cell dimensions, i.e. one cell dimension is much larger or smaller than the other two, will most likely lead to reduced strength and stiffness, undesired buckling behaviour or a reduced

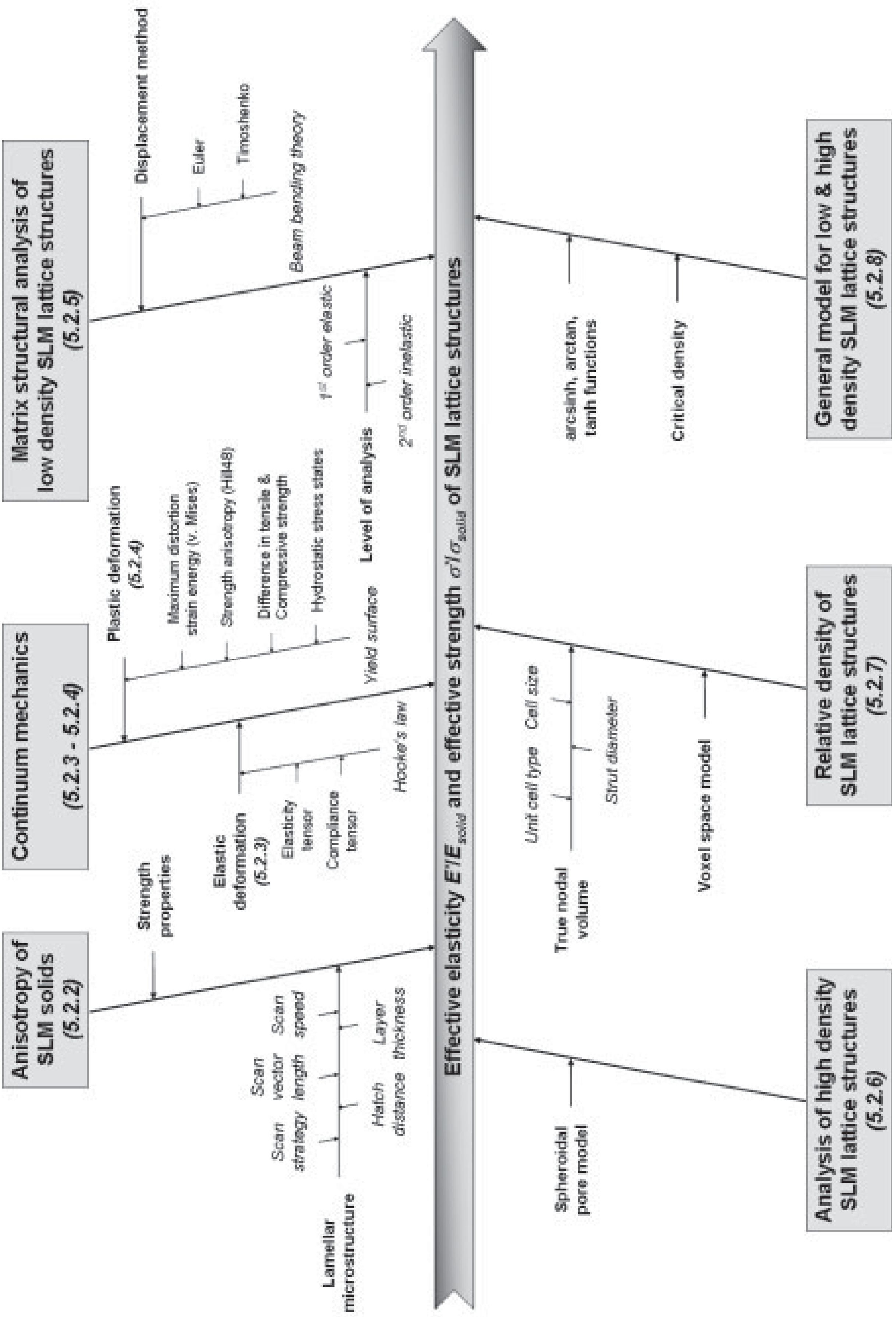
Anisotropy of SLM solids (5.2.2)
Continuum mechanics (5.2.3 - 5.2.4)
Matrix structural analysis of low density SLM lattice structures (5.2.5)
Strength properties
Plastic deformation (5.2.4)
Maximum distortion strain energy (v. Mises)
Strength anisotropy (Hill48)
Difference in tensile & Compressive strength
Hydrostatic stress states
Yield surface
Displacement method
Euler
Timoshenko
Beam bending theory
Lamellar microstructure
Scan strategy
Scan vector length
Scan speed
Hatch distance
Layer thickness
Elastic deformation (5.2.3)
Elasticity tensor
Compliance tensor
Hooke's law
Level of analysis
1st order elastic
2nd order inelastic
Effective elasticity E'/E_{solid} and effective strength σ'/σ_{solid} of SLM lattice structures
Spheroidal pore model
True nodal volume
Unit cell type
Cell size
Strut diameter
Voxel space model
arcsinh, arctan, tanh functions
Critical density
Analysis of high density SLM lattice structures (5.2.6)
Relative density of SLM lattice structures (5.2.7)
General model for low & high density SLM lattice structures (5.2.8)

Figure 5.2: Ishikawa diagram of a generalized theory for SLM lattice structures

surface-to-mass-ratio. In the case of other non-orthorhombic unit cells the ratio between the unit cell dimensions *a* and *b* as well as *a* and *c* will be set to a fixed value which complies best with these requirements.

5.2.2 Anisotropy of SLM solids

As explained in ***section 3.5.2*** SLM solids show anisotropic material properties due to their lamellar microstructure which is a direct result of the layerwise manufacturing. The formation of the lamellar microstructure is mainly influenced by the chosen process parameters such as laser beam power, scan strategy, scan vector length, scan speed, hatch distance and layer thickness. It is expected that the elastic properties of SLM solids remain unaffected since these depend rather on the interaction of atomic bonds than on the microstructure. The mechanical strength properties, however, depend on the microstructure. Therefore, in anisotropic SLM solids they limit the maximum strength which is typically found in directions in the x-y-plane.

If orthorhombic symmetry is assumed for the lamellar microstructure of SLM solids and if loads in directions other than the principal directions can be considered as combined principal stress states, then it should be expected that the Hill48 criterion introduced later in ***eq. (5.49)*** may be applied to define the yield surface of SLM solids. Unlike the v. Mises criterion, which gives a circular cylindrical yield surface, the Hill yield surface of SLM solids is expected to exhibit a flattened cylinder, i.e. an elliptic cylinder with a shorter semi axis along the z-direction due to reduced strength in z-direction. This elliptic cylinder is also more tilted towards the x-y-plane for the same reason. Therefore, in 3D principal stress space where σ_1, σ_2 and σ_3 are equivalent to the x-, y- and z-direction of the SLM process two major consequences prevail:

1. The flattened Hill cylinder has a rather elliptic cross section area, which in turn yields a rather circular projection in the σ_1-σ_2 plane according to the sketch shown in the left part of ***fig. 5.3***. Thus position vectors to each location along the yield surface in the σ_1-σ_2 plane

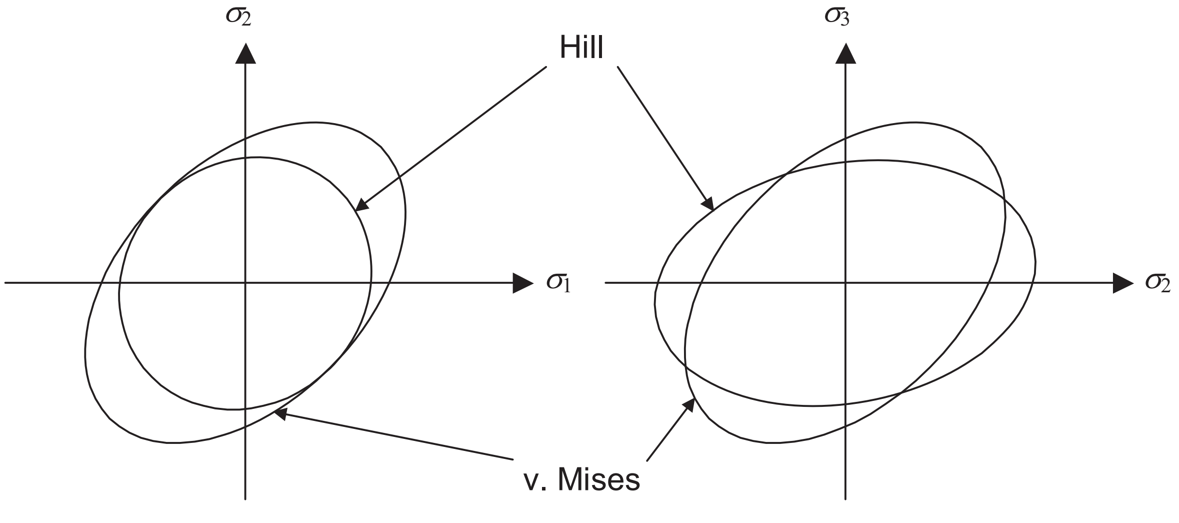

Figure 5.3: Hill vs. v. Mises yield surfaces for SLM solids

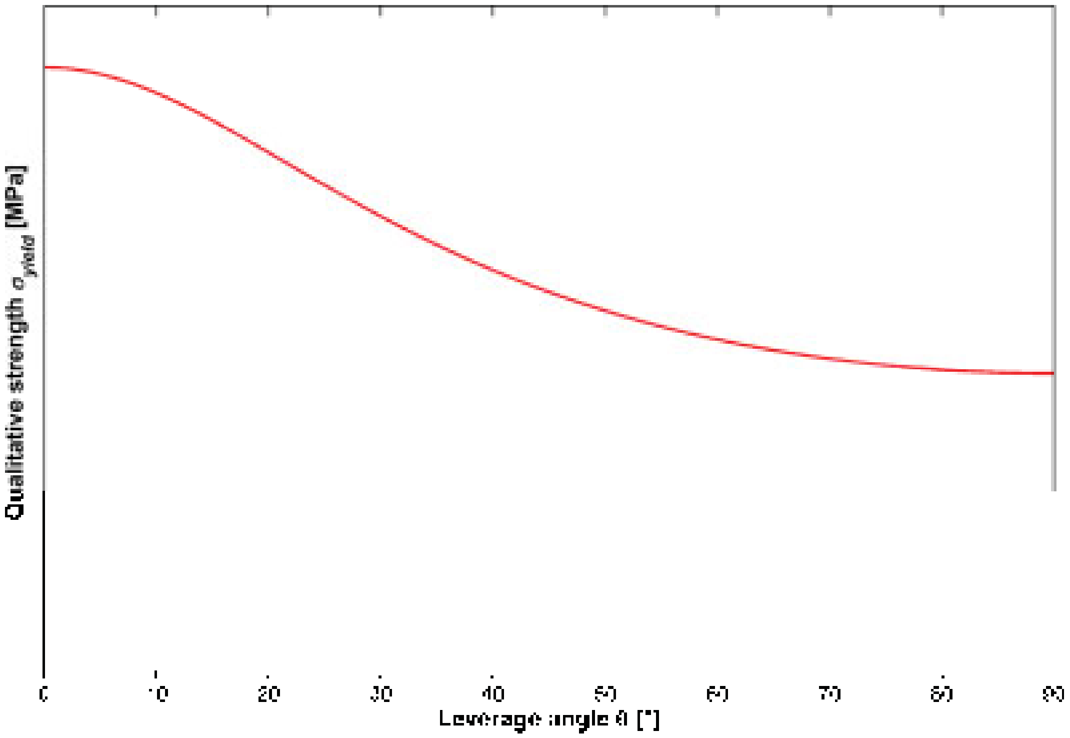

Figure 5.4: Theoretical trend of yield strength in dependence of leverage angle between force and x-y-plane

have approximately the same length and strength is independent of the direction of force.

2. In the σ_1-σ_3 or σ_2-σ_3 plane, the tilting of the Hill cylinder leads to rotation of the according projection as depicted in the right part of ***fig. 5.3*** where the length r of the position vector to the yield surface can be written as

$$r = \sqrt{\sigma_x^2 + \sigma_z^2} \text{ or } r = \sqrt{\sigma_y^2 + \sigma_z^2}\,. \tag{5.25}$$

   This position vector length is linked with the leverage angle θ – counted from the x-y-plane towards the acting force – by the correlation

$$\cos\theta = \frac{\sigma_x}{r}\,. \tag{5.26}$$

Fig. 5.4 is derived from these two formulae and it qualitatively shows the theoretical trend of how the yield strength decreases as the angle of leverage increases. This means strength is qualitatively highest in directions of the x-y-plane and lowest in z-direction. From the figure it is evident that the change of yield strength in dependence of leverage angle is not linear but rather depends on the inverse cosine of the angle θ.

5.2.3 Characterization of elastic deformation for SLM lattice structures

In engineering the existence of structure, e.g. like pores inherent in cellular materials, is neglected, if possible, to make the handling of bulk material properties easier. Continuum mechanics helps to achieve this goal by ignoring fine structure details and by replacing exact solutions for finite volume elements by a smoothed hypothetical continuum for the bulk material or smaller homogenized parts of it. This has been the preferred approach for isotropic cellular materials as presented in ***section 5.1*** and it proves to be as well suitable for anisotropic SLM lattice structures.

The specification of the stress state of a homogeneous volume element of a solid body requires the description of this volume element in e.g. a Cartesian coordinate system with unit vectors $\mathbf{e}_i$ where the surfaces of the volume element are perpendicular to the unit vectors. Each arbitrary traction $\mathbf{t}_i$ on the i^{th} plane of the volume element *dV* in ***fig. 5.5*** is represented by a linear combination

$$\mathbf{t}_i = \sum_i \sigma_{ij} \cdot \mathbf{e}_j \tag{5.27}$$

of stress components acting on the faces of the volume element. The overall stress state of the volume element *dV* is, therefore, expressed by the coefficients σ_{ij} in the second-rank Cauchy stress tensor

$$\boldsymbol{\sigma}_{ij} = \begin{bmatrix} \sigma_{11} & \sigma_{12} & \sigma_{13} \\ \sigma_{21} & \sigma_{22} & \sigma_{23} \\ \sigma_{31} & \sigma_{32} & \sigma_{33} \end{bmatrix}. \tag{5.28}$$

All indices *i* denote the plane on which a stress acts while *j* corresponds to the direction $\mathbf{e}_j$ in which the stress acts. This tensor is symmetric, i.e. $\boldsymbol{\sigma}_{ij} = \boldsymbol{\sigma}_{ji}$, due to the fulfillment of the couple equilibria along all three principal axes. All σ_{ij}, where $i = j$, are referred to as normal stresses whereas all σ_{ij}, where $i \neq j$, are referred to as shear stresses. Each stress state causes a corresponding state of deformation. Normal stresses lead to a change of volume in the finite volume element due to strain ε_{kl}, where $k = l$, along one or more of its sides. Shear stresses, however, produce angular deformation $\gamma_{kl} = 2 \cdot \varepsilon_{kl}$, where $k \neq l$, while the volume remains constant. Small deformations ε_{kl} of a finite volume element can be expressed as a symmetric second-rank tensor

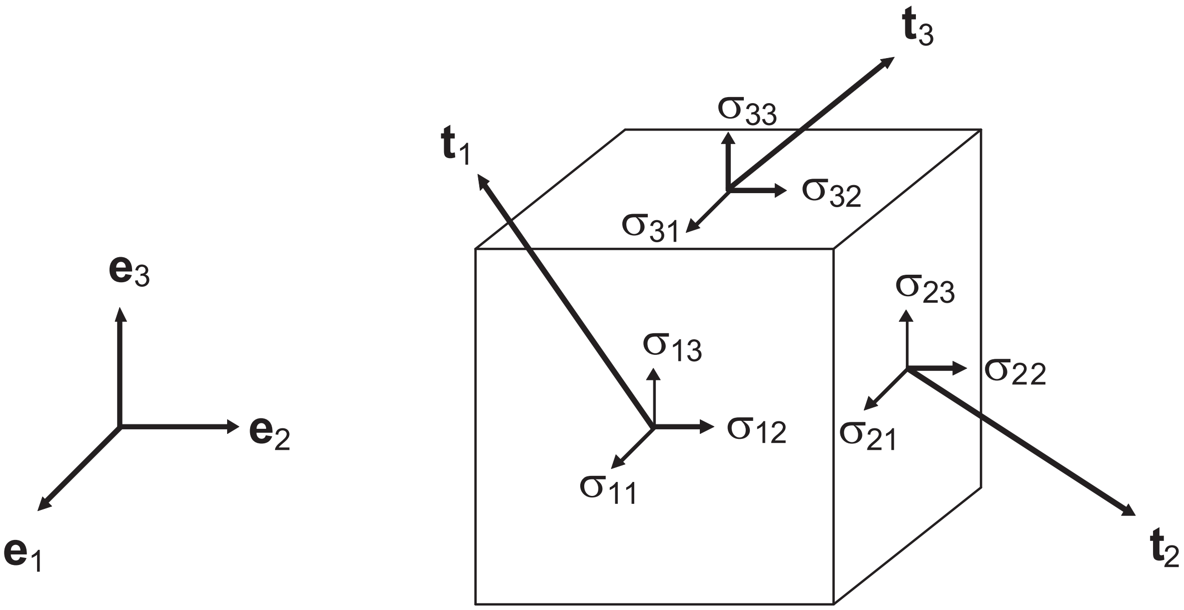

Figure 5.5: 3D stress state of a volume element *dV*

$$\boldsymbol{\varepsilon}_{kl} = \begin{bmatrix} \varepsilon_{11} & \varepsilon_{12} & \varepsilon_{13} \\ \varepsilon_{21} & \varepsilon_{22} & \varepsilon_{23} \\ \varepsilon_{31} & \varepsilon_{32} & \varepsilon_{33} \end{bmatrix} \tag{5.29}$$

similar to the stress tensor. Stress and strain are both linked by a constitutive relation which is sufficiently well approximated for small deformations by the linear Hooke's law

$$\sigma = E \cdot \varepsilon \,. \tag{5.30}$$

For linear, elastic deformations in the one-dimensional case E is the (Young's) modulus of elasticity. In three dimensions each of the six distinct components σ_{ij} of the two-dimensional stress tensor independently influences the six distinct components ε_{kl} of the strain tensor. To link both, the four-dimensional elasticity tensor $\mathbf{C}_{ijkl}$ is introduced which consists of $3^4 = 81$ independent coefficients C_{ijkl}. Thus the stress tensor is obtained from the double dot product of the elasticity and strain tensor:

$$\boldsymbol{\sigma}_{ij} = \mathbf{C}_{ijkl} \cdot\cdot \boldsymbol{\varepsilon}_{kl} \tag{5.31}$$

Since the elasticity tensor $\mathbf{C}_{ijkl}$ is difficult to handle the Voigt notation is introduced which reduces two-dimensional tensors to vectors as follows.

$$\boldsymbol{\sigma}_{\alpha}{}^{T} = \begin{pmatrix} \sigma_{11} & \sigma_{22} & \sigma_{33} & \sigma_{23} & \sigma_{13} & \sigma_{12} \end{pmatrix} \tag{5.32}$$

$$\boldsymbol{\varepsilon}_{\beta}{}^{T} = \begin{pmatrix} \varepsilon_{11} & \varepsilon_{22} & \varepsilon_{33} & 2\varepsilon_{23} & 2\varepsilon_{13} & 2\varepsilon_{12} \end{pmatrix} \tag{5.33}$$

This and the symmetry restrictions $C_{ijkl} = C_{jikl}$, $C_{ijkl} = C_{ijlk}$ and $C_{ijkl} = C_{klij}$ allow to express the elasticity tensor as a symmetric 6×6 matrix $\mathbf{C}_{\alpha\beta}$ of only 21 independent components instead of 81 (Cowin, 1989, pp. 249-252, [65]). Thus ***eq. (5.34)*** gives Hooke's law for the three-dimensional, anisotropic case, i.e. for the general case of triclinic symmetry.

$$\begin{pmatrix} \sigma_{11} \\ \sigma_{22} \\ \sigma_{33} \\ \sigma_{23} \\ \sigma_{13} \\ \sigma_{12} \end{pmatrix} = \begin{bmatrix} C_{11} & C_{12} & C_{13} & C_{14} & C_{15} & C_{16} \\ & C_{22} & C_{23} & C_{24} & C_{25} & C_{26} \\ & & C_{33} & C_{34} & C_{35} & C_{36} \\ & & & C_{44} & C_{45} & C_{46} \\ & \textbf{sym.} & & & C_{55} & C_{56} \\ & & & & & C_{66} \end{bmatrix} \cdot \begin{pmatrix} \varepsilon_{11} \\ \varepsilon_{22} \\ \varepsilon_{33} \\ 2\varepsilon_{23} \\ 2\varepsilon_{13} \\ 2\varepsilon_{12} \end{pmatrix} \tag{5.34}$$

The elasticity tensor $\mathbf{C}_{\alpha\beta}$ possesses even fewer independent coefficients $C_{\alpha\beta}$ for specific symmetries of SLM lattice structures. It is expected that SLM lattice structures yield most favourable properties if orthorhombic or cubic unit cell symmetries are applied, but it is also known from structural engineering that octet truss structures show very high stiffness. Nevertheless, this should be neglected since orthorhombic symmetries allow much easier handling of elasticity tensors. In the orthorhombic case only 9 independent coefficients $C_{\alpha\beta}$

remain in the elasticity tensor. If the stresses are known, then all deformations can be calculated according to

$$\begin{pmatrix} \varepsilon_{11} \\ \varepsilon_{22} \\ \varepsilon_{33} \\ 2\varepsilon_{23} \\ 2\varepsilon_{13} \\ 2\varepsilon_{12} \end{pmatrix} = \begin{bmatrix} \frac{1}{E_1} & -\frac{\nu_{21}}{E_2} & -\frac{\nu_{31}}{E_3} & 0 & 0 & 0 \\ -\frac{\nu_{12}}{E_1} & \frac{1}{E_2} & -\frac{\nu_{32}}{E_3} & 0 & 0 & 0 \\ -\frac{\nu_{13}}{E_1} & -\frac{\nu_{23}}{E_2} & \frac{1}{E_3} & 0 & 0 & 0 \\ 0 & 0 & 0 & \frac{1}{G_{23}} & 0 & 0 \\ 0 & 0 & 0 & 0 & \frac{1}{G_{13}} & 0 \\ 0 & 0 & 0 & 0 & 0 & \frac{1}{G_{12}} \end{bmatrix} \cdot \begin{pmatrix} \sigma_{11} \\ \sigma_{22} \\ \sigma_{33} \\ \sigma_{23} \\ \sigma_{13} \\ \sigma_{12} \end{pmatrix}, \qquad \textbf{\textit{(5.35)}}$$

where the elasticity tensor was replaced with its inverse matrix, the compliance tensor $\mathbf{S}_{\alpha\beta}$. Its technological components $S_{\alpha\beta}$ were replaced with the generalized engineering constants E_i, G_{ij} and ν_{ij}, where $i \neq j$ for the shear modulus and Poisson's ratio. It must be noted that this tensor is furthermore symmetric, i.e. $\nu_{21}\cdot E_2^{-1} = \nu_{12}\cdot E_1^{-1}$, $\nu_{31}\cdot E_3^{-1} = \nu_{13}\cdot E_1^{-1}$ and $\nu_{32}\cdot E_3^{-1} = \nu_{23}\cdot E_2^{-1}$, thus the coefficients S_{21}, S_{31} and S_{32} in ***eq. (5.35)*** are merely given for reasons of completeness. In order to calculate stresses from given deformations ***eq. (5.34)*** can be rewritten in where its elasticity tensor is the inverse of the above compliance tensor. Using the engineering constants gives the rather lengthy correlation

$$\begin{pmatrix} \sigma_{11} \\ \sigma_{22} \\ \sigma_{33} \\ \sigma_{23} \\ \sigma_{13} \\ \sigma_{12} \end{pmatrix} = \begin{bmatrix} \frac{E_1}{\Delta}\left(1-\nu_{23}\nu_{32}\right) & \frac{E_2}{\Delta}\left(\nu_{12}+\nu_{13}\nu_{32}\right) & \frac{E_3}{\Delta}\left(\nu_{13}+\nu_{12}\nu_{23}\right) & 0 & 0 & 0 \\ & \frac{E_2}{\Delta}\left(1-\nu_{13}\nu_{31}\right) & \frac{E_3}{\Delta}\left(\nu_{23}+\nu_{21}\nu_{13}\right) & 0 & 0 & 0 \\ & & \frac{E_3}{\Delta}\left(1-\nu_{12}\nu_{21}\right) & 0 & 0 & 0 \\ & & & G_{23} & 0 & 0 \\ & \textbf{sym.} & & & G_{13} & 0 \\ & & & & & G_{12} \end{bmatrix} \begin{pmatrix} \varepsilon_{11} \\ \varepsilon_{22} \\ \varepsilon_{33} \\ 2\varepsilon_{23} \\ 2\varepsilon_{13} \\ 2\varepsilon_{12} \end{pmatrix} \qquad \textbf{\textit{(5.36)}}$$

where

$$\Delta = 1 - \nu_{12}\nu_{21} - \nu_{23}\nu_{32} - \nu_{13}\nu_{31} - 2\nu_{21}\nu_{31}\nu_{32}\,. \qquad \textbf{\textit{(5.37)}}$$

Throughout this thesis all results for effective elasticity whether obtained from model experiments or from experimental work shall be given as ratios of some of the 9 engineering constants related to the bulk material's properties. Each ratio, after multiplication with the according bulk material constant can by directly used in ***eqs. (5.35)*** through ***(5.37)*** which indicate how to apply these constants in manual or numerical calculations.

5.2.4 Characterization of plastic deformation for SLM lattice structures

The characterization of plastic failure of a material is typically associated with the introduction of yield criteria and the so-called yield surface, which is a second order surface in the principal stress space. Any vectorial combination of the three principal stresses $\sigma_1 = \sigma_{11}$, $\sigma_2 = \sigma_{22}$, and $\sigma_3 = \sigma_{33}$, where $\sigma_1 \geq \sigma_2 \geq \sigma_3$, ending within the body formed by the second order surface results in elastic behaviour of the material whereas combined stresses ending outside of this body or on its surface result in plastic deformation. Therefore, the yield criterion is a function of the stress tensor $\boldsymbol{\sigma}_{ij}$ formulated as

$$f(\boldsymbol{\sigma}_{ij}) = \sigma_e - \sigma_{yield} \quad \begin{cases} < 0, \text{ for elastic deformation} \\ \geq 0, \text{ for plastic deformation} \end{cases} \tag{5.38}$$

where the equivalent stress σ_e is the substitute for all stress tensor components.

The two most important failure criteria assume that the hydrostatic stress or mean stress σ_m, usually defined as

$$\sigma_m = \frac{1}{3} I_1 = \frac{1}{3}(\sigma_{11} + \sigma_{22} + \sigma_{33}), \tag{5.39}$$

where I_1 is the first invariant of the stress tensor's characteristic polynomial, does not contribute to yield since hydrostatic stress states only cause a volumetric change in a finite volume element. Yield in metallic materials, however, is caused by shear effects between grain boundaries. Thus only the amount of stress deviating from the hydrostatic stress state (which theoretically can grow infinitely), i.e. the deviatoric stress, is responsible for the occurrence of yield. The deviatoric stress tensor is defined as

$$\mathbf{s}_{ij} = \boldsymbol{\sigma}_{ij} - \mathbf{I}_3 \cdot \sigma_m \tag{5.40}$$

with $\mathbf{I}_3$ being the 3×3 identity matrix. The second invariant J_2 derived from the characteristic polynomial of this tensor is

$$J_2 = s_{11}^2 + s_{22}^2 + s_{33}^2 + s_{11}s_{22} + s_{11}s_{33} + s_{22}s_{33} + s_{12}^2 + s_{13}^2 + s_{23}^2 \tag{5.41}$$

which can be rewritten by replacing the deviatoric tensor coefficients s_{ii} with $(\sigma_{ii}\text{-}\sigma_m)$ as

$$J_2 = \frac{1}{6}\left((\sigma_{11} - \sigma_{22})^2 + (\sigma_{22} - \sigma_{33})^2 + (\sigma_{33} - \sigma_{11})^2\right) + \sigma_{12}^2 + \sigma_{13}^2 + \sigma_{23}^2 . \tag{5.42}$$

After principal axis transformation of an arbitrary stress state the shear stresses disappear and ***eq. (5.42)*** can be expressed in terms of the principal stresses σ_1, σ_2 and σ_3 which gives

$$J_2 = \frac{1}{6}\left((\sigma_1 - \sigma_2)^2 + (\sigma_2 - \sigma_3)^2 + (\sigma_3 - \sigma_1)^2\right). \tag{5.43}$$

In the popular von Mises failure criterion of maximum distortion strain energy the stress σ_e equivalent to a combined stress state is defined as

$$\sigma_e = \sqrt{3J_2} = \sqrt{\frac{1}{2}\left((\sigma_1 - \sigma_2)^2 + (\sigma_2 - \sigma_3)^2 + (\sigma_3 - \sigma_1)^2\right)}. \qquad \textit{(5.44)}$$

This gives the yield function

$$f(\boldsymbol{\sigma}_{ij}) = \sqrt{\frac{1}{2}\left((\sigma_1 - \sigma_2)^2 + (\sigma_1 - \sigma_3)^2 + (\sigma_2 - \sigma_3)^2\right)} - \sigma_{yield}. \qquad \textit{(5.45)}$$

In contrast, the as well popular Tresca failure criterion of maximum shear stresses gives the yield function

$$f(\boldsymbol{\sigma}_{ij}) = (\sigma_{11} - \sigma_{33}) - \sigma_{yield} = (\sigma_{11} - \sigma_{33}) - 2\tau_{yield}. \qquad \textit{(5.46)}$$

Both failure criteria, von Mises and Tresca, shown in ***fig. 5.6***, give a cylindrical or prismatic yield surface in principal stress space, respectively, around the hydrostatic axis as their center. The deviatoric stresses are found in the plane perpendicular to the hydrostatic axis, also known as the π-plane.

These criteria are well suitable for isotropic materials but do not hold for anisotropic materials. Solid SLM parts exhibit slightly anisotropic mechanical properties (as will be shown in ***section 6.1***) due to their laminate structure received from the SLM process as described in ***section 3.3.1***. The expected anisotropy of SLM lattice structures may be even

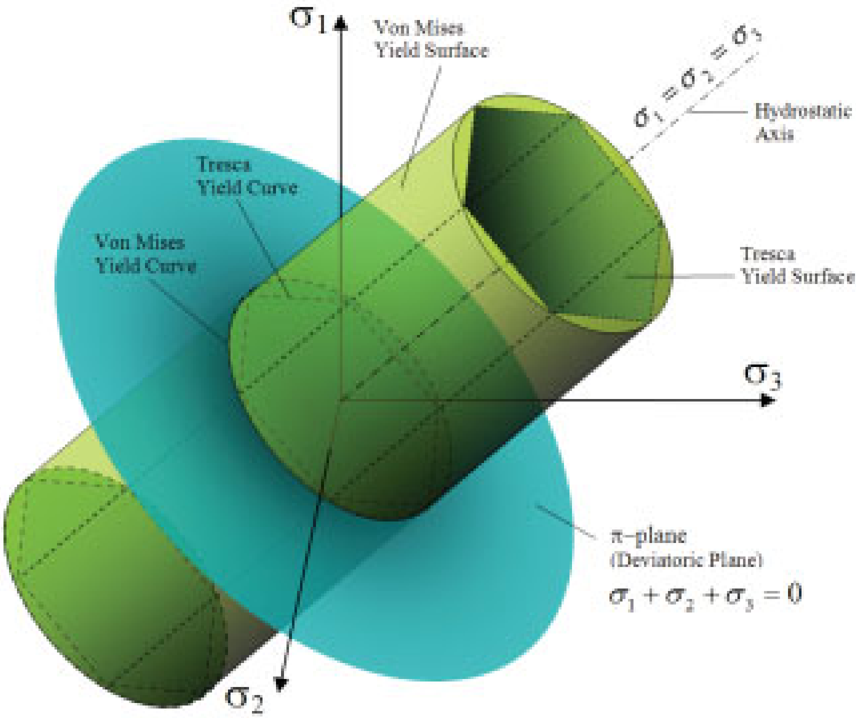
σ_1
Von Mises Yield Surface
$\sigma_1 = \sigma_2 = \sigma_3$
Hydrostatic Axis
Tresca Yield Curve
Von Mises Yield Curve
Tresca Yield Surface
σ_3
π-plane (Deviatoric Plane)
$\sigma_1 + \sigma_2 + \sigma_3 = 0$
σ_2

Figure 5.6: Von Mises and Tresca yield surfaces for isotropic materials [318]

higher than that of SLM solids. Furthermore, the assumption that SLM lattice structures undergo no volumetric change if loaded hydrostatically does not hold at all due to the void space within the unit cells. These allow volumetric deformation even under hydrostatic load conditions. This implies that a different yield criterion is required, which incorporates a closed second order surface. This new criterion should

- account for hydrostatic stress states,
- consider the anisotropy in SLM solids,
- consider the topology of SLM lattice structures and thus their relative density and anisotropy,
- account for possible deviations of tensile and compressive strengths of SLM lattice structures and
- reduce to the von Mises criterion, if solid materials of full density are considered and neither anisotropy nor difference in tensile and compressive strength prevails.

A summary of various yield criteria was given by Abrate (2008, pp. 10-45, [3]), especially criteria for cellular materials that account for the effect of hydrostatic stress states. Among these Abrate suggested different categories from which appears most suitable what he defined as category 3:

$$J_2 + c_1 \cdot I_1^2 = c_2 \tag{5.47}$$

Replacing both invariants with stresses from ***eqs. (5.43)*** and ***(5.39)*** this expression becomes

$$\sigma_e^2 + c_3 \cdot \sigma_m^2 = \sigma_{yield}^2 . \tag{5.48}$$

This results in an ellipse in the σ_m-σ_e stress plane which will ensure a closed surface ellipsoid in the principal stress space. In order to account for the anisotropy, whether produced by the solid material's anisotropy or by the topology of the lattice structure, the criterion known as Hill48 (Hill, 1948, p. 285, [142]) is incorporated into the effective stress:

$$\sigma_e^2 = c_\alpha (\sigma_1 - \sigma_2)^2 + c_\beta (\sigma_2 - \sigma_3)^2 + c_\gamma (\sigma_3 - \sigma_1)^2 \tag{5.49}$$

Using the three principal stress directions implies that orthorhombic symmetry is expected for SLM lattice structures as derived in ***section 5.2.3***. To keep the new criterion simple the coefficients c_α, c_β and c_γ are calculated solely from the tensile strengths of the solid material in the principal stress directions without consideration of each principal direction's dependency of strength on relative density to the power of varying shape factors as follows.

$$\begin{aligned} c_\alpha &= \frac{1}{2} \sigma_{1,tensile} \cdot \sigma_{2,tensile} \cdot \left(\frac{1}{\sigma_{1,tensile}^2} + \frac{1}{\sigma_{2,tensile}^2} - \frac{1}{\sigma_{3,tensile}^2} \right) \\ c_\beta &= \frac{1}{2} \sigma_{2,tensile} \cdot \sigma_{3,tensile} \cdot \left(\frac{1}{\sigma_{2,tensile}^2} + \frac{1}{\sigma_{3,tensile}^2} - \frac{1}{\sigma_{1,tensile}^2} \right) \end{aligned} \tag{5.50}$$

$$c_{\gamma} = \frac{1}{2}\sigma_{3,tensile} \cdot \sigma_{1,tensile} \cdot \left(\frac{1}{\sigma_{3,tensile}^2} + \frac{1}{\sigma_{1,tensile}^2} - \frac{1}{\sigma_{2,tensile}^2} \right)$$

The effect of hydrostatic stress is accounted for by the term σ_m in ***eq. (5.48)***. Therefore, ***eq. (5.39)*** is extended such that the influence of hydrostatic stress increases with decreasing relative density. Hence, if solid material is considered, the diagram in the σ_m-σ_e stress plane will show two lines parallel to the σ_m-axis similar to the von Mises criterion rather than an ellipse. Additionally, ***eq. (5.39)*** is extended according to a suggestion made by Raghava (1973, pp. 225-232, [238]) who considered different strengths in tension and compression for isotropic materials. This approach implies several modifications of the terms σ_m and σ_{yield} in ***eq. (5.48)*** to meet the requirements of anisotropic, cellular materials. First, the center of the ellipse in the σ_m-σ_e plane is translated along the σ_m-axis according to the squared mean difference between the uniaxial, solid tensile and compressive strengths in all principal stress directions to comply with anisotropic behaviour. The mean difference is then weighted by the overall relative density since differences in tensile and compressive behaviour reduce with decreasing relative density. To further meet Raghava's criterion the modification of the term σ_{yield} in ***eq. (5.48)*** incorporates the multiplication of each principal direction's uniaxial, solid tensile and compressive strengths to account for anisotropy. Again, if all tensile and compressive strengths are identical the expression reduces to the von Mises case. Finally, the σ_{yield} term is as well weighted by the material's relative density. The relative density expressions used here include only one exponent *n* rather than different exponents in different principal directions in order to not complicate the new yield criterion. However, it might be required for future applications to refine this criterion accordingly. The complete failure criterion can now be written as

$$\begin{aligned} & c_{\alpha}(\sigma_1 - \sigma_2)^2 + c_{\beta}(\sigma_2 - \sigma_3)^2 + c_{\gamma}(\sigma_3 - \sigma_1)^2 + \\ & \frac{1}{3}\left(1 - \frac{\rho^*}{\rho_{solid}}\right) \cdot \left(\sigma_1 + \sigma_2 + \sigma_3 - \left(\frac{\rho^*}{\rho_{solid}}\right)^n \cdot \begin{pmatrix} (\sigma_{1,tensile} - \sigma_{1,compressive}) + \\ (\sigma_{2,tensile} - \sigma_{2,compressive}) + \\ (\sigma_{3,tensile} - \sigma_{3,compressive}) \end{pmatrix} \right)^2 = \\ & \frac{1}{3}\left(\frac{\rho^*}{\rho_{solid}}\right)^n \cdot \begin{pmatrix} (\sigma_{1,tensile} \cdot \sigma_{1,compressive}) + \\ (\sigma_{2,tensile} \cdot \sigma_{2,compressive}) + \\ (\sigma_{3,tensile} \cdot \sigma_{3,compressive}) \end{pmatrix} \end{aligned} \qquad \textbf{(5.51)}$$

which will give ellipsoidal yield surfaces as in ***fig. 5.7*** for relative densities smaller than unity. If applied on solids the second line of ***eq. (5.51)*** will be eliminated and prismatic yield surfaces comparable to ***fig. 5.6*** will result which makes this failure criterion consistent with the existing ones.

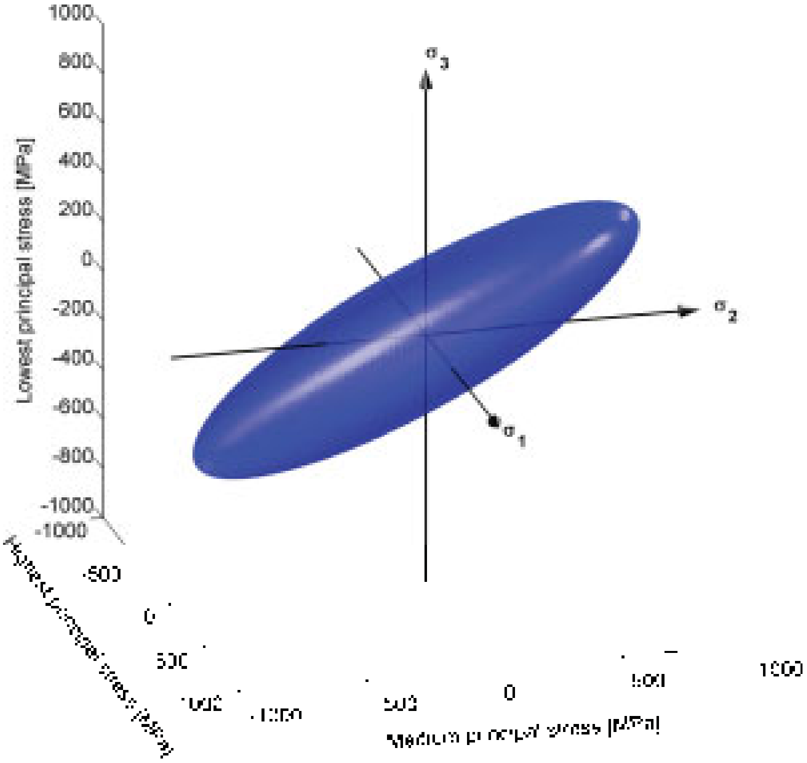

Figure 5.7: Yield surface for SLM lattice structure

5.2.5 Matrix structural analysis for low density SLM lattice structures

The benefits of applying continuum mechanics on SLM lattice structures are manifold. Derived scaling laws allow to describe material properties as effective bulk material properties which makes their handling easier. However, continuum models break down if small enough volume elements are considered that resolve features of the subordinate structure. Therefore, a refined model for this structure is necessary which also delivers satisfactory explanations for expected effects within the bulk material that continuum mechanics alone cannot account for. This refined model could possibly contribute to explain the elastic and plastic deformation behaviour inside of the framework of a SLM lattice structure.

Generally, in engineering mechanics frameworks are handled with the help of beam bending theories and matrix structural analysis methods. These theories are only briefly reviewed here to account for a better appreciation of the approaches used to understand the failure mechanisms of SLM lattice structures. Among other literature especially two references by Bažant (1991, [34]) and McGuire (2000, [197]) are strongly recommended for further reading.

One typical approach in structural engineering is the direct stiffness method. It is a refinement of the displacement method which requires less effort in obtaining the required matrices. It calculates the reaction of axial force members in a network of struts and nodes upon external forces by displacement of its nodes due to their translation and rotation. The displacements and the support reactions are considered unknown and they are calculated from the elastic axial compression and tension of all members, i.e. struts, as well as their elastic bending. The elastic deformation of each member is on one hand derived from its stiffness which is calculated from elementary material and geometry properties and on the other hand from the forces which act on each element's nodes. One such line element of length L with nodes 1 and 2 is shown in ***fig. 5.8*** where all forces and moments act on both nodes in positive directions of the element's local coordinate system which is denoted by an apostrophe. This is typically selected such that the x'-direction extends along the element whereas the y'- and z'-direction are perpendicular to it. Each node can exhibit three degrees of freedom for translation (u', v' and w') and three for rotation (θ_x', θ_y' and θ_z'). This gives a total of 12 degrees of freedom for each element. The vector of all forces and moments $\mathbf{F}'_i$ of the i-th element is linked to its vector of all displacements Δ'_i by the 12×12 element stiffness matrix $\mathbf{k}'_i$ according to Hooke's law:

$$\mathbf{F}_i^{'} = \mathbf{k}_i^{'} \cdot \mathbf{\Delta}_i^{'} \tag{5.52}$$

This stiffness matrix is determined from the equilibrium equations of all forces which have to yield a zero sum in each principal direction and from the equilibrium equations of all moments which have to yield a zero sum per node around each principal axis, respectively. The equilibrium equations are derived from superpositioning the considered element as an axial force member, as a beam bent about its z-axis as well as a beam bent about its y-axis and as a pure torsional member. The displacement u'_1 in axial direction is hence given by

$$u_1^{'} = \frac{F_{x1}^{'} \cdot L}{EA}, \tag{5.53}$$

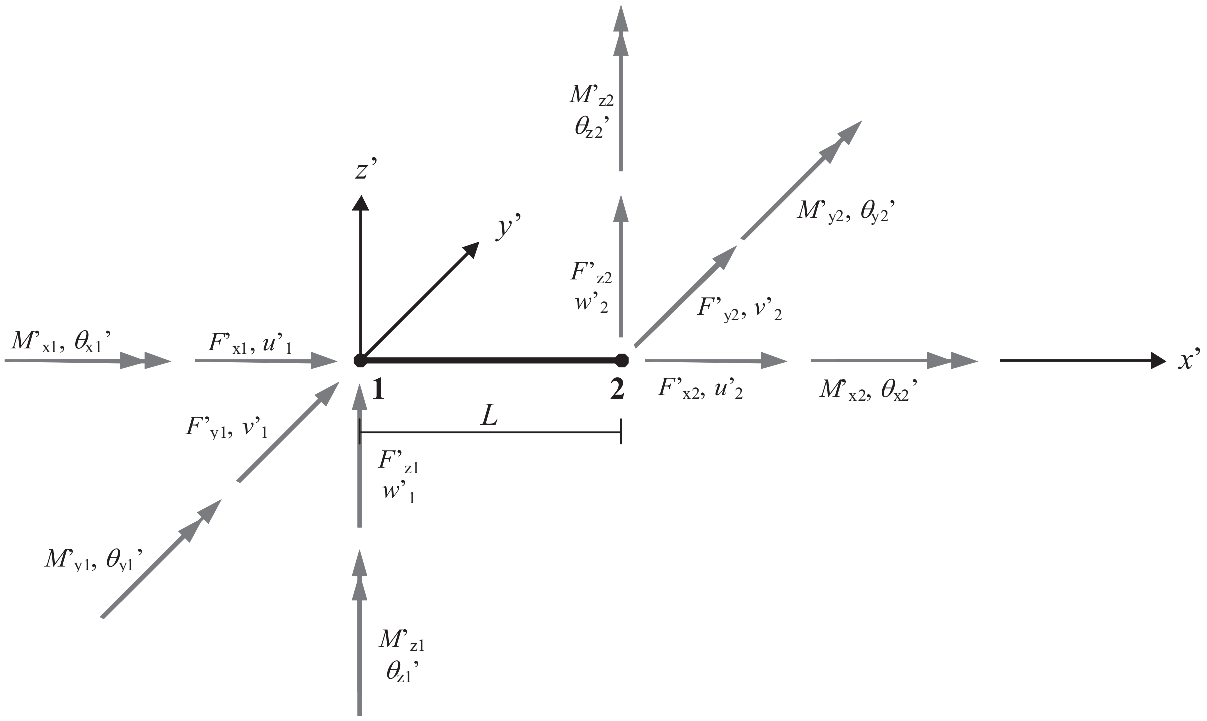

Figure 5.8: Nodal forces and moments acting on a framework member in local coordinates

while double integration of the Euler-Bernoulli differential equation of a flexural beam

$$\frac{d^2v'}{dx'^2} = \frac{M'_z(x')}{EI_z} = \frac{1}{EI_z}\cdot\left(F'_y\left(x'_{F_y} - x'\right) + M'_z(x')\right) \tag{5.54}$$

gives the general elastic curve equations

$$\frac{dv'}{dx'} = \frac{1}{EI_z}\cdot\left(F'_y\left(x'_{F_y}\cdot x' - \frac{x'^2}{2}\right) + M'_z(x')\cdot x'\right) + C_1 \tag{5.55}$$

$$v'(x') = \frac{1}{EI_z}\cdot\left(F'_y\left(x'_{F_y}\cdot\frac{x'^2}{2} - \frac{x'^3}{6}\right) + M'_z(x')\cdot\frac{x'^2}{2}\right) + C_1x' + C_2 \tag{5.56}$$

where C_1 and C_2 are the integration constants. These are obtained from evaluating the different boundary conditions for the beam in ***fig. 5.8***. When a node of the beam is subsequently loaded with unit displacements and unit rotations, superpositioning of these loads gives the correlations for a beam deflected and bent about axes other than the longitudinal axis:

$$F'_{y1} = \frac{12EI_z}{L^3}v'_1 \tag{5.57}$$

$$M'_{z1} = \frac{6EI_z}{L^2}\theta'_{z1} \tag{5.58}$$

From the St. Venant correlation of a beam under torsion with polar area moment of inertia J

$$\theta'_{x1} = \frac{M'_{x1}\cdot 2\cdot(1+\nu)\cdot L}{JE} \tag{5.59}$$

the equilibrium equations are supplemented such that the complete element stiffness matrix $\mathbf{k}'_i$ can be assembled in ***eq. (5.60)*** which shows all equilibrium equations in local coordinates.

$$\begin{pmatrix} F'_{x1} \\ F'_{y1} \\ F'_{z1} \\ M'_{x1} \\ M'_{y1} \\ M'_{z1} \\ \hline F'_{x2} \\ F'_{y2} \\ F'_{z2} \\ M'_{x2} \\ M'_{y2} \\ M'_{z2} \end{pmatrix} = E\cdot \underbrace{\left[\begin{array}{cccccc|cccccc}
\frac{A}{L} & 0 & 0 & 0 & 0 & 0 & -\frac{A}{L} & 0 & 0 & 0 & 0 & 0 \\
0 & \frac{12I_z}{L^3} & 0 & 0 & 0 & \frac{6I_z}{L^2} & 0 & -\frac{12I_z}{L^3} & 0 & 0 & 0 & \frac{6I_z}{L^2} \\
0 & 0 & \frac{12I_y}{L^3} & 0 & -\frac{6I_y}{L^2} & 0 & 0 & 0 & -\frac{12I_y}{L^3} & 0 & -\frac{6I_y}{L^2} & 0 \\
0 & 0 & 0 & \frac{J}{2(1+\nu)L} & 0 & 0 & 0 & 0 & 0 & -\frac{J}{2(1+\nu)L} & 0 & 0 \\
0 & 0 & -\frac{6I_z}{L^2} & 0 & \frac{4I_Y}{L} & 0 & 0 & 0 & \frac{6I_y}{L^2} & 0 & \frac{2I_y}{L} & 0 \\
0 & \frac{6I_z}{L^2} & 0 & 0 & 0 & \frac{4I_z}{L} & 0 & -\frac{6I_z}{L^2} & 0 & 0 & 0 & \frac{2I_z}{L} \\ \hline
-\frac{A}{L} & 0 & 0 & 0 & 0 & 0 & \frac{A}{L} & 0 & 0 & 0 & 0 & 0 \\
0 & -\frac{12I_z}{L^3} & 0 & 0 & 0 & -\frac{6I_z}{L^2} & 0 & \frac{12I_z}{L^3} & 0 & 0 & 0 & -\frac{6I_z}{L^2} \\
0 & 0 & -\frac{12I_y}{L^3} & 0 & \frac{6I_y}{L^2} & 0 & 0 & 0 & \frac{12I_y}{L^3} & 0 & \frac{6I_y}{L^2} & 0 \\
0 & 0 & 0 & \frac{J}{2(1+\nu)L} & 0 & 0 & 0 & 0 & 0 & \frac{J}{2(1+\nu)L} & 0 & 0 \\
0 & 0 & -\frac{6I_y}{L^2} & 0 & \frac{2I_Y}{L} & 0 & 0 & 0 & \frac{6I_y}{L^2} & 0 & \frac{4I_y}{L} & 0 \\
0 & \frac{6I_z}{L^2} & 0 & 0 & 0 & \frac{2I_z}{L} & 0 & -\frac{6I_z}{L^2} & 0 & 0 & 0 & \frac{4I_z}{L}
\end{array}\right]}_{\mathbf{k}'_i} \cdot \begin{pmatrix} u'_1 \\ v'_1 \\ w'_1 \\ \theta'_{x1} \\ \theta'_{y1} \\ \theta'_{z1} \\ \hline u'_2 \\ v'_2 \\ w'_2 \\ \theta'_{x2} \\ \theta'_{y2} \\ \theta'_{z2} \end{pmatrix} \tag{5.60}$$

These equilibrium equations correlate all forces, moments and resulting displacements for a beam under elastic deformation. Beyond the standard Euler-Bernoulli beam bending theory it is worthwile to extend this stiffness matrix when SLM lattice structures are considered. Typically, the achievable slenderness ratio of single struts, i.e. their length to radius ratio *L*/*r*, is below 30 which implies a higher significance of the influence of transverse shear strain. Therefore, the Timoshenko beam bending theory should be employed which considers the influence of transverse shear deformation by relaxing the normality assumption, i.e. cross sections perpendicular to the beam axis in the undeformed state remain plane after deformation but not necessarily normal to the beam axis. This yields a less stiff beam and results in the increased deflection

$$v'_{Timoshenko}\left(x'\right)=\underbrace{v'\left(x'\right)}_{\substack{\text{Euler–}\\ \text{Bernoulli}\\ \text{deflection}}}+\frac{\overbrace{F'_y\left(x'_{F_y}-x'\right)+M'_z\left(x'\right)}^{\text{Euler–Bernoulli moment}}}{GAK_s}+C_1\left(\frac{x'^3}{6}-\frac{EI_z x'}{GAK_s}\right)+C_2\frac{x'^2}{2}+C_3x'+C_4 \qquad \textbf{\textit{(5.61)}}$$

where GA is the shear rigidity, K_s is the shear correction coefficient and C_1 through C_4 are integration constants (Wang, 1995, pp. 763-765, [306]) which need to be obtained from the boundary conditions according to the beam in ***fig. 5.8***. ***Eq. (5.57)*** is then supplemented with the additional Timoshenko deflection. It should be noted that the slenderness ratio is always twice the value of the above mentioned aspect ratio *a*/*d*. Although throughout this thesis the aspect ratio is generally considered a major design parameter, this section will mainly refer to the slenderness ratio commonly used in elastic beam theories to be consistent with these.

After obtaining all element stiffness matrices they can be transformed into the global coordinate system. Each element's local principal axes x', y' and z' are portrayed as three rotations of the global principal axes x, y and z by the angles α, β and γ according to ***fig. 5.9***. The rotation matrix of three orthogonal forces F'_x, F'_y and F'_z (or moments or displacements) of the i-th element from global into local coordinates is φ_i in ***eq. (5.62)*** which is the product of

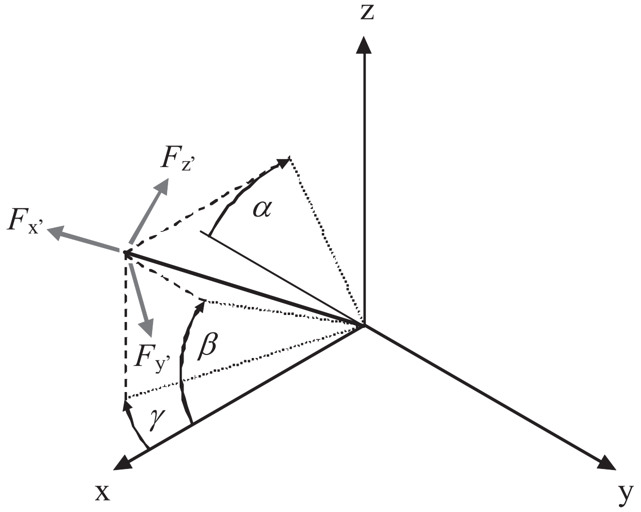

Figure 5.9: Coordinate transformation from local to global coordinates by means of 3 consecutive rotations

the passive rotation matrices for each of the three angles. These angles can be derived from a vector calculated from both global node coordinates of the considered element. Since the choice of angles is not unambiguous they are typically selected such that the cross section of the element is oriented in the preferred way.

$$\begin{pmatrix} F_x \\ F_y \\ F_z \end{pmatrix} = \underbrace{\begin{bmatrix} 1 & 0 & 0 \\ 0 & \cos\alpha & \sin\alpha \\ 0 & -\sin\alpha & \cos\alpha \end{bmatrix} \cdot \begin{bmatrix} \cos\beta & 0 & -\sin\beta \\ 0 & 1 & 0 \\ \sin\beta & 0 & \cos\beta \end{bmatrix} \cdot \begin{bmatrix} \cos\gamma & \sin\gamma & 0 \\ -\sin\gamma & \cos\gamma & 0 \\ 0 & 0 & 1 \end{bmatrix}}_{\boldsymbol{\varphi}_i} \cdot \begin{pmatrix} F_x' \\ F_y' \\ F_z' \end{pmatrix} \tag{5.62}$$

The transformation of all 12 degrees of freedom of the i-th element simultaneously requires the rotation matrix $\mathbf{\Phi}_i$ which is composed of diagonal entries of the matrix $\boldsymbol{\varphi}_i$ according to:

$$\mathbf{\Phi}_i = \begin{bmatrix} \boldsymbol{\varphi}_i & & & \\ & \boldsymbol{\varphi}_i & & \\ & & \boldsymbol{\varphi}_i & \\ & & & \boldsymbol{\varphi}_i \end{bmatrix} \tag{5.63}$$

Local forces and moments $\mathbf{F}_i$' as well as local displacements $\mathbf{\Delta}_i$' are transformed into global coordinates $\mathbf{F}_i$ and $\mathbf{\Delta}_i$ by the following two equations.

$$\mathbf{F}_i = \mathbf{\Phi}_i \cdot \mathbf{F}_i' \tag{5.64}$$

$$\mathbf{\Delta}_i = \mathbf{\Phi}_i \cdot \mathbf{\Delta}_i' \tag{5.65}$$

Using the orthogonality properties of $\mathbf{\Phi}_i$, i.e. its inverse is equal to its transpose, and substituting both previous formulae into ***eq. (5.52)*** gives the equilibrium equation of the i-th element:

$$\mathbf{F}_i = \mathbf{\Phi}_i \cdot \mathbf{k}_i \cdot \mathbf{\Phi}_i^{\mathrm{T}} \cdot \mathbf{\Delta}_i \,. \tag{5.66}$$

The equilibrium equations of the complete system of all *n* elements are then assembled in accordance with ***eq. (5.52)*** which yields:

$$\begin{pmatrix} \mathbf{F}_1 \\ \vdots \\ \mathbf{F}_i \\ \vdots \\ \mathbf{F}_n \end{pmatrix} = \underbrace{\begin{bmatrix} \mathbf{\Phi}_1 & & & & \\ & \ddots & & & \\ & & \mathbf{\Phi}_i & & \\ & & & \ddots & \\ & & & & \mathbf{\Phi}_n \end{bmatrix} \begin{bmatrix} \mathbf{k}_1 & & & & \\ & \ddots & & & \\ & & \mathbf{k}_i & & \\ & & & \ddots & \\ & & & & \mathbf{k}_n \end{bmatrix} \begin{bmatrix} \mathbf{\Phi}_1^{\mathrm{T}} & & & & \\ & \ddots & & & \\ & & \mathbf{\Phi}_i^{\mathrm{T}} & & \\ & & & \ddots & \\ & & & & \mathbf{\Phi}_n^{\mathrm{T}} \end{bmatrix}}_{\mathbf{K}} \begin{pmatrix} \mathbf{\Delta}_1 \\ \vdots \\ \mathbf{\Delta}_i \\ \vdots \\ \mathbf{\Delta}_n \end{pmatrix} \tag{5.67}$$

This system of equilibrium equations can be rearranged by grouping the support reactions and support degrees of freedom together. ***Eq. (5.67)*** can hence be rewritten as

$$\begin{pmatrix} \mathbf{F}_f \\ \hline \mathbf{F}_s \end{pmatrix} = \left[\begin{array}{c|c} \mathbf{K}_{ff} & \mathbf{K}_{fs} \\ \hline \mathbf{K}_{sf} & \mathbf{K}_{ss} \end{array}\right] \cdot \begin{pmatrix} \mathbf{\Delta}_f \\ \hline \mathbf{\Delta}_s \end{pmatrix} \tag{5.68}$$

where the subscript s denotes support reactions and degrees of freedom while the subscript f represents all remaining forces and nodal displacements. The displacements at supported nodes are all zero, i.e. $\Delta_s = 0$, therefore, ***eq. (5.68)*** can be rewritten as

$$\mathbf{F}_f = \mathbf{K}_{ff} \cdot \mathbf{\Delta}_f \tag{5.69}$$

which solved for the unknown nodal displacements Δ_f yields

$$\mathbf{\Delta}_f = \mathbf{K}_{ff}^{-1} \cdot \mathbf{F}_f = \mathbf{S}_{ff} \cdot \mathbf{F}_f \tag{5.70}$$

where $\mathbf{S}_{ff}$ is the global compliance tensor. In the final step the unknown support reactions $\mathbf{F}_s$ are as well obtained from ***eq. (5.68)*** by deriving

$$\mathbf{F}_s = \mathbf{K}_{sf} \cdot \mathbf{\Delta}_f \tag{5.71}$$

and substituting from ***eq. (5.70)*** gives

$$\mathbf{F}_s = \mathbf{K}_{sf} \cdot \mathbf{S}_{ff} \cdot \mathbf{F}_f \, . \tag{5.72}$$

The above presented first-order linear elastic approach allows the calculation of nodal displacements in a framework of line elements due to linear elastic deformation. However, the linear elastic regime of each element's deformation capabilities is typically limited to stresses characterized by the yield point as shown in ***fig. 2.12***. McGuire (2000, pp. 217-218, [197]) names a number of sources for nonlinearity which, mainly, can be found in geometrical effects such as the influence of axial forces on the flexural stiffness of an individual element or in the influence of large displacements, in material effects such as the change of material properties under load e.g. due to plastic deformation and in the combination of both effects. In order to account for these effects various levels of analysis were established, i.e. first- and second-order, elastic and inelastic analyses. The second-order inelastic analysis serves the purpose best to describe actual material behaviour since the equilibrium equations are written in terms of the geometry of the deformed system which may include all sources of nonlinearity. It is conducted by applying a step-wise linear analysis based on ***eq. (5.68)*** in the general form

$$d\mathbf{F} = \mathbf{K}_t \cdot d\mathbf{\Delta} \tag{5.73}$$

where d denotes the change of forces and displacements in each increment. Typically, the so-called tangent stiffness matrix $\mathbf{K}_t$ portrays the tangent of a section of the nonlinear stress-strain curve. It consists of linear elastic components and additional components as functions of forces and/or displacements such as the geometric stiffness matrix and the plastic reduction matrix which are developed according to McGuire (2000, pp. 242-300, [197]). In regard to the use for SLM lattice structures the geometric stiffness matrix is sufficiently accounted for if the concepts of nonlinear response due to interactions between axial forces and bending as well as combined axial forces and torsion are considered. At the onset of plasticity, i.e. at the yield point, the plastic reduction matrix is derived from the gradient to that point on the yield surface which correlates with the current state at each considered force increment. Therefore, this gradient depends on the general shape of the yield surface as well as the force increment considered. For SLM lattice structures the yield surface introduced in ***eq. (5.51)*** and displayed in ***fig. 5.7*** should be employed for this purpose.

In the application of several load increments true nonlinear behaviour is approximated more or less exact depending on the choice of the tangent stiffness matrix in each increment. In simple load steps, i.e. the Euler method, each increment's tangent stiffness matrix is determined from the deformed geometry and element forces before applying the increment. This implies a deviation between the end of the increment's linear response and the true nonlinear behaviour and hence an increasing overall deviation to that extent that the strength of a structure is overestimated. Other approaches employ the use of weighted tangent stiffness matrices obtained at the start of the increment and at some point within the increment. The 'average' tangent stiffness matrix of the *i*-th increment

$$\mathbf{K}_{t,i} = c_1 \cdot \mathbf{K}_{t,i1} + c_2 \cdot \mathbf{K}_{t,i2} + \ldots + c_j \cdot \mathbf{K}_{t,ij} \qquad \textbf{\textit{(5.74)}}$$

is influenced by the weighting factors c_j whose sum yields unity while any tangent stiffness matrix $\mathbf{K}_{t,ij}$ for $j > 1$ is calculated for a defined load ratio μ of the full increment. One popular approach is the second-order midpoint Runge-Kutta method which uses two weighting factors $c_1 = 0$ and $c_2 = 1$ and a load ratio $\mu = 0.5$.

Plastic deformation of SLM lattice structures as discussed in ***section 5.2.4*** can be caused from two fundamental failure mechanisms. Besides the plastic flow of material discussed above, buckling is another important mechanism. It occurs at stresses below yield if the slenderness ratio of a beam is high enough and is, therefore, undesired. Wang (2005, pp. 125-128, [307]) asserted that elastic buckling cannot occur in typical cellular structures made from steel struts due to the material's high critical slenderness ratio of approximately 100, which is beyond the build capabilities of LFF systems. For beams loaded like the one in ***fig. 5.8***, i.e. clamped at both ends, the critical stress at which buckling occurs is

$$\sigma_{buckle} = \frac{4\pi \cdot EI}{L^2 / r^2} \quad \left(= \frac{16\pi \cdot EI}{a^2 / d^2} \right) \qquad \textbf{\textit{(5.75)}}$$

which gives the hyperbolic Euler curve of buckling strength vs. slenderness ratio. However, towards lower slenderness ratios below the critical value

$$\frac{L}{r} \leq \sqrt{\frac{E \cdot \pi^2}{\sigma_{yield}}} \qquad \textbf{\textit{(5.76)}}$$

the buckling strength exceeds the yield strength and the path of the critical stress bifurcates from the Euler curve to a linear, constant stress. For stainless steel the approximate critical slenderness ratio is thus 63 which is still beyond typical build capabilities of LFF systems. This implies that inelastic buckling, i.e. buckling during plastic flow, is very likely to occur as the compressive experiments in ***section 6.4*** show. Therefore, buckling may not necessarily be the initial failure mechanism of SLM lattice structures but for most cell types it can be expected to contribute to accelerated deformation of cell struts. Thus it should be included in determination of the tangent stiffness matrix $\mathbf{K}_t$. Observations made by Zhu (1997, p. 323, [333]) were reported where even struts with aspect ratios as little as 3, i.e. slenderness ratios of 6, involved buckling during deformation. Another detail that should be considered for SLM lattice structures on one hand is the above mentioned influence of shear deformation which in extension of ***eq. (5.75)*** reduces the buckling strength to

$$\sigma_{buckle,shear} = \frac{\sigma_{buckle}}{1 + \frac{c \cdot \sigma_{buckle}}{AG}} \qquad \textbf{\textit{(5.77)}}$$

where c is a numerical factor depending on the shape of the cross section. For circular cross sections c becomes 1.11 (Timoshenko, 1961, p. 133, [293]). On the other hand in the regime of slenderness ratios where failure is governed by the yield strength rather than the Euler-buckling stress, ***eq. (5.76)*** has to be slightly modified to the extent that past the yield point Young's modulus is replaced by the smaller tangent modulus E_t similar to ***eq. (5.73)***. Hence, at the critical slenderness ratio a transition from the hyperbolic Euler-curve to another shifted hyperbolic curve given in ***eq. (5.78)*** can be found which describes inelastic material behaviour (Timoshenko, 1961, pp. 178-179, [293]).

$$\sigma_{buckle,inelastic} = \frac{E_t \cdot \pi^2}{L^2 / r^2} \qquad \textbf{\textit{(5.78)}}$$

The truss framework approach presented in this section is expected to work well within certain limits of relative density of SLM lattice structures. However, beyond a certain relative density the aspect ratio of struts becomes very small or is even unexistent when the circumferences of adjacent struts begin to interfere with each other. Then the SLM fabricated part is no longer a lattice structure which can be dealt with truss framework methods but it is rather a solid with pores as shown in ***section 5.2.6***.

5.2.6 Effective material properties for high density SLM lattice structures

The effective material properties for SLM lattice structures of high relative density could be derived from the considerations presented in ***section 5.1.3***. However, these models are not expected to be fully sufficient for SLM lattice structures and some are impractical to use. Moreover, it is assumed that for relative densities around unity, which is equivalent to porosities around zero, the considered material property scales either linearly with porosity or with a power of the porosity. If it scales with a power of the porosity of greater than one it is expected that in diagrams of this property versus relative density a negative curvature results in the regime of high relative density. This assumption is regarded accordingly in construction of the general model for SLM lattice structures of low and high relative density in ***section 5.2.8***.

5.2.7 Determination of relative density for SLM lattice structures

For the scaling laws given in ***section 5.1.1*** mass concentrated in a unit cell's joints where struts intersect was repeatedly included. The resulting error is acceptable for typical cellular materials which possess a low relative density. For SLM lattice structures, however, this error is not acceptable since a much greater variety of relative densities can be produced. Therefore, the true relative density must be derived from the total volume contribution of all intersecting micro struts to one unit cell divided by the unit cell volume. The total volume of all intersecting micro struts is obtained from adding up all fractions of micro strut volumes in one unit cell less the sum of all intersection volumes.

The axes of two cylinders of radius r_1 and r_2 intersecting each other under angle α as shown in ***fig. 5.10 a)*** span a planar area in the x-z-plane as illustrated in ***fig. 5.10 b)***. The intersection volume V can be calculated from integrating in the y-direction over all resulting rhombic cross section areas that are found in the x-z-plane according to ***fig. 5.10 c)*** which gives

$$V = \int_{-r_2}^{r_2} \left(2\sqrt{r_1^2 - y^2} \cdot \frac{2}{\sin\alpha} \sqrt{r_2^2 - y^2} \right) dy \,. \qquad \textbf{\textit{(5.79)}}$$

Since all micro strut diameters in SLM lattice structures are assumed to be equal $r_1 = r_2 = d/2$ this integral can be rewritten as

$$V = \frac{4}{\sin\alpha} \cdot \int_{-\frac{d}{2}}^{\frac{d}{2}} \left(\frac{d^2}{4} - y^2 \right) dy \,. \qquad \textbf{\textit{(5.80)}}$$

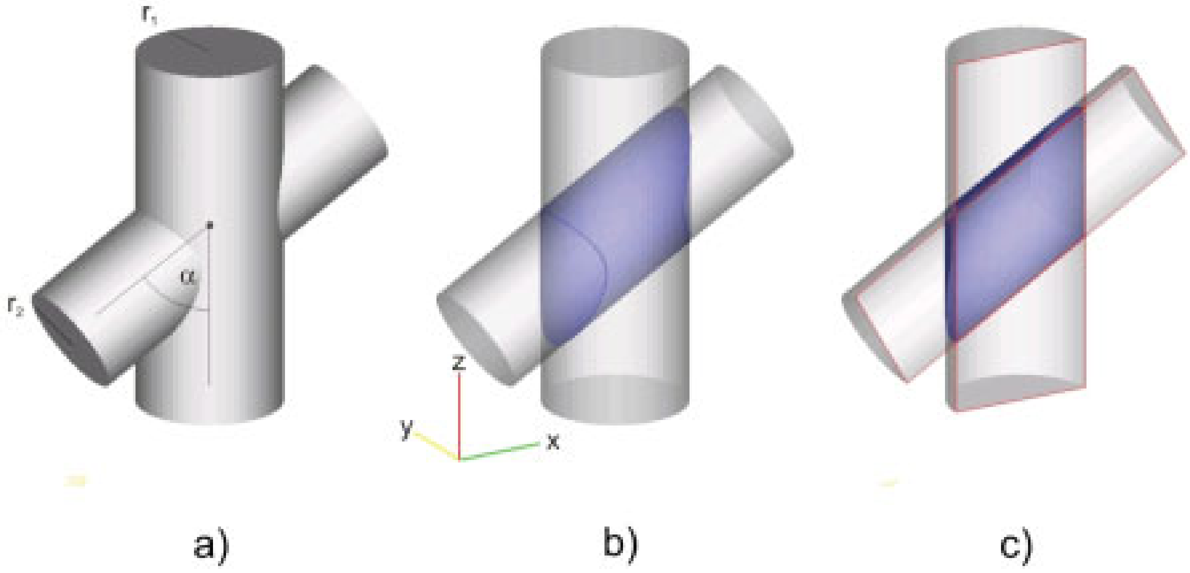

Figure 5.10: Intersection of two struts of radius r_1 and r_2

After integration between the given bounds the volume results to

$$V = \frac{2}{3} \cdot \frac{d^3}{\sin\alpha}. \tag{5.81}$$

The true relative density of one unit cell is thus given by

$$\frac{\rho^*}{\rho} = \frac{\pi \frac{d^2}{4} \cdot \sum_n f_n \cdot l_n - \frac{2}{3} d^3 \cdot \sum_m \frac{1}{\sin\alpha_m}}{a^3}, \tag{5.82}$$

where:
n – number of struts in one unit cell
f_n – volume fraction of each strut which belongs to one unit cell, typically $f_n = \{1, \frac{1}{2}, \frac{1}{4}\}$
l_n – strut length, typically $l_n = \{a, \sqrt{2}a, \sqrt{3}a\}$ in orthorhombic (cubic) cell types with face and body diagonals
m – number of intersection volumes

The volume fraction f_n describes which portion of one strut has to be accounted to a particular unit cell. For a strut from one edge to another edge e.g. only a quarter of its mass contributes to the considered unit cell and for face diagonals only half its mass. The number of intersection volumes m is determined from the number of nodes in the unit cell and the amount of struts meeting in one node. Per node the number of intersection volumes is equal to the amount of struts less one, meaning that the intersection volume has to be calculated for one randomly chosen strut paired with all remaining struts in that node. Rewriting this correlation for the aspect ratio *a*/*d* as the main design parameter yields

$$\frac{\rho^*}{\rho} = \left(\frac{d}{a}\right)^3 \cdot \left(\frac{\pi}{4d} \cdot \sum_n f_n \cdot l_n - \frac{2}{3} \cdot \sum_m \frac{1}{\sin\alpha_m}\right). \tag{5.83}$$

It is obvious that the relative density of a unit cell is proportional to the third power of the inverse of the aspect ratio. ***Eq. (5.83)*** results for considering one unit cell but also holds for bulk cellular materials provided that it is composed of a unit cell type that is space filling without leaving gaps.

Above a certain critical relative density, i.e. below a critical aspect ratio, it is expected that all behaviour typical for frameworks (especially bending-dominated behaviour) vanishes and that the scaling laws valid up to this point break down. This is assumed because above the critical relative density the cellular material can no longer be represented by a framework of struts, i.e. it stops being a lattice structure and becomes a solid with pores in it, which is strictly stretch-dominated. The critical relative density has to be determined individually for each unit cell type. ***Eq. (5.83)*** may well be employed for relative densities significantly higher than zero and will deliver more exact results as opposed to calculations which neglect the intersection volume in nodes. However, near the critical relative density this model fails as the overlap geometry of the involved struts at the cell border causes increased error. Such geometries cannot be easily assessed and expressed in a simple formula. It is, therefore, suggested to derive the critical relative density as well as relative densities beyond this point from numerical calculations in voxelized space.

5.2.8 General model for SLM lattice structures of low and high relative density

As shown above a generalized theory for the effective Young's moduli and strengths of SLM lattice structures must take into account both models for framework structures and for solids with pores. Around the occurrence of the critical relative density a brisk transition from one law to the other law is expected. This is supported by examinations made for high-density open-cell aluminum foams (Huschka, 1998, p. 109, [150]) where the exponent in the scaling law for the Young's modulus according to ***eq. (2.11)*** was significantly reduced for relative densities near unity.

Apparently, in the low relative density regime properties scale with a power of the relative density and in the high relative density they scale with a power of the porosity. Hence it can be derived that the three functions of inverse tangent (arctan), hyperbolic tangent (tanh) and inverse hyperbolic sine (arcsinh) can be employed to find mathematical expressions for the behaviour of a property across the full range of relative densities. These functions fulfill the correct change from a positive curvature in the low relative density regime to a negative curvature in the high relative density regime as shown in ***fig. 5.11***.

$$\sigma^*_{yield} = c_1 \cdot \arctan\left(c_2 \cdot \left(\frac{\rho^*}{\rho_{solid}} - c_3\right)\right) + c_4 \qquad \textbf{\textit{(5.84)}}$$

$$\sigma^*_{yield} = c_1 \cdot \tanh\left(c_2 \cdot \left(\frac{\rho^*}{\rho_{solid}} - c_3\right)\right) + c_4 \qquad \textbf{\textit{(5.85)}}$$

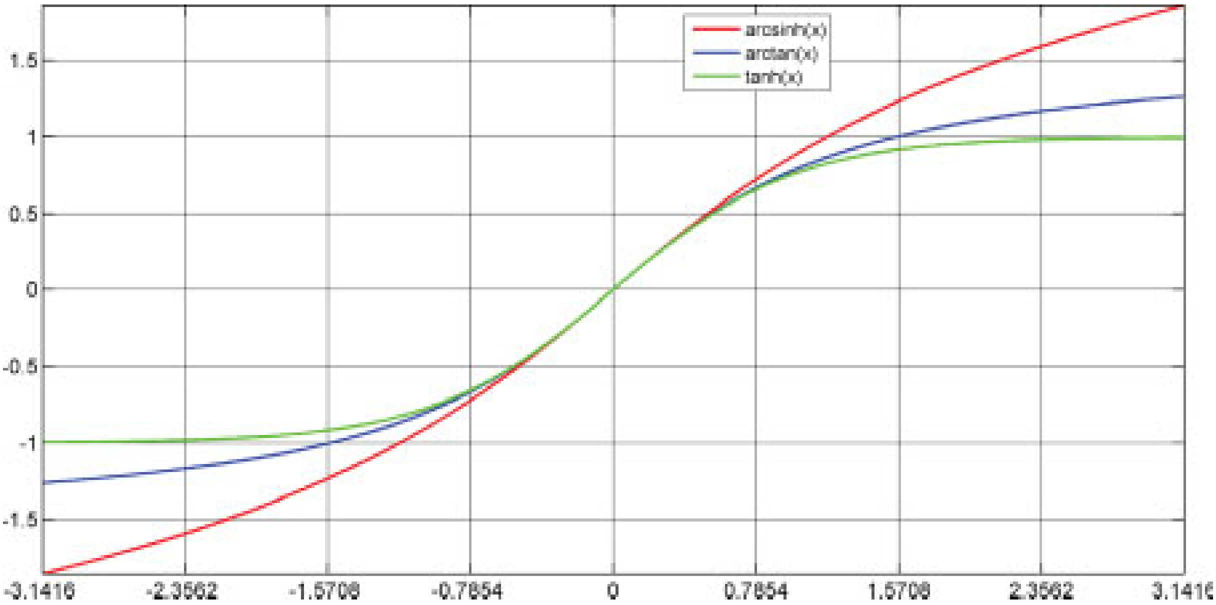

Figure 5.11: Suitable functions which can describe a property over the full range of relative densities

$$\sigma^*_{yield} = c_1 \cdot \operatorname{arcsinh}\left(c_2 \cdot \left(\frac{\rho^*}{\rho_{solid}} - c_3\right)\right) + c_4 \qquad \textbf{\textit{(5.86)}}$$

Eqs. (5.84) through ***(5.86)*** are according examples for the property of yield strength. Which function is best suitable should be decided individually e.g. based on fitting of experimental data. The factors c_1 and c_4 allow to adjust the functions along the y-axis. The slope of the transition between low and high relative density regime is controlled by c_2 and the critical relative density can be found in value c_3.

5.3 Development of SLM lattice structure designs

5.3.1 General producibility

Before deciding for open- or closed-cell lattice structure designs it is mandatory to ponder the advantages and disadvantages of either solution. Both allow to speed up the SLM process and manufacture parts of significant size and strength in less time thus saving cost. Generally, open-cell structures allow removing the unmelted powder in order to optimize part weight while in closed-cell structures unmelted powder would remain encapsulated. Nevertheless, the density of powder enclosed in closed-cell structures can be as low as 0.618 times the density of the according solid material as shown in ***section 3.4.2.2***. This implies that such structures still allow the reduction of part weight while the remaining unmelted powder contributes to the parts compressive and shear strength. However, here open-cell structures are preferred in order to obtain the maximum possible benefits in terms of e.g. strength-to-weight-ratio.

The term 'Laser Freeform Fabrication' suggests that objects of arbitrary shape can be produced from the SLM process, however, three major constraints apply. SLM lattice structures cannot be designed of struts in arbitrary directions or of arbitrary diameter or of arbitrary length at a given diameter. The first constraint of directional limitations result from the poor effective heat conductivity properties of the powder bed as indicated in ***section 3.4.3.2***. In ***section 3.4.3.6*** it was shown that this leads to the so-called balling effect which will prevent the successful production of horizontal or near horizontal struts in SLM lattice structures as observed during the precursor experiment documented in ***section 4.1***. An examination conducted by Sutcliffe (2005, p. 1087, [286]) demonstrated that SLM lattice micro struts could be built with high reproducibility at a leverage angle of 38° from the building platform. At an angle of as little as 11° some struts could still be produced successfully. However, this number was no acceptable benchmark for industrial measures. Thus, depending on the strut diameter and hence the melt energy per exposure point, leverage angles around 38° should be considered the minimum.

The second major constraint of minimum strut diameter is limited to values that depend on several parameters mainly according to ***eq. (3.34)*** such as the minimum possible melt energy per exposure point, the laser beam focus diameter, the effective heat conductivity of the powder bed and also the layer thickness. For a given layer thickness an upper bound for the minimum strut diameter can be derived from the melt front propagation in the x-y-plane compared to the z-direction. In order to ensure a solid connection to the previous layer the melt front must propagate at least as deep as one layer thickness in z-direction. At the same time it propagates laterally, starting from the focus edge. This simple estimation gives an upper bound for the minimum strut diameter d depending on the focus diameter $d_{0,86.5}$ plus twice the layer thickness l_z.

$$d = d_{0,86.5} + 2 \cdot l_z \tag{5.87}$$

If the focus diameter is 110 µm and the layer thickness 75 µm, then this bound becomes 260 µm. However, in reality smaller minimum strut diameters can be realized due to mainly three effects:

1. The laser beam has a certain penetration depth into the powder bed which depends on the average particle size according to ***eq. (3.4)***.
2. The laser beam has a lateral intensity profile which limits the available beam power towards the focus edge. Therefore, the melt front propagation in z-direction takes place faster compared to the above shown rule of thumb while the lateral melt front propagation is slower.
3. Heat is lost at the powder bed surface which limits the propagation of the melt front.

All three effects combined give a minimum value of manufacturable strut diameters of roughly 10 to 20 % below the values from ***eq. (5.87)*** but this might vary depending on material and machine or process parameters. More exact estimations can be expected from FEM heat transfer calculations. The example mentioned above for a layer thickness of 75 µm and a focus diameter of 110 µm is considered with machine and material parameters according to the data given in ***sections 4.2.2*** and ***4.2.3***, i.e. 100 W laser beam power, 850 µs

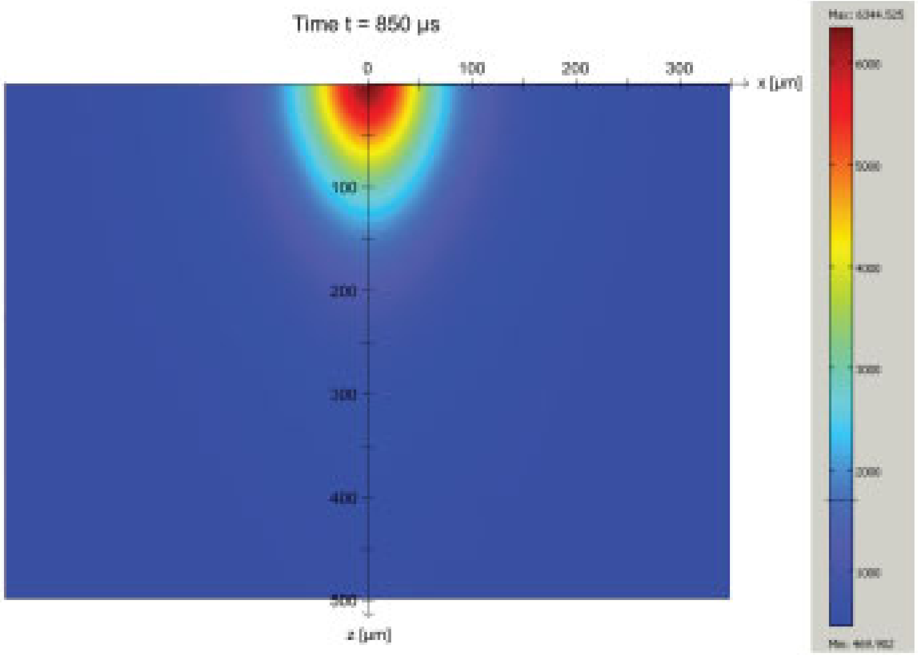

Figure 5.12: FEM calculation of melt front propagation in unconsolidated powder

point exposure time (giving 85 mJ of melt energy) and stainless steel powder of 20 to 53 µm particle size (median size $d_{50} = 35.546$ µm) with a powder bed density of 0.618 and an effective heat conductivity according to ***eq. (3.12)***. A preheated powder bed of 473.15 K was assumed whose surface loses heat to the process chamber environment which presumably heats up to 313.5 K. The result for an unconsolidated powder bed which absorbs 60 % of the incident laser beam power is shown in ***fig. 5.12*** where after 850 µs exposure time the melt temperature of stainless steel at approximately 1700 K is reached at a depth of 153.4 µm (approximately twice the layer thickness to ensure sufficient coherence) while the melt pool width is 202.5 µm, hence defining the minimum producible strut diameter for this constellation.

The third major constraint of maximum manufacturable strut length at a given strut diameter is the issue of maximum obtainable aspect ratio. The term aspect ratio is usually applied to express limits of producibility for a particular process. An example is the ratio of the depth of a bore and the bore diameter typically resulting in a value greater than unity. For SLM lattice structures the quotient of cell size divided by lattice micro strut diameter is suggested as a definition of the aspect ratio. The maximum aspect ratio of an individual SLM lattice structure cell type yields the minimum possible relative density. Either one of these values will typically be considered when build limitations are estimated. Another observation is that the relative density value is slightly above the percolation threshold, which indicates the beginning of coherence in a structure, as introduced in ***section 2.1.4***. The precursor experiments presented in ***section 4.1*** proved that for small strut diameters obtained from low melt energy per exposure point, robust lattice structures could only be produced for small cell sizes. For larger diameters obtained from higher melt energy, stable structures could be achieved for much greater cell sizes. The main reason for unsuccessful builds is the deflection of micro struts in the SLM lattice structure during the recoating of the powder bed.

Therefore, a general consideration on the stability of struts oriented in the z-direction during the layerwise powder application process is performed. It takes into account that the elastic Euler-Bernoulli beam deflection formula analog to ***eq. (5.56)*** but in global coordinates

$$v(z) = \frac{Fa^3}{6EI}\left(3\frac{z^2}{a^2} - \frac{z^3}{a^3}\right) \qquad \text{where } I = \frac{\pi d^4}{64} \tag{5.88}$$

is applicable since the environment of each strut is the easily movable powder bed. The powder near the surface is subject to friction with the silicon wiper which is responsible for spreading the powder material evenly. Therefore, if the silicon wiper deflects a strut during powder application, it might not be able to move back to its original position which is then filled with powder. This is most likely to occur particularly for vertical struts, which explains why struts in z-direction were chosen to derive this model. Additionally, friction forces exerted in the y-direction by the silicon wiper do not cause compressive or tensile loads in vertical struts. Thus friction forces on them cause load mainly in bending. A previous examination conducted at iLAS revealed that the maximum force occurring in the powder bed in z-direction during powder application is in the range of up to 10 N (Rehme, 2005). According to Lin (2001, p. 2, [184]) the friction coefficient for stainless steel and silicon is between 0.01 and 0.04. Thus the maximum deflection force is $F = 0.4$ N. It is assumed that for building stable unit cells the allowed deflection v should be less than the strut diameter d and that an area moment of inertia I for a circular strut cross section is applicable together with a Young's modulus E of 200 GPa. Solving ***Eq. (5.88)*** for the maximum cell size a for a given strut diameter d gives

$$a = \sqrt[3]{\frac{3d \cdot EI}{F}} \qquad \text{for } v(z = a) = d\,. \tag{5.89}$$

When incorporating the results presented above for minimum strut diameters of e.g. 202.5 µm the calculated maximum cell size becomes 2.927 mm which gives the aspect ratio of 14.45. For a strut diameter of e.g. 500 µm, however, the theoretically possible cell size becomes 13.2 mm which is equal to an aspect ratio of 26.4. This implies that theoretically the aspect ratio rises with increasing micro strut diameter.

5.3.2 Tesselation of 3D space

The options to arrange self-consistent symmetry elements in 3D space such that no gaps are left are constricted. The possibilities are defined by the seven crystallographic systems of triclinic, monoclinic, orthorhombic, tetragonal, trigonal, hexagonal and cubic symmetries, listed in order of increasing symmetry. These systems are subdivided into 14 Bravais lattice types to indicate the centering, 32 point groups to reflect translatory and rotatory symmetry operations and a total of 230 space groups resulting from combining these. Crystallographic models describe the positions of atoms in corners, on faces or in the center of all polyhedra resulting from the 230 space groups. In the case of SLM lattice structures built from identical unit cells, however, mass is distributed differently. Here, the mass is found along the edges or between corners of the polyhedra. This is important to know since the naming of SLM lattice structures developed in this thesis to characterize their structure is based on names used in material sciences but the meaning is slightly different.

The number of general convex or concave polyhedra that are also space-filling are limited. The group of platonic solids e.g., also called the regular polyhedra, are composed of equivalent faces of congruent, convex polygons. Besides the cube (6 faces), there are icosahedron (20 faces), dodecahedron (12 faces), octahedron (8 faces) and tetrahedron (4 faces). However, among these only the cube is space-filling. Other possibilities to fill space without gaps are given by combinations of platonic solids such as octahedron and tetrahedron, also known as the octet truss structure. As shown in ***fig. 5.13*** further options are the use of single polyhedra without equal, congruent faces such as

- truncated octahedron also known as tetrakaidecahedron (14 faces, often used to model foams due to surface minimization),
- rhombic dodecahedron,
- rhombo-hexagonal dodecahedron,

- trapezo-rhombic dodecahedron,
- gyrobifastigium (8 faces),
- four variations of hendecahedra (11 faces), i.e. ((elongated) bisymmetric/sphenoid),
- rhombic dodecahemioctahedron (16 faces) built from 4 octahedrons, two of which are rotated and even
- 18- or 38-sided polyhedra.

This list is completed by prismatic bodies such as

- triangular prism (5 faces) and
- hexagonal prism (8 faces).

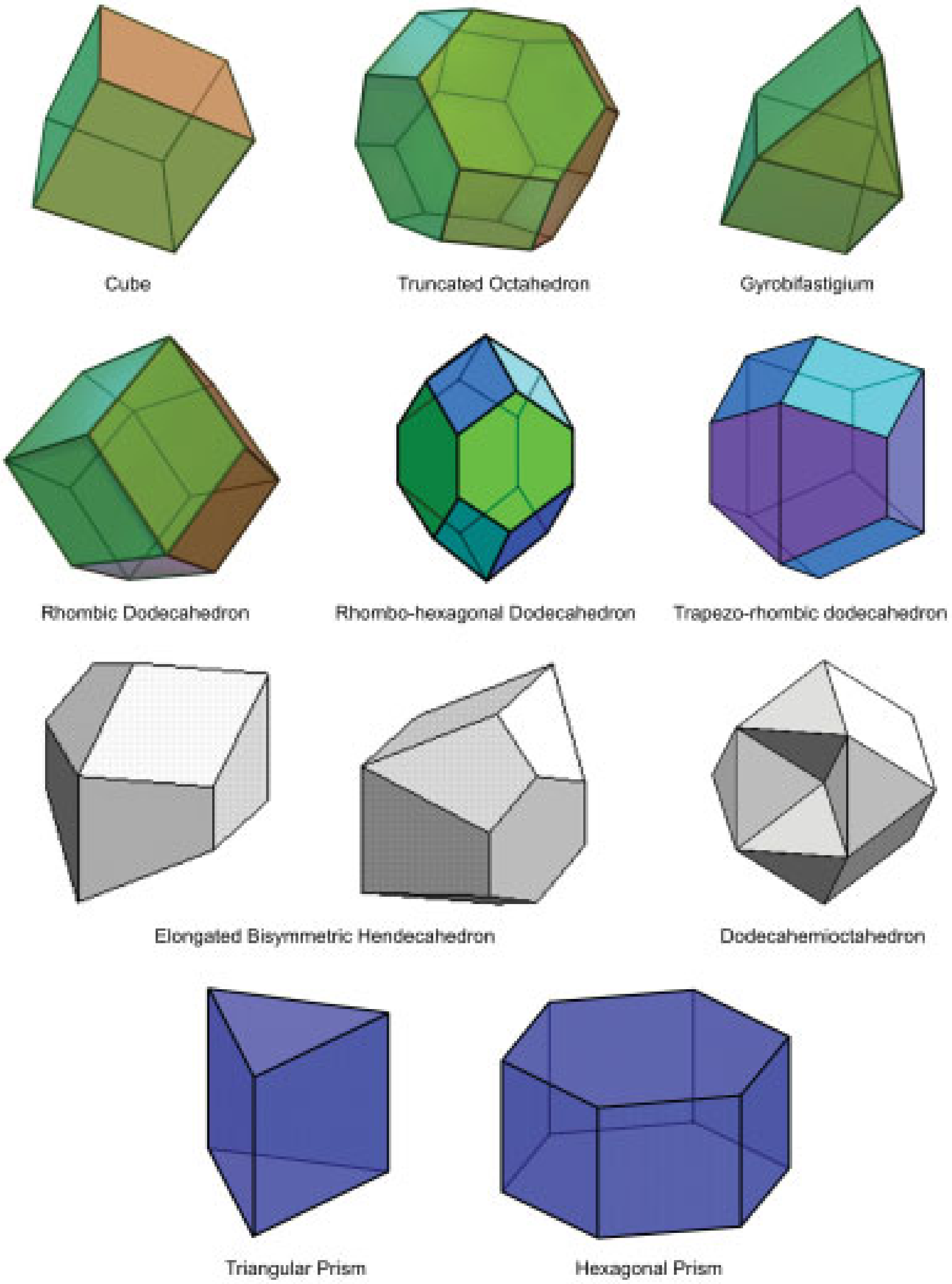
Cube
Truncated Octahedron
Gyrobifastigium
Rhombic Dodecahedron
Rhombo-hexagonal Dodecahedron
Trapezo-rhombic dodecahedron
Elongated Bisymmetric Hendecahedron
Dodecahemioctahedron
Triangular Prism
Hexagonal Prism

Figure 5.13: Space-filling polyhedra (1st and 2nd row: [317], 3rd row: [151])

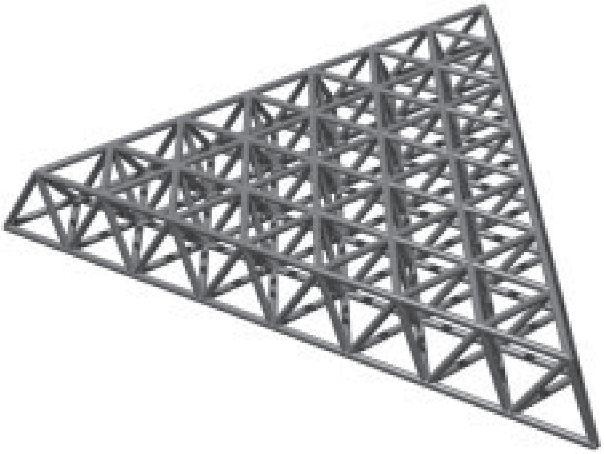

Figure 5.14: Octet truss framework [263]

However, some of these polyhedra must be excluded from further consideration due to several reasons. The truncated octahedron, gyrobifastigium, rhombic dodecahemioctahedron as well as the triangular and hexagonal prism are excluded since they exhibit struts in the x-y-plane. These polyhedra could be tilted such that a minimum leverage angle is applied between all struts and the powder bed plane, however, this is not considered reasonable, if the mechanical properties of SLM lattice structures of such design should be found in the directions of the principal axes. After comparing the rhombo-hexagonal and the trapezo-rhombic dodecahedron, the rhombo-hexagonal variation is excluded because it shows 6-sided polygons while the trapezo-rhombic shows a maximum of 4-sided polygons which is considered more stable in terms of Maxwell's rule given in ***eq. (5.22)***. The 18- or 38-sided polyhedra are eliminated from the list as well for the same reason since these are expected to comprise mechanisms and undesired failure behaviour. Finally, all versions of hendecahedra are excluded due to their complicated stacking which involves many different rotations and translations of the unit cell in order to fill space self-comsistently. This is expected to yield detrimental mechanical properties.

Thus, the only remaining polyhedra are cube, rhombic dodecahedron and trapezo-rhombic dodecahedron. From the combinations of polyhedra (octahedron and tetrahedron) the octet truss structure shown in ***fig. 5.14*** is the framework of highest mechanical performance (Buckminster Fuller, 1983, p. 167, [48]). Unfortunately, this structure comprises struts in the x-y-plane and again, if it was built at an angle versus the horizontal plane the design direction would be inconsistent with the principal axes. Additionally, this method would still yield struts with only very small minimum angle and, therefore, has to be dismissed.

5.3.3 Selected SLM lattice structures

As explained before, highly periodic structures give the highest mechanical stability and stiffness. Therefore, optimum results can be expected from simple approaches of dividing 3D space into equal unit cells. One simple approach is the use of orthorhombic or, when the unit cell size is equal in all three directions of space, cubic unit cells. Besides struts along the edges of a cubic or cuboidal unit cell it is reasonable to place struts on faces as face diagonals or between two most remote corners as body diagonals. Thus, unit cells

- with or without struts in z-direction,
- with single, double or without face diagonal struts in the x-z-plane or in the y-z-plane or
- with or without body diagonal struts

become possible. From these options a representative total of 8 different cubic unit cells was selected according to ***fig. 5.15*** for further theoretical and experimental study. These comprise unit cell variations of single face diagonals (*fcc*), single face diagonals with vertical struts in z-direction (fcc_z), double face diagonals (f_2cc), double face diagonals with vertical struts (f_2cc_z), body diagonals (*bcc*), body diagonals with vertical struts (bcc_z), double face diagonals with body diagonals (f_2bcc) and double face diagonals with body diagonals and vertical struts (f_2bcc_z). The face diagonals in ***fig. 5.15*** are solid lines and they exhibit an angle of 45° to the x-y-plane. The body diagonals have an angle of 35.3° and are dashed lines while the vertical struts are dotted lines. Despite of the considerations from ***section 5.3.1*** all angles are considered sufficient for a robust cell design. These 8 unit cell types were developed under the aspect of offering a variety between smallest density and highest strength for various load situations. The names of the basic cell types such as *fcc* and *bcc* were derived according to conventions in material sciences for cubic cells. Since there is the choice of providing either one or two face diagonals per face, *fcc* cells are indexed f_2cc, if double face diagonals are applied. The existence of vertical struts is stated by the index '*z*' after the structure's full name.

Other possibilities for SLM lattice structure frameworks are the two remaining polyhedra, which were not excluded, the rhombic dodecahedron and trapezo-rhombic dodecahedron. In

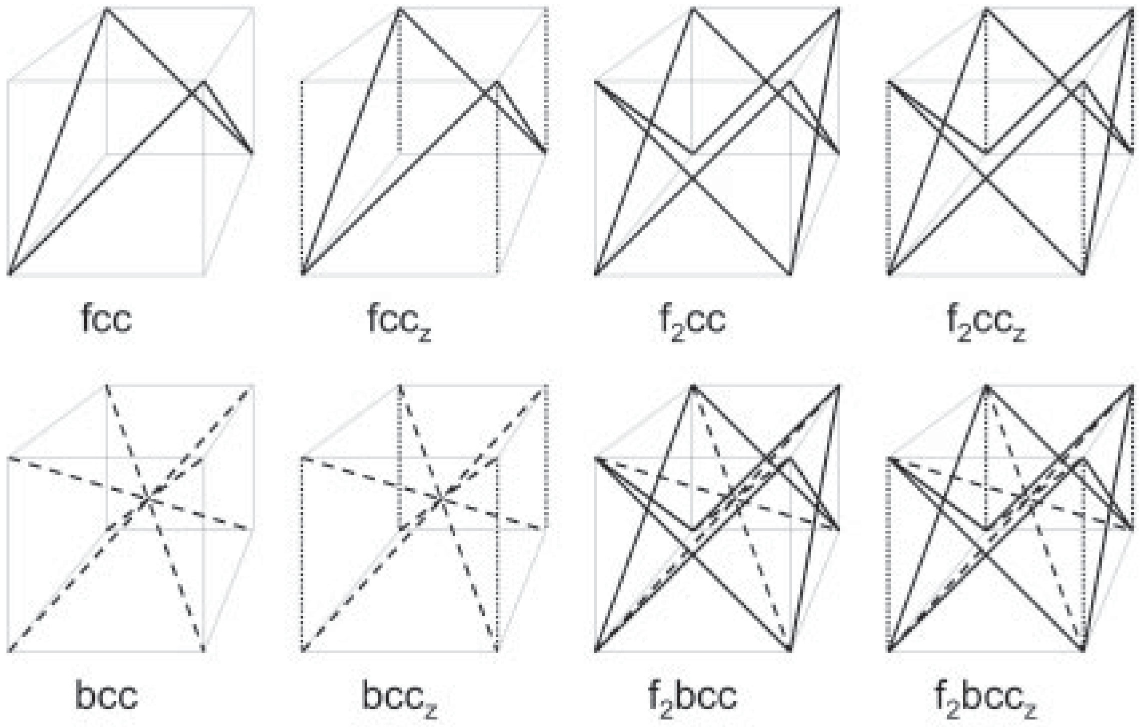

Figure 5.15: Selected cubic unit cell types

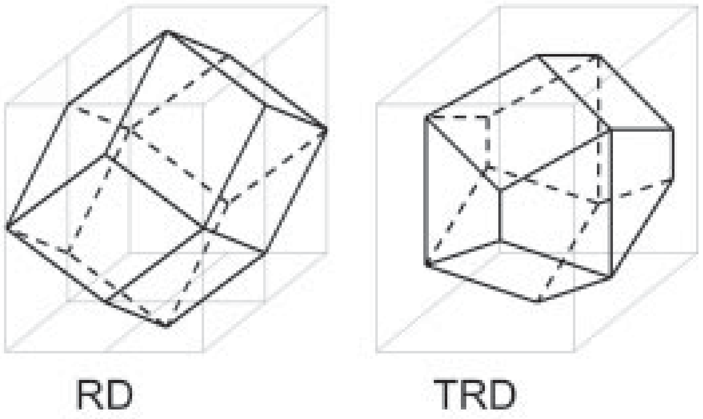

Figure 5.16: Selected polyhedral unit cell types

order to study their mechanical behaviour, these structures are not further modified by additional struts and are selected as shown in ***fig. 5.16*** where the dashed lines represent hidden lines, if the polyhedra were solid. For future reference they obtain the names *RD* (rhombic dodecahedron) and *TRD* (trapezo-rhombic dodecahedron). The most critical part about this unit cell design is the smallest angles that occur in both dodecahedra. The *TRD* framework exhibits a minimum strut angle of 18.4° against the x-y-plane and the *RD* framework even possesses a minimum angle of 16.3°. Such low angles might be detrimental in terms of robust unit cell design, therefore, these SLM lattice structures have to be evaluated carefully in the experimental producibility study in ***section 6.2.2***.

In ***section 5.3.2*** the octet truss structure was excluded from the list of feasible SLM lattice structures. Nevertheless, its high mechanical performance stays tempting enough to employ a slightly modified framework. Therefore, if all horizontal struts are removed from the structure shown in ***fig. 5.14*** then a new framework comprising tetrahedra made from three non-horizontal struts develops. This structure has triangular faces which, according to Maxwell's rule given in ***eq. (5.22)***, should promise high stiffness. In its most simple arrangement shown in the upper left part of ***fig 5.17*** these tetrahedra all have four equivalent sides made from equilateral triangles and the packing is such that in one layer each tetrahedron has six neighbours and the voids between the tetrahedra have hexagonal shape (observed in z-direction). In crystallography tetrahedra are members of the trigonal (rhombohedral) system, also known as trigonal pyramids. However, trigonal systems are often elegantly described in hexagonal representation. Thus, this structure is named simple hexagonal packing (*hp*). In the upper right part of ***fig 5.17*** the framework is extended by filling each hexagonal void with tetrahedra which are rotated 180° around the z-axis (dashed lines). This pattern is named hp_{2u} where the subscript indicates the additional filling with tetrahedra pointing upwards. In the bottom left part of ***fig 5.17*** the framework is filled similarly with additional tetrahedra that are rotated 180° around the x-axis. The result is named hp_{2d} where the index '*d*' stands for the additional tetrahedra pointing downwards. Finally, in the bottom right of ***fig 5.17*** the framework combines both previously introduced structures by placing upward and downward pointing tetrahedra in the hexagonal voids. Accordingly, this framework is named hp_{2ud}.

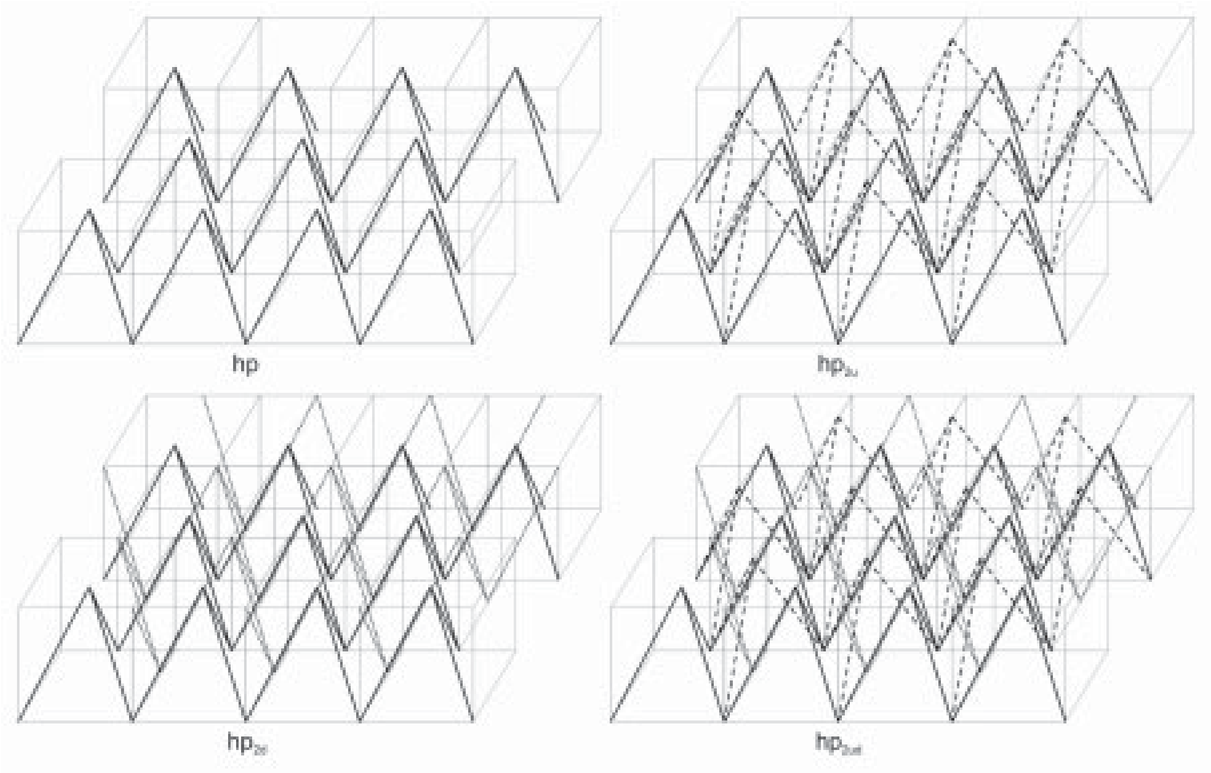

Figure 5.17: Tetrahedral unit cell types

5.4 Theoretical analysis of preselected SLM lattice structures

5.4.1 Evaluation of expected critical relative densities

The 14 preselected SLM lattice structure cell types are expected to show various types of mechanical behaviour and only some may be optimal for specific load situations. Therefore, the above developed theories are verified as far as possible in order to narrow down the amount of specimens for the experimental validation especially for the stages of compression, tensile and shear tests of various cell sizes. The Maxwell approach presented in ***section 5.1.2*** can predict behaviour for isotropic cellular materials and might be suitable as a first order estimate to determine bending- and stretch-dominated behaviour. For single unit cells the number of degrees of freedom M according to ***eq. (5.22)*** is negative for all 14 cell types including obviously stretch-dominated cell types such as f_2bcc_z which would erroneously be considered bending-dominated. If, however, a bulk arrangement of unit cells is considered to have a more realistic approach, i.e. struts and joints are shared among adjacent cells, then the number of degrees of freedom is above zero for all 14 cell types. This incorrectly implies stretch-dominated behaviour even for those cell types which are obviously bending-dominated such as *fcc*. Therefore, the Maxwell approach is not suitable for an estimation of bending- and stretch-dominated behaviour in this case and will have to be derived from the stress-strain diagrams during the compression tests in ***section 6.7.1***.

In order to assemble the generalized theory for SLM lattice structures the model suggested in ***section 5.2.8*** has to be supplemented with estimations of the critical relative density to determine the transition between the models for framework structures and for solids with pores. The critical relative density is considered to occur when the length-to-diameter-ratio of struts in a unit cell becomes so small that two struts joined at a given angle virtually reduce to only one strut along a prescribed amount of their elongation or, secondly, when the distance between two adjacent struts becomes so small that they are directly connected. When this occurs the struts have no room left for bending and the structure ceases to be a framework. The case of angled struts can be derived from determination of the overlap length x of two struts joined at an angle α as shown in ***fig. 5.18***. One of the two struts involved, usually the shorter one, has a critical length l below which and a critical diameter d above which it stops being a strut due to merging with adjacent struts. The length of each strut is directly linked to the unit cell size a, therefore, the aspect ratio as defined above can be determined when the appropriate corner of a unit cell is known where the first strut literally vanishes. This strut is called the critical strut. It could be found at a node where the smallest angle between two struts occurs, however, the smallest angle does not necessarily yield the critical strut, it is merely an indicator where to search. The critical strut may also be found at a bigger angle or in a longer strut if this strut comprises further intersections with other struts. The critical length l of this critical strut can then be equated with the appropriate amount of multiples of the overlap length x and additionally with the strut diameter d for each further intersection. The resulting equation can be rewritten to yield a relation of the type a/d.

In the second case where a unit cell ceases to be a framework due to the collision of two adjacent struts which are not joined at all, both critical struts are usually less obvious to find.

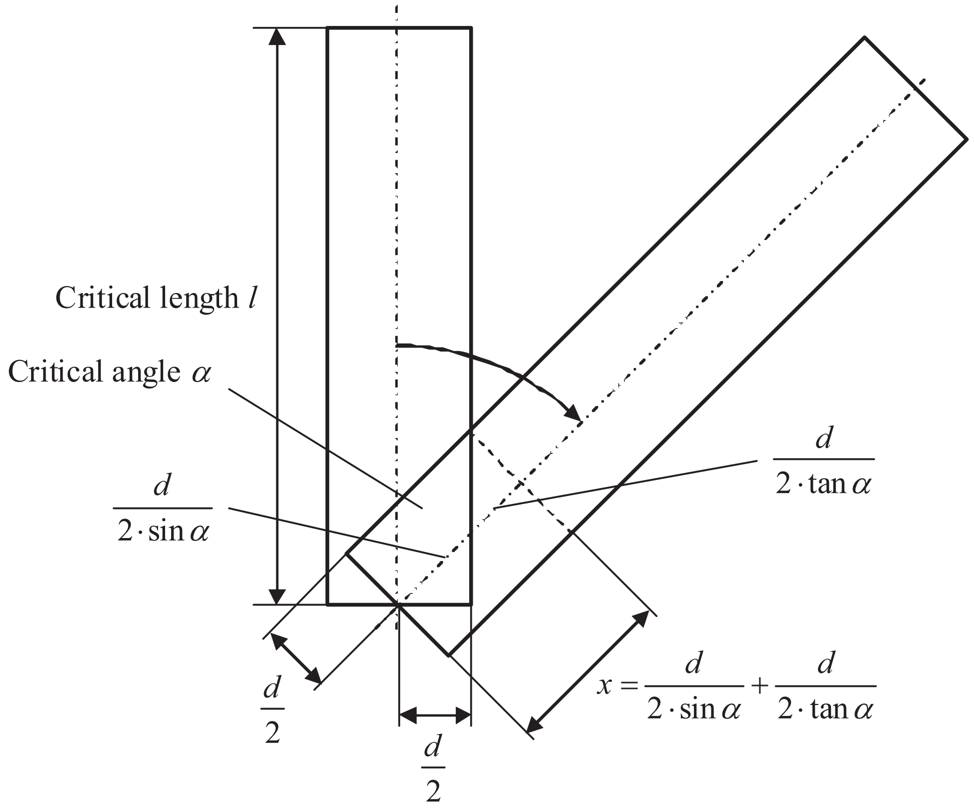
Critical length l
Critical angle α
$\frac{d}{2\cdot\sin\alpha}$
$\frac{d}{2\cdot\tan\alpha}$
$x=\frac{d}{2\cdot\sin\alpha}+\frac{d}{2\cdot\tan\alpha}$
$\frac{d}{2}$
$\frac{d}{2}$

Figure 5.18: Determination of overlap length between two adjacent struts

Depending on the complexity of a unit cell the analytical derivation of a relation for the aspect ratio might be difficult to obtain. Therefore, a numerical simulation, where the aspect ratio is gradually reduced, can help to find the critical struts and the according critical aspect ratio.

However, a sole analytical estimation of the critical relative density is difficult to conduct as explained above in ***section 5.2.7***. Therefore, a mixed approach of analytical determination of the critical aspect ratio and numerical simulation of the resulting critical relative density is applied on all 14 preselected cell types. The analytical part is in accordance with ***fig. 5.18*** for cell types *fcc* through hp_{2u} in ***table 5.1***. The remaining cell types hp_{2d} and hp_{2ud} represent the second case where the numerical calculations of the aspect ratio are manually adjusted to the collision geometry of both critical struts which were found in the simulation. The numerical modelling of the critical relative density is owed to a simulation performed with the MATLAB software package (version R2008a). For this simulation a copy of each unit cell is

Table 5.1: Estimation of critical relative densities

Cell type	Critical angle α	Overlap x	Critical length l	Critical aspect ratio a/d [1]	Critical relative density [1]
fcc	60°	$\frac{\sqrt{3}d}{2}$	$\sqrt{2}a = 2x$	$\frac{\sqrt{3}}{\sqrt{2}}$	0.7789
fcc_z	45°	$\frac{d}{2}\left(1+\sqrt{2}\right)$	$\sqrt{2}a = 2x$	$\frac{1+\sqrt{2}}{\sqrt{2}}$	0.6206
f_2cc	60°	$\frac{\sqrt{3}d}{2}$	$\sqrt{2}a = 2x + d$	$\frac{1+\sqrt{3}}{\sqrt{2}}$	0.6494
f_2cc_z	45°	$\frac{d}{2}\left(1+\sqrt{2}\right)$	$\sqrt{2}a = 2x + d$	$\frac{2+\sqrt{2}}{\sqrt{2}}$	0.5125
bcc	70.5288°	$d\left(\sqrt{\frac{3}{2}}+\sqrt{\frac{1}{2}}\right)$	$\sqrt{3}a = 2x$	$\frac{2\sqrt{2}}{\sqrt{3}}$	0.9130
bcc_z	54.7356°	$\frac{d}{2}\left(\sqrt{\frac{3}{2}}+\sqrt{\frac{1}{2}}\right)$	$\sqrt{3}a = 2x + d$	$\left(\sqrt{\frac{3}{2}}+\sqrt{\frac{1}{2}}+1\right)/\sqrt{3}$	0.9078
f_2bcc	35.2644°	$\frac{d}{2}\left(\sqrt{3}+\sqrt{2}\right)$	$\sqrt{2}a = 2x + d$	$\frac{\sqrt{3}+\sqrt{2}+1}{\sqrt{2}}$	0.6424
f_2bcc_z	35.2644°	$\frac{d}{2}\left(\sqrt{3}+\sqrt{2}\right)$	$\sqrt{2}a = 2x + d$	$\frac{\sqrt{3}+\sqrt{2}+1}{\sqrt{2}}$	0.6736
RD	70.5288°	$\frac{d}{2}\cdot\frac{3}{2\sqrt{2}}$	$\frac{a}{4}\sqrt{6} = 2x$	$\sqrt{3}$	0.8079
TRD	105.8942°	$\frac{d}{2}\left(\sin\alpha + \cos\alpha\left(1+\cos\alpha\right)\right)$	$\frac{a}{3} = 2x$	$3\cdot\left(\sin\alpha + \cos\alpha\left(1+\cos\alpha\right)\right)$	0.6321
hp	60°	$\frac{\sqrt{3}d}{2}$	$a = 2x$	$\sqrt{3}$	0.5964
hp_{2u}	33.5603°	$\frac{d}{2}\left(\frac{1}{\sin\alpha}+\frac{1}{\cos\alpha}\right)$	$a = x$	$\frac{1}{2}\left(\frac{1}{\sin\alpha}+\frac{1}{\cos\alpha}\right)$	0.6725
hp_{2d}	–	–	–	3.7764	0.2418
hp_{2ud}	–	–	–	3.7764	0.3134

defined in three-dimensional space represented by 250 x 250 x 250 voxels. Struts are defined as vectors which are translated and rotated in three-dimensional space to take their according positions. Their lengths are calculated from the length of the voxel space borders, i.e. $a = 250$ voxels, and their radius is derived accordingly from the aspect ratio. This information is sufficient to determine whether each voxel is penetrated by at least one strut or not. This accounts for intersection volumes in joints of a unit cell where otherwise mass misleadingly contributes repeatedly to the relative density as explained in ***section 5.2.7***. An exemption to the voxel space size is made for both polyhedral cell types and all four tetrahedral cell types since either one or both of the conditions $a \neq b$ and $a \neq c$ are fulfilled. However, in the simulation's voxel space the length a is kept constant while b and c are adjusted, i.e. their lengths become greater than 250. Increasing the length of the voxel space increases the accuracy in calculating the critical relative density, however, a base length of 250 voxels was found to yield sufficient accuracy. It is also the limit for calculations of the critical relative density on a standard dual processor desktop computer with 4 GB of memory. Higher accuracy would require more memory.

The results of this mixed analytical and numerical approach are compiled in ***table 5.1*** where for each cell type according to ***fig. 5.18***, if applicable, the derived critical angle α, the length of the overlap x at the critical angle and the approach for the critical length l at which the first strut is constrained are given. In the calculation of the critical relative density the radii of all struts are taken from the critical aspect ratio by substitution of the diameter d.

From the results table it becomes obvious that typical critical relative densities are expected to show values around 60 to 70 %. Especially cell types with only few struts in one unit cell such as *fcc* and *bcc* show quite high values. It is, however, remarkable that both *bcc* and bcc_z outperform all other cell types which makes them well suitable for applications where bending of struts is required over a broad range of relative densities, e.g. envisioned in applications of energy absorbers. Usually those cell types which comprise a complex arrangement of unit cell struts such as f_2cc_z and all four tetrahedral cell types can exhibit collision of struts at low relative densities. In regard of ***fig. 5.11*** and due to the leap in strength and stiffness at the point of critical relative density portrayed there, it can be concluded that these cell types show highest possible strength and stiffness at low densities. Especially hp_{2d} and hp_{2ud} show very low values for the critical relative density. Due to their complexity they are expected to possess several points of critical relative density, one for each occuring collision. This, however, is not further investigated.

5.4.2 Matrix structural analysis of preselected SLM lattice structures

In order to learn about the expected effective strengths of all 14 preselected SLM lattice structures in the regime of low relative densities another simulation is employed using the MASTAN2 software (version 3.2) provided by Prof. Ziemian and Prof. McGuire which is also based on MATLAB. This software performs matrix structural analysis of given frameworks for which the foundations are laid in ***section 5.2.5***. The goal is to obtain data which can later be compared to results from the experimental investigations in ***section 6***.

The simulation requires some assumptions, the main one being that matrix structural analysis of a framework can only be performed at relative densities below the critical relative density. Therefore, strut diameters of 0.5 mm are assumed from which the critical cell size can be derived according to ***table 5.1***. As far as applicable, cell sizes of 0.5, 1, 1.5, 2, 2.5, 3, 4, 5 and 6 mm are examined for each of the 14 cell types. Before the MASTAN2 simulation is performed, the relative density of all cell types and cell sizes is calculated with the same MATLAB simulation used previously to calculate the critical relative densities in ***section 5.4.1***. The resulting relative densities are given in ***appendix 10.3*** in ***table 10.1***.

For each combination of cell type and cell size the yield strength is then calculated in all three directions of space using MASTAN2 simulations of lattice structure blocks with 4 x 4 x 4 unit cells which comprise a maximum of around 1300 elements for most cell types and can be computed on a standard dual processor desktop computer with 4 GB of memory. In order to avoid size effects, which are discussed more in-depth in ***section 6.3.1***, yield strengths can be calculated for many different lattice structure block sizes (e.g. 3 x 3 x 3). The result is one calibration curve per cell type and direction of force with a distribution of yield strengths over number of cells according to a power law with positive or negative exponent which asymptotically approaches a constant value. This value is usually achieved for 10 x 10 x 10 unit cell blocks, i.e. the size effect disappears. In order to provide a common base for comparing simulation results to experimental results, the calibration curve power law allows to derive the yield strength of 10 x 10 x 10 unit cell blocks from 4 x 4 x 4 simulation.

All strut intersections in each unit cell are defined as nodes which are not simulated as pin-joints like in many other simulations but as rigid nodes with fixed warping conditions. This is justified by the fact that intersecting struts are welded together in the SLM process and therefore rigid. On all nodes of one of the six faces of each simulated lattice structure block external forces are applied according to the desired stress level. Usually stress from a total force slightly larger than the expected yield strength can be selected since the deformation is calculated stepwise until the onset of yield. The nodes on the opposite side of the loaded face are supported such that each node is supported against the direction of force. One corner node is additionally supported in both directions perpendicular to the direction of force and both two corner nodes adjacent to this node are each additionally supported in one direction perpendicular to the direction of force. This boundary condition is required to implement a stabilized structure on which computations can be successfully performed. Furthermore, some important strut element properties are defined for the simulation. The cross sections are assumed to be circular, hence their area is determined to 0.1963 mm^2, the moments of inertia around each strut's local y- and z-axis I_{yy} and I_{zz} are determined to $3.067 \cdot 10^{-3}$ mm^4, the torsion constant J is determined to $6.136 \cdot 10^{-3}$ mm^4 and the warping coefficient Cw to 0 mm. The plastic section moduli around the y- and z-axis Z_{yy} and Z_{zz} are set to 0.01227 mm^4 while the shear areas A_{yy} and A_{zz} are determined to 0.1785 mm^2. Since SLM lattice structures made from stainless steel 1.4404 are considered in this thesis the material properties of the struts are set accordingly to 210 GPa for the modulus of elasticity, 0.33 for the Poisson's ratio, 500 MPa for the yield strength and $7.783 \cdot 10^{-5}$ N/mm^3 for the weight density.

Table 5.2: Resulting theoretical power laws for preselected cell types

Cell type	$\sigma^*_{yield,x}/\sigma_{yield,solid,x}$	$\sigma^*_{yield,y}/\sigma_{yield,solid,y}$	$\sigma^*_{yield,z}/\sigma_{yield,solid,z}$	Yield strength/relative density [MPa]		
				x	y	z
fcc	$0.1671\cdot(*)^{1.5962}$	$0.1711\cdot(*)^{1.5962}$	$0.1686\cdot(*)^{1.5958}$	18.18	18.18	17.42
fcc_z	$0.1272\cdot(*)^{1.1274}$	$0.1302\cdot(*)^{1.1274}$	$0.5313\cdot(*)^{1.3428}$	47.46	47.46	127.1
f_2cc	$0.2693\cdot(*)^{1.6426}$	$0.2756\cdot(*)^{1.6426}$	$0.2513\cdot(*)^{1.6648}$	38.5	38.5	30.94
f_2cc_z	$0.1502\cdot(*)^{1.1206}$	$0.1538\cdot(*)^{1.1206}$	$0.336\cdot(*)^{1.2458}$	58.01	58.01	99.55
bcc	$0.1468\cdot(*)^{1.657}$	$0.1503\cdot(*)^{1.657}$	$0.1554\cdot(*)^{1.6571}$	22.21	22.21	22.36
bcc_z	$0.1710\cdot(*)^{1.7003}$	$0.1751\cdot(*)^{1.7003}$	$0.1998\cdot(*)^{1.1653}$	25.65	25.65	68.01
f_2bcc	$0.1712\cdot(*)^{1.2239}$	$0.1752\cdot(*)^{1.2239}$	$0.1108\cdot(*)^{1.3406}$	60.14	60.14	30.3
f_2bcc_z	$0.1594\cdot(*)^{1.1952}$	$0.1632\cdot(*)^{1.1952}$	$0.1434\cdot(*)^{1.1646}$	61.15	61.15	49.99
RD	$0.4651\cdot(*)^{1.6052}$	$0.4761\cdot(*)^{1.6052}$	$0.2451\cdot(*)^{1.7115}$	77.99	77.99	31.26
TRD	$0.2459\cdot(*)^{1.6344}$	$0.1321\cdot(*)^{1.5596}$	$0.1201\cdot(*)^{1.5076}$	46.09	26.94	25.98
hp	$0.07856\cdot(*)^{1.646}$	$0.0677\cdot(*)^{1.6162}$	$0.2835\cdot(*)^{1.6202}$	8.896	8	31.89
hp_{2u}	$0.1837\cdot(*)^{1.6323}$	$0.1456\cdot(*)^{1.6593}$	$0.4756\cdot(*)^{1.6597}$	25	17.46	57.23
hp_{2d}	$0.1446\cdot(*)^{1.5513}$	$0.0857\cdot(*)^{1.5646}$	$0.2928\cdot(*)^{1.5383}$	24.83	13.99	48.77
hp_{2ud}	$0.1408\cdot(*)^{1.6035}$	$0.1449\cdot(*)^{1.614}$	$0.3103\cdot(*)^{1.6345}$	25.95	26.29	51.64

The simulation allows only the estimation of the yield behaviour but not the post-yield behaviour. This yield behaviour is calculated from a second order inelastic analysis which calculates the tangent modulus in a stepwise process by employing the mid-point Runge-Kutta method (McGuire, 2000, p. 343, [197]), i.e. the predictor-corrector method, where the recommended initial load increment of 10 % of the maximum load (McGuire, 2000, p. 340, [197]) is used and the number of steps must be sufficiently high in order for the simulation to converge. The calculated relative densities and yield strengths of all cell types are summarized in ***appendix 10.3***. All values belong to the low relative density regime. Therefore, power laws can be derived from these results which are given in ***table 5.2*** where $\sigma_{yield,solid}$ is taken from the experimental results for solid, compressive specimens presented in ***section 6.7.1*** and the relative density ρ^*/ρ_{solid} is replaced by (*) for improved readibility. These power laws can later be compared to power laws derived from experimental data in the low relative density regime. However, only some of the 14 cell types will be investigated sufficiently in experiments to allow deriving according power laws. Additionally, ***table 5.2*** contains the yield strength results in all three directions of space per each cell type at 2.5 mm cell size divided by the calculated relative density at this cell size. This is a representation of the specific yield strength which is also examined experimentally later. It is an estimate for the interaction of the proportionality factor and the exponent in the power laws and gives an early indication which cell type might be promising for further investigation.

5.5 Summary

This chapter starts with correlations for strength and elastic properties of isotropic cellular materials in the regime of low as well as high relative densities. The concepts of bending and stretch-dominated deformation behaviour are pointed out and it is established that Maxwell's criterion for the stability of framework structures is not sufficient for SLM lattice structures.

Therefore, a newly developed structural hypothesis for anisotropic SLM lattice structures comprises considerations of the anisotropy of SLM solids of which the SLM struts are made of as well as continuum mechanics to provide simple means of describing SLM lattice structures as a homogenous body in which its fine inherent structure is denied. Thus elastic deformations are described by the threedimensional, orthorhombic elasticity tensor and plastic deformations by a newly derived yield criterion. This criterion is characterized by an ellipsoidal yield surface which accounts for failure due to hydrostatic stress states, anisotropy in SLM solids, cell type and cell size of SLM lattice structures and possible deviations between tensile and compressive strengths. This hypothesis further comprises the displacement method for matrix structural analysis of frameworks in order to correlate the mechanical properties to the inner structure of low relative density SLM lattice structures. Since micro struts in SLM lattice structures have a rather small ratio of length-to-diameter the Timoshenko beam theory is considered as well to account for shear stresses. At high relative densities SLM lattice structures become rather solids with pores which causes framework theories to break down completely. Therefore, an assumption for the material properties in this regime is given. Next, the problem of determining the true relative density from the design parameters is dealt with and approaches for a more exact determination are presented. Finally, a generalized model which considers both SLM lattice structures of low and high relative density in one function is presented and the concept of the critical relative density where the transition from one regime to the other takes place is introduced.

Next, the general producibility of SLM lattice structures is theoretically analyzed. Constraints for strut direction, minimum strut diameters and maximum strut length are derived for the point-like exposure strategy developed in ***section 4***. Furthermore, the maximum expected aspect ratio, i.e. the achievable cell size at given strut diameter, is calculated. Then some light is shed on the possibilities to fill threedimensional space with self-consistent symmetry elements without leaving gaps. From the considered polyhedrae some are selected and turned into framework elements by equipping their edges with struts or by e.g. filling their interior with diagonal struts. Thus 14 cell types which are deemed producible by the SLM process are derived and presented. Finally, these are analyzed theoretically by calculating their respective critical relative density from the critical strut length where the transition from the regime of low relative density to high relative densitiy is expected to take place. This requires that in order for a SLM lattice structure to become a solid with pores, at least one strut, i.e. the critical strut, is obstructed from bending due to overlap with an adjacent strut in the unit cell. Below the critical relative density power laws for the yield strength of all 14 cell types are calculated in a simulation using the MASTAN2 software based on MATLAB. The results are compiled for later comparison with the experimental data.

6 Experimental analysis of SLM solids and cellulars

6.1 Mechanical properties of SLM solids

Before experimental results on the mechanical properties of SLM lattice structures can be assessed it is mandatory to obtain the mechanical properties for SLM solids as they outline the framework of the failure criterion for SLM lattice structures given in ***eq. (5.51)***. This reduces to the Hill48 criterion if all porosity is neglected, i.e. the relative density becomes unity. As explained in ***section 3.5.2*** the anisotropic behaviour of the mechanical properties of SLM solids has been recognized for quite some time, however, no in-depth analysis of a large number of specimens has been previously conducted.

The laminated structure received from the SLM process was previously described in ***section 3.3.1***. It is evident that laminates involve anisotropic strength properties. In the SLM process the build direction, which is labeled the z-direction, could be phrased as the direction of lamination. If the exposure strategy in the SLM process is chosen such that neither the x- nor the y-direction is the preferred direction of scanning, i.e. an alternating x- and y-scan is applied, then the special case of orthotropic strength properties is expected. Previous examinations conducted by Meiners (1999, pp. 96-99, [201]) and other researchers show decreased strength in z-direction. This result is expected here as well. However, all recent examinations suffered from insufficient sample amounts to statistically confirm the exact anisotropic mechanical behaviour of SLM solids. Therefore, the directional dependence of mechanical properties such as yield strength, ultimate strength, break strain and Young's modulus was scrutinized closely. This analysis was conducted by using 290 test specimens made from stainless steel (1.4404) according to the process conditions presented in ***section 4.2***. All specimens were orientated in 145 different directions normal to the surface of a hemisphere separated into a grid of 15° meridians for the leverage angle θ as well as 15°

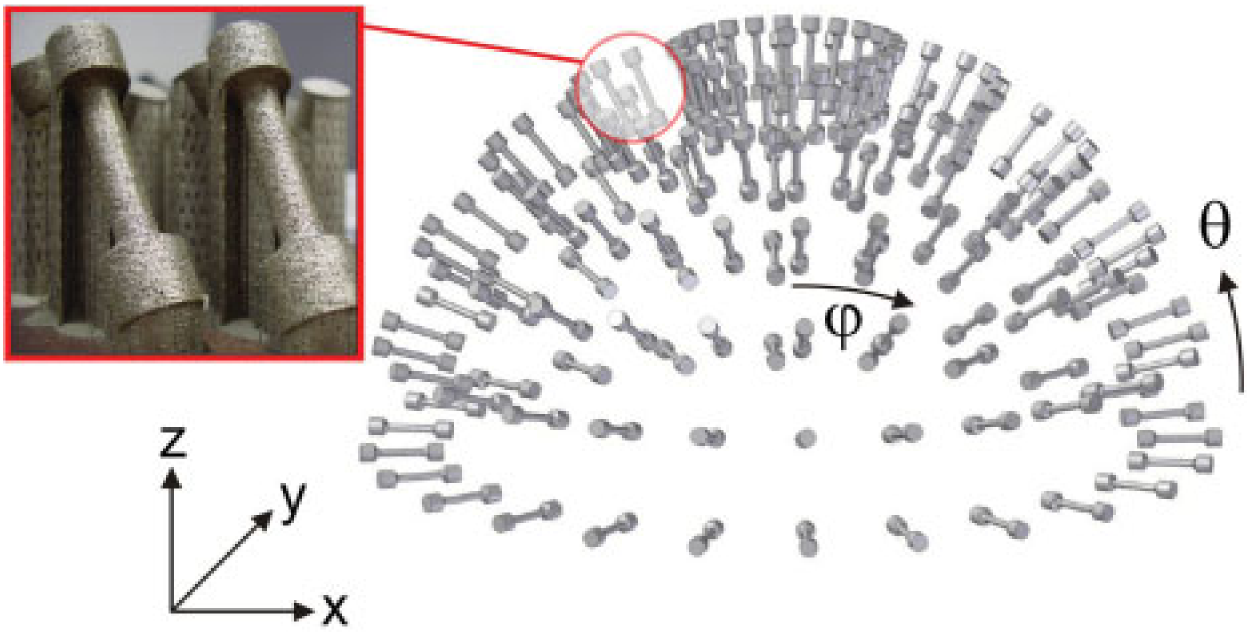

Figure 6.1: SLM tensile specimens orientated in directions normal to the surface of a hemisphere

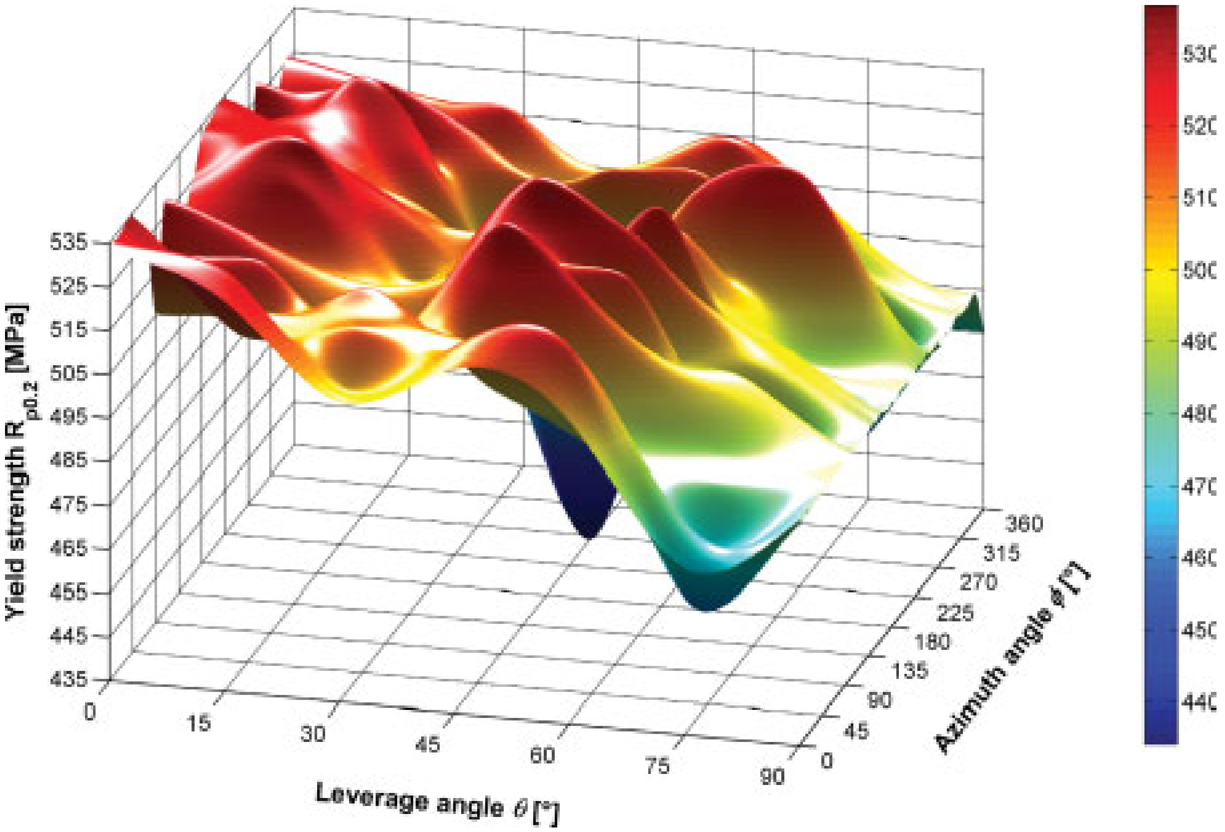

Figure 6.2: Directional dependence of tensile yield strength $R_{p0.2}$ for SLM solids

latitudes for the azimuth angle φ as shown in ***fig. 6.1***. Positive increments of angle θ were counted against the x-y-plane while positive increments of angle φ started at the positive y-axis and were counted clockwise in the x-y-plane. All test specimens received identical dimensions showing 24 mm in effective core length and 5 mm in core diameter in compliance with regulations given in DIN EN 10002 (2001, p. 1, [90]) and DIN 50125 (2004, pp. 4-7, [85]). In order to avoid stress concentration due to notch effects and surface roughness they were all post-processed on a turning center and received a final core diameter of 4 mm.

The tensile tests were conducted on a Zwick 1474 universal testing machine. ***Fig. 6.2*** through ***6.5*** show the results for all obtained yield strengths $R_{p0.2}$, ultimate strengths R_m, break strains A and Young's moduli E over all variations of azimuth angle φ and leverage angle θ. For the yield strength a clear decline was found for a rising angle of leverage as shown in ***fig. 6.2***. Test specimens that were built in the x-y-plane ($\theta = 0°$) showed an average yield strength of 525 MPa while those built in z-direction ($\theta = 90°$) showed an average of 486 MPa. The decline of the mean values for different angles θ can be roughly approximated by a linear correlation, however, if considered more precisely, the trend predicted theoretically in ***section 5.2.2*** and shown in ***fig. 5.4*** can be found here. The ultimate strength in ***fig. 6.3*** shows a similar behaviour with an average value of 604 MPa at $\theta = 0°$ though this is not the maximum here. Surprisingly, the maximum is obtained at $\theta = 15°$ with an average value of 616 MPa. The minimum average value does not occur in z-direction either but at $\theta = 75°$ and

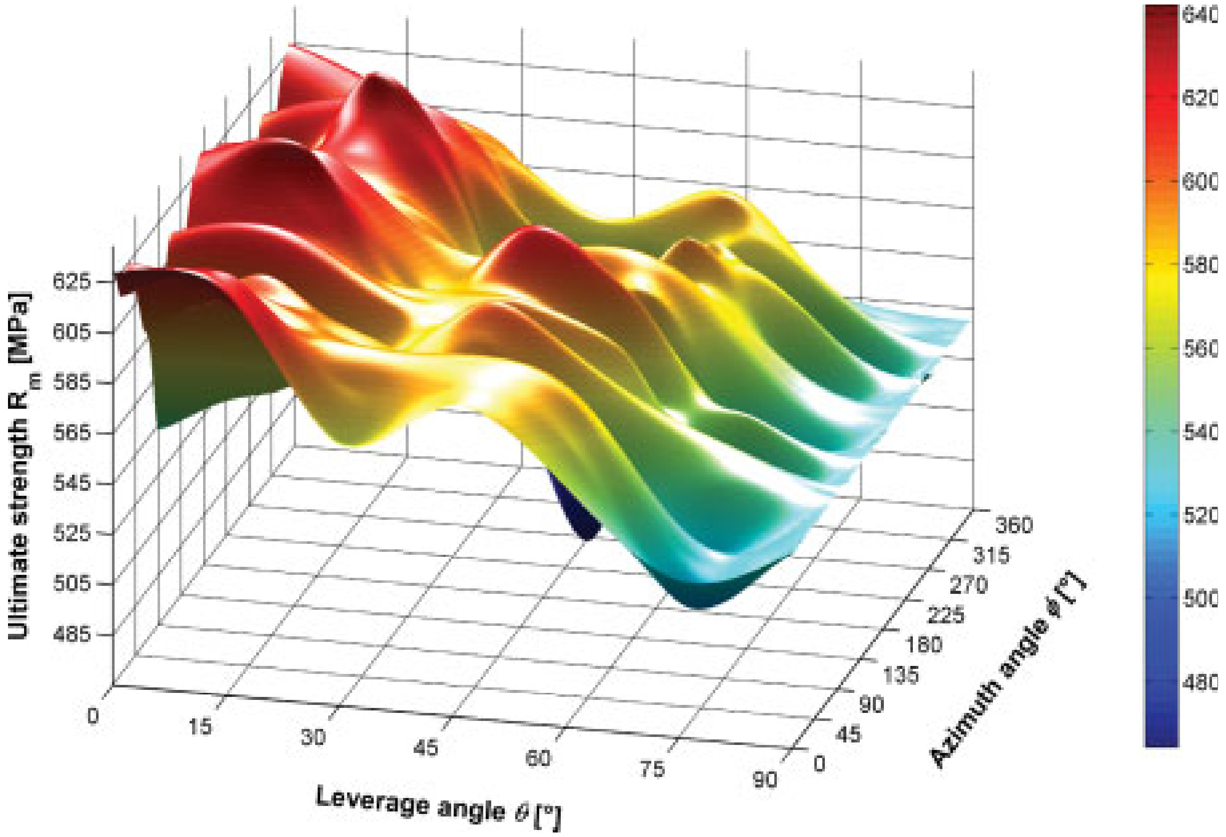

Figure 6.3: **Directional dependence of ultimate strength R_m for SLM solids**

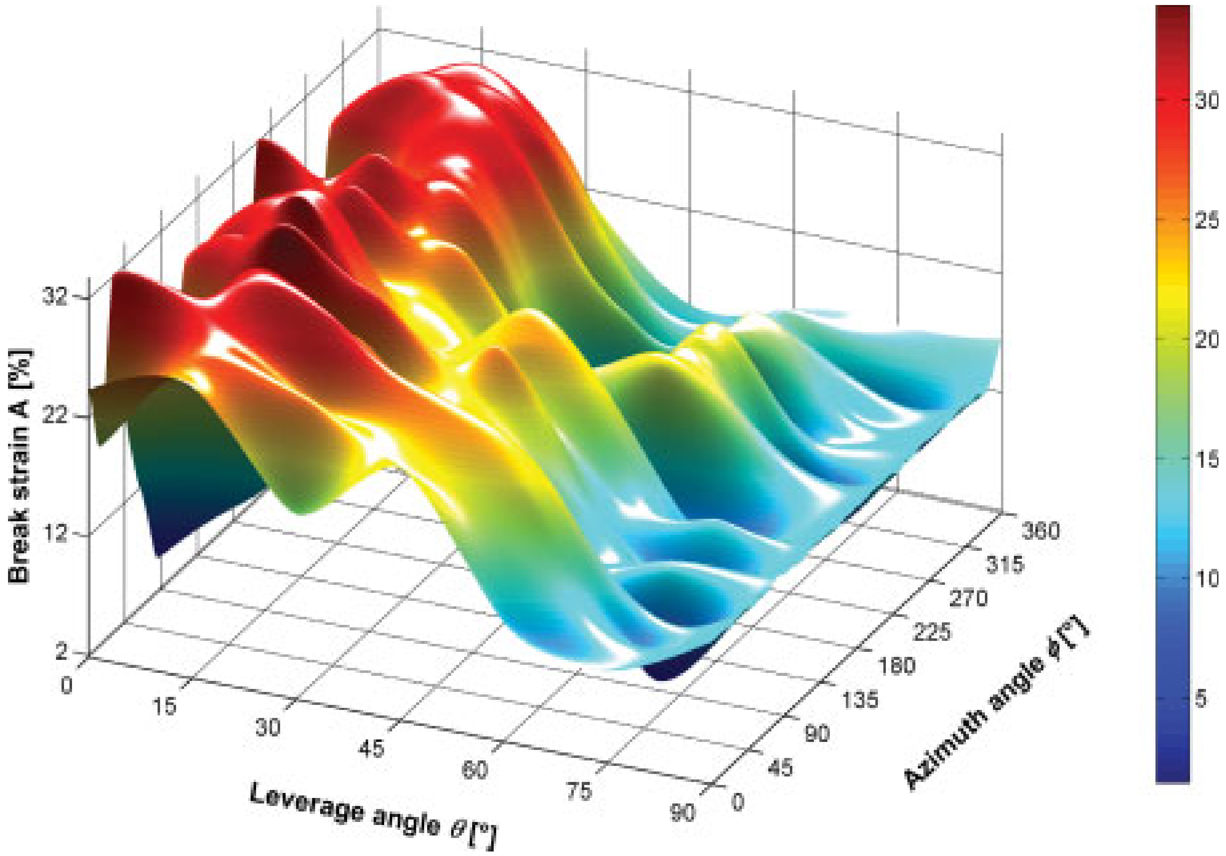

Figure 6.4: **Directional dependence of break strain for SLM solids**

540 MPa. In z-direction the average value for ultimate strength is slightly higher at 543 MPa. Like before the correlation between the average ultimate strength and angle θ is roughly linear. The results for the break strain A are given in ***fig. 6.4***. As observed before for the yield and the ultimate strength, the break strain decreases as the angle θ increases. Again, the maximum average value of 28.98 % is found at $\theta = 15°$ while at $\theta = 0°$ the average value yields 19.56 %. The average minimum break strain of 10.52 % is also found at $\theta = 75°$ while in z-direction the average break strain equals 13.7 %.

For the three quantities of yield strength, ultimate strength and break strain no clear dependency on the azimuth angle φ was observed. However, along the examined angles φ the results showed varying spread. If one extreme outlier is disregarded, the maximum spread for constant angle of leverage θ in terms of yield strength is 37.50 MPa and the average of all standard deviations over all angles θ is 10.47 MPa. For the ultimate strength the maximum spread for constant θ is 77.97 MPa and and the average of all standard deviations over all angles θ is 16.71 MPa. Accordingly the break strain yields a maximum spread of 0.1925 and overall standard deviation of 4.427 %. After averaging all values for each constant angle θ, the resulting best linear fits for the yield strength, ultimate strength and break strain are given in ***eqs. (6.1)*** through ***(6.3)***.

$$R_{p0.2} = 525.16\,\text{MPa} - \left(0.4273 \cdot \theta\right)\text{MPa} \tag{6.1}$$

$$R_{m} = 614.92\,\text{MPa} - \left(0.8324 \cdot \theta\right)\text{MPa} \tag{6.2}$$

$$A = 0.2532 - \left(0.0015 \cdot \theta\right) \tag{6.3}$$

These correlations smoothen the variations of all three quantities that were observed in dependency of the leverage angle θ. Typically, as mentioned above, global maxima and minima of the mechanical strength properties were observed at leverage angles of 15 and 75°, respectively. Furthermore, local minima and maxima could be observed at angles of $\theta = 30°$ and $\theta = 60°$. These were distinctly developed for the yield strength and the ultimate strength. The best explanation for the spread along the examined angles θ is the distribution of specimens over several batches of build processes. Each 48 specimens of identical leverage angle were fabricated simultaneously in one build process and received, therefore, identical process conditions. Although the process parameters remained unchanged throughout the whole procedure of manufacturing all specimen batches it is apparent that each build process and thus all specimens of identical leverage angle were slightly influenced individually by unknown conditions. This caused slight improvement of the mechanical properties for the 15 and 60° batches as well as slight degradation of the mechanical properties for the 0, 30 and 75° batches.

The main finding up to this point is that the mechanical strength properties of SLM solids are transversely isotropic, i.e. in the principal stress space two planes of symmetry exist. The failure surface of SLM solids is sufficiently described by the Hill48 criterion given in ***eq. (5.49)*** whose coefficients are determined according to ***eqs. (5.50)***. For the results obtained

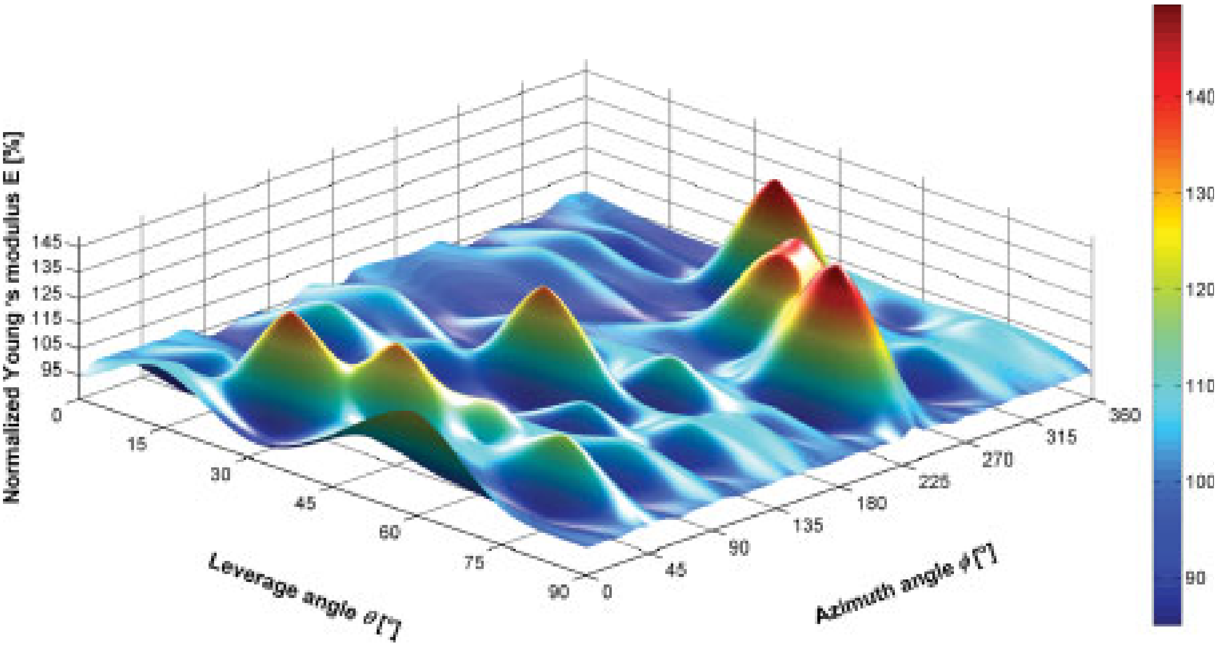

Figure 6.5: Directional dependence of Young's modulus for SLM solids

here the coefficients yield the following values: $c_\alpha = 0.4122$, $c_\beta = 0.5347$ and $c_\gamma = 0.5495$. The value for c_α differs significantly from both other values due to the reduced strength in z-direction. Theoretically, c_β and c_γ should be equal thus representing the two symmetry planes. In 3D stress space the failure surface is a cylinder which is tilted to the x-y-plane more or less depending on the deviation of coefficient c_α. Cross sections of this cylinder perpendicular to the hydrostatic axis give nearly circular shape.

Fig. 6.5 summarizes the results of the experimental analyis of the Young's moduli of all solid SLM tensile specimens. Evidently, the Young's modulus E does not dependent on the angles of leverage θ and azimuth φ. The figure shows a total of six outliers, however, most results remain close to the average value, which is normalized to 100 % here since the method of measurement allowed no determination of true absolut elasticity values. This implies that the Young's modulus is isotropic which appears reasonable since it depends on the interaction of atomic bonds of a material rather than on its microstructure, which influences the above discussed strength properties. This fact is supported by ***eq. (6.4)*** given by Gibson (1997, p. 75, [123]), which states a proportionality between the Young's modulus E, the Boltzmann constant k_B, the melt temperature of the material T_{melt} and the atomic volume Ω.

$$E \propto \frac{k_B T_{melt}}{\Omega} \tag{6.4}$$

Since, in contrast to the mechanical strength properties, the elasticity and hence Poisson's ratio of SLM solids are isotropic, their elasticity tensor according to ***eq. (5.34)*** contains only 3 distinct values, i.e. only the two engineering constants E and ν are required to fully describe the elastic behaviour of SLM solids, which are expressed more easily in the according compliance tensor **S**:

$$\begin{pmatrix} \varepsilon_{11} \\ \varepsilon_{22} \\ \varepsilon_{33} \\ 2\varepsilon_{23} \\ 2\varepsilon_{13} \\ 2\varepsilon_{12} \end{pmatrix} = \begin{pmatrix} \frac{1}{E} & -\frac{\nu}{E} & -\frac{\nu}{E} & 0 & 0 & 0 \\ & \frac{1}{E} & -\frac{\nu}{E} & 0 & 0 & 0 \\ & & \frac{1}{E} & 0 & 0 & 0 \\ & & & \frac{2(1+\nu)}{E} & 0 & 0 \\ & & & & \frac{2(1+\nu)}{E} & 0 \\ & & & & & \frac{2(1+\nu)}{E} \end{pmatrix} \cdot \begin{pmatrix} \sigma_{11} \\ \sigma_{22} \\ \sigma_{33} \\ \sigma_{23} \\ \sigma_{13} \\ \sigma_{12} \end{pmatrix} \qquad \textbf{\textit{(6.5)}}$$

In accordance with ***eq. (2.16)*** the components S_{44} through S_{66} comply with the inverse of the engineering constant G for the shear modulus.

6.2 Producibility of SLM lattice structures

6.2.1 Minimum positive feature size

After clarifying the boundary conditions for the fabrication of SLM solids the next issue is to determine the true realms of producibility for the several SLM lattice structures that were developed in ***section 5.3.3*** according to the theoretical producibility considerations made in ***section 5.3.1***. The producibility of any SLM lattice structure depends mainly on the stability of its struts. Therefore, it is important to assess the primary stability of such struts for various diameters. The lower limit of producible strut diameters, i.e. their minimum positive feature size according to the definition in ***section 3.5.2***, typically depends on the SLM technology used. If the machine configuration was changed e.g. by modifying the focal length and hence the focus diameter, then the minimum strut diameter would change accordingly. Especially the minimum strut diameter is of high interest for the ability of producing filigree yet durable lattice structures in order to obtain optimized stiffness- and strength-to-mass-ratio and to achieve the goals set out in ***section 2.2.3*** of overcoming the restrictions of alternative fabrication processes.

Some earlier experiments (Rehme, 2004) have shown that it is well possible to achieve a reproducible wall thickness of approximately 0.2 mm with stainless steel powder at particle sizes between 10 and 55 µm, which appears reasonable in regard of the expected dimensions of the melt pool width according to ***eq. (3.34)***. However, in the strategy of point-like exposure patterns as presented in ***fig. 4.2*** the melt pool width and thus the strut diameter depend mainly on the effective heat conductivity of the powder material as well as on the power of the laser beam, its focus diameter and the exposure time. The exposure time replaces the scan speed from ***eq. (3.34)*** since it has no use here. The effective heat conductivity for any powder material is much worse than for the same solid material and allows only a limited melt pool width. Therefore, the melt energy as a product of laser beam power P_L and exposure time $t_{exposure}$ according to ***eq. (6.6)*** mainly determines the resulting strut diameter. If, however, the laser beam power is kept constant, the exposure time is significantly relevant. Due to the limitations of the effective heat conductivity it is expected that for rising amounts of melt energy the additional increase of strut diameter is much smaller.

$$E_{melt} = P_L \cdot t_{\text{exposure}} \tag{6.6}$$

The goal of the minimum positive feature size experiments was to analyze the primary stability of vertical struts, to evaluate their optical appearance, which should disclose no obvious flaws and to obtain a correlation of melt energy and strut diameter. This experiment was conducted on two different SLM machines one being the machine introduced in ***section 4.2.3*** where the laser beam power was set to a constant value of 100 W in order to determine the basic correlation between melt energy and obtained strut diameter. The second machine used was a nearly identical system by the same manufacturer, however, built in 2007 and equipped with a 200 W Ytterbium fiber laser from IPG Photonics. With this machine the laser beam power was varied in steps of 20 W from 60 to 200 W.

The amount of melt energy coupled into the stainless steel powder material (previously described in ***section 4.2.2***) was determined by control of exposure time set to values between 850 and 8500 µs for the 100 W SLM machine and 250 to 20000 µs for the 200 W SLM machine. The resulting melt energies were between 0.02 and 4 J vice versa. At 100 W beam power exposure times of roughly 1000 µs at point distances of roughly 100 µm, thus giving a scan speed of 100 mm/s, allow processing of stainless steel powder materials to solid objects. However, precursor attempts at building SLM lattice structures showed that increasing the exposure time might be mandatory for the production of stable lattice structures. Therefore, the above given melt energy values represent a suitable bandwidth to achieve this goal.

In total 436 different SLM lattice micro struts were analyzed from random SLM lattice structures built at different melt energy quantities obtained from varying the exposure time and the laser beam power as indicated above. This revealed the dependency between the strut diameter and the required amount of melt energy. In the log-log diagram in ***fig. 6.6*** the obtained diameters are marked according to the given legend where the 100 W SLM machine is referred to as ‘SLM #1’ while the results for the 200 W SLM system are identified by the tag ‘SLM #2’. Each marker represents the average of measured values for a particular SLM machine at a specific laser beam power and exposure time. The standard deviations are shown as vertical error bars. As expected, the strut diameter d increases less with rising melt energy quantities E_{melt} which is best described by the power law in ***eq. (6.7)*** for which the results are given in ***table 6.1***.

$$d = c_1 \cdot \left(E_{melt}\right)^m . \tag{6.7}$$

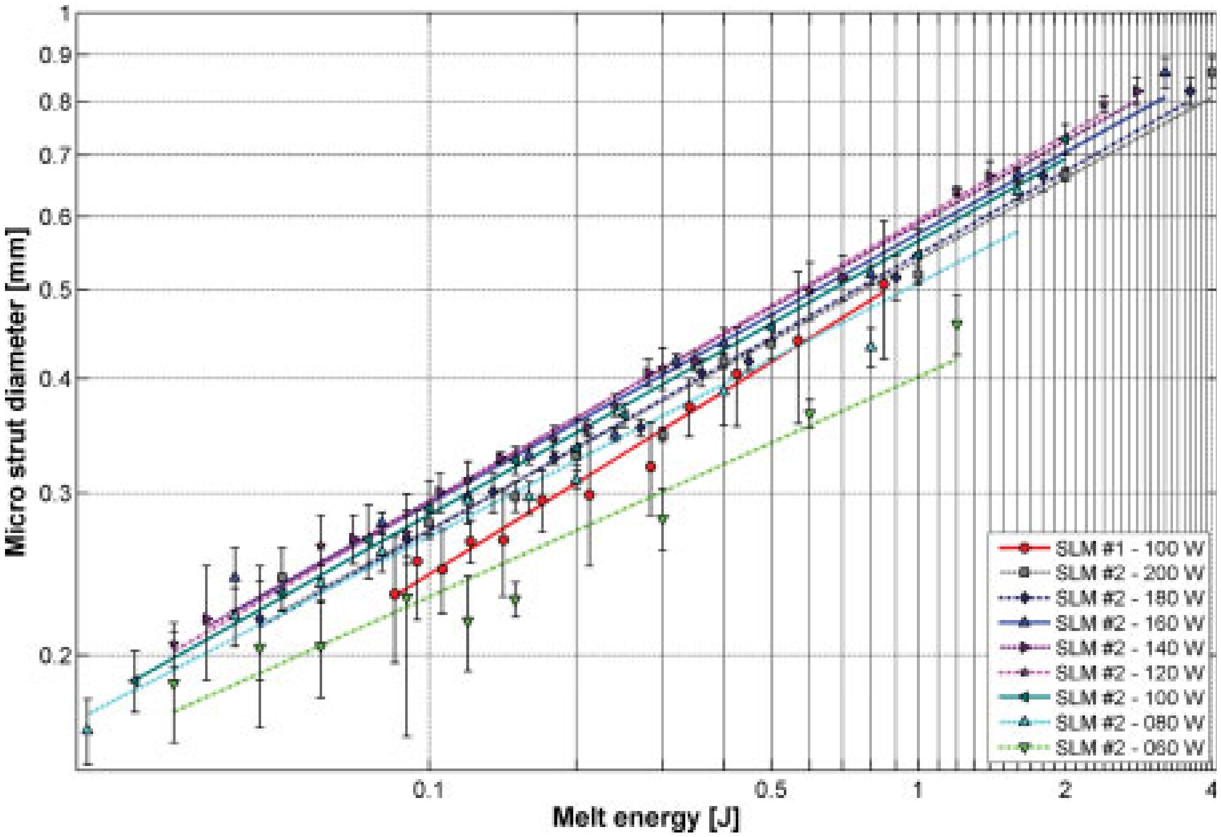

Figure 6.6: Lattice strut diameter vs. melt energy

The best fit curves in ***fig. 6.6***, which are given per each combination of SLM machine and laser beam power as solid, dashed or dash-dotted lines, show values for the exponent m in the range of 0.2393 and 0.3309 and for the factor c_1 between 0.4018 and 0.5949, provided E_{melt} is given in Joule and d should be obtained in millimeters. As apparent from the figure both investigated machines show nearly similar average strut diameters at identical melt energies independently of the laser beam power used. Only one outlier exists at 60 W which obviously yields too low beam intensity and causes a significant deviation. It is also evident that a slight

Table 6.1: Best fit coefficients for average strut diameter

SLM machine / Laser beam power P_L [W]	Factor c_1	Exponent m
#1 / 100	0.5245	0.3309
#2 / 60	0.4018	0.2393
#2 / 80	0.5083	0.2762
#2 / 100	0.5645	0.2976
#2 / 120	0.5951	0.3078
#2 / 140	0.589	0.3008
#2 / 160	0.5754	0.2939
#2 / 180	0.5461	0.3008
#2 / 200	0.5389	0.2939

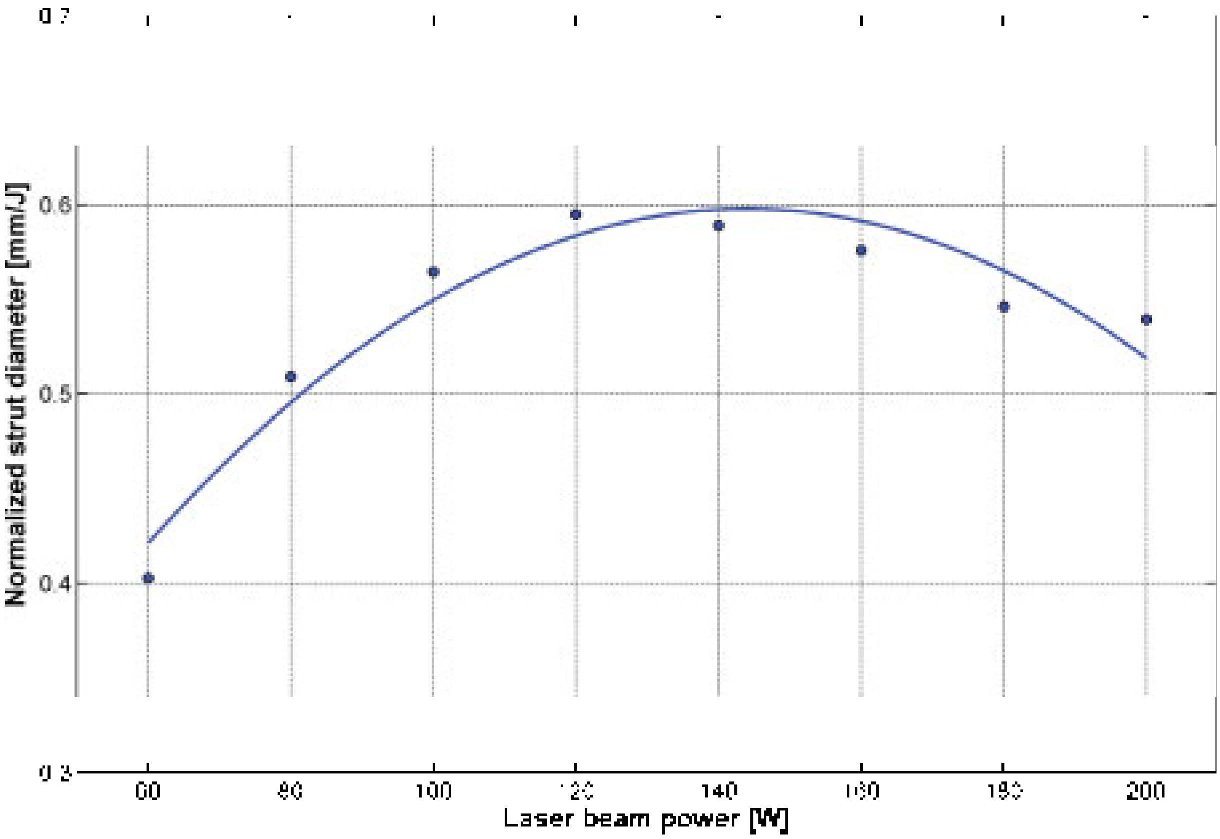

Figure 6.7: Normalized strut diameter in dependency of laser beam power

deviation exists between both considered SLM machines which is not further investigated. A detailed overview of all obtained mean strut diameters and their standard deviations is given in ***appendix 10.4*** in ***table 10.3***.

The slight displacement of each best fit curve along the y-axis of the log-log diagram in ***fig. 6.6***, observed for the experiments conducted on the 200 W SLM machine (SLM #2), appears to depend on laser beam power. In order to evaluate this for the 200 W SLM machine, each average strut diameter obtained per combination of melt energy and laser beam power is normalized to millimeters per unit melt energy of 1 J. This overall average of all normalized average strut diameters per laser beam power is identical with the proportionality factor c_1 from ***table 6.1*** of each laser beam power's according best fit power law or it can be found at the intersection of each best fit curve with the 1 J mark on the melt energy axis in ***fig. 6.6***. These overall averages are displayed versus their according laser beam power in ***fig. 6.7*** where a clear dependency between the laser beam power and the normalized average strut diameter is disclosed. A maximum of 0.5951 mm/J is found at a laser beam power of 120 W. This implies that high beam power is not necessarily beneficial to the process. A slightly greater absolute melt pool diameter can be achieved at higher laser beam power but despite of a greater focus diameter an increasingly rising part of the beam energy does not influence the lateral propagation of the melt pool such that the normalized melt pool diameter decreases. Instead the beam energy is coupled deeper into the material which is in accordance with the theory of laser deep penetration welding. Etched cross sections of stainless steel SLM solids have shown that the intensity threshold for laser deep penetration welding is easily surpassed at 200 W beam power which is usually detrimental to the SLM solid due to additional porosity developing at the bottom of the keyhole (Rehme, 2008).

The fit of the data points in the diagram are best described by a quadratic correlation which supplements ***eq. (6.7)*** to determine the expected strut diameter where the factor c_2 must be negative. ***Table 6.1*** gives all values of c_1 and m in ***eq. (6.8)*** found in the experiments. The factors c_2, c_3 and c_4 are $-2.518 \cdot 10^{-5}$, $7.244 \cdot 10^{-3}$ and 0.07708, respectively.

$$d = c_1 \cdot \left(E_{melt}\right)^m + c_2 \cdot \left(P_L\right)^2 + c_3 \cdot P + c_4 \qquad \textbf{\textit{(6.8)}}$$

6.2.2 Stability of SLM lattice structures

The stability of any SLM lattice structure is mainly affected by the primary stability of its struts and by the overall stability of the cell network. The strut stability is rather influenced by process parameters as explained in the previous section whereas the stability of the cell network depends strongly on

- unit cell type,
- length, width and height of one unit lattice cell as well as
- micro strut diameter

in considered SLM lattice structures. Subsequently, these three factors are investigated. In such an examination the unit cell edge lengths may be chosen arbitrarily which offers a wide range of variations for producibility examinations. As mentioned in ***section 5.2.1*** the theoretical analysis in this thesis considers only identical dimensions for all unit cell edges for two reasons. The same assumption is valid for the experimental analysis in order to not increase the complexity of the examinations, and secondly, because higher strength and stiffness should be expected from SLM lattice structures with identical unit cell edge lengths. Therefore, the main unit cell design parameters remain the unit cell size a and the strut diameter d along with the 14 unit cell types as developed in ***section 5.3.3***. The ratio of unit cell size to strut diameter a/d is the aspect ratio which was used throughout ***section 5*** for considerations of struts as flexible beams. This term is as well useful to describe dimensions that a manufacturing process can produce such as ratios of e.g. bore hole depth and diameter. Therefore, the goal of the next experimental investigation is to determine the producibility limitations of SLM lattice structures when cell sizes and strut diameters are varied, i.e. each cell type's maximum aspect ratio is obtained. Apparently, aspect ratios here must be greater than one otherwise no lattice structures but solids with pores will be obtained.

The cell stability may be influenced by process deficiencies. Build errors can occur e.g. by lack of proper attaching of the first few layers of some struts to the building platform. This may be caused by poor preparation of the building platform, unleveled powder application leading to a partially too thick layer of powder, insufficient strength of supports or many other reasons. Typically, this type of build error is self-repairing to a certain degree since struts can still develop over areas with such deficiencies. With increasing progress in the build process these struts can grow along face and body diagonals of adjacent unit cells as shown in one extreme example in the left part of ***fig. 6.8*** where initially nearly all except for two supports of the SLM lattice structure did not attach to the building platform. However, over the course of the build process this lattice structure recovered due to growth along the directions indicated by red arrows. Generally, for functional parts such process deficiencies are not acceptable, however, an important conclusion drawn from this observation is that a smaller build error in e.g. a single strut, which is not properly connected in the inner SLM lattice structure, is compensated as shown in the red circle of the right part in ***fig. 6.8***.

The likelihood of the occurence of such build errors can be reduced if the maximum aspect ratio is regarded for each specific cell type. In order to assess these build limitations a total of 1680 test specimens were produced. All 14 different unit cell types were built on the SLM machine introduced in ***section 4.2.3*** with variable melt energies from 0.085 to 0.85 J (according to the red, circular data points in ***fig 6.6***) in order to obtain variable strut diameters while applying a constant laser beam power of 100 W which is near the optimum power according to ***fig. 6.7***. The diameters were combined with variable cell sizes of 1, 1.5, 2, 2.5, 3, 4, 5, 6, 8 and 10 mm. From the resulting specimens of which a sample result for cell type *bcc* is presented in ***fig. 6.9*** it is clearly recognizable that the robustness of SLM lattice structures is reduced with decreased melt energy and with increased cell size. An overview of all specimens is given in ***appendix 10.5*** in ***fig. 10.7***.

Before evaluating the specimens, three different grades of cell stability are distinguished. The desired grade is where SLM lattice structures show no build errors at all whereas the second grade comprises minor imperfections and the third grade shows major imperfections or no cell network coherence at all. A sample result for the cell type *bcc* is given in the log-log diagram in ***fig. 6.10*** where the cell size is displayed versus the melt energy. The results for all remaining cell types are given in ***appendix 10.5*** in ***fig. 10.8***. In ***fig. 6.10*** the area of perfect cell stability with no build errors at all is found below the green curve, i.e. the lower curve. Above the green and below the orange (upper) curve minor imperfections are found in the lattice structures. Above the orange curve major imperfections or no cell coherence prevails. Additionally, a best fit derived from the green curve is represented by a black, solid line.

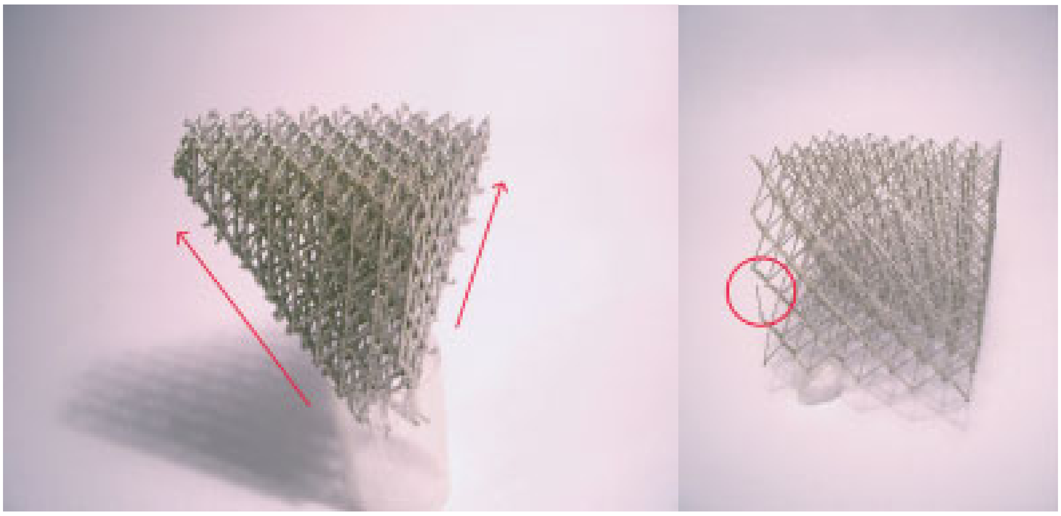

Figure 6.8: Build errors in SLM lattice structures

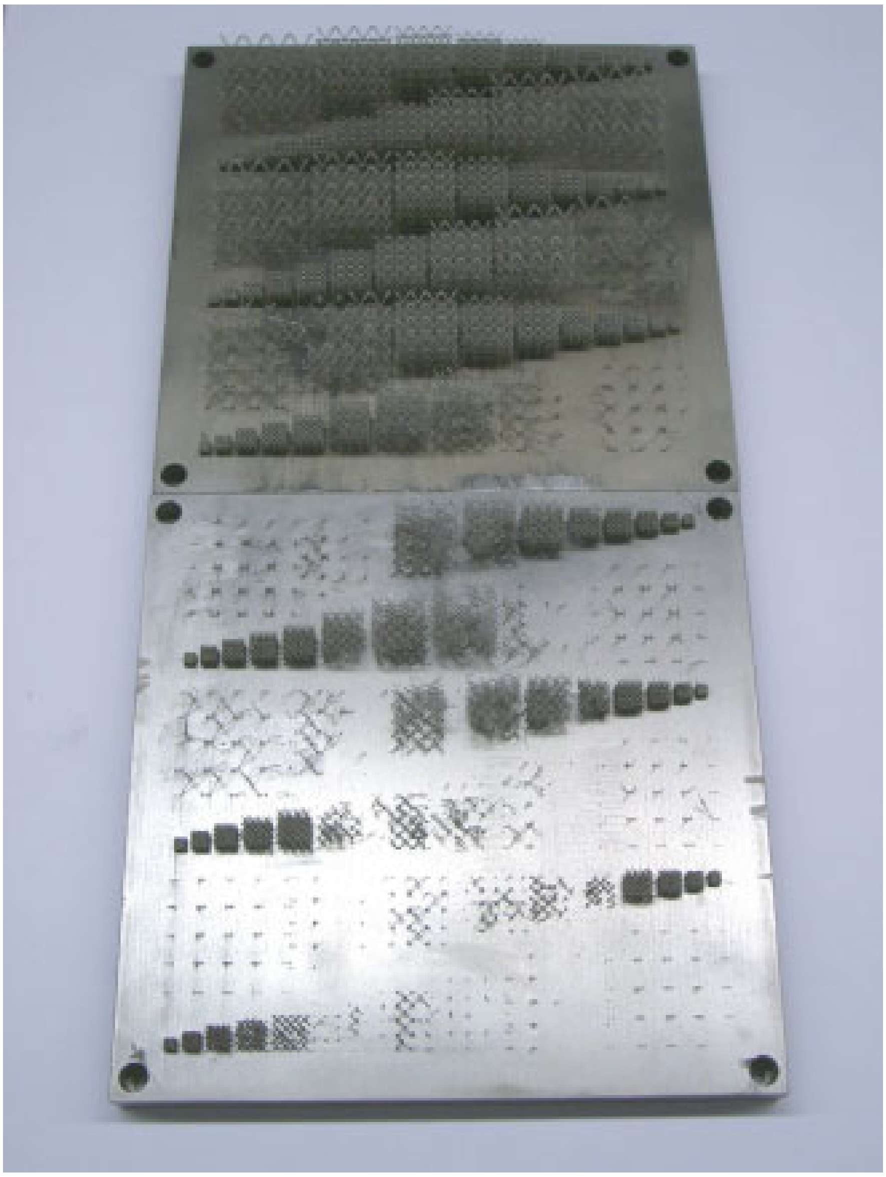

Figure 6.9: Obtainable aspect ratio experiment for cell type *bcc*

In 7 out of all 14 cell types logarithmic fits give the highest coefficient of determination R^2 while power law fits are more suitable for the remaining 7 cell types. However, a power law fit is more recommendable since the strut diameter correlation in ***eq. (6.8)*** is similar, which involves a power law depending on the melt energy as well. Additionally, the average coefficient of determination for power law fits of all 14 cell types is higher than for logarithmic fits of all cell types, i.e. $R^2 = 0.9343$ compared to 0.9179. Therefore, a power law SLM lattice structure stability criterion is derived which describes the maximum obtainable cell size a (in millimeters) in dependence of the applied melt energy E_{melt} (given in Joule). The coefficients c_5 and n in ***eq. (6.9)*** represent each according best fit of the green curve for all 14 cell types according to ***table 6.2***.

$$a = c_5 \cdot \left(E_{melt}\right)^n \tag{6.9}$$

Eq. (6.9) cannot be simply expressed by the obtainable aspect ratio but with ***eq. (6.7)*** it can be rewritten as

$$a = c_5 \left(\sqrt[m]{\frac{d}{c_1}} \right)^n \qquad \textbf{\textit{(6.10)}}$$

where m and n are taken from ***tables 6.1*** and ***6.2***, respectively.

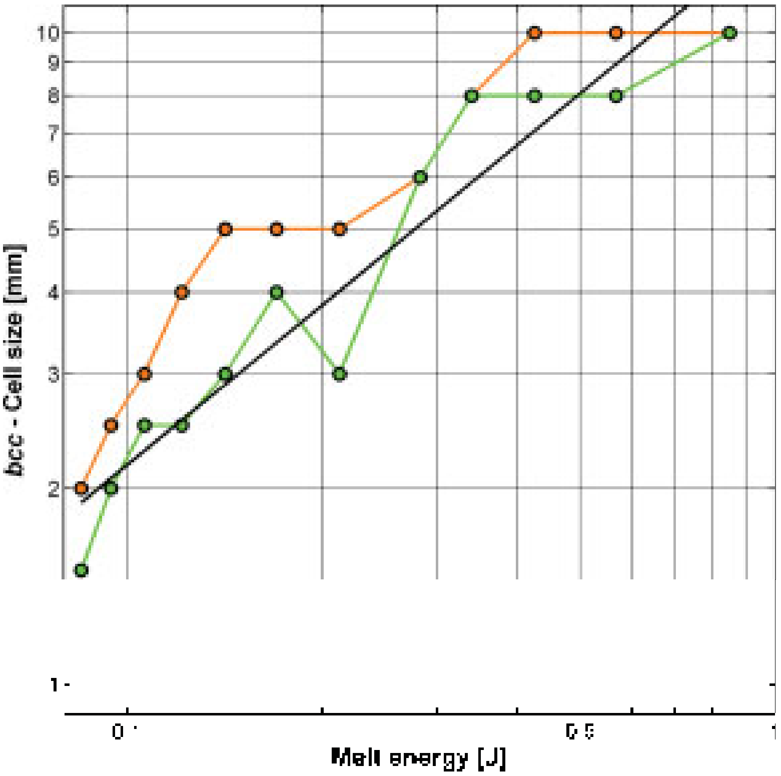

Figure 6.10: Results for obtainable stability of cell type *bcc*

Table 6.2: Best fit coefficients for SLM lattice structure stability criterion in *eq. (6.9)*

Rank	Unit cell type	Factor c_5	Exponent n
1	f_2bcc_z	14.73	0.8964
2	*bcc*	14.19	0.8149
3	f_2cc_z	13.04	0.8965
4	bcc_z	12.98	0.725
5	f_2bcc	11.91	0.808
6	f_2cc	11.09	0.9814
7	fcc_z	9.013	0.7934
8	hp_{2d}	8.439	0.4937
9	*RD*	8.399	0.6491
10	hp_{2ud}	8.248	0.4667
11	*TRD*	7.370	0.5859
12	hp_{2u}	7.305	0.4877
13	*fcc*	6.859	0.8928
14	*hp*	5.757	0.5904

Subsequently, the experiments revealed a large bandwidth of possible aspect ratios for each cell type, however, at specific strut diameters noteworthy aspect ratios were found. The overall maximum value obtained was 22.73 for cell type *f_2bcc_z* at an average strut diameter of 0.44 mm (0.5677 J melt energy) whereas the minimum was 3.390 for *fcc* at an average strut diameter of 0.295 mm (0.17 J melt energy). The theoretical approach in ***section 5.3.1***, ***eq. (5.89)*** predicted aspect ratio ranges between 14.45 and 26.4 which rise non-linearly with increasing strut diameter and an approximate possible cell size of 13.2 mm at a strut diameter of 500 µm. The experimental results are of the same magnitude and, therefore, in good agreement with these theoretically predicted values.

The best fit of the (green) curves of all cell types in ***fig. 10.8*** representing stable cell networks are compared in ***fig. 6.11***. The best fit coefficients are given in ***tables 6.2*** where all cell types are ranked according to the intercept value c_5 of the best fit curve, hence those types with the potentially highest obtainable aspect ratio at low melt energies are listed first. For easier comparison the results from ranks 1 to 5 in ***tables 6.2*** are given as solid, green lines, while ranks 6 to 7 are given as dot-dashed, blue lines and ranks 8 to 14 as dashed, red lines. Surprisingly, the cell types *f_2cc_z*, *bcc* and *bcc_z* rank very high although they comprise a significantly lower relative density than e.g. *f_2bcc_z*. Therefore, these cell types should be of

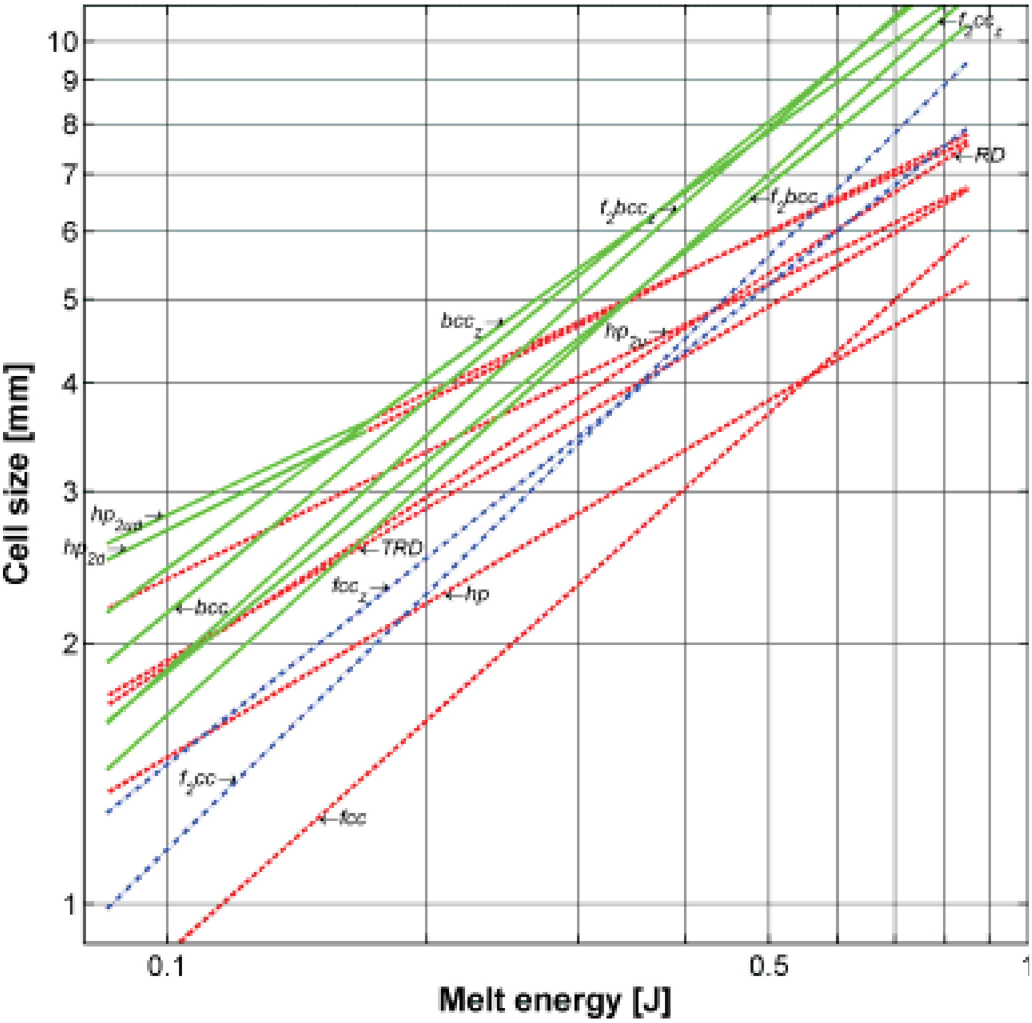

Figure 6.11: Best fit evaluation of obtainable aspect ratios for all cell types

special interest for further considerations. The main characteristic of the green curves is that they show a suitable combination of high intercept and high slope values in the log-log-diagram which yields high average aspect ratios. However, two cell types are an exemption to this. The slopes of cell types hp_{2d} and hp_{2ud} are too low to be seriously considered, however, at very small strut diameters below approximately 0.295 mm (0.17 J melt energy) they appear to exhibit high aspect ratio values.

To ensure primary stability of SLM lattice structures it is recommended that unit cells are designed such that the stability criterion in ***eq. (6.9)*** is fulfilled. The experimental results found here suggest that cubic unit cell types and among these preferably those with body diagonals allow the best producibility over a broad range of cell sizes and strut diameters. However, in specific applications other cell types may be beneficial. Therefore, all cell types are subject to further investigation.

6.3 Development of test procedures

6.3.1 Test utilities, test conditions and sample sizes

All mechanical testing for this thesis was conducted using a Zwick single lead-screw universal testing machine model 1455 (20 kN maximum force, 1000 mm maximum travel) and a Hegewald & Peschke double lead-screw universal testing machine (150 kN maximum force, 1100 mm maximum travel). In order to ensure precise results the stiffness of either testing machine was determined before specimens were tested. The machine stiffnesses were obtained indirectly from testing cylindrical, solid stainless steel specimens of known Young’s modulus in the compressive elastic region. This approach can be considered as a serial connection of springs of spring constant D_i according to ***eq. (6.11)*** in which the constant of one spring, i.e. a stainless steel specimen, is known and the constant of the second spring, i.e. the universal testing machine, can be derived from the measured total spring constant as shown in ***eq. (6.13)***. The spring constant of the compressive test specimen is derived according to ***eq. (6.12)*** from its geometry where A is the cross section area and l_0 is the length as well as from the Young’s modulus of stainless steel. Thus the spring constant D of the Zwick 1455 testing machine is determined to 59.33 kN/mm and of the Hegewald & Peschke testing machine to 48.01 kN/mm.

$$\frac{1}{D_{total}} = \sum_i \frac{1}{D_i} \tag{6.11}$$

$$D = \frac{EA}{l_0} \tag{6.12}$$

$$D_{\text{testing machine}} = \frac{1}{\frac{1}{D_{total}} - \frac{l_0}{EA}} \tag{6.13}$$

Subsequently, it becomes possible to determine the true Young's modulus of solid as well as cellular specimens based on ***eq. (6.14)*** where *A* and l_0 determine the specimen's initial geometry and *ΔF* and *Δl* are force and displacement measured in the elastic region.

$$E_{true} = \frac{\sigma}{\varepsilon} = \frac{\Delta F}{A} \cdot \frac{l_0}{\Delta l_{true}} = \frac{\Delta F \cdot l_0}{A \cdot \left(\Delta l - \frac{\Delta F}{D_{\text{testing machine}}} \right)} \qquad \textbf{\textit{(6.14)}}$$

Before conducting full-factorial strength tests on SLM lattice structures it is important to not only narrow down the most promising cell types and produce the required test specimens in accordance with the results from ***section 6.2*** but to also consider size effects in the specimens. These size effects can occur, which distort the obtained results such that e.g. specimen strengths or stiffnesses appear smaller than they actually are, if the number of unit cells perpendicular to the load direction is chosen too small. They can arise from mainly two sources. One is the reduced constraint of cells and their struts at the side of specimens compared to those cells in the bulk of specimens. A second effect, though of minor significance for SLM lattice structures, is the influence of stress-free struts in cut cell edges due to e.g. inappropriate post-processing. Based on theoretical considerations from Onck (2001, pp. 682-688, [221]) it is apparent that the Young's modulus and the strength of specimens scale with the inverse of the amount of cells perpendicular to the load direction. For higher number of cells both properties quickly converge against those of specimens of infinite width. The calculations made by Onck suggest that using specimen widths of at least eight cells perpendicular to the load direction leaves a remaining error of approximately 6 % for stiffness results and of even 12 % for strength results. This appears too high, however, it is acceptable since due to this error stiffness and strength of specimens are rather underestimated. Ashby (2000, pp. 26-27, [17]) conducted experimental investigations which back these results. In uniaxial compressive testing specimens made from the open-cell aluminum sponge ERG Duocel and from the closed-cell aluminum foam Alporas showed clearly that specimen widths of seven or more cell sizes showed no further increase in Young's modulus and strength. Experimental results for the exact same materials obtained by Andrews (2001, p. 704, [12]) even gave rise to a minimum specimen width of six cells as a sufficient lower limit. From these results it is concluded that all compressive and tensile specimens tested in this thesis must at least comprise eight unit cells in sample width perpendicular to the direction of the applied test force. For shear experiments Ashby determined a minimum specimen width of three unit cells. This, however, is exceeded for all shear specimens in this thesis as they were equipped with a minimum of eight unit cells in each direction.

In order to achieve optimal specimen preparation the post-processing must be chosen carefully. Therefore, throughout the fabrication of specimens for this thesis all samples were separated from the building platform solely by wire EDM. Thus plain surfaces without fractions of cells were obtained in all samples which is of highest importance especially in compressive tests in z-direction.

6.3.2 Compression strength tests

For all compressive specimens the constraints from DIN 50134 (2007, pp. 3-9, [86]) apply. This implies that all testing has to be conducted at temperatures of 23±5°C. The effective Young's modulus of specimens is derived from the secant of the elastic unloading curve and a subsequent elastic loading curve in the stress-strain diagram according to Lu (1999, p. 7531, [189]) and Ashby (2000, p. 42, [17]). Each specimen is tested until significantly crushed during which the first unloading should be initiated at 70 % of the plateau stress, which is e.g. shown in ***fig. 2.10***. Characterization of elastic properties is generally not trivial, therefore, some researchers have previously used ultrasound analyses which, however, are not employed here. As opposed to solid materials where yield is typically characterized by 0.2 % plastic deformation DIN 50134 suggests to define the yield point at 1 % plastic deformation in which the according yield strength σ_{yield} is also referred to as R_{p1}. The onset of densification of cellular specimens is defined as 130 % of the plateau stress. Therefore, energy absorption is measured up to this point according to ***eq. (2.33)*** unless it is defined as the energy absorption at 20, 40 or 60 % strain due to lack of e.g. a clearly distinguishable plateau stress.

The requirements mentioned regarding the universal testing machine are met by the boundary conditions introduced in ***section 6.3.1***. All compressive specimens are held fixed by two parallel plates with minimum hardness of 60 HRC. The interface between the plates and the specimens are lubricated with e.g. graphite.

The norm recommends specimen sizes of at least 10 cells in each direction of space. However, this recommendation is made due to the stochastic nature of foams and sponges. Since the specimens investigated here are strictly periodic and due to the results presented in ***section 6.3.1*** the minimum specimen size for all compressive specimens is determined to 8 cells and to 10 cells for smaller cell sizes. It is also recommended that the length-to-width ratio of compressive specimens be 1.5 to 2. However, this recommendation is not followed due to the high number of expected specimens which require considerable build-time. This procedure is supported by some results obtained from Mukai (1999, p. 923, [213]) who found that the specific yield strengths of compression samples of one type of cellular material give constant values provided that the specimen height does not fall below a minimum value. From these results it is derived that the minimum specimen height should be at least 2/3 of the width. Therefore, a length-to-width ratio of 1 is determined for all compressive specimens.

The norm also recommends a minimum of at least three specimens. This is approved as the minimum number of specimens for each direction of space to be tested. Also, all outer dimensions of the individual specimens should be measured with better than 1 % accuracy at a minimum of at least three different reading points. For the specimens of this thesis a digital calliper with an accuracy of 0.01 mm was used which fulfills the accuracy requirements for the specimen dimensions defined below. The norm recommends a strain rate of 10^{-3} s^{-1} which for specimen lengths between 15 and 50 mm gives absolute displacement velocities between 0.3 and 3 mm/min. For reasons of simplification the displacement speed is set to a constant value of 3 mm/min which is considered quasi-static.

The compressive testing is divided into two stages for which cuboid shaped specimens are made with the SLM machine introduced in ***section 4.2.3***. The first stage is conducted with all 14 cell types at one specific cell size of 2.5 mm and the average strut diameter of 0.507 mm which was found in ***section 6.2.1*** for 0.85 J of melt energy. The second stage is conducted only with the most promising cell types from the first stage, however, regarding the results from the producibility investigations. In this stage cell sizes from 0.5 to 6 mm are examined. The strut diameter is not varied but kept constant for all specimens for one particular reason. For larger cell sizes the maximum obtainable aspect ratio may be exceeded if too small strut diameters are applied and specimens might not be producible. Therefore, to ensure comparable results across all specimens, only the expected average strut diameter of 0.507 mm and thus a melt energy of 0.85 J are employed.

6.3.3 Tensile strength tests

Generally, all boundary conditions introduced in ***section 6.3.2*** apply to the tensile strength test specimens and procedures as well. All methods are maintained in a likewise fashion in compliance with the norms DIN EN 10002 (2001, pp. 1-43, [90]) and DIN 50125 (2004, pp. 1-11, [85]). However DIN 50125 suggests that the initial length L_0 of tensile specimens should be five times the initial diameter d_0. In order to reduce build-time for the numerous specimens this recommendation is disregarded and the length of all specimens is determined to 1.5 times the width.

The shape of the flanges deviates from the norm as well. The end faces are equipped with plate-like flanges which can be accommodated in both grooves of the bracket shown in ***fig. 6.12***. Two such brackets are required for attaching one tensile specimen to the universal testing machine. The flanges are fabricated as solids simultaneously with the specimens in such a way that the end face cell rows grow partially into the flanges to ensure a safe bond between the flanges and the SLM lattice structure. The norm ASTM C 297 (1988, p. A-4, [20]) gives suggestions on the design of tensile sandwich structures. The composition of SLM lattice structures with solid SLM flanges is similar to sandwich structures. ASTM C 297 derives the minimum facing area for the bond which for cell sizes up to 6 mm should be at

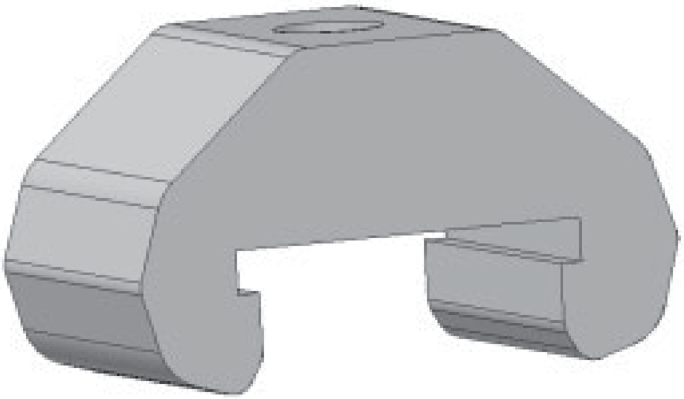

Figure 6.12: Bracket for retaining one flange of a tensile specimen

least 625 mm^2, i.e. 25 mm length on each side for specimens with rectangular cross section. The norm also implies that the bond between the flange and the actual specimen should not affect its core. In order to meet this criterion and to avoid failure of the cells near the flanges all struts within two cell rows of the flanges are subject to double laser beam exposure in the point-like exposure strategy, giving a total melt energy of 1.7 J per point. This increases the strut diameter to approximately 0.7 mm as opposed to 0.507 mm in the core.

The tensile testing is conducted with the same cell types from the second stage of the compressive testing. Again, the strut diameter is kept constant at an average of 0.507 mm to ensure specimen stability while the cell sizes vary from 1.5 to 6 mm. All specimens comprise 15 cells in length and 10 cells in width except for the 6 mm cell specimens which comprise 12 cells in length and 8 cells in width to limit specimen sizes and build-time. All tensile specimens are tested at the same displacement velocity as the compressive specimens at 3 mm/min. According to the norm DIN EN 10002 strain rates between 0.00025 and 0.0025 s^{-1} and temporal stress gradients between 2 and 20 MPa/s should be used if the Young's modulus of the material is below 150 GPa, which applies to SLM lattice structures made of stainless steel with relative densities significantly lower than unity. These requirements are met as the resulting strain rates for 5 and 1.5 mm are $6.667 \cdot 10^{-4}$ and $2.222 \cdot 10^{-3}$ s^{-1} which gives maximum stress gradients of 2.269 MPa/s.

6.3.4 Shear tests

Shear specimens are more intricate to fabricate than compressive or tensile specimens due to the relatively large area of the cover plates which surround the core and due to the additional fixtures that have to be attached for clamping the specimens in the testing machine. In order to avoid having to build large solid areas in the x-y-plane the shear specimens are restricted to shear testing in the y-z-plane only. The norm ASTM C 273 (1988, p. A-1, [19]) recommends a minimum width of twice the thickness and minimum length of 12 times the thickness for shear specimens. This further restricts the possible range of specimen sizes since the thickness must meet the minimum number of cells requirement introduced in ***section 6.3.1***. Here, all shear specimens receive a thickness according to the size of eight unit cells.

According to the norm DIN 53294 (1982, pp. 1-2, [89]) a typical setup for shear experiments comprises a specimen which is loaded such that the effective stress direction runs diagonally across the specimen's core, from one cover plate to the other. However, if the minimum length criterion is not fulfilled, the error produced from diagonal loading without adjusting the calculation of shear strength and modulus is unacceptable. Therefore, a symmetric design is chosen where one middle plate is placed between two cores, to which two additional cover plates were attached. Consequently, only half of the measured forces can be accounted for the estimation of shear strengths and moduli. In order to avoid failure of the cells near the middle or cover plates all struts within two cell rows of the plates are subject to double laser beam exposure in the exact same way as described for the tensile specimens in ***section 6.3.3***. Likewise, this increases the strut diameter to approximately 0.7 mm near the plates as opposed to 0.507 mm.

Due to the size limitations of the building platform only one set of shear specimens is considered for testing of the same cell types from the second stage of the compressive testing. For each cell type three specimens are examined. To ensure usable results a cell size of 3 mm is chosen which gives a core thickness of 24 mm. According to DIN 53294 length and width of such cores should be 400 and 100 mm, respectively, whereas compared to ASTM C 273 it should be 288 and 48 mm, respectively. The size limitations require that the core length has to be reduced to 200 and the width to 50 mm, in compliance with cores of less than 20 mm thickness as described by DIN 53294. Recently, some investigators have also disobeyed the minimum length requirements with still satisfying results as reported by Saenz (1998, p. 84, [262]). Therefore, the final core dimensions become 24 by 204 by 51 mm or 8 by 68 by 17 unit cells. For stiff cores the norm requires that all dimensions of the individual specimens should be measured with better than 1 % or 0.001 mm accuracy. The exact same procedure described in ***section 6.3.2*** using a digital calliper satisfies the relative accuracy requirement, however, its resolution remains limited to 0.01 mm. On one side of each specimen both outer cover plates are connected with a flange which is arranged perpendicularly to them. Likewise, the other end receives a flange attached to the middle plate, parallel to the first flange. Both flanges are compatible with those from the tensile tests, therefore, the shear specimens could as well be investigated by means of the brackets shown in ***fig. 6.12***.

The displacement velocity of 3 mm/min equals that of both the compressive and the tensile tests, however, the resulting strain rate of $2.451 \cdot 10^{-4}\ s^{-1}$ is higher than the strain rate of $8.333 \cdot 10^{-5}\ s^{-1}$ suggested by ASTM C 273. This is considered not harmful as the stress gradient of 0.04194 MPa/s is far below the maximum value of 10 MPa/s given by DIN 50141 (1982, p. 2, [87]). This norm as well as DIN 53290 (1982, p. 3, [88]) define the shear strength of a specimen as the ultimate stress which occurs during testing. This definition deviates substantially from the strength definition in compression and tension and is adapted here. The effective shear modulus should be derived from the secant in the elastic regime of the stress-strain diagram obtained from the tests as suggested by ASTM C 273. This method is adapted as well, however, the suggestion to calculate the effective shear modulus from the Young's moduli of the plates and the cores is neglected since in the specimens considered here, the plate's modulus is typically much higher than that of the core.

6.4 Test of specific strength in dependence of cell type

Before testing the elasticity and strength properties of numerous specimens of various cell types and cell sizes, the range of cell types is reasoned on the basis of precursor experiments. In order to investigate the specific strengths of different cell types, i.e. their strength per unit weight, compressive specimens of constant cell size and constant strut diameter are defined. A set of 126 specimens is designed accordingly, 9 of each of the above developed 14 cell types of which each three were tested under uniaxial compression in the x-, y- and z-direction. For reasons of good comparibility between all cell types the cell size is chosen to 2.5 mm and the strut diameter is defined according to the maximum melt energy in ***fig. 6.6*** used with the

SLM machine introduced in ***section 4.2.3***, i.e. 0.85 J giving an average strut diameter of 0.507 mm, in order to avoid insufficient strut stability especially in cell types of low relative density. All specimens are of cubic shape with 10 x 10 x 10 cells as shown in ***fig. 6.13***.

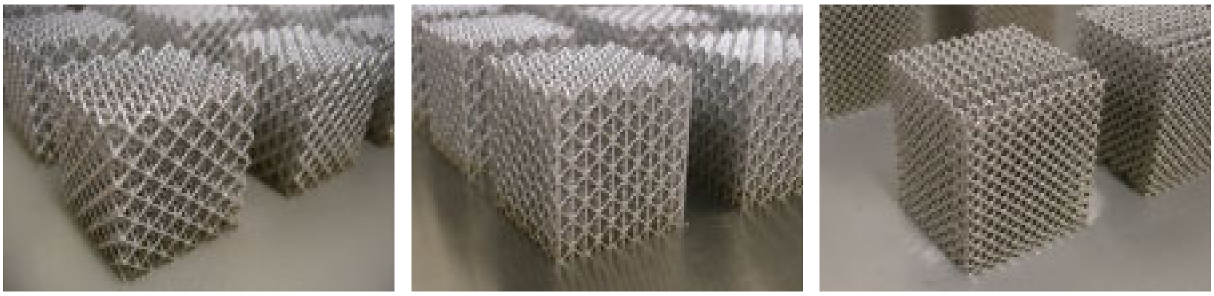

fcc *fcc_z* *f_2cc*

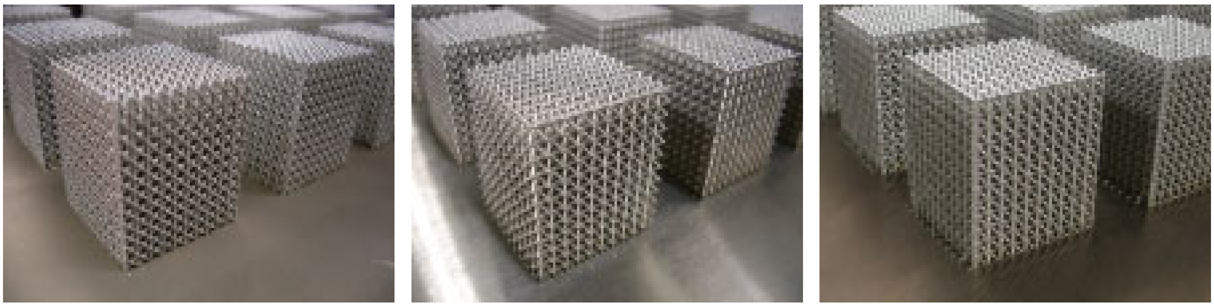

f_2cc_z *bcc* *bcc_z*

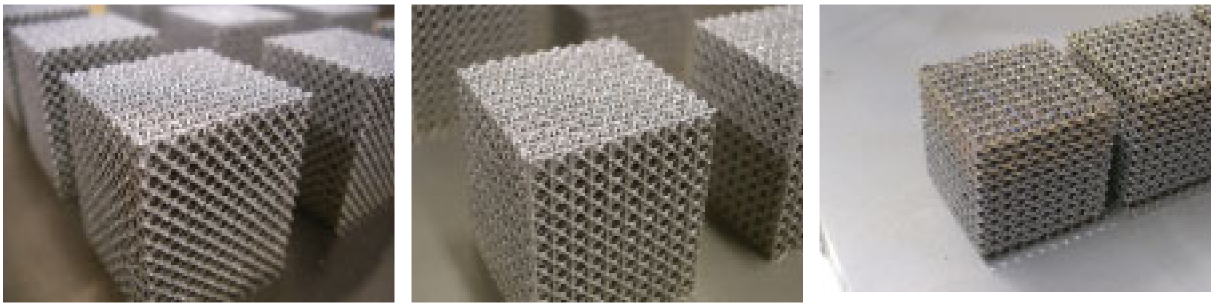

f_2bcc *f_2bcc_z* *RD*

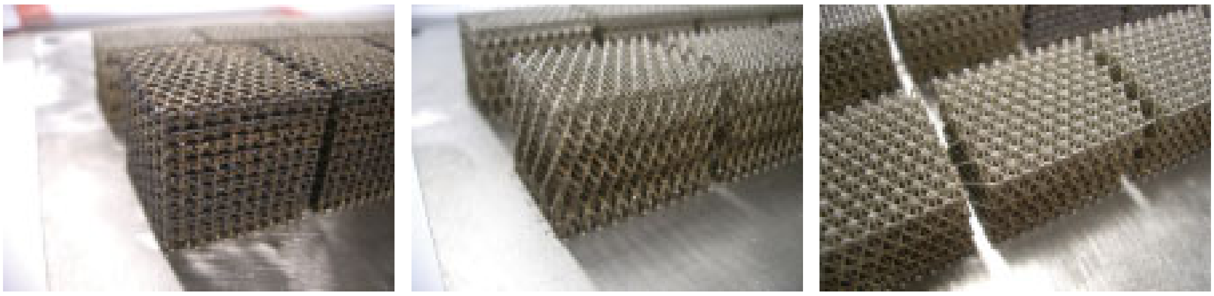

TRD *hp* *hp_{2u}*

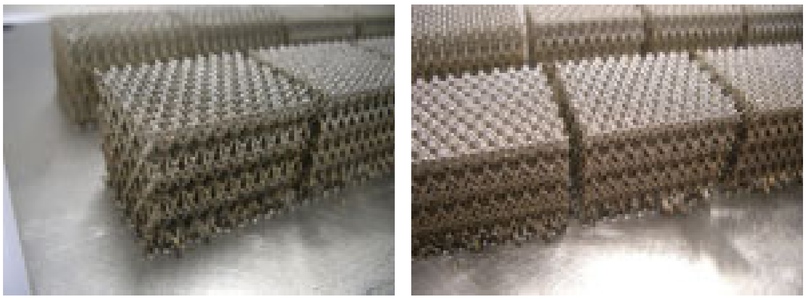

hp_{2d} *hp_{2ud}*

Figure 6.13: Test specimens for specific strength tests on all cell types

Table 6.3: Results for average relative density, strengths, specific strengths and energy absorption

Cell type	ρ^*/ρ_{solid} [1]	Std. dev. [1]		Yield strength R_{p1} [MPa]	Std. dev. [MPa]	Specific yield strength [MPa/kg]	Energy absorption W [MJ/m^3]
fcc	0.05571	$8.403\cdot10^{-4}$	x	1.146	$2.222\cdot10^{-2}$	138.7	0.4064
			y	1.267	$1.384\cdot10^{-2}$	149.1	0.4624
			z	1.173	0.1235	137.9	0.5335
fcc_z	0.08098	$1.911\cdot10^{-3}$	x	3.254	$8.945\cdot10^{-2}$	268.2	0.5999
			y	3.081	$7.146\cdot10^{-2}$	254.8	0.6443
			z	6.599	0.4391	543.6	1.872
f_2cc	0.1051	$8.933\cdot10^{-4}$	x	5.775	0.2277	374.9	1.456
			y	5.560	0.3420	349.3	1.502
			z	6.849	0.3863	449.6	3.243
f_2cc_z	0.1273	$2.393\cdot10^{-3}$	x	8.078	0.4599	421.0	1.612
			y	7.900	0.8313	418.5	1.765
			z	14.39	0.7396	773.6	6.657
bcc	0.1685	$1.882\cdot10^{-3}$	x	6.242	0.6639	264.0	2.926
			y	5.256	$9.200\cdot10^{-2}$	213.7	2.604
			z	6.238	0.4024	256.7	3.637
bcc_z	0.1860	$3.645\cdot10^{-3}$	x	7.397	0.1127	267.1	3.693
			y	7.084	0.4312	249.6	3.410
			z	12.53	0.3280	444.0	7.580
f_2bcc	0.2485	$3.218\cdot10^{-3}$	x	19.39	0.7575	515.5	8.964
			y	15.74	1.100	410.1	7.538
			z	15.08	0.4132	408.4	7.683
f_2bcc_z	0.2687	$4.777\cdot10^{-3}$	x	21.49	0.7705	539.0	11.78
			y	17.40	0.4087	431.0	8.987
			z	22.18	0.9214	539.0	14.23
RD	0.2183	$2.169\cdot10^{-3}$	x	22.91	0.4331	752.4	14.25
			y	20.40	0.2914	673.9	13.30
			z	14.83	0.2246	494.3	8.644
TRD	0.2695	$5.794\cdot10^{-3}$	x	20.85	0.4968	568.1	11.52
			y	21.10	0.4447	550.2	12.75
			z	17.22	2.186	450.6	13.74
hp	0.09293	$5.943\cdot10^{-3}$	x	0.9633	$6.545\cdot10^{-2}$	126.4	0.4175
			y	0.5457	$2.472\cdot10^{-2}$	69.5	0.2743
			z	4.330	0.1402	557.1	1.221
hp_{2u}	0.1402	$3.135\cdot10^{-3}$	x	4.404	0.3026	368.0	1.761
			y	2.105	0.1266	170.6	1.281
			z	11.86	0.5570	1004	3.943
hp_{2d}	0.1386	$3.423\cdot10^{-3}$	x	3.602	0.3134	305.9	1.623
			y	2.457	0.1187	196.0	1.235
			z	12.18	1.077	1034	4.113
hp_{2ud}	0.1997	$7.706\cdot10^{-3}$	x	6.033	0.8106	335.7	3.359
			y	3.870	0.2266	228.4	2.001
			z	10.30	$9.265\cdot10^{-2}$	606.5	6.297

All specimens are tested according to the boundary conditions set in ***section 6.3.2*** after their dimensions and their weight are measured to calculate their relative density. During testing, force-displacement values are recorded from which stress-strain diagrams are derived. These are evaluated and the most important mechanical results such as the achieved average relative densities and their standard deviations, the yield strengths under compressive loads in x-, y- and z-direction as well as their standard deviations, the specific yield strength and the energy absorption in each direction are assessed. All values are summarized in ***table 6.3***. The specific yield strength and energy absorption are derived at this point since these figures are very suitable to judge the performance of different cell types.

The main findings obtained from the compressive tests are that some SLM lattice structures fulfill certain tasks better than others depending on the requirements. Cell types such as *fcc*, f_2cc, *bcc*, f_2bcc and f_2bcc_z show rather isotropic mechanical behaviour, whereas e.g. fcc_z, f_2cc_z and bcc_z are highly anisotropic with a distinct difference of the strength in z-direction compared to the other directions. All tetrahedral structures show even a significantly higher strength in z-direction compared to the other directions. To further assess the use of certain SLM lattice structures it is helpful to consider their specific yield strengths. Apparently, SLM lattice structures normally achieve higher specific yield strengths than other cellular materials. Aluminum foams typically range around 200 MPa/kg. The cell types hp_{2u} and hp_{2d}, however, even achieve values of above 1000 MPa/kg in at least one direction. For the first eight cell types in ***table 6.3*** it was expected that the yield strengths in x- and y-direction are identical. However, average strengths are slightly reduced in the y-direction. The reason for this behaviour remains unclear. The cell type *bcc*, which in ***section 6.2.2*** was found to show high stability during build-time despite a comparatively low relative density, turns out to be disappointing since its specific yield strength is the second lowest overall.

Most of the 14 unit cell types can be clustered in certain groups. If the results from ***table 6.3*** are arranged in log-log diagrams such that yield strengths are displayed versus relative densities for each direction of compression, then three diagrams like those in ***fig. 6.14*** through ***6.16*** are obtained. The results for cubic unit cells without body diagonals (blue), for cubic unit cells with body diagonals (green) and for tetrahedrals (red), which are all highlighted with result markers according to the legends in the three figures, can be linked with power law fits. Since only two data points exist for the polyhedral cell types (yellow), no best fit is derived for *RD* and *TRD*. The best fit curves yield power laws which are given in the diagrams as well.

From this procedure suitable SLM lattice structures for given tasks may be found as well. As mentioned in ***section 2.1.4.15*** the exponent of power laws should be as small as possible in correlations of strength in dependence of relative density in order to allow high strengths at low relative densities. From this as well as the position of the best fit curves in the diagrams three conclusions become evident. One is that most cell types with body diagonals (green, solid line) and the both investigated polyhedral cell types show the highest absolute strengths.

This is not surprising due to their higher relative density. Secondly, in the x- and y-direction all cell types without body diagonals (blue, solid line) show the highest strengths at given relative densities since their best fit curve is shifted to the extreme left in the diagram and exhibits the lowest or nearly lowest slope, respectively. The third conclusion is that in z-direction the best fit curve for tetrahedral cell types (red, solid line) shows a significantly lower slope compared to the other cell types. The obtained power law exponent of 1.2289 in

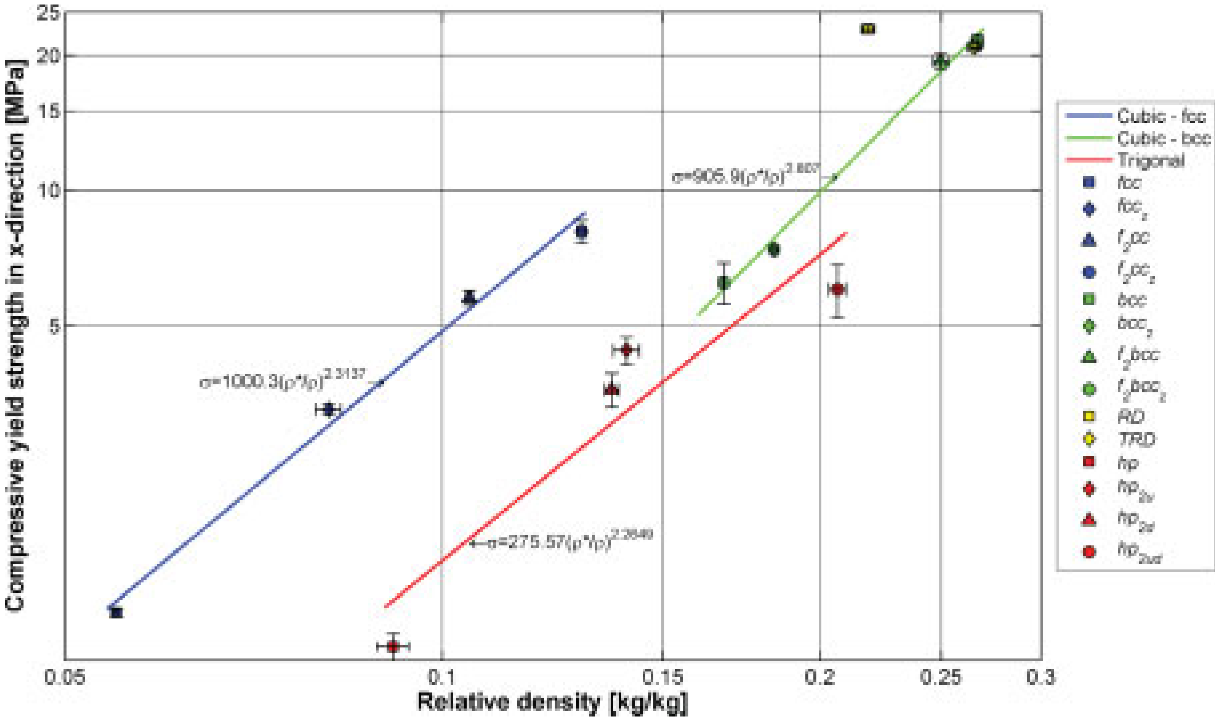

Figure 6.14: Results of compression tests at constant cell size in x-direction

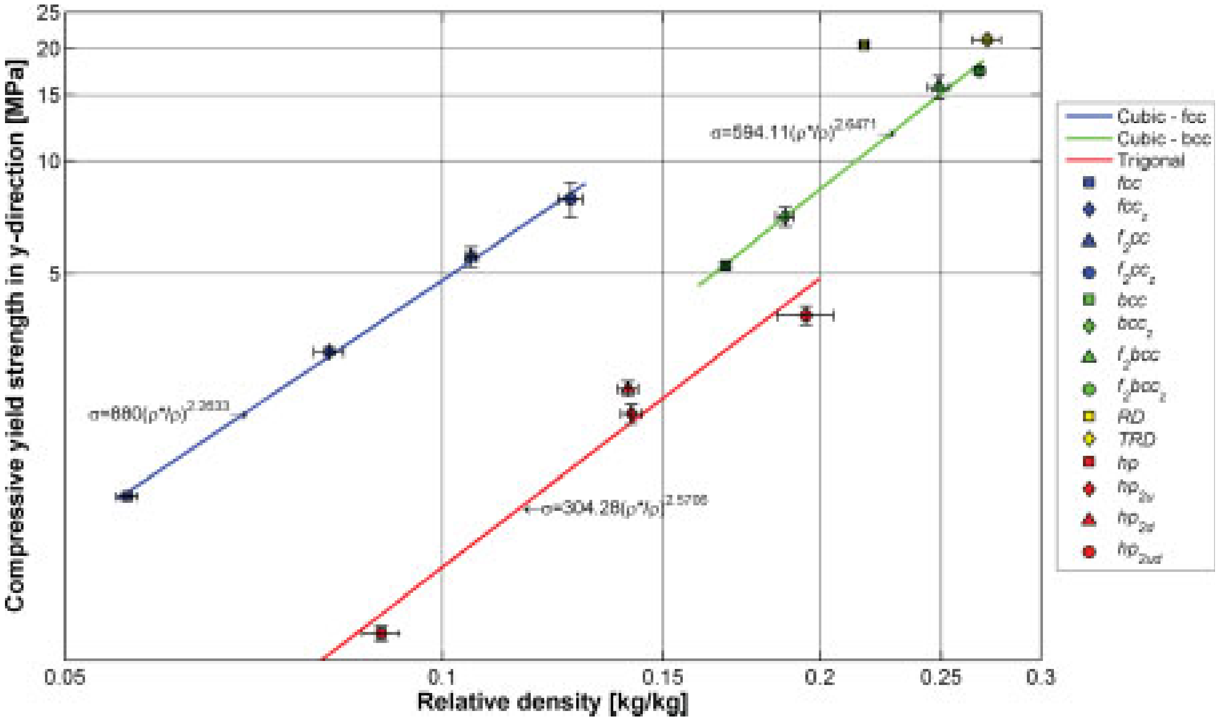

Figure 6.15: Results of compression tests at constant cell size in y-direction

fig. 6.16 indicates an outstanding capability for high strength even at low relative density.

The compression tests reveal that depending on structure and direction of compressing three different failure modes prevail which are shown in a qualitative stress-strain diagram in ***fig 6.17*** from a choice of actual test data. The most dominating failure mode I, given as a green, dash-dotted line in ***fig 6.17***, occurs for all cell types with body diagonals as well as for all non-cubic cell types. It comprises two linear inclines, one elastic, the other one plastic before total compaction of the specimens takes place and it represents stretch-dominated behaviour in accordance with ***fig. 2.10***. The second dominating failure mode II, given as a blue, solid line, occurs mainly in x- and y- direction due to the absence of struts in these directions and is, therefore, bending-dominated. After the linear elastic incline a peak strength merges into a plateau of wavy curves before total compaction takes place. This is best explained with a layerwise failure of the cell network in the test specimens where the observable wavelength in the force-displacement diagram equals the cell size in the direction of compression. The third least observed failure mode III, given as a red, dashed line in the figure, comprises a linear elastic incline, a peak strength and a constant plateau strength before total compaction is reached. ***Table 6.4*** summarizes the failure modes of all 14 cell types obtained in all three directions of compression. It is useful for future design of SLM lattice structures for given applications where e.g. either stretch- or bending-dominated behaviour is required.

The evaluation of the energy absorption per unit volume in three directions of space of all 14 cell types is given as well in ***table 6.3***. Due to the ocurrence of the above introduced three failure modes with distinctly different stress-strain curves the rule of measuring energy absorption at 130 % of the plateau stress cannot be applied. However, the experimental data

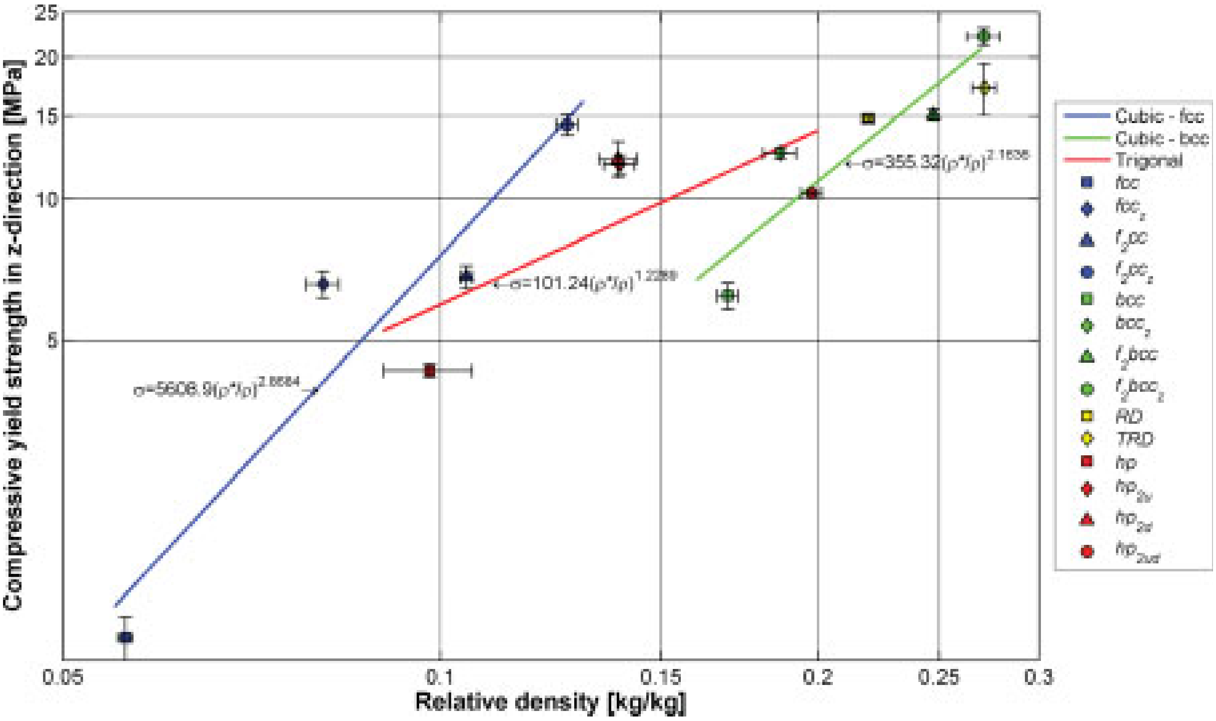

Figure 6.16: Results of compression tests at constant cell size in z-direction

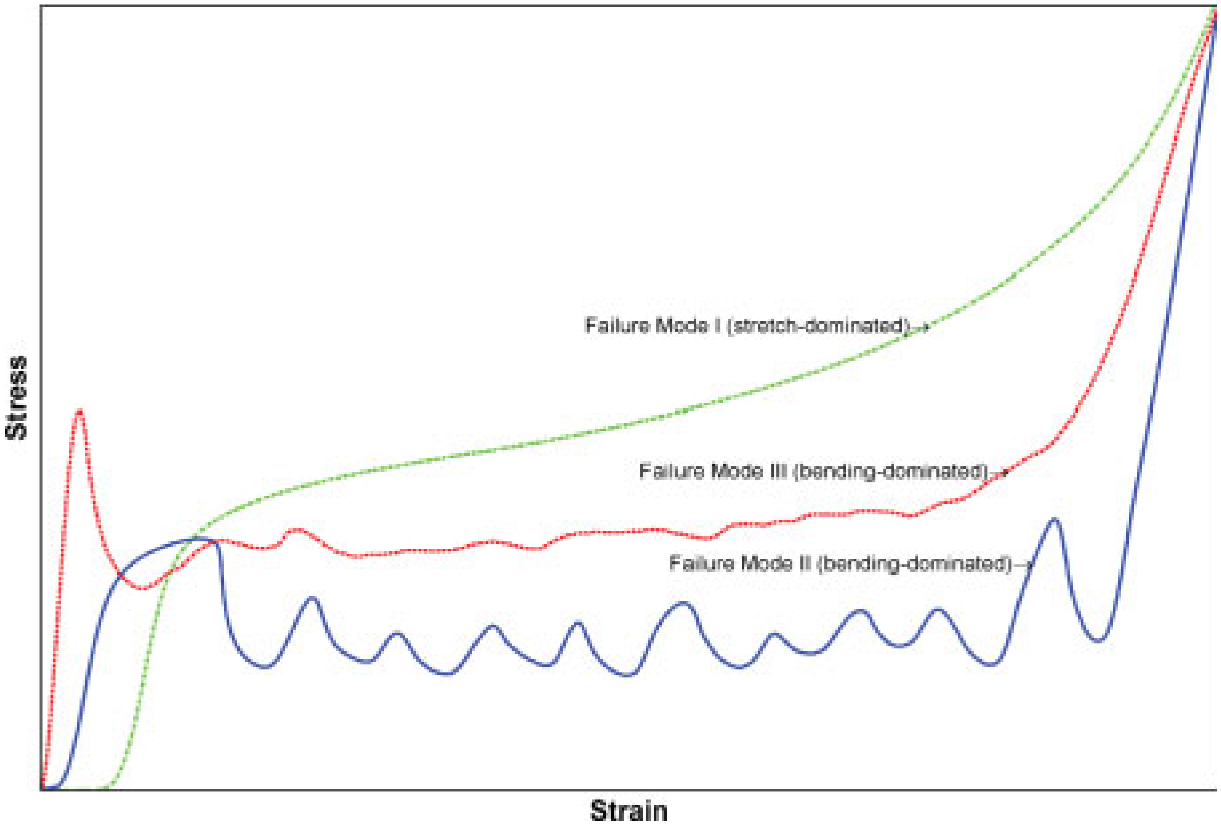

Figure 6.17: Typical failure modes for SLM lattice structures (type I, II and III)

from the compressive tests at 2.5 mm cell size allow reasonable evaluation of the amount of absorbed energy at 40 % compression from the initial length of all specimens. As ***table 6.3*** indicates the absorped energy per unit volume can be roughly correlated with the specific strength. The cell types f_2bcc_z, *TRD* and *RD* deliver the highest (up to 14.25 MJ/m^3) and the cell types *hp* and *fcc* the lowest (as little as 0.2743 MJ/m^3) energy absorption per unit volume which is in accordance with their respective relative densities.

Most cell types easily excel the performance of energy absorbers made from aluminum foams as presented in ***section 2.1.4.14*** in terms of energy absorption per unit volume. If, however, the ratio of energy absorption per unit volume-to-weight is considered the ranking derived from ***table 6.3*** changes slightly but not significantly. In this regard f_2bcc_z, f_2cc_z and *TRD* are

Table 6.4: Failure modes of various SLM lattice structure cell types

Cell type	x	y	z	Cell type	x	y	z
fcc	II	II	III	f_2bcc_z	I	I	I
fcc_z	II	II	III	*RD*	I	I	I
f_2cc	II	II	I	*TRD*	I	I	I
f_2cc_z	II	II	III	*hp*	I	I	III
bcc	I	I	I	hp_{2u}	I	I	III
bcc_z	I	I	I	hp_{2d}	I	I	II
f_2bcc	I	I	I	hp_{2ud}	I	I	I

the best performing cell types which deliver specific values in z-direction of 6.675, 6.591 and 6.425 kJ/kg, respectively. The overall best energy absorbing cell type in the x- and y-direction is *RD* which shows specific values of up 8.229 kJ/kg. Compared to values between 3.284 and 3.983 kJ/kg obtained for static loading of aluminum foams up to even 55 % compression, some SLM lattice structures outperform these values significantly. All tetrahedral cell types, however, especially hp_{2u} and hp_{2d} which show extraordinary high specific strengths in z-direction are disappointing in terms of energy absorption. It has to be noted that the choice of a suitable cell type for a specific task also requires consideration of the anisotropy properties. Cell type f_2cc_z exhibits a distinct anisotropic energy absorption characteristic whereas the cell types f_2bcc_z, *RD* and *TRD* are more or less balanced. However, in applications of single, predetermined impact directions such anisotropic behaviour may be even desired.

6.5 Selection of cell types for tests in dependence of cell size

All previous theoretical and experimental analyses have involved the examination of 14 different cell types. Before the next experimental stage, however, the amount of cell types has to be narrowed down in order to reduce the effort of specimen fabrication and test procedures to a reasonable dimension. Therefore, the three most promising cell types are selected, derived from the conclusions drawn from all results available up to this point.

The selection criteria (underlined) comprise the following issues:

1. Attractive cell types must offer high cell network stability and should allow a high aspect ratio over a broad range of cell sizes and strut diameters. The results from ***fig. 6.11*** are used to evaluate this category.
2. It is desired to cover a large span of relative densities as given in ***table 6.3*** among the three to-be-selected cell types for an ability to observe possible effects from very high or very low relative densities. Preferably those cell types which exhibit the absolute or nearly highest and lowest relative densities should be involved in further testing.
3. Typically, high yield strengths should be obtained at low relative densities. An indicator for this is given in ***figs. 6.14*** through ***6.16*** where the location of the best fit curves for certain groups of cell types are shown. Generally, a group of cell types performs better if its best fit curve is placed as much left in the log-log-diagrams as possible, meaning that identical strength can be achieved with less relative density, and if this curve exhibits a low power law exponent, i.e. its slope is as low as possible, which means that with decreasing density the strength is reduced less quickly.
4. Opposed to insights gained from the absolute yield strength, the specific yield strength can be significantly different. High specific yield strength is usually desired, therefore, all cell types are ranked according to the results from ***table 6.3***.
5. In specific applications it might be required that the (specific) yield strengths in all three directions of space shows specifically isotropic or anisotropic behaviour. Thus the results from ***table 6.3*** are evaluated for cell types that show very balanced values in the x-, y- and z-direction as well as very unbalanced values.

Table 6.5: Evaluation matrix of all cell types

Cell type	High stability	High/low relative density	Power law	High specific yield strength	High isotropy or anisotropy	High specific energy absorption and failure mode suitability		Build time	Total score
fcc	○	+	+	−	+	−	+	+	3
fcc_z	○	○	+	○	+	○	+	+	4
f_2cc	○	○	+	○	○	○	+	+	3
f_2cc_z	+	○	+	+	+	+	+	+	7
bcc	+	−	−	−	○	○	−	○	-3
bcc_z	+	−	−	○	○	○	−	○	-2
f_2bcc	+	+	−	○	−	○	−	○	-1
f_2bcc_z	+	+	−	○	−	+	−	○	0
RD	−	○	−	+	−	+	−	−	-3
TRD	−	+	−	○	−	+	−	−	-3
hp	−	○	○	○	+	−	○	+	0
hp_{2u}	−	−	○	+	+	○	○	○	0
hp_{2d}	○	−	○	+	+	○	○	○	1
hp_{2ud}	○	−	○	+	+	○	−	○	0

6. For energy absorbers it is usually mandatory to possess not only high energy absorption per unit volume but also high energy absorption per unit weight. The latter is derived from ***table 6.3*** and used to evaluate the suitability of all cell types.
7. In energy absorption applications cell types with failure modes II and III according to ***table 6.4*** should be preferred. A typical stress-strain diagram shows a nearly rectangular profile with a very steep slope at the linear-elastic regime and large regime of strain at a constant stress level, if possible. This requirement disqualifies failure mode I. The suitability is evaluated according to the amount of failure modes II and III each cell type shows in all three directions of space.
8. Apart from failure modes suitable for energy absorbers it is also desirable to include all three failure modes in further investigations and have hence such three cell types selected which allow for complete coverage in this regard.
9. For economical considerations it is important to evaluate the build time a specific cell type requires in relation to other cell types.

In ***table 6.5*** good fulfillment of the above listed criteria is represented by a '+', a mediocre fulfillment by a '○' and a poor fulfillment by a '–'. Additionally, these evaluations are given the values +1, 0 and -1 which are added up for each cell type. The higher a particular cell type's resulting total score is the higher the probability of selecting it for the subsequent experimental stages becomes. An undisputed winner is cell type f_2cc_z which scores highest at a value of 7. This cell type clearly outperforms all other cell types and is, therefore, selected.

However, it possesses only a medium relative density, hence it is evident that both remaining cell types to be selected should cover the lowest and the highest relative density values. Among the cell types of highest relative density the cell type *f$_2$bcc$_z$* stands out with a total score of 0 which does not appear high, however, all other high density cell types score even lower. The cell type of lowest relative density *fcc* (total score of 3) ranks slightly lower than *fcc$_z$* (total score of 4) but still higher than all other low density cell types. The cell type *fcc* is preferred over *fcc$_z$* to assess the possibilities of SLM lattice structures in the extreme regime of low relative density. In the total ranking the cell types *fcc* and *f$_2$bcc$_z$* take third and fifth position which is considered adequate. Hence, the cell types *fcc*, *f$_2$cc$_z$* and *f$_2$bcc$_z$* are selected for subsequent experimental testing.

6.6 Test of elasticity in dependence of cell size

6.6.1 Elastic compression tests

The elasticity of all three selected cell types is tested under compressive forces in order to assess the range of possibilities on how to influence the effective stiffness, i.e. Young's modulus, in dependence of cell types and cell size while the strut diameter is kept constant. Cell sizes are chosen to 0.5, 1, 1.5, 2, 3, 4, 5 and 6 mm while the strut diameter is defined according to the maximum melt energy in ***fig. 6.6*** used with the SLM machine introduced in ***section 4.2.3***, i.e. 0.85 J giving an average strut diameter of 0.507 mm, in order to allow sufficient strut stability especially at large cell sizes of 5 and 6 mm. Although, according to ***fig. 10.8*** the manufacture of 6 mm cells of cell type *fcc* is possible, the obtained specimens are not satisfactory as can be seen in the left part of ***fig. 6.18*** where some sample specimens of cell types *fcc* and *f$_2$bcc$_z$* are shown. Due to slight damage these cells are excluded from testing, therefore, a set of initially 216 accordingly designed specimens, 9 of all 8 cell sizes and all 3 cell types is reduced to 207 specimens which are tested under uniaxial compression

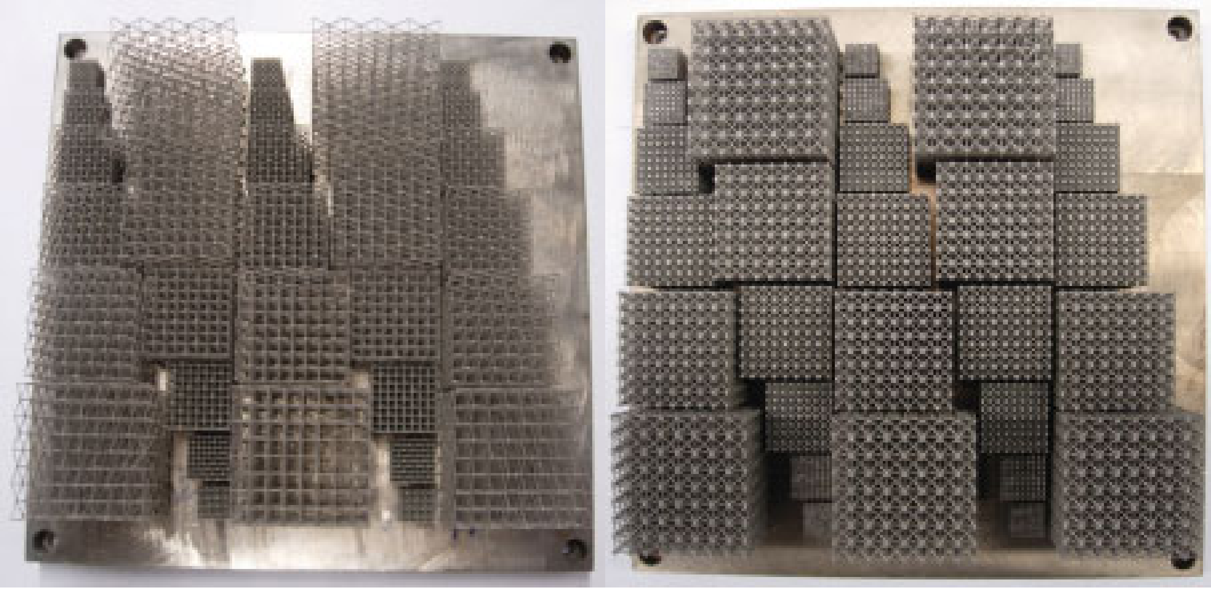

Figure 6.18: Compressive test specimens of cell types *fcc* and *f$_2$bcc$_z$* for effective elasticity at variable cell sizes

in the x-, y- and z-direction. Each distinct test of cell type, cell size and direction of compression is repeated with three identical specimens. All specimens possess cubic shape featuring 8 cells in each direction of space in order to limit build-time.

The testing is conducted in accordance with the boundary conditions set in ***section 6.3.2*** after the specimens' dimensions and weights are determined in order to calculate their relative densities. During testing, force-displacement values are recorded from which stress-strain diagrams are derived. The unloading modulus in the obtained stress-strain diagrams is calculated from a linear best fit of an unload/reload cycle during each respective compression test. Each Young's modulus is calculated from ***eq. (6.14)*** where the stiffness of the respective testing machine used for the compression of the specimens is applied.

The averaged results of all three compression tests for each combination of cell type, cell size and direction are summarized in ***appendix 10.6*** in ***tables 10.4*** through ***10.6***. The results for cell type f_2bcc_z are given in a linear diagram in ***fig. 6.19*** where the obtained Young's moduli are shown versus the measured relative densities. The values in the x-, y- and z-direction are indicated by red triangles, green circles and blue squares as result markers with best fit curves of the same colour in solid, dashed and dotted line style. The effective Young's moduli at relative densities equal to unity are set to the literature value for stainless steel of 200 GPa due to nonexistence of influence from the SLM process on the Young's modulus of solid materials as explained in ***section 6.1***. Both diagrams for cell types *fcc* and f_2cc_z can be found in ***appendix 10.6*** in ***fig. 10.9*** and ***10.10***. All diagrams have linear axes in order to better show the regime where the low relative density power law breaks down and the transition to

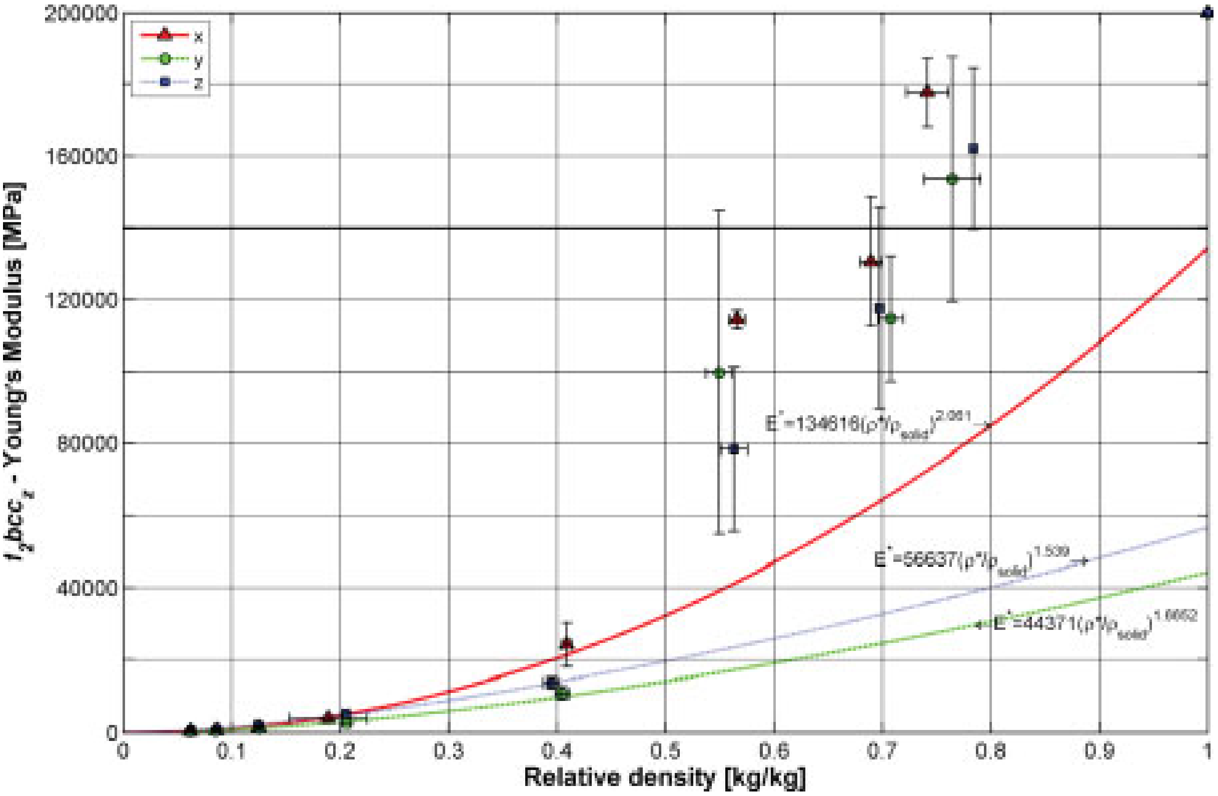

Figure 6.19: Results for effective Young's modulus of cell type f_2bcc_z

another model takes place in accordance with the explanations given in ***section 5.2.8***. In all three diagrams the best fit curves represent the resulting power laws of the effective Young's modulus E^* for each respective direction of compression. They are given directly in the diagrams and calculated only from data points in the low relative density regime below the critical relative density as derived in ***table 5.1***. It should be noted that for cell type f_2bcc_z, opposed to the tests presented in ***section 6.7.1***, the data points for cell sizes of 1.5 mm, i.e. a relative density of approximately 0.56, are not included in the best fit curves although they are found below the critical relative density. The apparent early power law breakdown at this point could be due to the large standard deviations of the measured values at 1.5 mm cell size.

From ***fig. 6.19*** it becomes evident that beyond the critical relative density the standard deviations increase excessively. The rise in standard deviation for higher relative density is due to increased inaccuracies at smaller cell sizes resulting from varying pore diameters. The massive increase in standard deviation for Young's modulus, however, is explained by inaccuracies of the measurement itself. Small errors in the evaluation of the compression test force-displacement diagrams can yield infinitely large Young's moduli if specimens have the same spring constant D as the testing machine as ***eq. (6.14)*** suggests. For specimens of high Young's modulus most of the displacement takes place rather in the testing machine. Cell types of high relative density such as f_2bcc_z are hence more difficult to handle in experimental analysis. As assumed in ***section 6.3.2*** ultrasound might be a better approach to assess the effective elasticity of SLM lattice structures. Nevertheless, all three diagrams show quite clearly the power law breakdown and the transition to a regime where SLM lattice structures can be described as solids with pores which show different elastic properties.

6.6.2 Elastic shear tests

Some elastic shear tests are conducted as well according to the boundary conditions set in ***section 6.3.4*** in order to verify possible correlations between Young's modulus and shear modulus. For each of the three selected cell types three double core specimens are fabricated with a cell size of 3 mm and each core comprising 8 by 68 by 17 cells in the x-, y- and z-direction as shown in ***fig. 6.20***. The shear force is applied in the y-direction on all specimens and the linear-elastic regime from the resulting stress-strain curve is evaluated. Due to fabrication of all shear specimens in one step including the flanges, the core weight cannot be measured separately. Therefore, only the actual dimensions are measured and the relative density is used from the average values of all 3 mm compressive specimens of the same cell type given in ***tables 10.4*** through ***10.6***. ***Table 6.6*** summarizes the obtained average effective shear moduli G. For cell type *fcc* the ratio of shear modulus to Young's modulus is 0.4019. This is in good accordance with the prediction from ***eq. (2.16)*** which, for stainless steel materials, is approximately 3/8. This allows simple deriving of scaling laws for load in shear from scaling laws set up for compressive loads.

The shear modulus of cell type f_2cc_z increases, however, it falls far beyond the expectations in relation to its Young's modulus as the ratio yields merely 0.07169. It is assumed that in shear loading in the y-direction the additional struts compared to cell type *fcc*, i.e. the struts in z-

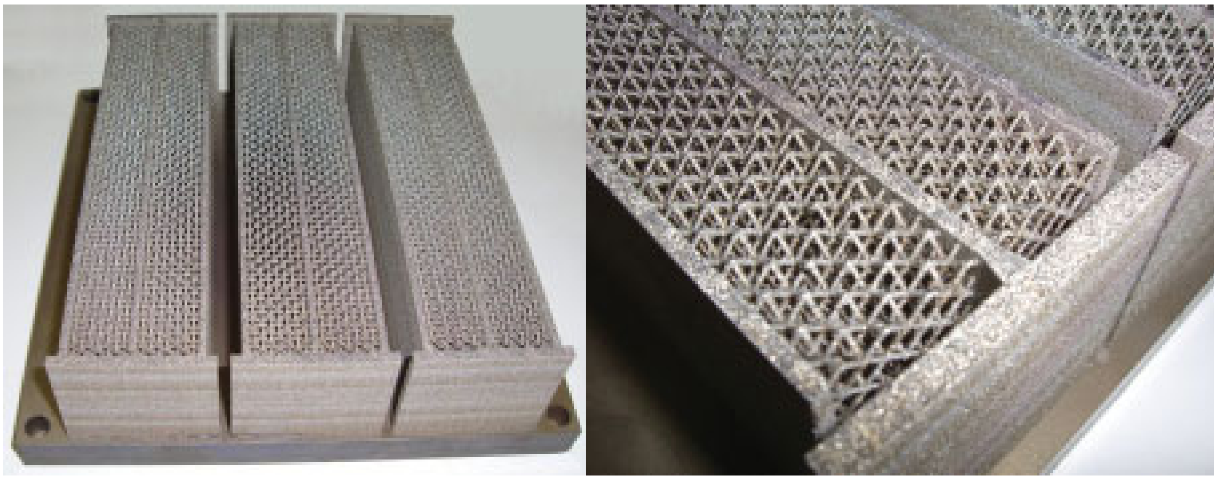

Figure 6.20: Shear specimens of cell type *fcc*

Table 6.6: Results for elastic shear tests

Cell type	ρ^*/ρ_{solid} [1]	Shear modulus y [MPa]	Std. dev. [MPa]	Young's Modulus y [MPa]
fcc	0.05264	35.93	8.850	89.41
f_2cc_z	0.1110	110.7	9.228	1544
f_2bcc_z	0.2002	116.2	24.12	2856

direction and the face diagonals, do not contribute much to the shear stiffness. However, this is presumably different if shear loading is considered for cell type f_2cc_z in z-direction along any arbitrary shear plane where a ratio of 3/8 predicted from ***eq. (2.16)*** is assumed to hold. The actual measurements in the y-direction with a y-z-shear plane neglect this assumption due to the anisotropy in this cell type.

The cell type f_2bcc_z does not deliver satisfactory results at all as obvious from ***table 6.6***. During the shear testing all three specimens suffered from premature failure of the bond between the flanges and the cores. It is assumed that the reason for this is the high stiffness of the cores. Therefore, the obtained values are not indicative for any derivations of scaling laws. The shear load experiments suggest that the chosen specimen configuration comprising two cores is inadequate for relative densities of 0.2 and higher. Specimens prescribed by DIN 53294 which are loaded diagonally need less complicated flanges and respective bonding and appear thus more suitable to serve the purpose regardless of the produced error explained in ***section 6.3.4***.

6.7 Test of strength in dependence of cell size

6.7.1 Compression strength tests

Measurement of the yield strengths of all three selected cell types is performed on the same specimens as shown in ***fig. 6.18*** and in the same test procedures as for the elastic compression tests presented in ***section 6.6.1***. Therefore, the same cell sizes, i.e. 0.5, 1, 1.5, 2, 3, 4, 5 and

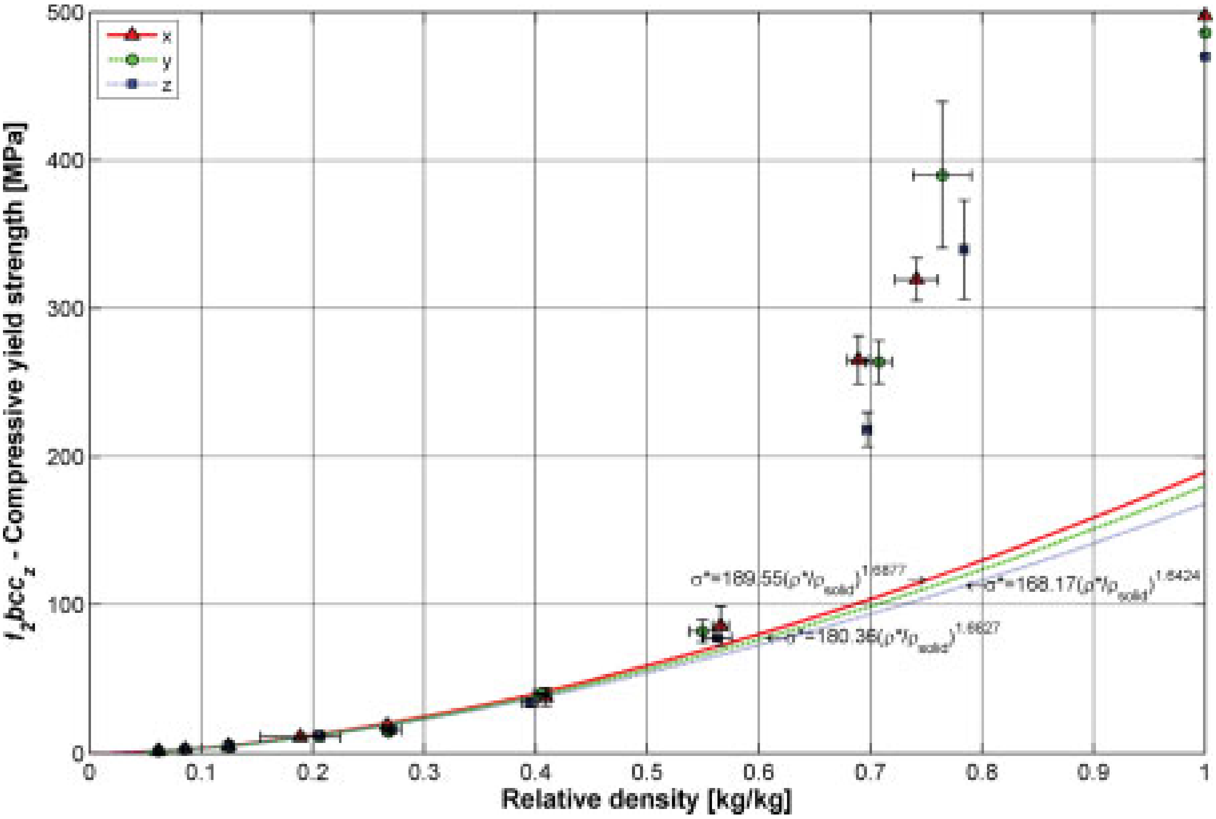

Figure 6.21: Results for effective compressive yield strength of cell type *f_2bcc_z*

6 mm, and three respective specimens in each x-, y- and z-direction are investigated under uniaxial compression. Additionally, the results from the specific strength tests for cell sizes of 2.5 mm presented in ***section 6.4*** are included to supplement the data. Moreover, yield strength results for cell type *fcc* at cell size 6 mm do not exist either which gives a total of 234 specimens available for analysis.

The averaged results of each three compression tests for each combination of cell type, cell size and direction are summarized in ***appendix 10.7*** in ***tables 10.7*** through ***10.9***. The results for cell type f_2bcc_z are given in a linear diagram in ***fig. 6.21*** where the obtained yield strength values R_{p1} are shown versus the measured relative densities. As with the elasticity tests, the values in the x-, y- and z-direction are indicated by red triangles, green circles and blue squares as result markers with best fit curves of the same colour in solid, dashed and dotted line style. Opposed to the elasticity tests, however, the effective yield strengths at relative densities equal to unity are not set to literature values. Instead results from a set of nine solid SLM compressive specimens made from stainless steel in the same batch as the tensile bars presented in ***section 6.1*** are used of which three are tested in each of the x-, y- and z-direction resulting in average yield strength values of 497.5, 486 and 470 MPa. Both diagrams for cell types *fcc* and f_2cc_z can be found in ***appendix 10.7*** in ***figs. 10.11*** and ***10.12***. Again the diagrams have linear axes in order to better show the regime of power law breakdown. The best fit curves are once again calculated only from data points at relative densities below the critical relative density as derived in ***table 5.1*** such that data points at or beyond the critical relative density can be clearly distinguished. The resulting power laws of the effective yield strength are given in the diagrams for each respective direction of compression.

The standard deviations for the measured yield strengths beyond the critical relative density are much higher than those below the critical relative density. However, apparently the increase is much smaller compared to the elasticity testing. This seems to confirm the assumption from ***section 6.6.1*** where non-linearities in the evaluation method are held responsible for the observed large standard deviations.

The failure modes explained in ***fig. 6.17*** and derived for all 14 cell types in ***table 6.4*** can be found in different cell sizes of the three scrutinized cell types as well. However, for cell sizes of 1.5 mm and smaller the failure modes are less distinct and more difficult to observe. ***Fig. 6.22*** shows some selected samples of 4 mm cell size where results for compression in the y-direction are omitted because they are qualitatively identical with those for the x-direction. The top left shows cell type *fcc* compressed in x-direction (left) where failure mode II prevails (i.e. failure of complete layers while other layers remain stable) and z-direction (right) where failure mode III is dominant (i.e. simultaneous and even failure of all cell layers). The top right of the figure displays cell type f_2bcc_z compressed in x- and z-direction (left and right). Both directions yield the stretch-dominated failure mode I which develops so-called crush bands in the specimens due to shear forces. These crush bands are observed in planes parallel to the direction of compression as either one or two crossed bands of diagonally compressed cells. The bottom of ***fig. 6.22*** shows cell type f_2cc_z compressed in x- and z-direction (left and right) as well. As suggested by the crushed cell structures compression in the x-direction

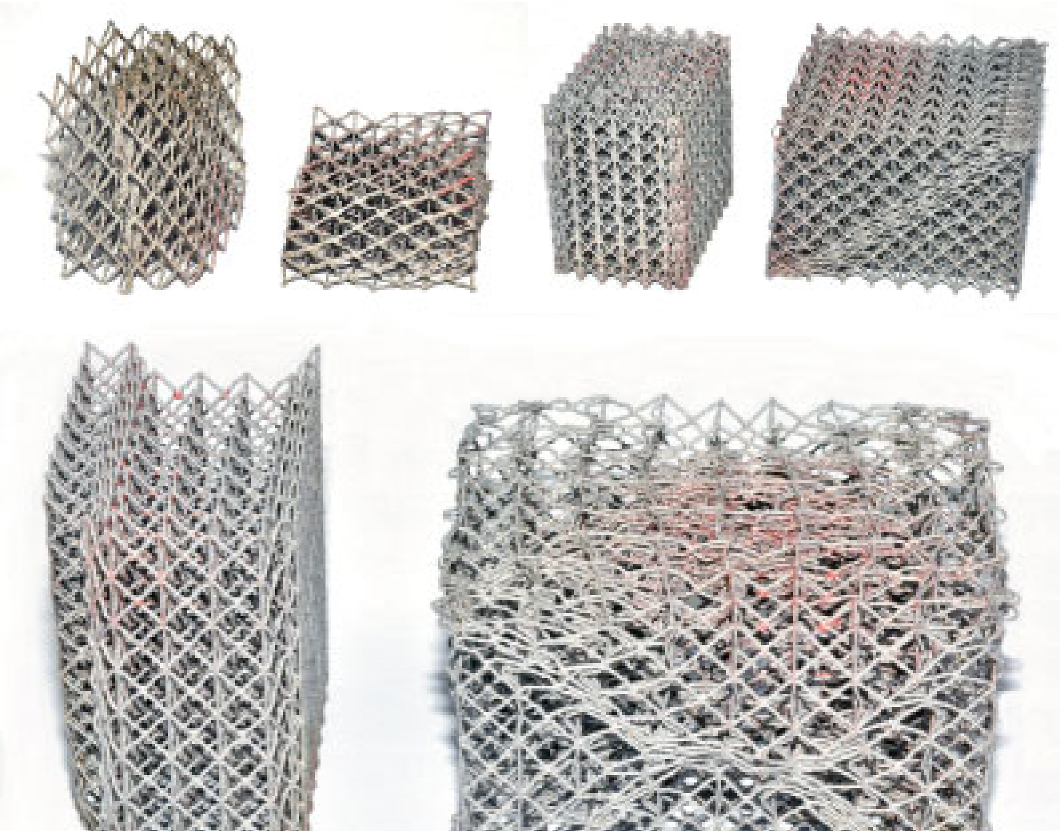

Figure 6.22: Crushed compressive specimens (cell types *fcc* top left, f_2bcc_z top right, f_2cc_z bottom)

gives failure mode II while the z-direction gives failure mode I. However, stress-strain diagrams for compression of cell type *f_2cc_z* in z-direction clearly show the development of a plateau stress, i.e. the cell structure fails from mode III instead. Apparently, this cell type combination renders a quite useful combination of failing at constant stress level while shear stresses develop. This confirms the assumptions from ***section 6.4*** that this cell type promises to perform well in energy absorption applications which makes it even more appealing.

6.7.2 Tensile strength tests

The tensile yield and ultimate strengths of all three selected cell types are investigated as well according to the boundary conditions introduced in ***section 6.3.3***. Therefore, the cell sizes of 1.5, 2, 3, 4, 5 and 6 mm, and three respective specimens in each x-, y- and z-direction are examined under uniaxial tensile stress. Smaller cell sizes are not considered in order to avoid too large stresses and premature failure in the bond between specimen and flange. Results for cell type *fcc* and 6 mm cell size do not exist for all three directions of testing, neither do they exist for testing of the same cell type of 5 mm cell size in z-direction. This gives a total of 150 specimens available for analysis.

For each combination of cell type, cell size and direction, averaged results of the obtained ultimate and yield strengths of each three tensile tests are summarized in ***appendix 10.8*** in ***tables 10.10*** through ***10.15***. For easy comparison with the results from the compression tests in ***section 6.7.1*** the yield strength results R_{p1} for cell type *f_2bcc_z* are shown versus the relative density in a linear diagram in ***fig. 6.23***. Again, the values in the x-, y- and z-direction are indicated by red triangles, green circles and blue squares as result markers with best fit curves

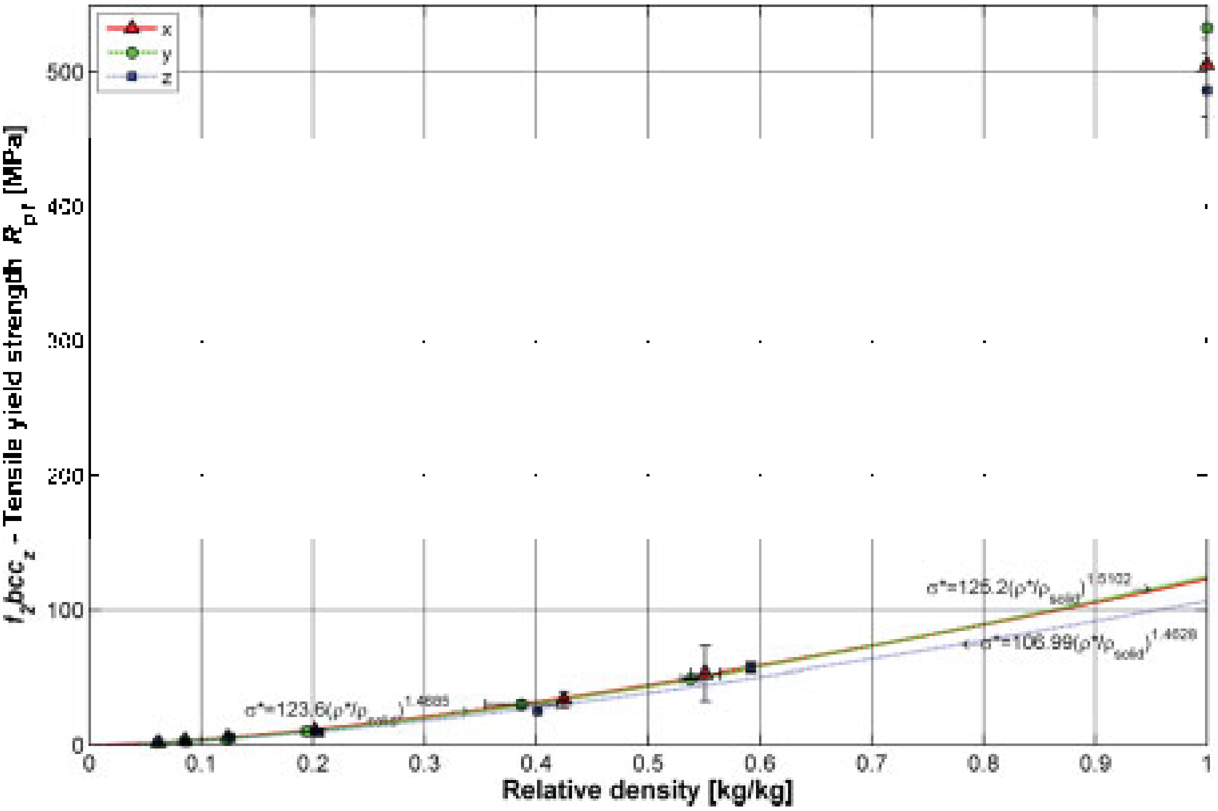

Figure 6.23: Results for effective tensile yield strength of cell type *f_2bcc_z*

of the same colour in solid, dashed and dotted line style. The effective yield strengths at relative densities equal to unity are set to values obtained from those tensile bars presented in ***section 6.1*** which were tested in the x-, y- and z-direction. Their average yield strengths are 505.5, 533.0 and 486.1 MPa, respectively. Another diagram for the ultimate strength of cell type f_2bcc_z is given in ***appendix 10.8*** in ***fig. 10.17*** where the average ultimate strengths at relative densities equal to unity are 543.6, 629.0 and 543.2 MPa. Likewise, diagrams for ultimate and yield strengths of cell types *fcc* and f_2cc_z can be found in ***appendix 10.8*** in ***fig. 10.13*** through ***10.17***. Power law breakdown cannot be observed in any of the tensile tests due to limitation of the minimum cell size to 1.5 mm. However, the data points at relative densities of unity and the best fit curves suggest that similar behaviour should be expected at higher relative densities beyond the critical relative densities according to ***table 5.1***.

Another observation made during tensile testing can be seen in ***fig. 6.24*** where tensile specimens from the three investigated cell types are analyzed in regard of their mechanical behaviour. All three specimens in the figure were tested in x-direction. Perpendicular to the direction of tension cell type f_2bcc_z (on the right in ***fig. 6.24***) clearly shows lateral contraction in z-direction as expected and nearly no contraction in y-direction. This implies a Poisson's ratio of close to zero in that direction. Both cell types *fcc* and f_2cc_z (on the left and in the middle in the same figure) also show a clear lateral contraction in z-direction, slightly more distinct for cell type *fcc*. However, in the y-direction both cell types exhibit negative Poisson's ratio as they bulge out perpendicular to the direction of tension. Judging from the deformations of all specimens the cell type *fcc* shows the largest amount of bulging out. At large cell sizes (5 mm) it can show lowest Poisson's ratios of down to $\nu = -1.2$ (below -1 due to the anisotropic structure of cell type *fcc*), which can be exploited in engineering applications according to ***section 2.1.4.9***. In this context the development of crush bands in compressive specimens should be seen in a completely new light, too. The cell type f_2cc_z in the bottom part of ***fig. 6.22*** e.g. develops such crush bands if compressed in the z-direction which allows a Poisson's ratio of nearly zero. This implies that using this cell type and direction of compression in applications of energy absorption will yield no significant lateral expansion which can cause unwanted damage to other components.

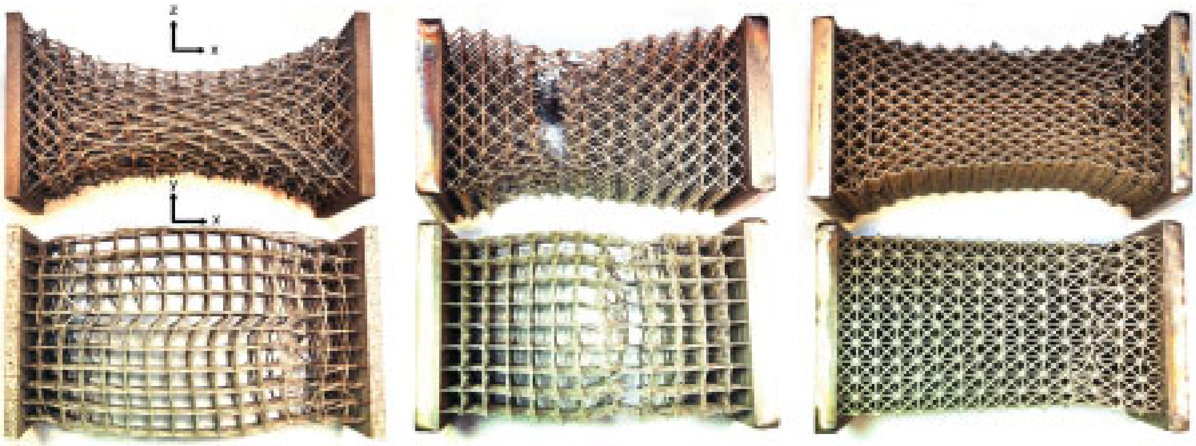

Figure 6.24: Crushed tensile specimens of cell types *fcc*, f_2cc_z and f_2bcc_z (from left to right)

6.7.3 Shear tests

Measurement of the shear strengths of all three selected cell types, i.e. ultimate strength according to the boundary conditions set in ***section 6.3.4***, is performed on the same specimens as shown in ***fig. 6.20*** and in the same test procedures as for the elastic shear tests presented in ***section 6.6.2***. These tests are conducted in order to verify possible correlations between compressive or tensile strength and shear strength. ***Table 6.7*** summarizes the obtained average shear strengths. For cell type *fcc* the ratio of shear strength to tensile ultimate strength is 0.2802 and for cell type f_2cc_z it is 0.3376. These are as well in good accordance with the ratio predicted in ***eq. (2.16)*** for shear and elastic moduli of approximately 3/8. The ratio for cell type f_2bcc_z of 0.09974 falls far behind the expectations for the same reasons noted before in ***section 6.6.2***. In order to make the results directly comparable the shear values are compared to the tensile ultimate strengths since shear strengths are also taken as ultimate strengths during testing.

With this limited amount of usable results a correlation for the effective shear strength in dependence of relative density according to ***eq. (2.6)*** is not easy to set up, however, the average values for cell types *fcc* and f_2cc_z yield

$$\frac{\tau^*}{\sigma_{tensile,ultimate,solid}} = 0.06418 \cdot \left(\frac{\rho^*}{\rho_{solid}} \right)^{1.3019} \tag{6.15}$$

which delivers an attractive result for the power law exponent. Nevertheless, the proportionality factor is one order of magnitude smaller than expected which might be an error caused by the availability of too few data.

Table 6.7: Results for shear strength testing

Cell type	ρ^*/ρ_{solid} [1]	Shear strength y [MPa]	Std. dev. [MPa]	Tensile ultimate strength y [MPa]
fcc	0.05264	0.7400	0.1329	2.641
f_2cc_z	0.1110	1.955	0.4569	5.789
f_2bcc_z	0.2002	1.300	0.2271	13.03

6.8 Results discussion

6.8.1 Comparison to literature results

The experimental results presented in this section allow some insight into the mechanical behaviour of SLM solids and SLM lattice structures. The strength properties of SLM solids are anisotropic and the z-direction is generally weaker than directions in the x-y-plane. However, three of the top four best producible cell types, i.e. ranked for highest stability during fabrication, include micro struts in z-direction as countermeasures against the anisotropic strength deficiencies. These results and the analysis of the performance comparison of all 14 cell types developed in ***section 6.5*** have led to the selection of cell types *fcc*, f_2cc_z and f_2bcc_z for which in-depth results of some selected mechanical properties depending on the choice of cell type and design parameters are herewith available.

Ratio of tensile and compressive strength

The literature cited in ***sections 2.1.4.1*** and ***2.1.4.2*** is unclear about whether compressive and tensile strengths are about equal or differ significantly from each other. ***Table 6.8*** gives an explanation as to why different sources do not agree. It clearly shows that the ratio between tensile and compressive strengths of SLM lattice structures increases with cell size. For cell sizes between 2 and 3 mm tensile and compressive strengths appear to be about equal. There is also a tendency that such cell types that yield lower relative density at identical cell size are stronger in tensile than in compressive strengths. Evidently, additional struts in a unit cell contribute to compressive rather than tensile strength.

Table 6.8: Ratios of tensile and compressive yield strengths of SLM lattice structures

Cell size [mm]	2		3		5	
Cell type	**x/y**	**z**	**x/y**	**z**	**x/y**	**z**
fcc	0.9738	1.180	1.278	1.005	1.939	n/a
f_2cc_z	0.9920	0.7700	1.190	0.8606	1.484	1.322
f_2bcc_z	0.8226	0.7387	0.9294	0.7622	1.238	0.6717

Power laws in the low relative density regime

Numerous power laws were derived to describe the mechanical strength of SLM lattice structures depending on the cell type, cell size as well as direction and type of load. It has to be noted that these power laws are solely based on results obtained below the individual critical relative density, since inclusion of results beyond the critical relative density would give useless power law fits which cannot be compared to other results. Therefore, a specific construction of function sets that describe mechanical properties of SLM lattice structures over the full bandwidth of relative densities is postponed to ***section 7.1***. If the power laws found in the experimental investigations are rewritten as correlations of relative strength like those for the compressive yield strengths in ***table 6.9*** they can be compared to the literature values presented in ***section 2.1.4.1***. Generally, the power laws found for compressive yield

Table 6.9: Comparison of power laws for the low relative density regime

Cell type	$\sigma^*_{yield,x}/\sigma_{yield,solid,x}$	$\sigma^*_{yield,y}/\sigma_{yield,solid,y}$	$\sigma^*_{yield,z}/\sigma_{yield,solid,z}$
fcc	$0.5007\cdot\left(\frac{\rho^*}{\rho_{solid}}\right)^{1.9461}$	$0.526\cdot\left(\frac{\rho^*}{\rho_{solid}}\right)^{1.9431}$	$0.6352\cdot\left(\frac{\rho^*}{\rho_{solid}}\right)^{2.0026}$
f_2cc_z	$0.5420\cdot\left(\frac{\rho^*}{\rho_{solid}}\right)^{1.7997}$	$0.4403\cdot\left(\frac{\rho^*}{\rho_{solid}}\right)^{1.7148}$	$0.5964\cdot\left(\frac{\rho^*}{\rho_{solid}}\right)^{1.5992}$
f_2bcc_z	$0.3900\cdot\left(\frac{\rho^*}{\rho_{solid}}\right)^{1.6877}$	$0.3837\cdot\left(\frac{\rho^*}{\rho_{solid}}\right)^{1.6827}$	$0.3380\cdot\left(\frac{\rho^*}{\rho_{solid}}\right)^{1.6424}$

strength of SLM lattice structures comprise proportionality factors between 0.3380 and 0.6352 as opposed to values around 0.3 confirmed by actual experiments with metal foams. This means higher strengths at lower relative density for SLM lattice structures.

The power law exponents derived analytically for metal foams predict values around 1.5 which, however, do not hold in experimental investigations. Due to structural flaws realistic values found in experiments are rather around 1.9 to 2. As shown in ***table 6.9*** SLM lattice structures offer a bandwidth of experimental values from 1.5992 to 2.0026 where in most cell types the exponents are smaller than for metal foams. Generally, a low power law exponent n is desired for both strength and stiffness scaling laws. The lower n is the higher the relative strength or stiffness becomes at low relative densities. Especially for very small relative densities (less than 0.1) a low power law exponent n has significant influence. Therefore, it can be concluded that SLM lattice structures outperform metal foams in terms of mechanical strength. This holds as well for the other examined properties such as tensile yield and ultimate strength, shear strength and elasticity. A tendency of decreasing power law exponent with an increasing number of struts in the unit cell can be observed for the three examined cell types.

6.8.2 Comparison to theory

The aspect ratios calculated in ***section 5.3.1*** with values between 14.45 and 26.4 are in good agreement with the values found experimentally between 3.390 and 22.73. Comparing the experimental results of compressive yield strengths to the findings of the simulation in ***section 5.4.2*** it becomes obvious that the power laws from ***table 5.2*** for the three examined SLM lattice structure cell types show similar but somewhat more optimistic results. It should be noted that the exponents from the simulation are 0.3534 to 0.6791 smaller and the proportionality factors are decreased between 1.88 and 4.25. Hence using a safety factor (e.g. 2) is recommended when structural design on the basis of SLM lattice structures is calculated purely on simulation results. From ***figs. 6.21***, ***10.11*** and ***10.12*** critical relative densities of 0.60, 0.75 and 0.55 can be observed for cell types f_2bcc_z, *fcc* and f_2cc_z which comes close to the theoretical calculations given in ***table 5.1*** where values of 0.6736, 0.7789 and 0.5125 were predicted. Therefore, it can be concluded that the experimental data are in good agreement with the theory and that theoretical calculations of mechanical properties of SLM lattice structures are permissible in the range of relative densities below the critical relative density.

6.8.3 Conclusion

Overall, judging from the conclusions drawn here in this section as well as in previous sections cell type f_2cc_z is the overall best performing cell type in many regards. It allows high specific strength, high specific energy absorption, high specific stiffness and high anisotropy of the strength properties when loaded under compressive stresses, especially in z-direction. Among the found power laws presented in ***table 6.9*** cell type f_2cc_z clearly shows the optimum combination of high proportionality factor and low exponent. It yields e.g. 50 and 100 MPa of compressive yield strength roughly at relative densities of 0.4 and 0.55 while such strengths can be achieved for cell types *fcc* and f_2bcc_z only at relative densities of approximately

0.45/0.6 and 0.5/0.7. The fact that cell type *f_2cc_z* exhibits a lower critical relative density compared to cell types *f_2bcc_z* and *fcc* is not necessarily detrimental since most typical applications of cellular materials require relative densities typically below 0.5.

6.9 Summary

This chapter summarizes the results of all experimental efforts conducted to assess some mechanical properties of SLM cellular materials. Before these are investigated the yield and ultimate strength as well as break strain and Young's modulus of 290 solid SLM tensile bars are presented which were built in 145 distinct directions of space evenly distributed over half a hemisphere. The result is that both, strength properties and break strain are anisotropic and deliver the highest values approximately in the x-y-plane of the build platform. Opposed to this, Young's moduli are not affected by the direction of testing and are therefore isotropic.

Next, the producibility of SLM lattice structures is investigated which begins with an examination of the influence of the process parameters on the shape of the obtained micro struts. A large range of cell sizes and strut diameters is tested on all 14 cell types developed in ***section 5.3*** in order to find those of highest stability at large ratios of cell size to strut diameter. Especially, cell types *f_2bcc_z*, *bcc* and *f_2cc_z* prove to be most promising in this regard.

The procedures of mechanical testing for strength and elastic properties of compressive, tensile and shear specimens are described which are in accordance with current norms and standards where deemed applicable. To narrow down the amount of cell types for mechanical testing, all 14 cell types are examined at 2.5 mm cell size in order to compare the properties of relative density, absolute and specific strength, energy absorption capabilities and build time, which are all useful in various applications. From all experimental results up to this point all cell types are ranked and *fcc*, *f_2cc_z* and *f_2bcc_z* are selected to be scrutinized in further mechanical tests in dependency of the cell size. These comprise elastic compression and shear tests as well as compressive, tensile and shear strength tests.

The results reveal dependencies of cell type and relative density. Power laws are derived for the regime of low relative density which allows direct comparison with results for other cellular materials given in the literature and in ***section 2.1.4***. The existence of a low as well as a high relative density regime, as suggested in ***section 5.2.8***, is confirmed by the experimental data since SLM lattice structures allow to exploit the full range of relative densities. For the three investigated cell types the experimentally determined critical relative densities, which separate both regimes, are in good accordance with the theoretical calculations.

In a concluding discussion it is found that from all analyzed cell types the overall best performing cell type is *f_2cc_z* as it allows high specific strength, high specific energy absorption and some other particular features of mechanical behaviour which emphasizes its outstanding position. It may be outperformed by other cell types in single, specific regards, but in total it is balanced best compared to all other investigated cell types.

7 Development of cellular design for SLM parts

7.1 Development of scaling laws for engineering design

7.1.1 Conversion of relative density into the main design parameters

Most correlations in the literature in ***section 2***, in the theoretical considerations in ***section 5*** and in the experimental investigations in ***section 6*** are given in dependency of relative density. Design engineers, however, require statements of expected product quality, e.g. mechanical strength, in terms of the main design parameters used by them according to ***fig 2.15***. The main design parameters for SLM lattice structures are defined in ***section 5.2.1***, these are the cell size a and the strut diameter d. Therefore, it is helpful for design engineers to provide a translation of the combined design parameter of aspect ratio a/d into relative densities which is valid across the full range of relative densities.

The experimental results from the three investigated cell types in ***sections 6.6*** through ***6.7*** suggest that relative density in dependency of cell size and hence aspect ratio can be described by functions where the curvature changes from negative to positive along positive direction of the x-axis. The functions of inverse tangent (arctan), hyperbolic tangent (tanh) and inverse hyperbolic sine (arcsinh) presented in ***eqs. (5.84)*** through ***(5.86)*** can fulfill this requirement if factors c_1 and c_2 have opposite signs. From these three functions one should be determined which gives the best fit to the experimental data and which shows the highest coefficient of determination R^2. The best fits for each of the three investigated cell types are given in ***table 7.1***. Additionally, the best fit curves are visualized in ***fig 7.1*** which can be used to convert relative densities and aspect ratios in either direction. In the figure the experimental data are given as red triangles for cell type *fcc*, as green circles for cell type f_2cc_z and as blue squares for cell type f_2bcc_z. Each best fit curve is given as a solid line of the according colour. It should be noted that the best fit for cell type f_2bcc_z does not approach a relative density of one. Alternatively, this could be set as a boundary condition in the best fit procedure which, however, would yield a lower coefficient of determination.

There is no clear trend as to which of the three functions from ***eqs. (5.84)*** through ***(5.86)*** is best suitable for fitting the experimental data. The function of inverse hyperbolic sine (arcsinh) appears to be neglectable, however, all three functions should be considered independently and judgement made from the fitting results. It is recommended to use the coefficients from ***table 7.1*** as start values. Typically, across different cell types and even

Table 7.1: Relative density in dependency of aspect ratio

Cell type	ρ/ρ_{solid}	R^2
fcc	$0.3986 \cdot \arctan\left(-1.236 \cdot \left(\frac{a}{d} - 1.225\right)\right) + 0.6076$	0.9991
f_2cc_z	$0.7193 \cdot \tanh\left(-0.3461 \cdot \left(\frac{a}{d} - 0.9989\right)\right) + 0.7639$	0.9958
f_2bcc_z	$0.5461 \cdot \tanh\left(-0.2705 \cdot \left(\frac{a}{d} - 2.479\right)\right) + 0.606$	0.9897

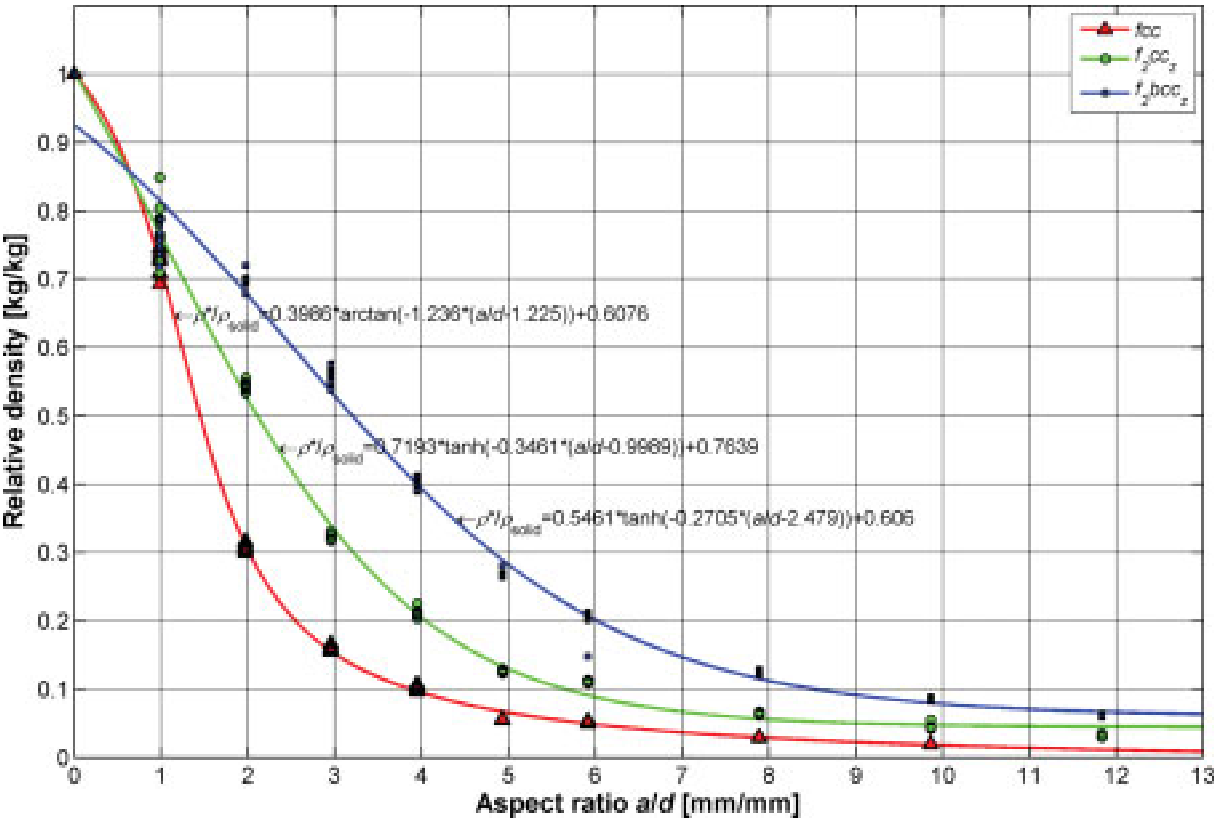

Figure 7.1: Relative density in dependency of aspect ratio

across the three functions the coefficients are of the same magnitude. In rare cases it might become necessary to base judgement for a best fit not merely on the coefficient of determination R^2 but also on reasonable curvature of the fit, if a best fit does not show a clear change of curvature as presented in ***fig 7.1***.

7.1.2 Scaling laws in dependency of aspect ratio in the low relative density regime

For the regime of low relative densities, i.e. below the critical relative density, the experimental investigations in ***sections 6.6*** through ***6.7*** revealed results in the form of power laws which describe a mechanical property in dependence of the relative density of a SLM lattice structure and two constants, i.e. one proportionality factor and one exponent. If considerations during the phase of engineering design are restricted to the regime of low relative density then scaling laws in dependency of aspect ratio can be found, based on power laws. These are simpler compared to the correlations given in ***section 7.1.1*** and, therefore, easier to use.

Table 7.2 gives the relative densities of the three examined cell types in dependency of the aspect ratio a/d. These expressions can be used to convert power law results from ***sections 6.6*** through ***6.7*** into correlations of aspect ratio. Furthermore, ***table 7.2*** reveals examples for the effective compressive yield strengths σ^*_{yield} in all three directions of space, based on the power law results from ***section 6.7.1***. Evidently, the resulting correlations yield dependencies proportional to approximately the inverse of the aspect ratio to the third power. It should be noted that all correlations in ***table 7.2*** are only valid for aspect ratios which yield relative densities below each cell type's critical value according to ***table 5.1***.

Table 7.2: Compressive yield strength in dependency of aspect ratio in the low relative density regime

Cell type	ρ^*/ρ_{solid}	$\sigma^*_{yield,x}$	$\sigma^*_{yield,y}$	$\sigma^*_{yield,z}$
fcc	$0.7158\cdot\left(\frac{a}{d}\right)^{-1.389}$	$202.7\cdot\left(\frac{a}{d}\right)^{-3.018}$	$131.7\cdot\left(\frac{a}{d}\right)^{-2.467}$	$176.8\cdot\left(\frac{a}{d}\right)^{-2.594}$
f₂cc_z	$1.934\cdot\left(\frac{a}{d}\right)^{-1.645}$	$1097\cdot\left(\frac{a}{d}\right)^{-3.142}$	$1033\cdot\left(\frac{a}{d}\right)^{-3.136}$	$582.4\cdot\left(\frac{a}{d}\right)^{-2.37}$
f₂bcc_z	$2.911\cdot\left(\frac{a}{d}\right)^{-1.497}$	$1957\cdot\left(\frac{a}{d}\right)^{-2.884}$	$1809\cdot\left(\frac{a}{d}\right)^{-2.844}$	$1669\cdot\left(\frac{a}{d}\right)^{-2.832}$

7.1.3 Scaling laws in dependency of aspect ratio for the full range of relative densities

SLM parts can be built in arbitrary relative densities and, therefore, the power law break down beyond the critical relative density can be easily observed in the experimental results in ***sections 6.6*** through ***6.7***. They suggest that similar to the approach in ***section 7.1.1*** the functions of inverse tangent (arctan), hyperbolic tangent (tanh) and inverse hyperbolic sine (arcsinh) introduced in ***eqs. (5.84)*** through ***(5.86)*** can be employed in order to describe mechanical strength properties in dependency of aspect ratio across the full range of relative densities. However, these functions are not necessarily easy to handle in terms of fitting them to experimental data. Therefore, some guidelines are given and example results presented on

Table 7.3: Best fits for compressive yield strength over full range of relative density

Cell type		σ^*_{yield}	R^2	*RMSE*
fcc	x	$273.4\cdot\tanh\left(-1.28\cdot\left(\frac{a}{d}-0.8012\right)\right)+274.9$	0.9999	1.686
	y	$166.2\cdot\arctan\left(-4.495\cdot\left(\frac{a}{d}-0.7943\right)\right)+254.4$	0.9998	2.934
	z	$346.2\cdot\tanh\left(-0.9947\cdot\left(\frac{a}{d}-0.4676\right)\right)+347.2$	1	0.9896
f₂cc_z	x	$185.2\cdot\arctan\left(-1.801\cdot\left(\frac{a}{d}-1.184\right)\right)+275.5$	0.9993	5.644
	y	$304.9\cdot\tanh\left(-0.6605\cdot\left(\frac{a}{d}-0.9037\right)\right)+306.6$	0.9998	2.901
	z	$336.7\cdot\tanh\left(-0.6176\cdot\left(\frac{a}{d}-0.8124\right)\right)+341.5$	0.9996	4.232
f₂bcc_z	x	$301.7\cdot\tanh\left(-0.4752\cdot\left(\frac{a}{d}-1.367\right)\right)+301.8$	0.9833	27.19
	y	$240.2\cdot\tanh\left(-0.7578\cdot\left(\frac{a}{d}-1.996\right)\right)+246.6$	0.9975	10.9
	z	$318.9\cdot\tanh\left(-0.513\cdot\left(\frac{a}{d}-1.175\right)\right)+321.8$	0.997	11.63

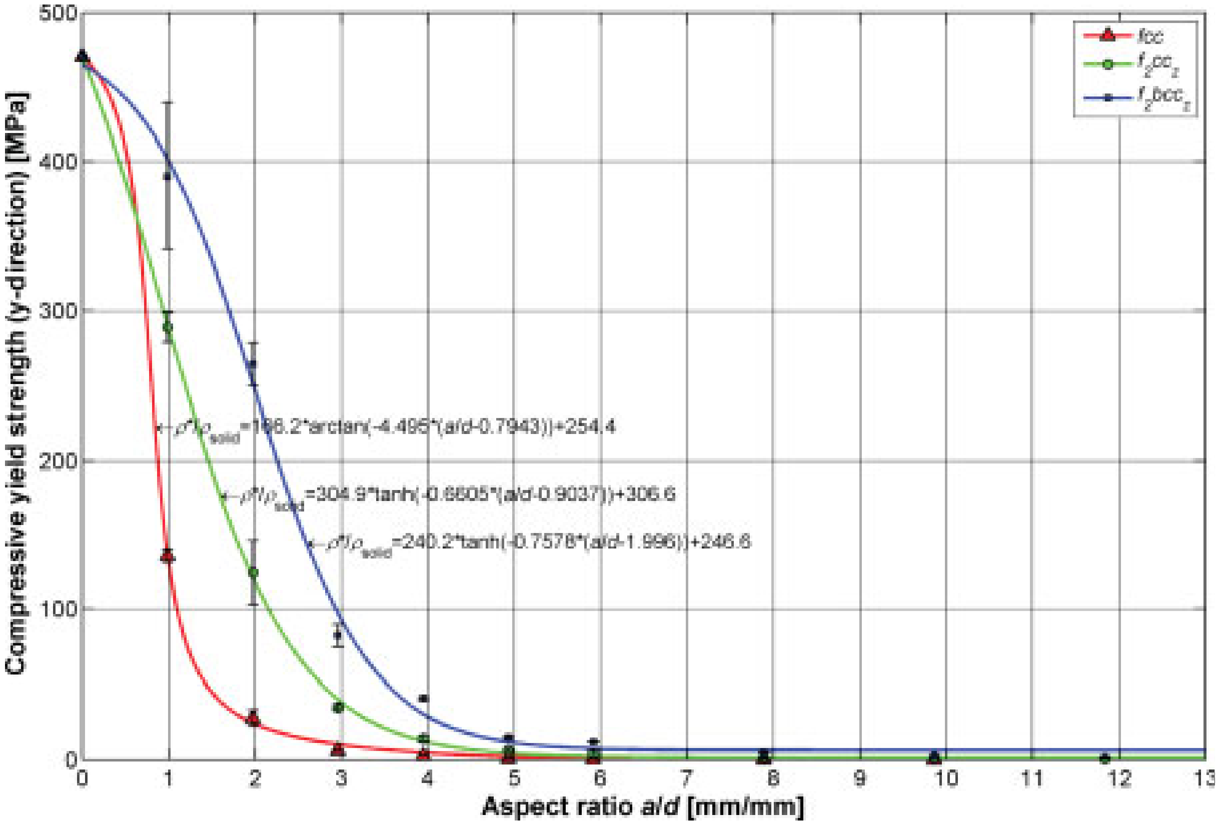

Figure 7.2: Compressive yield strengths in y-direction of different cell types vs. aspect ratio

the basis of the findings from ***section 6.7.1*** for compressive yield strength.

The results for compressive yield strengths in all three directions of space for all three investigated cell types are fitted to the three ***eqs. (5.84)*** through ***(5.86)*** where c_1 through c_4 are the coefficients of each best fit. These three functions may initially not yield satisfactory fits with coefficients of determination R^2 far below 0.9. Numerical approaches of determining the best fit coefficients may not converge if poor start values are given. An educated guess of suitable start values usually helps to obtain R^2 values close to unity.

Table 7.3 shows the resulting best fits and their coefficient of determination R^2 as well as the root mean square error (*RMSE*). If two best fits for one property yield identical R^2 values the lowest *RMSE* can be used to decide which fit is better. From ***table 7.3*** there is a clear trend as to which of the three functions is best suitable for fitting the experimental data. Evidently, this is the function of hyperbolic tangent (tanh), however, occasionally the inverse tangent (arctan) must be considered as well while the inverse hyperbolic sine (arcsinh) can be neglected. The hyperbolic tangent (tanh) usually shows the smallest slope in the transition zone from low to high relative densities whereas the the inverse hyperbolic sine (arcsinh) shows the largest slope while the inverse tangent (arctan) is balanced between both other functions.

Similar to ***section 7.1.1*** it is recommended to use the coefficients from ***table 7.3*** as start values in further development of scaling laws. Across different cell types and across the three different functions the coefficients are of the same magnitude. However, it has to be noted that the function whose best fit offers the highest coefficient of determination R^2 for a specific cell type and direction of load is not always the best choice. E.g. in the case of cell type *fcc* the value of R^2 for the best fit of hyperbolic tangent (tanh) in the y-direction is 1, however, the coefficient c_3 is negative which implies a change of curvature only for negative aspect ratios. This is considered unsuitable since the regime of high relative density, i.e. low aspect ratio, is best described by negative curvature. Therefore, the function of inverse tangent (arctan) is preferred although it shows a slightly reduced R^2 value. It is generally recommended to base judgement for best fits not merely on the coefficient of determination R^2 but also on reasonable curvature of the fit as shown in the example curves in ***fig. 7.2*** for the results from ***table 7.3*** for compressive yield strengths in the y-direction. In this figure the experimental data are given as red triangles for cell type *fcc*, as green circles for cell type f_2cc_z and as blue squares for cell type f_2bcc_z. Each best fit curve is given as a solid line of the according colour.

7.2 General design rules for SLM lattice structures and for hybrid parts

7.2.1 Design rules for stand-alone SLM lattice structures

The general design rules for SLM solids apply as well to design for SLM lattice structures, be it merely for SLM lattice structures without any solids attached or for hybrid parts consisting of SLM lattice structures with attached solid parts like e.g. walls, housings or flanges.

Heat transfer

The important issue of heat conduction through the part to the building platform due to part geometry or part orientation must be regarded in any SLM application. This is valid for SLM solids and likewise for SLM lattice structures.

Dimensional accuracy

Another important design issue which is important to SLM solids as well as SLM lattice structures is dimensional accuracy. Inaccuracies of dimensions due to systematic deviations in the used machine must be avoided by countermeasures based on mathematic expressions which relate the CAD dimensions with the dimensions actually obtained from the process. Inaccuracies due to coincidental spread around a desired dimension cannot be reduced by proper part design. This issue is left to system design instead, i.e. the quality of the SLM machine components.

Minimum feature size

Minimum feature size is on one hand limited by the hardware, i.e. the laser beam source, the focussing optics, etc. However, on the other hand the design engineer has some influence by choice of materials (heat transfer properties) and possible process parameters (beam power, scan speed, etc.) which the chosen material can be processed with as ***eq. (3.34)*** suggests.

Mechanical strength

The mechanical strength of any SLM part, whether it is a lattice structure, a solid or a combination of both, is subject to anisotropy as presented in ***section 6.1***. Besides regarding the anisotropy the design engineer must also take into account that the material properties depend severly on the process parameters. Therefore, it has to be concluded that design engineers are obliged to use material properties from trustworthy sources only where the considered material properties have repeatedly been made reproducible.

Producibility

Design rules for the producibility of SLM lattice structures as stand-alone parts as well as components of hybrid parts are given in ***section 6.2.2*** where rules for the achievable aspect ratio in SLM lattice structures are presented. The stability criterion in ***eq. (6.9)*** should be employed to predict the producibility of desired cell sizes for specific cell types.

7.2.2 Design rules for hybrid parts

Hybrid parts offer completely new design possibilities which should be exploited by design engineers. One example could be the increase of bending strength of sandwich panels by optimizing internal cellular structures. If graded cells are provided perpendicular to the face sheets where the cell size increases from the face sheet to the center of the core, then the area moment of inertia and hence the bending stiffness is maximized. Design engineers can easily develop many more such ideas and integrate them especially into hybrid parts which optimize a part for a given application. Nonetheless, it is also mandatory to mention that the field of topology optimization can contribute a great deal of help in finding optimum part design for given mechanical or thermal load situations. Therefore, these methods should be considered by the design engineer as well.

Stair step effect

One constraint which needs to be considered for solid fractions of hybrid parts is the stair step effect. In additive layer manufacturing the stair step effect is literally unavoidable. However, it can be minimized if design engineers prescribe suitable process parameters such as the layer thickness and define a proper part orientation. The latter can be obtained from mathematical optimization suggested in ***section 3.4.1.1***.

Residual stresses

Thermally induced residual stresses can develop in solid fractions of hybrid parts from unsuitable geometries such as longish features extending in the x-y-plane while the scan vector lengths are not significantly limited. Other improper geometries involve insufficient heat conduction into the building platform which functions as a heat sink. Hence, the cross section areas of successive slices of a part should decrease in positive z-direction. Other than that the support design takes major influence on successful handling of residual stresses. Again, the design engineer should rely on trustworthy material property databases which prescribe the process parameters since these take significant influence as well, as shown in ***section 3.4.3.7***.

Bonding of solid parts with SLM lattice structures

In hybrid parts with SLM lattice structures similar to the part drafted in ***fig. 3.1*** another issue of producibility must not be ignored. The bonding of any type of lattice structure on top of a horizontal bottom plane is generally easy to accomplish. However, connecting a lattice

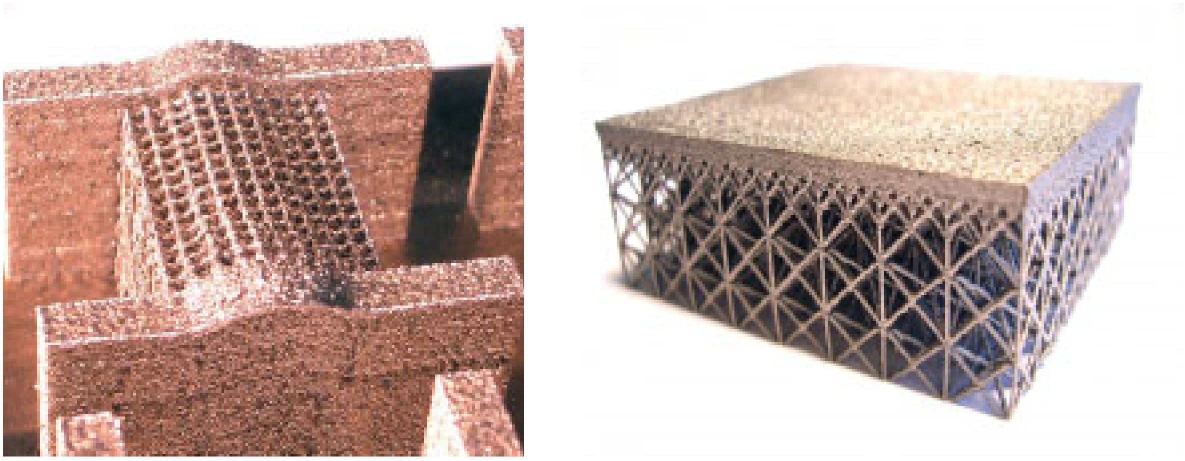

a) b)

Figure 7.3: Bonding of SLM lattice structures with solid walls in hybrid parts

structure to side walls in a hybrid part may cause build errors due to residual thermal stresses in those walls. The layerwise manufacturing process and the shrinkage of each layer during cooling down can cause the attached lattice structure to warp. Secondly, when placing a solid wall horizontally on top of a lattice structure one faces the problem that the gaps between the struts of the lattice structure underneath contain only powder. This yields potential process instabilities since metallic powders have a rather low thermal conductivity and excess process heat might not be carried away quick enough leading to the balling effect where powder particles form droplets before solidification (see ***section 3.4.3.6***). Especially this second issue depends strongly on the cell size of the lattice structure.

The three above investigated cell types with cell sizes of 6, 5, 4, 3, 2 and 1.5 mm were analyzed (Rehme, 2007, pp. 17-18, [257]) to study their behaviour of bonding them with side walls and horizontal top planes and to assess the range of cell sizes that allow building error-free parts. The experiments showed that shrinkage of solid side walls in direction of their elongation affects the attached lattice structure similar as in compressive testing in the x- or y-direction, respectively. Depending on its cell type and the load direction each lattice structure exhibits specific lateral expansion behaviour perpendicular to the direction of side wall elongation due to its positive Poisson's ratio or due to buckling. In the process of manufacturing a lattice structure, which is surrounded by side walls, the only degree of freedom for the lattice struts is the positive z-direction. Therefore, if the cell size at a given strut diameter is below a critical minimum, the lattice structure develops a hump in positive z-direction as seen in ***fig. 7.3 a)***. The results suggest that reasonable cell sizes to be attached to solid side walls should possess a minimum diameter of 1.5 mm for cell type *fcc* and a minimum of 2 mm for cell types f_2cc_z and f_2bcc_z to avoid hump development.

Solid, horizontal top planes can be manufactured over a wide range of cell sizes for all cell types tested. If the structure shown in ***fig. 7.3 b)*** is applied where the gaps between 6 mm cells are filled in with cells of 3 and 1.5 mm size, the balling effect can be overcome and a smooth, solid top plane is obtained. Gradually reducing the cell size as shown in the figure is strongly recommended for large cell sizes since upon cooling down solid layers can compress the lattice structure attached underneath in x- and y-direction similar as side walls do.

7.3 Cellular Design for SLM lattice structures in medical implants

7.3.1 Advantages of SLM lattice structures in implant applications

This ***section 7.3*** provides sample applications where SLM lattice structures and hybrid parts with included SLM lattice structure are implemented. According to press releases (MCP-HEK Tooling GmbH, 2006, pp. 1-2, [199]) and publications (Bibb, 2006, pp. 95-99, [38]) SLM solids have successfully served as hip endoprostheses and denture frameworks that were actually implanted into human bodies. Currently, cellular materials do not earn much attention in use with medical implants as shown at the bottom of ***table 2.1***. Nevertheless, open-cell structures in sub-millimeter dimensions promise great progress in design of medical implants where a maximum interaction between the implant and the surrounding tissue and a high resulting adhesion strength is desired. They allow better ingrowth of bone and other tissue as control of pore size is important for promoting growth of tissue cells and blood vessels. Recently, porous materials made from sintering or plasma spraying processes were tested to achieve increased elasticity in an attempt to match the Young's modulus of cortical bone. However, the sintered materials did not show sufficient fatigue strength and they showed low adhesion strength of the porous layer to the bulk material in the case of plasma spraying (Helsen, 1998, pp. 154-158, [141]). Therefore, solid open-cell SLM lattice structures could be well capable of delivering all advantages: acceptable osseointegration, customized elasticity and sufficient fatigue strength.

Especially the factor of customized elasticity of implants is often given particular attention in order to reduce so-called stress shielding. Stress shielding means the routing of stresses through the implant material rather than bone. It typically leads to bone resorption, i.e. loss of bone tissue, occuring at the interface between bone and implant which has the drastic effect of loosening of the implant. As a consequence the patient will require a revision in which a new prosthesis with greater dimensions is implanted in order to make up for the lost bone material. Instead researchers have suggested to employ so-called isoelastic implants where the effective stiffness of the used material matches the stiffness of the surrounding bone. However, according to Bobyn (1992, p. 91, [39]), equal ('iso') stiffnesses of the implant material and the surrounding bone are not necessarily desirable. More often the stiffness of the implant needs to be rather physioelastic, i.e. optimized for the total stiffness of bone and implant together. SLM lattice structures allow to achieve physioelastic stiffnesses in implants.

7.3.2 Example 1: Optimization of bending stiffness of a hip endoprosthesis stem

This subsection gives a sample application for a stand-alone SLM lattice structure implemented into a hip endoprosthesis. Generally, for hip endoprostheses it is beneficial for the implant to possess a bending stiffness of about one third to one half of that of the human femur (the long bone in the human thigh) (Bobyn, 1992, p. 79, [39]). The bending stiffness is dictated by the product of Young's modulus and area moment of inertia. For typical implant stem diameters of 13 mm and femur diameter of 19.5 mm the ratio of area moment of inertia of the implant and surrounding bone material results to 0.25. This implies that the effective Young's modulus of the implant stem should be around 1.2 to 2 times higher than that of the human femur's cortical tissue which can be expected to show values around 19.9 GPa according to Bayraktar (2004, p. 33, [33]). According to the results from ***section 6.6*** implant stems manufactured completely from SLM lattice structures should possess cell sizes of 1.5 up to nearly 2 mm for cell type f_2cc_z and around 2 mm for cell type f_2bcc_z. In regard of these cell sizes and the strut diameters at which the experimental findings from ***section 6.6*** were obtained, typical pore diameters between 1 and 1.5 mm result. This matches roughly the structure of the trabecular structure in the proximal femur and should, therefore, be considered suitable.

7.3.3 Example 2: Optimization of bending stiffness of a tibial base plate

An application for hybrid parts made from SLM lattice structures combined with SLM solids can be found in knee endoprostheses located at the distal end of the femur where the knee is located. Such implants connect the femur to the tibia (shinbone) and replace the natural joint either partially or completely. The tibial component in these implants typically consists of a base plate with a stem and a so-called tibial spacer which both reside in a horizontal plane on top of the tibia. The tibial base plate is usually a solid part which is rough on the bottom side to improve the bone-implant bond. ***Fig. 7.4*** shows a redesigned tibial base plate fabricated as a SLM hybrid part with its bottom side pointing towards the camera. For demonstration purposes the cell type was chosen to f_2cc_z of 2.5 mm cell size. In the above presented calculation of the required effective Young's modulus of a hip endoprosthesis an implant stem and bone give a circumferential interface. The tibial base plate, however, exhibits an interface parallel to the long bone's cross section, i.e. the stiffness of bone and implant are not additive but behave like a serial connection of springs as described by ***eq. (6.11)***. This implies that if the bending stiffness of the whole assembly should be appropriate, i.e. physioelastic, then both bone and implant must have equal bending stiffnesses. The bending stiffness of a typical human tibia comprising cortical as well as trabecular bone is around 246 Nm^2 according to studies conducted by Liang (2008, lb 131, [182]). Calculating the effective

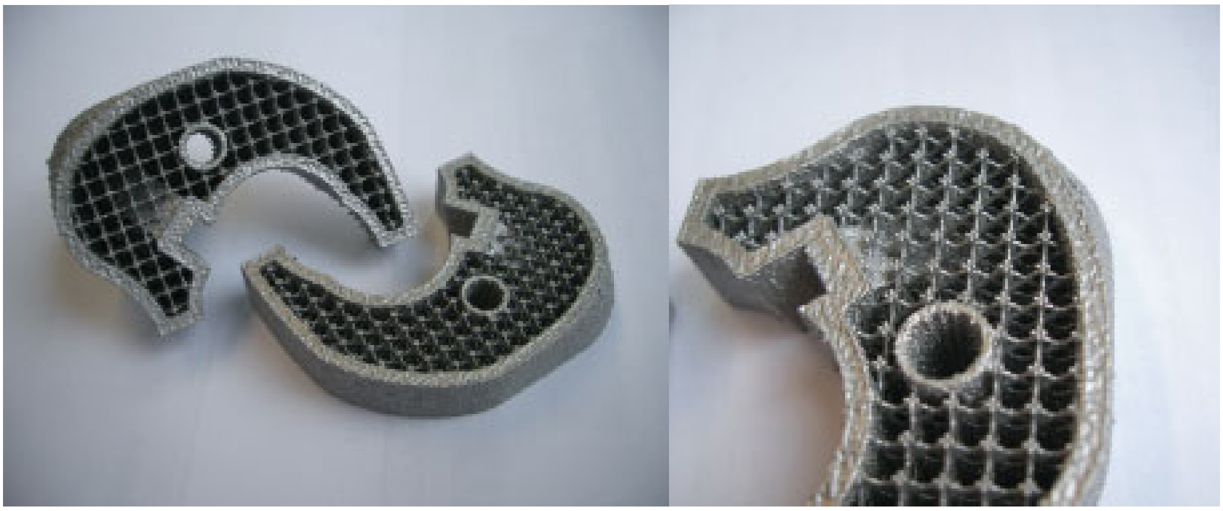

Figure 7.4: Redesigned tibial base plate as an example of a hybrid part with SLM lattice structure

Young's modulus as well as the area moment of inertia of freeform SLM lattice structures to which a freeform solid structure is attached is a tedious task which should be left to FEM calculations or estimated by piecewise calculation of the area moment of inertia. For a tibial base plate similar to the one shown in ***fig. 7.4*** which has a wall thickness of 1.5 mm it is expected that a cell size between 1 and 2 mm is required in order for it to be physioelastic. The combined Young's modulus of such a solid wall and a SLM lattice structure of cell type f_2cc_z and cell size of 1 mm (of effective elasticity according to ***table 10.5***) results to approximately 30522 MPa and the combined area moment of inertia is approximately 12708 mm^4. For cell size 1.5 mm values of 17450 MPa and 8514 mm^4 and for a cell size of 2 mm values of 10671 MPa and 6224 mm^4 result, respectively. From these values a quadratic fit of bending stiffness versus cell size can be found and a required cell size of 1.257 mm is derived in order to exactly match the above given bending stiffness of human tibia.

7.3.4 Example 3: Optimization of extensional stiffness of a tibial base plate

Since the tibial base plate is placed at the proximal end of the tibia, bending stiffness might be of lesser significance than compressive or tensile, i.e. extensional, stiffness. In order to obtain identical extensional stiffnesses of both implant and tibia, the above mentioned combined Young's modulus of SLM lattice structure and solid wall has to match the Young's Modulus of the tibia (again including cortical and trabecular bone). The Young's modulus of a human tibia in tension is given to 18.4 GPa (Fung, 1993, p. 511, [118]). A quadratic fit of the above found combined Young's moduli versus cell size gives a required cell size of 1.454 mm in order to exactly match the Young's modulus of the tibia. Depending on the fulfillment of rather one or the other task the design engineer has to compromise between both results obtained for physioelastic cell size. In cases like in ***section 7.3.2*** where only bending stiffness has to be matched no compromise is necessary, however, for interfaces between bone and implant of even more complex geometry it might be required to compromise between more results.

7.3.5 Example 4: Verification of compressive yield strength of a tibial base plate

Usually, the compressive strength of a conventional, solid tibial base plate is regarded sufficient and not subject to investigation. Evidently, the compressive strength of a tibial base plate as shown in ***fig. 7.4*** is much lower than that of a solid tibial base plate. Therefore, it should be estimated what forces can be expected to act on the tibial base plate and what strength might be obtained from the SLM hybrid part in ***fig. 7.4*** which employs the cell sizes for optimum elasticity calculated in ***sections 7.3.3*** and ***7.3.4***.

The maximum forces that an average, healthy person can tolerate for a short amount of time should be estimated to nine times the gravitational acceleration of earth, i.e. 9*g*. Thus the tibial base plate might have to bear forces as high as nine times the person's weight. If the person is assumed to weigh 100 kg this results in a force of 8829 N. Assuming further that this force is distributed evenly across the cross section of the tibial base plate, the solid wall (area of 234 mm^2) has to tolerate 2350 N while the lattice structure (area of 645.1 mm^2) has to bear 6479 N. Both forces are equivalent to 10.04 MPa of stress which is of no significance for the solid wall. According to the experimental results from ***table 10.8*** at a cell size of 1.5 mm the cell type f_2cc_z shows compressive yield strengths of at least 34.41 MPa with a standard deviation of 1.639 MPa. At smaller cell sizes as calculated in ***sections 7.3.3*** and ***7.3.4*** the strength even increases further. Therefore, it can be assumed that the redesigned tibial base plate will not fail due to static loads.

7.3.6 Example 5: Optimization of manufacturing time and cost of a tibial base plate

According to the implant manufacturer the conventional tibial base plate is produced in batches of 30 parts where each tibial base plate costs roughly 150 Euros. One lot requires approximately a lead time of one week. Using the SLM process with a 250 by 250 mm build platform 24 tibial base plates similar to the one in ***fig. 7.4*** can be manufactured simultaneously. Each one has a solid volume of 4086 mm^2 without the lattice structure. Typical process parameters for the SLM system introduced in ***section 4.2.3*** which use a layer thickness of 75 µm yield a build rate of 0.9 mm^3/s. It is assumed that the recoating of the powder bed requires approximately 20 s per layer and that the recoating is repeated for 144 layers, based on the layer thickness and the part height of 10.8 mm. Additionally it is provided that each tibial base plate in each layer has on average 460 exposure points for fabricating the lattice structure and each exposure point requires 0.0085 s of laser beam exposure time. Altogether this yields a total build time of 34.82 hours. If machine operation cost of 100 Euros per hour is assumed then the price per part results to approximately 145 Euros. In fact it is expected that the machine operation cost per hour will be severely reduced in the near future as the initial investment cost will decrease.

Nevertheless, today’s SLM technology already allows to produce a batch of 24 parts at approximately the same cost per part. The production time is also reduced, however, additionally to those two days of SLM production another two days should be calculated for post-processing which gives a lead time reduced from 7 to 4 days. Most importantly the value of the added functionality of improved osseointegration which is received from the SLM lattice structure must be considered.

7.4 Summary

This chapter shows how the experimental results from ***section 6*** can be converted into scaling laws which may be employed by design engineers in a convenient way. This implies mainly conversions between relative density and aspect ratio, where the latter is the main design parameter which is familiar to design engineers. Sample scaling laws based on the aspect ratio are derived for the three investigated cell types. Since SLM lattice structures can be fabricated with nearly any arbitrary relative density it was shown in ***section 6*** that power laws alone do not allow sufficient characterization of their mechanical properties due to break down of the power laws beyond the critical relative density. Therefore, this chapter gives suitable correlations for the power law regime where low relative density (or vice versa high aspect ratio) prevails. It also gives scaling laws for the full range of relative densities (or aspect ratios) that are based on some trigonometric functions. From these functions usually the hyperbolic tangent (tanh) is most suitable to describe both regimes of low and high relative density as well as the transition between them.

Next, general rules are given on how to design SLM solids, SLM lattice structures and SLM hybrid parts which combine both solids and lattice structures. Specific insight is given into hybrid parts where SLM lattice structures are bonded to solid walls. The specific design limitations inherent in these parts are discussed.

Finally, it is shown how SLM lattice structures and SLM hybrid parts can be implemented into products like medical implants. One example each is given for a hip endoprosthesis and a knee endoprosthesis which employ either a stand-alone SLM lattice structure or a SLM hybrid part. It is expected that these applications benefit from the implementation of SLM lattice structures by promoting faster ingrowth of bone tissue, increased stability of the implant and physioelastic properties which increase the lifetime expectation of the bond between bone tissue and the implant due to reduced stress shielding. In five examples the impact of the implementation of SLM lattice structures into both parts is analyzed. The examples involve analysis of effective bending stiffness, extensional stiffness, compressive yield strength as well as manufacturing cost and time to reflect the goals set out in ***section 1*** where cellular design was intended to be incorporated into LFF processes in order to reduce manufacturing cost and time while product quality is enhanced.

8 Conclusion

The work in this thesis was set out to develop a new class of metallic, cellular materials which provide new interesting characteristics and properties from an innovative manufacturing process called Laser Freeform Fabrication (LFF). The approach of combining the benefits of cellular design with an innovative production process was on one hand expected to have an impact on the reduction of manufacturing cost and time. On the other hand product quality was expected to be enhanced by establishing intelligent designs and new functionalities.

It was shown that by using cellular materials the functionality of a product and hence its quality typically depends on characteristics from the fabrication process rather than independently chosen design parameters. Furthermore, conventional manufacturing methods for periodic, cellular materials were found to be not sufficient in terms of achieving small cell sizes in the range of few millimeters while high periodicity, high strength, little flaws and the potential for topology optimization is given. Therefore, the Selective Laser Melting (SLM) process was analyzed thoroughly to correlate its influence parameters with quality properties of SLM solid parts before it was developed for the manufacture of so-called SLM lattice structures. It could be shown that employing CAD data is not sufficient to obtain micro-sized struts. Therefore, a new point-like exposure strategy was developed which allows the manufacture of SLM lattice structures with micro-sized struts in the submillimeter range and cell sizes in the range of few millimeters down to the submillimeter range made from stainless steel powder materials.

In order to give guidelines for design engineers who wish to employ SLM lattice structures in future product development the mechanical properties of SLM lattice structures were assessed by development of an anisotropic structural hypothesis and by intensive experimental investigations. All single steps and results of this approach are summarized at the end of each chapter. It was shown that SLM lattice structures allow a very high degree of design freedom compared to conventional cellular materials. From this the most important finding of this thesis was derived that power laws, which are normally used to describe mechanical properties of cellular materials, break down above a certain critical relative density. After three most promising cell types of SLM lattice structures were identified, new correlations were developed for these cell types which allow to represent the full range of relative densities, i.e. both regimes of low and high relative density as well as the transition zone. Furthermore, one specific cell type called f_2cc_z was identified which excels other cell types by far and is overall best performing due to its high specific strength, high specific energy absorption and high specific stiffness when loaded under compressive stresses, especially in z-direction.

This thesis contributes to the improvement of products manufactured with LFF processes. The approach of cellular design allows not only to reduce manufacturing time due to reduced exposure time and hence less production cost, but it also allows to employ new degrees of design freedom and, therefore, increased product quality due to new product functionalities. This work further accounts for changing conventional approaches of product design and provides tools for design engineers to successfully implement SLM lattice structures into their products. For this reason design rules were recommended for the application of SLM lattice structures as stand-alone parts as well as hybrid parts.

In order to further substantiate the implementation of SLM lattice structures into applications, two examples from the field of medical endoprostheses were scrutinized in order to prove how innovative products can be furnished with new functionalities. In these applications new functionalities involve faster ingrowth of bone tissue, increased stability of the implant and physioelastic properties which increase the lifetime expectation of the bond between bone tissue and the implant. It could be shown that the integration of SLM lattice structures is on one hand feasible and on the other hand suitable to manufacture hip endoprostheses with matching bending stiffness and knee endoprosthesis components with matching bending stiffness, matching extensional stiffness and sufficient compressive yield strength. Additionally, it was shown that in the case of knee endoprosthesis components produced with SLM, manufacturing time and cost can be reduced as well.

Despite of the comprehensive results compiled in this work some unanswered questions remain. It is expected that these present results can be easily applied on any other ductile metallic material. For brittle materials, however, it is expected that rescaling of the results is only permissible in very low relative density regimes where cellular materials behave rather ductile. More particular questions such as variability of specific strengths in dependency of the cell size or energy absorption in dependency of the cell size were not further investigated in this thesis and are left for future work. Any type of topological optimization of SLM lattice structures was not dealt with in this thesis either. This field in particular breaks ground for further improved design methods. SLM lattice structures in products could be further optimized in respect of expected load cases. In structural or thermal applications modifications on the level of single struts could improve their overall performance. These modifications could mean e.g. the removal of struts or customization of strut diameters according to stress or heat propagation. This would require the implementation of the design rules for SLM lattice structures presented here into software for finite element methods.

9 Bibliography

[1] **Abdel Ghany, K. ; Moustafa, S. F.:** *Comparison between the products of four RPM systems for metal.* In: Rapid Prototyping Journal, Vol. 12, No. 2, 2006, Bradford, UK : MCB University Press, 2006, Pages 86-94, ISSN 1355-2546

[2] **Abramenko, A. N. ; Kalinichenko, A. S. ; Burtser, Y. et al.:** *Determination of the Thermal Conductivity of Foam Aluminum.* In: Journal of Engineering Physics and Thermophysics, Vol. 72, No. 3, 1999, New York City, NY, USA : Springer, 1999, Pages 369-373, ISSN 1062-0125

[3] **Abrate, S.:** *Criteria for Yielding or Failure of Cellular Materials.* In: Journal of Sandwich Structures and Materials, Vol. 10, No. 1, 2008, London, UK : Sage Publications, 2008, Pages 5-51, ISSN 1099-6362

[4] **Agarwala, M. ; Bourell, D. ; Beaman, J. et al.:** *Direct selective laser sintering of metals.* In: Rapid Prototyping Journal, Vol. 1, No. 1, 1995, Bradford, UK : MCB University Press, 1995, Pages 26-36, ISSN 1355-2546

[5] **Agarwala, M. ; Bourell, D. ; Beaman, J. et al.:** *Post-processing of selective laser sintered metal parts.* In: Rapid Prototyping Journal, Vol. 1, No. 2, 1995, Bradford, UK : MCB University Press, 1995, Pages 36-44, ISSN 1355-2546

[6] **Aizenberg, J. ; Weaver, J. C. ; Thanawala, M. S. et al.:** *Skeleton of Euplectella sp.: Structural Hierarchy from the Nanoscale to the Macroscale.* In: Science, Vol. 309, No. 5732, 2005, Washington, DC, USA : AAAS, 2005, Pages 275-278, ISSN 0036-8075

[7] **Akhtar, S. ; Wright, C. S. ; Youseffi, M.:** *Direct Selective Laser Sintering of Tool Steel Powders to High Density: Part B – The Effects on Microstructural Evolution.* In: Bourell, D. L. ; Crawford, R. H. ; Beaman, J. J. ; Wood, K. L. ; Marcus, H. L. : 14th Solid Freeform Fabrication Proceedings 2003, Austin, TX, USA : University of Texas, 2003, Pages 656-667, ISSN 1053-2153

[8] **Almeida, H. ; Bártolo, P. J.:** *Computer Aided Design of Scaffolds for Rapid Prototyping.* In: Proceedings RPD 2006 Rapid Product Development Event, Marinha Grande, Portugal, Marinha Grande, Portugal : Centimfe, 2006, Pages P6050.1-P6050.6

[9] **Andersen, O. ; Studnitzky, T. ; Bauer, J.:** *Direct Typing – a New Method for the Production of Cellular P/M Parts.* In: Proceedings of Euro PM 2004, Powder Metallurgy World Congress & Exhibition, Vienna, Austria, Editors : Danninger, H. ; Ratzi, R. ; Vol. 4, Shrewsbury, UK : European Powder Metallurgy Association, 2004, Pages 189-194, ISBN 1-899072-15-2

[10] **Andrews, E. W. ; Sanders, W. ; Gibson, L. J.:** *Compressive and tensile behaviour of aluminum foams.* In: Materials Science and Engineering A, Vol. 270, No. 2, 1999, Amsterdam, Netherlands : Elsevier, 1999, Pages 113-124, ISSN 0921-5093

[11] **Andrews, E. W. ; Huang, J.-S. ; Gibson, L. J.:** *Creep behavior of a closed-cell aluminum foam.* In: Acta Materialia, Vol. 47, No. 10, 1999, Kidlington, UK : Elsevier, 1999, Pages 2927-2935, ISSN 1359-6454

[12] **Andrews, E. W. ; Gioux, G. ; Onck, P. et al.:** *Size effects in ductile cellular solids. Part II: experimental results.* In: International Journal of Mechanical Sciences, Vol. 43, No. 3, 2001, Kidlington, UK : Elsevier, 2001, Pages 701-713, ISSN 0020-7403

[13] **Andrews, E. W. ; Gibson, L. J. ; Ashby, M. F.:** *The creep of cellular solids.* In: Acta Materialia, Vol. 47, No. 10, 1999, Kidlington, UK : Elsevier, 1999, Pages 2853-2863, ISSN 1359-6454

[14] **Andrews, K. W.:** *Empirical formulae for the calculation of some transformation temperatures.* In: Journal of the Iron and Steel Institute, Vol. 203, 1965, London, UK : Iron and Steel Institute, 1965, Pages 721-727, ISSN 0021-1567

[15] **Angel, S.:** *Das SchlickerReaktionsSchaumSinter(SRSS)-Verfahren im Vergleich im Vergleich zu Aluminium- und Nickelschaum.* Institut für Eisenhüttenkunde (iEHK), RWTH, 2005

[16] **Apprill, J. M. ; Poirier, D. R. ; Maguire, M. C. et al.:** *GASAR Porous Metals Process Control.* In: Porous and Cellular Materials for Structural Applications, Symposium 1998, San Francisco, CA, USA, Editors : Schwartz, D. S. ; Shih, D. S. ; Evans, A. G. ; Wadley, H. N. G. ; Vol. 521, Warrendale, PA, USA : Materials Research Society, 1998, Pages 291-296, ISBN 1-55899-427-0

[17] **Ashby, M. F. ; Evans, A. G. ; Fleck, N. A. et al.:** *Metal Foams : A Design Guide.* Boston, MA, USA : Butterworth-Heinemann, 2000, ISBN 0-7506-7219-6

[18] **ASTM B 213 – 03:** *Standard Test Method for Flow Rate of Metal Powders.* West Conshohocken, PA, USA : American Society for Testing and Materials, 2003

[19] **ASTM C 273 – 61:** *Standard Test Method for Shear Properties in Flatwise Plane of Flat Sandwich Constructions or Sandwich Cores.* Philadelphia, PA, USA : American Society for Testing and Materials, 1988

[20] **ASTM C 297 – 61:** *Standard Test Method for Tensile Strength of Flat Sandwich Constructions in Flatwise Plane.* Philadelphia, PA, USA : American Society for Testing and Materials, 1988

[21] **Babcsán, N. ; Banhart, J. ; Leitlmeier, D.:** *Metal Foams – Manufacture and Physics of Foaming.* In: Proceedings of the International Conference "Advanced Metallic Materials", Bratislava, Slovakia : Institute of Materials and Machine Mechanics, 2003, Pages 5-15, ISBN 80-969011-7-6

[22] **Babcsán, N. ; Mészáros, I. ; Hegman, N.:** *Thermal and Electrical Conductivity Measurements on Aluminum Foams.* In: Materialwissenschaft und Werkstofftechnik, Vol. 34, No. 4, 2003, Weinheim, Germany : Wiley-VCH Verlag, 2003, Pages 391-394, ISSN 0933-5137

[23] **Badiche, X. ; Forest, S. ; Guibert, T. et al.:** *Mechanical properties and non-homogeneous deformation of open-cell nickel foams: application of the mechanics of cellular solids and of porous materials.* In: Materials Science and Engineering A, Vol. 289, No. 1-2, 2000, Amsterdam, Netherlands : Elsevier, 2000, Pages 276-288, ISSN 0921-5093

[24] **Badrinarayan, B. ; Barlow, J. W.:** *Metal Parts From Selective Laser Sintering of Metal-Polymer Powders.* In: Marcus, H. L. ; Beaman, J. J. ; Barlow, J. W. ; Bourell, D. L. ; Crawford, R. H. : 3rd Solid Freeform Fabrication Proceedings 1992, Austin, TX, USA : University of Texas, 1992, Pages 141-146, ISSN 1053-2153

[25] **Banhart, J. ; Baumeister, J. ; Weber, M.:** *Damping properties of aluminium foams.* In: Materials Science and Engineering A, Vol. 205, No. 1-2, 1996, Amsterdam, Netherlands : Elsevier, 1996, Pages 221-228, ISSN 0921-5093

[26] **Banhart, J.:** *Eigenschaften und Anwendungsgebiete offenporiger metallischer Werkstoffe.* In: Materialwissenschaft und Werkstofftechnik, Vol. 31, No. 6, 2000, Weinheim, Germany : Wiley-VCH Verlag, 2000, Pages 501-504, ISSN 0933-5137

[27] **Banhart, J. ; Brinkers, W.:** *Fatigue Behavior of Aluminum Foams.* In: Journal of Material Sciences Letters, Vol. 18, No. 8, 1999, Dordrecht, Netherlands : Kluwer, 1999, Pages 617-619, ISSN 0261-8028

[28] **Banhart, J.:** *Manufacture, characterisation and application of cellular metals and metal foams.* In: Progress in Material Science, Vol. 46, No. 6, 2001, Amsterdam, Netherlands : Elsevier, 2001, Pages 559-632, ISSN 0079-6425

[29] **Banhart, J.:** *Manufacturing Routes for Metallic Foams.* In: JOM, Vol. 52, No. 12, 2000, Warrendale, PA, USA : The Minerals, Metals & Materials Society, 2000, Pages 22-27, ISSN 1047-4838

[30] **Banhart, J.:** *Foam Metal: The Recipe.* In: europhysics news, Vol. 30, No. 1, 1999, Berlin, Germany : Springer, 1999, Pages 17-20, ISSN 0531-7479

[31] **Banhart, J. ; Knüwer, M.:** *Powder Injection and Formation of Porosity in Spray Forming.* In: Proceedings of Euro PM 1998, Powder Metallurgy World Congress & Exhibition, Granada, Spain, Vol. 5, Bellstone, UK : European Powder Metallurgy Association, 1998, Pages 265-270, ISBN 1-899072-09-8

[32] **Banhart, J. ; Baumeister, J.:** *Production Methods for Metallic Foams.* In: Porous and Cellular Materials for Structural Applications, Symposium 1998, San Francisco, CA, USA, Editors : Schwartz, D. S. ; Shih, D. S. ; Evans, A. G. ; Wadley, H. N. G. ; Vol. 521, Warrendale, PA, USA : Materials Research Society, 1998, Pages 121-132, ISBN 1-55899-427-0

[33] **Bayraktar, H. H. ; Morgan, E. F. ; Niebur, G. L. et al.:** *Comparison of the elastic and yield properties of human femoral trabecular and cortical bone tissue.* In: Journal of Biomechanics, Vol. 37, No. 1, 2004, Amsterdam, Netherlands : Elsevier, 2004, Pages 27-35, ISSN 0021-9290

[34] **Bažant, Z. P. ; Cedolin, L.:** *Stability of Structures.* Oxford, UK : Oxford University Press, 1991, ISBN 0-19-505529-2

[35] **Beal, V. E. ; Erasenthiran, P. ; Hopkinson, N. et al.:** *Fabrication of x-graded H13 and Cu powder mix using high power pulsed Nd:YAG laser.* In: Bourell, D. L. ; Crawford, R. H. ; Beaman, J. J. ; Wood, K. L. ; Marcus, H. L. : 15th Solid Freeform Fabrication Proceedings 2004, Austin, TX, USA : University of Texas, 2004, Pages 187-197, ISSN 1053-2153

[36] **Bell, L. H. ; Bell, D. H.:** *Industrial Noise Control : Fundamentals and Applications.* Second edition, New York City, NY, USA : Dekker, 1994, ISBN 0-8247-9028-6

[37] **Berggreen, K. M.:** *Findung geeigneter Prozessparameter für das Lasergenerieren von Funktionsbauteilen der Medizintechnik aus Titan-Werkstoffen unter besonderer Berücksichtigung der Qualitätssicherung.* Diploma thesis at Hamburg University of Technology (TUHH), Institute of Laser and System Technologies (iLAS), 2005, Supervisor : Rehme, O.

[38] **Bibb, R. ; Eggbeer, D.:** *Rapid manufacture of removable partial denture frameworks.* In: Rapid Prototyping Journal, Vol. 12, No. 2, 2006, Bradford, UK : MCB University Press, 2006, Pages 95-99, ISSN 1355-2546

[39] **Bobyn, J. D. ; Mortimer, E. S. ; Glassman, A. H. et al.:** *Producing and Avoiding Stress Shielding: Laboratory and Clinical Observations of Noncemented Total Hip Arthroplasty.* In: Clinical orthopaedics and related research, Vol. 274, No. 1, 1992, Philadelphia, PA, USA : Lippincott Williams & Wilkins, 1992, Pages 79-96, ISSN 0009-921X

[40] **Boccaccini, A. R.:** *Zur Abhängigkeit der mechanischen Eigenschaften zweiphasiger und poröser Werkstoffe von der Gefüge- bzw. Porositätsstruktur.* Dissertation RWTH Aachen, Germany, 1994, Aachen, Germany : Verlag Mainz, ISBN 3-930085-38-0

[41] **Boomsma, K. S. ; Poulikakos, D.:** *On the effective thermal conductivity of a three-dimensonally structured fluid-saturated metal foam.* In: International Journal of Heat and Mass Transfer, Vol. 44, No. 4, 2001, Amsterdam, Netherlands : Elsevier, 2001, Pages 827-836, ISSN 0017-9310

[42] **Boomsma, K. S.:** *Metal Foams as Novel Compact High Performance Heat Exchangers for the Cooling of Electronics.* Dissertation ETH Zürich, Switzerland, 2002 http://e-collection.ethbib.ethz.ch/ecol-pool/diss/fulltext/eth14708.pdf Updated last: February, 3rd 2003 ; Retrieved: April, 16th 2006

[43] **Bourell, D. L. ; Marcus, H. L. ; Barlow, J. W. et al.:** *Selective Laser Sintering of Metals and Ceramics.* In: The International Journal of Powder Metallurgy, Vol. 28, No. 4, 1992, Princeton, NJ, USA : American Powder Metallurgy Institute, 1992, Pages 369-381, ISSN 0888-7462

[44] **Bram, M. ; Nelles, H. ; Buchkremer, H. P. et al.:** *Charakterisierung, mechanische Eigenschaften und Verformungsverhalten von hochporösen Formkörpern aus Titan und rostfreien Stählen (316L).* In: Materialwissenschaft und Werkstofftechnik, Vol. 31, No. 6, 2000, Weinheim, Germany : Wiley-VCH Verlag, 2000, Pages 497-500, ISSN 0933-5137

[45] **Brettschneider, M.:** *Untersuchung der Anisotropie der mechanischen Eigenschaften von lasergenerierten Probekörpern.* Project thesis at Hamburg University of Technology (TUHH), Institute of Laser and System Technologies (iLAS), 2006, Supervisor : Rehme, O.

[46] **Brothers, A. H. ; Dunand, D. C.:** *Plasticity and damage in cellular amorphous metals.* In: Acta Materialia, Vol. 53, No. 16, 2005, Kidlington, UK : Elsevier, 2005, Pages 4427-4440, ISSN 1359-6454

[47] **Brunauer, S. ; Emmet, P. H. ; Teller, E.:** *Adsorption of Gases in Multimolecular Layers.* In: Journal of the American Chemical Society. Vol. 60, No. 2, 1938, Pages 309-319, ISSN 0002-7863

[48] **Buckminster Fuller, R.:** *Inventions: The Patented Works of R. Buckminster Fuller.* New York City, NY, USA : St. Martin's Press, 1983, ISBN 0-31243-479-0

[49] **Bugeda, G. ; Cervera, M. ; Lombera, G.:** *Numerical prediction of temperature and density distribution in selective laser sintering processes.* In: Rapid Prototyping Journal, Vol. 5, No. 1, 1999, Bradford, UK : MCB University Press, 1999, Pages 21-26, ISSN 1355-2546

[50] **Calladine, C. R.:** *Buckminster Fuller's "Tensegrity" structures and Clerk Maxwell's rules for the construction of stiff frames.* In: International Journal of Solids and Structures, Vol. 14, No. 2, 1978, Oxford, UK : Pergamon Press, 1978, Pages 161-172, ISSN 0020-7683

[51] **Calmidi, V. V. ; Mahajan, R. L.:** *The effective thermal conductivity of high porosity fibrous metal foams.* In: Journal of Heat Transfer, Vol. 121, No. 2, 1999, New York City, NY, USA : ASME, 1999, Pages 466-471, ISSN 0022-1481

[52] **Cambridge Technologies / N. N.:** *Model 6650 Moving Coil Closed Loop Galvanometer Based Optical Scanner with Capacitive Position Detector.* http://www.camtech.com/products/6450/6650.html
Updated last: 2003 ; Retrieved: November, 25th 2007

[53] **Castillo, L.:** *Study about the rapid manufacturing of complex parts of stainless steel and titanium.* TNO and AIMME report 2005, Instituto Tecnológico Metalmecánico

[54] **Chen, C. P. ; Lakes, R. S.:** *Holographic study of conventional and negative Poisson's ratio metallic foams: elasticity, yield and micro-deformation.* In: Journal of Materials Sciences, Vol. 26, No. 20, 1991, Dordrecht, Netherlands : Kluwer, 1991, Pages 5397-5402, ISSN 0022-2461

[55] **Chen, T. ; Zhang, Y.:** *Thermal Modeling of Metal Powder-Based Selective Laser Sintering.* In: Bourell, D. L. ; Crawford, R. H. ; Beaman, J. J. ; Wood, K. L. ; Marcus, H. L. : 16th Solid Freeform Fabrication Proceedings 2005, Austin, TX, USA : University of Texas, 2005, Pages 356-369, ISSN 1053-2153

[56] **Choe, H. ; Dunand, D. C.** *Synthesis, structure and mechanical properties of Ni-Al and Ni-Cr-Al superalloy foams.* In: Acta Materialia, Vol. 52, No. 5, 2004, Kidlington, UK : Elsevier, 2004, Pages 1283-1295, ISSN 1359-6454

[57] **Choi, J. B. ; Lakes, R. S.:** *Fracture Toughness of Re-entrant Foam Materials with a Negative Poisson's Ratio: Experiment and Analysis.* In: International Journal of Fracture, Vol. 80, No. 1, 1996, Dordrecht, Netherlands : Kluwer Academic Publication, 1996, Pages 73-83, ISSN 0020-7268

[58] **Choi, J. B. ; Lakes, R. S.:** *Nonlinear Analysis of the Poisson's Ratio of Negative Poisson's Ratio foams.* In: Journal of Composite Materials, Vol. 29, No. 1, 1995, London, UK : Sage Publications, 1995, Pages 113-128, ISSN 0021-9983

[59] **Choi, J. B. ; Lakes, R. S.:** *Nonlinear Properties of metallic cellular materials with a negative Poisson's ratio.* In: Journal of Materials Sciences, Vol. 27, No. 19, 1992, Dordrecht, Netherlands : Kluwer, 1992, Pages 5373-5381, ISSN 0022-2461

[60] **Chou, K.-S. ; Song, M.-A.:** *A novel method for making open-cell aluminum foams with soft ceramic balls.* In: Scripta Materialia, Vol. 46, No. 5, 2002, Oxford, UK : Elsevier, 2002, Pages 379-382, ISSN 1359-6462

[61] **Chu, C. L. ; Chung, C. Y. ; Lin, P. H. et al.:** *Fabrication of porous NiTi shape memory alloy for hard tissue implants by combustion synthesis.* In: Materials Science and Engineering A, Vol. 366, No. 1, 2004, Amsterdam, Netherlands : Elsevier, 2004, Pages 114-119, ISSN 0921-5093

[62] **Chung, H. ; Das, S.:** *Scaling Laws for Melting and Resolidification in Direct Selective Laser Sintering of Metals.* In: Bourell, D. L. ; Crawford, R. H. ; Beaman, J. J. ; Wood, K. L. ; Marcus, H. L. : 13th Solid Freeform Fabrication Proceedings 2002, Austin, TX, USA : University of Texas, 2002, Pages 322-330, ISSN 1053-2153

[63] **Cocks, A. C. F. ; Ashby, M. F.:** *Creep-buckling of cellular solids.* In: Acta Materialia, Vol. 48, No. 13, 2000, Kidlington, UK : Elsevier, 2000, Pages 3395-3400, ISSN 1359-6454

[64] **Costa, L. ; Vilar, R. ; Réti, T.:** *Simulating the effects of substrate pre-heating on the final structure of steel parts built by laser powder deposition.* In: Bourell, D. L. ; Crawford, R. H. ; Beaman, J. J. ; Wood, K. L. ; Marcus, H. L. : 15th Solid Freeform Fabrication Proceedings 2004, Austin, TX, USA : University of Texas, 2004, Pages 643-654, ISSN 1053-2153

[65] **Cowin, S. C.:** *Properties of the Anisotropic Elasticity Tensor.* In: The Quarterly Journal of Mechanics and Applied Mathematics, Vol. 42, No. 2, 1989, Oxford, UK : Oxford University Press, 1989, Pages 249-266, ISSN 0033-5614

[66] **Crames, I.:** *Untersuchung und Aufnahme spezifischer Kenngrößen einer Anlage für das Lasergenerieren.* Project thesis at Hamburg University of Technology (TUHH), Institute of Laser and System Technologies (iLAS), 2005, Supervisor : Rehme, O.

[67] **Curran, J. A.:** *Micrograph 631 and full record.* Department of Materials Science and Metallurgy, University of Cambridge http://www.msm.cam.ac.uk/doitpoms/miclib/micrograph_record.php?id=631 Updated last: October, 2nd 2003 ; Retrieved: January, 16th 2007

[68] **Dalgarno, K. W. ; Childs, T. H. C. ; Rowntree, I. et al.:** *Finite Element Analysis of Curl Development in the Selective Laser Sintering Process.* In: Bourell, D. L. ; Beaman, J. J. ; Marcus, H. L. ; Crawford, R. H. ; Barlow, J. W. : 7th Solid Freeform Fabrication Proceedings 1996, Austin, TX, USA : University of Texas, 1996, Pages 559-566, ISSN 1053-2153

[69] **Dalgarno, K. W. ; Stewart, T.:** *Production tooling for polymer moulding using the RapidSteel process,* In: Rapid Prototyping Journal, Vol. 7, No. 3, 2001, Bradford, UK : MCB University Press, 2001, Pages 173-179, ISSN 1355-2546

[70] **Dalgarno, K. W. ; Goodridge, R. D.:** *Compression testing of layer manufactured metal parts:the RAPTIA compression benchmark.* In: Rapid Prototyping Journal, Vol. 10, No. 4, 2004, Bradford, UK : MCB University Press, 2004, Pages 261-264, ISSN 1355-2546

[71] **Dalgarno, K. W. ; Pallari, J. H. ; Woodburn, J.:** *Mass Customisation of Medical Devices and Implants: State of the Art and Future Directions.* http://www.rm-platform.com/index.php?option=com_docman&task=doc_download&gid=122&Itemid=38 Updated last: August, 21st 2006 ; Retrieved: July, 10th 2007

[72] **Dannemann, K. A. ; Lankford Jr., J.:** *High strain rate compression of closed-cell aluminium foams.* In: Materials Science and Engineering A, Vol. 293, No. 1-2, 2000, Amsterdam, Netherlands : Elsevier, 2000, Pages 157-164, ISSN 0921-5093

[73] **Darcy, H (1856) ; Bobeck, P. (english translation, 2004):** *The Public Fountains of the City of Dijon.* Dubuque, IA, USA : Kendall / Hunt Publishing Company, 2004, ISBN 0-7575-0540-6

[74] **Das, S. ; Chung, H.:** *A Model of Laser-Powder Interaction in Direct Selective Laser Sintering,* In: Bourell, D. L. ; Beaman, J. J. ; Crawford, R. H. ; Marcus, H. L. ; Wood, K. L. ; Barlow, J. W. : 12th Solid Freeform Fabrication Proceedings 2001, Austin, TX, USA : University of Texas, 2001, Pages 357-365, ISSN 1053-2153

[75] **Deckard, C. R.:** *Selective Laser Sintering.* Dissertation University of Texas, Austin, TX, USA, 1989, Ann Arbor, MI, USA : UMI, 1989

[76] **Degischer, H. P.:** *Heterogeneous Metals Designed for Structural Applications.* In: Proceedings of the International Conference “Advanced Metallic Materials”, Bratislava, Slovakia : Institute of Materials and Machine Mechanics, 2003, Pages 40-47, ISBN 80-969011-7-6

[77] **Deloro Stellite Holding GmbH & Co. KG / Hofmann, D.:** *Werkszeugnis nach DIN EN 10204/2.2, Nr. 554466.* Koblenz, Germany : Deloro Stellite, 2006

[78] **Deshpande, V. S. ; Fleck, N. A.:** *Collapse of truss core sandwich beams in 3-point bending.* In: International Journal of Solids and Structures, Vol. 38, No. 36, 2001, New York City, NY, USA : Elsevier, 2001, Pages 6275-6305, ISSN 0020-7683

[79] **Deshpande, V. S. ; Fleck, N. A.:** *Isotropic constitutive model for metallic foams.* In: Journal of the Mechanics and Physics of Solids, Vol. 48, No. 6-7, 2000, Amsterdam, Netherlands : Elsevier, 2000, Pages 1253-1283, ISSN 0022-5096

[80] **Dharmasena, K. P. ; Wadley, H. N. G.:** *Electrical conductivity of open-cell metal foams.* In: Journal of Materials Research, Vol. 17, No. 3, 2002, Warrendale, PA, USA : Materials Research Society, 2002, Pages 625-631, ISSN 0884-2914

[81] **DIN 1304-1:1994-03:** *Formelzeichen – Allgemeine Formelzeichen.* Berlin, Germany : Beuth Verlag, 1994

[82] **DIN 8580:2003-09:** *Fertigungsverfahren: Begriffe, Einteilung.* Berlin, Germany : Beuth Verlag, 2003

[83] **DIN 32532:2006-11:** *Schweißen – Laserstrahlverfahren zur Materialbearbeitung – Begriffe für Prozesse und Geräte (draft version):* Berlin, Germany : Beuth Verlag, 2006

[84] **DIN 50100:1978-02:** *Dauerschwingversuch.* Berlin, Germany : Beuth Verlag, 1978

[85] **DIN 50125:2004-01:** *Prüfung metallischer Werkstoffe – Zugproben.* Berlin, Germany : Beuth Verlag, 2004

[86] **DIN 50134:2007-12:** *Prüfung von metallischen Werkstoffen – Druckversuch an metallischen zellularen Werkstoffen.* Berlin, Germany : Beuth Verlag, 2007

[87] **DIN 50141:1982-01:** *Prüfung metallischer Werkstoffe – Scherversuch.* Berlin, Germany : Beuth Verlag, 1982

[88] **DIN 53290:1982-02:** *Prüfung von Kernverbunden – Begriffe.* Berlin, Germany : Beuth Verlag, 1982

[89] **DIN 53294:1982-02:** *Prüfung von Kernverbunden – Schubversuch.* Berlin, Germany : Beuth Verlag, 1982

[90] **DIN EN 10002-1:2001-12:** *Zugversuche – Metallische Werkstoffe.* Berlin, Germany : Beuth Verlag, 2001

[91] **DIN EN ISO 9000:2005-12:** *Quality Management Systems – Fundamentals and vocabulary.* Berlin, Germany : Beuth Verlag, 2005

[92] **DIN EN ISO 10534-1:2001-10:** *Akustik – Bestimmung des Schallabsorptionsgrades und der Impedanz in Impedanzrohren.* Berlin, Germany : Beuth Verlag, 2001

[93] **DIN EN ISO 10534-2:2001-10:** *Akustik – Bestimmung des Schallabsorptionsgrades und der Impedanz in Impedanzrohren.* Berlin, Germany : Beuth Verlag, 2001

[94] **DIN EN ISO 11145:2002-03:** *Optik und optische Instrumente – Laser und Laseranlagen – Begriffe und Formelzeichen.* Berlin, Germany : Beuth Verlag, 2002

[95] **DIN EN ISO 11146-1:2005-04:** *Lasers and laser-related equipment – Test methods for laser beam widths, divergence angles and beam propagation ratios – Part 1: Stigmatic and simple astigmatic beams.* Berlin, Germany : Beuth Verlag, 2005

[96] **DIN EN ISO 12737:2005-10:** *Metallische Werkstoffe – Bestimmung der Bruchzähigkeit (ebener Spannungszustand).* Berlin, Germany : Beuth Verlag, 2005

[97] **DIN ISO 4022:1990-10:** *Ermittlung der spezifischen Durchströmbarkeit.* Berlin, Germany : Beuth Verlag, 1990

[98] **DIN ISO 9277:2003-05:** *Bestimmung der spezifischen Oberfläche von Feststoffen durch Gasadsorption nach dem BET-Verfahren.* Berlin, Germany : Beuth Verlag, 2003

[99] **DIN ISO 80000-8:2006-01:** *Größen und Einheiten – Teil 8: Akustik.* Berlin, Germany : Beuth Verlag, 2006

[100] **Dormal, T.:** *3D Printing Metal: The Fastest Solution for Complex Metal Parts and Inserts.* In: Proceedings RPD 2004 Rapid Product Development Event, Marinha Grande, Portugal, Marinha Grande, Portugal : Centimfe, 2004, Pages P4011.1-P4011.4

[101] **E-Eleser, N. S.:** *Herstellung von Senkerodierelektroden durch selektives Lasersintern – Ein Beitrag zu Rapid Tooling.* Dissertation TU Chemnitz, Germany, 2000, Chemnitz, Germany : TU Chemnitz, 2000

[102] **Eichler, J. ; Eichler, H. J.:** *Laser: Bauformen, Strahlführung, Anwendungen.* 5. Auflage, Berlin, Germany : Springer, 2003, ISBN 3-540-00376-2

[103] **Eichler, J. ; Dünkel, L. ; Eppich, B.:** *Die Strahlqualität von Lasern.* In: Laser Technik Journal, Vol. 1, No. 2, 2004, Weinheim, Germany : Wiley-VCH Verlag, 2004, Pages 63-66, ISSN 1613-7728

[104] **Eisen, M.:** *Systematische Entwicklung geeigneter Prozessparameter für das Lasergenerieren von Bauteilen aus Edelstahlwerkstoffen.* Project thesis at Hamburg University of Technology (TUHH), Institute of Laser and System Technologies (iLAS), 2004, Supervisor : Rehme, O.

[105] **Eisenberg, C. ; Ramge, T. ; Helbig, O.:** *Offen für Innovationen: Eine Serie in brand eins, Folge 7: Laser.* In: brand eins Wirtschaftsmagazin, Vol. 9, 2005, Hamburg, Germany : brand eins Verlag, 2005, Pages 51-60, ISSN 1438-9339

[106] **Elzey, D. M. ; Wadley, H. N. G.:** *The limits of solid state foaming.* In: Acta Materialia, Vol. 49, No. 5, 2001, Kidlington, UK : Elsevier, 2001, Pages 849-859, ISSN 1359-6454

[107] **ERG Materials and Aerospace Corporation / n. n.:** *Duocel Aluminum Foam – Information Brochure.* Oakland, CA, USA : ERG, 2006

[108] **Emmelmann, C. ; Rehme, O. ; Petersen, M. et al.:** *Innovationsanalyse für das Laser Rapid Manufacturing – Produkt, Zeit, Kosten.* Talk at the laser forum, Nortec, 10th trade fair for production technology, Hamburg, Germany : Institute of Laser and System Technologies, 2006

[109] **Emmelmann, C. ; Rehme, O.:** *Generative Fertigung von Ti-Legierungen: Laserstrahl vs. Elektronenstrahl.* In: Werkstoffe für die Fertigung, Vol. 44, No. 3, 2007, Mering, Germany : HW-Verlag, 2007, Pages 52-55, ISSN 0930-2629

[110] **Emmelmann, C. ; Rehme, O. ; Petersen, M,:** *Laser Freeform Fabrication for Medical Applications.* In: Proceedings of the Fourth International WLT-Conference “Lasers in Manufacturing 2007”, Editors : Vollertsen, F. ; Emmelmann, C. ; Schmidt, M. ; Otto, A. ; Stuttgart, Germany : AT-Fachverlag, 2007, Pages 249-254, ISBN 978-3-00-021449-3

[111] **Emmelmann, C. ; Rehme, O. ; Schwarze, D.:** *Selective Laser Melting of Lattice Structures in Solid Shells.* In: Proceedings of the 3rd International Conference on Advanced Research in Virtual and Rapid Prototyping, 2007, Leiria, Portugal, Editors : Bartolo, P. J. et al., London, UK : Taylor & Francis Group, 2007, Pages 529-535, ISBN 978-0-415-41602-3

[112] **Emmelmann, C.:** *Laser system engineering I: Systems for beam guidance and forming.* Lecture notes Hamburg University of Technology (TUHH), winter term 2007/08

[113] **Fackler, I.:** *Fertigungstechnik für zellulare Mikrostrukturen.* In: Produktion, Vol. 44, No. 36, 2005, Landsberg, Germany : verlag moderne industrie, 2005, Page 11, ISSN 0344-6166

[114] **Führer, J.:** *Ganzheitliche Optimierung des indirekten Metall-Lasersinterprozesses.* Dissertation TU München, Germany, 2002, München, Germany : Herbert Utz Verlag, 2002, ISBN 3-8316-0124-0

[115] **Feng, Y. ; Zheng, H. ; Zhu, Z. et al.:** *The microstructure and electrical conductivity of aluminium alloy foams.* In: Materials Chemistry and Physics. Vol. 78, No. 1, 2003, Amsterdam, Netherlands : Elsevier, 2003, Pages 196-201, ISSN 0254-0584

[116] **Fratzl, P.:** *Biologischer Glaskäfig aus der Tiefsee.* Presseinformation, Max-Planck-Institut für Kolloid- und Grenzflächenforschung, Potsdam, Germany : MPI Kolloid- und Grenzflächenforschung, 2005, Pages 1-4, ISSN 0170-4656

[117] **Friis, E. A. ; Lakes, R. S. ; Park, J. B.:** *Negative Poisson's Ratio Polymeric and Metallic Foams.* In: Journal of Materials Sciences, Vol. 23, No. 12, 1988, Dordrecht, Netherlands : Kluwer, 1988, Pages 4406-4414, ISSN 0022-2461

[118] **Fung, Y.-C.:** *Biomechanics: Mechanical Properties of Living Tissue.* Second Edition, New York City, NY, USA : Springer, 1993, ISBN 0-387-97947-6

[119] **Gers, H. ; Nijhof, K. ; Baumgärtner, F.:** *Powder Metallurgical Production of Aluminium Foam Sandwiches.* In: Materials Week and Materialica 2000 Proceedings, Editor : Werkstoffwoche-Partnerschaft GbR, Frankfurt, Germany : Werkstoffinformationsgesellschaft mbH, 2000
http://www.dgm.de/download/tg/523/523_0555.pdf
Updated last: September, 2000 ; Retrieved: January, 3rd 2007

[120] **German, R. M.:** *Particle Packing Characteristics.* Princeton, New Jersey : Metal Powder Industries Federation, 1989, ISBN 0-918404-83-5

[121] **Ghanekar, A. ; Crawford, R.:** *Optimization of SLS Process Parameters using D-optimality.* In: Bourell, D. L. ; Crawford, R. H. ; Beaman, J. J. ; Wood, K. L. ; Marcus, H. L. : 14th Solid Freeform Fabrication Proceedings 2003, Austin, TX, USA : University of Texas, 2003, Pages 348-362, ISSN 1053-2153

[122] **Gibson, L. J.:** *Biomechanics of cellular solids.* In: Journal of Biomechanics, Vol. 38, No. 3, 2005, Amsterdam, Netherlands : Elsevier, 2005, Pages 377-399, ISSN 0021-9290

[123] **Gibson, L. J. ; Ashby, M. F.:** *Cellular Solids: Structure & Properties.* Second Edition, Cambridge, UK : Cambridge University Press, 1997, ISBN 0-521-49911-9

[124] **Gioux, G. ; McCormack, T. M. ; Gibson, L. J.:** *Failure of aluminum foams under multiaxial loads.* In: International Journal of Mechanical Sciences, Vol. 42, No. 6, 2000, Kidlington, UK : Elsevier, 2000, Pages 1097-1117, ISSN 0020-7403

[125] **Glaßer, M.:** *Low volume- and Volume Production of Plastic and Metal Parts by Using Laser Sintering Technologies.* In: Proceedings RPD 2004 Rapid Product Development Event, Marinha Grande, Portugal, Marinha Grande, Portugal : Centimfe, 2004, Pages P4015.1-P4015.5

[126] **Glaßer, M. ; Stotko, C. M.:** *Mass Customization by using Laser Sintering Technologies on its way up.* In: Proceedings RPD 2006 Rapid Product Development Event, Marinha Grande, Portugal, Marinha Grande, Portugal : Centimfe, 2006, Pages P6032.1-P6032.7

[127] **Golovin, I. S. ; Sinning, H.-R.:** *Internal friction in metallic foams and some related cellular structures.* In: Materials Science and Engineering A, Vol. 370, No. 1-2, 2004, Amsterdam, Netherlands : Elsevier, 2004, Pages 504-511, ISSN 0921-5093

[128] **Golovin, I. S. ; Sinning, H.-R. ; Arhipov, I. K. et al.:** *Damping in some cellular materials due to microplasticity.* In: Materials Science and Engineering A, Vol. 370, No. 1-2, 2004, Amsterdam, Netherlands : Elsevier, 2004, Pages 531-536, ISSN 0921-5093

[129] **Golovin, I. S. ; Sinning, H.-R. ; Göken, J. et al.:** *Fatigue-related damping in some cellular metallic materials.* In: Materials Science and Engineering A, Vol. 370, No. 1-2, 2004, Amsterdam, Netherlands : Elsevier, 2004, Pages 537-541, ISSN 0921-5093

[130] **Gradinger, R. ; Rammerstorfer, F. G.:** *On the influence of meso-inhomogeneities on the crush worthiness of metal foams.* In: Acta Materialia, Vol. 47, No. 1, 1999, Kidlington, UK : Elsevier, 1999, Pages 143-148, ISSN 1359-6454

[131] **Grenestedt, J. L.:** *Influence of Imperfections on Effective Properties of Cellular Solids.* In: Porous and Cellular Materials for Structural Applications, Symposium 1998, San Francisco, CA, USA, Editors : Schwartz, D. S. ; Shih, D. S. ; Evans, A. G. ; Wadley, H. N. G. ; Vol. 521, Warrendale, PA, USA : Materials Research Society, 1998, Pages 3-13, ISBN 1-55899-427-0

[132] **Grenestedt, J. L.:** *Effective elastic behavior of some models for 'perfect' cellular solids.* In: International Journal of Solids and Structures, Vol. 36, No. 10, 1999, New York City, NY, USA : Elsevier, 1999, Pages 1471-1501, ISSN 0020-7683

[133] **von Hagen, H. ; Bleck, W.:** *Compressive, tensile and shear testing of melt-foamed aluminium.* In: Porous and Cellular Materials for Structural Applications, Symposium 1998, San Francisco, CA, USA, Editors : Schwartz, D. S. ; Shih, D. S. ; Evans, A. G. ; Wadley, H. N. G. ; Vol. 521, Warrendale, PA, USA : Materials Research Society, 1998, Pages 59-64, ISBN 1-55899-427-0

[134] **Han, F. ; Seiffert, G. ; Zhao, Y. et al.:** *Acoustic absorption behaviour of an open-celled aluminium foam.* In: Journal of Physics D: Applied Physics, Vol. 36, No. 3, 2003, Bristol, UK : Institute of Physics Publishing, 2003, Pages 294-302, ISSN 0022-3727

[135] **Harte, A.-M. ; Fleck, N. A. ; Ashby, M. F.:** *Fatigue failure of an open cell and a closed cell aluminium alloy foam.* In: Acta Materialia, Vol. 47, No. 8, 1999, Kidlington, UK : Elsevier, 1999, Pages 2511-2524, ISSN 1359-6454

[136] **Hauser, C. ; Childs, T. H. C. ; Dalgarno, K. W. et al.:** *Atmospheric Control during Direct Selective Laser Sintering of Stainless Steel 314S powder.* In: Bourell, D. L. ; Beaman, J. J. ; Crawford, R. H. ; Marcus, H. L. ; Barlow, J. W. : 10th Solid Freeform Fabrication Proceedings 1999, Austin, TX, USA : University of Texas, 1999, Pages 265-272, ISSN 1053-2153

[137] **Hauser, C. ; Childs, T. H. C. ; Dalgarno, K. W.:** *Selective Laser Sintering of Stainless Steel 314 HC processed using room temperature powder beds.* In: Bourell, D. L. ; Beaman, J. J. ; Crawford, R. H. ; Marcus, H. L. ; Barlow, J. W. : 10th Solid Freeform Fabrication Proceedings 1999, Austin, TX, USA : University of Texas, 1999, Pages 273-280, ISSN 1053-2153

[138] **Hauser, C. ; Childs, T. H. C. ; Taylor, C. M. et al.:** *Direct Selective Laser Sintering of Tool Steel Powders to High Density. Part A: Effects of Laser Beam Width and Scan Strategy.* In: Bourell, D. L. ; Crawford, R. H. ; Beaman, J. J. ; Wood, K. L. ; Marcus, H. L. : 14th Solid Freeform Fabrication Proceedings 2003, Austin, TX, USA : University of Texas, 2003, Pages 644-655, ISSN 1053-2153

[139] **Hauser, C. ; Childs, T. H. C. ; Badrossamay, M.:** *Further Developments in Process Mapping and Modelling in Direct Metal Selective Laser Melting.* In: Bourell, D. L. ; Crawford, R. H. ; Beaman, J. J. ; Wood, K. L. ; Marcus, H. L. : 15th Solid Freeform Fabrication Proceedings 2004, Austin, TX, USA : University of Texas, 2004, Pages 448-459, ISSN 1053-2153

[140] **Hebsur, M. G. ; Whittenberger, J. D. ; Krause, D. L.:** *Superalloy Lattice Block Developed for Use in Lightweight, High-Temperature Structures.* In: Research & Technology 2002, Hanover, MD, USA : NASA Center for Aerospace Information, 2003, Pages 19-20

[141] **Helsen, J. A. ; Breme, H. J.:** *Metals as Biomaterials.* Chichester, UK : John Wiley & Sons, 1998, ISBN 0-471-96935-4

[142] **Hill, R.:** *A Theory of the Yielding and Plastic Flow of Anisotropic Metals.* In: Proceedings of the Royal Society of London, Series A, Vol. 193, 1948, London, UK : Royal Society, 1948, Pages 281-297, ISSN 0962-8444

[143] **Hodge, A. M. ; Dunand, D. C.:** *Measurement and Modeling of Creep in Open-Cell NiAl Foams.* In: Metallurgical and Materials Transactions A, Vol. 34A, October, 2003, Warrendale, PA, USA : The Minerals, Metals & Materials Society, 2003, Pages 2353-2363, ISSN 1073-5623

[144] **Hohe, J.:** *Stochastic homogenization of polymeric foams.* In: Advancing with Sandwich Structures, Proceedings of the 7th International Conference on Sandwich Structures, Aalborg, Denmark, Editors : Thomesen, O. T. ; Bozhevolnaya, E. ; Lyckegaard, A. ; Part 9, Dordrecht, Netherlands : Springer, 2005, Pages 925-934, ISBN 978-1-4020-3444-2

[145] **Hohenhoff, G. ; Haferkamp, H. ; Meier, O.:** *Herstellung individueller Endoprothesen mittels Laserstrahlauftragschweißen.* Talk at WLT Laser-Summerschool conference, Hannover, Germany : Laser Zentrum Hannover e.V., 2006

[146] **Housholder, R. F.:** *Molding process.* United States Patent 4247508, filed December 3rd, 1979, published January 27th, 1981
http://www.freepatentsonline.com/4247508.html
Updated last: 2007 ; Retrieved: May, 9th 2007

[147] **Huang, J. S. ; Lin, J. Y.:** *Modeling of fatigue for cellular materials.* In: Porous and Cellular Materials for Structural Applications, Symposium 1998, San Francisco, CA, USA, Editors : Schwartz, D. S. ; Shih, D. S. ; Evans, A. G. ; Wadley, H. N. G. ; Vol. 521, Warrendale, PA, USA : Materials Research Society, 1998, Pages 27-32, ISBN 1-55899-427-0

[148] **Hull, C. W.:** *Apparatus for production of three-dimensional objects by stereolithography.* United States Patent 4575330, filed August 8th, 1984, published March 11th, 1986
http://www.freepatentsonline.com/4575330.html
Updated last: 2007 ; Retrieved: May, 9th 2007

[149] **Hurysz, K. M. ; Clark, J. L. ; Nagel, A. R. et al.:** *Steel and Titanium Hollow Sphere Foams.* In: Porous and Cellular Materials for Structural Applications, Symposium 1998, San Francisco, CA, USA, Editors : Schwartz, D. S. ; Shih, D. S. ; Evans, A. G. ; Wadley, H. N. G. ; Vol. 521, Warrendale, PA, USA : Materials Research Society, 1998, Pages 191-203, ISBN 1-55899-427-0

[150] **Huschka, S.:** *Modellierung eines Materialgesetzes zur Beschreibung der mechanischen Eigenschaften von Aluminiumschaum.* Dissertation, Germany, 1998, Fortschrittsberichte VDI Reihe 5 Nr. 525, Düsseldorf, Germany : VDI Verlag, ISBN 3-18-352505-4

[151] **Inchbald, G.:** *Five space-filling polyhedra.* In: The Mathematical Gazette, Vol. 80, No. 11, 1996, Leicester, UK : The Mathematical Association, 1996, Pages 466-475, ISSN 0025-5572

[152] **Jacobs, P. F.:** *A Brief History of Rapid Prototyping & Manufacturing: The Early Years.* In: Proceedings of the 2002 International Conference on Metal Powder Deposition for Rapid Manufacturing, Princeton, NJ, USA : Metal Powder Industries Federation, 2002, Pages 1-4, ISBN 1-878954-87-3

[153] **Jacobs, P. F.:** *A Brief History of Rapid Prototyping & Manufacturing: The Growth Years.* In: Proceedings of the 2002 International Conference on Metal Powder Deposition for Rapid Manufacturing, Princeton, NJ, USA : Metal Powder Industries Federation, 2002, Pages 5-8, ISBN 1-878954-87-3

[154] **Jancek, R. ; Kottar, A. ; Kriszt, B. et al.:** *Cellular Aluminum Foam Panels Under Tensile Loading.* In: Proceedings of the International Conference “Advanced Metallic Materials”, Bratislava, Slovakia : Institute of Materials and Machine Mechanics, 2003, Pages 132-134, ISBN 80-969011-7-6

[155] **Kanahashi, H. ; Mukai, T. ; Yamada, Y. et al.:** *Dynamic compression of an ultra-low density aluminium foam.* In: Materials Science and Engineering A, Vol. 280, No. 2, 2000, Amsterdam, Netherlands : Elsevier, 2000, Pages 349-353, ISSN 0921-5093

[156] **Karapatis, N. P. ; Guidoux, Y. ; Gygax, P. E. et al.:** *Thermal Behavior of Parts Made by Direct Metal Laser Sintering.* In: Marcus, H. L. ; Beaman, J. J. ; Bourell, D. L. ; Barlow, J. W. ; Crawford, R. H. : 9th Solid Freeform Fabrication Proceedings 1998, Austin, TX, USA : University of Texas, 1998, Pages 79-87, ISSN 1053-2153

[157] **Karapatis, N. P. ; Egger, G. ; Gygax, P.-E. et al.:** *Optimization of Powder Layer Density in Selective Laser Sintering.* In: Bourell, D. L. ; Beaman, J. J. ; Crawford, R. H. ; Marcus, H. L. ; Barlow, J. W. : 10th Solid Freeform Fabrication Proceedings 1999, Austin, TX, USA : University of Texas, 1999, Pages 255-263, ISSN 1053-2153

[158] **Kathuria, Y. P.:** *Influence of Process Parameters on Laser Assisted Aluminium Foaming.* In: Materials Week and Materialica 2000 Proceedings, Editor : Werkstoff-woche-Partnerschaft GbR, Frankfurt, Germany : Werkstoffinformationsgesellschaft, 2000 http://www.dgm.de/download/tg/523/523_0340.pdf
Updated last: April, 2001 ; Retrieved: January, 3rd 2007

[159] **Kaviany, M.:** *Principles of Heat Transfer in Porous Media.* Second Edition, New York City, NY, USA : Springer, 1995, ISBN 0-387-94550-4

[160] **Klocke, F. ; Wagner, C.:** *Direct Selective Laser Sintering of Superalloys.* In: Bourell, D. L. ; Crawford, R. H. ; Beaman, J. J. ; Wood, K. L. ; Marcus, H. L. : 13th Solid Freeform Fabrication Proceedings 2002, Austin, TX, USA : University of Texas, 2002, Pages 187-198, ISSN 1053-2153

[161] **Klocke, F. ; Wagner, C.:** *Coalescence Behaviour of Two Metallic Particles as Base Mechanism of Selective Laser Sintering.* In: CIRP Annals Manufacturing Technology, Vol. 52, No. 1, 2003, Paris, France : CIRP, 2003, Pages 177-180, ISBN 3-905277-40-2

[162] **Klocke, F. ; Wagner, C. ; Ader, C.:** *Development of an Integrated Model for Selective Metal Laser Sintering.* In: Proceedings of 36th CIRP International Seminar on Manufacturing Systems, 2003, Editors : Weber, C. ; Bley, H. ; Hirt, G. ; Saarbrücken, Germany : Universität des Saarlandes, 2003, Pages 387-392, ISBN 3-930429-58-6

[163] **Ko, W. L.:** *Deformations of Foamed Elastomers.* In: Journal of Cellular Plastics, Vol. 1, No. 1, 1965, London, UK : Sage Publications, 1965, Pages 45-50, ISSN 0021-955X

[164] **Kooistra, G. W. ; Deshpande, V. S. ; Wadley, H. N. G.:** *Compressive behavior of age hardenable tetrahedral lattice struss structures made from aluminium.* In: Acta Materialia, Vol. 52, No. 14, 2004, Kidlington, UK : Elsevier, 2005, Pages 4229-4237, ISSN 1359-6454

[165] **Kováčik, J. ; Simančik, F.:** *Aluminium Foam – Modulus of Elasticity and Electrical Conductivity According to Percolation Theory.* In: Scripta Materialia, Vol. 39, No. 2, 1998, Oxford, UK : Elsevier, 1998, Pages 239-246, ISSN 1359-6462

[166] **Krause, D. L. ; Whittenberger, J. D. ; Kantzos, P. T. et al.:** *Mechanical Testing of IN718 Lattice Block Structures.* In: Processing and Properties of Lightweight Cellular Metals and Structures, Proceedings of Third Global Symposium on Materials Processing and Manufacturing, Editors : Ghosh, A. K. ; Sanders, T. H. ; Claar, T. D. ; Warrendale, PA, USA : The Minerals, Metals & Materials Society, 2002, Pages 233-242, ISBN 0-87339-527-1

[167] **Kretz, R. ; Hausberger, K. ; Götzinger, B.:** *Energy-Absorbing Behavior of Aluminum Foams: Head Impact Tests on the A-Pillar of a Car.* In: Advanced Engineering Materials, Vol. 4, No. 10, 2002, Weinheim, Germany : Wiley-VCH Verlag, 2002, Pages 781-785, ISSN 1438-1656

[168] **Kruth, J. P. ; Froyen, L. ; Rombouts, M. et al.:** *New Ferro Powder for Selective Laser Sintering of Dense Parts.* In: CIRP Annals Manufacturing Technology, Vol. 52, No. 1, 2003, Paris, France : CIRP, 2003, Pages 139-142, ISBN 3-905277-40-2

[169] **Kruth, J. P. ; Mercelis, P. ; Froyen, L. et al.:** *Binding Mechanisms in Selective Laser Sintering and Selective Laser Melting.* In: Bourell, D. L. ; Crawford, R. H. ; Beaman, J. J. ; Wood, K. L. ; Marcus, H. L. : 15th Solid Freeform Fabrication Proceedings 2004, Austin, TX, USA : University of Texas, 2004, Pages 44-59, ISSN 1053-2153

[170] **Kyogoku, H. ; Ramos, J. A. ; Bourell, D. L. :** *Laser Melting of Ti-Ni Shape Memory Alloy.* In: Bourell, D. L. ; Crawford, R. H. ; Beaman, J. J. ; Wood, K. L. ; Marcus, H. L. : 14th Solid Freeform Fabrication Proceedings 2003, Austin, TX, USA : University of Texas, 2003, Pages 668-675, ISSN 1053-2153

[171] **Lakes, R. S.:** *Deformation mechanisms in negative Poisson's ratio materials: structural aspects.* In: Journal of Materials Sciences, Vol. 26, No. 9, 1991, Dordrecht, Netherlands : Kluwer, 1991, Pages 2287-2292, ISSN 0022-2461

[172] **Lakes, R. S.:** *Design consideration for negative Poisson's ratio materials.* In: Journal of Mechanical Design, Vol. 115, No. 4, 1993, New York City, NY, USA : ASME, 1993, Pages 696-700, ISSN 1050-0472

[173] **Lakes, R. S.:** *Foam Structures with a Negative Poisson's Ratio.* In: Science, Vol. 235, No. 4792, 1987, Washington, DC, USA : AAAS, 1987, Pages 1038-1040, ISSN 0036-8075

[174] **Lakes, R. S.:** *Materials with structural hierarchy.* In: Nature : International weekly journal of science, Vol. 361, No. 6412, 1993, London, UK : Nature Publishing Group, 1993, Pages 511-515, ISSN 0028-0836

[175] **Lankford Jr., J. ; Dannemann, K. A.:** *Strain Rate Effects In Porous Materials.* In: Porous and Cellular Materials for Structural Applications, Symposium 1998, San Francisco, CA, USA, Editors : Schwartz, D. S. ; Shih, D. S. ; Evans, A. G. ; Wadley, H. N. G. ; Vol. 521, Warrendale, PA, USA : Materials Research Society, 1998, Pages 103-108, ISBN 1-55899-427-0

[176] **Laoui, T. ; Wang, X. ; Childs, T. H. C. et al.:** *Laser Penetration in a Powder Bed During Selective Laser Sintering of Metal Powders: Simulations Versus Experiments.* In: Bourell, D. L. ; Beaman, J. J. ; Crawford, R. H. ; Marcus, H. L. ; Barlow, J. W. : 11th Solid Freeform Fabrication Proceedings 2000, Austin, TX, USA : University of Texas, 2000, Pages 453-460, ISSN 1053-2153

[177] **Laoui, T. ; Santos, E. ; Osakada, K. et al.:** *Properties of Titanium Implant Models Made by Laser Processing.* In: Proceedings of the 4th International Conference on Laser Assisted Net Shape Engineering, LANE 2004, Erlangen, Germany, Vol. 1, Editors : Geiger, M. ; Otto, A. ; Bamberg, Germany : Meisenbach Verlag, 2004, Pages 475-484, ISBN 3-87525-202-0

[178] **Last, B. J. ; Thouless, D. J.:** *Percolation Theory and Electrical Conductivity,* In: Physical Review Letters, Vol. 27, No. 25, 1971, College Park, MD, USA : American Physical Society, 1971, Pages 1719-1721, ISSN 0031-9007

[179] **Lee, D. N.; Han, H N. ; Oh, K. H. et al.:** *Analysis of deformation of porous metals.* In: Porous and Cellular Materials for Structural Applications, Symposium 1998, San Francisco, CA, USA, Editors : Schwartz, D. S. ; Shih, D. S. ; Evans, A. G. ; Wadley, H. N. G. ; Vol. 521, Warrendale, PA, USA : Materials Research Society, 1998, Pages 33-38, ISBN 1-55899-427-0

[180] **Lemke, S.:** *Untersuchung metallischer und nichtmetallischer Werkstoffe auf ihre Eignung für das Lasergenerieren.* Project thesis at Hamburg University of Technology (TUHH), Institute of Laser and System Technologies (iLAS), 2005, Supervisor : Rehme, O.

[181] **Levy, G. N. ; Schindel, R. ; Kruth, J. P.:** *Rapid Manufacturing and Rapid Tooling with Layer Manufacturing (LM) Technologies, State of the Art and Future Perspectives.* In: CIRP Annals Manufacturing Technology, Vol. 52, No. 2, 2003, Paris, France : CIRP, 2003, Pages 589-609, ISBN 3-905277-40-2

[182] **Liang, M. T. C. ; Lewis, K. M. ; Spalding, T. W.:** *Bone Bending Stiffness and BMD in trained Cyclists, Runners and Untrained Men.* In: The FASEB Journal, Vol. 22, Late Breaking Meeting Abstracts, 2008, Bethesda, MD, USA : The Federation of American Societies for Experimental Biology, 2008, lb 131

[183] **Lin, F. ; Sun, W. ; Yan, Y.:** *Optimization with minimum process error for layered manufacturing fabrication.* In: Rapid Prototyping Journal, Vol. 7, No. 2, 2001, Bradford, UK : MCB University Press, 2001, Pages 73-81, ISSN 1355-2546

[184] **Lin, T.-W. ; Wendland, D. ; Shapiro, B.:** *Friction Dynamic Characterization of Micro-Ball Bearings.* MEMS Sensors and Actuators Lab (MSAL), Dept. of Electrical and Computer Engineering, Univ. of Maryland, 2001

[185] **Lorenz, A. ; Rehme, O. ; Emmelmann, C.:** *Statistische Versuchsplanung in der Lasermaterialbearbeitung.* In: Photonik – Fachzeitschrift für die Optischen Technologien, Vol. 37, No. 3, 2005, Stuttgart, Germany : AT-Fachverlag, 2005, Pages 92-96, ISSN 1432-9778

[186] **Low, K. H. ; Leong, K. F. ; Chua, C. K. et al.:** *Characterization of SLS parts for drug delivery devices.* In: Rapid Prototyping Journal, Vol. 7, No. 5, 2001, Bradford, UK : MCB University Press, 2001, Pages 262-267, ISSN 1355-2546

[187] **Lu, T. J. ; Stone, H. A. ; Ashby, M. F.:** *Heat transfer in open-cell metal foams.* In: Acta Materialia, Vol. 46, No. 10, 1998, Kidlington, UK : Elsevier, 1998, Pages 3619-3635, ISSN 1359-6454

[188] **Lu, T. J. ; Chen, C.:** *Thermal transport and fire retardance properties of cellular aluminum alloys.* In: Acta Materialia, Vol. 47, No. 5, 1999, Kidlington, UK : Elsevier, 1999, Pages 1469-1485, ISSN 1359-6454

[189] **Lu, T. J. ; Hess, A. ; Ashby, M. F.:** *Sound absorption in metallic foams* In: Journal of Applied Physics Vol. 85, No. 11, 1999, Melville, NY, USA : American Institute of Physics, 1999, Pages 7528-7539, ISSN 0021-8979

[190] **Ma, L. ; Song, Z. ; He, D.:** *Cellular structure controllable aluminium foams produced by high pressure infiltration process.* In: Scripta Materialia, Vol. 41, No. 7, 1999, Oxford, UK : Elsevier, 1999, Pages 785-789, ISSN 1359-6462

[191] **Manriquez-Frayre, J. A. ; Bourell, D. L. :** *Selective Laser Sintering of Binary Metallic Powder.* In: Beaman, J. J. ; Marcus, H. L. ; Bourell, D. L. ; Barlow, J. W. : 1st Solid Freeform Fabrication Proceedings 1990, Austin, TX, USA : University of Texas, 1990, Pages 99-106, ISSN 1053-2153

[192] **Martínez-García, A. ; Sánchez-Reche, A. ; Pomposo-Alonso, J. A. et al.:** *Use of the Selective Laser Sintering to Obtain Electrodes to Manufacture Prototype Moulds by Electrical Discharge Machining.* In: Proceedings RPD 2004 Rapid Product Development Event, Marinha Grande, Portugal, Marinha Grande, Portugal : Centimfe, 2004, Pages P4079.1-P4079.5

[193] **Martz, E. O. ; Lee, T. ; Lakes, R. S. et al.:** *Re-entrant Transformation Methods in Closed Cell Foams.* In: Cellular Polymers, Vol. 15, No. 4, 1996, Shawbury, UK : Rapra Technology, 1996, Pages 229-249, ISSN 0262-4893

[194] **Maxwell, J. C.:** *On the calculation of the equilibrium and stiffness of frames.* In: Philosophical Magazine, Vol. 27, 1864, London, UK : Taylor & Francis, 1864, Pages 294-299, ISSN 1478-6435

[195] **McCullough, K. Y. G. ; Fleck, N. A. ; Ashby, M. F.:** *Toughness of aluminium alloy foams.* In: Acta Materialia, Vol. 47, No. 8, 1999, Kidlington, UK : Elsevier, 1999, Pages 2331-2343, ISSN 1359-6454

[196] **McCullough, K. Y. G. ; Fleck, N. A. ; Ashby, M. F.:** *Unixaxial stress-strain behaviour of aluminium alloy foams.* In: Acta Materialia, Vol. 47, No. 8, 1999, Kidlington, UK : Elsevier, 1999, Pages 2323-2330, ISSN 1359-6454

[197] **McGuire, W. ; Gallagher, R. H. ; Ziemian, R. D.:** *Matrix Structural Analysis.* Second Edition, New York, NY, USA : John Wiley & Sons, 2000, ISBN 0-471-12918-6

[198] **MCP-HEK Tooling GmbH:** *MCP Rapid Tooling Machines.*
In: MCP Rapid Tooling Technologies
http://www.mcp-group.de/data/pics/20050718144557_0.jpg
Updated last: June, 2006 ; Retrieved: June, 14th 2006

[199] **MCP-HEK Tooling GmbH:** *SLM – Medizinische Anwendungen: Durch Rapid Manufacturing erhalten Patienten in Australien individuell hergestellte Hüftimplantate.* Pressemitteilung, 02/2006

[200] **Meena, V. K. ; Nagahanumaiah:** *Optimization of EDM machining parameters using DMLS electrode.* In: Rapid Prototyping Journal, Vol. 12, No. 4, 2006, Bradford, UK : MCB University Press, 2006, Pages 222-228, ISSN 1355-2546

[201] **Meiners, W.:** *Direktes Selektives Laser Sintern einkomponentiger metallischer Werkstoffe.* Dissertation RWTH Aachen, Germany, 1999, Aachen, Germany : Shaker Verlag, 1999, ISBN 3-8322-3104-8

[202] **Meiners, W. ; Over, C. ; Wissenbach, K. et al.:** *Direct Generation of Metal Parts and Tools by Selective Laser Powder Remelting (SLPR).* In: Bourell, D. L. ; Beaman, J. J. ; Crawford, R. H. ; Marcus, H. L. ; Barlow, J. W. : 10th Solid Freeform Fabrication Proceedings 1999, Austin, TX, USA : University of Texas, 1999, Pages 655-661, ISSN 1053-2153

[203] **Mercelis, P. ; Kruth, J.-P.:** *Residual stresses in Selective Laser Sintering and Selective Laser Melting.* In: Bourell, D. L. ; Crawford, R. H. ; Beaman, J. J. ; Wood, K. L. ; Marcus, H. L. : 16th Solid Freeform Fabrication Proceedings 2005, Austin, TX, USA : University of Texas, 2005, Pages 109-131, ISSN 1053-2153

[204] **Miani, F. ; Kuljanic, E. ; Sortino, M.:** *Modelling the Mechanical Properties of Direct Metal Selectively Laser Sintered Parts.* In: Proceedings of the 3rd International Conference on Laser Assisted Net Shape Engineering, LANE 2001, Erlangen, Germany, Editors : Geiger, M. ; Otto, A. ; Bamberg, Germany : Meisenbach Verlag, 2001, Pages 383-390, ISBN 3-87525-154-7

[205] **Mirahmadi, A. ; Saedodin, S. ; Shanjani, Y.:** *Manufacturing time optimization in additive and removal methods by ACS approach.* In: Proceedings RPD 2006 Rapid Product Development Event, Marinha Grande, Portugal, Marinha Grande, Portugal : Centimfe, 2006, Pages P6006.1-P6006.5

[206] **Miyoshi, T. ; Itoh, M. ; Akiyama, S. et al.:** *Aluminum Foam, "Alporas": The Production Process, Properties and Applications.* In: Porous and Cellular Materials for Structural Applications, Symposium 1998, San Francisco, CA, USA, Editors : Schwartz, D. S. ; Shih, D. S. ; Evans, A. G. ; Wadley, H. N. G. ; Vol. 521, Warrendale, PA, USA : Materials Research Society, 1998, Pages 133-137, ISBN 1-55899-427-0

[207] **Miyoshi, T. ; Itoh, M. ; Mukai, T. et al.:** *Enhancement of energy absorption in a closed-cell aluminum by the modification of cellular structures.* In: Scripta Materialia, Vol. 41, No. 10, 1999, Oxford, UK : Elsevier, 1999, Pages 1055-1060, ISSN 1359-6462

[208] **Mohr, U. ; Bleck, W.:** *A Novel Method for the Processing of Metallic Foams by Slipcasting.* In: Materials Week and Materialica 2000 Proceedings, Editor : Werkstoff-woche-Partnerschaft GbR, Frankfurt, Germany : Werkstoffinformationsgesellschaft, 2000 http://www.dgm.de/download/tg/523/523_0377.pdf
Updated last: September, 2000 ; Retrieved: January, 3rd 2007

[209] **Morgan, R. ; Sutcliffe, C. J. ; O'Neill, W.:** *Experimental investigation of nanosecond pulsed Nd:YAG laser re-melted pre-placed powder beds.* In: Rapid Prototyping Journal, Vol. 7, No. 3, 2001, Bradford, UK : MCB University Press, 2001, Pages 159-172, ISSN 1355-2546

[210] **Motz, C. ; Pippan, R.:** *Deformation behaviour of closed-cell aluminium foams in tension.* In: Acta Materialia, Vol. 49, No. 13, 2001, Kidlington, UK : Elsevier, 2001, Pages 2463-2470, ISSN 1359-6454

[211] **Motz, C. ; Pippan, R.:** *Fracture behaviour and fracture toughness of ductile closed-cell metallic foams.* In: Acta Materialia, Vol. 50, No. 8, 2002, Kidlington, UK : Elsevier, 2002, Pages 2013-2033, ISSN 1359-6454

[212] **Mukai, T. ; Kanahashi, H. ; Yamada, Y. et al.:** *Dynamic compressive behavior of an ultra-lightweight magnesium foam.* In: Scripta Materialia, Vol. 41, No. 4, 1999, Oxford, UK : Elsevier, 1999, Pages 365-371, ISSN 1359-6462

[213] **Mukai, T. ; Kanahashi, H. ; Miyoshi, T. et al.:** *Experimental study of energy absorption in a close-celled aluminum foam under dynamic loading.* In: Scripta Materialia, Vol. 40, No. 8, 1999, Oxford, UK : Elsevier, 1999, Pages 921-927, ISSN 1359-6462

[214] **Naing, M. W. ; Chua, C. K. ; Leong, K. F. et al.:** *Fabrication of customised scaffolds using computer-aided design and rapid prototyping techniques*, In: Rapid Prototyping Journal, Vol. 11, No. 4, 2005, Bradford, UK : MCB University Press, 2005, Pages 249-256, ISSN 1355-2546

[215] **Nelson, C. ; McAlea, K. ; Gray D.:** *Improvements in SLS Part Accuracy.* In: Marcus, H. L. ; Beaman, J. J. ; Bourell, D. L. ; Barlow, J. W. ; Crawford, R. H. : 6th Solid Freeform Fabrication Proceedings 1995, Austin, TX, USA : University of Texas, 1995, Pages 159-169, ISSN 1053-2153

[216] **Niebling, F.:** *Qualifizierung einer Prozesskette zum Laserstrahlsintern metallischer Bauteile.* Dissertation Universität Erlangen-Nürnberg, Germany, 2002, Bamberg, Germany : Meisenbach Verlag, 2005, ISBN 3-87525-219-5

[217] **Nieh, T. G. ; Higashi, K. ; Wadsworth, J.:** *Effect of cell morphology on the compressive properties of open-cell aluminum foams.* In: Materials Science and Engineering A, Vol. 283, No. 1-2, 2000, Amsterdam, Netherlands : Elsevier, 2000, Pages 105-110, ISSN 0921-5093

[218] **Niu, H. J. ; Chang, I. T. H.:** *Liquid phase sintering of M3/2 high speed steel by selective laser sintering,* In: Scripta Materialia, Vol. 39, No. 1, 1998, Oxford, UK : Elsevier, 1998, Pages 67-72, ISSN 1359-6462

[219] **Niu, H. J. ; Chang, I. T. H.:** *Selective laser sintering of gas and water atomized high speed steel powders.* In: Scripta Materialia, Vol. 41, No. 1, 1999, Oxford, UK : Elsevier, 1999, Pages 25-30, ISSN 1359-6462

[220] **Niu, H. J. ; Chang, I. T. H.:** *Instability of scan tracks of selective laser sintering of high speed steel powder.* In: Scripta Materialia, Vol. 41, No. 11, 1999, Oxford, UK : Elsevier, 1999, Pages 1229-1234, ISSN 1359-6462

[221] **Onck, P. R. ; Andrews, E. W. ; Gibson, L. J.:** *Size effects in ductile cellular solids. Part I: modeling.* In: International Journal of Mechanical Sciences, Vol. 43, No. 3, 2001, Kidlington, UK : Elsevier, 2001, Pages 681-699, ISSN 0020-7403

[222] **Ott, E. A.:** *Superalloy Lattice Block.* NASA Glenn Research Center, 2003 http://gltrs.grc.nasa.gov/reports/2003/CR-2003-212719.pdf Updated last: December, 2003 ; Retrieved: January, 4th 2007

[223] **Over, C.:** *Generative Fertigung von Bauteilen aus Werkzeugstahl X38CrMoV5-1 und Titan TiAl6V4 mit „Selective Laser Melting“.* Dissertation RWTH Aachen, Germany, 2003, Aachen, Germany : Shaker Verlag, 2003, ISBN 3-8322-2245-6

[224] **Paradies, C. J. ; Tobin, A. ; Wolla, J.:** *The Effect of GASAR Processing Parameters on Porosity and Properties in Aluminum Alloy.* In: Porous and Cellular Materials for Structural Applications, Symposium 1998, San Francisco, CA, USA, Editors : Schwartz, D. S. ; Shih, D. S. ; Evans, A. G. ; Wadley, H. N. G. ;Vol. 521, Warrendale, PA, USA : Materials Research Society, 1998, Pages 297-302, ISBN 1-55899-427-0

[225] **Park, C. ; Nutt, S. R.:** *PM synthesis and properties of steel foams.* In: Materials Science and Engineering A, Vol. 288, No. 1, 2000, Amsterdam, Netherlands : Elsevier, 2000, Pages 111-118, ISSN 0921-5093

[226] **Pawlicki, J. ; Koza, E. ; Zurawski, P. et al.:** *Mechanical Properties of Closed Cell Al foams based on tetrakaidecahedronal Model of Structure.* In: Proceedings of the International Conference "Advanced Metallic Materials", Bratislava, Slovakia : Institute of Materials and Machine Mechanics, 2003, Pages 235-238, ISBN 80-969011-7-6

[227] **Petersen, M.:** *Lasergenerieren von Metall-Keramik-Verbundwerkstoffen.* Dissertation TU Hamburg-Harburg, Germany, 2006, Göttingen, Germany : Cuvillier Verlag, 2007, ISBN 978-3-86727-146-2

[228] **Pintat, T. ; Greul, M. ; Greulich M. et al.:** *Accuracy and Mechanical Behavior of Metal Parts Produced by Lasersintering.* In: Marcus, H. L. ; Beaman, J. J. ; Bourell, D. L. ; Barlow, J. W. ; Crawford, R. H. : 6th Solid Freeform Fabrication Proceedings 1995, Austin, TX, USA : University of Texas, 1995, Pages 72-79, ISSN 1053-2153

[229] **Pogson, S. R. ; Fox, P. ; Sutcliffe, C. J. et al.:** *The production of copper parts using DMLR.* In: Rapid Prototyping Journal, Vol. 9, No. 5, 2003, Bradford, UK : MCB University Press, 2003, Pages 334-343, ISSN 1355-2546

[230] **Pohl, H. ; Simchi, A. ; Issa, M. et al.:** *Thermal Stresses in Direct Metal Laser Sintering.* In: Bourell, D. L. ; Beaman, J. J. ; Crawford, R. H. ; Marcus, H. L. ; Wood, K. L. ; Barlow, J. W. : 12th Solid Freeform Fabrication Proceedings 2001, Austin, TX, USA : University of Texas, 2001, Pages 366-372, ISSN 1053-2153

[231] **Prall, D. ; Lakes, R. S.:** *Properties of a chiral honeycomb with a Poisson's ratio -1.* In: International Journal of Mechanical Sciences, Vol. 39, No. 3, 1997, Kidlington, UK : Elsevier, 1997, Pages 305-314, ISSN 0020-7403

[232] **Queheillalt, D. T. ; Wadley, H. N. G.:** *Cellular metal lattices with hollow trusses.* In: Acta Materialia, Vol. 53, No. 2, 2005, Kidlington, UK : Elsevier, 2005, Pages 303-313, ISSN 1359-6454

[233] **Queheillalt, D. T. ; Wadley, H. N. G. ; Schwartz, D. S.:** *Elastic Properties of Low Density Core (LDC) Ti-6Al-4V Sandwich Cores.* In: Porous and Cellular Materials for Structural Applications, Symposium 1998, San Francisco, CA, USA, Editors : Schwartz, D. S. ; Shih, D. S. ; Evans, A. G. ; Wadley, H. N. G. ; Vol. 521, Warrendale, PA, USA : Materials Research Society, 1998, Pages 237-242, ISBN 1-55899-427-0

[234] **Queheillalt, D. T. ; Katsumi, Y. ; Wadley, H. N. G.:** *Electron Beam-Directed Vapor Deposition of Multifunctional Structures.* In: Mechanisms of Surface and Microstructure Evolution in Deposited Films and Film Structures, Symposium 2001, San Francisco, CA, USA, Editors : Sanchez Jr., J. ; Amar, J. G. ; Murty, R. ; Gilmer, G. ; Vol. 672, Warrendale, PA, USA : Materials Research Society, 2001, Pages O5.6.1-O5.6.6, ISBN 1-55899-608-7

[235] **Queheillalt, D. T. ; Choi, B. W. ; Wadley, H. N. G. et al.:** *In-situ Sensing of the Expansion of Low Density Core (LDC) Ti-6Al-4V Sandwich Structures.* In: Porous and Cellular Materials for Structural Applications, Symposium 1998, San Francisco, CA, USA, Editors : Schwartz, D. S. ; Shih, D. S. ; Evans, A. G. ; Wadley, H. N. G. ; Vol. 521, Warrendale, PA, USA : Materials Research Society, 1998, Pages 243-248, ISBN 1-55899-427-0

[236] **Queheillalt, D. T. ; Wadley, H. N. G.:** *Pyramidal lattice truss structures with hollow trusses.* In: Materials Science and Engineering A, Vol. 397, No. 1-2, 2005, Amsterdam, Netherlands : Elsevier, 2005, Pages 132-137, ISSN 0921-5093

[237] **Queheillalt, D. T. ; Hass, D. D. ; Sypeck, D. J. et al.:** *Synthesis of open-cell metal foams by templated directed vapor deposition.* In: Journal of Materials Research, Vol. 16, No. 4, 2001, Warrendale, PA, USA : Materials Research Society, 2001, Pages 1028-1036, ISSN 0884-2914

[238] **Raghava, R. S. ; Caddell, R. M. ; Yeh, G. S.:** *The Macroscopic Yield Behaviour of Polymers.* In: Journal of Material Science, Vol. 8, No. 2, 1973, Dordrecht, Netherlands : Kluwer, 1973, Pages 225-232, ISSN 1573-4803

[239] **Rajan, V. T. ; Srinivasan, V. ; Tarabanis, K. A.:** *The optimal zigzag direction for filling a two-dimensional region.* In: Rapid Prototyping Journal, Vol. 7, No. 5, 2001, Bradford, UK : MCB University Press, 2001, Pages 231-240, ISSN 1355-2546

[240] **Ramos, J. A. ; Murphy, J. ; Lappo, K.:** *Single-layer Deposits of Nickel Base Superalloy by means of Selective Laser Melting.* In: Bourell, D. L. ; Crawford, R. H. ; Beaman, J. J. ; Wood, K. L. ; Marcus, H. L. : 13th Solid Freeform Fabrication Proceedings 2002, Austin, TX, USA : University of Texas, 2002, Pages 211-223, ISSN 1053-2153

[241] **Ramos, J. A. ; Bourell, D. L.:** *Solidification Morphology Analysis of SLM of Cu Powder.* In: Bourell, D. L. ; Crawford, R. H. ; Beaman, J. J. ; Wood, K. L. ; Marcus, H. L. : 15th Solid Freeform Fabrication Proceedings 2004, Austin, TX, USA : University of Texas, 2004, Pages 203-213, ISSN 1053-2153

[242] **Rattanawong, W.:** *A Generic Part Build Orientation in Rapid Prototyping.* In: Proceedings RPD 2004 Rapid Product Development Event, Marinha Grande, Portugal, Marinha Grande, Portugal : Centimfe, 2004, Pages P4050.1-P4050.5

[243] **Rausch, G. ; Baumeister, J. ; Lehmhus, D. et al.:** *FOAMINAL – Eigenschaftsübersicht, Konstruktionsrichtlinien.* Version 1.4, Bremen, Germany : Fraunhofer IFAM, 2002

[244] **Rausch, G. ; Weber, M.:** *Powder Metallurgical Production of Steel Foams.* In: Materials Week and Materialica 2000 Proceedings, Editor : Werkstoffwoche-Partnerschaft GbR, Frankfurt, Germany : Werkstoffinformationsgesellschaft mbH, 2000 http://www.dgm.de/download/tg/523/523_0687.pdf
Updated last: October, 2000 ; Retrieved: January, 3rd 2007

[245] **Regenfuß, P. ; Hartwig, L. ; Klötzer, S. et al.:** *Industrial freeform generation of microtools by laser micro sintering.* In: Bourell, D. L. ; Crawford, R. H. ; Beaman, J. J. ; Wood, K. L. ; Marcus, H. L. : 15th Solid Freeform Fabrication Proceedings 2004, Austin, TX, USA : University of Texas, 2004, Pages 709-719, ISSN 1053-2153

[246] **Regenfuß, P. ; Ebert, R. ; Klötzer, S. et al.:** *Industrial Laser Micro Sintering.* In: Proceedings of the 4th International Conference on Laser Assisted Net Shape Engineering, LANE 2004, Erlangen, Germany, Vol. 1, Editors : Geiger, M. ; Otto, A. ; Bamberg, Germany : Meisenbach Verlag, 2004, Pages 413-424, ISBN 3-87525-202-0

[247] **Regenfuß, P. ; Ebert, R. ; Exner, H.:** *Laser Micro Sintering.* In: Laser Technik Journal, Vol. 4, No. 1, 2007, Weinheim, Germany : Wiley-VCH Verlag, 2007, Pages 26-30, ISSN 1613-7728

[248] **Rehme, O. ; Emmelmann, C. ; Daniel, A.:** *Laserinnovationen für den Werkzeug- und Formenbau.* In: MB Guide, 09/2004, Heiden, Switzerland : Publica-Press Heiden, 2004, Pages 20-29

[249] **Rehme, O. ; Emmelmann, C.:** *Laser Rapid Manufacturing patientenangepasster Implantate aus Titanwerkstoffen.* Talk at conference on “Innovative Medicine and Biotechnology in Hamburg”, 05/2005, Hamburg, Germany : Institute of Laser and System Technologies, 2005

[250] **Rehme, O. ; Emmelmann, C.:** *Reproducibility for Properties of Selective Laser Melting Products.* In: Proceedings of the Third International WLT-Conference “Lasers in Manufacturing 2005”, Editors : Beyer, E. ; Dausinger, F. ; Ostendorf, A. ; Otto, A. ; Stuttgart, Germany : AT-Fachverlag, 2005, Pages 227-232, ISBN 3-00-016402-2

[251] **Rehme, O. ; Emmelmann, C.:** *Rapid Manufacturing of Lattice Structures with Selective Laser Melting.* In: Proceedings of SPIE Photonics West, LASE 2006 Symposium, conference on “Laser-based Micropackaging III”, Editors : Bachmann, F. G. ; Hoving, W. ; Lu, Y. ; Washio, K. ; Vol. 6107, Bellingham, WA, USA : The International Society for Optical Engineering, 2006, Pages 0K1-0K12, ISBN 0-8194-6149-0

[252] **Rehme, O. ; Emmelmann, C.:** *Selective Laser Melting offenzellulärer Strukturen und Charakterisierung ihrer mechanischen Eigenschaften.* Talk at WLT Laser-Summerschool conference 06/2006, Hamburg, Germany : Institute of Laser and System Technologies, 2006

[253] **Rehme, O. ; Schwarze, D. ; Emmelmann, C.:** *Selective Laser Melting of Customized Implants with Cellular Structures for Optimized Elasticity and Improved Osseointegration.* In: Proceedings RPD 2006 Rapid Product Development Event, Marinha Grande, Portugal, Marinha Grande, Portugal : Centimfe, 2006, Pages P6001.1-P6001.5

[254] **Rehme, O. ; Emmelmann, C.:** *MedLAS – LaserKompetenzSystem im LaserZentrumNord (LZN).* Talk at 21st Laserstammtisch meeting of Hansephotonik e.V., 03/2007, Hamburg, Germany : Institute of Laser and System Technologies, 2007

[255] **Rehme, O. ; Schwarze, D. ; Emmelmann, C.:** *Isoelastic Properties and Improvement of Osseointegration of Laser Freeform Fabrication Implants.* In: Rapid Prototyping, Technical Quarterly, Vol. 13, No. 1, 2007, Dearborn, MI, USA : Society of Manufacturing Engineers, 2007, Pages 1-9, ISSN 1544-9491

[256] **Rehme, O. ; Emmelmann, C.:** *Cellular Design for Laser Freeform Fabrication.* In: Proceedings of the Fourth International WLT-Conference "Lasers in Manufacturing 2007", Editors : Vollertsen, F. ; Emmelmann, C. ; Schmidt, M. ; Otto, A. ; Stuttgart, Germany : AT-Fachverlag, 2007, Pages 243-248, ISBN 978-3-00-021449-3

[257] **Rehme, O. ; Schwarze, D. ; Emmelmann, C.:** *Selective Laser Melting of Lattice Structures in Solid Shells.* Talk at 3rd International Conference on Advanced Research in Virtual and Rapid Prototyping, 2007, Leiria, Portugal, 09/2007 : Hamburg, Germany : Institute of Laser and System Technologies, 2007

[258] **Rice, R. W.:** *Comparison of stress concentration versus minimum solid area based mechanical property-porosity relations.* In: Journal of Materials Sciences, Vol. 28, No. 8, 1993, Dordrecht, Netherlands : Kluwer, 1993, Pages 2187-2190, ISSN 0022-2461

[259] **Roberts, A. P. ; Garboczi, E. J. :** *Elastic moduli of model random three-dimensional closed-cell cellular solids,* In: Acta Materialia, Vol. 49, No. 2, 2001, Kidlington, UK : Elsevier, 2001, Pages 189-197, ISSN 1359-6454

[260] **Roberts, A. P. ; Garboczi, E. J. :** *Elastic properties of model random three-dimensional open-cell solids.* In: Journal of the Mechanics and Physics of Solids, Vol. 50, No. 1, 2002, Amsterdam, Netherlands : Elsevier, 2002, Pages 33-55, ISSN 0022-5096

[261] **Rohsenow, W. M. ; Hartnett, J. P.:** *Handbook of Heat Transfer.* New York City, NY, USA : McGraw-Hill, 1973, ISBN 0-07-053576-0

[262] **Saenz, E. ; Baranda, P. S. ; Bonhomme, J.:** *Shear Properties on Aluminum Metal Foams Prepared by the Melt Route.* In: Porous and Cellular Materials for Structural Applications, Symposium 1998, San Francisco, CA, USA, Editors : Schwartz, D. S. ; Shih, D. S. ; Evans, A. G. ; Wadley, H. N. G. ; Vol. 521, Warrendale, PA, USA : Materials Research Society, 1998, Pages 83-89, ISBN 1-55899-427-0

[263] **Salsbury, P.**
http://www.sculptors.com/~salsbury/Gifs/Graphics/octet-truss-003-v2.png
Updated last: April, 4th 2001 ; Retrieved: May, 1st 2008

[264] **Sanders, W. S. ; Gibson, L. J.:** *Mechanics of BCC and FCC hollow-sphere foams.* In: Materials Science and Engineering A, Vol. 352, No. 1-2, 2003, Amsterdam, Netherlands : Elsevier, 2003, Pages 150-161, ISSN 0921-5093

[265] **Sanders, W. S. ; Gibson, L. J.:** *Reduction in Young's Modulus Of Aluminum Foams Due To Cell Wall Curvature and Corrugation.* In: Porous and Cellular Materials for Structural Applications, Symposium 1998, San Francisco, CA, USA, Editors : Schwartz, D. S. ; Shih, D. S. ; Evans, A. G. ; Wadley, H. N. G. ; Vol. 521, Warrendale, PA, USA : Materials Research Society, 1998, Pages 53-57, ISBN 1-55899-427-0

[266] **Santos, E. C. ; Abe, F. ; Kitamura, Y. et al.:** *Mechanical Properties of Pure Titanium Models Processed by Selective Laser Melting.* In: Bourell, D. L. ; Crawford, R. H. ; Beaman, J. J. ; Wood, K. L. ; Marcus, H. L. : 13th Solid Freeform Fabrication Proceedings 2002, Austin, TX, USA : University of Texas, 2002, Pages 180-186, ISSN 1053-2153

[267] **Santos, E. C. ; Shiomi, M. ; Osakada, K. et al.:** *Rapid manufacturing of metal components by laser forming.* In: International Journal of Machine Tools & Manufacture, Vol. 46, No. 12-13, 2006, Oxford, UK : Elsevier, 2006, Pages 1459-1468, ISSN 0890-6955

[268] **Sauer, A.:** *Optimierung der Bauteileigenschaften beim Selektiven Lasersintern von Thermoplasten.* Dissertation Universität Duisburg-Essen, Germany, 2005, Aachen, Germany : Shaker Verlag, 2005, ISBN 978-3-8322-4428-6

[269] **Schatt, W. ; Wieters, K.-P.:** *Pulvermetallurgie: Technologien und Werkstoffe.* Düsseldorf, Germany : VDI-Verlag, 1994, ISBN 3-18-401343-X

[270] **Scheffler, M. ; Colombo, P.:** *Cellular Ceramics: Structure, Manufacturing, Properties and Applications.* Weinheim, Germany : Wiley-VCH Verlag, 2005, ISBN 3-527-31320-6

[271] **Schwartz, D. S. ; Shih, D. S. ; Lederich, R. J. et al.:** *Development and scale-up of the low density core process for Ti-64.* In: Porous and Cellular Materials for Structural Applications, Symposium 1998, San Francisco, CA, USA, Editors : Schwartz, D. S. ; Shih, D. S. ; Evans, A. G. ; Wadley, H. N. G. ; Vol. 521, Warrendale, PA, USA : Materials Research Society, 1998, Pages 225-230, ISBN 1-55899-427-0

[272] **Shapovalov, V. I.:** *Formation of ordered gas-solid via solidification in metal-hydrogen systems.* In: Porous and Cellular Materials for Structural Applications, Symposium 1998, San Francisco, CA, USA, Editors : Schwartz, D. S. ; Shih, D. S. ; Evans, A. G. ; Wadley, H. N. G. ; Vol. 521, Warrendale, PA, USA : Materials Research Society, 1998, Pages 281-290, ISBN 1-55899-427-0

[273] **Shellabear, M. ; Lenz, J. ; Junior, V.:** *E-Manufacturing with Laser-Sintering – to Series Production and Beyond.* In: Proceedings of the 4th International Conference on Laser Assisted Net Shape Engineering, LANE 2004, Erlangen, Germany, Vol. 1, Editors : Geiger, M. ; Otto, A. ; Bamberg, Germany : Meisenbach Verlag, 2004, Pages 435-444, ISBN 3-87525-202-0

[274] **Sherman, A. J. ; Tuffias, R. H. ; Kaplan, R. B.:**
Refractory Ceramic Foams: A Novel High Temperature Structure.
http://www.ultramet.com/foamtech.htm
Updated last: October, 9th 1999 ; Retrieved: March, 2nd 2006

[275] **Sih, S. ; Barlow, J. W.:** *Measurement and prediction of the thermal conductivity of powders at high temperatures.* In: Marcus, H. L. ; Beaman, J. J. ; Barlow, J. W. ; Bourell, D. L. ; Crawford, R. H. : 5th Solid Freeform Fabrication Proceedings 1994, Austin, TX, USA : University of Texas, 1994, Pages 321-329, ISSN 1053-2153

[276] **Simančik, F. ; Mináriková, N. ; Čulák, S. et al.:** *Effect of foaming parameters on the pore size.* In: Proceedings of the 1st International Conference on Metal Foams and Porous Metal Structures (MetFoam '99), Editors : Banhart, J. ; Ashby, M. F. ; Fleck, N. A. ; Berlin, Germany : MIT-Verlag, 1999, Pages 105-108, ISBN 3-9805748-7-3

[277] **Stampfl, J. ; Cano Vives, R. ; Seidler, S. et al.:** *Rapid Prototyping – A Route for the Fabrication of Biomimetic Materials.* In: Proceedings of the 1st International Conference on Advanced Research in Virtual and Rapid Prototyping, Leiria, Portugal, 2003, Editors : Bartolo, P. J. ; Mitchell, G. et al. ; Leira, Portugal : 2003, Pages 659-666

[278] **Stauffer, D. ; Aharony, A.:** *Introduction to percolation theory.* Revised second Edition, London, UK : Taylor & Francis, 1994, ISBN 0-7484-0253-5

[279] **Steinberger, J.:** *Optimierung des Selektiven-Laser-Sinterns zur Herstellung von Feingussteilen für die Luftfahrtindustrie.* Dissertation TU München, Germany, 2001, Düsseldorf, Germany : VDI Verlag, 2001, ISBN 3-18-357302-4

[280] **Stöbener, K. ; Baumeister, J. ; Rausch, G.:** *Aluminiumschäume für die industrielle Produktion.* In: ATZ – Automobiltechnische Zeitschrift, Vol. 107, No. 1, 2005, Wiesbaden, Germany : Vieweg Verlag, 2005, Pages 10-15, ISSN 0001-2785

[281] **Stöbener, K. ; Baumeister, J. ; Lehmhus, D. et al.:** *Composites Based on Metallic Foams: Phenomenology; Production; Properties and Principles.* In: Proceedings of the International Conference "Advanced Metallic Materials". Bratislava, Slovakia : Institute of Materials and Machine Mechanics, 2003, Pages 281-286, ISBN 80-969011-7-6

[282] **Ströhla, S. ; Winter, W. ; Kuhn, G.:** *Numerische Ermittlung elastischer Eigenschaften von Metallschäumen mit Polyeder-Einheitszellen.* In: Materialwissenschaft und Werkstofftechnik, Vol. 31, No. 6, 2000, Weinheim, Germany : Wiley-VCH Verlag, 2000, Pages 444-446, ISSN 0933-5137

[283] **Stucker, B. E. ; Bradley, W. L. ; Norasetthekul S. et al.:** *The Production of Electrical Discharge Machining Electrodes Using SLS: Preliminary Results.* In: Marcus, H. L. ; Beaman, J. J. ; Bourell, D. L. ; Barlow, J. W. ; Crawford, R. H. : 6th Solid Freeform Fabrication Proceedings 1995, Austin, TX, USA : University of Texas, 1995, Pages 278-286, ISSN 1053-2153

[284] **Stucker, B. E. ; Malhotra, M. ; Qu, X. et al.:** *RapidSteel Part Accuracy.* In: Bourell, D. L. ; Beaman, J. J. ; Crawford, R. H. ; Marcus, H. L. ; Barlow, J. W. : 11th Solid Freeform Fabrication Proceedings 2000, Austin, TX, USA : University of Texas, 2000, Pages 133-140, ISSN 1053-2153

[285] **Sun, M.-S. M.:** *Physical Modeling of the Selective Laser Sintering Process.* Dissertation University of Texas, Austin, TX, USA, 1991, Ann Arbor, MI, USA : UMI, 1992

[286] **Sutcliffe, C. ; Brooks, W. ; Cantwell, W. et al.:** *The Rapid Manufacture of Micro Hierarchical Structures by Selective Laser Melting.* In: ICALEO 2005 Congress Proceedings, LIA Publication 598, Vol. 98, Orlando, Florida : Laser Institute of America, 2005, Pages 1082-1088, ISBN 0-912035-82-X

[287] **Swainson, W. K.:**
Method, medium and apparatus for producing three-dimensional figure product.
United States Patent 4041476, filed July 23rd, 1971, published August 9th, 1977
http://www.freepatentsonline.com/4041476.html
Updated last: 2007 ; Retrieved: May, 9th 2007

[288] **Sypeck, D. J. ; Wadley, H. N. G.:** *Cellular Metal Truss Core Sandwich Structures.* In: Advanced Engineering Materials. Vol. 4, No. 10, 2002, Weinheim, Germany : Wiley-VCH Verlag, 2002, Pages 759-764, ISSN 1438-1656

[289] **Sypeck, D. J. ; Parrish, P. A. ; Wadley, H. N. G.:** *Novel Hollow Powder Porous Structures.* In: Porous and Cellular Materials for Structural Applications, Symposium 1998, San Francisco, CA, USA, Editors : Schwartz, D. S. ; Shih, D. S. ; Evans, A. G. ; Wadley, H. N. G. ; Vol. 521, Warrendale, PA, USA : Materials Research Society, 1998, Pages 205-210, ISBN 1-55899-427-0

[290] **Tabata, T. ; Masaki, S.:** *Estimation of Flow Stress of Porous Sintered Metals From Hardness Test With Pyramidal and Spherical Indenters.* In: Journal of Engineering Materials and Technology, Vol. 112, No. 1, 1990, New York City, NY, USA : ASME, 1990, Pages 95-98, ISSN 0094-4289

[291] **Tangwiriyasakul, C.:** *Systematic development and verification of design rules for laser generated metallic parts suitable for medical applications.* Master thesis at Hamburg University of Technology (TUHH), Institute of Laser and System Technologies (iLAS), 2004, Supervisor : Rehme, O.

[292] **Thomson, W. (aka Lord Kelvin):** *On the division of space with minimum partitional energy.* In: Philosophical Magazine, Vol. 24, No. 151, 1887, London, UK : Taylor & Francis, 1887, Pages 503-514, ISSN 1478-6435

[293] **Timoshenko, S. P. ; Gere, J. M.:** *Theory of elastic stability.* Second Edition, New York, NY, USA : McGraw-Hill, 2000, ISBN 0-07-085821-7

[294] **Tolochko, N. K. ; Laoui, T. ; Khlopkov, Y. V. et al.:** *Absorptance of powder materials suitable for laser sintering.* In: Rapid Prototyping Journal, Vol. 6, No. 3, 2000, Bradford, UK : MCB University Press, 2000, Pages 155-160, ISSN 1355-2546

[295] **Tolochko, N. K. ; Mozzharov, S. E. ; Laoui, T.:** *Selective laser sintering of single- and two-component metal powders.* In: Rapid Prototyping Journal, Vol. 9, No. 2, 2003, Bradford, UK : MCB University Press, 2003, Pages 68-78, ISSN 1355-2546

[296] **Tolochko, N. K. ; Arshinov, M. K. ; Gusarov, A. V. et al.:** *Mechanisms of selective laser sintering and heat transfer in Ti powder.* In: Rapid Prototyping Journal, Vol. 9, No. 5, 2003, Bradford, UK : MCB University Press, 2003, Pages 314-326, ISSN 1355-2546

[297] **Tolochko, N. K. ; Mozzharov, S. E. ; Yadroitsev, I. A. et al. :** *Balling process during selective laser treatment of powders.* In: Rapid Prototyping Journal, Vol. 10, No. 2, 2004, Bradford, UK : MCB University Press, 2004, Pages 78-87, ISSN 1355-2546

[298] **Triantafillou, T. C. ; Gibson, L. J.:** *Multiaxial Failure Criteria for Cellular Materials.* In: Mechanical Properties of Porous and Cellular Materials, Symposium 1990, Boston, MA, USA, Editor : Sieradzki, K. ; Vol. 207, Pittsburgh, PA, USA : Materials Research Society, 1991, Pages 9-14, ISBN 1-558-99099-2

[299] **Uckelmann, I. :** *Generative Serienfertigung von individuellen Produkten aus CoCr mit dem Selektiven Laser-Schmelzen.* Dissertation RWTH Aachen, Germany, 2006, Aachen, Germany : Shaker Verlag, 2007, ISBN 3-8322-4989-3

[300] **Van der Schueren, B. ; Kruth, J. P.:** *Powder deposition in selective metal powder sintering.* In: Rapid Prototyping Journal. Vol. 1, No. 3, 1995, Bradford, UK : MCB University Press, 1995, Pages 23-31, ISSN 1355-2546

[301] **Van Elsen, M.:** *Complexity of Selective Laser Melting: A new optimisation approach.* Dissertation Katholieke Universiteit Leuven, Belgium, 2007, Heverlee, Belgium : Katholieke Universiteit Leuven, 2007

[302] **Waag, U. ; Schneidereit, H. ; Schulze, F. et al.:** *Metallic Hollow Sphere Structures – Processing, Properties and Applications.* In: Materials Week and Materialica 2000 Proceedings, Editor : Werkstoffwoche-Partnerschaft GbR, Frankfurt, Germany : Werkstoffinformationsgesellschaft mbH, 2000
http://www.dgm.de/download/tg/523/523_0684.pdf
Updated last: March, 2001 ; Retrieved: January, 3rd 2007

[303] **Wadley, H. N. G.:** *Cellular Metals Manufacturing.* In: Advanced Engineering Materials, Vol. 4, No. 10, 2002, Weinheim, Germany : Wiley-VCH Verlag, 2002, Pages 726-733, ISSN 1438-1656

[304] **Wadley, H. N. G. ; Fleck, N. A. ; Evans, A. G.:** *Fabrication and structural performance of periodic cellular metal sandwich structures.* In: Composites Science and Technology, Vol. 63, No. 16, 2003, Barking, UK : Elsevier, 2003, Pages 2331-2343, ISSN 0266-3538

[305] **Wagner, C.:** *Untersuchungen zum Selektiven Lasersintern von Metallen.* Dissertation RWTH Aachen, Germany, 2003, Aachen, Germany : Shaker Verlag, 2003, ISBN 3-8322-1538-7

[306] **Wang, C. M.:** *Timoshenko Beam-Bending Solutions in Terms of Euler-Bernoulli Solutions.* In: Journal of Engineering Mechanics, Vol. 121, No. 6, 1995, Reston, VA, USA : ASCE, 1995, Pages 763-765, ISSN 0733-9399

[307] **Wang, H. V.:**
A Unit Cell Approach for Lightweight Structure and Compliant Mechanism
Ph. D. Thesis, Mechanical Engineering, Georgia Institute of Technology, 2005
http://etd.gatech.edu/theses/available/etd-11222005-162952/unrestricted/wang_hongqing_v_200512_phd.pdf
Updated last: November, 28th 2005 ; Retrieved: August, 1st 2006

[308] **Wang, X. ; Lu, T. J.:** *Optimized acoustic properties of cellular solids.* In: Journal of the Acoustical Society of America, Vol. 106, No. 2, 1999, Melville, NY, USA : American Institute of Physics, 1999, Pages 756-765, ISSN 0001-4966

[309] **Wang, Y. C. ; Lakes, R. S. ; Butenhoff, A.:** *Influence of Cell Size on Re-entrant Transformation of Negative Poisson's Ratio Reticulated Polyurethane Foams.* In: Cellular Polymers, Vol. 20, No. 6, 2001, Shawbury, UK : Rapra Technology, 2001, Pages 373-385, ISSN 0262-4893

[310] **Wanner, A. ; Kriszt, B.:** *Charakterisierung des linear-elastischen Verhaltens von Metallschäumen mittels Ultraschall Phasenspektroskopie.* In: Materialwissenschaft und Werkstofftechnik, Vol. 31, No. 6, 2000, Weinheim, Germany : Wiley-VCH Verlag, 2000, Pages 481-483, ISSN 0933-5137

[311] **Warren, W. E. ; Kraynik, A. M.:** *Linear Elastic Behavior of a Low-Density Kelvin Foam With Open Cells.* In: Journal of Applied Mechanics, Vol. 64, No. 4, 1997, New York City, NY, USA : ASME, 1997, Pages 787-794, ISSN 1528-9036

[312] **Weaire, D. ; Cox, S. J. ; Banhart, J.:** *Methods and models of metallic foam fabrication.* In: Proceedings of the 8th International Conference on Composites Engineering (ICCE/8), 2001, Tenerife, Spain, Editor : Hui, D. ; Orlando, FL, USA : International Community for Composites Engineering, 2001, Pages 977-978

[313] **Weber, M.:** *Herstellung von Metallschäumen und Beschreibung der Werkstoffeigenschaften.* Dissertation TU Clausthal, Germany, 1995

[314] **Wegst, C. W. ; Wegst, M.:** *Stahlschlüssel / Key to Steel.* 20. Auflage 2004, Marbach, Germany : Verlag Stahlschlüssel Wegst, 2004, ISBN 3-922599-20-6

[315] **Wicklein, M. ; Sauer, M. ; Klomfass, A. et al.:** *Mesomechanical simulation of cellular aluminium.* In: Proceedings of the 3rd International Conference on Cellular Metals and Metal Foaming Technology (MetFoam 2003), Editors : Banhart, J. ; Fleck, N. A. ; Mortensen, A. ; Berlin, Germany : MIT-Verlag, 2003, Pages 369-374, ISBN 3-935538-12-X

[316] **Wikipedia Contributors:** *Metal foam.* In: Wikipedia, The Free Encyclopedia
http://en.wikipedia.org/wiki/Metal_foam
Updated last: February, 19th 2006 ; Retrieved: March, 4th 2006

[317] **Wikipedia Contributors:** *Polyhedron.* In: Wikipedia, The Free Encyclopedia
http://en.wikipedia.org/wiki/Polyhedron
Updated last: April, 25th 2008 ; Retrieved: May, 1st 2008

[318] **Wikipedia Contributors:** *Von Mises yield criterion.*
In: Wikipedia, The Free Encyclopedia
http://en.wikipedia.org/wiki/Von_Mises_stress
Updated last: March, 17th 2008 ; Retrieved: March, 22nd 2008

[319] **Williams, C. B. ; Mistree, F. ; Rosen, D. W.:** *Towards the Design of a Layer-Based Additive Manufacturing Process for the Realization of Metal Parts of Designed Mesostructure.* In: Bourell, D. L. ; Crawford, R. H. ; Beaman, J. J. ; Wood, K. L. ; Marcus, H. L. : 16th Solid Freeform Fabrication Proceedings 2005, Austin, TX, USA : University of Texas, 2005, Pages 217-230, ISSN 1053-2153

[320] **Williams, J. D. ; Miller, D. ; Deckard, C.:** *Selective Laser Sintering Part Strength as a Function of Andrew Number, Scan Rate and Spot Size.* In: Bourell, D. L. ; Beaman, J. J. ; Marcus, H. L. ; Crawford, R. H. ; Barlow, J. W. : 7th Solid Freeform Fabrication Proceedings 1996, Austin, TX, USA : University of Texas, 1996, Pages 549-553, ISSN 1053-2153

[321] **Williams, J. D. ; Deckard, C. R.:** *Advances in modeling the effects of selected parameters on the SLS process.* In: Rapid Prototyping Journal, Vol. 4, No. 2, 1998, Bradford, UK : MCB University Press, 1998, Pages 90-100, ISSN 1355-2546

[322] **Wirtz, T. P.:** *Herstellung von Knochenimplantaten aus Titanwerkstoffen durch Laserformen.* Dissertation RWTH Aachen, Germany, 2005
http://deposit.d-nb.de/cgi-bin/dokserv?idn=978158687&dok_var=d1&dok_ext=pdf&filename=978158687.pdf
Updated last: January, 19th 2006 ; Retrieved: November, 05th 2007

[323] **Wöß, A. ; Stampfl, J. ; Fratzl, P.:** *Cellular Solids beyond the Apparent Density – an Experimental Assessment of Mechanical Properties.* In: Advanced Engineering Materials, Vol. 6, No. 3, 2004, Weinheim, Germany : Wiley-VCH Verlag, 2004, Pages 134-138, ISSN 1438-1656

[324] **Wohlers, T. T.:** *Wohlers Report 2003.* First Edition 2003, Fort Collins, CO, USA : Wohlers Associates, 2003

[325] **Wolfangel, F.:** *Untersuchung des Einflusses von Pulverkorngrößenverteilungen auf qualitätsrelevante Ergebnisgrößen des SLM-Prozesses.* Project thesis at Hamburg University of Technology (TUHH), Institute of Laser and System Technologies (iLAS), 2006, Supervisor : Rehme, O.

[326] **Xu, F. ; Loh, H. T. ; Wong, Y. S.:** *Considerations and selection of optimal orientation for different rapid prototyping systems.* In: Rapid Prototyping Journal, Vol. 5, No. 2, 1999, Bradford, UK : MCB University Press, 1999, Pages 54-60, ISSN 1355-2546

[327] **Yagi, S. ; Kunii, D.:** *Studies on effective thermal conductivities in packed beds.* In: AIChE Journal, Vol. 3, No. 3, 1957, New York City, NY, USA : American Institute of Chemical Engineers, 1957, Pages 373-381, ISSN 0001-1541

[328] **Yang, Y. ; Loh, H. T. ; Fuh, J. Y. H. et al.:** *Equidistant path generation for improving scanning efficiency in layered manufacturing.* In: Rapid Prototyping Journal, Vol. 8, No. 1, 2002, Bradford, UK : MCB University Press, 2002, Pages 30-37, ISSN 1355-2546

[329] **Zettl, B. E. ; Stanzl-Tschegg, S. E. ; Gradinger, R. et al.:** *High cycle fatigue properties of aluminium foams.* In: Porous and Cellular Materials for Structural Applications, Symposium 1998, San Francisco, CA, USA, Editors : Schwartz, D. S. ; Shih, D. S. ; Evans, A. G. ; Wadley, H. N. G. ; Vol. 521, Warrendale, PA, USA : Materials Research Society, 1998, Pages 97-102, ISBN 1-55899-427-0

[330] **Zhang, D.:** *Entwicklung des Selective Laser Melting (SLM) für Aluminiumwerkstoffe.* Dissertation RWTH Aachen, 2004, Aachen, Germany : Shaker Verlag, 2004, ISBN 3-8322-3104-8

[331] **Zhao, C. Y. ; Lu, T. J. ; Hodson, H. P. et al.:** *The temperature dependence of effective thermal conductivity of open-celled steel alloy foams.* In: Materials Science and Engineering A, Vol. 367, No. 1-2, 2004, Amsterdam, Netherlands : Elsevier, 2004, Pages 123-131, ISSN 0921-5093

[332] **Zhu, H. H. ; Fuh, J. Y. H. ; Lu, L.:** *Microstructural evolution in direct laser sintering of Cu-based metal powder.* In: Rapid Prototyping Journal, Vol. 11, No. 2, 2005, Bradford, UK : MCB University Press, 2005, Pages 74-81, ISSN 1355-2546

[333] **Zhu, H. X. ; Knott, J. F. ; Mills, N. J.:** *Analysis of the elastic properties of open-cell foams with tetrakaidecahedral cells.* In: Journal of the Mechanics and Physics of Solids, Vol. 45, No. 3, 1997, Amsterdam, Netherlands : Elsevier, 1997, Pages 319-343, ISSN 0022-5096

10 Appendices

10.1 Cellular material properties

10.1.1 Acoustical properties

Sound is mechanical energy propagating through matter as a longitudinal wave. In air at standard atmosphere it travels at a speed of approximately 343 m/s, however, in solid, elastic materials the sound velocity is typically much faster (Ashby, 2000, p. 171, [17]). In e.g. steel and aluminum the velocities are 5920 m/s and 6300 m/s at a temperature of 20° C. Thus it becomes obvious that closed-cell porosities act rather like the solid material due to low intrinsic damping of the rigid cell walls (Han, 2003, p. 295, [134]) and do not contribute much to a specific type of energy absorption which is the annihilation of sound pressure (Lu, 1999, p. 7528, [189]). Therefore, open-cell materials perform much better, especially if they are backed by an appropriate air gap which increases the height and width of the absorption peak and shifts the peak towards lower frequencies (Han, 2003, p. 294, [134]).

Sound pressure has an audible range of about 10^6 Pa and is given in a logarithmic scale for reasons of convenience by refering the squared sound pressure p to a squared reference pressure of $p_0 = 2 \cdot 10^{-5}$ Pa. The sound pressure level L_p is measured in decibels as stated in ***eq. (10.1)***. Alternatively, the sound power level L_P can be calculated according to ***eq. (10.2)*** as a quotient of sound power P and a reference power $P_0 = 10^{-12}$ W (DIN EN ISO 80000-8, 2006, p. 14, [99]).

$$L_p = 10 \cdot \log_{10}\left(\frac{p^2}{p_0^2}\right) = 20 \cdot \log_{10}\left(\frac{p}{p_0}\right) \tag{10.1}$$

$$L_P = 10 \cdot \log_{10}\left(\frac{P}{P_0}\right) \tag{10.2}$$

$$\alpha = 1 - r^2 \qquad \text{where: } \begin{array}{l} p_i = p_{max} \cdot \cos(2\pi f t) \\ p_r = r p_{max} \cdot (-\cos(2\pi f t)) \end{array} \tag{10.3}$$

For acoustic absorption in engineering applications the important frequency range is between 20 and 4000 Hz (Han, 2003, p. 301, [134]). The sound absorption coefficient α describes the fraction of energy that is absorbed at given frequencies and is defined in ***eq. (10.3)*** by the pressure p_i of an incident sound wave impinging normally on an absorber and the pressure p_r of the reflected wave. In accordance with DIN EN ISO 10534-1 (2001, pp. 6-7, [92]) the incident and the reflected wave must be in phase (standing wave tube method) when the relation between their amplitudes r is measured. DIN EN ISO 10534-2 (2001, pp. 1-15, [93]) describes an alternative procedure to obtain the sound absorption coefficient by using a standing wave tube method which utilizes a broadband random sound source (noise generator) and two microphone positions. The complex acoustic transfer function then delivers the ratio between the incident and the reflected wave (Han, 2003, pp. 295-296, [134]). A third, however, due to lack of reproducibility less favourable way to obtain the sound absorption coefficient is the reverberation-room method where the sound waves impinge randomly upon the sample (Lu, 1999, p. 7530, [189]). To characterize the overall performance of a sound absorber better it is helpful to make also use of either the peak half-width which is defined as the width of the frequency band at an absorption coefficient of 50 % of the peak value or the noise reduction coefficient (NRC) which is the arithmetic average of the absorption coefficient at the frequencies of 250, 500, 1000 and 2000 Hz (Bell, 1994, p. 203, [36]). For completeness it must be added that the sound absorption coefficient and the related values are not material properties as they depend on sample thickness. True material properties are the complex values of characteristic impedance $\bar{Z}$ and the propagation constant (aka wave number) $\bar{k}_0$. They can be calculated from the complex density and the complex compressibility of the sound carrier medium (typically air) which both derive from the porosity and the tortuosity of the sample material as suggested by Wang (1999, p. 757, [308]) and Lu (1999, pp. 7529-7530, [189]). Conventional sound absorbers such as polymer foams and glass wool can achieve wideband absorption of up to $\alpha = 0.99$.

The annihilation of sound energy can happen in multiple ways (Lu, 1999, p. 7528, [189]) (Han, 2003, p. 300, [134])

- such as viscous losses as the sound pressure pumps the medium in and out of cavities in the absorber where it suffers from flow resistance,
- thermal-elastic attenuation due to heat exchange between the medium and the solid absorber structure,
- by Helmholtz-type resonators where the cross-sectional area of the absorber changes abruptly in the direction normal to sound wave propagation such that micro channels are connected to large volumes,
- by vortex shedding from sharp edges of the rigid walls in the absorber and
- by direct mechanical damping in the material itself.

Applied to metallic cellulars it is widely perceived that vortex shedding can be neglected for linear sound behaviour and direct mechanical damping can be ignored due to large stiffness of the metallic framework. Different researchers studied the influence of cellular material properties on sound energy dissipation. Altogether they found that in rigid-framed porous materials the cell size, the cell shape, the cell topology, the density, the airflow resistance, the sample thickness and the air cavity depth take major influence on sound absorption. These factors are highly interlinked. Values of up to 95 % sound absorption for an open-cell aluminum sponge were measured (Banhart, 2000, p. 503, [26]). In contrast, Lu (1999, pp. 7530-7535, [189]) described the use of a closed-cell aluminum foam named Alporas which is generally a poor sound absorber unless compressed or rolled leading to cell fracture and formation of sharp-edged crack openings. Untreated Alporas absorbs sound best if the least relative density tested of 0.09 and a medium sample thickness between 10 and 20 mm (from the range of 6 to 50 mm) is applied. Here, an absorption coefficient of 0.6 can be obtained. If Alporas with initial density of 0.09 is rolled or compressed to 60 % of its original thickness, then the sound absorption can be enhanced to a peak of 0.8 at frequencies around 1500 Hz. To further improve the transparency to air motion the effect of hole drilling was also investigated and sound absorption close to unity was found for frequencies between 1200 and

1600 Hz. In this case the effects of viscous forces, thermal damping and Helmholtz resonance contribute to optimized sound absorption for samples not thinner than 10 mm. Han (2003, pp. 296-301, [134]) also confirmed that the sound absorption coefficient for closed-cell aluminum foams achieves poor values below 0.5 while their open-cell counterparts can exceed values of 0.99 at certain frequencies with peak half-widths of up to 3500 Hz. Here, for thin samples without air cavity the smallest pore size of 0.5 mm from a range of up to 5 mm and densities between 0.14 and 0.34 delivered best results, whereas with the use of an air cavity pore sizes of 1.5 and 2.5 mm showed higher and broader absorption peaks between 0.95 and 0.99. Generally, the shift of the sound absorption peak towards lower frequencies is proportional to the depth of the air cavity, however, it takes virtually no influence on the maximum. Air-gap backing contributes much to absorption by Helmholtz resonance though each single cell of an open-cell material can be considered a small Helmholtz resonator. Further examinations indicated that the influence of a great sample thickness is in most cases beneficial. If considered in combination, the density, the cell size and the cell shape are responsible for the airflow resistance which is another criterion for energy dissipation and thus a reliable way to estimate the sound absorption capabilities of an open-cell material. According to Han (2003, p. 294, [134]) it should range at medium values between 0.04 and 0.045 Ns/m^4 regardless of the cell parameters. Wang (1999, p. 757, [308]) developed optimization strategies for aluminum foams and honeycombs and found from theoretical analysis that the cell shape has minor impact on sound absorption, whereas the influence of density is significant. Low density means a larger area of surface which the passing air exchanges heat with and suffers friction losses from. Aside from some possible exemptions to the rule the sound absorption coefficient generally increases with sample thickness. The effect of cell size is much more complicated since increasing the cell size for an infinitely thick sample will improve the sound absorption. However, computations revealed that for thinner absorbers of 3 to 4 cm thickness with an air cavity depth of 4 to 5 cm and a density of less than 0.4 an optimium cell size lies in the range of approximately 0.1 mm where the best sound absorption occurs at frequencies between 500 and 2000 Hz. These values were obtained by calculating effective pore properties from the complex density and the complex compressibility for air passing through a given honeycomb structure.

Though some specific findings from different researchers may appear contradictory the overall outcome is that viscous and thermal losses contribute most to sound absorption especially for cell sizes in the submillimeter range and for high frequencies. Thus the air flow resistance is a viable quantity to measure sound absorption. Helmholtz resonance can interfere with the above mentioned effects if the cell size is clearly greater e.g. in the range of 3 mm. Nevertheless, obtaining high sound absorption is always a compromise of finding the optimum combination among the different effects.

In contrast to the examinations introduced in ***section 2.1.4.6*** (Wanner, 2000, pp. 481-483, [310]) applied ultrasonic sound of frequencies between 50 and 400 kHz on open-cell metallic sponges to obtain linear-elastic material properties such as Young’s modulus.

10.1.2 Mechanical damping properties

A property of cellular metallic materials related to acoustics to some extent was described by Ashby (2000, pp. 176-179, [17]) where foam panels and sandwich panels with foam cores were found to be very attractive due to their flexural stiffness and thus inherent high damping capacity. According to Golovin (2004, pp. 504-511, [127]) the relative density, the cell size, the cell shape, the pre-deformation, the number of vibrations (fatigue) and air pressure influence the damping of a cellular material. Four different mechanisms exist that can possibly contribute to mechanical damping. These are

- thermoelastic damping (amplitude-independent),
- string-like vibrations of dislocations, which is enhanced in porous structures by localized stresses (reversible, amplitude-dependent),
- magnetomechanical damping (reversible, amplitude-dependent),
- microplastic deformation (irreversible, amplitude-dependent) and
- growth and propagation of microcracks due to fatigue (irreversible, amplitude-dependent).

To obtain the damping capacity the loss factor ϑ is typically determined either as the generally exponential decay behaviour in resonance or by the resonance width which is the bandwidth around resonance frequency where the amplitude is greater than $1/\sqrt{2}$ times the resonance amplitude. Banhart (1996, pp. 221-228, [25]) used the resonance width to examine aluminum foam samples of relative densities between 0.26 and 0.89 with cell sizes ranging from 0.3 to 2 mm. The resonance frequency of the cuboid shaped, elongated samples was adjusted by changing the length of the sample. The best average loss factors achieved were between $25\cdot10^{-4}$ to $30\cdot10^{-4}$ though single outliers could attain values of up to $40\cdot10^{-4}$. It became clear that the loss factor is independent of frequency, however, some variations occurred probably caused by inhomogeneous spatial material distribution. Nevertheless, a significant dependency was found as the loss factor decreases while the relative density increases. This context is described by the power function in ***eq. (10.4)*** which matches well with the widely accepted perception that porosities generally enhance damping due to stress concentration and mode conversion around pores on microscopic as well as on macroscopic scales. All results obtained here were amplitude-independent since the strain level was kept as small as possible ($\varepsilon \leq 10^{-4}$) to reduce damping effects from clamping of the samples.

$$\vartheta = 1.1798\cdot10^{-3}\left(\frac{\rho^{*}}{\rho_{solid}}\right)^{-0.5526} \tag{10.4}$$

Porous parts made from stainless steel 316L and titanium powder with relative densities between 0.14 and 0.78 were analyzed by Golovin (2004, pp. 531-535, [128]). Some of the specimens contained only microporosities with voids of 10 µm size while others also comprised macroporosities with gaps between 350 and 500 µm. Strain of the specimens was varied such that amplitude-dependent damping occurred. The loss factor was determined from the logarithmic decrement of vibration amplitudes to values between 10^{-3} and 10^{-1}. The experiments showed that damping was not sensitive to frequency variations in the range between 10^{-4} and 10^{-2} Hz and that only the overall relative density has major influence rather than micro- or macropores.

In a further study Golovin (2004, pp. 537-541, [129]) exposed similar specimens to vibrational load. Generally, an increase of damping was observed for all specimens with continuous number of vibrations. However, the lower the relative density of the specimens was the higher the increase in damping became. This was assumed to occur due to a decrease in modulus of elasticity caused by microplastic deformation and growth as well as movement of microcracks due to fatigue.

10.1.3 Permeability

This property applies only to open-cell materials where a gas, or more generally a fluid, is pumped through. The permeability is characterized by the pressure drop Δp the gas or fluid will suffer as it passes through a constant cross sectional area A for a given length l. The pressure drop is proportional to the free stream velocity of the fluid specified by the volume stream velocity Q divided by the cross sectional area as derived by Darcy (1856, Appendix D, [73]). According to DIN ISO 4022 (1990, p. 7, [97]) three different types of flow are established. Laminar flow is a non-turbulent flow where all losses are only due to the dynamic viscosity η. It results in the linear term given in ***eq. (10.5)***. If e.g. a stochastic distribution of pores in the material causes constant change in the direction of flow, then energy loss and therefore pressure drop occurs due to local turbulences. This so-called inertia flow depends on the density ρ of the gas or fluid and results in the quadratic term added in ***eq. (10.5)***. However, for small stream velocities Q/A of the gas or fluid this term is negligible and ***eq. (10.5)*** can be simplified accordingly. A third flow type is called slip flow which only gains significance if the pore size is in the range of the average free path length of the gas' or fluid's molecules. For all cellular materials considered in this thesis the resulting term can therefore be neglected. The parameters Ψ_v and Ψ_i in the equation are named the laminar permeability coefficient and the turbulent inertia permeability coefficient. Both can be determined experimentally.

$$\frac{\Delta p}{l} = \underbrace{\left(\frac{\eta}{\Psi_v}\right) \cdot \frac{Q}{A}}_{\text{laminar}} + \underbrace{\left(\frac{\rho}{\Psi_i}\right) \cdot \left(\frac{Q}{A}\right)^2}_{\text{turbulent}} \qquad \textbf{\textit{(10.5)}}$$

Typically gases are more suitable than fluids as a test medium (DIN ISO 4022, 1990, p. 8, [97]). The inferiority of fluids can be substantiated due to

- capillary action especially for small pore sizes,
- formation of gas cushions or
- absorption reactions with some metals.

However, gases are more likely to show inertia flow behaviour. Therefore, in most cases ***eq. (10.5)*** will be applied as given above including the quadratic term.

Banhart (2000, pp. 502-503, [26]) conducted permeability measurements of aluminum sponges with average pores sizes of 0.45, 0.75, 0.85 and 1.45 mm. For average pore sizes of 0.45 mm a pressure drop of approximately $4 \cdot 10^5$ Pa/m occurs at stream velocities of 0.4 m/s, whereas for 1.45 mm average pore size it is only $0.5 \cdot 10^5$ Pa/m at the same velocity. Thus values for the permeability coefficients were derived for Ψ_v in the range of $4 \cdot 10^{-12}$ to 10^{-10} m² and for Ψ_i between $8 \cdot 10^{-7}$ to $4 \cdot 10^{-6}$ m.

Another experiment was also carried out by Boomsma (2002, pp. 75-91, [42]) with deionized and degassed water as a liquid coolant pumped through uncompressed and compressed ERG Duocel aluminum sponges. The uncompressed material showed pore sizes between 2.3 and 6.9 mm and its relative density ranged between 0.072 and 0.08. At the smallest pore size a pressure drop of approximately $0.62 \cdot 10^5$ Pa/m occurred at stream velocities of 0.4 m/s while the largest pore size allowed only $0.2 \cdot 10^5$ Pa/m at the same velocity. The least-squares curve fit delivered values in the range of $712 \cdot 10^{-10}$ to $3529 \cdot 10^{-10}$ m² for Ψ_v and between $2.762 \cdot 10^{-3}$ to $8.3 \cdot 10^{-3}$ m for Ψ_i. However, for the same material compressed by factors 2 to 8 with final relative densities between 0.118 and 0.392 a much higher pressure drop of values between 15 to $82 \cdot 10^5$ Pa/m at stream velocities of up to 1.04 m/s was achieved. In this case the permeability coefficients ranged between $2.46 \cdot 10^{-10}$ to 44.4^{-10} m² for Ψ_v and between $1.149 \cdot 10^{-4}$ to $8.757 \cdot 10^{-4}$ m for Ψ_i. An important observation made during the experiment was the relation found that at constant density a smaller cell size will increase the flow resistance and hence the pressure drop per unit length.

A different approach was chosen by Ashby (2000, pp. 186-187, [17]). The pressure drop is characterized by a single, non-linear yet not quadratic term since the stochastic open-cell sponges examined there exhibit preferably turbulent flow (Ashby, 2000, p. 181, [17]). Converted into the symbols used in DIN ISO 4022 (1990, p. 3, [97]) the formula given reads as denoted in ***eq. (10.6)*** where d is the diameter of one ligament in the sponge structure, a is the cell size given by ***eq. (10.7)*** and c and m were calibrated experimentally to the values of $c = 4$ and $m = 0.4$.

$$\frac{\Delta p}{l} = \frac{c \cdot d^m}{a} \cdot \frac{\eta^m \cdot \rho_{fluid}}{(1 - \Psi_v)^{2-m}} \cdot \left(\frac{Q}{A}\right)^{2-m} \tag{10.6}$$

$$a = 1.24 d \sqrt{\frac{3\pi}{\frac{\rho^*}{\rho_{solid}}}} \tag{10.7}$$

According to Kaviany (1995, p. 29, [159]) no general relationship exists between the permeability of a porous medium and the relative density as observed for most other cellular material properties since the permeability is strongly affected by shape and structure of the porosities.

10.1.4 Thermal properties

In cellular materials the properties of melting point, specific heat and thermal expansion do not differ from the solid they were made from (Ashby, 2000, p. 47, [17], Scheffler, 2005, p. 10, [270]). However, the properties of thermal conductivity λ, thermal diffusivity a and heat transfer coefficient α strongly depend on whether the porosity is the open- or closed-cell type. Closed-cell foams generally exhibit low thermal conductivity and unsuitable heat transfer attributes while open-cell sponges show much better thermal conductivity and promising heat transfer capabilities. According to Ashby (2000, p. 181, [17]) closed-cell foam insulation is approx. 8-30 times greater than for solids. However, it is still one order of magnitude below that of their non-metallic counterparts which makes them generally unsuitable for heat insulation purposes on one hand though on the other hand they exhibit quite interesting fire retardance properties (Lu, 1999, pp. 1481, 1484, [188]). A first order estimate of the effective thermal conductivity of a porous medium that is filled with gas or fluid can be made simply by accounting for the volume fractions of both solid and voids (Boomsma, 2001, pp. 828, [41]). The relative density and e.g. thermal conductivity of each phase then provide the effective value as suggested in ***eq. (10.8)***. However, for small relative densities the structure of the solid matrix, i.e. the cell size and shape, becomes very important (Kaviany, 1995, p. 119, [159]) thus ***eq. (10.8)*** is assumed to be applicable only around relative densities near unity.

$$\lambda^* = \frac{\rho^*}{\rho_{solid}} \cdot \lambda_{solid} + \left(1 - \frac{\rho^*}{\rho_{solid}}\right) \cdot \lambda_{gas} \qquad \textbf{\textit{(10.8)}}$$

One approach for the thermal conductivity of closed-cell materials was given by Ashby (2000, p. 47, [17]) through a non-linear relation derived from percolation theory (explained at the beginning of ***section 2.1.4***) which is presented in ***eq. (10.9)*** where the relative thermal conductivity only depends on the relative density to the power of n.

$$\frac{\lambda^*}{\lambda_{solid}} = \left(\frac{\rho^*}{\rho_{solid}}\right)^n \qquad \text{with:} \quad n = 1.65 \text{ to } 1.8 \qquad \textbf{\textit{(10.9)}}$$

Babcsán (2003, pp. 392-393, [22]) conducted experimental examinations on closed-cell Alporas foams with relative densities between 0.066 and 0.171 by comparing their thermal conductivity to known reference materials. The results made a linear correlation for increasing thermal conductivity with increasing density apparent, according to ***eq. (10.10)***. The coefficient C showed a minor dependence on ambient temperature but was best matched with an average value of 0.4686 at room temperature. However, this correlation does not hold out against high relative densities because as the relative density becomes unity the relative thermal conductivity must converge towards one. Thus it is valid only for low relative densities.

$$\frac{\lambda^*}{\lambda_{solid}} = C \cdot \frac{\rho^*}{\rho_{solid}} \tag{10.10}$$

This relation was confirmed and somewhat extended to account for the contribution of radiation by Lu (1999, pp. 1469, 1479, [188]) who calculated the thermal conductivity for different periodic and stochastic closed-cell structures and found the coefficient *C* to depend mainly on the tortuosity of the cell walls but also on breakage of cell walls, missing cells or cell misalignments. Besides heat transport in solid cell walls other mechanisms such as gaseous conduction or natural convection within the cells can be ignored since thermal conductivity in metallic solids is generally three to four orders of magnitude greater than in gases and, additionally, convection in cells of less than 10 mm size can hardly develop. However, according to their FE calculations radiation can become important if the thermal conductivity of the solid cell walls falls below a value of 20 W/mK which exceeds the value of only few metal alloys. Radiation is assumed to be dependent on cell size, temperature and relative density. Lu (1999, p. 1482, [188]) claimed that the thermal diffusivity is the same as that of the bulk material. Though experimental data supposedly supports this conclusion this fact remains controversial since the thermal diffusivity *a* is defined according to ***eq. (10.11)*** (Rohsenow, 1973, p. I-2, [261]) where c_p stands for the specific heat of the material. It is obvious that for a cellular solid of low relative density this relation cannot be applied.

$$a = \frac{\lambda}{\rho \cdot c_p} \tag{10.11}$$

Like the other researchers mentioned above Abramenko (1999, pp. 369-373, [2]) examined closed-cell foams made from aluminum with relative densities between 0.21 and 0.31 and found overall low thermal conductivity. The measurements conducted on some specimens were best matched with a formula considering both solid and gas conductivity. Hence, ***eq. (10.12)*** specifies a correlation where the term preceded by coefficient c_2 follows the assumption that heat conduction takes place successively in both phases, whereas the term preceded by coefficient c_1 incorporates simultaneous heat conduction. Both coefficients c_1 and c_2 must always add up to unity and were determined to $c_1 = 0.13$ and $c_2 = 0.87$. Generally, the thermal conductivity of these foams was up to 30 times lower than for the solid material but still twice as high as that of state-of-the-art insulating materials.

$$\lambda^* = c_1 \cdot \frac{\lambda_{solid}}{1 - \frac{\rho^*}{\rho_{solid}} \cdot \left(1 - \frac{\lambda_{gas}}{\lambda_{solid}}\right)} + c_2 \cdot \frac{\lambda_{gas}}{1 + \frac{\rho^*}{\rho_{solid}} \cdot \left(\frac{\lambda_{solid}}{\lambda_{gas}} - 1\right)} \tag{10.12}$$

As anounced above the properties for open-cell materials show different behaviour. Scheffler (2005, pp. 9-10, [270]) developed a correlation from the assumption that of all cell struts on average one third is situated in direction of thermal transport to which only these contribute. Thus the thermal conductivity is proportional to one third of the relative density, however, for near solid bodies this would yield only one third of the solid's conductivity. Therefore, the first term in brackets in ***eq. (10.13)*** is supplemented with a non-linear component ensuring the correct value of thermal conductivity for a fully dense solid. The second term accounts for gaseous heat conduction in the open cells. Regarding the thermal diffusivity a^* one can neglect conductivity through gas to simplify ***eq. (10.13)*** and rewrite ***eq. (10.11)*** as shown in ***eq. (10.14)***. Opposed to the opinion of Lu (1999, p. 1482, [188]) the thermal diffusivity does depend on the relative density, however, surprisingly enough this dependency is to the power of 0.5 and hence much weaker than for thermal conductivity.

$$\lambda^* = \frac{1}{3} \cdot \left(\frac{\rho^*}{\rho_{solid}} + 2 \cdot \left(\frac{\rho^*}{\rho_{solid}} \right)^{3/2} \right) \cdot \lambda_{solid} + \left(1 - \frac{\rho^*}{\rho_{solid}} \right) \cdot \lambda_{gas} \tag{10.13}$$

$$a^* = \frac{1}{3} \cdot \left(1 + 2 \cdot \sqrt{\frac{\rho^*}{\rho_{solid}}} \right) \cdot \frac{\lambda_{solid}}{\rho_{solid} \cdot c_p} \tag{10.14}$$

Another study conducted by Zhao (2004, pp. 123-131, [331]) revealed experimental data on the thermal conductivity at ambient and vacuum conditions of an open-cell steel alloy (FeCrAlY) sponge with relative densities between 0.05 and 0.1. Hollow ligaments are a distinctive feature of this material. At ambient pressure the thermal conductivity was twice the value as for vacuum conditions. Therefore, unlike for closed-cell materials, natural convection has a great influence on heat conductivity even for comparatively small cell sizes which reside in the range of 0.1 to 7 mm for this sponge. If the density is fixed and the cell size is varied, one can even observe increasing thermal conductivity with increasing cell size, especially for high temperatures. This confirms the significance of natural convection, however, though no correlation was given all evaluations from Zhao (2004, pp. 126-129, [331]) indicate the validity of ***eq. (10.9)*** and ***eq. (10.10)***.

A first assessment of heat transfer properties was done by Lu (1998, pp. 3619-3635, [187]) using experimental results from the ERG Duocel open-cell sponge made from aluminum. In the attempt to obtain maximum heat transfer versus least pumping power of a fluid pumped through the cell structure a model of the sponge comprising simple cubic cells was developed. The result found was that the heat transfer coefficient α rises with increased relative density as well as with increased fluid velocity. However, the pressure drop per unit length yields a minimum at a relative density of approx. 0.1 for different fluid velocities. Furthermore, the calculations showed that the overall optimum of heat exchanging performance prevails at relative densities between 0.35 and 0.4.

Boomsma (2001, pp. 827-836, [41]) developed a rather lengthy formula for the effective thermal conductivity derived from a model for aluminum sponges involving a tetrakaidecahedral geometry which imitates the actual geometry received from surface minimization during the foaming process well enough. The resulting equation was compared to experimental data obtained by Calmidi (1999, pp. 466-471, [51]) for air and water as the void-filling medium. It was found to deliver acceptable predictions on the effective thermal conductivity. Since only low relative densities between 0.02 and 0.12 were considered the resulting correlation matched ***eq. (10.10)*** where the coefficient C showed values of 0.308 for air and 0.3113 for water as the medium filling the porosities. Boomsma (2002, pp. 66-103, [42]) also acquired own experimental data on the heat exchange properties of aluminum sponges. This was achieved by using compressed ERG Duocel aluminum sponges with relative densities between 0.118 and 0.392. These specimens originated from the same batch that was previously examined for its hydraulic behaviour (see ***appendix 10.1.3***). The performance capability for heat exchanging applications was evaluated by obtaining results for the dimensionless Nusselt number Nu in dependence of the stream velocity, for the Colburn factor J versus the Reynolds number Re and for the pumping power versus the thermal resistance R_{th}. The Nusselt number measures the enhancement of heat transfer under real conditions where convection occurs compared to heat conduction only. A typical application is the transfer of heat to a fluid stream. The highest Nusselt number obtained was 134.6 at a stream velocity of 1.33 m/s. The Colburn factor gives a heat transfer performance estimate by comparing a heat exchanger's convection coefficient to the required stream velocity while the Reynolds number gives the ratio of inertial to viscous forces and can be used to determine whether a flow will be laminar or turbulent. Some of the aluminum sponges achieved Colburn factors of less than 0.05 at Reynolds numbers of greater than 100. One sponge with a relative density of 0.331 showed least values for both pumping power (1.29 W) and thermal resistance (8.00 K/kW) at the optimum operation point where the stream velocity is 0.356 m/s. Generally, the data showed significant improvements in terms of performance efficiency over conventional heat exchangers.

10.1.5 Electrical properties

Among the electrical properties of cellular materials there are supposedly only few attributes of interest which are the resistance R, the electrical conductivity σ which is the reciprocal of the resistivity ρ (i.e. resistance multiplied with the cross-sectional area and divided by the length of the conductor) and the permittivity ε_r (i.e. the relative dielectric constant). A pure empiricism yet again in accordance with the percolation theory (explained at the beginning of ***section 2.1.4***) was given by Ashby (2000, p. 48, [17]) through ***eq. (10.15)*** as a correlation between resistance and relative density of the cellular material without distinguishing open- or closed-cell materials or other parameters. Especially for low relative densities in the range of less than 0.2 this equation describes a highly non-linear increase of resistance and thus decrease of conductivity.

$$\frac{R^*}{R_{solid}} \approx \left(\frac{\rho^*}{\rho_{solid}}\right)^{-n} \qquad \text{with:} \quad n = 1.6 \sim 1.85 \qquad \textbf{\textit{(10.15)}}$$

An approach for electrical conductivity of open-cell materials was given by Scheffler (2005, pp. 9-10, [270]) where analogous to the derivation of ***eq. (10.13)*** for thermal conductivity a simple geometric model of electrical conductivity was developed. All explanations from ***appendix 10.1.4*** apply accordingly to ***eq. (10.16)*** which also provides a non-linear increase of conductivity with increasing density. Only the conductivity of the gas filling the open-cell space can be neglected here.

$$\frac{\sigma^*}{\sigma_{solid}} = \frac{1}{3} \cdot \left(\frac{\rho^*}{\rho_{solid}} + 2 \cdot \left(\frac{\rho^*}{\rho_{solid}} \right)^{3/2} \right) \tag{10.16}$$

Real experimental analysis for open-cell materials was conducted by Badiche (2000, p. 287, [23]) who examined the resistivity of a nickel sponge and found a similar slightly non-linear correlation as proposed in ***eq. (10.15)*** where the resistivity ρ substitutes the resistance R. However, the exponent n deviates and exhibits values between 0.98 and 1.18. In contrast to this finding Dharmasena (2002, pp. 625-631, [80]) examined an open-cell ERG Duocel aluminum material of relative densities between 0.04 and 0.12 and found a rather linear behaviour when a direct current is passed through the outer two probes of an inline four-point probe. Here, the electrical conductivity can be calculated from the measured potential difference of the two inner probes. According to Dharmasena (2002, p. 625, [80]) the relative density and cell morphology contribute most to the electrical properties. Thus calculations of the equivalent resistance and hence the conductivity were made based on a tetrakaidecahedral approximation of the cell morphology with triangular ligaments for a given density. Both experiment and model showed a linearly increasing conductivity with increasing relative density, however, the slope of the hypothetical derivation is clearly higher. Damaged or missing cell ligaments account quite well for this and if instead of 36 ligaments per unit cell two less ligaments are assumed the slopes match nearly perfectly. Another minor calculative influence was found from varying the cross sectional area of the ligaments. ***Eq. (10.17)*** depicts the relative conductivity in dependence of the relative density found in the experimental results (Dharmasena, 2002, p. 626, [80]) that delivered an average value of approx. 0.3781 for parameter C.

$$\frac{\sigma^*}{\sigma_{solid}} = C \cdot \frac{\rho^*}{\rho_{solid}} \tag{10.17}$$

Experimental results on electrical conductivity for three different relative densities between 0.066 and 0.171 for the closed-cell aluminum foam Alporas were obtained by Babcsán (2003, p. 393, [22]). A low frequency eddy current method was applied and again a linear correlation for increasing conductivity versus increasing relative density was found. Conversion of the results yields a value of approximately 0.5976 for the parameter C in ***eq. (10.17)***. This method is said to be also a cost effective way for fast determination of thermal conductivity for metals. According to the Wiedemann-Franz law (Weber, 1995, p. 92, [313]) the ratio of thermal and electrical conductivity of a metal is proportional to its temperature as mobile electrons are the only carriers of both transport mechanisms unless temperatures are too high (convection and radiation). However, Babcsán (2003, p. 393, [22]) did not clarify how the given ratios between thermal and electrical conductivity should be correlated especially regarding that the ratio was not constant at steady temperatures unlike expected. Another closed-cell aluminum foam material was examined by Feng (2003, pp. 196-201, [115]) who tested foams with almost identical relative densities between 0.194 and 0.197 but different cell diameters between 1.7 and 3.6 mm to investigate the influence of cell size on electrical conductivity. The results obtained from wheatstone bridge circuit measurements with DC current showed that the morphology (here i.e. the cell size) does not contribute to electrical conductivity and merely variations in relative density take influence. The range of relative densities tested was from 0.129 to 0.313. It was correlated best with the reciprocal to ***eq. (10.15)*** given in ***eq. (10.18)*** comprising a similar value for parameter n as in ***eq. (10.15)***. ***Eq. (10.18)*** is said to be valid for the typical range of densities looked at throughout this section, however, for very high densities close to unity a different formula originally developed for two-phase composites and not further detailed here exhibits less deviation. Since the linear correlation from ***eq. (10.17)*** seems to be valid for only very low relative densities, ***eq. (10.18)*** appears to be the approach of best applicability over the full range of densities. These experimental data also confirm previous examinations from Weber (1995, pp. 92-97, [313]) who inferred the same formula and found a value of $n = 1.7$ after predicting a range between 1.5 and 3.1 due to assumptions made from a form factor and an orientation factor for pores in a cellular material.

$$\frac{\sigma^*}{\sigma_{solid}} = \left(\frac{\rho^*}{\rho_{solid}}\right)^n \qquad \text{with:} \quad n = 1.504 \qquad \textbf{\textit{(10.18)}}$$

Scheffler (2005, p. 10, [270]) suggested cellular materials for electrical insulation applications due to their resulting low permittivity which converges towards the value of the gas filling in the pores of the cellular material as the relative density decreases. ***Eq. (10.19)*** is an adapted formula from this source.

$$\varepsilon_r^* = \varepsilon_{r,gas} + \left(\varepsilon_{r,solid} - 1\right) \cdot \left(\frac{\rho^*}{\rho_{solid}}\right) \qquad \textbf{\textit{(10.19)}}$$

10.1.6 Specific surface area

Compared to solids cellular materials naturally have a high specific surface area. The precise measurement of the specific surface area, however, is only feasible for open-cell materials. This can be achieved by gas adsorption using the volumetric-static multi point method according to Brunauer, Emmet and Teller (BET) (DIN ISO 9277, 2003, p. 12, [98]). At the surface of a solid the bond between atoms and molecules is not as saturated as internally. The resulting surface forces can cause accumulation of foreign atoms from a substrate there which exists in either liquid or gas phase. This process is called adsorption where with increasing concentration of the liquid phase or with increasing partial pressure of the gas phase the amount of adsorped substrate can either converge asymptotically against a maximum or steady initially in a linear range as seen in ***fig. 10.1 (left)*** provided it is measured at constant temperature. This maximum or linear range is the capacity limit of the adsorped substrate and equals the equilibrium state of adsorption and desorption processes where the surface of the solid is completely covered by a single layer of substrate.

The BET-method measures the amount of substrate adsorped by the surface. Nitrogen at its boiling point (77.4 K) is typically used as substrate unless argon or krypton is applied.

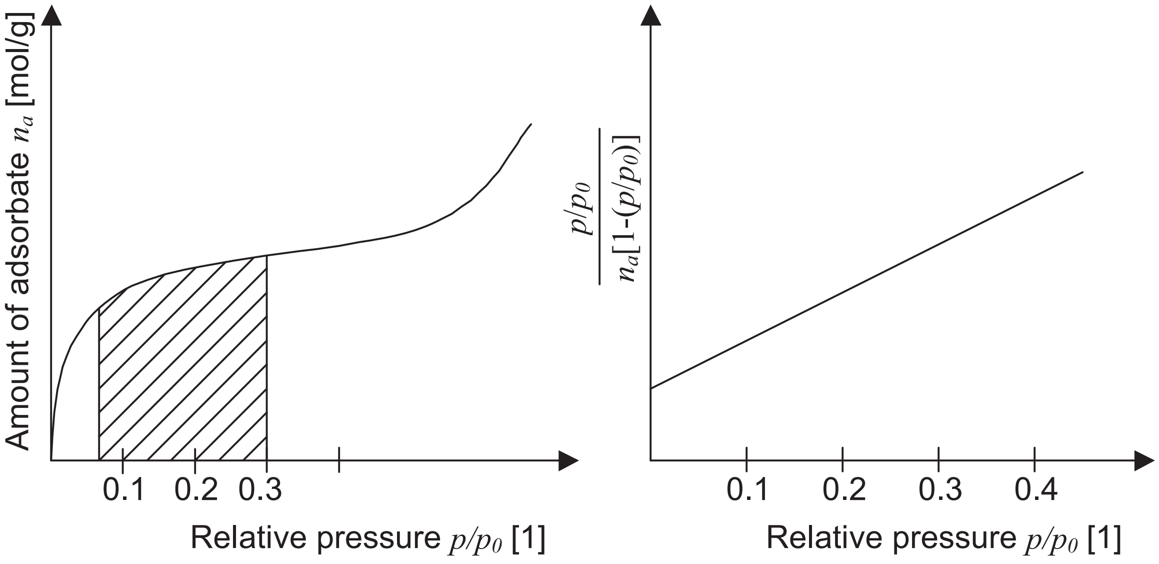

Figure 10.1: Adsorption isotherm (left) and BET diagram (right) [98]

Evaluation of the BET diagram ***fig. 10.1 (right)*** between relative pressures p/p_0 of 0.05 and 0.3 for the substrate yields the specific adsorbate volume V_a required for a monomolecular layer. For nitrogen at 77.4 K a surface area of 0.162 nm² per molecule results (Brunauer, 1938, pp. 309-319, [47]) thus allowing to calculate the specific surface area a_s according to ***eq. (10.20)*** where n_m is the specific amount of adsorbate molecules required for a monomolecular layer, a_m is the average surface area covered by one molecule and L is the Avogadro constant (DIN ISO 9277, 2003, p. 15, [98]). However, despite the high sensitivity of the BET method, obtaining an exact monomolecular layer on all edges and in all corners of a cell structure is subject to uncertainty. Therefore, the minimum feature size should not be smaller than 20 µm. If using nitrogen as substrate, then the test specimens should exhibit a specific surface area of at least 1 m²/g. Krypton can provide better results for smaller values (Schatt, 1994, pp. 76-78, [269]).

$$a_s = n_m a_m L \tag{10.20}$$

So far only few measurements were conducted for metallic sponges delivering values between 1 and 2 m²/g (Banhart, 2000, p. 503, [26]).

10.1.7 Buoyancy

For completeness the list of cellular material properties is closed with buoyancy. Naturally, it only applies for closed-cell materials containing a gas (or fluid) of significantly less density in its voids than the fluid (or gas) the cellular material is floating in and where the density of the solid material is much greater than this fluid's density. Buoyancy can be defined as the state of equilibrium where the gravitational force on a body matches the lifting force due to the amount of displaced fluid. Assuming that a random part comprising the volume V contains a defined gas of density ρ_{gas} and floats in a fluid of density ρ_{fluid} then ***eq. (10.21)*** gives the condition as where the part will not sink or will even float upwards (Rehme, 2006). Solving this equation gives the formula for the maximum absolute density allowed for buoyancy of a part (***eq. (10.22)***). Provided that the gas is air and the fluid is water, the density ratio between both is roughly 10^3 and the density ratio between air and metallic solids is in the range of 10^3 to 10^4. In this case the last equation can be simplified and rewritten as ***eq. (10.23)*** where in accordance with previous formulae the relative density is used for a general design rule.

$$F_{buoyancy} > F_{gravitational}$$

$$\Rightarrow \rho_{fluid} \cdot Vg > \left(\frac{\rho^*}{\rho_{solid}} \right) \cdot \rho_{solid} \cdot Vg + \left(1 - \frac{\rho^*}{\rho_{solid}} \right) \cdot \rho_{gas} \cdot Vg \tag{10.21}$$

$$\Leftrightarrow \qquad \rho^* < \frac{\rho_{fluid} - \rho_{gas}}{1 - \frac{\rho_{gas}}{\rho_{solid}}} \tag{10.22}$$

$$\frac{\rho^*}{\rho_{solid}} < \frac{\rho_{fluid}}{\rho_{solid}} \tag{10.23}$$

10.2 Fabrication of stochastic cellular materials: foams and sponges

Stochastic cellular materials made from metals are either formed in liquid-state processing, produced from the solid state, formed from the vapor phase or electro-deposited from the ionic state in an aqueous solution. Metal foams and sponges are still a fairly new class of cellular materials with low densities and novel physical, mechanical, thermal, electrical und acoustic properties. These materials are typically being obtained from metal melt under application of gas during solidification. Although the literature often describes foams as both open- and closed-cell materials this work strictly refers to closed-cell materials as foams. Here, sponges represent open-cell micro structures and can result from what was initially a foam during solidification if the process parameters are chosen such that the cell walls of the foam thin out and start to vanish leaving behind the former cell edges as a network of struts. For metal foams and sponges several different manufacturing approaches were developed which can be distinguished by the raw material and the manufacturing process as well as the resulting relative density and the open- or closed-cell pore structure. The most important technologies of which approximately eleven are commercially established are introduced here as follows.

10.2.1 Pressing from solid phase

The process of pressing can be more or less distinct such that green parts with low strength or highly consolidated parts with only few remaining pores result.

Sintering of metal powders

A simple method of obtaining a stochastic cellular material from a variety of metals such as stainless steel, bronze, titanium or superalloys is the use of sintering processes where the remaining porosity can give relative densities between 0.5 and 0.8. The interconnected open spaces as seen in ***fig. 10.2 a)*** are smaller than the powder particles used, typically smaller than 100 μm. The finest voids can be as small as 1 μm (Banhart, 2001, pp. 587-588, [28]). Often, the strength of these green parts is comparatively low and other follow-up processes such as HIPing or roll compaction might be required. It might also be necessary to break up oxide

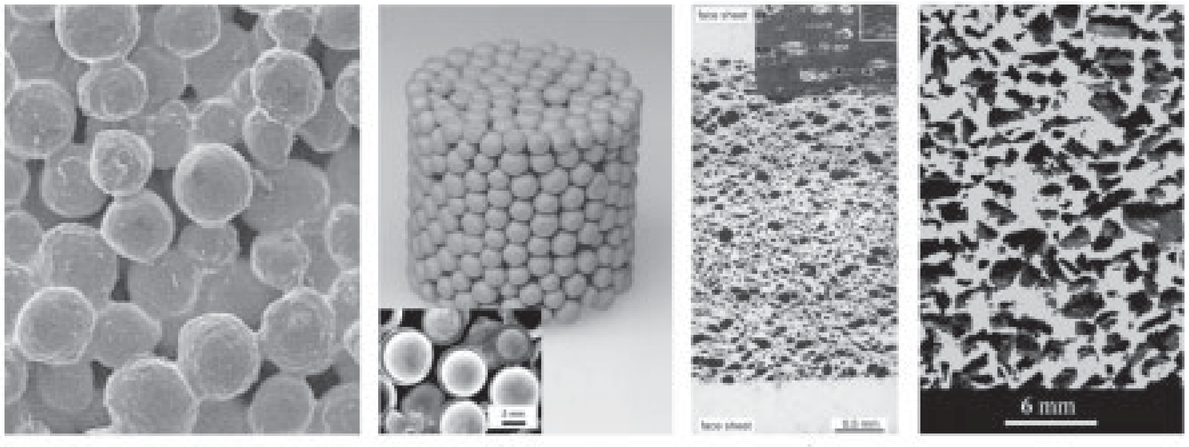

Figure 10.2: Stochastic cellular materials made by pressing from solid phase [28], [303], [271], [106], [67]

layers on the powder particles prior to sintering in order to ensure a metallic bond between them. A new development in this field is the sintering of metal fibers.

HIPing, vacuum sintering or liquid-phase sintering of hollow spheres
A limited fraction of hollow metal spheres can be obtained from inert gas atomization for the preparation of powder metallurgy particles. The separation of hollow and solid powder particles was described by Sypeck (1998, pp. 206-208, [289]). Such hollow spheres show diameters of up to 1 mm and can be consolidated using processses such as HIPing, vacuum sintering or liquid-phase sintering as shown in ***fig. 10.2 b)***. Thus cellular parts can be fabricated from nickel superalloys and TiAl6V4 with relative densities of 0.06 and closed or, depending on the intensity of compaction, also open pore sizes between 100 µm and several millimeters (Ashby, 2000, pp. 16-19, [17]).

In a different process low price styrofoam spheres are spraycoated with a metalpowder slurry (Waag, 2000, pp. 1-2, [302]). Subsequently, a heat treatment is applied on the green spheres to remove the styrofoam core by pyrolysis and to sinter the metallic shell. This can take place individually with single spheres such that the above mentioned consolidation processes can be used afterwards or the spheres are joined together in a mould to shape a desired geometry. Typical materials in this process are stainless steel and the cell size can range between 0.5 and 10 mm. Considering the available cell sizes, the possible cell wall thickness between 20 and 1500 µm and a maximum density of 74 % for a *hcp* configuration of single sized spheres, a broad range of possible relative densities between 0.01 and 0.73 results. Another process was reported by Hurysz (1998, p. 193, [149]) who produced stainless steel and titanium hollow spheres from metal powder slurries without the use of styrofoam templates by injecting the slurry through the outer jet of a coaxial nozzle while passing gas through the inner jet.

Entrapped gas expansion
A solid thin-walled container is filled with powder from the same material, then evacuated to remove all oxygen and finally refilled with argon gas at pressure of up to 5 bar before it is sealed. This container is successively consolidated by HIPing and hot rolled such that the relative density increases to approx. 0.98. Eventually, during heat treatment at 900°C for 20 to 30 hours the pressurized inert gas entrapped inside the powder particles expands. Thus the pore pressure increases and the pores slowly grow by creep of the surrounding metal. This process is applicable to TiAl6V4 materials and is used in industrial manufacture of sandwich structures for aerospace applications where it is also known as the Low Density Core (LDC) process (Schwartz, 1998, p. 225, [271]), (Elzey, 2001, p. 850, [106]). It yields closed-cell structures with a minimum relative density of 0.5 and pore sizes from 10 to 300 µm similar to those in ***fig. 10.2 c)*** (Ashby, 2000, pp. 14-16, [17]), (Banhart, 2001, pp. 588-589, [28]). An in-depth examination of the characteristics of LDC sandwich structures was conducted by Queheillalt (1998, pp. 237-242, [233], 1998, pp. 243-248, [235]) which is recommended for further reading.

Co-compaction of two powder materials, one leachable
Two powders e.g. aluminum alloys and sodium chloride (salt) are consolidated until sufficient

coherence between the particles of both phases is achieved. Then the salt is leached out in a suitable solvent (e.g. water) leaving behind an open-cell sponge with relative densities between 0.3 and 0.5. The cell sizes lie in the range of 10 µm to 10 mm and are determined by the leachable powder particle size (Ashby, 2000, pp. 19-20, [17]). ***Fig. 10.2 d)*** shows a typical result from such a process. Other materials like titanium, stainless steel and some nickel based superalloys can also be processed this way. In the case of titanium a non-leachable but thermally decomposable space-holder such as polymer granules also give satisfying results (Banhart, 2001, p. 589-591, [28]).

10.2.2 Foaming from solid phase

Foam usually means that a gas is dispersed in a liquid by formation of bubbles. However, in this context foams also include solid foams where gas is enclosed in solidified bubbles. In the case of foaming from the solid phase the bubbles are typically generated by use of a blowing agent.

Combustion reaction

Babcsán (2003, p. 7, [21]) described the blending and compacting of aluminum and nickel powder with Ti, B_4C and TiC as additives. When such a precursor is heated above the melting temperature of the aluminum an exothermal reaction takes place between the components where the oxides and hydrates in the powder surfaces form the blowing gas. Thus minimum relative densities of 0.15 can be obtained. A similar process was used by Chu (2004, pp. 114-116, [61]) who used a compressed mixture of titanium and nickel powders. Once ignited with a TiC ignition reagent, the combustion propagates along the compact in a very short time leading to a porous NiTi shape memory alloy of mostly open porosity. The relative densities were around 0.427 and pore sizes between 200 and 500 µm as depicted in ***fig. 10.3 a)***.

Foaming of slurries

Foaming can also be initiated at room temperature by a chemical reaction. A metallic powder is mixed with a dispersant and a blowing agent before a solvent with phosphoric acid and

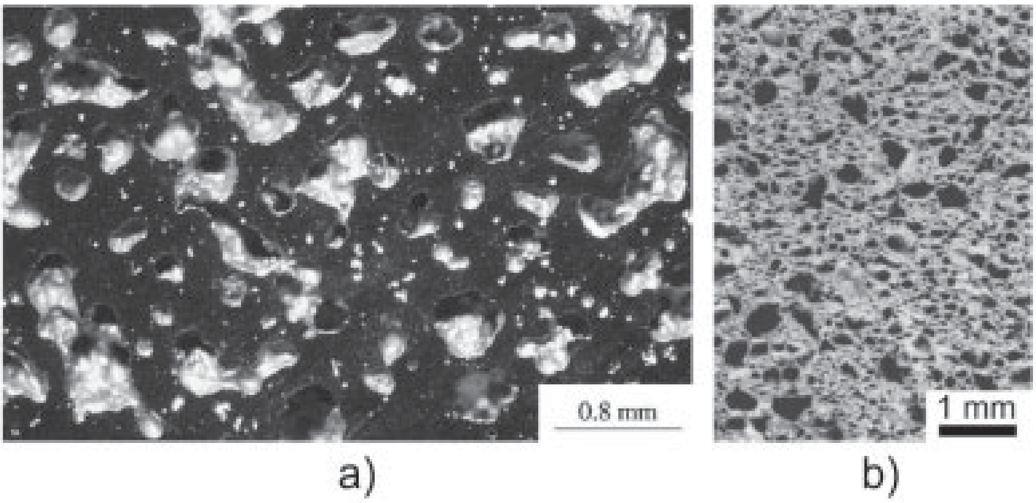

Figure 10.3: Stochastic cellular materials made by foaming from solid phase [61], [15]

water or alcohol is added. In the resulting slurry two different chemical reactions take place: The metal-acid reaction creates hydrogen bubbles causing the slurry to foam while simultaneously metal phosphates form which is a strong binder that freezes the bubbles in the slurry. At this stage the result is a green part in which closed-cell porosity prevails. Subsequently, it has to be sintered under reductive conditions to achieve proper metallic bonds and reasonable strength attributes. During this process the solvent evaporates turning the mostly interconnected pores into an open-cell porosity. Mohr (2000, pp. 1-2, [208]) and Angel (2005, pp. 1-3, [15]) obtained relative densities between 0.11 and 0.45 at pore sizes of 0.01 up to 3.5 mm. One of their samples is shown in ***fig. 10.3 b)***.

10.2.3 Foaming from liquid phase

In the case of foaming from the liquid phase blowing agents can be used as well, however, in some processes a simple feed of gas into the metal melt is sufficient.

Melt gas injection (gas bubbling)

Either CO_2, O_2, N_2, inert gas or water can be injected into liquid aluminum and distributed with rotating impellers. The resulting fine gas bubbles float to the surface where they drain and solidify giving a structure like the one in ***fig. 10.4 a)***. This process produces closed-cell foams (commercially known under the names Cymat Metcomb and formerly Hydro Aluminum) with relative densities of 0.02 to 0.2 depending on the amount of gas injected and

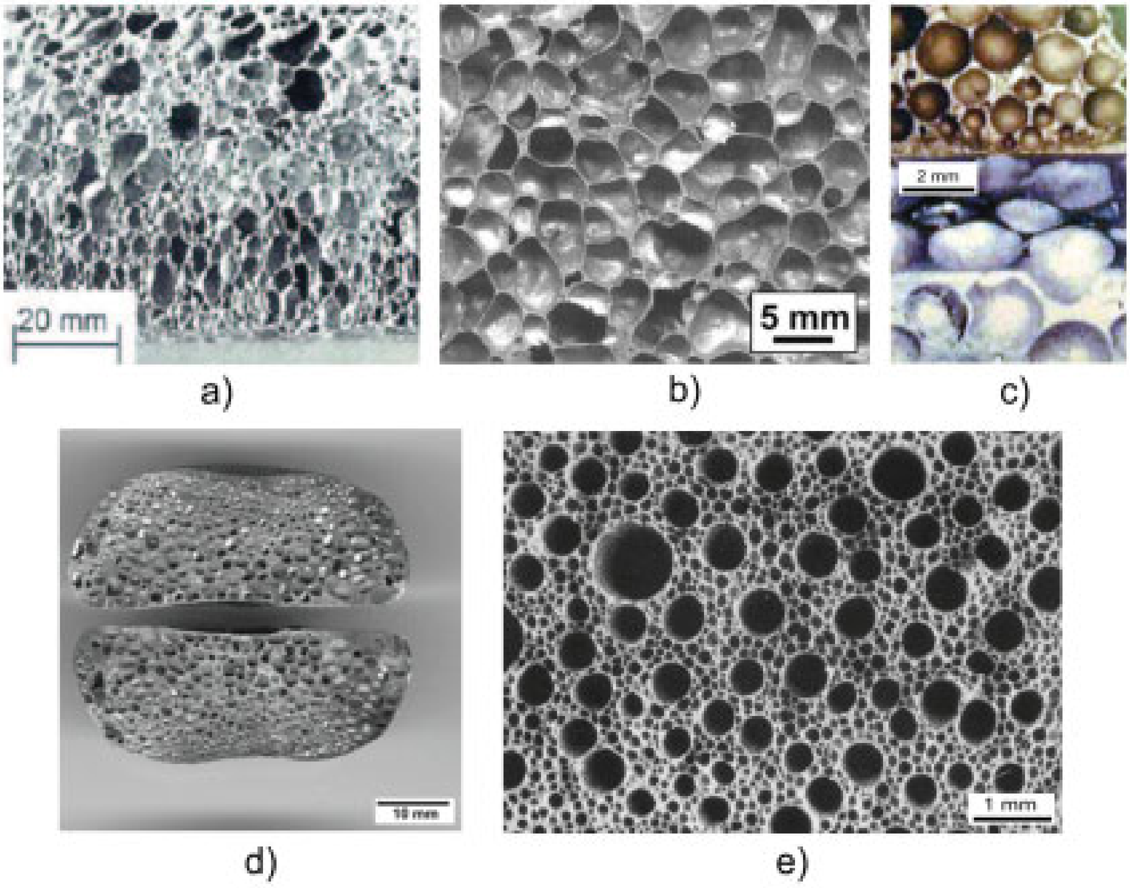

a) b) c)

d) e)

Figure 10.4: Stochastic cellular materials made by foaming from liquid phase [76], [316], [244], [158], [28]

the cooling rate of the foam. The cell diameter can vary between 3 and 20 mm (Ashby, 2000, pp. 8-9, [17]), (Banhart, 2001, pp. 564-567, [28]).

Gas-releasing particle decomposition
Foaming agents such as titanium hydride (TiH_2) powder particles (each 5 to 20 µm in diameter) decompose at temperatures significantly below the melting temperature of aluminum. After the melt is vigorously stirred while the foaming agent is added the emerging hydrogen gas forms bubbles. As soon as all particles have decomposed, the foam is cooled down to avoid collapse of the bubbles. This would typically lead to a closed-cell structure if the foam drainage is sufficiently slow due to high viscosity of the melt. Control parameters in this process are temperature, time and pressure. These determine the obtainable range of cell sizes between 0.5 and 5 mm leading to relative densities of 0.2 to 0.07. The fact that titanium hydride decomposes too quickly at higher temperatures and that hydrogen embrittles most engineering metals allows this process only for the production of aluminum foams of which the commercial product Alporas in ***fig. 10.4 b)*** is well established and the Formgrip process is at bench-scale level (Ashby, 2000, pp. 9-10, [17]), (Miyoshi, 1998, pp. 133-137, [206]), (Banhart, 2000, pp. 23, [29]).

Metal powder with blowing agent
A related method that employs the powder metallurgical process uses the same type of powder agent, however, this time it is mixed with the metal powder and compacted to a dense precursor by hot pressing or extruding. The precursor is then heated to the melting point of the metal at which the blowing agent has already begun releasing gas. The melt of the liquid or near-liquid metal expands and is cooled down to freeze the structure after sufficient foaming has taken place (Banhart, 1999, p. 18, [30]) which gives structures similar to that of ***fig. 10.4 d)***. This method is also known as the Fraunhofer process which was originally applied on aluminum powders. It yields material with closed-cell porosities and a dense outer skin (Stöbener, 2005, p. 11, [280]) also known under the brand names Foaminal and Alulight. Rausch (2000, pp. 2-5, [244]) and Park (2000, pp. 112-113, [225]) developed this process for low alloyed steel. In contrast to the titanium hydride used as a blowing agent for aluminum alloys a different substance had to be found which releases gas near below the melting point of steel. Especially metal nitrides and alkaline earth metal carbonates such as Mn_4N, CrN, MoN, $CaCO_3$, $SrCO_3$ and $BaCO_3$ fulfill this task. Generally, these foaming processes yield relative densities between 0.08 and 0.37 whereas the pore size can range from 1 to 5 mm.

The most important parameters in the foaming of metals using the powder metallurgical process were determined by Simančik (1999, p. 106, [276]). Besides the chemical composition of the matrix material also the maximum temperature of the foam, the heating time of the precursor before the maximum temperature is achieved, the time period in which the foam is in liquid or semisolid state and the external pressure are of greatest influence. Weaire (2001, pp. 977-978, [312]) modeled the process of solidification and drainage using a foam drainage equation to derive parameters for the foaming of arbitrary materials.

A way to produce near-net-shape parts from sandwich foam structures was developed by Gers (2000, pp. 2-3, [119]) where the precursor is extruded and forced through a tool while sheets of non-expandable aluminum are joined to it by roll-bonded cladding. Next, other forming processes like e.g. deep drawing can be conducted before a heat treatment causes the onset of expansion by decomposition of the blowing agent. In a way this process is similar to the above mentioned entrapped gas expansion process, except that here no pressurized gas exists in the precursor.

Laser foaming

The above described powder compact foaming technology was slightly modified by Kathuria (2000, pp. 1-8, [158]) who applied CO_2 laser beam energy as an alternative source of heat on consolidated but unfoamed aluminum samples shown in ***fig. 10.4 c)***. Due to the limited spot size of a laser beam only a local, small fraction of the precursor is foamed at a time which allows a graded distribution of pore sizes for customized properties by changing the process parameters. In experiments the processing speed, i.e. the speed at which the laser moves across the surface of a sample, was identified as the dominant influence on pore size. At lower speeds a high amount of beam energy was transferred into the material and greater pores developed. Their size ranged between 0.2 and 3 mm giving relative densities of 0.33 up to 0.68.

A similar process is currently under development by Hohenhoff (2006, pp. 13-18, [145]) where a solid outer skin for titanium implants is prepared by laser cladding and, in a second step, the internal volume is filled with a mixture of titanium powder and $CaCO_3$ as a blowing agent without compaction. Then the same laser source used in the first process step does the foaming. Preliminary tests resulted in relative densities around 0.65 and pore sizes from few tens of microns to 3 mm.

Gas-metal eutectic solidification

Fig. 10.4 e) illustrates the structure of GASARs (aka GASERITE) which are produced from either Al-, Be-, Cr-, Cu-, Fe-, Mg-, Mn- or Ni-based alloys that exhibit a eutectic. The liquid phase at this point is saturated with hydrogen under pressure and cooled down as the pressure is progressively reduced. Thus a directional solidification takes place resulting in a material with longish tube-like cavities filled with hydrogen. The relative density can vary from 0.25 to 0.95 (Shapovalov, 1998, p. 282, [272]). Here, the pore size (between 10 µm and 10 mm) depends vastly on the process parameters which are difficult to handle (Apprill, 1998, pp. 291-296, [16], Paradies, 1998, pp. 297-302, [224]). Typical process parameters are the chemistry of the alloy, melt-overpressure, temperature gradient and the rate of solidification. This manufacturing process is not yet commercially available (Ashby, 2000, p. 20, [17]).

Spray foaming

In this process a metallic melt is atomized and sprayed onto a substrate. If a powder such as a blowing agent is injected into the stream of melt droplets, then pores are generated in the solidifying deposit. The implementation of this process was reported by Banhart (1998, pp. 265-267, [31]) who injected silicon oxide into a carbon steel spray. The silicon oxide decomposed upon contact with the melt and closed-cell porosities with relative densities between 0.44 and 0.6 and pores, presumably in the range of several millimeters or greater, were obtained. Nonetheless, it has to be noted that this process delivers pore shapes far from spherical with a very inhomogeneous distribution.

10.2.4 Casting from liquid phase

The different types of casting introduced here are conducted with templates that supply stochastic structures. Some processes can be conducted as simple gravity casting while others require the application of pressure or heating of the mold. However, all processes are subject to the typical issues involved with casting in terms of accuracy, residual stress and distortion.

Investment casting
Open-cell polymer sponges that are commonly available are used as mould templates. The desired cell size and density is selected and coated with casting slurry and casting sand. The mould is baked to harden the casting material and to decompose the polymer template. Any metal alloy which is suitable for investment casting can be used to obtain a copy of the original polymer foam (Ashby, 2000, pp. 11-14, [17]). Depending on the polymer foam template the resulting structures can possess pore sizes of 1 to 5 mm and relative densities from 0.03 up to 0.2. ***Fig. 10.5 a)*** gives an example of the commercially successful product by the name of Duocel.

Infiltration of compacted substrate spaceholders
Closely related to the above mentioned process where two powders are consolidated and one is leached out, this process can be combined with a casting step where a bed of leachable powder particles is infiltrated by a metal melt under pressure. After cooling has taken place the leachable component, e.g. salt, is washed out leaving behind an open-cell sponge (Ashby, 2000, pp. 19-20, [17]). An improved and more efficient version of this process was suggested by Ma (1999, p. 786, [190]) wo used high pressure infiltration to obtain aluminum foams with relative densities from 0.142 to 0.27 and pores sizes between 1.19 and 2.85 mm. Chou (2002,

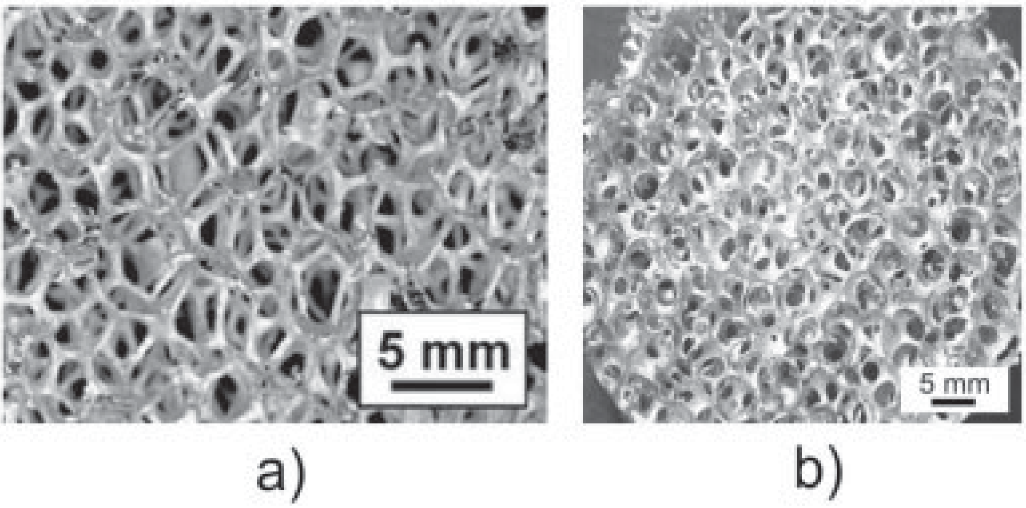

Figure 10.5: Stochastic cellular materials made by casting from liquid phase [316], [60]

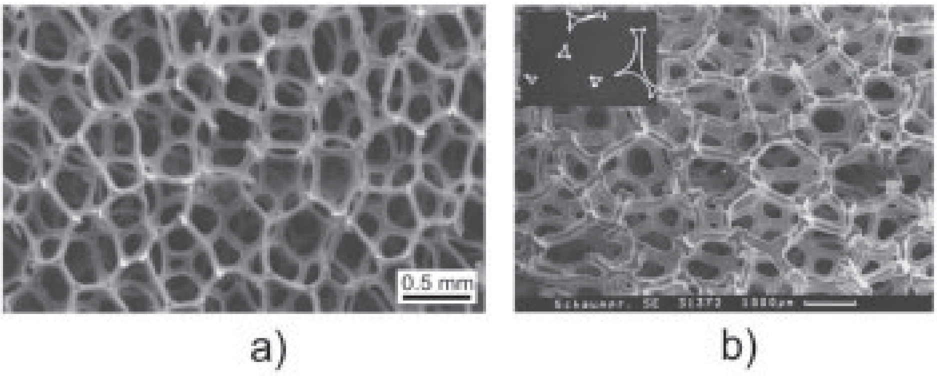

Figure 10.6: Stochastic cellular materials made by deposition techniques [28]

pp. 379-380, [60]) presented a process where an open-cell porosity in aluminum with a relative density as low as 0.115 and a pore size of 4 mm was achieved by the application of soft ceramic balls which can be easily removed after casting with ultrasonic vibration in water as seen ***fig. 10.5 b)***. All these processes have the advantage of minimizing the pore size variations, however, this is at the cost of not being able to achieve high relative densities (Banhart, 2001, pp. 583-584, [28]).

10.2.5 Deposition techniques from vapor or ionic phase

Chemical Vapor Deposition (CVD) and Physical Vapor Deposition (PVD)

Ashby (2000, p. 14, [17]) and Banhart (2001, p. 597, [28]) described a CVD process, industrially known as Incofoam, where a nickel containing gas $Ni(CO_4)$ decomposes thermally at temperatures above 120°C to nickel and carbon monoxide. The nickel vapor condenses on a cold open-cell polymer template. After layers of tens or hundreds of micrometers of nickel are applied, the polymer is removed by chemical or thermal treatment. Thus hollow ligaments result and subsequent sintering is necessary to densify these ligaments. Finally, sponges with open pore sizes between 100 and 300 µm are obtained as depicted in ***fig. 10.6 a)***. The possible densities range between 0.02 to 0.05. The toxicity of nickel is an important issue that must not be underestimated, however, this process is also available for titanium. A similar method used by Sherman (1999, pp. 1-3, [274]) incorporates Chemical Vapor Infiltration (CVI) of a porous carbon sponge gained from a polymer sponge by pyrolysis. In this process, commercially available under the name Ultramet, layers of up to 1000 µm thickness of materials such as zirconium, niobium, hafnium, tantalum, tungsten or rhenium can be deposited onto the substrate.

A PVD process where atomic vapor of an Inconel alloy is generated with an electron beam was suggested by Queheillalt (2001, pp. 1028-1030, [237]). After the deposition onto a polyurethane sponge the template is decomposed thermally and the remaining metallic sponge with pore sizes from 0.85 to more than 1 mm has to be sintered. This approach extends to the production of copper sponges with pore sizes of approximately 1.25 mm (Queheillalt, 2001, p. O5.6.2, [234]). All foam samples achieved relative densities between 0.01 and 0.1.

Electro-deposition

The electro-deposition technique is applied in a similar way as the investment casting process. The available commercial products by the names of Retimet and Celmet (Banhart, 1998, p. 130, [32]) are used as sacrificial open-cell polymer sponge templates which first have to be made electrically conductive by either coating it with slurry based on graphite or carbon or by cathode sputtering. Then the sponge is coated in an electrolyte, i.e. a solution of metal ions, by application of voltage between the anode and the cathode which is the sponge template. Nickel, nickel-chromium and copper are the preferred metals for this method. After the electro-plating is complete the polymer is removed by thermal treatment and thus hollow struts remain giving the structure in ***fig. 10.6 b)***. Banhart (2001, pp. 595-596, [28]) reported that for the fabrication of nickel sponges this process yields relative densities between 0.044 and 0.073 at cell sizes between 0.5 and 3.2 mm.

10.3 Simulation results: relative densities and compressive yield strengths

Table 10.1: Calculated relative density for all cell types and cell sizes

	Cell size [mm]								
Cell type	**0.5**	**1**	**1.5**	**2**	**2.5**	**3**	**4**	**5**	**6**
fcc	0.9347	0.3974	0.2019	0.1209	0.08076	0.05732	0.03373	0.02191	0.01550
fcc_z	0.9818	0.4998	0.2625	0.1595	0.1075	0.07659	0.04541	0.02975	0.02121
f_2cc	0.9901	0.6261	0.3534	0.2205	0.1505	0.1082	0.06469	0.04242	0.03019
f_2cc_z	0.9901	0.6378	0.3846	0.2466	0.1706	0.1237	0.07471	0.04940	0.03538
bcc	1	0.7474	0.4238	0.2634	0.1784	0.1286	0.07576	0.04896	0.03494
bcc_z	1	0.7881	0.4658	0.2941	0.2010	0.1455	0.08641	0.05627	0.04033
f_2bcc	1	0.8944	0.6280	0.4208	0.2963	0.2179	0.1323	0.08725	0.06269
f_2bcc_z	1	0.9058	0.6591	0.4468	0.3164	0.2334	0.1424	0.09423	0.06788
RD	0.9969	0.7139	0.4158	0.2619	0.1786	0.1296	0.07657	0.05059	0.03611
TRD	1	0.8441	0.5305	0.3426	0.2365	0.1725	0.1029	0.0681	0.0486
hp	0.9648	0.4939	0.2649	0.1615	0.1081	0.07724	0.04493	0.02922	0.02056
hp_{2u}	0.9760	0.5848	0.3311	0.2061	0.1394	0.1002	0.05866	0.03845	0.02712
hp_{2d}	0.9779	0.6168	0.3560	0.2183	0.1457	0.1039	0.06025	0.03928	0.02761
hp_{2ud}	0.9848	0.696	0.4407	0.2859	0.1973	0.1435	0.0852	0.0563	0.0399

Table 10.2: Calculated yield strengths [MPa] in x-, y- and z-direction for all cell types and cell sizes

	Cell size [mm]								
Cell type	**0.5**	**1**	**1.5**	**2**	**2.5**	**3**	**4**	**5**	**6**
fcc	104.0	19.66	6.417	2.804	1.468	0.8615	0.3677	0.1891	0.1094
	104.0	19.66	6.417	2.804	1.468	0.8615	0.3677	0.1891	0.1094
	100.7	18.52	6.146	2.692	1.407	0.8242	0.3510	0.1798	0.1039
fcc_z	96.53	28.08	14.21	7.637	5.102	3.667	2.162	1.247	0.7222
	96.53	28.08	14.21	7.637	5.102	3.667	2.162	1.247	0.7222
	279.1	84.15	39.83	23.45	13.66	9.098	4.330	2.206	1.135
f_2cc	301.8	65.58	23.75	11.07	5.795	3.362	1.472	0.7582	0.4419
	301.8	65.58	23.75	11.07	5.795	3.362	1.472	0.7582	0.4419
	330.0	59.37	20.50	9.216	4.656	2.841	1.218	0.6302	0.3675
f_2cc_z	248.8	57.68	26.75	15.32	9.896	7.177	4.004	2.629	1.786
	248.8	57.68	26.75	15.32	9.896	7.177	4.004	2.629	1.786
	493.0	118.2	50.38	27.71	16.98	11.30	5.900	3.757	2.595
bcc	253.2	50.19	17.19	7.576	3.963	2.332	0.9963	0.5143	0.2973
	253.2	50.19	17.19	7.576	3.963	2.332	0.9963	0.5143	0.2973
	252.9	50.12	17.16	7.566	3.989	2.329	0.9949	0.5136	0.2969
bcc_z	377.7	65.64	22.39	9.850	5.155	3.027	1.298	0.6694	0.3889
	377.7	65.64	22.39	9.850	5.155	3.027	1.298	0.6694	0.3889
	271.0	77.97	37.00	21.47	13.67	9.729	5.512	3.611	2.149
f_2bcc	661.6	143.3	55.26	28.98	17.82	12.02	6.684	4.353	3.197
	661.6	143.3	55.26	28.98	17.82	12.02	6.684	4.353	3.197
	385.9	87.69	32.34	16.06	8.977	6.292	3.323	2.037	1.378
f_2bcc_z	502.5	124.7	53.03	29.68	19.35	12.74	7.522	4.780	3.385
	502.5	124.7	53.03	29.68	19.35	12.74	7.522	4.780	3.385
	470.7	110.6	48.69	25.30	15.82	10.98	7.135	4.491	3.074
RD	707.8	151.3	53.84	24.89	13.93	8.569	3.828	1.957	1.157
	707.8	151.3	53.84	24.89	13.93	8.569	3.828	1.957	1.157
	47.47	75.64	24.53	10.72	5.584	3.285	1.401	0.7291	0.4222
TRD	721.4	134.5	46.08	21.05	10.90	6.76	2.966	1.538	0.8934
	421.3	72.01	25.28	11.99	6.371	4.058	1.839	0.9839	0.5887
	408.1	67.58	23.24	10.98	6.144	3.833	1.826	0.9921	0.6101
hp	86.77	13.43	4.254	1.844	0.9617	0.5600	0.2356	0.1193	0.06836
	71.91	11.51	3.730	1.646	0.8648	0.5087	0.2172	0.1115	0.06463
	266.7	46.19	15.18	6.664	3.447	2.017	0.8724	0.4463	0.2577
hp_{2u}	225.7	41.64	14.64	6.642	3.485	2.077	0.8857	0.4579	0.2651
	187.8	33.11	10.93	4.841	2.434	1.504	0.6429	0.3298	0.1882
	610.7	104.4	34.25	15.17	7.978	4.690	2.008	1.033	0.5973
hp_{2d}	210.3	40.92	14.71	6.768	3.618	2.146	0.9306	0.4761	0.2721
	157.4	26.46	8.769	3.870	2.038	1.198	0.5134	0.2639	0.1514
	526.9	91.23	30.28	13.27	7.106	4.221	1.824	0.9449	0.5521
hp_{2ud}	316.0	58.54	21.03	9.311	5.119	3.199	1.364	0.6940	0.3951
	279.3	51.48	19.96	9.131	5.188	3.090	1.348	0.6784	0.3819
	748.7	132.0	43.83	19.39	10.19	5.960	2.560	1.323	0.7692

10.4 Average strut diameter in dependence of melt energy

Table 10.3: Results for average strut diameters for variable melt energies

Melt energy	Average strut diameter *d* [mm] Standard deviation [mm]	} at beam power P_L [W]						
E_{melt} [J]	60	80	100	120	140	160	180	200
0.02		0.1658 0.01340						
0.025			0.1878 0.01429					
0.03	0.1865 0.02565			0.2058 0.01118				
0.035					0.219 0.03100			
0.04		0.2205 0.01593				0.2428 0.01882		
0.045	0.2038 0.03686						0.219 0.03010	
0.05			0.2338 0.01053					0.2428 0.01882
0.06	0.2045 0.02469	0.239 0.01105		0.263 0.02093				
0.07					0.2675 0.01626			
0.075			0.267 0.02483					
0.08		0.259 0.01283				0.2783 0.007455		
0.085			0.233 0.03683					
0.09	0.2313 0.06791			0.2718 0.01565			0.2675 0.01626	
0.0944			0.253 0.03434					
0.1			0.2888 0.02105					0.2783 0.007455
0.105					0.301 0.01517			
0.1063			0.248 0.02573					
0.12	0.218 0.02560	0.2943 0.01646		0.3103 0.01473		0.2975 0.01139		
0.1214			0.266 0.01430					
0.135							0.301 0.01517	
0.14					0.3278 0.004787			
0.1417			0.267 0.03529					

Table 10.3 **(continued)**

Melt energy	**Average strut diameter d [mm]** **Standard deviation [mm]** } **at beam power P_L [W]**							
E_{melt} [J]	**60**	**80**	**100**	**120**	**140**	**160**	**180**	**200**
0.15	0.23 0.009900		0.326 0.01143					0.2975 0.01139
0.16		0.297 0.01219				0.3295 0.007		
0.17			0.295 0.02273					
0.18				0.344 0.01143			0.3278 0.004787	
0.2		0.3105 0.006856	0.336 0.02546					0.3295 0.007
0.21					0.3538 0.007632			
0.2125			0.299 0.04932					
0.24				0.374 0.01039		0.3475 0.006403		
0.25			0.3653 0.01097					
0.27							0.3538 0.007632	
0.28					0.406 0.01386			
0.2833			0.321 0.03725					
0.3	0.2815 0.02138			0.4103 0.02155				0.3475 0.006403
0.32						0.4178 0.0075		
0.34			0.373 0.02710					
0.35					0.4175 0.009747			
0.36							0.406 0.01385	
0.4		0.3873 0.03131				0.4365 0.01745		0.4178 0.0075
0.425			0.405 0.04994					
0.45							0.4175 0.009747	
0.5			0.4545 0.01420					0.4365 0.01745
0.5677			0.44 0.08246					
0.6	0.3665 0.01308			0.4988 0.03620				
0.7					0.5153 0.02868			

Table 10.3 (continued)

Melt energy	Average strut diameter *d* [mm] Standard deviation [mm] } at beam power P_L [W]							
E_{melt} [J]	60	80	100	120	140	160	180	200
0.8		0.433 0.02077				0.5193 0.01215		
0.85			0.507 0.08655					
0.9							0.5153 0.02868	
1.0			0.545 0.03575					0.5193 0.01215
1.2	0.4585 0.0342			0.6395 0.007550				
1.4					0.6645 0.02464			
1.6		0.639 0.01347				0.6673 0.01193		
1.8							0.6645 0.02464	
2			0.729 0.02678					0.6673 0.01193
2.4				0.7963 0.01548				
2.8					0.8215 0.02877			
3.2						0.8608 0.03244		
3.6							0.8215 0.02877	
4								0.8608 0.03244

10.5 Results for stability of SLM lattice structures

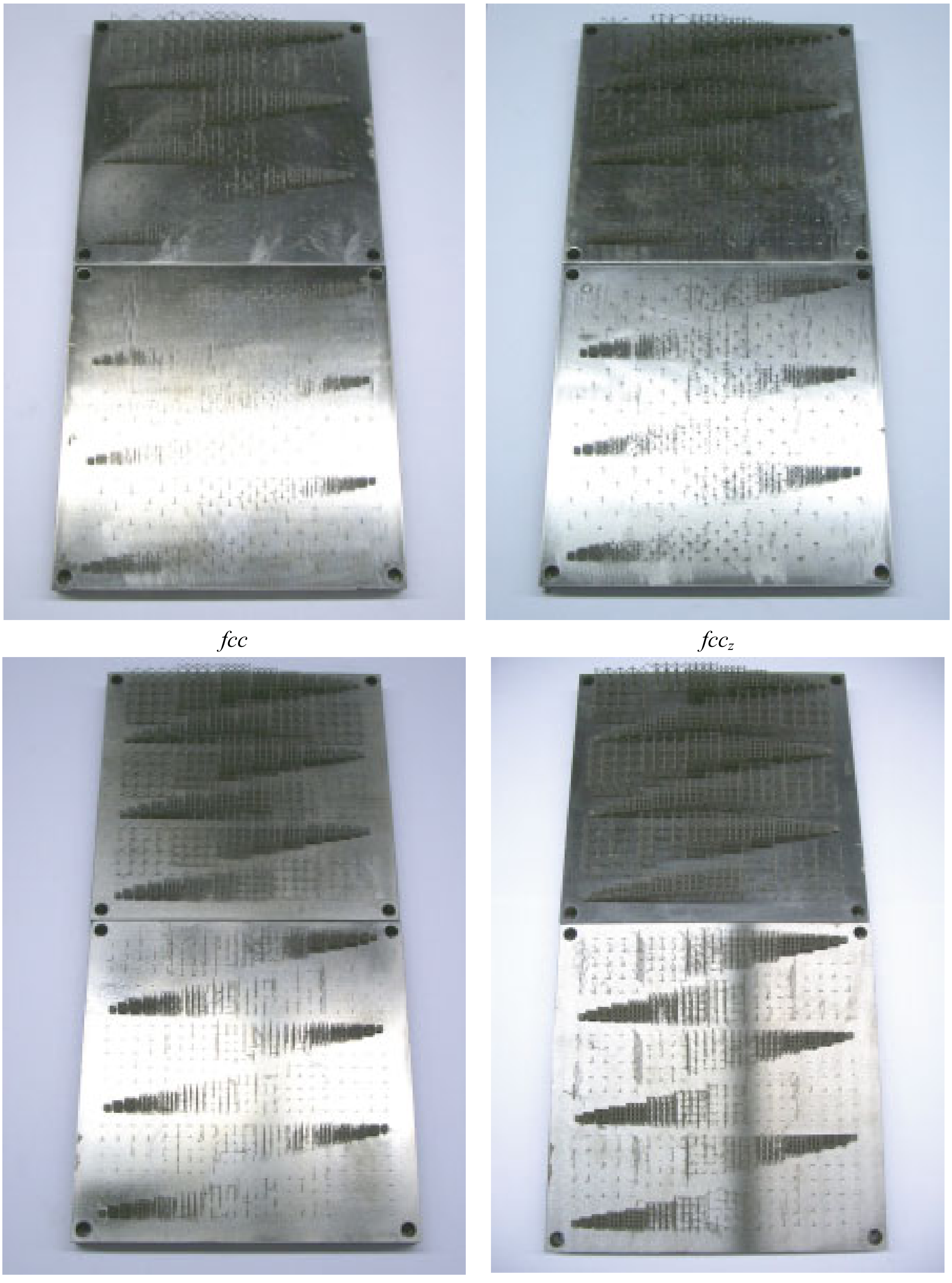

fcc

fcc$_z$

f$_2$*cc*

f$_2$*cc*$_z$

Figure 10.7: Test specimens for examination of obtainable aspect ratio

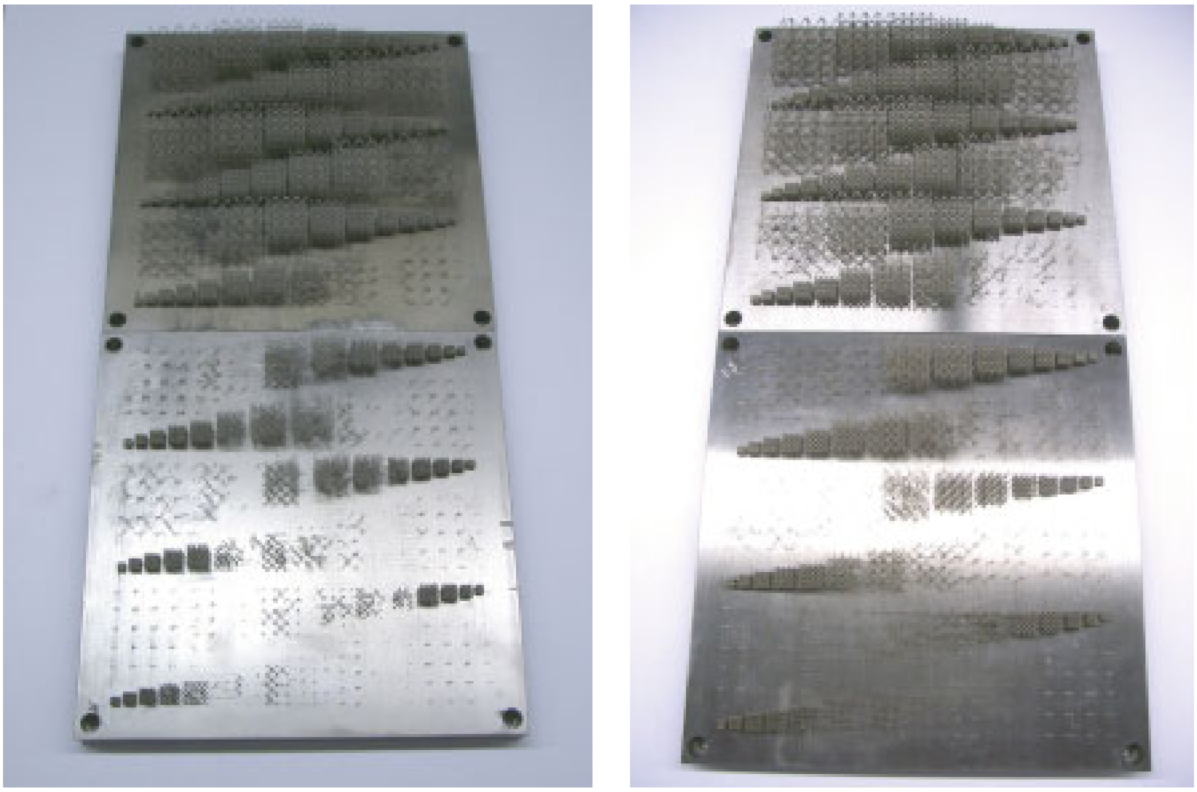

bcc *bcc*$_z$

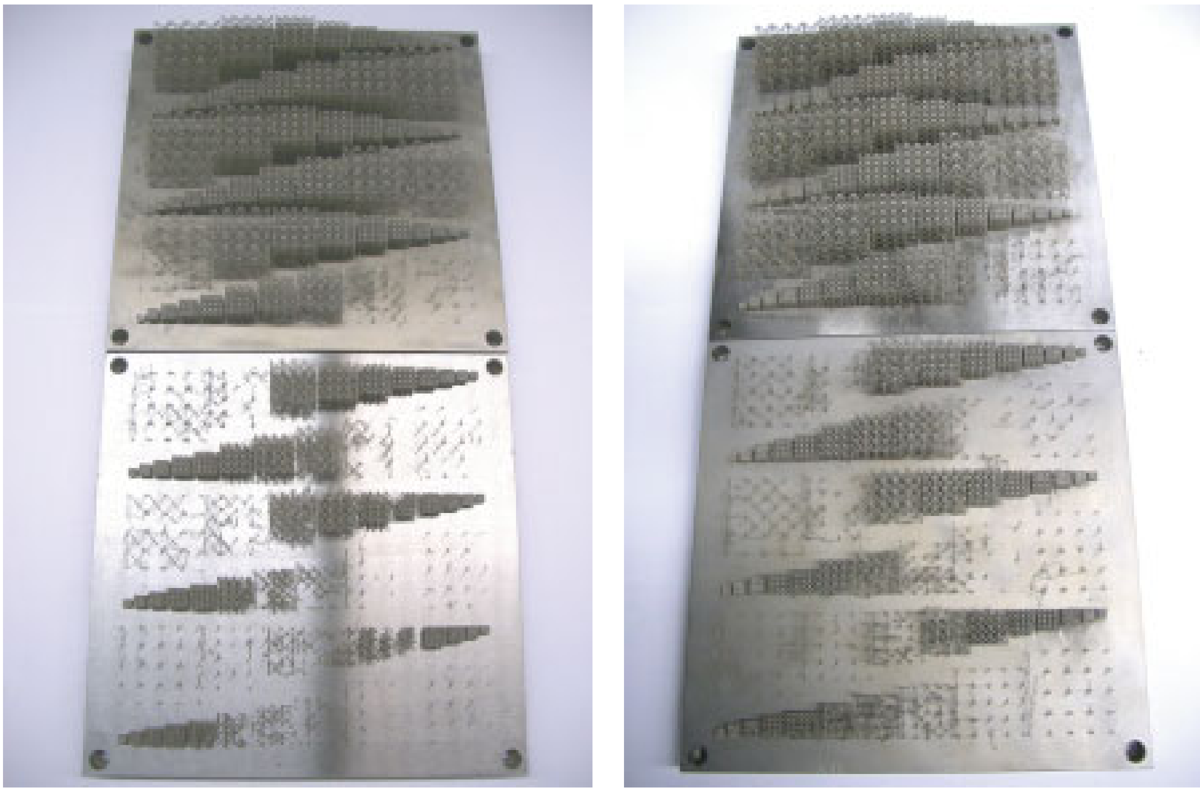

f_2*bcc* f_2*bcc*$_z$

Figure 10.7 (continued)

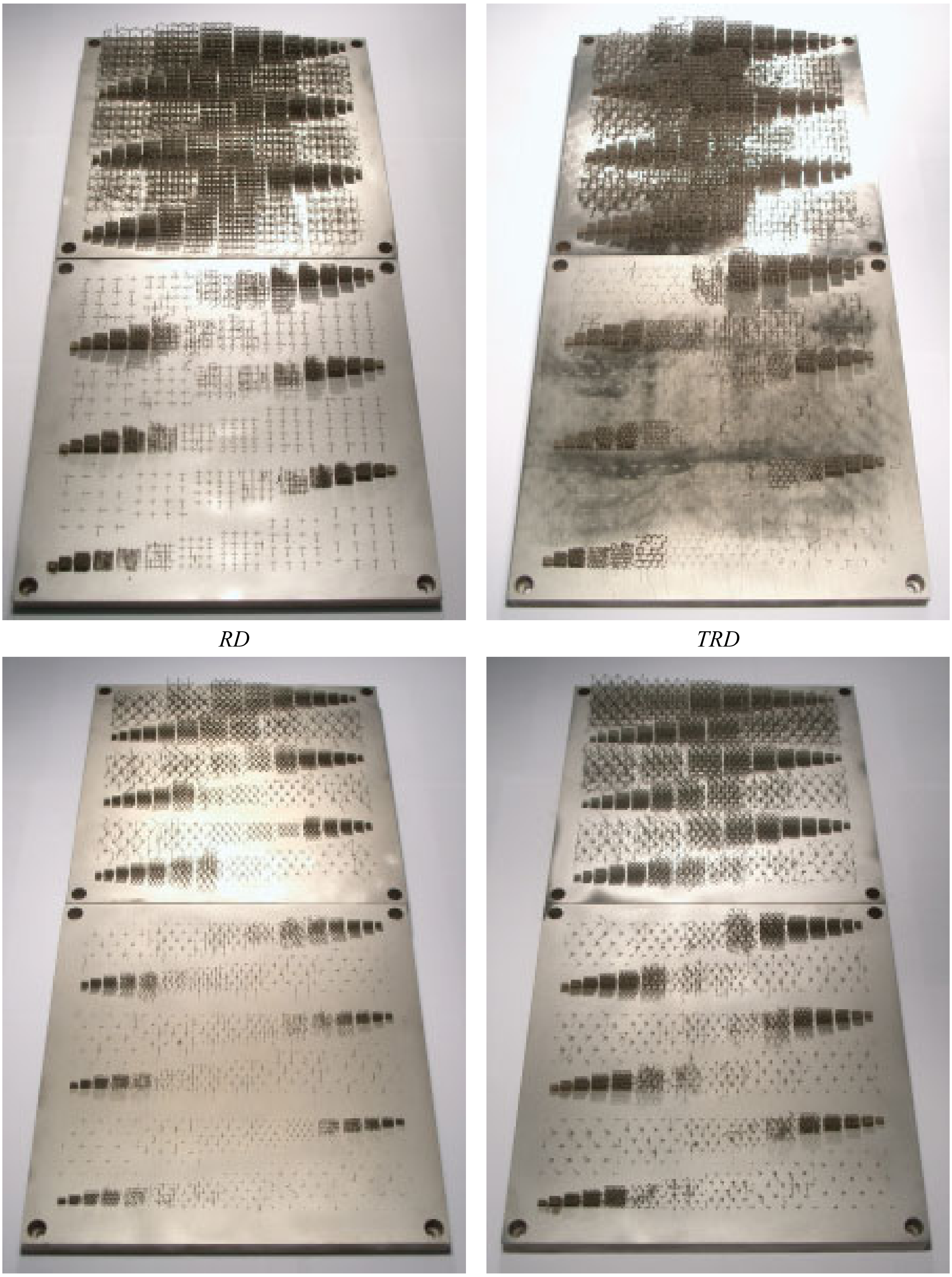

RD *TRD*

hp *hp*$_{2u}$

Figure 10.7 (continued)

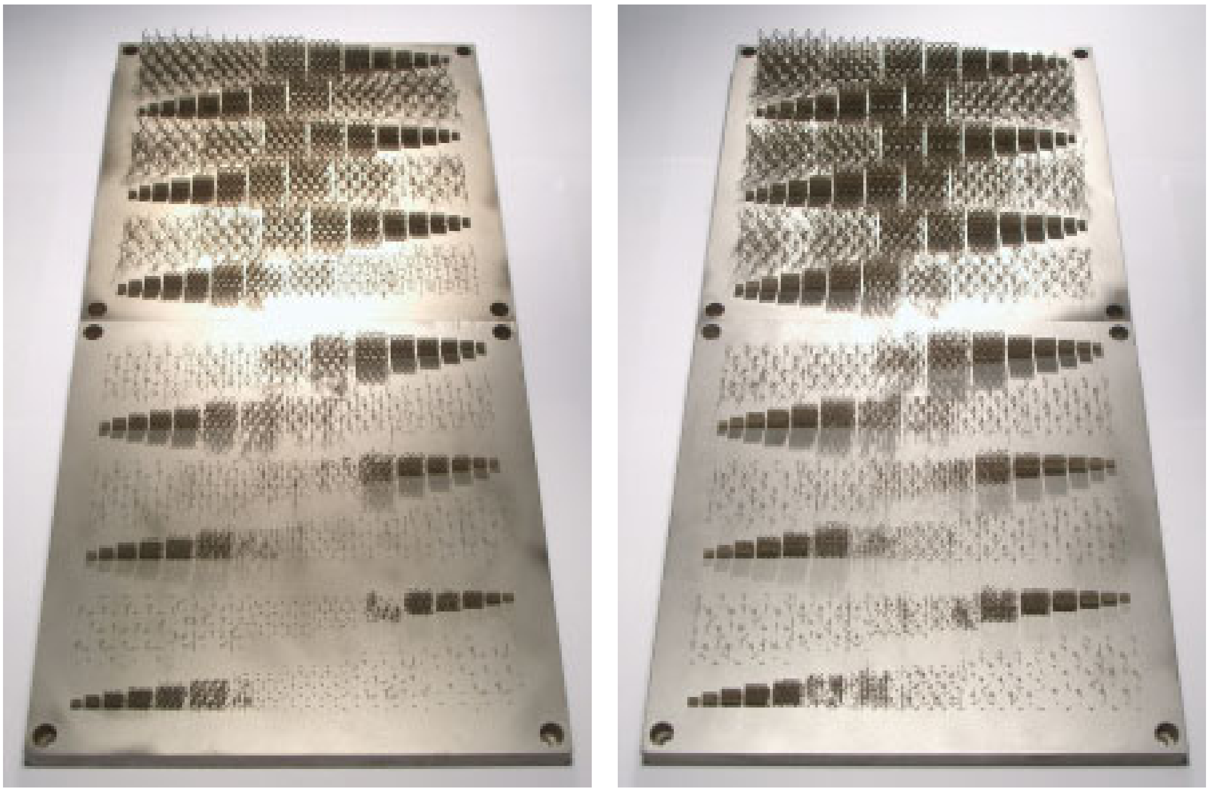

hp$_{2d}$ *hp*$_{2ud}$

Figure 10.7 (continued)

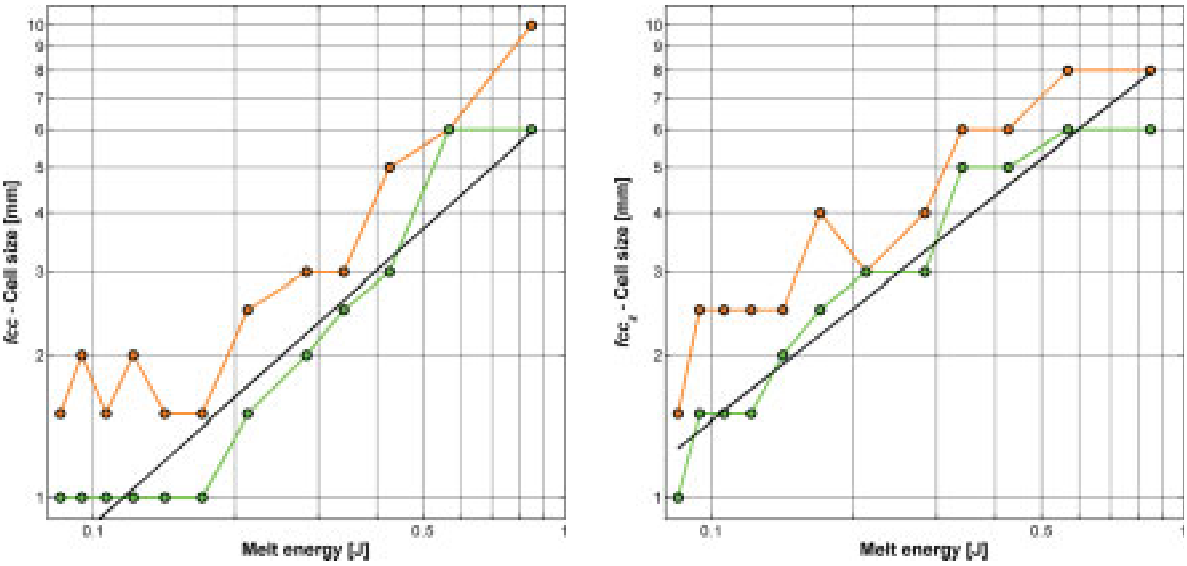

fcc *fcc*$_z$

Figure 10.8: Results for obtainable stability of SLM lattice structures

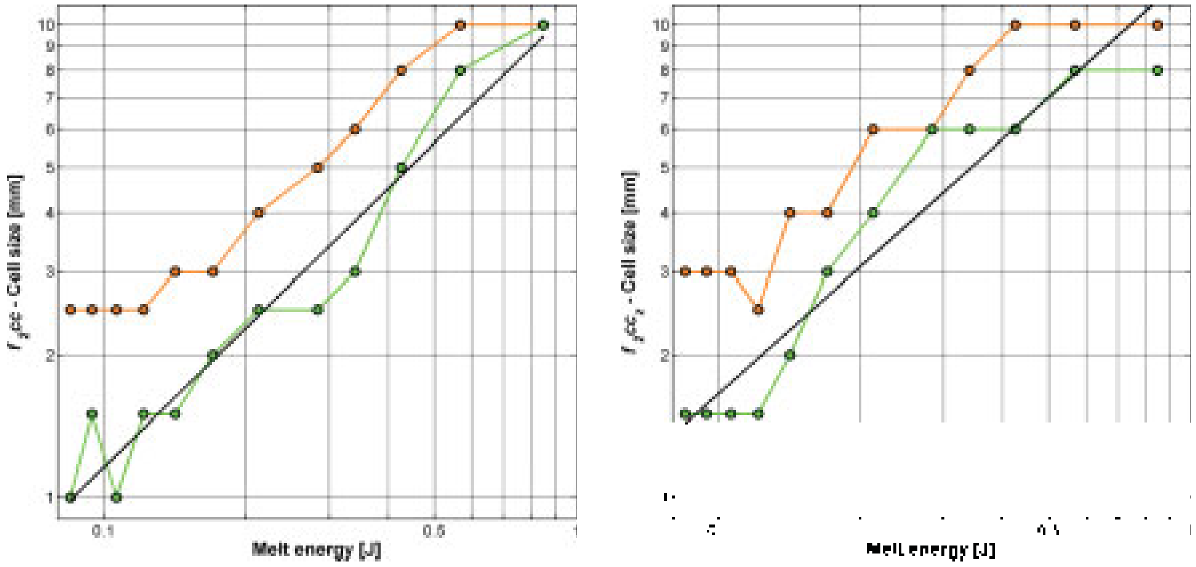

f_2cc f_2cc_z

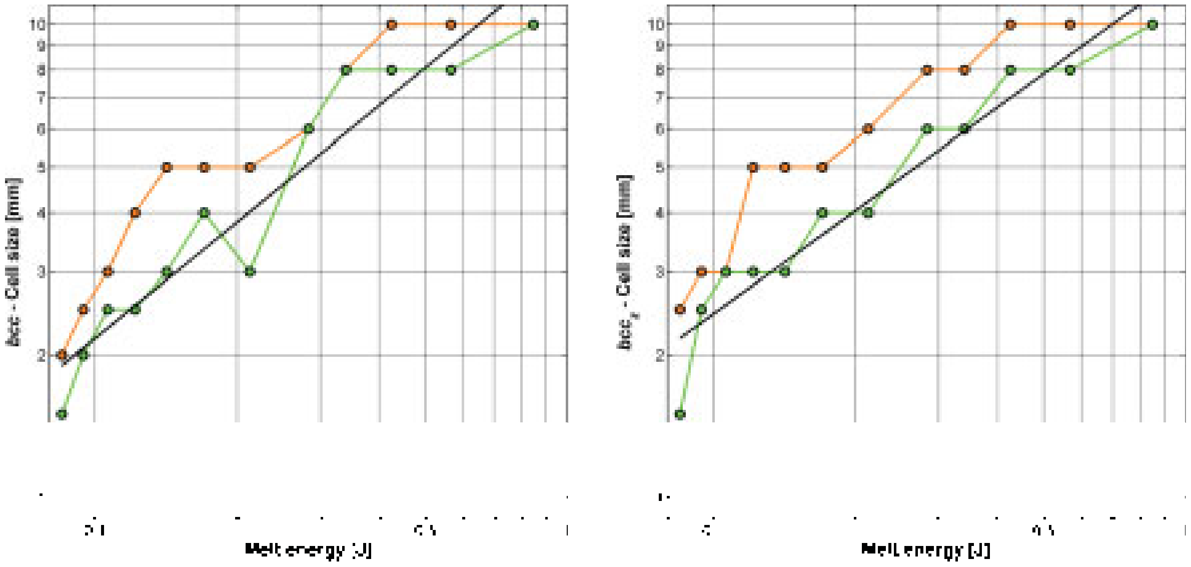

bcc bcc_z

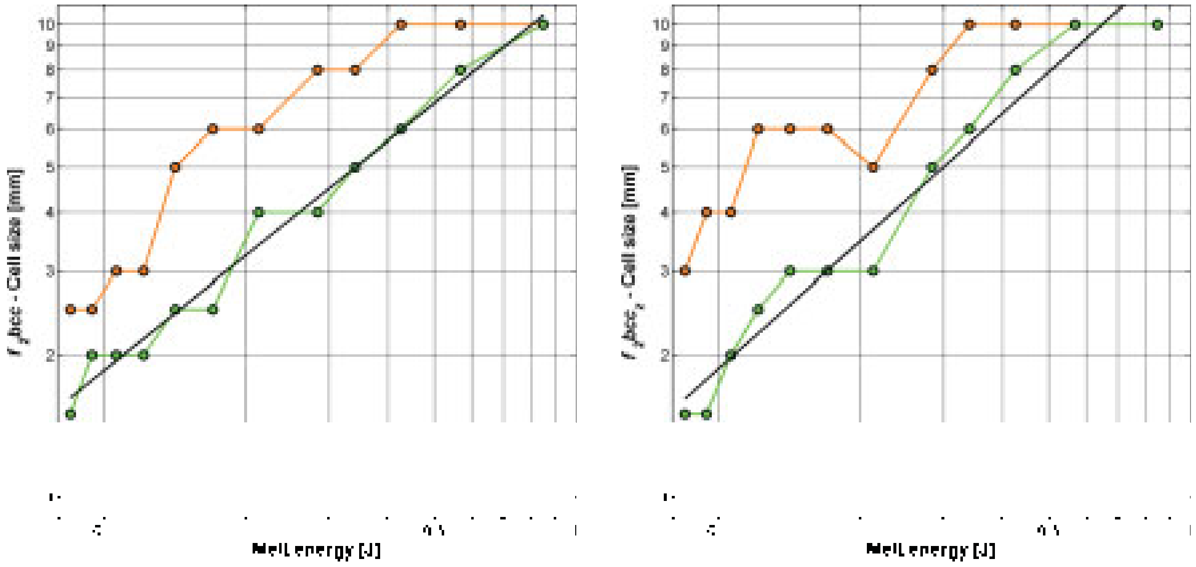

f_2bcc f_2bcc_z

Figure 10.8 (continued)

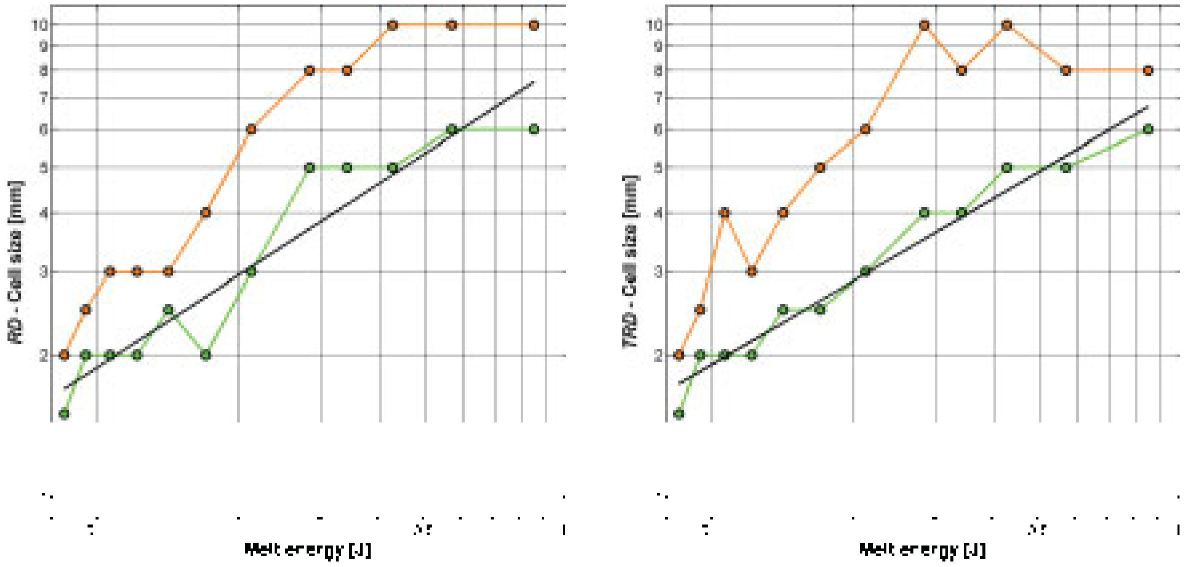

RD *TRD*

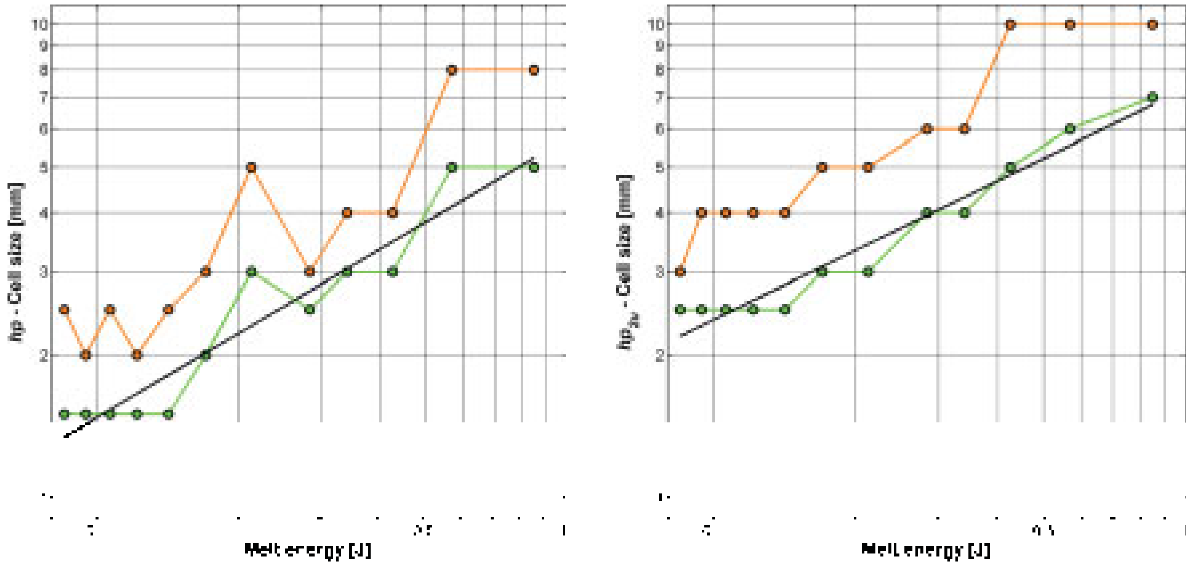

hp hp_{2u}

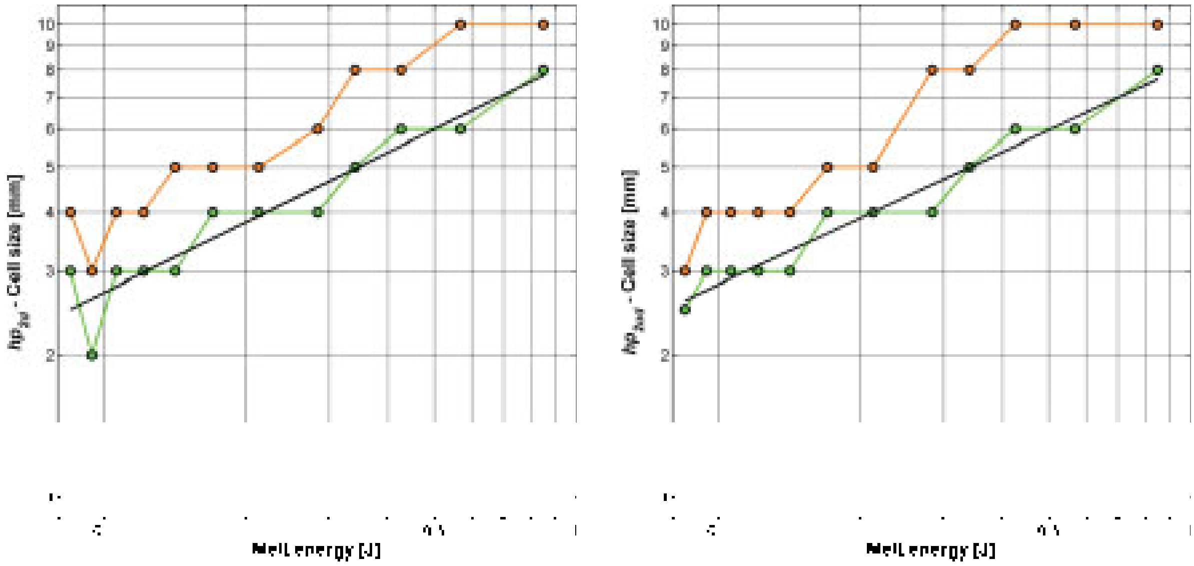

hp_{2d} hp_{2ud}

Figure 10.8 (continued)

10.6 Results of elasticity in dependence of cell size

Table 10.4: Elasticity in dependence of cell size for cell type *fcc*

Cell size [mm]		ρ^*/ρ_{solid} [1]	Std. dev. [1]	Young's modulus [MPa]	Std. dev. [MPa]
0.5	x	0.7319	0.005393	70324.94	25814.38
	y	0.7159	0.02685	85522.68	11395.32
	z	0.7211	0.02234	76457.47	14239.99
1	x	0.3072	0.006296	5044.943	402.0407
	y	0.3091	0.006887	3451.252	352.2513
	z	0.3071	0.007029	3809.681	723.8173
1.5	x	0.1642	0.003603	1054.724	64.05661
	y	0.1584	0.001385	1071.658	143.11092
	z	0.1578	0.002931	1262.849	72.48161
2	x	0.1043	0.003289	381.9270	33.30294
	y	0.1025	0.002569	382.7848	26.05994
	z	0.09943	0.003244	360.0063	45.21097
3	x	0.05291	0.001162	101.8850	10.72360
	y	0.05298	0.001212	89.40685	7.220951
	z	0.05202	0.002006	98.36402	25.56175
4	x	0.03022	0.00009562	26.13207	0.8427954
	y	0.02955	0.0005267	25.98721	1.107685
	z	0.02921	0.0007367	29.46380	1.377111
5	x	0.01968	0.0005200	7.676058	0.9624769
	y	0.01976	0.0007248	8.144237	1.654876
	z	0.01940	0.0003863	8.684064	0.9629966

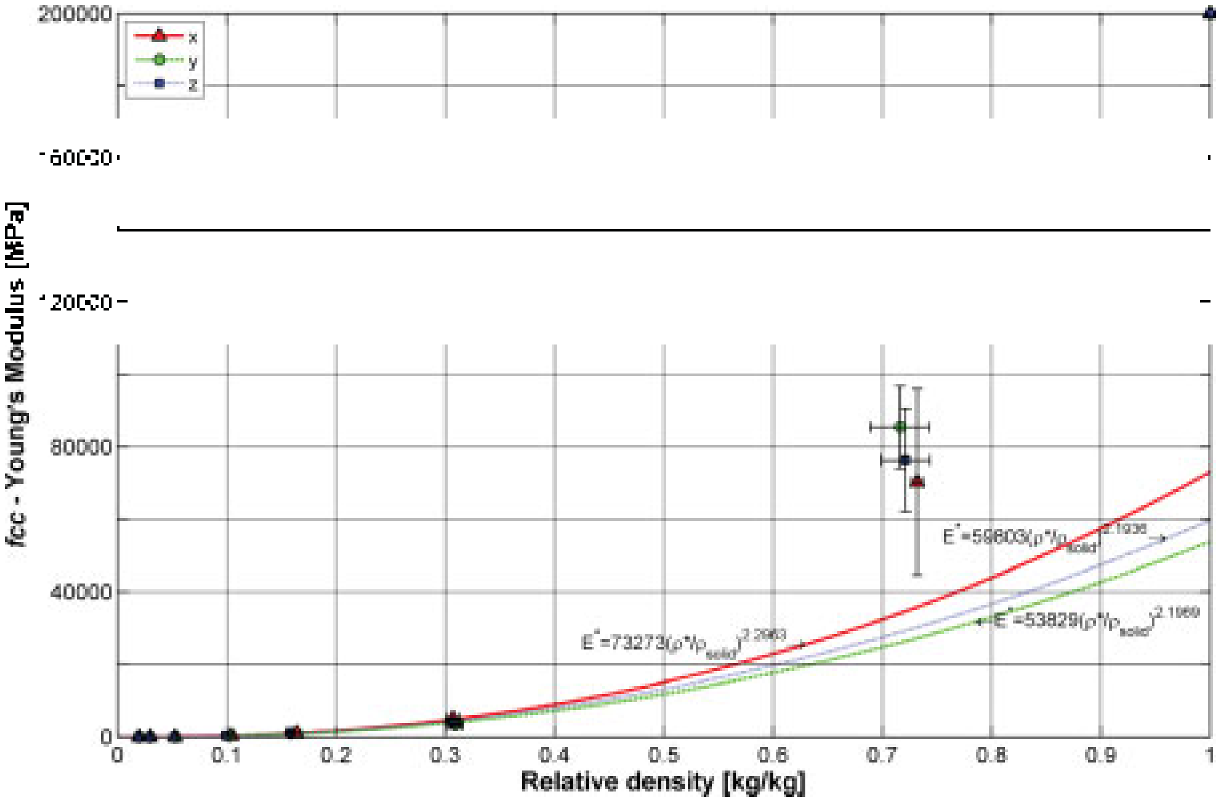

Figure 10.9: Results for effective Young's modulus of cell type *fcc*

Table 10.5: Elasticity in dependence of cell size for cell type f_2cc_z

Cell size [mm]		ρ^*/ρ_{solid} [1]	Std. dev. [1]	Young's modulus [MPa]	Std. dev. [MPa]
0.5	x	0.7800	0.06279	132329.9	9345.499
	y	0.7482	0.04970	98772.88	5557.102
	z	0.7701	0.01668	148289.4	12159.67
1	x	0.5481	0.007922	68255.42	17982.00
	y	0.5403	0.004263	66596.42	6804.210
	z	0.5382	0.006745	79101.62	4753.861
1.5	x	0.3228	0.007682	17780.64	1804.0344
	y	0.3254	0.001037	17344.20	1377.812
	z	0.3202	0.003659	26819.77	534.3343
2	x	0.2155	0.008732	5927.633	154.2177
	y	0.2109	0.002625	5127.558	328.1876
	z	0.2074	0.002833	13569.79	3296.271
3	x	0.1099	0.002270	1908.374	164.2917
	y	0.1122	0.0003626	1544.171	31.88279
	z	0.1109	0.002226	4734.769	607.2245
4	x	0.06426	0.001088	752.2235	50.66221
	y	0.06476	0.002439	591.4213	13.78450
	z	0.06429	0.0008273	1728.191	80.52403
5	x	0.04308	0.001244	451.8372	26.16690
	y	0.04788	0.006078	333.5845	53.00918
	z	0.04333	0.0005433	1127.786	254.6167
6	x	0.03085	0.0006554	147.5074	20.32277
	y	0.03130	0.0003583	142.6571	2.716023
	z	0.03173	0.003285	706.1404	193.0971

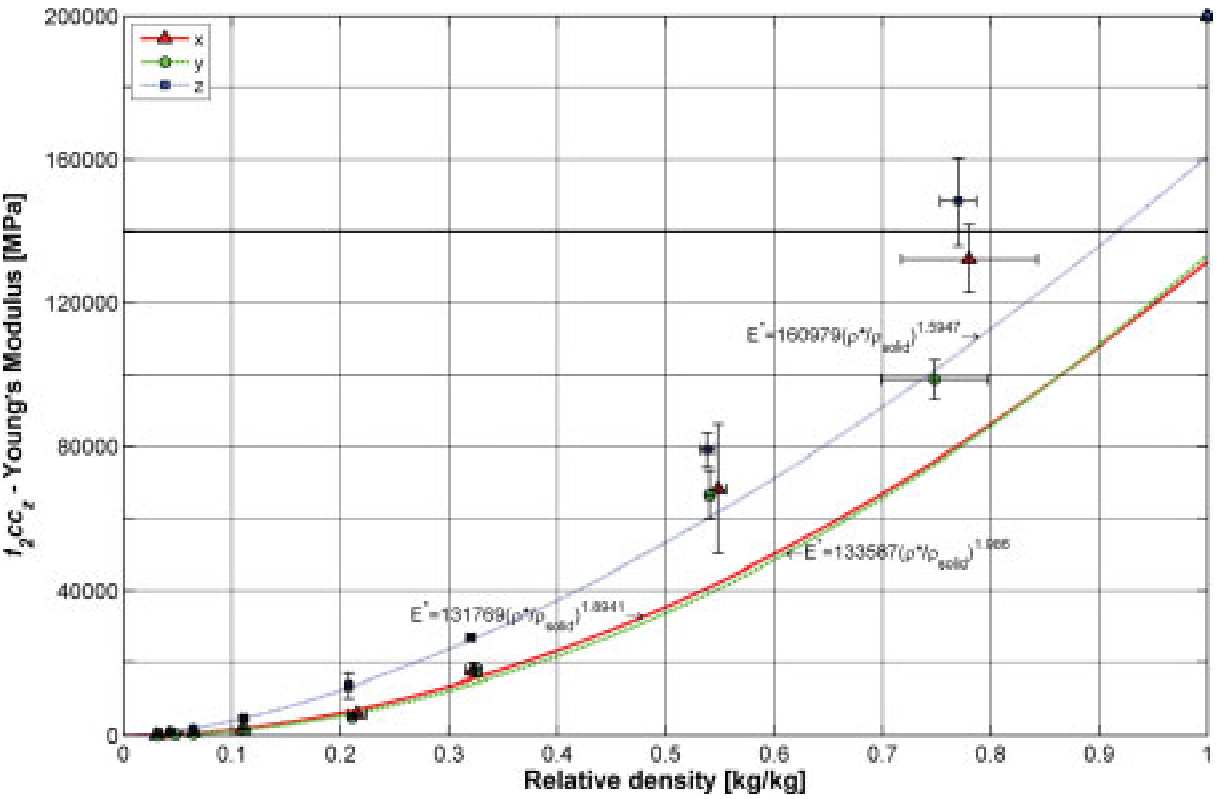

Figure 10.10:Results for effective Young's modulus of cell type f_2cc_z

Table 10.6: Elasticity in dependence of cell size for cell type f_2bcc_z

Cell size [mm]		ρ^*/ρ_{solid} [1]	Std. dev. [1]	Young's modulus [MPa]	Std. dev. [MPa]
0.5	x	0.7414	0.019250	177660.2	9511.102
	y	0.7644	0.025980	153608.7	34028.70
	z	0.7838	0.003477	162136.6	22352.15
1	x	0.6892	0.009944	130590.5	17957.73
	y	0.7074	0.011820	114768.5	17425.63
	z	0.6970	0.003887	117668.7	27969.20
1.5	x	0.5657	0.007144	114478.8	2473.448
	y	0.5491	0.011490	99789.11	44876.47
	z	0.5630	0.012430	78473.60	22813.41
2	x	0.4090	0.004346	24116.71	6131.699
	y	0.4047	0.006515	10810.91	1778.663
	z	0.3948	0.007331	13529.31	1540.197
3	x	0.1891	0.035820	3992.206	595.5205
	y	0.2063	0.004166	2855.645	127.4465
	z	0.2053	0.002812	5272.407	32.97271
4	x	0.1249	0.001251	1565.0595	47.61223
	y	0.1251	0.004332	1341.437	71.59357
	z	0.1242	0.002948	2175.186	70.83098
5	x	0.08566	0.002361	801.3574	98.45070
	y	0.08516	0.002142	706.1907	15.04904
	z	0.08640	0.001746	1165.395	26.22821
6	x	0.06174	0.002467	523.0812	22.16693
	y	0.06147	0.001292	469.5320	13.21640
	z	0.06244	0.001143	879.8037	140.8449

10.7 Results of compressive strength in dependence of cell size

Table 10.7: Compressive yield strength in dependence of cell size for cell type *fcc*

Cell size [mm]		ρ^*/ρ_{solid} [1]	Std. dev. [1]	Yield strength [MPa]	Std. dev. [MPa]
0.5	x	0.7319	0.005393	211.3357	4.520051
	y	0.7159	0.02685	136.0219	24.71505
	z	0.7211	0.02234	183.0107	11.98972
1	x	0.3072	0.006296	26.84000	5.160920
	y	0.3091	0.006887	27.44370	1.959789
	z	0.3071	0.007029	33.57393	2.366198
1.5	x	0.1642	0.003603	6.487814	0.4449330
	y	0.1584	0.001385	6.244218	0.4270624
	z	0.1578	0.002931	7.103183	0.1324941
2	x	0.1043	0.003289	2.933588	0.1677093
	y	0.1025	0.002569	2.865535	0.1259842
	z	0.09943	0.003244	3.003023	0.1056495
2.5	x	0.05495	0.0002876	1.145924	0.0222213
	y	0.05606	0.001082	1.267459	0.01383706
	z	0.05610	0.0007762	1.173462	0.1235421
3	x	0.05291	0.001162	0.7060155	0.04893041
	y	0.05298	0.001212	0.7104437	0.006582082
	z	0.05202	0.002006	0.8040166	0.05238325
4	x	0.03022	0.00009562	0.2531991	0.01974674
	y	0.02955	0.0005267	0.2683062	0.01160895
	z	0.02921	0.0007367	0.2678653	0.01766124
5	x	0.01968	0.0005200	0.1244398	0.000945424
	y	0.01976	0.0007248	0.1227422	0.004169324
	z	0.01940	0.0003863	0.1281610	0.003594573

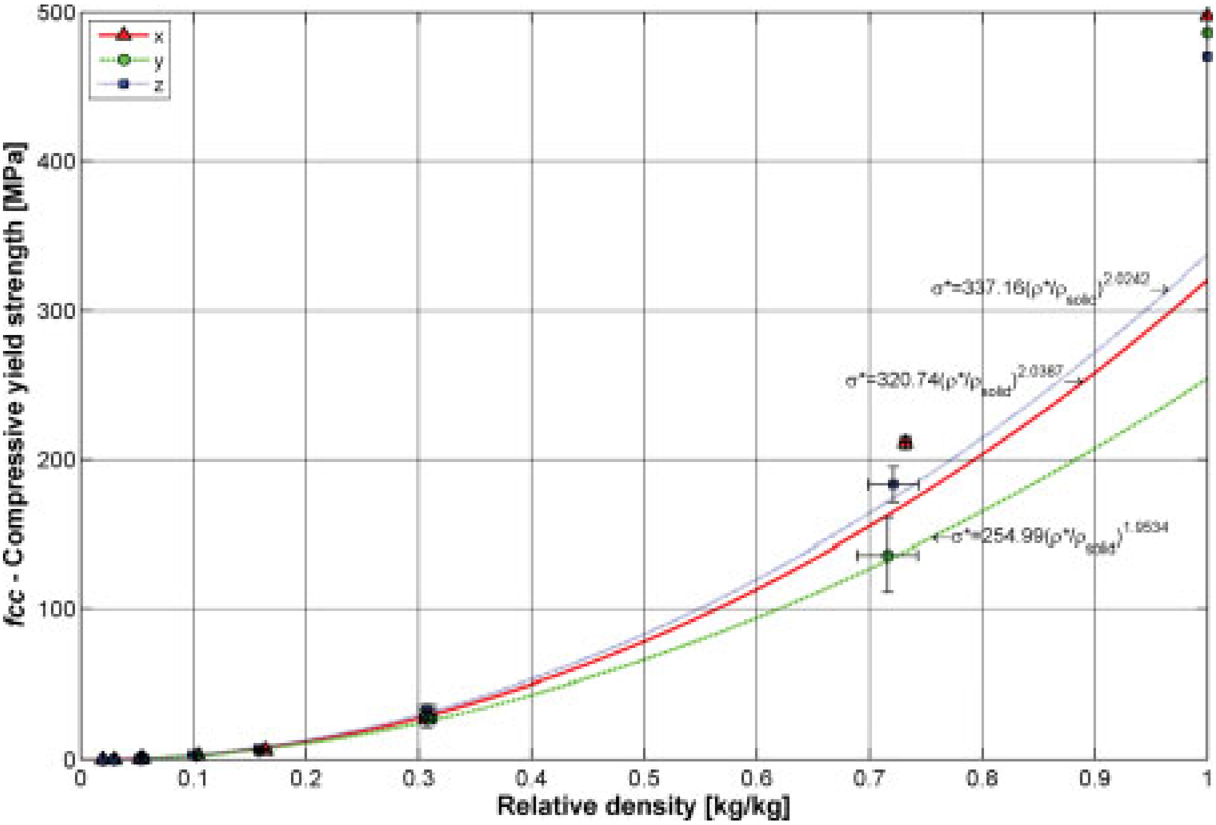

Figure 10.11:Results for effective compressive yield strength of cell type *fcc*

Table 10.8: Compressive yield strength in dependence of cell size for cell type f_2cc_z

Cell size [mm]		ρ^*/ρ_{solid} [1]	Std. dev. [1]	Yield strength [MPa]	Std. dev. [MPa]
0.5	x	0.7800	0.06279	337.4964	9.091748
	y	0.7482	0.04970	288.7387	10.14441
	z	0.7701	0.01668	305.6047	6.720428
1	x	0.5481	0.007922	103.6648	29.24108
	y	0.5403	0.004263	124.6537	21.87540
	z	0.5382	0.006745	135.6168	41.08935
1.5	x	0.3228	0.007682	36.37177	0.6021191
	y	0.3254	0.001037	34.41261	1.639387
	z	0.3202	0.003659	43.89996	0.9938072
2	x	0.2155	0.008732	14.68336	1.029899
	y	0.2109	0.002625	14.14142	1.921465
	z	0.2074	0.002833	24.95599	1.331856
2.5	x	0.1291	0.0009910	8.078290	0.4598662
	y	0.1265	0.002880	7.899946	0.8313113
	z	0.1262	0.002466	14.39365	0.7396261
3	x	0.1099	0.002270	4.366211	1.651666
	y	0.1122	0.0003626	4.075505	1.858601
	z	0.1109	0.002226	8.906507	0.2232127
4	x	0.06426	0.001088	2.360155	0.06129356
	y	0.06476	0.002439	1.456909	0.4754023
	z	0.06429	0.0008273	3.707285	0.2966491
5	x	0.04308	0.001244	1.155571	0.03732514
	y	0.04788	0.006078	1.161940	0.09616898
	z	0.04333	0.0005432	2.162396	0.2524185
6	x	0.03085	0.0006554	0.3797341	0.2589068
	y	0.03130	0.0003582	0.6681042	0.000741453
	z	0.03173	0.003285	1.050036	0.2420546

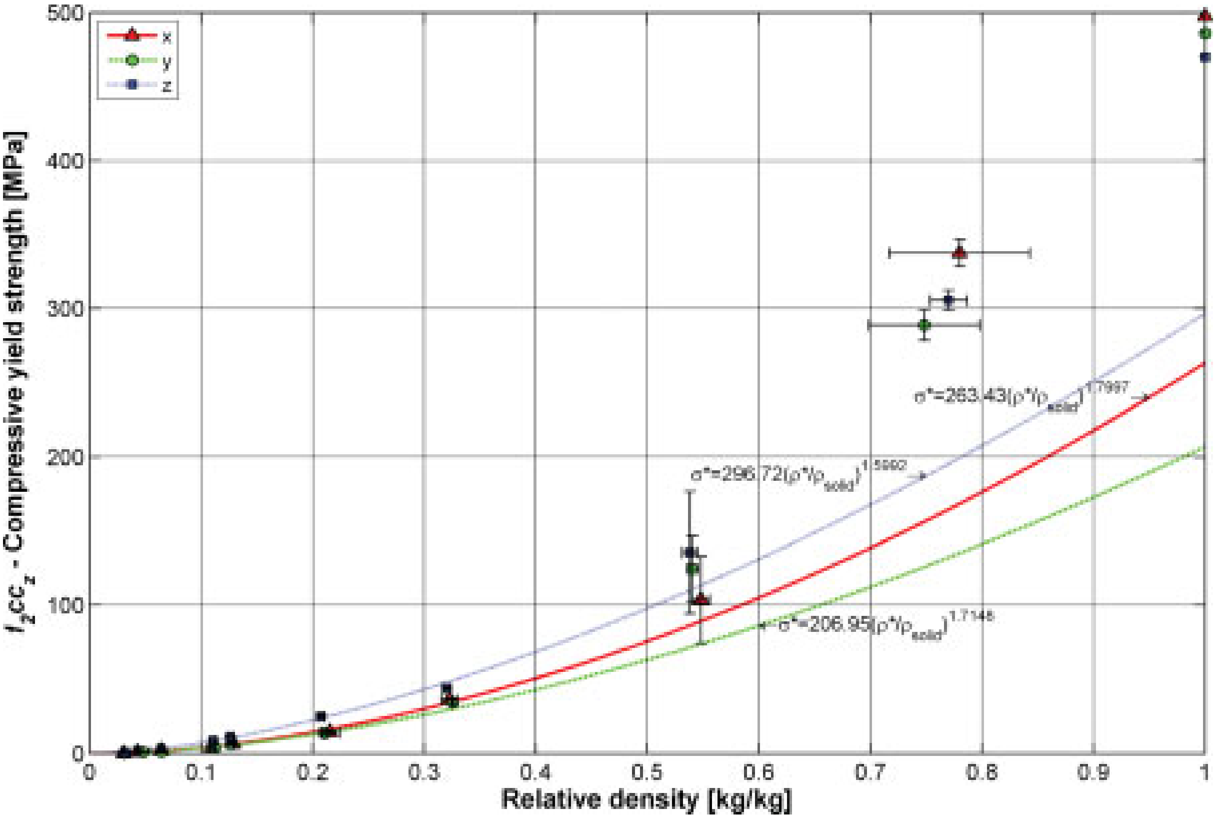

Figure 10.12: Results for effective compressive yield strength of cell type f_2cc_z

Table 10.9: Compressive yield strength in dependence of cell size for cell type f_2bcc_z

Cell size [mm]		ρ^*/ρ_{solid} [1]	Std. dev. [1]	Yield strength [MPa]	Std. dev. [MPa]
0.5	x	0.7414	0.01925	319.5197	14.17212
	y	0.7644	0.02598	389.9215	49.22645
	z	0.7838	0.003477	339.7262	33.30114
1	x	0.6892	0.009944	265.2046	16.34907
	y	0.7074	0.01182	263.8122	14.63700
	z	0.6970	0.003887	218.3029	11.78176
1.5	x	0.5657	0.007144	85.57575	13.41934
	y	0.5491	0.01149	82.04504	7.421785
	z	0.5630	0.01243	77.48601	1.247228
2	x	0.4090	0.004346	38.10226	6.067721
	y	0.4047	0.006515	40.26938	0.9474444
	z	0.3948	0.007331	34.29378	2.979271
2.5	x	0.2670	0.002838	21.49203	0.7704601
	y	0.2679	0.001596	17.39830	0.4086528
	z	0.2711	0.008171	22.17791	0.9213618
3	x	0.1891	0.03582	11.39595	1.673025
	y	0.2063	0.004166	11.98434	0.1589706
	z	0.2053	0.002812	12.47400	0.333555
4	x	0.1249	0.001251	5.333595	0.1089364
	y	0.1251	0.004332	5.009902	0.2698251
	z	0.1242	0.002948	5.706168	0.04912603
5	x	0.08566	0.002361	2.794167	0.1130363
	y	0.08516	0.002142	2.960198	0.05187003
	z	0.08640	0.001746	3.147753	0.1804370
6	x	0.06174	0.002467	1.988787	0.09184072
	y	0.06147	0.001292	1.900715	0.03836245
	z	0.06244	0.001143	1.788424	0.06527527

10.8 Results of tensile strength in dependence of cell size

Table 10.10: Tensile ultimate strength in dependence of cell size for cell type *fcc*

Cell size [mm]		ρ^*/ρ_{solid} [1]	Std. dev. [1]	Ultimate strength [MPa]	Std. dev. [MPa]
1.5	x	0.1642	0.0008546	13.52744	2.943169
	y	0.1563	0.006209	10.81395	1.472472
	z	0.1602	0.003699	9.316869	1.646833
2	x	0.1054	0.0007086	7.679464	0.6891940
	y	0.1037	0.001151	7.915896	0.1417868
	z	0.09765	0.004246	6.987728	0.4559954
3	x	0.05228	0.0005553	2.850898	0.05388902
	y	0.05203	0.0005516	2.641218	0.08776910
	z	0.05364	0.0007274	2.709449	0.05954093
4	x	0.02938	0.0001050	1.320110	0.03344039
	y	0.02907	0.0001577	1.394324	0.08490001
	z	0.03070	0.002364	1.388641	0.2870225
5	x	0.01952	0.00007731	0.7481693	0.07602761
	y	0.01971	0.0001997	0.7625283	0.1101278
	z	n/a	n/a	n/a	n/a

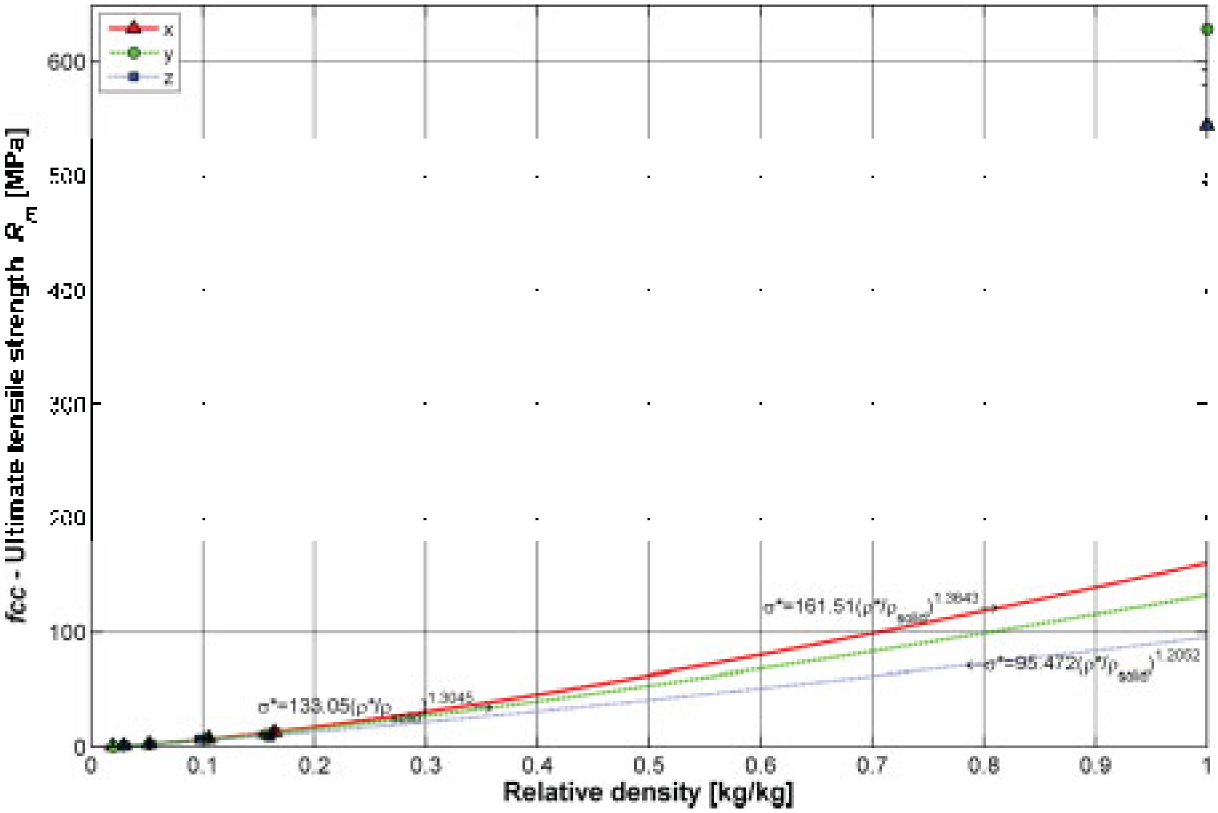

Figure 10.13:Results for effective tensile ultimate strength of cell type *fcc*

Table 10.11: Tensile yield strength in dependence of cell size for cell type *fcc*

Cell size [mm]		ρ^*/ρ_{solid} [1]	Std. dev. [1]	Yield strength [MPa]	Std. dev. [MPa]
1.5	x	0.1642	0.0008546	6.230970	0.09588025
	y	0.1563	0.006209	5.959505	0.6681618
	z	0.1602	0.003699	7.396967	0.1939795
2	x	0.1054	0.0007086	2.696892	0.07160374
	y	0.1037	0.001151	2.949306	0.1080302
	z	0.09765	0.004246	3.543943	0.1609094
3	x	0.05228	0.0005553	0.9125240	0.02539924
	y	0.05203	0.0005516	0.8978507	0.06487079
	z	0.05364	0.0007274	0.8077647	0.006415707
4	x	0.02938	0.0001050	0.4431192	0.01061919
	y	0.02907	0.0001577	0.4962734	0.01482189
	z	0.03070	0.002364	0.5386845	0.06554013
5	x	0.01952	0.00007731	0.2398164	0.01140726
	y	0.01971	0.0001997	0.2395344	0.02084842
	z	n/a	n/a	n/a	n/a

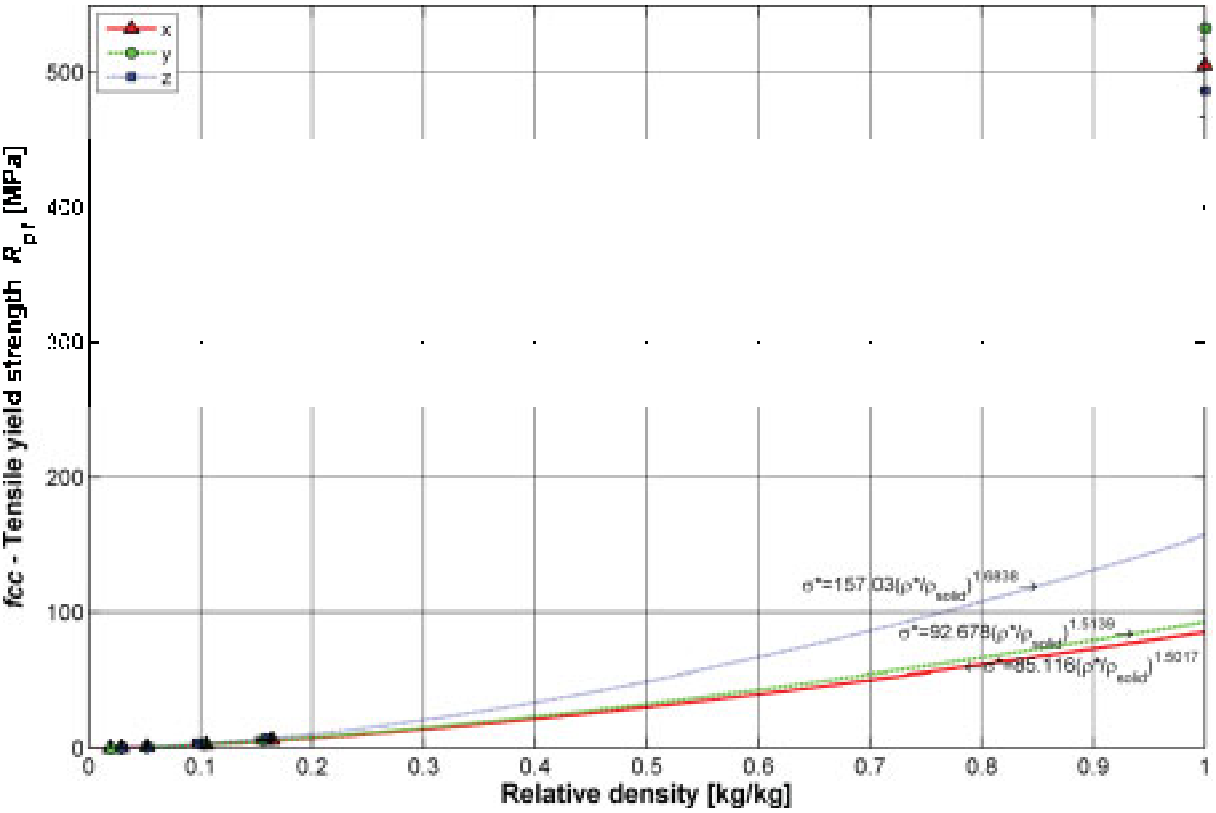

Figure 10.14:Results for effective tensile yield strength of cell type *fcc*

Table 10.12: Tensile ultimate strength in dependence of cell size for cell type f_2cc_z

Cell size [mm]		ρ^*/ρ_{solid} [1]	Std. dev. [1]	Ultimate strength [MPa]	Std. dev. [MPa]
1.5	x	0.3271	0.004975	24.48712	3.655664
	y	0.3142	0.007979	26.19863	1.783611
	z	0.3277	0.005015	36.06314	5.539250
2	x	0.2133	0.0004357	18.57771	0.1839981
	y	0.2134	0.003124	14.56220	1.472861
	z	0.2074	0.006582	19.92172	2.624338
3	x	0.1101	0.001240	8.452828	0.2740119
	y	0.1080	0.0004617	5.789299	0.2006724
	z	0.1151	0.0004325	9.766044	0.7065397
4	x	0.06406	0.00008842	4.537603	0.1225906
	y	0.06438	0.0001311	3.389133	0.1056211
	z	0.06488	0.0009561	5.149446	0.3398153
5	x	0.04422	0.0001418	2.395082	0.1237231
	y	0.04397	0.000068702	1.754039	0.3290348
	z	0.04616	0	3.094054	0
6	x	0.03143	0.0001486	1.396047	0.01606429
	y	0.03116	0.0001533	1.107049	0.05007971
	z	0.03129	0	1.706402	0

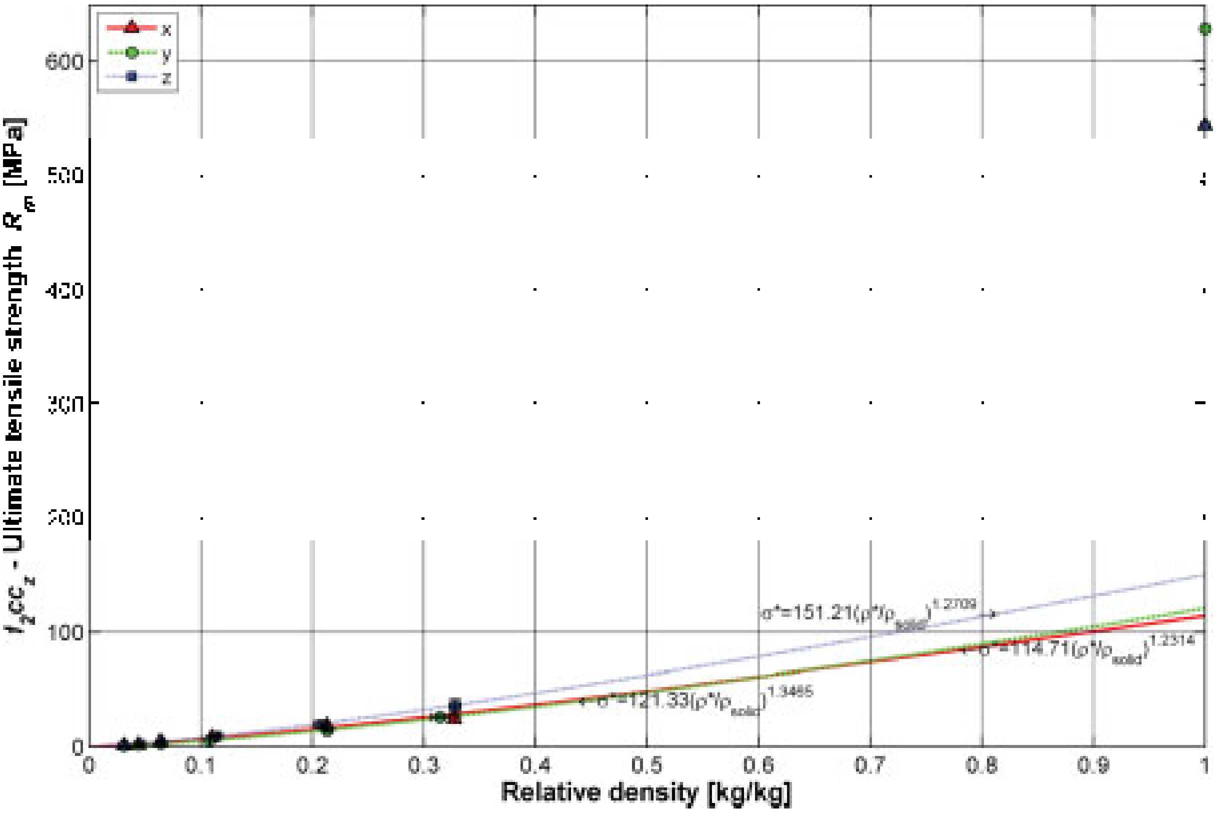

Figure 10.15:Results for effective tensile ultimate strength of cell type f_2cc_z

Table 10.13: Tensile yield strength in dependence of cell size for cell type f_2cc_z

Cell size [mm]		ρ^*/ρ_{solid} [1]	Std. dev. [1]	Yield strength [MPa]	Std. dev. [MPa]
1.5	x	0.3271	0.004975	23.17568	1.878816
	y	0.3142	0.007979	22.84294	0.8742290
	z	0.3277	0.005015	34.81252	4.599663
2	x	0.2133	0.0004357	16.41850	0.2162401
	y	0.2134	0.003124	12.16747	0.6612789
	z	0.2074	0.006582	19.21849	1.406358
3	x	0.1101	0.001240	5.515304	0.2615662
	y	0.1080	0.0004617	4.531903	0.1880945
	z	0.1151	0.0004325	7.665431	0.2455295
4	x	0.06406	0.00008842	3.034698	0.0556187
	y	0.06438	0.0001311	2.931283	0.2182124
	z	0.06488	0.0009561	4.222869	0.09578134
5	x	0.04422	0.0001418	1.770060	0.07873619
	y	0.04397	0.000068702	1.670323	0.2616664
	z	0.04616	0	2.856582	0
6	x	0.03143	0.0001486	1.025022	0.01364938
	y	0.03116	0.0001533	1.035007	0.03266133
	z	0.03129	0	1.544834	$2.71948 \cdot 10^{-16}$

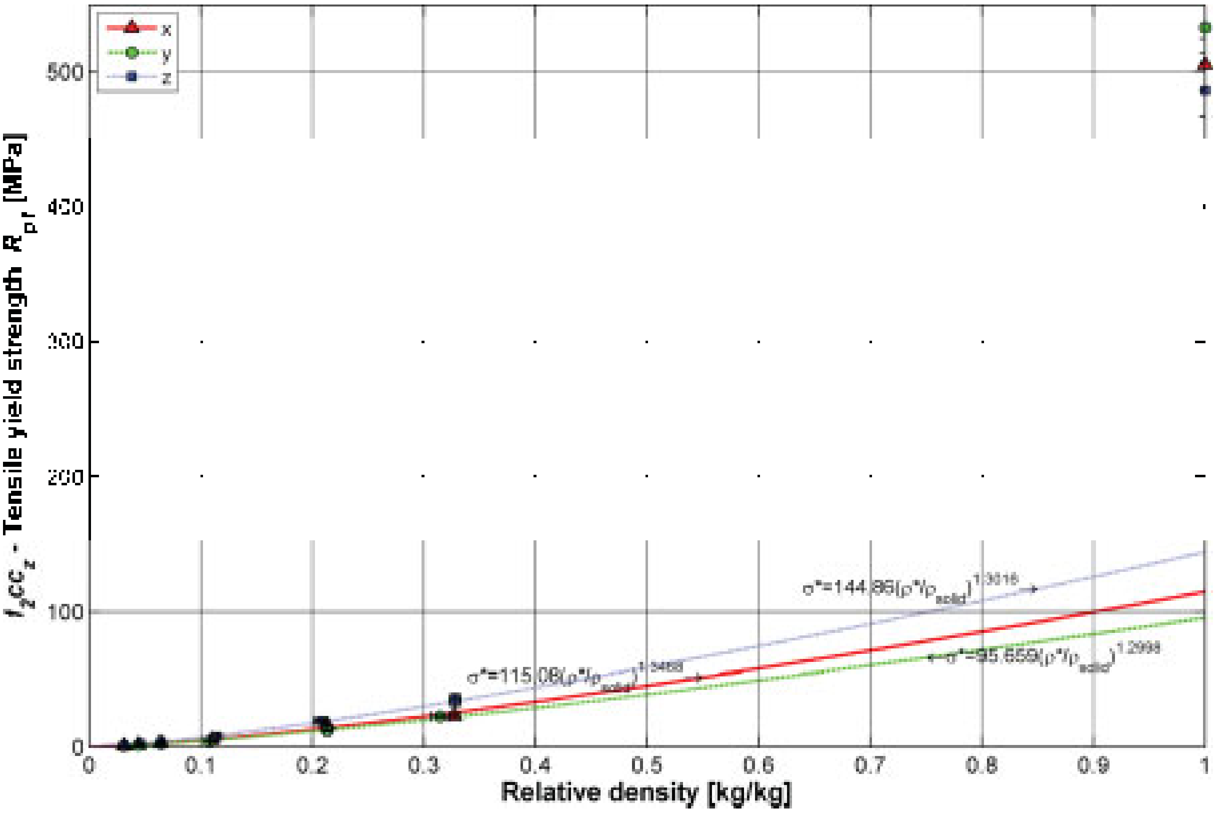

Figure 10.16:Results for effective tensile yield strength of cell type f_2cc_z

Table 10.14: Tensile ultimate strength in dependence of cell size for cell type f_2bcc_z

Cell size [mm]		ρ^*/ρ_{solid} [1]	Std. dev. [1]	Ultimate strength [MPa]	Std. dev. [MPa]
1.5	x	0.5512	0.01339	61.50592	21.64749
	y	0.5380	0.008438	67.35081	1.056380
	z	0.5916	0.003436	61.59918	5.777136
2	x	0.4247	0.002505	34.93768	5.080239
	y	0.3863	0.03165	31.89434	5.287430
	z	0.4011	0	25.32544	0
3	x	0.2018	0.001177	15.79927	1.740645
	y	0.1945	0.004074	13.03333	0.7283442
	z	0.2048	0.004820	10.77679	2.967118
4	x	0.1242	0.0005705	7.866570	1.715572
	y	0.1237	0.00009465	5.203556	1.021247
	z	0.1263	0.001260	6.705514	0.2339938
5	x	0.08573	0.00004440	4.862888	0.3552093
	y	0.08502	0.0002817	4.373553	0.1392551
	z	0.08644	0.001220	2.154079	0.4198663
6	x	0.06194	0.00006464	3.035404	0.2181083
	y	0.06167	0.0001487	2.911827	0.2000488
	z	0.06205	0.0002384	2.790455	0.1260134

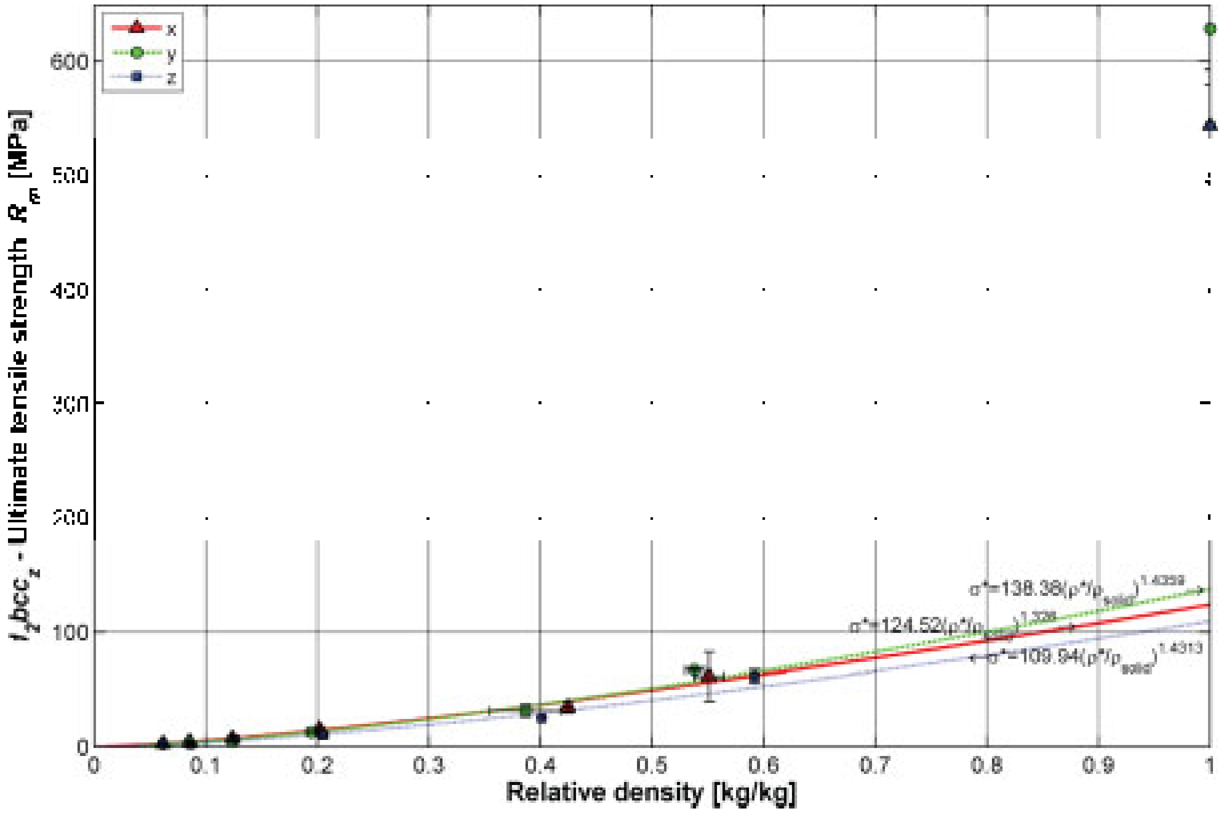

Figure 10.17:Results for effective tensile ultimate strength of cell type f_2bcc_z

Table 10.15: Tensile yield strength in dependence of cell size for cell type f_2bcc_z

Cell size [mm]		ρ^*/ρ_{solid} [1]	Std. dev. [1]	Yield strength [MPa]	Std. dev. [MPa]
1.5	x	0.5512	0.01339	52.76307	20.20672
	y	0.5380	0.008438	49.43672	0.7754022
	z	0.5916	0.003436	57.44162	3.528123
2	x	0.4247	0.002505	33.95091	6.121776
	y	0.3863	0.03165	30.51949	2.915271
	z	0.4011	0	25.32544	0
3	x	0.2018	0.001177	11.42474	0.2433519
	y	0.1945	0.004074	10.31859	0.2206899
	z	0.2048	0.004820	9.504707	1.960112
4	x	0.1242	0.0005705	5.962128	0.06073683
	y	0.1237	0.00009465	4.784225	0.8162202
	z	0.1263	0.001260	5.977933	0.1375145
5	x	0.08573	0.00004440	3.671426	0.2656813
	y	0.08502	0.0002817	3.450438	0.08354475
	z	0.08644	0.001220	2.114350	0.3510537
6	x	0.06194	0.00006464	1.917921	0.1251686
	y	0.06167	0.0001487	1.807753	0.1328781
	z	0.06205	0.0002384	2.379987	0.07620639

Curriculum Vitae

Name	Olaf Rehme
Birth date	May 23rd 1971
Birth place	Hamburg, Germany

Professional activities

08/2008 – today	Project engineer, Siemens AG, Corporate Technology, Berlin
01/2003 – 07/2008	Research assistant, Institute of Laser and System Technologies, Hamburg University of Technology (TUHH)
11/2000 – 12/2002	Executive project manager (COO), Ventas AG, Hamburg
02/1999 – 10/2000	Project manager, SDM GmbH, Hamburg
01/1993 – 01/1999	Software development and customer consulting, SDM GmbH, Hamburg

Education

10/1992 – 01/1999	Studies in mechanical engineering / production technologies, TUHH Degree: Diplom-Ingenieur
08/1977 – 06/1990	Elementary and secondary high school, Degree: Abitur

Military services

07/1990 – 06/1991	German Federal Armed Forces based at Stade

Extracurricular

07/1991 – 07/1992	Work and travel in Canada and USA